Title	Laboratory scale modelling of a point absorber wave energy converter
Authors	Flannery, Brian
Publication date	2018
Original Citation	Flannery, B. 2018. Laboratory scale modelling of a point absorber wave energy converter. PhD Thesis, University College Cork.
Type of publication	Doctoral thesis
Rights	© 2018, Brian Flannery. - http://creativecommons.org/licenses/by-nc-nd/3.0/
Download date	2024-04-19 00:22:01
Item downloaded from	https://hdl.handle.net/10468/6980

National University of Ireland – Cork (NUIC)

Department of Civil and Environmental Engineering

"Laboratory Scale Modelling of a Point Absorber Wave Energy Converter"

Brian Flannery BE(Hons) MEngSC

Supervisor: Prof. Tony Lewis

Head of Department: Prof. Gerald Kiely

Submitted in fulfilment of the requirements for the degree of

Doctor of Philosophy (PhD)

May 2018

"Laboratory scale modelling of a point absorber wave energy converter"

Declaration

"The work contained in this thesis has not been previously submitted to meet the requirements for an award at University College Cork (UCC) or any other higher education institution. To the best of my knowledge and belief, this thesis contains no material previously published or written by another person except where due reference is made."

Signed:_____ Date: _____

Brian Flannery BE(Hons) MEngSC

"Laboratory scale modelling of a point absorber wave energy converter"

Acknowledgements:

Abstract

Finding an effective Power Take Off (PTO) system, that can deal with the low power levels (< 1W), associated with laboratory scale testing of Wave Energy Converts (WEC) is a notoriously difficult problem. This thesis investigates the use a magnetic particle brake to address the issue. The work describes 1:50 scale tests of a generic point absorber device, restricted to heave motions only. The model set-up is not intended to replicate any existing WEC device but rather to provide a good case study for examining performance characteristics such as exciting forces, response amplitudes and power absorption for both regular and irregular wave conditions.

The PTO was found to be an effective low cost solution for the scale of operations considered. The brake adequately met the requirements of supplying resistive damping at the typically low speeds and could supply enough force to hold device at the stillwater level for wave force excitation tests. The characteristics of the PTO proved to be ineffective to study the advanced control technique known as latching. A new control method based on Wavelet analysis, utilising the PTOs ability to vary the damping in real time is described. The method yielded marginally improved energy capture.

Three different shapes of float have been tested: simple right cylinder, a right cylinder with conical and hemispherical ends. Experimental testing was carried out using the (25m long, 18m wide and 1m deep) wave basin at the Hydraulics & Maritime Research Centre. The cone shape was found to be the most efficient with the use of mechanically induced control forces.

A numerical model predicts the theoretical response of the buoy using linear theory, allowing for a validation study between the experimental and numerical results. A time domain model has been developed using Simulink and the boundary element method package WAMIT enabling non-linearity's in the set-up to be examined. It was found that using a linear hydrostatic restoring force underestimated the resonance frequency of the cone and hemisphere. The numerical models yielded poor prediction results due the increased device motions, violating the linear assumptions.

Glossary

AC	-	Alternating Current
AMETS	-	Atlantic Marine Energy Test Site
AWS	-	Archimedes Wave Swing
BEM	-	Boundary Element Method
BIBO	-	Bounded Input Bounded Output
CNC	-	Computer Numerical Controlled
CWE	-	Carnegie Wave Energy
DC	-	Direct Current
DFT	-	Discrete Fourier Transform
ESB	-	Electricity Supply Board
FDI	-	Frequency Domain Identification
FFT	-	Fast Fourier Transform
GUI	-	Graphical User Interface
HMRC	-	Hydraulics and Marine Research Centre
HSVD	-	Hankel Singular Value Decomposition
IEEE	-	Institute of Electrical and Electronic Engineers
IFFT	-	Inverse Fast Fourier Transform
JONSWAP	-	Joint Wave Observation Program
LTD	-	Private Limited Company

LWT	-	Linear wave theory
NASA	-	National Aeronautics & Space Administration
NUIC	-	National University of Ireland
OE	-	Ocean Energy
OWC	-	Oscillating Water Column
PC	-	Personal Computer
PI	-	Proportional Integral
PTO	-	Power Take Off
RAO	-	Response Amplitude Operator
RPE	-	Relative Percentage Error
SDOF	-	Single Degree Of Freedom
SEAI	-	Sustainable Energy Authority of Ireland
STFT	-	Short-Time Frequency Transform
TPL	-	Technology Performance Level
TRL	-	Technology Readiness Level
UCC	-	University College Cork
WEC	-	Wave Energy Converter
WT	-	Wavelet Transform

Contents

List of Figures

List of Tables

Chapter 1: Introduction

Renewable energy is a vital research area due to our overdependence on diminishing supplies of fossil fuels; rising levels of carbon dioxide emissions leading to climate change and the potentially disastrous socio-economic consequences for the poorest and most vulnerable people in society. The Mary Robinson Foundation on Climate Justice (MRFCJ, 2018) emphasises that "those in vulnerable situations are particularly susceptible to the impacts of climate change".

1.1 Ocean energy

Currently ocean energies represent only 0.01% of electricity production from renewable sources. With the exception of tidal range technology, no other marine energy technology is widely deployed being still at an early stage of development. Total worldwide installed ocean power was about 530 MW in 2012, of which 517 MW came from tidal range power plants (Ernst & Young, 2013). Despite such relatively low installed capacity, the worldwide ocean wave resource is vast as is illustrated in Figure 1:1.
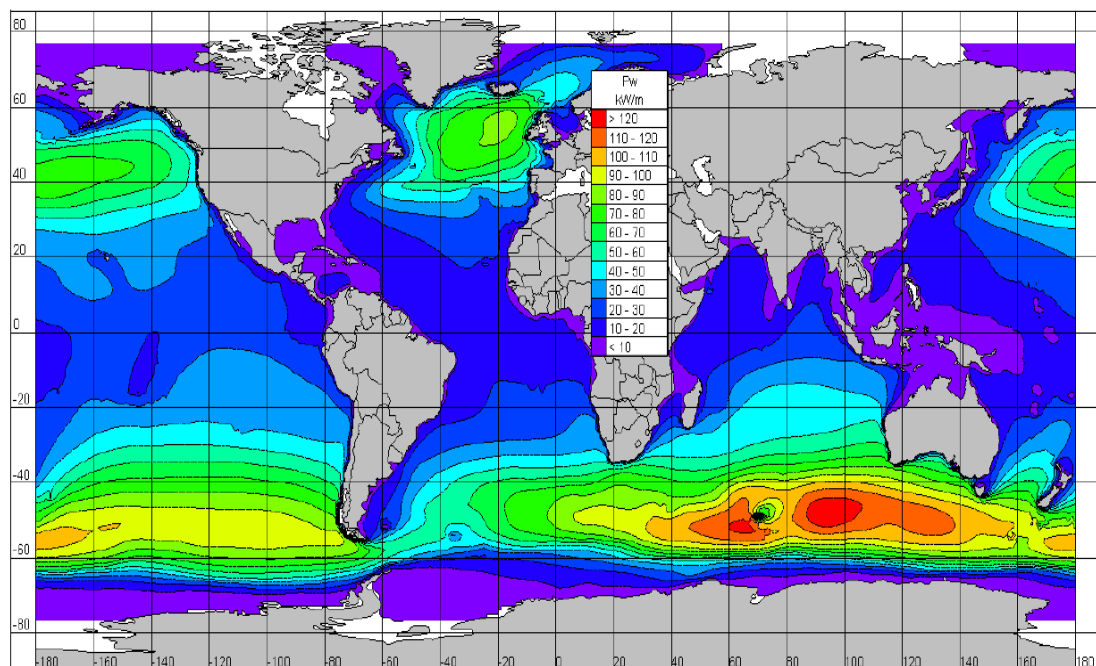
Figure 1:1: Global distribution of annual mean wave power. {source Cornett (2008)}

1.2 Wave energy

Wave energy is created by wind, as a by-product of the atmosphere's redistribution of solar energy. The rate of energy input to waves is typically .01 to .1 W/m2. This is a small fraction of the gross solar energy input, which averages 350 W/m2, but waves can build up over oceanic distances to energy densities averaging over 100 kW/m (note that the typical measure is power per metre width of wave front). Because of its origin from oceanic winds, the highest average levels of wave power are found on the lee side of temperate zone oceans (Barstow et al, 2008).

1.2.1 Wave energy in Ireland

Wave energy is potentially an important sector for Ireland, with its wave resource off the west coast placing the country in an ideal position to become a world leader in this field. According to an assessment of Ireland's wave energy resource carried out by Electricity Supply Board Ireland (ESBI) & Marine Institute (2005), much of the western coast lies in an area subject to theoretical available wave power of 50-70 kW per metre of wave crest, with an estimated 6000 MW or 59TWh of realisable resource. In addition to being an untapped resource, investment in arrays or farms of wave energy converters (WECs) would be beneficial as a means of producing 'cleaner' energy, reducing carbon emissions and also reducing Ireland's existing heavy reliance on importing the majority of its energy needs {Ireland imports 90% of total primary energy requirement Clancy et al. (2010)}.

1.2.2 Future developments

The Electricity Supply Board (ESB) is developing the Westwave project and is seeking to deliver Ireland's first electricity from Atlantic wave energy. ESB is investigating and developing a site near Doonbeg, Co Clare for a 5 MW array of wave energy devices (Sharkey, 2012). Carnegie Wave Energy (CWE) have also proposed a 5MW demonstration project off Spanish Point in Co Clare (Carnegie Wave Energy, 2012). The Irish company Ocean Energy has announced that its wave energy convertor OE Buoy will be deployed at the U.S. Navy's Wave Energy Test Site on the windward coast of the Hawaiian Island of O'ahu.

1.3 Device development protocol

The staged development protocol is widely regarded as the ideal roadmap for advancing WEC technologies from an initial concept to commercial installation. Several different guidelines

exist, but they all share the same core principals; that is, to follow a prescribed sequence of stages, which consider various levels of technical complexity and investment requirements. The recommendation is to advance through this stages sequentially in order to gain the required understanding of the device characteristics while minimising the project's risk. One such example is Figure 1:2: IEA-OES 5 stage structured development plan (Figure 1:2) to progress a wave energy converter (WEC) from an idea to a marketable product. European and American developers are urged to adhere to this plan while developing marine energy technologies. The structured, phased programme is influenced by similar Technical Readiness approach utilised by the (US) National Aeronautics & Space Administration (NASA) Technical Readiness approach. In the case of ocean energy devices the stages can conveniently be linked to different device scales by following Froude Similitude Laws and geometric similarity (Holmes & Nielsen, 2010).

Figure 1:2: IEA-OES 5 stage structured development plan (source Cahill 2014)

In the wave energy protocol each stage includes defined Technology Readiness Levels (TRL) .A description of the different stages according to (Holmes & Nielsen, 2010) is given for clarity.

The concept validation stage (TRL 1-3) entails testing a small scale (~ 1:50) model in a set of monochromatic, regular waves (of a single frequency) followed by polychromatic (many frequencies combined), irregular sea states. Regular wave tests enable more control to the researcher to identify and describe physical processes at specific frequencies. Regular waves allow the research to investigate parameters such as the radiated wave height, which as we shall discuss later, is intrinsically linked to power capture, such that the device geometry can be optimised. Irregular sea states provide more realistic conditions in order to estimate potential device performance in conditions more closely resembling real seaways. Hull seaworthiness and mooring suitability can also be established at this early stage.

The design validation stage (TRL 4) involves using a larger, more sophisticated model (~ 1:10) and consequently often requires a larger testing facility capable of producing the necessary wave input conditions. Testing at this stage usually covers a more extensive number of sea states, including realistic survival conditions. During this phase, engineering is introduced in the form of a preliminary design and an elementary costing of the system components is established. Based on the measured power absorption in a range of sea states, the annual energy production is estimated using a set of generic wave conditions. More sophisticated numerically modelling techniques such as Computational Fluid Dynamics (CFD) & Finite Element Methods (FEM) are also recommend at this stage. Additionally porotype design feasibility and cost estimates should be considered.

The systems validation stage includes the testing of all sub-systems incorporating a fully operational PTO that enables demonstration of the energy conversion process from wave to wire. If the cost is acceptable, Stage 3 is entered in more detail with the aim to test the complete wave energy converter at a selected sub-prototype size (circa 1:4) that can safely be deployed at sea and produce power. The device is still small enough to facilitate easier handling and operation but large enough to experience deployment, recovery and maintenance techniques at sea. The first involvement with licences, permissions, certification and environmental requirements will be encountered. Also, design teams will experience manufacturing and production and supply chain issues, though the device may not be grid connected. Productivity remains a key stage gate requirement in these tests

The device validation stage is a critical part of the process and covers a solo machine pilot plant validation at sea in a scale approaching the final full size (circa 1:1). This stage is a proving programme of designs already established rather than actually experimenting with new options. Tests can be initially conducted at a moderate sea state site prior to extended

proving at an exposed ocean location. This is a very exacting requirement however, since it involves all components from each sub systems conversion process. The device as a whole must be proven fit for purpose before this stage is concluded. The device must also be grid connected before the end of the proving trials. Heavy engineering operations at sea are involved so health and safety requirements become important, as do O&M of the plant under realistic conditions. Since only a single unit is involved environmental impact will be minimal but monitoring of the machines presence in a given location must be undertaken.

The economics validation stage involves multiple device testing, initially in small arrays (circa 3-5 machines) which can be expanded as appropriate. By the conclusion of the previous sea trials, the technology and engineering of a device should be well established and proven. The technical risk of Stage 5 should, therefore, be minimized. However, the consequence of failure would be significant and the financial risks are less certain since it is the economic potential of the devices deployed as a generating wave park that are under investigation. Initially the hydrodynamic interactions of the devices will be investigated, together with the combined electricity supply stability possible via the power electronics. Availability and service scenarios will be important issues as more machines are deployed as will onshore and offshore O&M requirements. Environmental aspects, both physical and biological, can now be studied in detail as well as the socioeconomic effect the wave park will have on the local area. Early stakeholder involvement is recommended.

A wide variety of device concepts exist (as we shall see in section 1.6) and a set of procedures to allow fair comparison between them is described in the EquiMar project (Ingram et al (2011)). The project is a vast inter-disciplinary project that lays out protocols that cover site selection, device engineering design, scaling up designs, deployment of arrays, environmental impact on flora, fauna & landforms, as well as economic issues. The project emphasis the need for standardised methods of resource assessment, tank testing and all to way up to full sea trials, so that devices can be compared in an equitable way.

 Weber et al (2013) discuss the importance of technology performance level (TPLs) depicted in Figure 1:3. TPLs are an assessment of all cost and performance drivers grouped into high level categories; power conversion efficiency, availability, capital expenditure (CAPEX) and lifecycle operational expenditure (OPEX). In Figure 1:3, the lower x-axis plots the technology readiness level, the upper x axis shows the increasing costs associated with advancing through the TRL levels. The left y axis gives TPLs and right hand y axis cost of energy (COE). A

device developer would ideally enter the market at the upper right-hand section of the graph, indicating that the full scale device is operating at a relatively low cost of energy.

Often device developers will take the same un-optimised device through the early TRL levels (or worse still skip levels entirely); only to be faced with the double dilemma of having a device that is not performing adequately, whilst also being stuck at a larger scale where operating costs are extremely prohibitive. This inefficient path is represented by the red curve in Figure 1:3. The ideal path as represented by the green curve is to maximise the performance of the device as early as possible, as cheaply as possible.
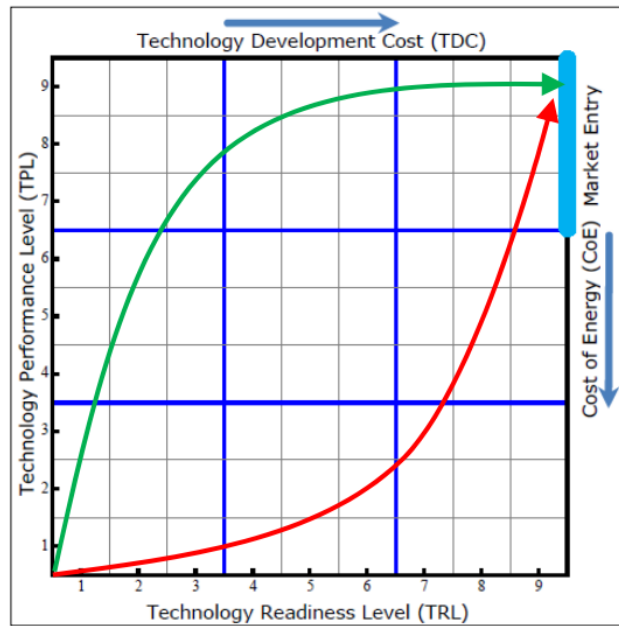
Figure 1:3: Metric for Successful Development of Economic WEC Technology (Weber et al., 2013)

Optimising device performance over the TRL levels between 1 to 4, can be achieved by using the best physical and numerical modelling techniques as well as developing and implementing advanced control algorithms, as early as possible. These sometimes separate but very much interrelated disciplines of research are essential in improving device performance. The main focus of this thesis is look at improved methodologies of physical modelling at early TRL levels. The research work also takes into consideration the other important areas of numerical modelling and control of wave energy devices.

1.4 Laboratory scale physical modelling

Given that the importance physical modelling has, as the focus of this work, a more in-depth discussion is given here before returning to the later stages of the development protocol (i.e. test sites).

Physical modelling is recognised as crucial element in the development of wave energy devices (constituting the first two stages of the plan). Physical modelling allows a smooth transition from the initial concept idea to the final energy producing prototype device. Investigations on device performance should be carried out at laboratory scale, where it is much easier (and more crucially, much cheaper) to make modifications to device parameters. Since physical models are the natural reproduction of the physical processes, they do not include any parameterizations or assumptions (as can be the case with numerical models) and can reproduce all the complex nonlinear physical phenomena accurately. Even more valuable is the fact that physical models can reproduce processes that are not fully understood so far and therefore cannot be sufficiently described mathematically. Examples of such phenomena are breaking wave impact forces, vortex generation and poor energy dissipation. These complex phenomena can be immediately apparent in a physical model. Additionally physical modelling is considered to be a very well established technique with a long tradition. The scientific community has built trust on physical modelling by performing physical tests for many centuries. For this reason, physical modelling is considered as the "gold standard" of almost all the modelling cases (Vyzikas, 2014)

Previous examples of developers who neglected to spend adequate testing time at model scale, only for their device to fail at prototype scale, should serve as valuable lessons as to the importance of physical model studies. In light of all this, it's not hyperbole to say that physical model studies are the foundations towards building a successful WEC.

1.4.1 Device Scaling

Figure 1:4 lists important dimensionless numbers used throughout fluid mechanics. Two particularly important modelling criteria are related to the Froude and Reynolds numbers. The Froude criterion is a parameter that expresses the relative influence of inertial and gravity forces in a hydraulic flow is given by the square root of the ratio of inertial to gravity forces, which is called the Froude Number. A physical interpretation of the Froude number is that it gives the relative importance of inertial forces acting on a fluid particle to the weight

of the particle (Munson et al 2009). Viscous forces occur in a fluid when adjacent particles have different velocities; there will be a momentum transfer between particles and hence a force. When viscous forces dominate in a hydraulic flow, the important parameter is the ratio of inertial to viscous forces (Reynolds number). A physical interpretation of the Reynolds number is that it gives the relative importance of the inertial force on a fluid particle to the viscous force on the particle. Reynolds first used this number to distinguish between laminar and turbulent flows (Reynolds, 1883).

Variables: Acceleration of gravity, g; Bulk modulus, E_v; Characteristic length, ℓ; Density, ρ; Frequency of oscillating flow, ω; Pressure, p (or Δp); Speed of sound, c; Surface tension, σ; Velocity, V; Viscosity, μ

Dimensionless Groups	Name	Interpretation (Index of Force Ratio Indicated)	Types of Applications
$\dfrac{\rho V \ell}{\mu}$	Reynolds number, Re	$\dfrac{\text{inertia force}}{\text{viscous force}}$	Generally of importance in all types of fluid dynamics problems
$\dfrac{V}{\sqrt{g\ell}}$	Froude number, Fr	$\dfrac{\text{inertia force}}{\text{gravitational force}}$	Flow with a free surface
$\dfrac{p}{\rho V^2}$	Euler number, Eu	$\dfrac{\text{pressure force}}{\text{inertia force}}$	Problems in which pressure, or pressure differences, are of interest
$\dfrac{\rho V^2}{E_v}$	Cauchy number,[a] Ca	$\dfrac{\text{inertia force}}{\text{compressibility force}}$	Flows in which the compressibility of the fluid is important
$\dfrac{V}{c}$	Mach number,[a] Ma	$\dfrac{\text{inertia force}}{\text{compressibility force}}$	Flows in which the compressibility of the fluid is important
$\dfrac{\omega \ell}{V}$	Strouhal number, St	$\dfrac{\text{inertia (local) force}}{\text{inertia (convective) force}}$	Unsteady flow with a characteristic frequency of oscillation
$\dfrac{\rho V^2 \ell}{\sigma}$	Weber number, We	$\dfrac{\text{inertia force}}{\text{surface tension force}}$	Problems in which surface tension is important

Figure 1:4: Common Variables and Dimensionless Groups in Fluid Mechanics (source Munson, Young, Okiishi, & Huebsch, 2009)

The following discussion on whether Froude and Reynolds scaling is applicable is taken from Hughes (1993). For practically all coastal engineering problems (and at least 90 percent of all hydraulic flow problems), the forces associated with surface tension and elastic compression are relatively small, and thus, can be safely neglected. This leaves selection of an appropriate hydrodynamic scaling law to an evaluation of whether gravity or viscous forces are dominant in the phenomenon. For this reason the Froude and Reynolds number are important to coastal engineers because similarity of one of these numbers, combined with geometric similarity, provides the necessary conditions for hydrodynamic similitude in an overwhelming

majority of coastal models. Reynolds similitude is seldom invoked as it is recognized that gravity forces predominate in free-surface flows; and consequently, most models are designed using the Froude criterion. Nevertheless, the engineer must make efforts to reduce the effects of viscosity in the model, otherwise the dissimilar viscous effects will constitute a scale effect. For example, viscous bottom friction in small scale harbour models will be significantly greater than in the prototype. Therefore, waves that must travel over long distances in the model will undergo a decrease in wave height greater than what occurs in the prototype. For this particular problem the solution is either to avoid lengthy wave propagation distances in the model, or to theoretically correct for the frictional losses in the model by beginning with a larger initial wave height

1.4.2 Problems with tank testing

When one models according to the Froude criterion, then automatically the Reynolds (and other) criterions are not met. Other physical forces such as viscosity, friction and surface tension will not scale correctly. Additionally Le Mehaute (1976) warns that if a salt water prototype is modelled in fresh water, there is about a 3% difference in in density and this changes forces accordingly. Apart from the scale effects, there are some unavoidable model effects that have a negative impact on the quality of the results. For example unlike the real sea, generating waves within a confined basin results in phenomena such as reflections arising from waves reflecting off basin walls. It is essential that these phenomena be fully understood and quantified. Additionally there is the generation of spurious waves from the wave paddles and the unwanted generation of cross waves all which will be discussed in due course.

While the costs associated with physical modelling are certainly less than the larger scales; the cost of facilities and the personnel for physical experiments is not a trivial matter. Due to the expense, scheduling windows can often be tight, requiring a large amount of tests be squeezed into a small amount of time. From the authors experience, developers often underestimate the amount of time required to both initially setup the experiment correctly and to complete the intended schedule. It is quite common that the full schedule is not completed and often repeat runs are the first to be sacrificed. Limiting factors such as basin depth, wave height and period generation capabilities determine the scale of the study. Typical scale tests carried out at the HMRC are between 1:50 & 1:20 scale.

Table 1-1: Different scale power levels for 500 kW prototype device

Scale	Power in model
1/50	0.6 W
1/25	6.4 W
1/15	38 W
1/10	0.16 kW
1/4	3.9 kW
1/1	500 kW

Table 1-1 shows how power scales using the Froude criterion for a 500 kW prototype device. From the table it can be noted that a particular problem of testing at small scales; is that the power production levels are usually small (being less than one Watt). The low speeds and torque associated with such low power levels are generally not compatible with conventional off the shelf motors. Therefore, the task of modelling the complete system: the oscillating device and a means of resisting the motion of the device to produce power (the power take off {PTO} mechanism) is relatively difficult. Finding an effective PTO that can operate at these small scales is a goal of this work.

1.5 Test sites

Returning to the later stages of the development plan, which involves larger scale sites in an open sea environment. Real sea test sites are vital stages for the advancement of WECs as to allow for performance assessment of the device in real seas. This is in contrast to the controlled laboratory settings of physical models. As well as more realistic appraisal of power capture performance they also allow the developer to examine individual component reliability. The experience of installing (and if trials are sufficiently long, maintaining) the device in open seas are also of huge importance to any developer. To date, the most frequently utilised test site in the world has been the European Marine Energy Centre (EMEC) on the island of Orkney, which has hosted deployments by developers such as Aquamarine Power, AW Energy, Corpower ocean, Laminaria, Pelamis, Seatricity and Wello Oy (EMEC, 2018)

1.5.1 Galway bay quarter scale test site

Advancing the technology readiness scale requires testing the complete WEC at a larger sub-prototype scale (~ 1:4). Ireland's quarter scale marine test site is located 1.5 km off the coast Galway Bay. As the site is partially sheltered from the Atlantic Ocean by the Aran Islands the site generally experiences benign conditions, characterised by local, fetch-limited wind seas. Although the site is susceptible to long period swell waves entering from the west and south-west, in general the wind seas provide a good representation, at quarter scale, of the wave climate conditions that would be expected at exposed Atlantic Ocean locations (Barrett, 2010). The Galway Bay site has seen successful deployments by both Wavebob and Ocean Energy Buoy (Thiebaut et al., 2011)

Figure 1:5: Wavebob (left) and OE buoy (right) deployed at Galway bay

1.5.2 Atlantic Marine Energy Test Site (AMETS)

The final development stages involve a solo machine pilot plant validation at sea in a scale approaching the final full scale (~ 1:1). This stage is a proving programme of designs already established rather than actually experimenting with new options. The Atlantic Marine Energy Test Site (AMETS) located off Annagh Head, west of Belmullet in County Mayo is being developed by the Sustainable Energy Authority of Ireland (SEAI) to facilitate testing of full scale wave energy converters in an open ocean environment. AMETS will be connected to the national grid and will comprise of two testing areas in 50 and 100 meters water depth, respectively (Lewis, 2014). A resource assessment of the site carried out by Cahill (2014) showed that the 15 year average power values for the 50 m and 100 m points are 62 kW/m and 77kW/m respectively. According to a OES Annual Report (2017) a foreshore lease has

been awarded for the site, planning permission for onshore aspects have also been secured and grid connection work has commenced. The energetic sea states typical of the site should offer generous capture yield but also pose a significant design challenge from a survivability perspective.

1.6 Wave energy conversion principles

The oldest patent known for the conversion of wave energy dates back to 1799 (Babarit, 2017). Since then a host of different devices have been consider and according to Falcão (2010) more than one hundred individual and diverse designs of wave energy converters have been identified. Several different methods of categorizing devices exist, with the purpose of comparing similar type devices. According to Thomas (2008) early classification work was focused mainly on floating devices with the terms *Point Absorber, Attenuator* and *Terminator* (see Figure 1:6) being used to describe the principle of operation as well as provide information on the geometry of the device. The descriptive terms are still used to a certain extent.
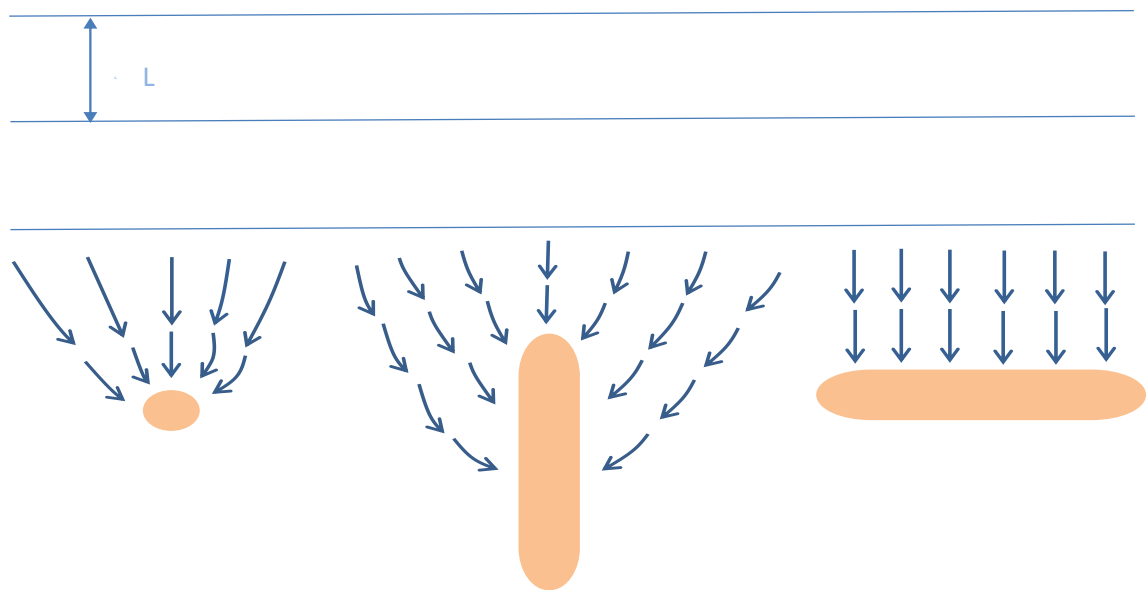
Figure 1:6: Point Absorber Attenuator and Terminator

Point Absorber

A point absorber is a floating structure which can absorb energy from any direction through its motion at or near the water surface. Point absorbers are often axisymmetric about a vertical axis and dimensionally small in comparison to the incident wavelength (as opposed to attenuators). Point absorbers are capable of absorbing the energy from a wavefront many times the key horizontal dimension (analogous to a radio antenna's ability to absorb much more power from the wave than is incident on to its physical cross section). In order to achieve such power levels however, the device must oscillate with an amplitude much greater than the incident wave. This behaviour not only violates the small amplitude assumptions of the foundational theory; it is also not permissible in practice due to stroke constraints of machinery etc.

Attenuator

An attenuator is a floating device which is orientated parallel to the direction of incoming waves, whose length dimension is much greater than the beam. Attenuators effectively ride the incident waves and can produce energy by resisting the motion along the length of the device. Thomas, (2008) states that the initial design concept was that the waves would attenuate along the device as power was extracted; this concept is generally incorrect and the motion of the attenuator may be almost symmetric about the mid-point of the device, so that the fore and aft portions of the device work equally hard. The Pelamis device is one example of the attenuator class and it uses hydraulics for the power take off (PTO) system.

Terminator

Terminators are devices whose beam is aligned perpendicular with the incident wave direction and the dimension of said beam is much greater than its length. They are named as so because they leave very little energy behind them when used. They may be designed to be either rigid or compliant type device Observing Figure 1:6 it can be seen that the main difference between an attenuator and a terminator is that the incoming wave angle varies by 90 degrees. Therefore a terminator can become an attenuator (and vice-versa) depending on wave climate conditions and mooring configuration.

Another classification is device location and water depth (Thorpe, 2000), i.e., *shoreline, bottom fixed, near shore* and *offshore* devices.

Offshore   *Nearshore*   *Onshore*
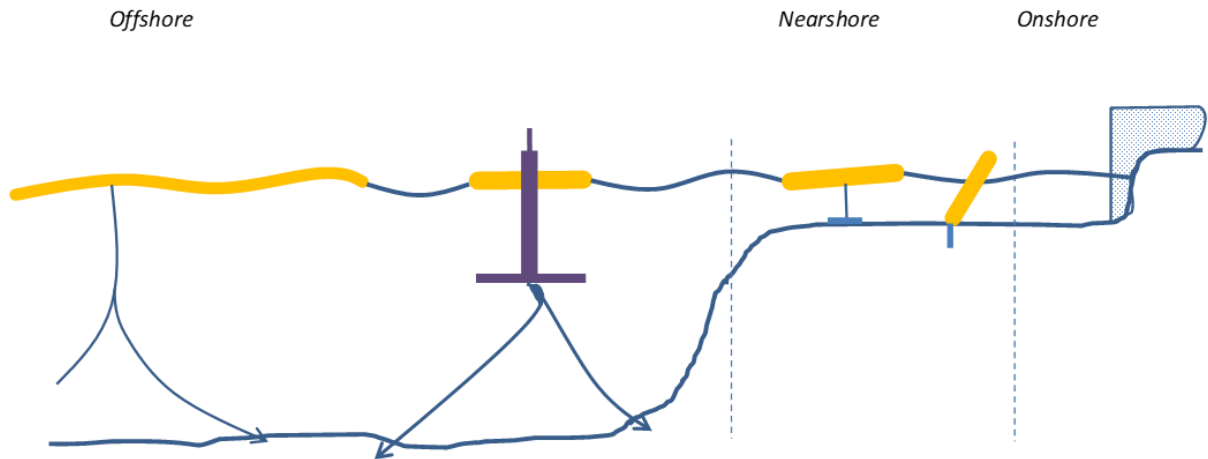
Figure 1:7: Classification by distance to shore

The descriptions *first, second* and *third generation system* is described by (Randløv, 1996) and was developed in the EU-funded OWEC-1 project. This classification system refers to the present status of a device, the development timescale and economic investment cost. The first, second and third generations roughly coincides with the location classifications shoreline, near shore and offshore. First generation devices are typically onshore or nearshore and utilise conventional power take off systems. Point absorbers are typically representative of second generation devices operating both nearshore and further offshore. Third generation systems can be large (in terms of physical size and power output) single devices or an array of smaller devices such the overall power output is still considerable. These systems are located offshore and encompass significant engineering challenges in terms of installation and operation and maintenance.

Alternatively, devices can be categorised by their primary conversion principle as is used by EMEC { http://www.emec.com}, depicted in Figure 1:8.
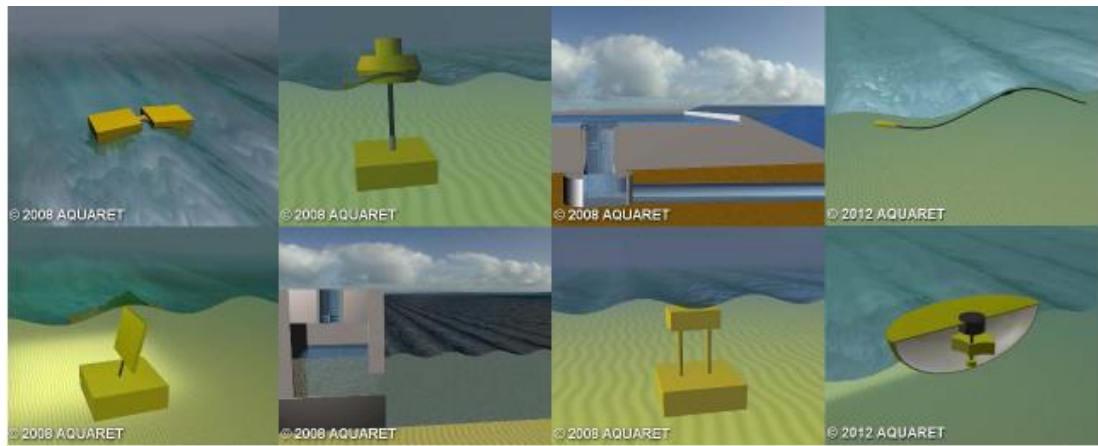
Figure 1:8: Methods of wave energy conversion, clockwise from top left: attenuator, point absorber, overtopping, bulge wave, gyroscopic, submerged pressure differential, oscillating water column and surge. Source { http://www.aquaret.com}

There is a certain amount of ambiguity in such category lists, as often devices will have features pertaining to one or more groups and a certain amount of crossover exists. A more detailed methodology of WEC classification is given by (Price, 2009). The following brief classification list is based on the EMEC method of conversion as per Figure 1:8 . The main categories are Point absorbers, attenuators (described previously), overtopping, bulge wave.

Overtopping

Overtopping devices tend to be large structures which can gather and store water waves in a reservoir. Electricity can be generated by releasing the water through conventional low-head turbines. The Wave Dragon is an example of an overtopping device. The wave dragon is also termed as a terminator device.

Bulge Wave

A bulge wave device consists of a rubber tube moored to the sea bed with some inlet valves at one end of the tube heading into to sea admitting water. The internal pressure created as the wave passes over the tube creates a 'bulge' of water. As the bulge traverses the tube it grows, gathering energy until till it passes through a turbine-generator at the opposite end of the tube. The Anaconda device is an example of a bulge wave type (Chaplin, Heller, Farley, Hearn, & Rainey, 2011).

Gyroscopic

Gyroscopic devices use the relative motion between a floating structure and an internal eccentric weight or gyroscope housed within the floating structure. The SEAREV developed at the Ecole Centrale, Nantes is composed essentially of a freely floating body enclosing a mechanical system featuring a large pendulum wheel oscillating around a horizontal axis (Durand et al., 2007).

Submerged Pressure Differential

A submerged pressure differential device such as the Archimedes Wave Swing (AWS) is a near-shore device which is fitted to the seabed. The device comprises of an enclosed air chamber just beneath the water surface. As a wave crest moves over the submerged device, the pressure differential pushes the device towards the seabed, this motion is then reversed over the trough of the wave cycle.

OWC

An oscillating water column is comprised of a chamber of air with an opening to the sea below the mean water level. The action of the waves causes the column to rise and fall, acting like a piston expanding and contracting the air. These pressure fluctuations within the volume of air can be used to drive a turbine which usually has the ability to rotate regardless of the direction of the airflow (e.g., a Wells Turbine). The rotation of the turbine is then used to generate electricity. An OWC can be fixed like the PICO plant on the Azores Island or floating like the OE buoy displayed in Figure 1:5.

Surging (Oscillating Wave Surge Convertor)

An oscillating wave surge converter is a hinged device which can move ('flap') with the motions of the waves. The base of the device, which serves as the fulcrum, is anchored to the sea bed while the top of the device can be just beneath the water surface like the Waveroller device or pierce the surface like the Oyster. Technically these are rotational devices rather moving in purely translational surge direction. In fact their movements are very similar to the wavemaking flaps used in wave tank facilities and are sometimes termed 'inverted wavemakers'.

1.7 Review of physical modelling

1.7.1 Introduction

What follows is a review of some of the previous methods employed for the physical modelling of wave energy converters in wave generation facilities. Given the previously discussed issue of power scaling, particular focus is given on different methodologies for modelling the power take off systems of WECs at laboratory scale. Bearing in mind the vast amount of device concepts conceived over the years, the list is by no means exhaustive. OWCs for example are only briefly discussed. The majority of experience at HRMC (during the authors' time) was related to this field and it was decided early on to branch out into other device types. The hope was that would lead to new expertise for the centre while at the same time posing as a considerable challenge. The objective of the review is to select a model which provides a good case study for laboratory experiments. The device is not intended to be any particular existing system but rather a generic wave energy converter. A discussion on how the different setups studied influenced the authors work is given at the end of this chapter.

There are typically three stages of power conversion involved in a wave energy device (see Figure 1:9). At the primary interface of the water and the floater, the frequency dependant power absorption is related to parameters such as shape, draft, wetted area etc. This first stage in the power chain is termed hydrodynamic or intercepted power. The second stage is the conversion of power from the moving floater/fluid by a PTO system which resists such motion. The third and final stage is electrical power conversion and grid supply. The focus of this thesis is exclusively with stages 1 & 2, (labelled mechanical energy in Figure 1:9) will be discussed in subsequent chapters.
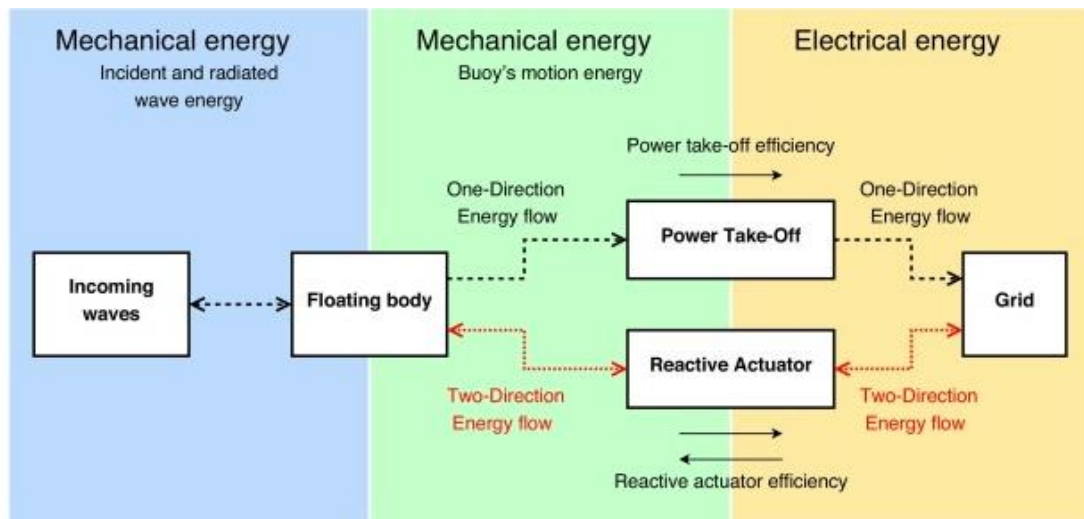
Figure 1:9: Energy flow from the waves to the grid. (source Genest et al (2014))

Laboratory PTO systems are usually less complex than their full scale counterparts because the later suffer difficulties associated with scaling down prototype generators, hydraulics motors etc. With this in mind, however, it is still important when designing a laboratory scale PTO system to be able to recreate the characteristic behaviour of the prototype arrangement as closely as possible. Efforts should be made to ensure correct modelling of the effect of the PTO on the overall hydrodynamic system, as its response are heavily linked.

For example, in a full scale OWC system there are predominately two types of turbine that can be used for PTO purposes; a Wells turbine, and an Impulse turbine. Neither of these designs is suitable for reconstructing a replica device at small laboratory scales (typically smaller than 1:15). The characteristic PTO damping curve (which can be force versus velocity or pressure versus velocity for an OWC) is also different for both these turbines, requiring alternative mechanisms of lab scale PTO.

Orifice plates are used to replicate the quadratic non-linear relation between pressure and the flowrate. For this reason, they are suited to the modelling of impulse turbines as was used by Sheng et al (2012) for example. A porous membrane or carpet-like material gives a linear response associated with a Wells turbine.

1.7.2 Methods of laboratory scale PTO

Frictional types

Kelly (2007) conducted physical experiments on a spar fork device that consisted of an active buoyant float moving with the waves and a reactive float (spar platform) opposing the motion of the active float (see Figure 1:10). The model was carried out such that the 0.8m depth flume would scale up to 20m i.e. a 1:25 scale. A frictional torque was applied at the joint between the spar fork components inducing a constant resistance between the two rotating structures of the spar fork. Standard helical springs were used at the pivot-joint between the arms in order to create compression forces in the joint that were both consistent and measurable. The amount of compression being applied to the springs between the two arms can be finely adjusted to give the desired friction value. As the device was floating, the author did not use a sensor to measure the torque. The torque was instead calculated using free decay test sand while the author reports satisfactory results, more precise measurements would be preferred for this work.

Figure 1:10: Spar fork design as used by Kelly (2007)

The Langlee wave energy converter is an oscillating wave surge converter comprised of a number of hinged flaps. The model PTO system consists of a load-adaptable friction wagon mounted on a rail, as shown in Figure 1:11 (Pecher et al, 2010). The device was testing using both 1:20 and 1:30 scaled sea state conditions.
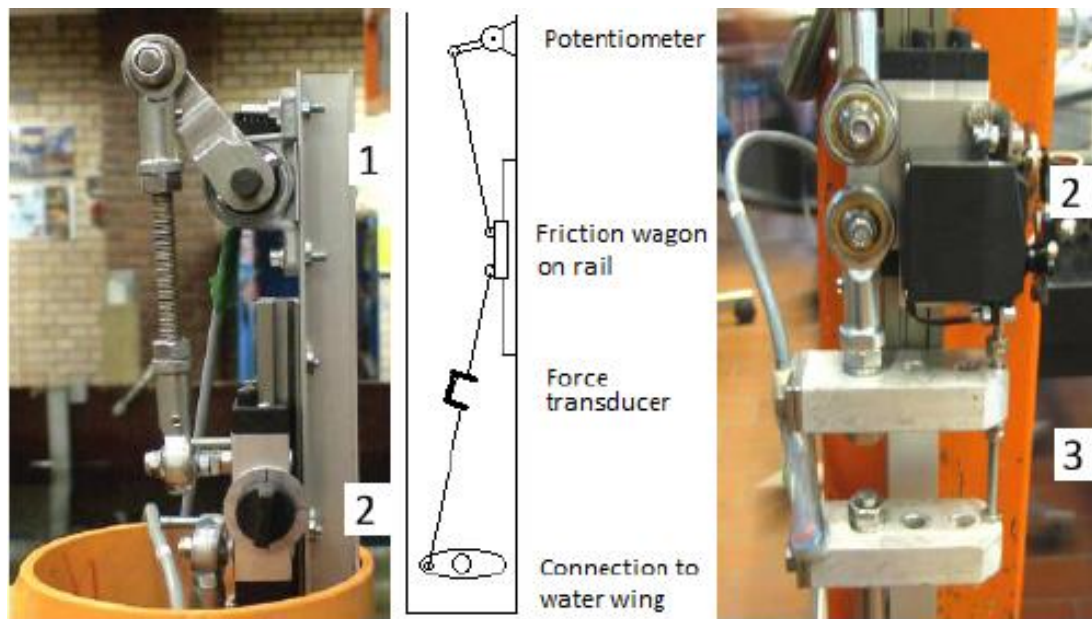
Figure 1:11: Model set up used in (Pecher et al., 2010). 1-Potentiometer, 2-load adjustable friction wagon wheel, 3-Force Transducer

Laboratory models in which the WEC turns a shaft can be damped by the friction of a pre-tensioned cable around a metallic wheel connected to the shaft of the WEC (Figure 1:12 left) as was used for a solo unit of the WEPTOS device used in (Rapuc, 2012). The device was tested for scale wave conditions at two Danish North Sea conditions resulting in scales of 1:23.4 and 1:8.33. Alternatively, mechanical braking can be achieved by applying direct compression to the rotating shaft (Figure 1:12 right) as was used in the PENWEST 1:30 scale model tests at Aalborg as part of the MARINET transnational wave basin access programme (Velar, 2013). The WEPTOS device is a replica of the seminal device, known as Salters duck (Salter 1974). This device despite being one of the earliest devices to be rigorously tank tested is reserved for the advanced PTO section as it is/was a highly sophisticated device.
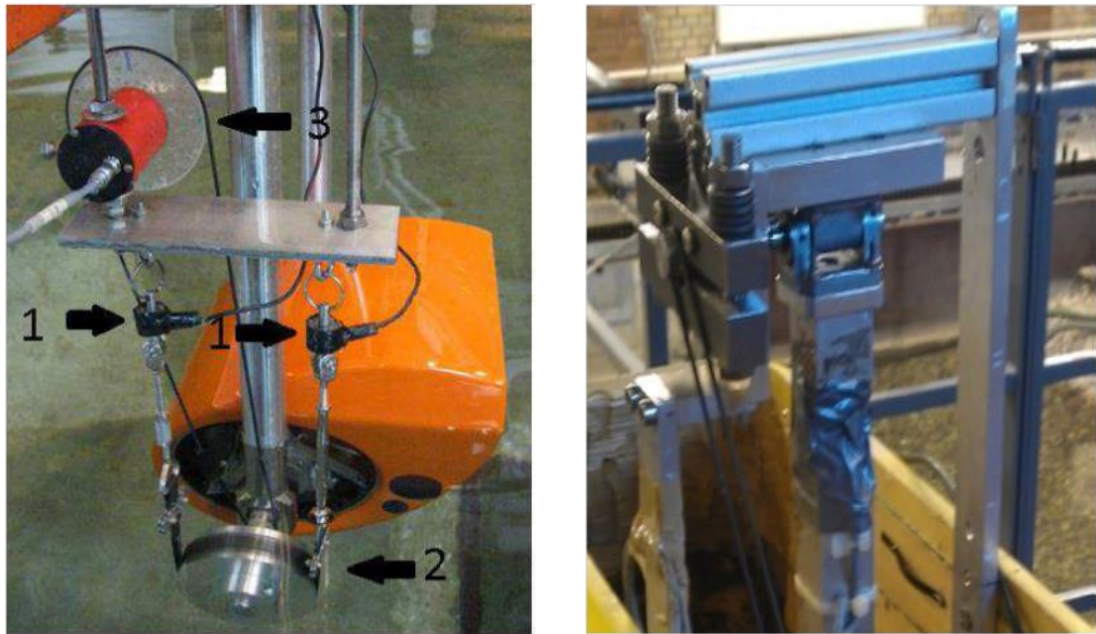
Figure 1:12: Left mechanical brake used in WEPTOS tests. 1: Load cells 2: pre-tensioned cable around a metallic wheel 3:Poteniometer. (source Rapuc, 2012) Right: mechanical brake used in PENWEST tests (source (Velar, 2013).

Dashpot type

Flocard & Finnigan, (2009), (2010) conducted a study on the power capture of bottom-pivoted pitching point absorbers. A sketch and picture of the device is shown in Figure 1:13. Test were carried out in a narrow (1 m wide) flume. A Froude scaling ratio of 1/33 was used to relate the wave flume water depth of 0.75m to a typical prototype mean water level of 25m. The experimental rig is composed of a buoyant cylinder mounted to an underwater shaft (labelled bottom shaft in sketch), rotating about low friction bearings. A second rotating shaft is mounted on top of the wave tank supporting the sensor equipment. The two shafts are coupled through thin pre-tensioned stainless steel wires. A rotary viscous dashpot is used as the external PTO. The device also has a ballast chamber to examine the effect of changing inertia on device performance. This is an interesting model setup, with the ability to test different ballast configurations a useful feature.
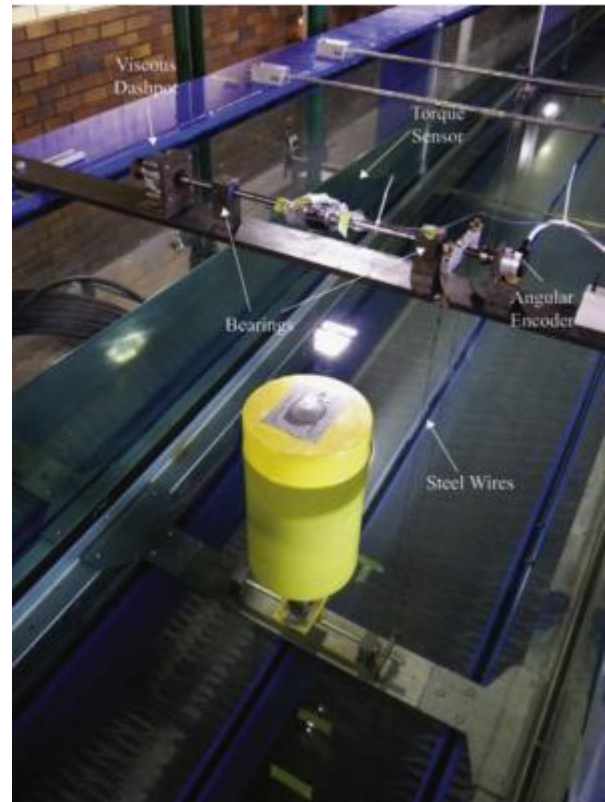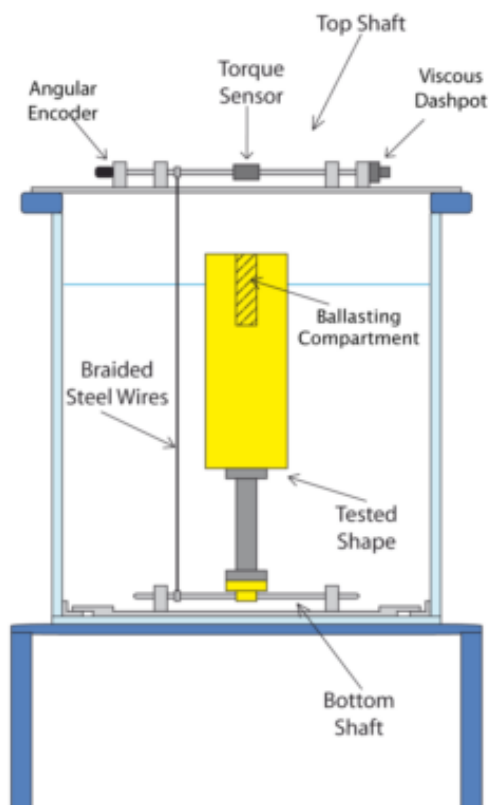
Figure 1:13: Model set up used by Flocard & Finnigan, (2009,2010)

Bailey & Bryden (2009) looked at a mono directional PTO system comprised of a linear spring and a damper (see Figure 1:14) that only produces a damping force in one direction of movement. The model experiments were carried out 1:40 scale in the curved tank facility at Edinburgh. The dampers are pneumatic and designed to have a linear response. Two types of dampers were used: a compression damper, which provides a resisting force when the piston of the damper is compressed into the unit, and an expansion damper, which provides a resisting force when the piston is expanding from the unit. The cylinder is restricted to heave motions by a stainless steel central rod which is held in place by an upper and lower external rod-end bearings, with PTFE liners. The internal mass is also limited to move in heave by being positioned on the central rod. The internal mass also has a PTFE bearing in contact with the central rod.
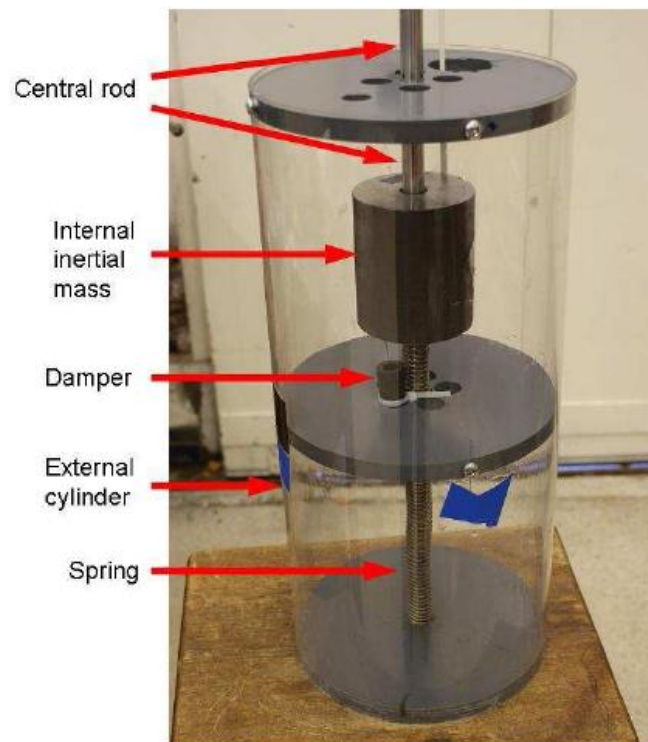
Figure 1:14: Experimental model used in Bailey, (2009)

Bailey (2009) reported that the reliability of the compression mono-directional damper constant is lower than the expansion mono-directional dampers. The author also reported possible air spring effects and nonlinearities in the dampers behaviour. While this is considered a worthy effort at PTO modelling, it was avoided due to the aforementioned complications.

Float-counterweight systems

Taneura et al (2010) conducted similar float-counterweight experiments in a larger test facility (A 3.2m deep, 30m wide and 160m long tank located at the Research and Development Center of Mitsubishi Heavy Industries LTD, Nagasaki, Japan). The larger scale of the experiment (float diameter was 1 m compared to prototype 1.5m) enabled a conventional motor to be used. It is interesting to note that despite the larger scale the experiment still required a gear box to increase the speed of the shaft as illustrated in Figure 1:15. The ratchet mechanism is used to only transmit the torque during the descent phase of the float.
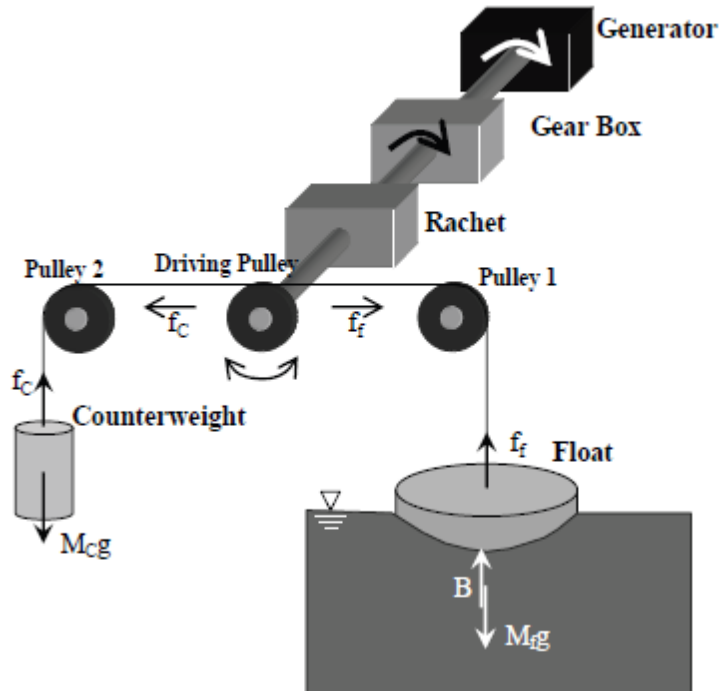
Figure 1:15: Schematic view of the laboratory set up used in (Taneura et al., 2010)

Vantorre, Banasiak, & Verhoeven, (2002) carried out a feasibility study for extracting wave energy from the Belgian coastal area of the North Sea. The initial study was a numerical one to determine the performance of heaving point absorbers in wave conditions that are representative of the region, calculated by means of a linear theory. The shape and dimensions of the heaving buoy, the external damping and a supplementary inertia were variable parameters in the study. Experimental model tests were reported in (Vantorre, Banasiak, & Verhoeven, 2004), where a cone shaped buoy was tested in regular and irregular waves. The experimental set up shown in Figure 1:16, consists of a buoy that is fixed to a steel rod that translates vertically, guided by two axial bearings attached to a frame. Supplementary mass used to increase the absorber inertia is implemented using a closed circuit of a timing belt guided by four pulleys. A mechanical compression brake was used for the PTO. The University of Ghent work was continued by (De Backer, 2010) who made improvements to the design such as replacing the circular guiding rod (which bent under the action of large surge forces) by a rectangular cross section.
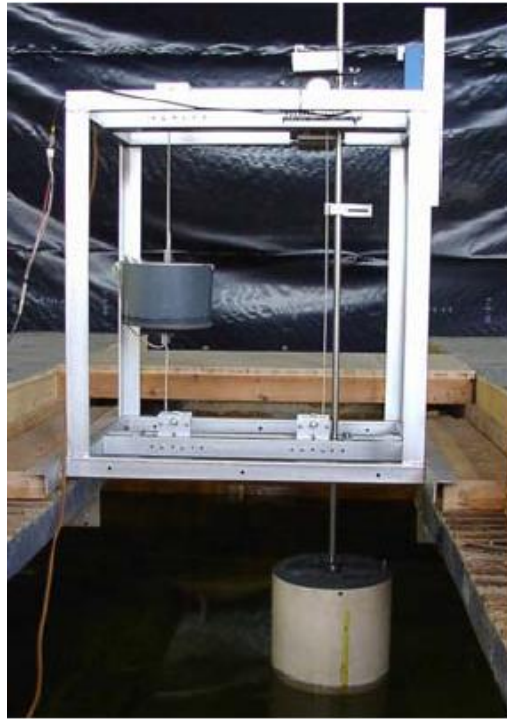
Figure 1:16: Float-counterweight model set up used in (Banasiak, Vantorre, & Verhoeven, 2003)

Higher quality bearings were used to reduce the amount of friction from previous tests by a factor of two. In addition to power absorption tests, the author also conducted drop tests to study the effects of bottom slamming as the buoy exits and re-enters the water. The scale of this experiment was 1:16 based on wave conditions off the Belgian coast.

1.7.3 Advanced methods of laboratory PTO

The following describes some of the more advanced methods of laboratory model PTO systems. No review would be complete without the foundational work carried out by Stephen Salter who is considered by many to be the 'father' of modern wave energy research. Salters (1974) nodding duck device was extremely efficient at converting the energy available in waves as the famous photo depicted in Figure 1:17 shows. An explanation for the picture is given by the Edinburgh Wave Power Group, (2018).

Waves are approaching from the right. Drops of a neutrally buoyant tracer-fluid consisting of a mixture of carbon tetrachloride and xylene with titanium oxide pigment have been injected to show the decaying orbits of wave motion. The amplitude of the incoming waves can be measured from the thickness of the bright band. Nodes and anti-nodes due to the small amount of reflection are evident. However the thickness of the bright band to the left of the model is largely due to the meniscus, as is confirmed by the very small orbits of tracer fluid

in this region. As the energy in a wave is proportional to the square of wave amplitude we can use the photograph to do energy accounting. If reflected and transmitted waves are one-fifth of the amplitude of the input they would have one twenty-fifth, or 4%, of its energy. This means that 96% has gone into the movement of the test model. The dynamometer showed that just over 90% of the power in the full width of the tank had been absorbed by the power take-off, leaving 6% loss through viscous skin friction
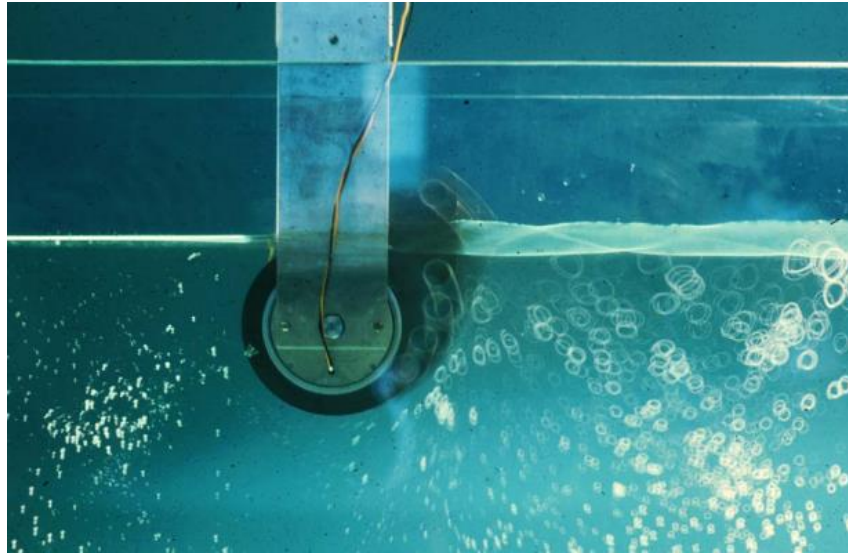
Figure 1:17: 1:100 scale Salters duck exhibiting approximately 90% efficiency. Photo taken by Jamie Taylor. (source Edinburgh Wave Power Group, 2018)
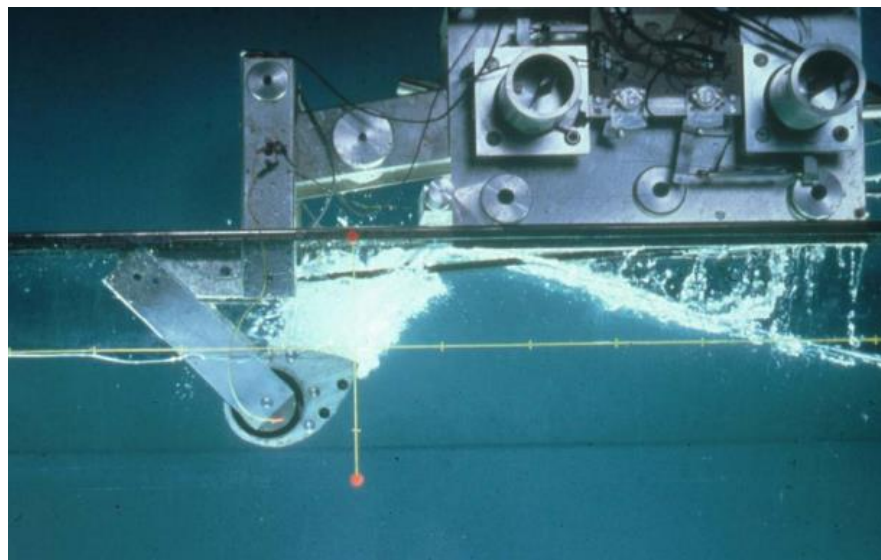
Figure 1:18: Later model of Salter's duck in the narrow test tank, photo by Jamie Taylor. (source Edinburgh Wave Power Group, 2018)

A later model mounting with controlled stiffness and damping in heave and surge is shown in Figure 1:18 where it is been subjected to a hundred year survival wave. The topic of control will be discussed in more detail in the theory section. For now it will be explained as putting power into the system at certain times during the wave cycle, to increase motion and power capture. The intention is that the increased energy yield from doing so will outweigh the power that was put into the device. The device had Aeroflex moving-magnet torque-motors at each end. One gave a velocity signal which could be processed by analogue operational amplifier networks built by David Jeffrey. These could implement variable damping, torque limiting, positive or negative spring and inertia, indeed any power take-off algorithm could be specified (Salter, 2008). Skyner (1987) tested a 1:33 scale pitching, heaving surging duck in the Edinburgh wide tank. Impressive efficiencies were observed through the implementation of control. The author also carried out extremely useful forced oscillation tests; whereby the device was driven in still water to determine the hydrodynamics properties of the device.

Unfortunately, a full sized prototype of the design was never built. The design was seen as overly complicated and too expensive to develop into a commercially viable project (Brooke, 2003).

Clutch

Weller (2010) used a float-counterweight setup for the Manchester bobber tank tests. The float was permitted to move in the surge direction to avoid mechanical friction associated with strut supported systems. The belt and pulley system was not a closed loop, and as the counterweight was lighter than the float, power was only extracted during the descent phase of the float. A sprag clutch was used to engage a shaft during the descent and disengage during ascent. On the other side of the clutch there is a flywheel providing inertia to the system. The flywheel is coupled to a 12V DC permanent magnet motor with custom made control circuit board used to specify a torque load to the drivetrain which simulates the load from a generator. Prior to testing, the magnitude of static friction in the system is quantified and accounted for so that compensation can be applied at low rotational speeds to avoid stall (Weller, Stallard, & Stansby, 2011).
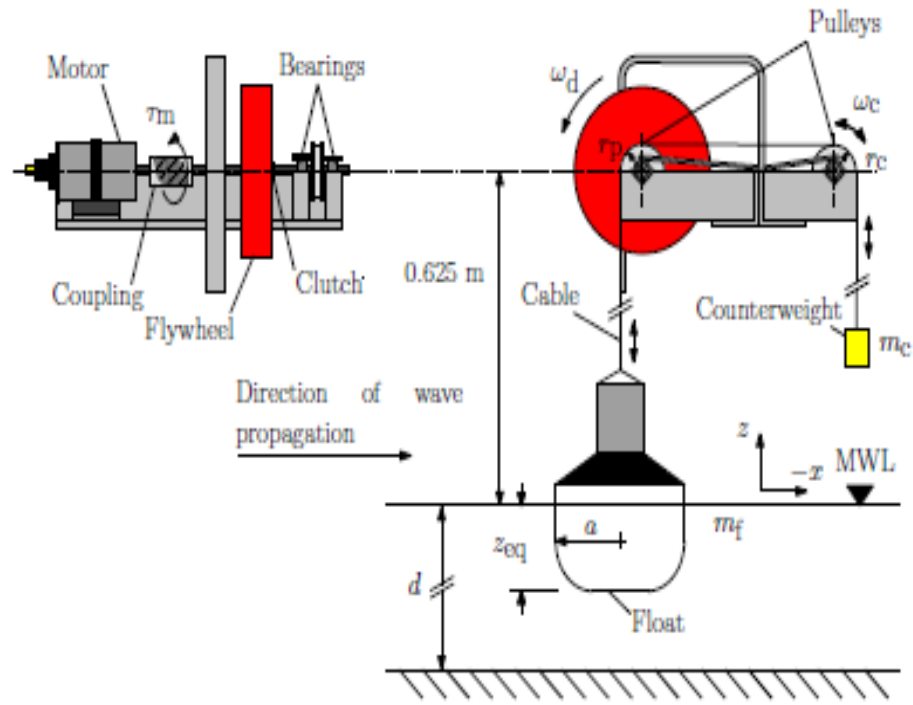
Figure 1:19: Schematic front and side views of the llaboratory model used in (source Weller et al., 2011)

Eddy current brakes

Eddy current brakes are based on the principle that a conductive material moving perpendicularly to a magnetic field generates a braking force that is proportional to its velocity.

Peiffer (2009) conducted experiments with a lab scale three phase linear generator acting as the PTO system (see Figure 1:20). The UC-Berkeley design consists of a cylindrical floater, acting as a rotor, which drives a stator consisting of two banks of wound coils.
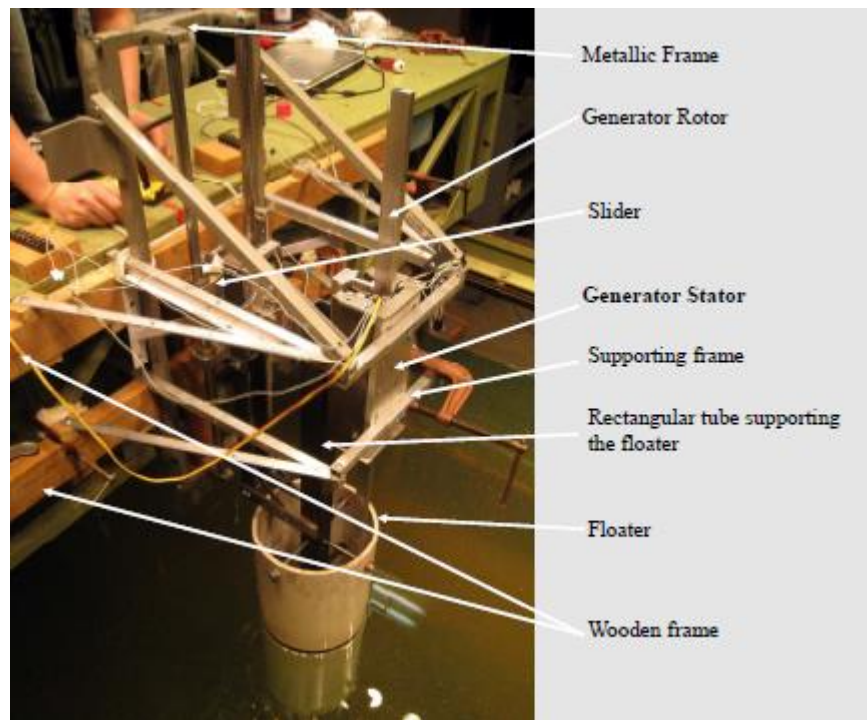
Figure 1:20: UC-Berkeley designed linear generator used in (Yeung, Peiffer, Tom, & Matlak, 2012)

The stator is comprised of two columns of 15 teeth (three sections of five teeth together for three individual phases) held firm by a U-shaped bracket. The rotor is comprised of 16 NeFeB high power magnets which pass between the columns of the stator creating a varying magnetic flux that induces an electromotive force and a current. The generator force is comprised of two types of force: a parasitic cogging force as the rotor moves past the magnetic poles and an electromagnetic force that opposes the motion of the buoy. The cogging force reduces the smoothness of the motion, and has no role in the conversion of the mechanical energy into electricity; only the electromagnetic force contributes useful electricity.

Lin (1999) conducted physical experiments on the IPS buoy, a point absorber device whose natural frequency can be altered by oscillating at an angle in between the heave and surge directions. The experimental model was constrained to move at an arbitrary but fixed angle. The buoy was constrained to move along a guiding rod by using water fed hydrostatic bearings. To load the buoy and simulate a full-scale power take-off mechanism, a fast-response linear-drive electric motor unit was used, that had earlier been developed by Richard Yemm. The design of a PTO system for a free floating IPS buoy is given in Taylor &

29

Mackay (2001.) and the experimental testing of such a buoy is given in Payne (2006) {see Figure 1:21 below}.
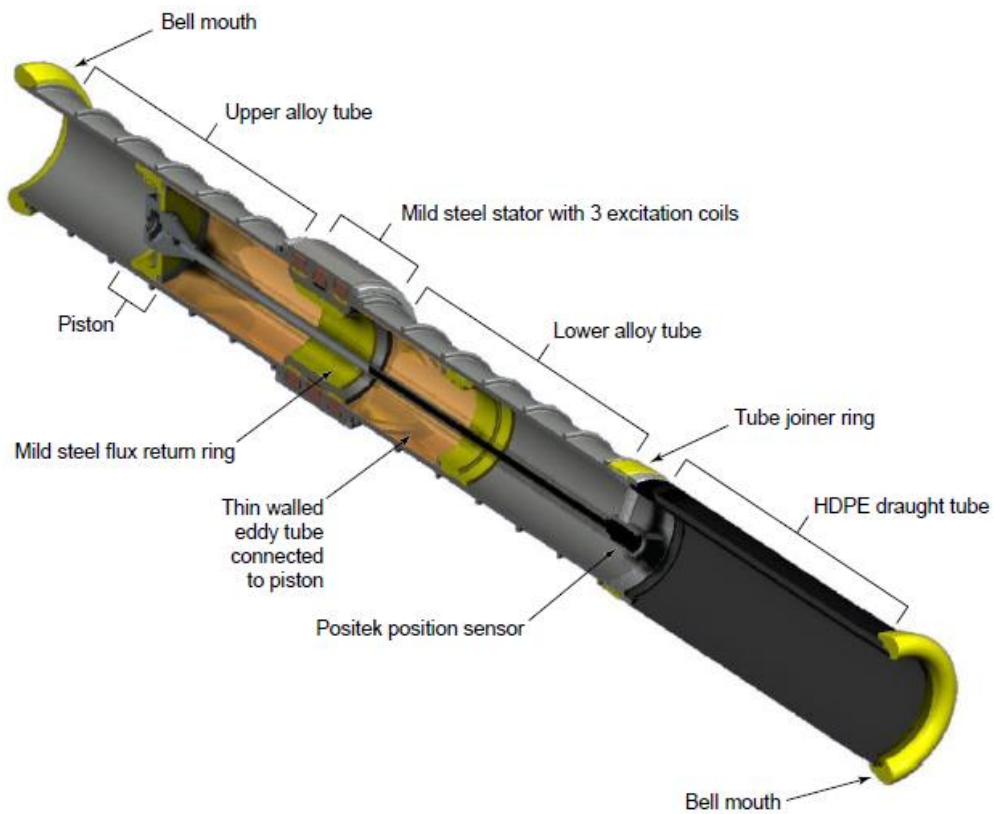
Figure 1:21: Section view of the PTO system used in Payne (2006)

The dynamometer circuit is made up of a tubular stator containing three coils, a return-ring and the radial water-filled gap between them. The eddy-tube moves through this gap and through the magnetic field produced by the coils. The dynamometer can be made to behave like an eddy current brake or as an induction motor depending on whether DC or AC current is used to energise the system.

Energising the three coils from a DC current source makes the machine behave as an eddy-current damper. The combination of radial flux and axial motion induces circumferential voltage in the eddy-tube which in turns drives a current. The combination of circumferential current and flux produces a force on the tube proportional to and opposing its velocity. Because both the voltage-to-velocity ratio and the current-to-force ratio are proportional to flux, the damping coefficient is proportional to the square of flux density and thus to the square of excitation current.

By energising the three coils from AC current sources that are mutually 120 degrees out of phase, the PTO machine behaves as a tubular induction motor comparable to a conventional linear induction motor.

(Lopes, Henriques, & Gato, 2009) constructed a rotary eddy current brake system for the 1:16 scale model testing of the WaveRoller wave energy converter. The model is shown in Figure 1:22. The six pairs of electromagnets create a magnetic field perpendicular to the aluminium disc, which produces a braking force on the disc proportional to its angular velocity.
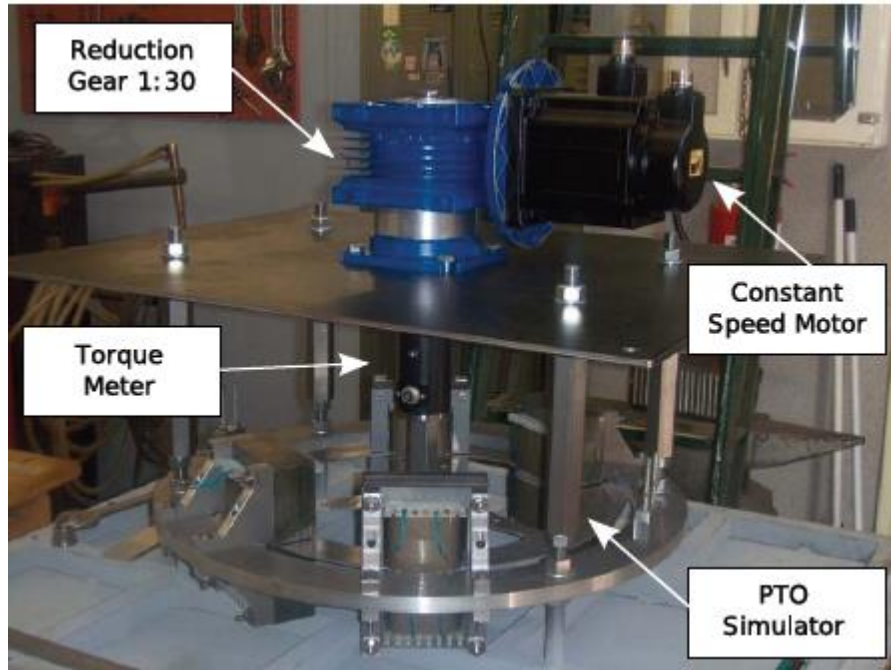
Figure 1:22: Dry bench set-up of the Waveroller PTO system used in (Lopes et al, n.d.)

Linear actuators

Villegas & Schaaf (2011) reported on a physical testing campaign carried out on the Wavebob point absorber WEC at the MARIN tank facilities in the Netherlands. A Copley Controls linear motor system was used consisting of a housing with windings (stator) and a moving rod with magnets (translator). The linear motor was controlled in current mode using a servo amplifier. The applied force is proportional to the electric current. This force is generated inside the motor and will not be equal to the force acting between the bodies since there are losses due to bearing friction and Eddy effects. By using a feedback system of the measured force, the linear motor control can compensate for such losses.
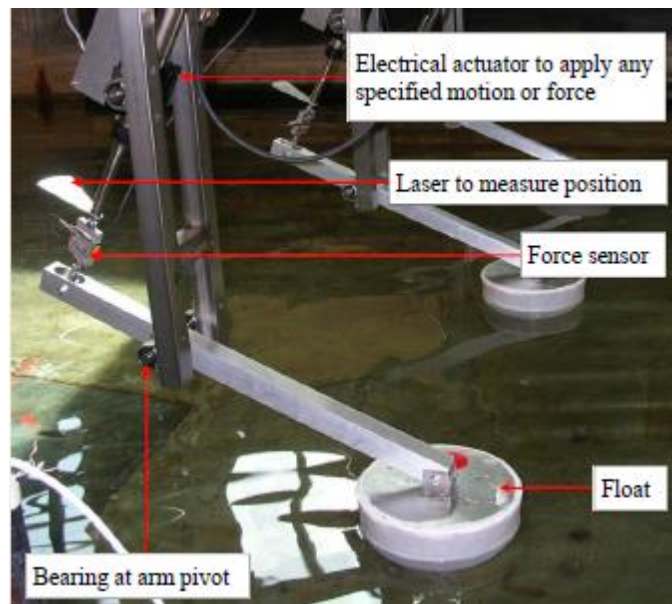
(Zurkinden, Kramer, & Alves, 2012) tested a model of the Wavestar WEC equipped with a sophisticated linear actuator acting as an electric power generator. A linear movement, as a result of wave motion, generates a direct electromagnetic force in the actuator. The motor consists of two main parts: the slider and the stator. The slider is a precision assembly that consists of a stainless steel tube, which is filled with neodymium magnets. The stator, also called the bearing of the slider, contains the position sensors and a microprocessor board. The device is supplemented by a force and displacement transducer. The displacement sensor consists of a laser measurement system which is mounted on top of the transducer.

1.7.4 Discussion on PTO selection.

The friction based PTO systems fall into a category one could label "Screwdriver Control". The PTO settings can be changed in-between tests with the use of said implement, but they are not suitable for changing the damping value while a test is ongoing. This is adequate for early proof of concept work. Additionally if it is a fully intended design decision that the full scale device will have a "pick and stick" damping value; That is to say the damping value over a certain period of time (usually 20 minutes to an hour) will remain a constant value. The damping value is usually tuned such that it will be optimum for the characteristics of the sea state the device is operating in. These sea state characteristics are usually supplied by measurement buoys and their output is typically given every 20 minutes to an hour (see Cahill (2014) for example). The specifics of the currently vaguely descriptive "sea state" will be

discussed in further detail later when introducing sea spectra; for now it is preferred to not get too technical, so that this opening chapter can be read by the layperson.

It would be advantageous of the damping of the PTO could be changed in real time such that advanced control techniques could be investigated as early as possible. It would naturally seem logical therefore to use one of the advanced PTO rigs described earlier, but this is not a trivial task. The early pioneering work of Salters duck and subsequent IPS devices is a testament to the ingenuity of the Edinburgh team. The bespoke nature of their work and original designs of Salter, Jeffrey, Taylor, Yemm and presumably many more, gifted electrical engineers is difficult to replicate. Such expertise is not available at every centre. The author's background as a luddite mechanical engineer, was certainly not adequate for the task. Consulting with the electrical team at HMRC (no slouches themselves) it was decided that while construction of a linear generator such as used by Yeung et al (2012), while possible would be very time consuming with many teething problems. It could then be regarded as a project in itself.

The next thing to look at then would be an off the shelf PTO system. The linear actuators are an excellent method of achieving this, but they are well designed high end components and the costs are prohibitive. A search for conventional rotational motors was carried out by liaising with several motor suppliers. The rotational speeds of the device are set by the wave frequencies that the basin is capable of generating (approximately 0.6-2.6 second for this particular basin). As mentioned previously the low speeds and power levels associated with model scaling do not match with the preferred operating speeds of continental motors. The problem of wave energy converters is that they are typically low speed high torque, whereas motors prefer high speed low torque environments. This usually necessitates the need of a gearbox which adds undesired non-linearity to the system.

It was hoped that the setups of Flocard & Finnigan, (2010) and De Backer (2010), which utilise additional mass, having the effect of amplifying buoy motions /velocities would shift the operating range into something more amiable for conventional motors. This turned not to be the case unfortunately. While investigating this line of inquiry it became apparent that the problem of finding a PTO mechanism that could operate effectively at typically low energy levels associated with model scale tests was adequately met by the utilisation of a magnetic particle brake.

The brake is comprised of an output shaft surrounded by a fine, dry stainless steel powder. The powder is free flowing, until a magnetic field is applied the brake. The powder particles form chains along the magnetic field lines providing frictional torque against the shaft. The torque is proportional to the magnetic field strength, and can be altered by suitably changing the D.C. input current. A more detailed description of the brake and its dynamics will be given in chapter where it is utilised for experimental work.

It was decided that a simple point absorber constrained to heave motions only such as used by De Backer (2010), would provide a good case study for examining details such as excitation forces, response amplitudes and power absorption which are typical measures that interest device developers. The inclusion of the more advanced PTO mechanism could be regarded as an improvement on the design and worthy of investigation. Although the PTO mechanism is a passive system, meaning it cannot put power into the device, the addition of supplementary inertia acts as a mechanical workaround, allowing control forces to be investigated. Incidentally the other interesting model set-up considered by the author, i.e. that of Flocard & Finnigan, (2010) was ruled out due to its degree of directional dependency. The reason why will be explained in more detail in Chapter 3 which as assessment of the wave basin characteristics at HMRC.

1.8 Thesis outline

This thesis will examine the early stage development of a heaving point absorber device. While the primary focus is on the physical modelling side; the important aspects of numerical modelling and control are also considered. Chapter two sets out some of the theoretical background material used throughout the thesis. Topics covered include: the theory of waves and, in particular laboratory generation of water waves, wave energy conversion principles, modelling a point absorber as a mass spring damper and an introduction to control techniques.

It is important for the experimentalist to understand the dynamics of the wave basin in which they operate. An existing wave basin characteristics study was not available to draw on. Chapter three therefore details research into HMRCs wave basin operation and performance: quantifying wave reflections in both regular and irregular waves, and assessing the spectral components of requested incident waves. Although an integral part of the work this chapter

is written such that it can be viewed in isolation by researchers whose sole interest is wave basin dynamics.

Chapter four describes the development of a numerical model of the heaving point absorber using linear theory. This entailed the use of WAMIT, a software package based on boundary element methods to first create a basic frequency domain model necessary for resolving the forces and response motions of the device. A time domain model was also created which could handle the non-linearity of the PTO system. The numerical model allows for a validation study between numerical results and experimental tests as well as allowing for a potential investigation into conditions outside of physical modelling.

Chapter five details the design and construction of the experimental test rig with the addition of the PTO simulation. An extensive series of experimental test results are given, including: heave excitation force tests, free decay tests, un-damped response and power absorption in regular and irregular waves.

Chapter six relates to the control of wave energy devices. Full scale WECs implement different control strategies with the aim of maximising energy yield. It would be beneficial to be able to test these control strategies at small scale. A signal can be sent to the particle brake to change its damping value in real time (during a test) allowing for some basic control techniques to be examined. A discussion is given of the strengths and weaknesses of the selected PTO device, being a passive device which limits its effectiveness in studying different control methods as most methods require reactive power (i.e., the ability to input power to the system).

Chapter 2: Theoretical Background

2.1 Linear Theory
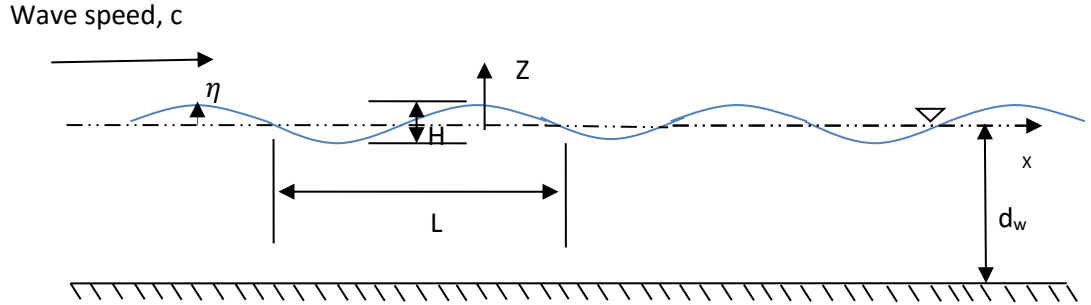
Figure 2:1: Definition sketch for a prgressive wave train

Figure 2:1 shows some of the fundamental parameters that will be used throughout this section. $\eta(x, z, t)$ is the wave elevation. L is the wavelength, k the wavenumber, i.e. the number of waves that exist over a specified distance $\left(k = \frac{2\pi}{L}\right)$ T is the wave period, ω is the angular frequency , $\left(\omega = \frac{2\pi}{T}\right)$ and d_w is the water depth.

Linear wave theory (LWT) is the most commonly applied description for wind-generated surface gravity waves. LWT assumes that the height of the wave is small compared to the wavelength (small amplitude assumption H/2L<<1) and that the water depth d_w is not small compared to the wavelength L (finite- depth assumption d_w/L<<1). Small amplitude LWT was originally developed by Airy (1845); and, consequently, LWT is also referred to as the Airy wave theory (Hudspeth, 2006b).

The fundamentals of linear theory, which form the theoretical basis of the numerical model used in this thesis, can be found in several text books including Falnes, (2002), and Holthuijsen, (2007). As such, it is assumed that the reader is familiar with the subject, so that what follows is a very brief synopsis of the underlying assumptions and significant results used in this work.
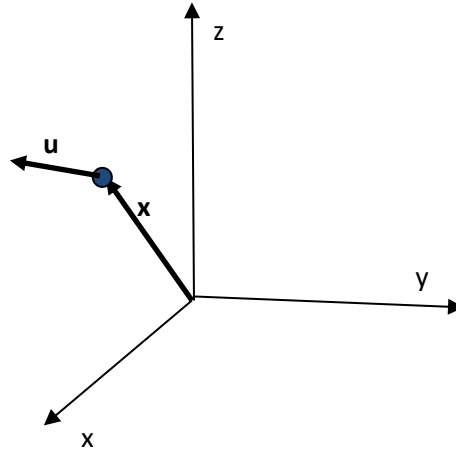
Figure 2:2: Position and velocity vectors in space

The position of a fluid particle in space is described by

$$x = \begin{pmatrix} x \\ y \\ z \end{pmatrix} = \begin{pmatrix} x_1 \\ x_2 \\ x_3 \end{pmatrix} \qquad (2.1)$$

Where the two representations (x,y,z) and (x_1,x_2,x_3) are equivalent and interchangeable.

The fluid velocity vector at that point is given by

$$u(x, y, z, t) = \begin{pmatrix} u_1 \\ u_2 \\ u_3 \end{pmatrix} \qquad (2.2)$$

Two fundamental fluid mechanics equations relate to the continuity of mass and momentum. The continuity equation

$$\frac{\partial \rho}{\partial t} + \nabla.(\rho u) = 0 \qquad (2.3)$$

And the Navier-Stokes equation (using the formulation of Feynman, 1965))

$$\frac{Du}{Dt} = -\frac{1}{\rho}\nabla p + \nabla\psi + \frac{f_{visc}}{\rho} \qquad (2.4)$$

Where $\frac{D}{Dt}$ is the total (or material derivative), ρ is the density of the fluid and p is the fluid pressure. ψ stands for the potential energy per unit mass, (for gravity for example φ is just

gz where g the gravitational constant). The viscosity force per unit volume $\boldsymbol{f}_{visc}$ has two components

$$\boldsymbol{f}_{visc} = \nu\nabla^2\mathbf{u} + (\nu + \nu')\boldsymbol{\nabla}(\boldsymbol{\nabla}.\boldsymbol{u}) \qquad (2.5)$$

The first term containing ν (the kinematic viscosity), relates to shear forces which exist in a moving fluid. The second term containing ν' (the second coefficient of viscosity) relates to internal forces during compression. If the fluid is assumed incompressible, this second term drops out and Eqn (2.3) reduces to $\boldsymbol{\nabla}.\boldsymbol{u} = 0$. The incompressibility assumption is usually valid, as the density of water increases by only 0.5% when the pressure is increased 1 to 100 atmospheres at constant (normal) temperature (Batchelor 1999).

Potential flow theory is employed where it is assumed that:

- The fluid is irrotational, so that $\boldsymbol{\nabla} \times \boldsymbol{u} = 0$

The concept of fluid irrationality can seem counterintuitive at first. A useful analogy is that of a Ferris wheel; the wheel itself can rotate but the individual carriages maintain the same orientation.

The fluid velocity **u** is related to a velocity potential Φ via

$$u_i = \frac{\partial\Phi}{\partial x_i} \qquad (2.6)$$

Where x_i and u_i are the components of displacement and velocity, respectively.

When the incompressible fluid criterion Eqn (2.3) is written in terms of the velocity potential Φ, one sees that the governing equation for the fluid is Laplacian, in that

$$\nabla^2\Phi = 0 \qquad (2.7)$$

This differential equation arises in many different areas of engineering and physics and is called Laplace's equation. It turns out that Laplace equation is all we have to know about the water motion away from the boundaries and the surface (Krogstad & Arntsen, 2000). Additionally it is assumed that the viscosity of the fluid is nil (being an ideal or inviscid fluid). The assumption of zero viscosity is a more troubling one. As Feynman (1965) puts it; John von Neumann was well aware of the tremendous difference between what happens when you don't have the viscous terms and when you do, and he was also aware that, during most

of the development of hydrodynamics until about 1900, almost the main interest was in solving beautiful *mathematical* problems with this approximation which had almost nothing to do with real fluids. He characterized the theorist who made such analyses as a man who studied "dry water." Nevertheless, for those of us without the mathematical abilities of Feynamn and von Neumann the omission of viscosity is commonplace, as it greatly simplifies the dynamics. In general the viscous effects are limited to a thin layer at the surface, at the seabed and next to an immersed body, called the boundary layer. The boundary layer will be discussed later when introducing a wave activated body.

The desired potential is then obtained by solving (2.7) subject to the appropriate l boundary conditions a given by (Sarpkaya & Isaacson, 1981)

$$\frac{\partial \Phi}{\partial z} = 0 \text{ at } z = -d_w \tag{2.8}$$

$$\frac{\partial \eta}{\partial t} + \frac{\partial \Phi}{\partial x}\frac{\partial \eta}{\partial x} - \frac{\partial \Phi}{\partial z} = 0 \ \ at \ z = \eta \tag{2.9}$$

The first condition is that there can be no flow through the closed seabed. The second known as the kinematic boundary condition states that the surface is always composed of the same particles. An intermediate step is taken leading to the formation of the last boundary condition; which states that the surface the pressure p must equal the atmospheric pressure, which we assume is constant. The pressure *p=p* (x,z,t) can be obtained using Bernoulli's equation:

$$\frac{p}{\rho} + \frac{\partial \Phi}{\partial t} + \frac{1}{2}(u_1^2 + u_3^2) + gz = C(t) \tag{2.10}$$

The function C(t) can be set to an arbitrary convenient constant. If we let C(t)=p_{atm}/ρ Bernoulli's equation gives us the dynamic boundary condition.

$$\frac{\partial \Phi}{\partial t} + \frac{1}{2}\left[\left(\frac{\partial \Phi}{\partial x}\right)^2 + \left(\frac{\partial \Phi}{\partial z}\right)^2\right] + g\eta = 0 \tag{2.11}$$

Sarpkaya & Isaacson (1981) summarise that at this point we have two-dimensional, progressive, permanent gravity waves over a smooth horizontal rigid bed. They are composed of a continuous, inviscid, incompressible fluid, with no temperature or salinity gradients, no vertical density gradient (even though gravitational force apply), no wind or wind shear, no surface tension, no bottom friction, no growth, and no attenuation. Two serious difficulties

arise in the attempt to obtain an exact solution for two dimensional wave train. The first is that the free surface boundary conditions are non-linear, and the second is that these conditions are prescribed at the free surface z=η which is initially unknown. The simplest and most fundamental approach is to seek a linear solution of the problem by taking the wave height H to be very much smaller than both the wave length and the still water depth d_w; that is H<<L,d_w. This approach is referred to as small amplitude wave theory, linear wave theory, or Airy theory. The non-linear terms which involve products of terms of order of the wave height are then assumed negligible in comparison with the remaining linear terms which are themselves the order of the wave height. Furthermore the free surface boundary conditions may now be applied directly at the still water level z=0.

With regard to the boundary conditions, one assumes that at the sea bed and at the free surface it is appropriate to linearise the equations as is depicted in the figure shown:
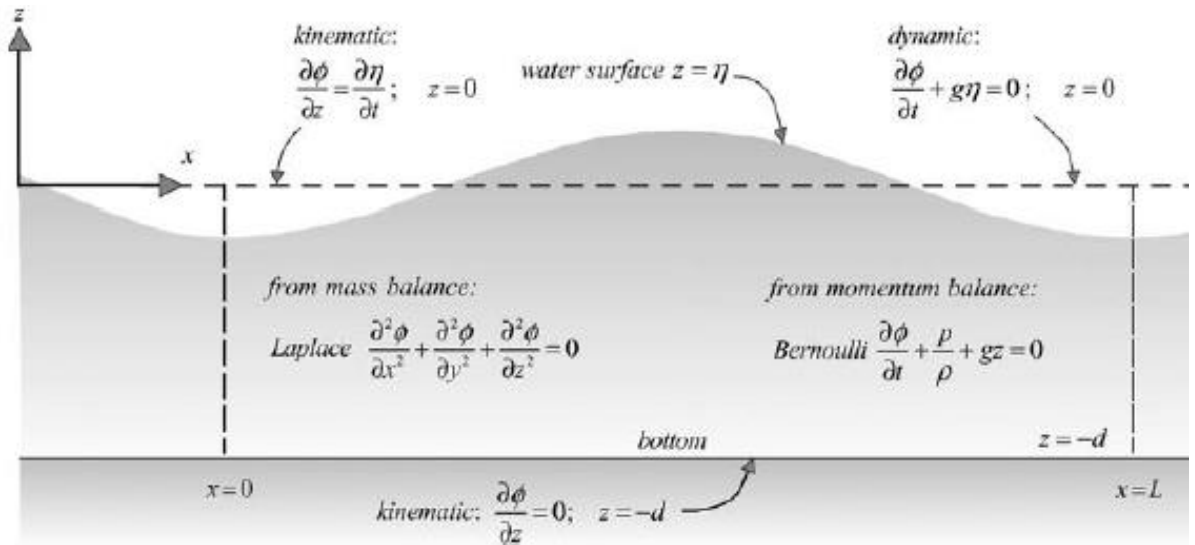
Figure 2:3: The linearised equations and boundary conditions in terms of the velocity potential. (source Holthuijsen, 2007)

The linearised boundary conditions may be combined to yield

$$\frac{\partial^2 \Phi}{\partial t^2} + g\frac{\partial \Phi}{\partial z} = 0 \ at \ z = 0 \tag{2.12}$$

$$\eta = -\frac{1}{g}\left(\frac{\partial \Phi}{\partial t}\right)_{z=0} \tag{2.13}$$

Bearing in mind that we are seeking solutions that are harmonic waves with sinusoidal time variation (using Falnes (2002) notation).

$$\Phi = \Phi(x, z, t) = \mathbb{R}\left\{\widehat{\Phi}(x, z)e^{-i\omega t}\right\} \tag{2.14}$$

The solution may be obtained by a separation of variables technique in which Φ is written in the form (Sarpkaya & Isaacson, 1981)

$$\widehat{\Phi}(x, z, t) = Z(z)X(x) \tag{2.15}$$

Inserting this into the Laplace equation (2.7) yields

$$\frac{\partial^2 Z}{\partial t^2} - k^2 \Phi = 0 \tag{2.16}$$

$$\frac{\partial^2 X}{\partial t^2} + k^2 \Phi = 0 \tag{2.17}$$

Where the sign of the separation constant k^2 has been chosen to provide a periodic rather than hyperbolic solution in the x dimension. The solutions of Z and X can be found in several textbooks (Sarpkaya & Isaacson, (1981), Mei, (1992), Falnes (2002) and the helpful website (WikiWaves, 2018). For conciseness the solution is given as

$$\widehat{\Phi} = \frac{igH}{2\omega} \frac{\cosh k(z + d_w)}{\cosh(kh)} \cos(\theta) \tag{2.18}$$

Where $\theta = kx - \omega t$ is the wave phase angle? The tremendous power of potential theory lies in the fact that once the potential is determined, one then easily obtains the velocity followed by the desired pressures and forces.

The linear dispersion relationship is formed from Eqn (2.12).

$$\omega^2 = gk \tanh(kd_w) \tag{2.19}$$

This is an equation which says that ω and k cannot be chosen at will. For a given k ≠ 0, only the two frequencies, ω and $-\omega$ which satisfies the equation are allowed (Krogstad & Arntsen, 2000). The dispersion relation tells us how the frequency and the wavenumber are related. Exploiting some characteristics of the tanh function, namely tanh(kd_w)≈1 when kd_w > π. (deep water), and tanh(kd_w) ≈kd_w when kd_w is small (≈ π/10). Thus the shallow water criteria is d_w<< L. This allows for the characterisation of different zones of water depth, (see Table 2-1). The phase velocity C of a regular wave crest is

$$C = \frac{\omega}{k} = \frac{L}{T} \qquad \text{(2.20)}$$

From Table 2-1 we observe that for shallow the phase velocity is independent of ω and k. and dependent on water depth. Shallow water waves are therefore non-dispersive. In deep water however, the celerity increases with increasing wave period and wavelength.

Table 2-1: Depth dependant wave characteristics

	Shallow Water	Intermediate Water	Deep Water
Relative Depth	$d_w < L_0/20$	$L_0/20 > d_w < L_0/2$	$d_w > L_0/2$
L	$L = T\sqrt{gd_w}$	$L = \frac{gT^2}{2\pi}\tanh\left(\frac{2\pi d_w}{L}\right)$	$L = \frac{gT^2}{2\pi} = L_0$
C	$C = \sqrt{gd_w}$	$C = \frac{gT}{2\pi}\tanh\left(\frac{2\pi d_w}{L}\right)$	$C = \frac{gT}{2\pi}$
Cg	$C_g = \sqrt{gd_w}$	$C_g = \frac{1}{2}\left(1 + \frac{2kd_w}{\sinh(2kd_w)}\right)$	$C_g = \frac{gT}{4\pi} = C_{g0}$

The other term introduce here is C_g is the group velocity. It relates to the speed at which energy is transferred. It's derivation is usually presented in one of two ways; the kinematic view is to take two very close proximity waves (in terms of ω).Anaysis of the resulting wave packet will eventually lead to the phase velocity of the component waves and the group velocity of the wave packet (see Mei et al (2005) for example). The other method preferred here is to use a dynamic view of energy flux. This is preferred, as in the authors opinion, formulation using one or more waves can lead to the misinterpretation, that group velocity is a phenomena of closely spaced frequencies. The theory is given according to Krogstad & Arntsen, (2000). The potential energy in a column of water with cross section dA is

$$dE_p = \int_{z=-dw}^{\eta} \rho gz dV = dA \int_{z=-dw}^{\eta} \rho gz dz = dA\rho g \frac{\eta^2 - dw^2}{2} \qquad \text{(2.21)}$$

Since only the excess potential energy is of interest, we subtract the part corresponding to the mean surface and obtain the potential energy per unit area

$$\frac{dE_p - dE_p(\eta = 0)}{dA} = \frac{1}{2}\rho g\eta^2 \qquad \text{(2.22)}$$

Instead of using the instantaneous value of surface elevation, it is more common to use the average of η^2 which for a sinusoidal wave is a^2.

$$\langle \frac{dE_p}{dA} \rangle = \frac{1}{4}\rho g a^2 \tag{2.23}$$

The kinetic energy is derived similarly by observing that

$$dE_k = \int\limits_{z=-dw}^{\eta} \frac{1}{2}\rho(u_1 + u_2 + u_3)^2 \, dV \tag{2.24}$$

If for simplicity we consider deep water and a plane wave $\eta(x,t) = A \sin(\omega t - kx)$; we obtain

$$(u_1 + u_2 + u_3)^2 = (\omega A)^2 e^{2kz} \tag{2.25}$$

And therefore

$$dE_k = \rho(\omega A)^2 \int\limits_{z=-dw}^{\eta} \frac{1}{2}e^{2kz}dz \approx \rho(\omega A)^2 \int\limits_{z=-dw}^{0} \frac{1}{2}e^{2kz}dz = \frac{1}{4}\rho g A^2 \tag{2.26}$$

The average kinetic and potential energies are equal, a property called *equipartition of energy*). The total energy being the sum of kinetic and potential parts is

$$E = E_p + E_k = \frac{1}{2}\rho g A^2 \tag{2.27}$$

Consider a vertical cross section of unit width along the crest. The average rate of energy flux (Power [P]) across this section is equal to the mean rate of work done by the dynamic pressure, that is

$$P = \int\limits_{z=-dw}^{\eta} \langle p(x,t)u(x,t)\rangle dz \approx -\rho \int\limits_{z=-dw}^{0} \langle \frac{\partial \Phi}{\partial t} \frac{\partial \Phi}{\partial x} \rangle dz \tag{2.28}$$

Which (Mei, 1992) calculates as, (recalling the definition of Φ given earlier)

$$P = \frac{1}{2}\rho g A^2 \left(\frac{1}{2}\frac{\omega}{k}\left(1 + \frac{2kd_w}{\sinh(2kd_w)} \right) \right) = E C_g \qquad \textbf{(2.29)}$$

Hence the group velocity has the dynamic meaning of the velocity of energy transport. One of the most interesting phenomena to observe (particularly early on in ones learning) is the group velocity in a wave tank. Send out a packet of say 8 (deep water) waves and follow the propagation from the paddles. The leading wave will travel at the individual phase velocity, however, the energy of the whole packet travels at the group velocity. The result of this is that waves at the front of the profile appear to "die out", as they lose some of their energy (height). Conversely at the back of the envelope new waves will appear to be "born". In the authors opinion, where possible, group velocity is a phenomena best observed, rather than described.

2.2 Wave generation and associative phenomena

We describe two wave maker types which are commonplace in wave basin facilities. Piston type wave makers are generally used for shallow water basins and generating shallow water waves. This is because the motion of the piston is better suited to create the elliptical motions of water particles in shallow waves. In shallow water the horizontal water particle motion is almost constant at all depths (see Figure 2:4 below).
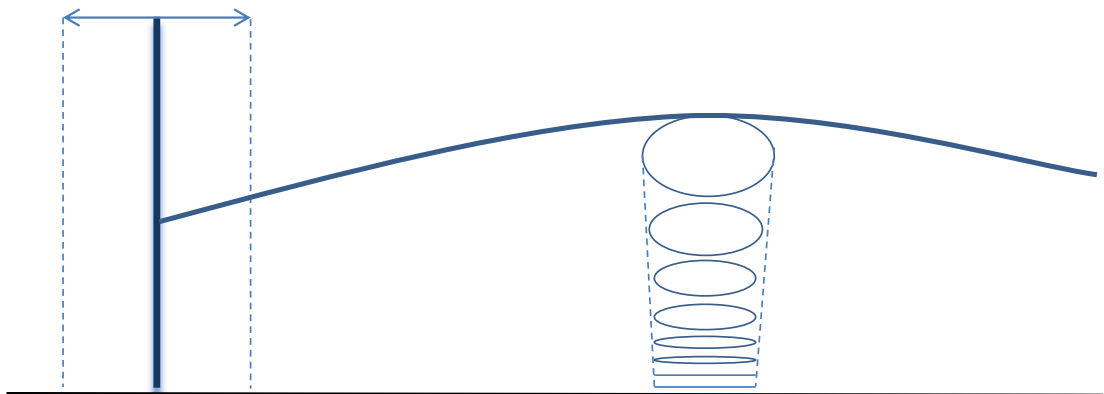
Figure 2:4: Sketch of piston paddle wave maker.

Flap paddle wave makers are flat vertical plates hinged at the bottom, so when driven with an oscillatory motion, they partially rotate in a fore and aft arc. In water that is deep compared to the wavelength, wave motion is confined to surface layers (see Figure 2:5 below).
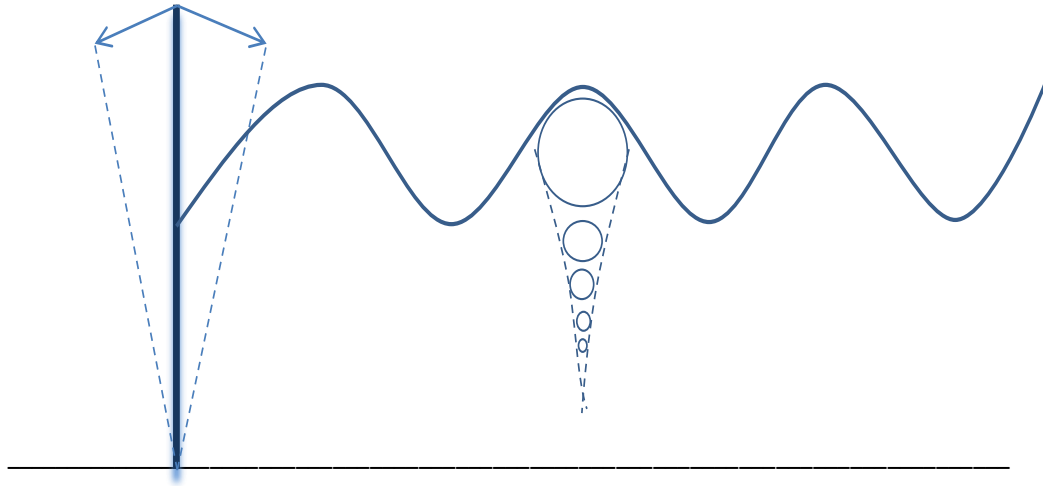
Figure 2:5: Sketch of flap paddle wave maker with particle motion matching deep water waves.

The actual paddle drive can be hydraulic, mechanical or electrical and paddle systems can be wet backed - water on both sides of paddle - or dry backed with a means of sealing the water. The wave height capability of a particular wavemaker (assuming adequate power to drive the wave board) is a function of its maximum usable stroke, coupled with water depth and wave period.

2.2.1 Regular Waves

Regular waves or monochromatic waves may be written mathematically in terms of a single amplitude A and frequency ω as

$$\eta(x, z, t) = \frac{H}{2} \, sin(\omega t - kx + \phi) = A \, sin(\omega t - kx + \phi) \qquad \textbf{(2.30)}$$

Needless to say, regular waves bear little resemblance to those in the sea which are comprised of multiple waves interacting from different directions. The figure overleaf gives

an example of how it possible to construct a more realistic wave by the simple superposition of component regular waves.
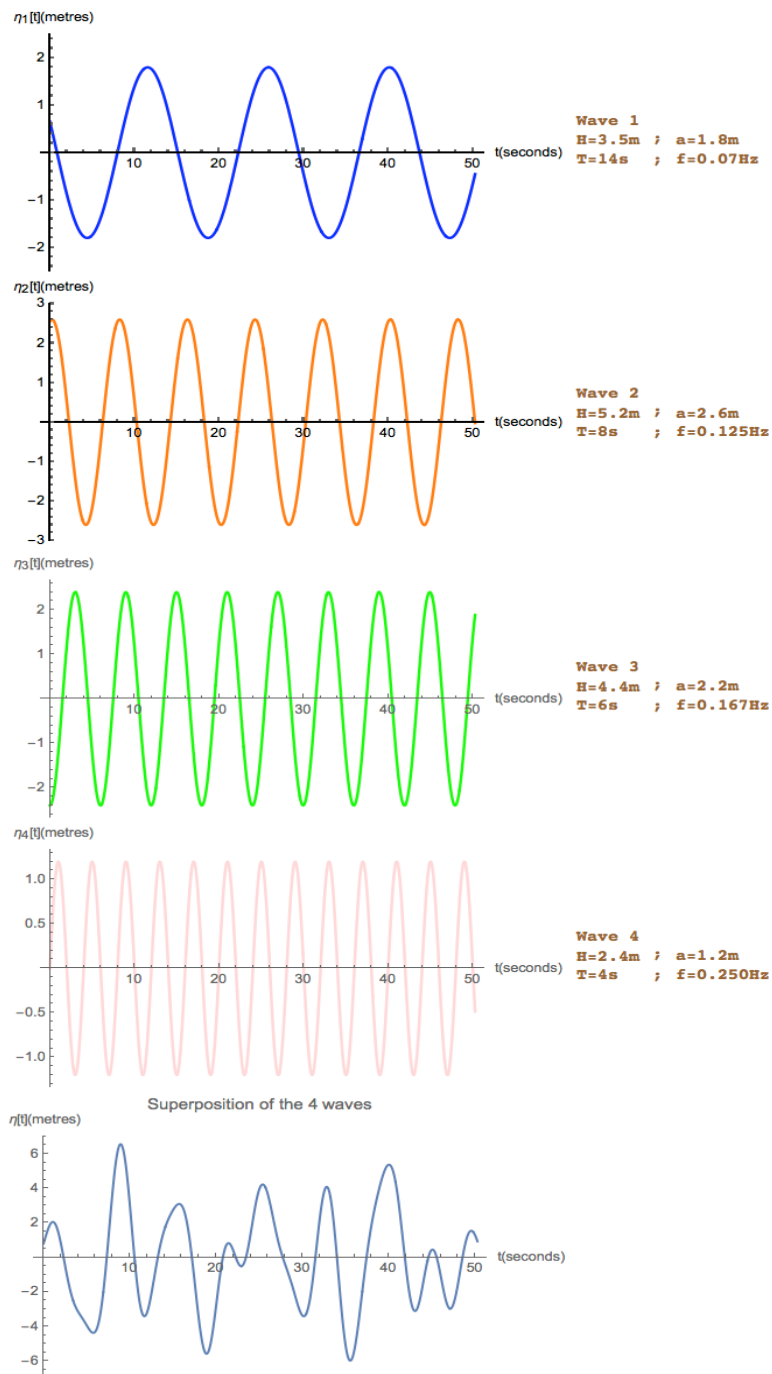
Figure 2:6: Example wave surface elevation, which is constructed by adding 4 regular waves of different height and period

Regular waves, however, offer a useful starting point for physical modelling as they allow for the observational response to very specific input conditions. This is crucial when one chooses to regard certain 'real' waves as a superposition of regular waves at different frequencies because, by linearity, the response of the real wave is then the sum of the individual responses of its constituent regular waves.

2.2.1 Regular Wave Reflection

If a monochromatic incident wave meets a plane vertical barrier then perfect reflection is said to occur. The interaction of the incident and reflected wave in this scenario sets up a standing wave with an antinode at the barrier and at half wavelength intervals thereafter, with nodes in between as depicted in Figure 2:7.

Wave record analys
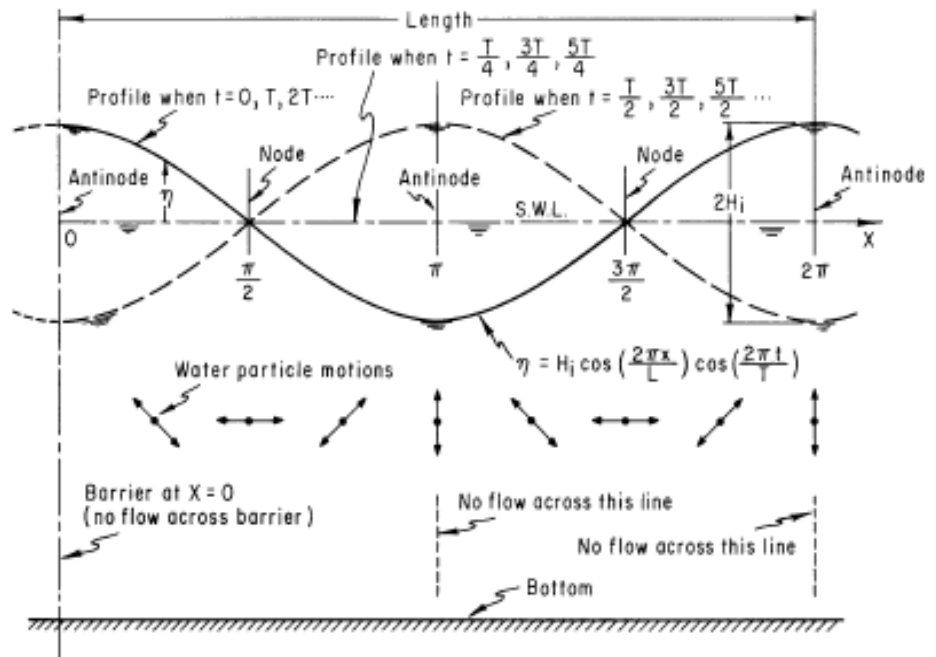
Figure 2:7: Standing wave (clapotis) system, perfect reflection from a vertical barrier (Coastal engineering research centre, 1984)

The following is the theory for partial standing waves as given by Ippen (1966).

Assuming a linear incident wave

$$\eta_i = a_i \sin(kx - \omega t) \tag{2.31}$$

47

and a linear reflected wave

$$\eta_r = a_r \sin(kx + \omega t + \varphi_r) \qquad \text{(2.32)}$$

Boccotti (2000), writes that one cannot exclude some phase angle between the reflected and the incident waves and this is why the phase angle φ_r is an unknown.

One obtains by superposition of the incident and reflected wave trains

$$n_{total} = \eta_i + \eta_r = \eta_i = a_i \sin(kx - \omega t) + a_r \sin(kx + \omega t + \varphi_r) \qquad \text{(2.33)}$$

Assuming that the barrier is at x = 0 and that φ_r = phase shift = π radians, then becomes

$$\eta_{total} = a_i \sin(kx - \omega t) - a_r \sin(kx + \omega t) \qquad \text{(2.34)}$$

Adding $a_r \sin(kx + \omega t)$ to both components of (2.34) in opposite directions we get

$$\eta_{total} = (a_i + a_r)\sin(kx - \omega t) - a_r[\sin(kx - \omega t) + \sin(kx + \quad \text{(2.35)}$$

The first component of the above equation describes a progressive wave of amplitude $(a_i + a_r)$ while the second component is a standing wave of amplitude a_r. The above can be re-written as

$$\eta_{total} = (a_i + a_r)\sin(kx)\cos(\omega t) - (a_i + a_r)\cos(kx)\sin(\omega t) \qquad \text{(2.36)}$$

Evaluating

$$\left. \frac{\partial \eta_{total}}{\partial t} \right|_x = 0 \qquad \text{(2.37)}$$

for any x,, i.e. at the nodes visible in Figure 2:7; gives

$$[\omega t]_{\eta_{total max}} = tan^{-1}\left[-\frac{a_i + a_r}{a_i + a_r}\cot(kx) \right] \qquad \text{(2.38)}$$

With

$$[kx]_{\eta_{total max}} = n\pi \ and \ (2n + 1)^{\pi}/_2 \ for \ n = 0,1,2, \dots \qquad \text{(2.39)}$$

Substituting these latter two expressions into (2.39) gives the following maximum and minimum amplitudes of the partial standing wave:

$$a_{max} = a_i + a_r \qquad\qquad \textbf{(2.40)}$$

$$a_{min} = a_i - a_r \qquad\qquad \textbf{(2.41)}$$

Therefore

$$H_{max} = 2(a_i + a_r) \qquad\qquad \textbf{(2.42)}$$

$$H_{min} = 2(a_i - a_r) \qquad\qquad \textbf{(2.43)}$$

With

$$\frac{H_{max} + H_{min}}{2} = H_i \qquad\qquad \textbf{(2.44)}$$

$$\frac{H_{max} - H_{min}}{2} = H_r \qquad\qquad \textbf{(2.45)}$$

Then

$$\frac{H_{max} - H_{min}}{H_{max} + H_{min}} = \frac{H_r}{H_i} = k_r \qquad\qquad \textbf{(2.46)}$$

Which is known as Healy's formula.

The pure standing wave profile occurs when the incoming wave train hits a breakwater orthogonally; however, this setup is rarely the case in basin facilities, except for specific coastal engineering studies. In practice wave reflections in a flume or basin are undesirable and measures and put in place to reduce them. Even though reflection in a basin can be reduced, they are still an ever present feature. This results in a partial standing wave profile which is discussed in more detail in section 3.7.

Ouellet & Datta (1986) state that after the wave generator, wave absorber is the most important mechanism in a wave flume or basin. Wave absorbers can be broadly classified into two main categories: active and passive wave absorbers. In their survey of wave generating facilities, the authors mention for passive absorbers, the beach of constant slope seems to be the most popular arrangement. Additionally other materials such as transversal bars, horsehair and wire screen are used in conjunction. The authors suggest that; reflections

of up to 10% are to be expected even for well-designed beaches and that the % reflection tends to increase with reduced wave height. It does not appear possible to attain reflection coefficients below 10% for absorbers shorter than 0.5 to 0.75 of a wavelength. It is also reported that parabola shaped beaches generally exhibit lower reflection coefficients.

Goda & Ippen (1963) theoretically analysed and tested wave absorbers composed of vertical mesh screens aligned normal to the direction of wave propagation. Four different screen absorbers where tested under deepwater wave conditions, and results compared favourably with theory. Reflection was shown to be dependent upon screen spacing, but not so dependent on the number of screens "provided the number is fairly large." They also stated that the screen absorber must be at least as long as the wavelength of the incident wave. Hughes (1993) summarises an extensive experimental program to develop an efficient wave absorber made of wire mesh screens carried out by Jamieson and Mansard (1987);

- The frontal area of the supporting framework should be minimal.
- High porosity mesh screens work best for absorbing energy from high steepness waves.
- Low porosity screens work best for absorbing energy from low steepness waves.
- Mesh screen porosity should decrease toward the rear of the wave absorber.
- Screen locations should be selected to correspond approximately to node locations of the partial standing waves.
- Wider screen spacing is required for steeper waves and longer wave periods, with sheet spacing progressively decreasing toward the rear of the wave absorber.

Active wave absorbers can be position or force feedback based. Milgram (1970) developed a position feedback controller which uses the signal from upstream wave gauges to estimate the reflected wave travelling towards to wavemaker. The driving signal to the wavemaker can then be adjusted based on the information attainable from the wave probes. The author reported that there was a significant level of error between the actual wave field generated compared to the desired result. Force feedback allows for direct measurement of the wave field at the wavemaker's surface. Salter (1981) noted that basin reflection made experimental measurements difficult (with amplitude variations of up to 30%) To address

this he developed a force feedback absorption system in the wide tank. This allowed the incident wave field to be determined and proved an effective way of cancelling out any reflected waves from the wavemaker surface. Active feedback systems like this eliminate the need for the wave board transfer function, and they also help to minimize second-order effects that arise when driving the wave board with a first-order signal. HMRCs basin at Pouladuff utilised such an active absorber developed by Edinburgh Designs (Bolton King & Rogers, 1997).

Several publications exist that explain different experimental techniques for measuring wave reflection. A good summary of these publications is presented by (Isaacson, 1991). The author compares three different reflection analysis methods. A two probe method, using one phase angle developed by Goda & Suzuki (1976), a three probe method using two phase angles by Funke & Mansard (1980) and three probe method developed by Isaacson himself. The author owns method was found to be the least accurate as it does not utilise the phase angles between the probes. The three probe method by Funke and Mansard was shown to give the best results, hence this method is utilised in this work.

2.2.2 Second Order Stokes Waves

In wave generation facilities, even though the experimentalist may desire to generate solely regular or monochromatic waves, it is often the case that higher harmonics will be present. These higher harmonic waves are sometimes termed, second order or Stokes waves. In 1847, Stokes published his work for nonlinear waves, according to which a wave can be approximated by adding extra harmonic waves to the basic harmonic. Each time a harmonic is added, the order of the wave increases by order of one. Every higher order correction is calculated by the previously obtained lower order correction, so that the process is successive. This theory, although usually extended to higher orders of accuracy than he was able to achieve, remains in use today and is based on the velocity potential (Dean & Dalrymple, 1991).
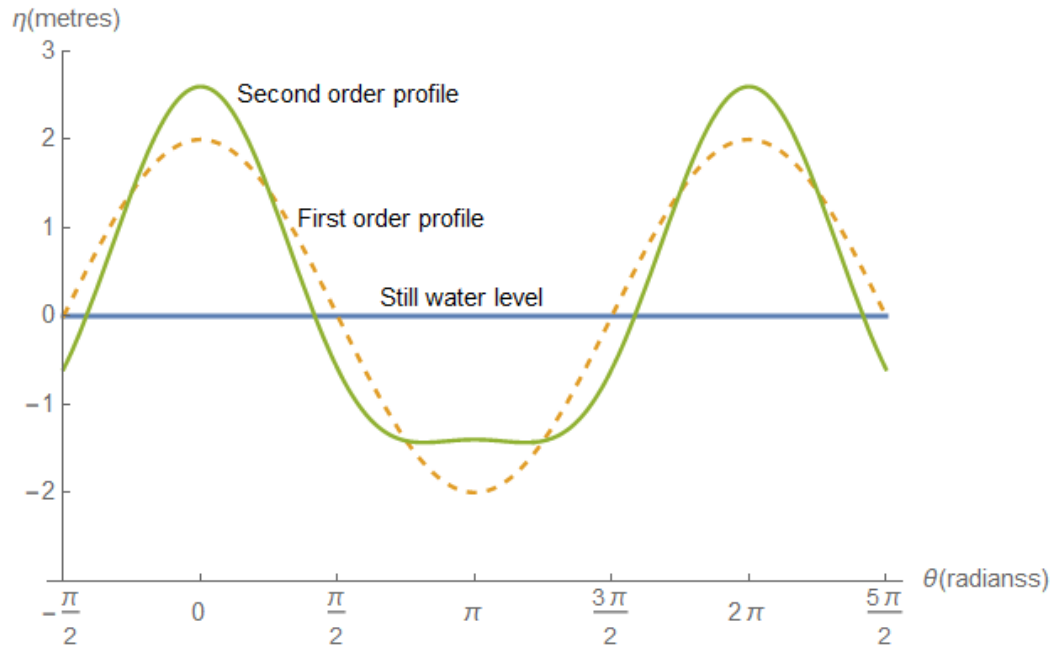
Figure 2:8: Linear and second order wave profile. Note the amplitude of the second harmonic is increased to illustrate the effect.

In the strictest sense, practically all laboratory generated waves violate the small-amplitude assumption invoked in deriving the first-order wavemaker theory. This results in unwanted wave nonlinearities being present in the forced waves in addition to naturally-occurring nonlinearities (Hughes, 1993). Examples of these naturally occurring non-liberalities are discussed further in Chapter 3:.

Attempts to generate regular waves in a wave flume using a sinusoidally varying wave board motion, as derived for first-order wavemaker theory, also produce unwanted free secondary waves which move at a speed that is slightly slower than the primary wave. The combination of the primary and secondary waves results in a combined wave form that varies both spatially and temporally. This modification to the primary wave becomes more pronounced as wave steepness (H/L) increases and/or relative depth (d_w/L) decreases, and experiments requiring uniform waves may be compromised if the wave distortion becomes severe (Hughes, 1993).

Madsen (1971) presented an expression for the second-order sea surface elevation far from the wavemaker for the case when a piston-type wave board is moved in a sinusoidal oscillation. This expression contained a second-order progressive Stokes wave and a free

second harmonic wave traveling at a slightly slower speed than the primary wave. This can be symbolically represented as (e.g. Svendsen, 1985)

$$n_{total=}a_{1s}\sin(kx - \omega t) + a_{2s}\sin 2(kx - \omega t)+a_{2f}\sin(kx - 2\omega t + \varphi))$$

(2.47)

Where the first term is the first-order wave component, the second term is the second-order Stokes contribution traveling at the same speed as the first-order wave, and the third term is the second-order free wave that propagates according to the dispersion relationship. The unwanted free wave can be removed from the wave field by adding a term to the wavemaker's first order driving signal to generate a wave component with the same frequency and wave height as the free wave but in anti-phase, this will effectively cancel the free wave.

The difficulty of wave tank generation is put succinctly by Madsen (1971);

"To generate a wave of permanent form the wavemaker should be given a motion, which as closely as possible, corresponds to the particle motion under the desired wave"

2.2.3 Irregular Waves & Spectra

While regular allow the experimenter a greater degree of control to investigate dynamics at specific frequencies, they bear little resemblance to a real sea/ocean water profile. As Hughes (1993) states, most physical models of coastal engineering problems involve forces resulting from the motion of gravity waves. In nature these waves are highly irregular and seldom exhibit anywhere near the uniformity of a sinusoidal wave train. Therefore, when it is appropriate, we should attempt to generate laboratory waves that closely approximate naturally occurring wave trains. As shown earlier the superposition of just a few sine waves with different amplitude and frequency can create a highly complicated signal, with amplitudes of the total signal that changes both in time and space. Svendsen (2005) states that this leads to the natural question: would it be possible to represent a real, irregular wave motion in the ocean by simple superposition of a large number of sine wave components? The answer to this question is: yes. However, it means we need to determine the amplitudes and phases of each of the (very) many wave components, and that turns out to be a nontrivial task. This leads to the introduction of wave spectra as a theoretical concept

The concept of spectrum can be attributed to Isaac Newton, who, with the aid of a prism, discovered that sunlight can be decomposed into a spectrum of colors from red to violet in

about 1700. This indicates that any light comprises numerous components of light of various colors (wave lengths). Analogous to the light spectrum it is commonplace to determine the different component frequencies of the sea, which introduces the concept of wave spectra. The task is to determine the amplitudes of the wave components that describe e.g. the surface variation in a given (measured) time series for a natural wave motion. Wave energy spectra are obtained by applying a Discrete Fourier Transform to the time series wave elevation data.

Figure 2:9: Wave record analysis taken from Journée & Massie, (2001)

Figure 2:9 above gives a graphical interpretation of the meaning of a wave spectrum and how it relates to the waves. This signal at the lower left hand part of the figure is called an irregular wave such that it's composed of several different individual wave frequencies interacting with each other. The irregular time domain wave history $\eta(t)$ (often termed ζ(t) as in used in the figure above) can be expressed via Fourier series analysis as the sum of a large number of regular wave components, each with its own frequency, amplitude and phase in the frequency domain. These phases will appear to be rather random, by the way. The value

54

$\frac{1}{2}\eta_a(\omega)/\Delta\omega$ associated with each wave component on the ω -axis - is plotted vertically in the middle; this is the wave energy spectrum, $S_\eta(\omega)$ (Journée & Massie, 2001).

The nth spectral moment is given by (2.48),

$$m_n = \int_0^\infty f^n S_\eta(f)df \qquad (2.48)$$

With m_0 being the total variance of the wave spectrum.

Various wave period parameters are determined using the ratio of different spectral moments such that

$$T_{(0,n)} = \left(\frac{m_0}{m_n}\right)^{\frac{1}{n}} \qquad (2.49)$$

The most notable periods are

- $T_{(0,1)}$ -   the mean wave period
- $T_{(0,2)}$ -   the zero crossing period
- $T_{(0,-1)}$ -   the energy period
- The peak frequency f_p, the frequency associated with the maximum amplitude in the spectrum

Another parameter, obtained from the wave spectra, is

- The variance wave height, $H_\sigma = 4\sqrt{m_0}$

The last parameter is often termed significant wave height H_s (and sometimes H_{m0}) H_s is more of a historical parameter and is closely related to the time series evaluated parameter $H_{1/3}$. That is; to take all of the individual wave heights from a time series zero crossing analysis, isolate the highest one third of all waves and take the average. This somewhat unusual parameter is an artefact of how average wave height was reported historically, with the human eye showing a bias towards smaller waves and discounting them. The ambiguity of different statistical parameters is explained in the work of Price (2009) and reproduced in Figure 2:10. Indeed the authors work does an excellent job of highlighting several

ambiguities/inconsistencies throughout wave energy (in what must have been a painstaking task).

Ambiguous parameter	Alternative definition	Explanation	Domain
H_s	$H_{1/3}$ [74]	mean highest third of crest to trough heights	time
H_s	$H_{m_0} = 4.004\sqrt{m_0}$ [74]	Rayleigh distribution : $H_{m_0} \approx H_{1/3}$	frequency
H_s	$H_\sigma = 4\sigma(\eta)$ [74]	Four times the variance of elevation.	time
H_s	$H_\sigma = 4\sqrt{m_0}$ [74]	if $\bar{\eta} = 0$ then $H_\sigma = 4\eta_{rms} = 4\sqrt{m_0}$	frequency
H_{rms}	H_{rms} [75]	rms of crest to trough heights	time
H_{rms}	$\sqrt{8\,m_0}$ [84]	Rayleigh distribution: $\sqrt{8\,m_0} \approx H_{rms}$	frequency
H_{rms}	η_{rms} [85]	rms of wave elevation	time
H_{rms}	η_{rms} [85]	if $\bar{\eta} = 0$ then $\eta_{rms} = \sqrt{m_0}$	frequency

Figure 2:10: Reproduction taken from Price (2009) listing ambiguous sea state parameters associated with wave height: the first column shows how a sea state parameter might be written in the literature, while the second column gives the possible interpretations of these parameters.

For a unidirectional wave system, the total energy E per unit area is (Tucker & Pitt, 2001)

$$E = \rho g \int_0^\infty S_\eta(f)df = \rho g m_0 \qquad (2.50)$$

The power transported per meter of crest length is

$$P_{avail} = \rho g \int_0^\infty C_g(f)S_\eta(f) \qquad (2.51)$$

Where $C_g(f)$ is the group velocity as defined previously. The formulas for theoretical spectra are derived from empirical studies of waves at different site locations, and are therefore statistical averages (or curves of best fit) for wave regimes found in different, lake, sea and ocean environments. There are a number of different spectra used in laboratory experiments, three well known spectra being the

- Pierson-Moskowitz spectrum
- Bretschneider spectrum
- JONSWAP spectrum

Pierson-Moskowitz spectrum

The Pierson-Moskowitz spectrum is derived from observations of fully-developed seas in the North Atlantic Ocean. Here

$$S_\eta(f) = \frac{\alpha g^2}{(2\pi)^4 f^5} exp\left[-0.74\left(\frac{f}{f_0}\right)^{-4}\right] \qquad (2.52)$$

Where α = Phillips constant = 0.0081 and f_0 is a reference frequency given by

$$f_0 = \frac{g}{2\pi U_{19.5}}$$

With $U_{19.5}$ being the wind speed measured 19.5 m above the still water level, is the sole variable parameter describing the spectrum (which does not depend on fetch or duration). The concept of a fully developed sea dates back to (Jeffreys, 1925) theory; that eddies on the leeward side of the waves resulted in a reduction of normal pressure as compared with the windward face and in a consequent transfer of energy from wind to waves. His results suggested that the wind could add energy to waves only so long as the wind speed was equal to or greater than the wave celerity, and that when the wave celerity became equal to the wind speed the waves reached maximum height and the sea was one of steady state.

 Bretschneider (1964) in his insightful review paper, states that the next great advance in the theory of wave generation in deep water was made by Sverdrup & Munk (1947), considering both normal and tangential stresses (whereas Jeffreys only considered normal stresses). According to their theory, the energy of waves can increase only if the normal and tangential stresses of the wind, exceeds the rate at which energy is dissipated by viscosity. The energy added by the wind goes into building the wave height and increasing the wave speed. The effect of the normal Stresses dominates for a short time only (during the early stages of wave development.) During the time that the waves are growing, the effect of the tangential stress is most important. When the average rate at which energy is transmitted to the waves by both tangential and normal stress is equal to the rate at which energy is dissipated by viscosity; the waves are said to have reached maximum height and celerity for a particular wind speed and are independent of fetch length and wind duration. This condition in which waves are in equilibrium with the wind is sometimes called the fully developed sea or fully arisen sea.

As a counterargument Hwang et al (2004) note that from the point of view of nonlinear wave–wave interaction (the re-distribution of energy in the variance density spectrum); if the wind event is truly unlimited in fetch and duration, the wave spectrum undergoes continuous frequency downshift. As the characteristic wavelength increases, the capacity of the wave field to absorb atmospheric forcing increases and the mechanism of wave breaking that limits the wave growth becomes weaker. Under such a scenario, it is difficult to imagine that the wave growth should be limited (i.e., reaching full development). The authors assert that the concept of ''full development'' of a wave field deserves more critical examination and additional observations in the field are needed to establish or disprove the growth limit of wind generated surface waves.

Bretschneider spectrum

In a report to the Beach Erosion Board of the US Army Corps of Engineers in 1959, Bretschneider proposed a spectral form that incorporated both the wave height and period of the sea state. This had the form

$$S_\eta(f) = Af^{-5}exp[-Bf^{-4}] \qquad\qquad (2.53)$$

$$where \; A = \frac{\alpha g^2}{(2\pi)^4} \;\; and \;\; B = \frac{5}{4f_p^{\;4}}$$

The coefficient B is proportional to the wave period and a combination of A and B are proportional to the significant wave height. The Bretschneider and Pierson–Moskowitz spectra differ only in the magnitudes assigned to αg^2 and B. Another form of the Bretschneider spectrum which illustrates the two input parameters is

$$S_\eta(f) = \frac{5}{16}\frac{H_s^{\;2}}{f}\left(\frac{f_p}{f}\right)^4 exp\left[-\frac{5}{4}\left(\frac{f_p}{f}\right)^4\right] \qquad\qquad (2.54)$$

When the steepness of the Bretschneider spectrum equals the fully developed case, the spectrum is equivalent to the Pierson-Moskowitz spectrum of Equation (2.91 (Barrett, 2010).

JONSWAP spectrum

Wind waves which develop rapidly in relatively restricted water by very strong wind usually exhibit a sharper spectral peak than the Bretschneider spectra. This feature has been taken

up by Hasselmann et al. (1973) in their proposal of wave spectrum, which was based on the results of the joint wave observation program for the North Sea (referred to as JONSWAP).

$$S_\eta(f) = G(f)\frac{\alpha g^2}{(2\pi)^4}\left(\frac{f_p}{f}\right)^4 exp\left[-\frac{5}{4}\left(\frac{f_p}{f}\right)^4\right] \qquad (2.55)$$

$$where \; G(f) = \gamma^{exp\left[-\frac{(f-f_p)^2}{2\sigma^2 f_p}\right]}$$

The JONSWAP spectrum is characterized by a parameter γ which is called the peak enhancement factor; this controls the sharpness of the spectral peak (see Figure 2:11) and is the ratio of the maximum spectral energy to the maximum of the corresponding Pierson-Moskowitz spectrum. σ defines the width on either side of the spectral peak, σ_a for f ≤ f_p and σ_b for f ≥f_p
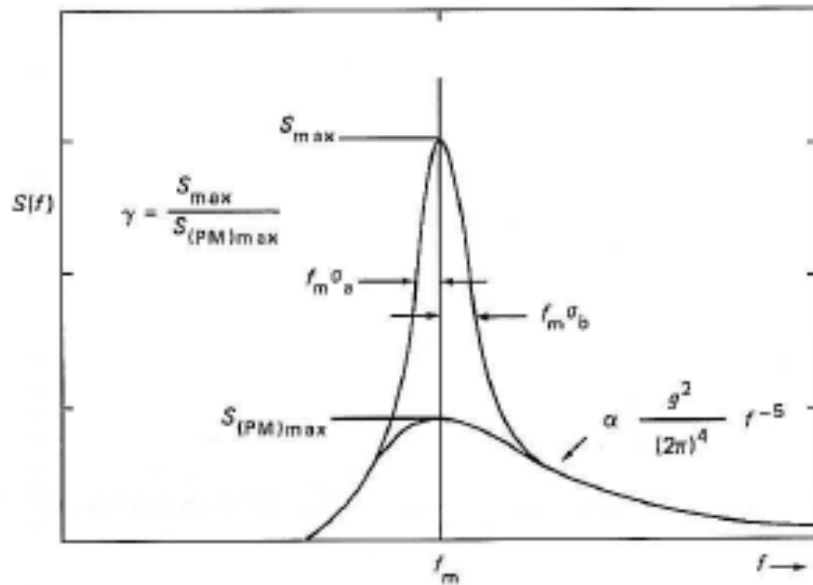
Figure 2:11: The JONSWAP spectrum, to illustrate the definitions of the parameters. The lower curve is the PM spectrum with the same f_p and α (source Tucker & Pitt (2001)

.A benefit of the JONSWAP spectra is that if one chooses a negative gamma factor, then it is possible to characterise double peaked spectra. These are spectra which occur when the sea is comprised of long period swell waves and local wind generated high frequency waves.

2.3 FFT

The link between the time domain representation of a wave signal and the amplitude of each frequency component in a wave spectrum is the Discrete Fourier Transform (DFT). The Fast Fourier Transform (FFT) algorithm revolutionised the computation of the Discrete Fourier Transform. Its efficiency rests on the fact, that it replaces the computationally infeasible procedure requiring $O(N^2)$ operations by a computationally feasible procedure requiring $O(N \log N)$ operations. Its discovery is attributed to Cooley and Tukey (Cooley & Tukey, 1965) but, it is now known that, the algorithm was first used by the eminent German mathematician, Carl Friedrich Gauss, in his determination of the coefficients of a finite Fourier series used by him to predict the orbits of celestial bodies. In the interim, it was rediscovered a number of times by other mathematicians, (most notably Karl Runge of Runge-Kutta fame), each of whom were unaware of its prior existence (Heideman, Johnson, & Burrus, 1985).

2.3.1 Short-Time Frequency Transform (STFT)

The short-time frequency transform (STFT) has been proposed as a tool to study the time frequency evolution of the properties of ocean wind waves (Guedes Soares & Cherneva, 2005). The STFT uses a window function to examine the frequency content over a certain time interval and then shifts the window along at each iteration.

A problem with the STFT lies in the selection of the window width and is actually related to the Heisenberg Uncertainty Principle: *the more precisely the position of a particle is determined, the less precisely its momentum can be known.* This principle also applies to the time–frequency information of a signal. The product of the time domain resolution and the frequency resolution is a constant, so one can have high resolution in one domain at the expense of the other but one cannot have high resolution in both the time frequency domains simultaneously.

2.4 Wavelet analysis

Wavelet analysis is fast becoming a common tool for analysing localised variations of power within a time series. By decomposing a time series into time–frequency space, one is able to determine both the dominant modes of variability and to ascertain how those modes vary in time (Torrence & Compo, 1998). According to Farge (1992) the wavelet transform originated in 1980 with Morlet working on the analysis of seismic data, and later developed further with the collaboration of Grossmann. Although, as is often the case in mathematics, the development of wavelet analysis can be linked to several different people dating as far back as 1909 with the first appearance of the Haar sequence.

Geophysical processes are often generated by complex systems which are not yet fully understood. Predictable behaviour in such systems, such as trends and periodicities, is therefore of great interest, making wavelet analysis an ideal tool in time series studies such as the Artic Oscillation index (Grinsted, Moore, & Jevrejeva, 2004), and in the El Nin˜o–Southern Oscillation (Torrence & Compo, 1998). Elsewhere, wavelet transforms have been applied in a variety of fields including signal processing, image coding, and numerical analysis. In an ocean wave energy context (Massel, 2001) used wavelet analysis to examine three separate scenarios:

- The rapid evolution of the deep-water wave field, due to the fast movement of an atmospheric front.
- The wave frequency structure transformation due to breaking on the top of a coral reef.
- A disintegration of a mechanically generated non-linear wave train in a wave tank (known as the Benjamin–Feir instability).

From an Irish wave resource perspective, Nolan, Ringwood, & Holmes, (2007) and Cahill, (2014) looked at the short term wave energy variability off the west coast of
Ireland.

Wavelet analysis is similar to Fourier analysis in that it breaks a signal down into its constituent parts. Whereas the Fourier transform breaks the signal into a series of sine waves of different frequencies, the wavelet transform breaks the signal into its wavelets which are scaled and shifted versions of the so called mother wavelet Massel, (2001).

In general, the wavelet transform (WT) of the signal, x(t), is given by

$$WT(s,\tau) = \langle x, \psi_{b,\tau} \rangle = \int_{-\infty}^{\infty} x(t)\psi_{s,\tau}(t)dt \qquad (2.56)$$

Where $\psi_{s,\tau}(t)$ is the mother wavelet given by

$$\psi_{s,\tau}(t) = \frac{1}{\sqrt{s}}\psi\left(\frac{t-\tau}{s}\right) \qquad (2.57)$$

Where τ is the translation parameter, corresponding to the position of the wavelet as it is shifted through the signal. The scale dilation parameter s determines the width of the wavelet. Small scales (s<1) compress the wavelet and are used to detect high frequency components whereas larger scales (s>1) expand the wavelet and are used to locate low frequency segments of the signal.

The wavelet coefficients $WT(s,\tau)$ are essentially a measure of the amount of correlation between the individually scaled and shifted wavelets and a localised section of the time series being analysed. Thus, if at a certain location in the signal, a particular scaled version of the mother wavelet shows a high degree of correlation with the signal, then the wavelet coefficients calculated at this point will be relatively large.

To be "admissible" as a mother wavelet, this function must have zero mean and be localized in both time and frequency space. The mother wavelet is itself of finite length and typically a fast decaying oscillating waveform. The Morlet wavelet is a very common mother wavelet and it has been used for analysis in this study. The Morlet wavelet is given by

$$\psi(t) = exp\left(\frac{-t^2}{2}\right)exp(ict) \qquad (2.58)$$

Whose real component is a plane wave of frequency c, modulated by a Gaussian envelope of unit width as depicted in Figure 2:12.
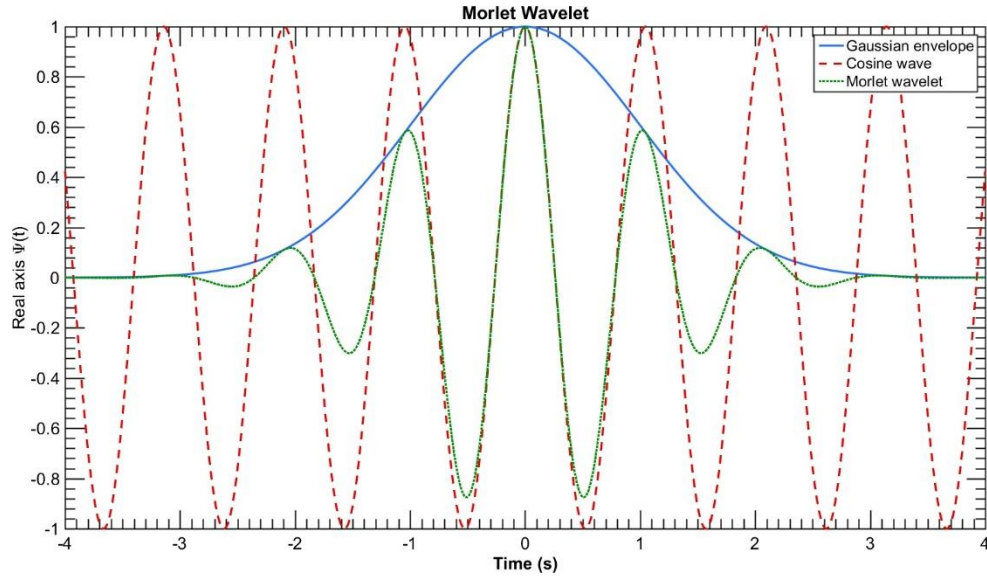
Figure 2:12: Morlet wavelet

Using the representation in (2.57) yields,

$$\psi_{s,\tau}(t) = \frac{1}{\sqrt{s}} \, exp\left[-\frac{1}{2}\left(\frac{t-\tau}{s}\right)^2\right] exp\left[ic\frac{t-\tau}{s}\right] \qquad \textbf{(2.59)}$$

The frequency nature of c is evident if we choose $c = 2\pi$, for then (2.59) becomes

$$\psi_{s,\tau}(t) = \frac{1}{\sqrt{s}} \, exp\left[-\frac{1}{2}\left(\frac{t-\tau}{s}\right)^2\right] exp\left[i\frac{2\pi}{s}(t-\tau)\right] \qquad \textbf{(2.60)}$$

With the exponential term $exp\left[i\frac{2\pi}{s}(t-\tau)\right]$ representing a sinusoidal wave of frequency $2\pi/s$. Therefore it is possible to treat the scale dilation parameter s as a period. In this study a c value of 6 is chosen in order to meet the admissibility criterion that the wavelet function has zero mean, a condition necessary to ensure that the inverse wavelet transform can be carried out smoothly. When c = 6, then the errors due to non-zero mean are smaller than the typical computer round-off errors (Farge, 1992). This study uses wavelet routines compiled by (Torrence & Compo, 1998) for Matlab. The usefulness of wavelets, in determining temporal variation in a wave train record will be discussed further in section 6.3.2.

2.5 Equation of motion of a heaving point absorber

A freely floating structure will have six degrees of freedom as depicted in the figure below.
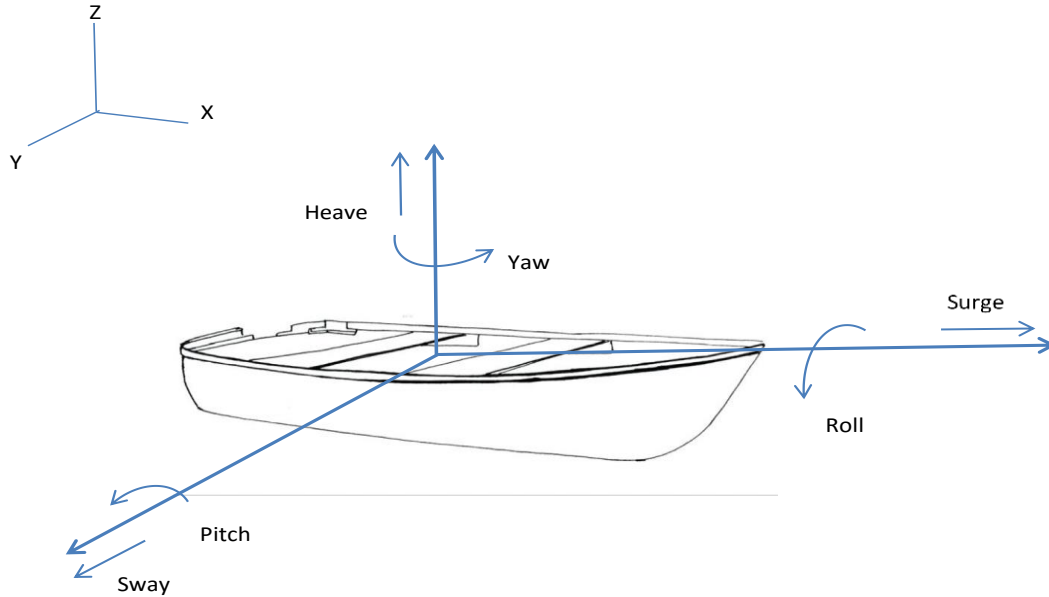
The three translation modes are, surge sway and heave, while the rotational modes are roll, pitch and yaw. The point absorber devices described in this thesis are constrained to move in a single degree of freedom (SDOF) only, and the direction is heave. The reason for constraining the device is to accommodate the PTO mechanism, which can only extract energy in a SDOF. Additionally the devices tested are axisymmetric about the z-axis.
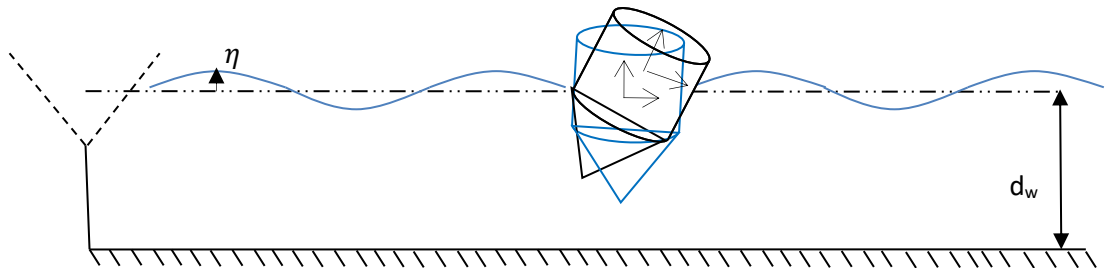
Figure 2:13: Sketch of wave body interaction

Using the methodology of Falnes (2002), select a coordinate system with the z axis through the centre of gravity of a body immersed in water. Further, we choose a reference point (z=z$_0$) on the z axis, for instance the centre of gravity or z=0. The body has a wet surface S, which separates it from the water. Consider a surface element dS at position $\vec{s}$. The vector $\vec{s}$ originates in the chosen reference point. Let $\vec{U}$ be the velocity of the reference point. The surface element dS has velocity

$$\vec{u} = \vec{U} + \vec{\Omega} x \vec{s} \qquad\qquad \textbf{(2.61)}$$

Where $\vec{\Omega}$ is the angular velocity vector corresponding to rotation about the reference point. Thus, with no rotation $\vec{u} = \vec{U}$ (as in our case restricted to heave) and with no translation $\vec{u} = \vec{\Omega} x \vec{s}$.

To account for wave-body interactions, a velocity potential needs to be found that satisfies

- the Laplace equation
- the boundary conditions on the seabed
- the boundary conditions at the free surface
- the boundary conditions on the submerged body surface
- the boundary condition at infinity.

Since the system is assumed linear, the resulting motion in waves can be seen as a superposition of the motion of the body in still water and the forces on the restrained body in waves (as shown in Figure 2:14). The hydrodynamic (radiation) loads are related to oscillating the device is otherwise still water (forced oscillation tests). The wave excitation forces are determined when waves are sent towards the buoy as it is held fixed in position.

The potential can therefore be separated into two components: a diffraction potential Φ_d, where the body is held fixed in the fluid and a radiation load Φ_r, where the body is oscillating in still water. The velocity potential for the entire problem is then the linear combination of the velocity potentials of each sub-problem:

$$\Phi = \Phi_d + \Phi_r \qquad\qquad \textbf{(2.62)}$$
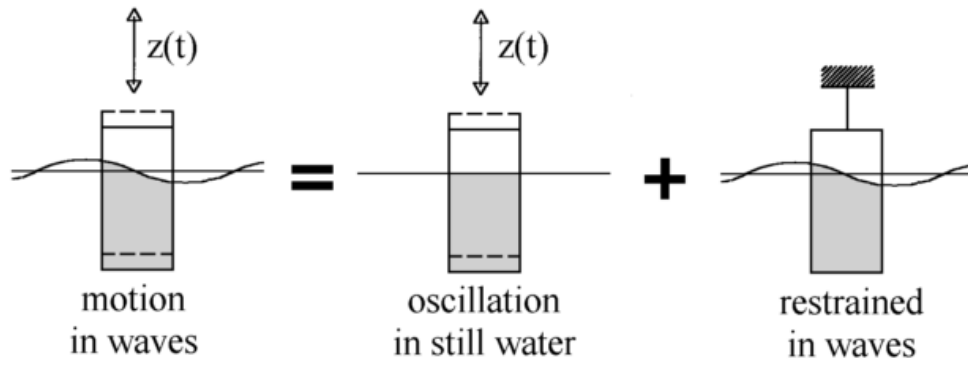
Figure 2:14: Superposition of hydrodynamic and wave excitation loads (source Journée & Massie, (2001))

The diffraction potential can be further subdivided into two parts: the incident wave field velocity potential Φ_I, which is the velocity potential due to the incident waves without the floating body being present, and the scattering velocity potential Φ_s, which is related to the disturbance felt by the wave field due to the presence of the floating body.

2.5.1 Radiation potential

When a body is oscillating in still water, radiated waves will travel away from the body. The force involved with this is called the radiation force. The radiated wave will have a velocity potential Φ_r which in the more general case is a superposition of radiated waves caused by each of the six oscillation modes. Adopting the formulation of Falnes (2002)

$$\Phi_r = \sum_{j=1}^{6} \varphi_j \vec{u}_j \qquad (2.63)$$

Where the j subscript represents the mode of motion. The radiation potential must satisfy the boundary conditions described previously as well additional boundary condition on the body

$$\frac{\partial \varphi_j}{\partial n} = n_j \qquad (2.64)$$

On the wetted surface S with n being the normal vector with six components corresponding to the modes of motion.

2.5.2 Diffraction potential

Referring to Figure 2:14, the diffraction potential is considered when the body is held fixed in the presence of incoming waves. As well as satisfying the Laplacian, free surface and seabed boundary conditions the diffraction potential must also satisfy a condition on the wetted body surface S.

$$\frac{\partial \Phi_D}{\partial n} = -\frac{\partial \Phi_I}{\partial n} \qquad (2.65)$$

Where Φ_I represents the undisturbed incident wave potential.

2.5.3 Pressures and forces

A great strength of linear theory is that once a solution is found for each of the component potentials. The total velocity potential can then be represented as the sum of the individual terms. For a body oscillating in six degrees of freedom the harmonic potential with angular frequency ω can be written

$$\Phi = \mathbb{R}\left[\left(\sum_{j=1}^{6} \varphi_j \vec{u}_j + \Phi_I + \Phi_S\right) e^{-i\omega t}\right] \qquad (2.66)$$

The pressure is obtained from Bernoulli's equation

$$p = -\rho \mathbb{R}\left[\left(\sum_{j=1}^{6} \varphi_j \vec{u}_j + \Phi_I + \Phi_S\right) e^{-i\omega t}\right] - \rho g z \qquad (2.67)$$

The hydrodynamic force acting on the body can be obtained by integrating the pressure over the surface area of the wetted surface.

$$F_H = \iint_S p \boldsymbol{n} dS \qquad (2.68)$$

Since we are restricting the device motion to heave as depicted in the sketch, we ignore the summation terms (dropping the index of mode of motion) and consider the forces involved for this specific case. A schematic of the setup is given in. The device of draft d is floating

in water of depth d_w. A belt and pulley system allows for the addition of supplementary mass. By placing mass on either side of the belt the total inertia of the system can be changed without altering the draft of the device.
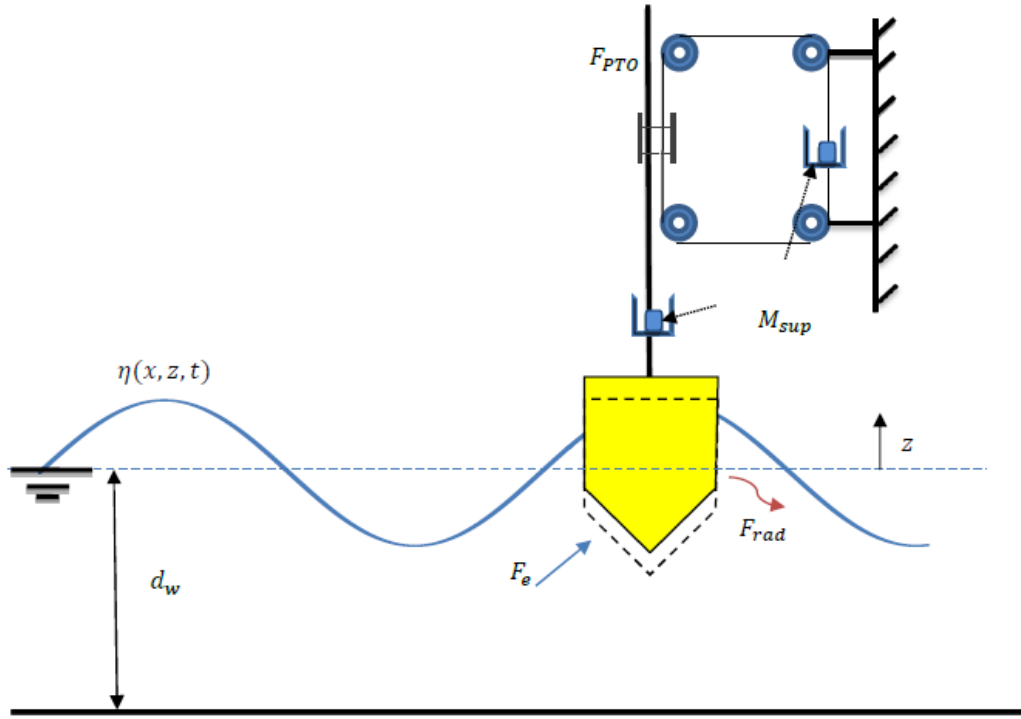
Figure 2:15: Sketch of point absorber set-up used

The equation of motion of the point absorber is given by

$$m\ddot{z}(t) = F_e(t) + F_{rad}(t) + F_{hyd}(t) + F_{PTO}(t) + F_{Tun}(t) \tag{2.69}$$

Where m is the mass of the buoy, F_e the excitation wave force and F_{rad} is the radiation force.

It is often useful to work in the frequency domain rather than the time domain. The frequency domain makes use of linear waves and the superposition principle. Making use of complex representation, the excitation force (often termed scattering force in older papers e.g. (Evans, 1981)) is the force the body would experience if it were held fixed in position.

$$F_e(t) = \mathbb{R}\{\mathbb{X}e^{-i\omega t}\} \tag{2.70}$$

$$\mathbb{X} = \mathbb{X}_i + \mathbb{X}_s \tag{2.71}$$

Note the double lettering style($\mathbb{X}$)is employed to signify a complex value as was used by Thomas (2008). The force is a comprised of two separate elements, the incident force and the diffracted force. The incident force $\mathbb{X}_i$ is obtained by integrating the known pressure due to the incident waves over the wetted body surface. The scattered force relates to the modulation of the incident wave due the presence of the device. This is often a difficult quantity to calculate and often numerical codes are employed to do so. It is common to see "scattered" and "diffracted" interchanged sometimes referring to the total force (comprised of two parts) and the part of the force relating to the pressure field of the altered wave integrated over the body. The form taken above is to maintain consistency with the potential discussed earlier.

The radiation force F_{rad} is the force related to the oscillatory motion of the device in otherwise still water. This is a complex quantity and is dependent on the shape of the device as well as the frequency of oscillation. It is customary to represent the force as containing both real and imaginary parts, one in phase with acceleration (added mass) and the other in phase with the velocity (damping) of the WEC.

$$F_{rad} = -\left[A(\omega)\ddot{Z} + B(\omega)\dot{Z}\right] \tag{2.72}$$

The frequency dependant added mass ($A(\omega)$, is often considered as the additional mass of the surrounding fluid, which is also excited by the device motions. Care must be given here however, as in certain scenarios the added mass can take a negative value. Mciver & Evans, (1984) write that for a deeply submerged body, the added-mass coefficient can be interpreted as the fluid mass accelerated by the body and is positive. However, when free-surface effects are important this need not be so. Ogilve (1963) calculated added-mass coefficients for a submerged horizontal cylinder. He found that when the depth of submergence is sufficiently small, compared to the diameter of the cylinder, the added mass is negative over a range of frequencies. Added mass depends on the type of motion of the body or of the fluid about the body: proximity of other bodies, free surface, etc. and time. It is not always possible or advisable to determine the instantaneous value of the added mass coefficient (Sarpkaya & Isaacson, 1981).

The hydrodynamic damping coefficient $B(\omega)$ is a measure of the energy flux in the waves radiating away from the oscillating body and is necessarily non-negative (Newman, 1977). Radiation damping is a function of frequency meaning waves of different height are radiated depending on the oscillation (or in forced oscillation tests the driven) frequency. The ability of a device to radiate waves depends on its shape, draft and mode of motion.

The hydrostatic restoring force F_{hyd} is equal to the Archimedes force F_{arch} minus the gravitational force F_g:

$$F_{hyd} = \rho g V(t) - Mg \tag{2.73}$$

Assuming the heave excursions are small, then the hydrostatic force can be approximated by

$$F_{hyd} = -CZ(t) = -\mathbb{R}\{CZe^{-i\omega t}\} \tag{2.74}$$

Where c is the hydrostatic spring constant $\rho g A_w$, with A_w being the waterline area.

The PTO force F_{PTO} is the force which opposes the motion of the floater with aim of capturing useful power. The tuning force arises form the supplementary mass added to the system (on either side of a closed loop pulley system as shown in Figure 2:15Figure 2:15: Sketch of point absorber set-up used. The purpose of the supplementary mass is to add inertia to the system, without changing the draft, thereby tuning the device towards different frequencies.

$$F_{tun} = M_{sup}\ddot{Z}(t) \tag{2.75}$$

2.5.4 Power absorption and capture width

The instantaneous power absorption is given by

$$P_{inst} = F_{PTO}(t) \; x \; \dot{Z}(t) = F_{PTO}(t) \; x \; U(t) \tag{2.76}$$

The average absorbed power over a time interval [T1 –T2] is therefore

$$P_{abs,avg} = \int_{T1}^{T2} \frac{P_{inst}}{T_2 - T_1} dt \tag{2.77}$$

An alternate form of the equation above is to make use of the $\langle \; \rangle$ brackets denoting time average over a specific period

$$P_{abs,avg} = \langle F_{PTO}(t) \; x \; U(t) \rangle \qquad \text{(2.78)}$$

The 'capture width', denoted by $\mathcal{L}$, is the ratio of the absorbed power to the average available power per unit crest length. i.e.

$$\mathcal{L} = \frac{P_{abs,avg}}{P_{avail}} \qquad \text{(2.79)}$$

The available power (per metre crest) was given earlier in equation (2.51)

Evans (1981) gives the result for total mean power absorbed by the device as

$$P_{abs,avg} = \frac{1}{8}|\mathbb{X}_s|^2/B - \frac{1}{2}|U_0/B - \mathbb{X}_s/B|^2 B \qquad \text{(2.80)}$$

Where U_0 is the complex amplitude of the body velocity, a parameter which can be controlled to yield the maxium potential power of.

$$P_{abs,avg} = \frac{1}{8}|\mathbb{X}_s|^2/B \qquad \text{(2.81)}$$

Which is theoretically attainable (ignoring losses) when the velocity has amplitude of

$$U_0 = \frac{\mathbb{X}_s}{2B} \qquad \text{(2.82)}$$

Falnes (2003) makes use of the Haskind relation between the hydrodynamic damping and excitation force vector; which for an axisymmetric buoy in heave is given as

$$B = \frac{k}{8P_{avail}}|\mathbb{X}_s|^2 \qquad \text{(2.83)}$$

Placing the value for B back into (2.81) and recalling the definition of capture width (2.79) leads to a key result of point absorber theory; that the maximum theoretical capture width depends only on the incoming wave length. For a point absorber oscillating in heave

$$\mathcal{L}_{max} = \frac{L}{2\pi} \qquad \text{(2.84)}$$

This is known as the 'point-absorber effect' or 'antenna effect' and is explained by the fact that the point absorber is able to absorb a larger fraction of the power than is available over its diameter. This result was discovered independently in the mid-70s

(during an era of increased interest in renewable energies due to an oil crisis) by Budal & Falnes (1975), Evans (1976), Newman (1976) and Mei (1976). While many heaving buoys can be classed as point absorbers, providing their characteristic dimension is small in comparison with the incoming wavelength, not all point absorbers need to be heaving buoys. Many OWC devices, OE buoy for example as well the oscillating flap Oyster device can also be classed as point absorbers. In fact Evans (1976) showed that for an axisymmetric device (symmetric about the vertical z-axis) oscillating in a single degree of freedom, the theoretical maximum capture width is

$$\mathcal{L}_{max} = \varepsilon \frac{L}{2\pi} \tag{2.85}$$

Where ε = 1 for heave as established previously and $\varepsilon = 2$ for pitch and surge. The maximum capture width is twice as much when using the horizontal motions of surge and pitch compared to the vertical motion of heave.

Dividing the capture width by the diameter D of the buoy gives the Capture Width Ratio (CWR) of the device. This metric will be used extensively throughout this thesis.

$$CWR = \frac{P_{abs,avg}}{P_{avail} \; x \; D} \tag{2.86}$$

2.6 Mass Spring Damper

Existing mass spring damper or vibration theory is directly applicable to point absorbers devices. Using standard notation, the governing equation is given by

$$m\ddot{z} + b\dot{z} + cz = 0 \tag{2.87}$$

Dividing by m yields,

$$\ddot{z} + 2\zeta\omega_n\dot{z} + \omega_n^2 z = 0 \tag{2.88}$$

Where

$$\zeta = \frac{b}{2m\omega_n} \qquad (2.89)$$

$$\omega_n = \sqrt{\frac{c}{m}} \qquad (2.90)$$

Here ω_n is the natural frequency (in rad/s) of the system and ζ is a measure of damping present in the system relative to the critical level of damping. In an actual vibration, there will always be some damping present. The solution of equation (2.88) must be a function which has the property that repeated differentiations do not change its form since the function and its first and second derivatives must be added together to give zero (Housner & Hudson, 1950). Assume a solution of the form;

$$z(t) = Ae^{\alpha t} \qquad (2.91)$$

Substituting equation (2.91) into equation (2.88) yields the characteristic equation,

$$\alpha^2 + 2\zeta\omega_n\alpha + \omega_n^2 = 0 \qquad (2.92)$$

An equation, whose roots are

$$\alpha_1 = \omega_n\left(-\zeta + \sqrt{\zeta^2 - 1}\right), \quad \alpha_2 = \omega_n\left(-\zeta - \sqrt{\zeta^2 - 1}\right) \qquad (2.93)$$

The general solution of the governing equation is therefore

$$z(t) = A_1 e^{\alpha_1 t} + A_2 e^{\alpha_2 t}$$

$$= A_1 e^{\left(-\zeta + \sqrt{\zeta^2 - 1}\right)\omega_n t} + A_2 e^{\left(-\zeta - \sqrt{\zeta^2 - 1}\right)\omega_n t} \qquad (2.94)$$

The physical significance of the solution depends on the amount of damping present. There are three distinct scenarios to be considered:

$\zeta > 1$: The system is said to be overdamped; the roots α_1, α_2 are real negative numbers. When an overdamped system is given an initial displacement, the damping is sufficiently large to ensure the mass never oscillates past the static equilibrium position but rather exponentially subsides.

$\zeta = 0$: The system is said to be critically damped with $\alpha_1 = \alpha_2 = -\omega_n$. A critically damped system when displaced will return to its equilibrium position without oscillating.

$\zeta < 0$: The system is underdamped. Such a system, when given a displacement, will oscillate about the equilibrium before eventually coming to rest. The frequency of oscillation is known as the damped angular frequency ω_d, and is given by

$$\omega_d = \omega_n \left(\sqrt{1 - \zeta^2}\right) \tag{2.95}$$

Rearranging equation (2.94) gives

$$z(t) = \left\{ A_1 e^{i\left(\sqrt{1-\zeta^2}\right)\omega_n t} + A_2 e^{-i\left(\sqrt{1-\zeta^2}\right)\omega_n t} \right\} e^{-\zeta\omega_n t}$$
$$= \left\{ A_1 e^{i\omega_d t} + A_2 e^{-i\omega_d t} \right\} e^{-\zeta\omega_n t} \tag{2.96}$$

Euler's identity $e^{i\theta} = \cos(\theta) + i\sin(\theta)$, allows the displacement to be written

$$z(t) = e^{-\zeta\omega_n t}\{ (A_1 + A_2)\cos(\omega_d t) + i(A_1 - A_2)sin(\omega_d t)\}$$
$$= e^{-\zeta\omega_n t}\{A_1' \cos(\omega_d t) + A_2' sin(\omega_d t)\} \tag{2.97}$$

Alternatively, equation (2.97) can be written in amplitude-phase form as

$$z(t) = C e^{-\zeta\omega_n t} \cos(\omega_d t + \phi) \tag{2.98}$$

In an effort to determine the hydrodynamic parameters of added mass and damping, it is usual to carry out a decay test. A decay test or extinction test is one where the buoy is initially displaced a distance z_0 from its equilibrium position and then released. The buoy then undergoes a damped free oscillation; parameters such as the natural frequency and hydrodynamic coefficients of added mass and damping can then be inferred from the recorded response of the buoy as it comes to rest. The unforced solution to a pure mass spring damper system is that of Equation (2.98) where the parameters C and ϕ are determined by the initial conditions. If the buoy is initially displaced a distance z_0, with an accompanying initial velocity $v_0 = 0$, then

$$C = \frac{z_0}{\sqrt{1 - \zeta^2}} \tag{2.99}$$

and

$$\phi = \tan^{-1}\left(\frac{-\zeta}{\sqrt{1 - \zeta^2}}\right) \tag{2.100}$$

A typical response of a damped free oscillation is shown in Figure 2:16(a). The envelope of decay is determined by the $Ce^{-\zeta\omega_n t}$ term, whilst the trigonometric term determines the frequency of oscillation.
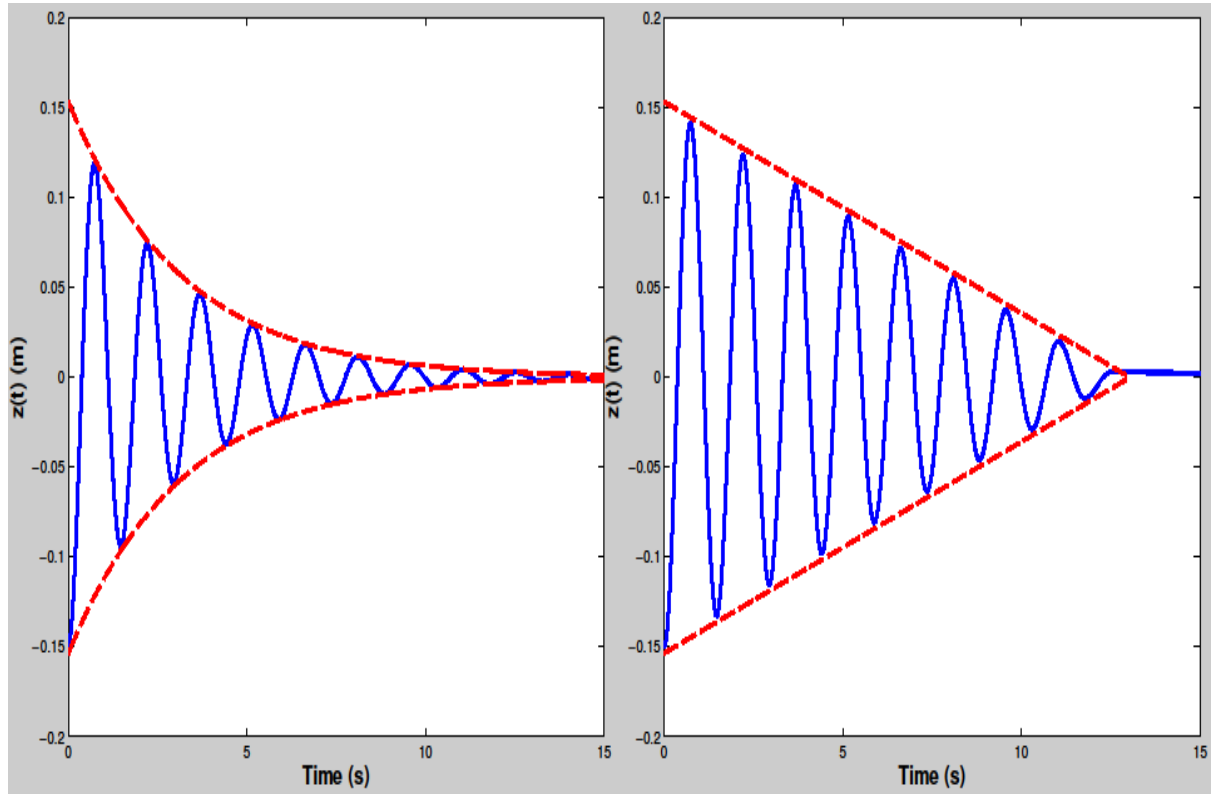
Figure 2:16: Typical free decay curve of (a) a viscously damped system; (b) Coulomb damping

According to (Feeny & Liang, 1996):

"In his *Theory of Sound*, Lord Rayleigh noted that, for the free vibration of a linear damped oscillator, 'the difference in the logarithms of successive extreme excursions is nearly constant, and is called the logarithmic decrement'. In fact, the idea goes back to Hermann Helmhotz, who in 1863 applied the logarithmic decrement to determine frequency information in musical tones given a known damping coefficient"

Therefore, the logarithmic ratio of successive peaks (called the logarithmic decrement δ) can be used to estimate the damping experimentally

75

$$\delta = \ln\left(\frac{z_1}{z_2}\right) = \zeta\omega_n T_d = \frac{2\pi\zeta}{\sqrt{1-\zeta^2}} \tag{2.101}$$

The influence of mechanical friction in any test set up cannot be ignored. If the energy dissipation in a system is achieved purely by friction, as is the case in the free response of a mass and spring with Coulomb friction, then the amplitude of successive peaks decays linearly with time as shown in Figure 2:16(b). Thus, to truly encapsulate all the dynamics of the experimental system both viscous and Coulomb damping must be considered. A method of identifying Coulomb and viscous friction from free vibration decrements is described in (Liang and Feeny 1998).

The equation of motion of a single degree of freedom SDOF mass spring damper with dry friction is

$$m\ddot{z} + b\dot{z} + cz + f(\dot{z}) = 0 \tag{2.102}$$

The dry friction will always oppose the direction of motion. Hence

$$f(\dot{z}) = f_k sign(\dot{z})$$

$$\dot{z} \neq 0, -f_s \leq f(0) \leq f_s \tag{2.103}$$

Where f_k, is the kinetic friction force and f_s is the static friction force. The equilibrium solution of Equation (2.102) can be obtained by letting $\ddot{z} = \dot{z} = 0$. A physical consequence of the friction is that the system doesn't have a single equilibrium point but rather a locus of equilibria $-z_s \leq z \leq z_s$ where $z_s = f_s/c$.

If follows from the above that if the buoy where to be submerged by some small distance $z < z_s$, then the restoring buoyancy force would not be able to overcome the stiction force so the buoy would remain stationary.

Equation (2.102) is piecewise solvable, when written as

$$\ddot{z} + 2\zeta\omega_n\dot{z} + \omega_n^2 z = -\omega_n^2 z_k \qquad \dot{z} > 0 \tag{2.104}$$

$$\ddot{z} + 2\zeta\omega_n\dot{z} + \omega_n^2 z = +\omega_n^2 z_k \qquad \dot{z} < 0 \tag{2.105}$$

Here $z_k = f_k/c$.

In a decay test the buoy is initially displaced $z(t_0) = Z_0 < -z_s$ with $\dot{z}(t_0) = 0$. Then the motion starts with $\dot{z} > 0$, and the response to equation (2.104) has the form

$$z(t) = (Z_0 + z_k)e^{-\zeta\omega_n(t-t_0)}\{cos(\omega_d(t - t_0)) + \beta sin(\omega_d(t - t_0))\} - z_k \qquad \textbf{(2.106)}$$

Where $\beta = \frac{\zeta}{\sqrt{1-\zeta^2}}$.

This equation is valid until the velocity vanishes after time $t = t_1 = t_0 + \pi/\omega_d$. If the next peak excursion point is denoted Z_1, then

$$Z_1 = z(t_1) = -e^{-\beta\pi}Z_0 + (e^{-\beta\pi} + 1)z_k \qquad \textbf{(2.107)}$$

If $Z_1 > z_s$ then the mass will reverse direction and continue moving only with $\dot{z} < 0$, so that the governing equation is now that given in equation (2.105). The solution for this interval is

$$z(t) = (Z_1 - z_k)e^{-\zeta\omega_n(t-t_1)}\{cos(\omega_d(t - t_1)) + \beta sin(\omega_d(t - t_1))\} + z_k \qquad \textbf{(2.108)}$$

This is valid until $\dot{z} = 0$ after time $t = t_2 = t_1 + \pi/\omega_d$. The next peak excursion point $Z_2 = z(t_2) = -e^{-\beta\pi}Z_1 - (e^{-\beta\pi} + 1)z_k$. If $Z_2 < -z_s$, motion will continue again. This process will repeat itself until $-z_s \leq Z_n \leq z_s$, at which time the motion stops. This iterated process leads to a recursive relation for the successive peaks and valleys in the oscillatory response:

$$Z_i = -e^{-\beta\pi}Z_{i-1} + (-1)^i(e^{-\beta\pi} + 1)z_k, \quad i=1,2,\dots,n. \qquad \textbf{(2.109)}$$

It is therefore possible to utilise successive maxima and minima points to isolate the viscous effect and then calculate the Coulomb effect. Taking the sum of extreme displacement values cancels out the friction contribution

$$\frac{Z_i + Z_{i+1}}{Z_{i-1} + Z_i} = -e^{-\beta\pi} \qquad \textbf{(2.110)}$$

Taking a logarithmic decrement gives the viscous dependence

$$\ln\left(\frac{Z_i + Z_{i+1}}{Z_{i-1} + Z_i}\right) = -\beta\pi \qquad \textbf{(2.111)}$$

2.7 Control

The most common modes of motion (in terms of energy capture are heave, surge and pitch, while yaw, roll and sway are rarely used. The natural frequency if the device is the square root of all the spring terms divided by all inertia terms.

$$\omega_n = \sqrt{\frac{\sum C}{\sum M}}$$ (2.112)

Heaving buoys and bodies that pitch about an axis close to the mean surface level naturally have high hydrostatic stiffness. Unless provided with some means of reducing the stiffness or controlling the motion, such heaving or pitching systems will have quite narrow response bandwidth, which makes them hydrodynamically inefficient wave absorbers in varying irregular seas. This flaw may be mitigated by active use of the machinery through a proper control strategy, or by including mechanical components to counteract the hydrostatic stiffness (Todalshaug, 2017). Control refers to any methods taken to achieve better power absorption, through the variation of physical parameters.
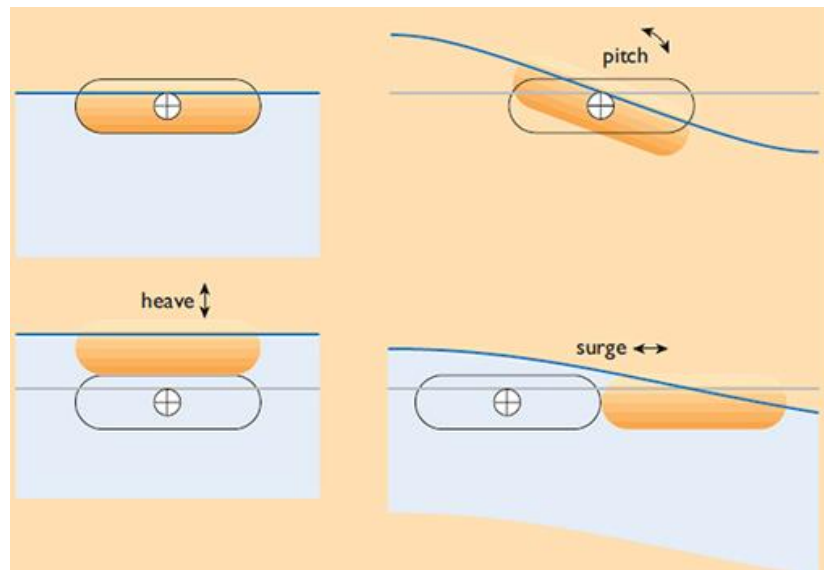
Figure 2:17: The pitch, heave and surge responses of a floating object to incident waves (source Open University (2018)

Pitching about an axis close to the surface is less volumetric efficient than surging When it comes to absorbing power. This is because such pitch motion gets its excitation from an area distributed along the direction of propagation for the wave. Surge motion on the in contrast gets its excitation mainly from areas of opposing vertical walls a distance apart (see Figure

2:17). On the other hand, it may be easier to design a practical machinery for pitching bodies than for surging bodies.(Todalshaug, 2013)

Todalshaug, (2017) states that for small bodies, heaving motion is the most volumetric efficient. This is because the heave excitation comes from a difference between atmospheric pressure at the top of the body and the full amplitude of hydrodynamic pressure at the bottom, see Figure 2:17. Surging and pitching take their excitation from a difference in hydrodynamic pressure along the wave, which is quite weak when the body is small. For large bodies the opposite is true, such that pitching and in particular surging motion are favoured over heaving motion. Systems combining power extraction from two or three modes of motion have the potential of giving a more efficient use of the installed structure.
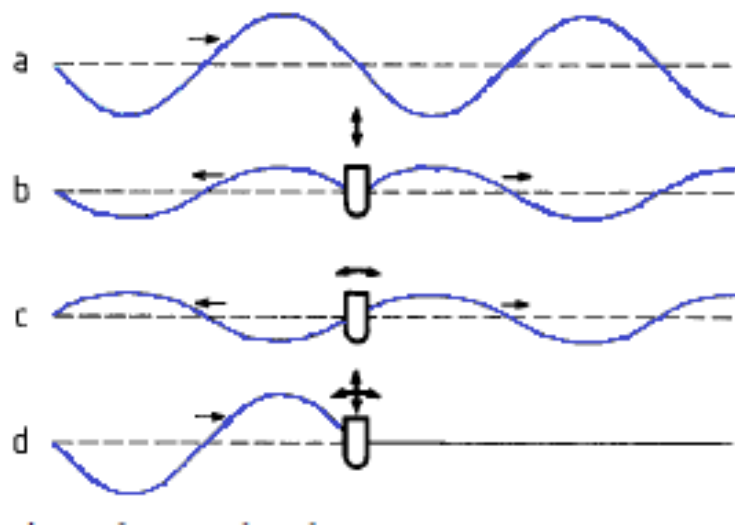
Figure 2:18: Sketch showing complete absorption of the incoming wave (source Falnes (2002))

To absorb waves means to generate waves. In Figure 2:18 curve (a) represents an undisturbed incident wave. Curve (b) illustrates symmetric wave generation (on otherwise calm water) by means of a straight array of evenly spaced, small floating bodies oscillating in heave. Curve (c) illustrates antisymmetric wave generation. Curve (d), which represents the superposition (sum) of the above three waves, illustrates complete absorption of the incident wave energy Falnes (2002). To absorb energy from an incident wave, the radiated waves emitted from the surface(s) of an oscillating system must destructively interfere with the incident wave (Wypych et al (2012))

The surge, sway and yaw modes have no restoring forces, and station-keeping forces must be supplied by moorings or other mechanisms. University of Exeter (Parish, 2015 for

example) are conducting interesting work into the use of dynamic moorings with a view to increase energy yield. This is a potentially advantageous avenue of research although the reliability of such systems as well as the economic considerations of mooring installation and operation and maintenance are crucial. Connecting moorings at sea is a difficult task and the larger the operational load the more expensive the charter vessel.

The fundamental purpose of control is to force the device to move in such a way as to increase power capture. For maximum power extraction, there exists an optimum motion path (position and velocity) that should be followed, and such a path depends on the incident wave. The response is governed by the combination of inertia, stiffness, damping and machinery (PTO) forces. This means that the response may be improved either by the design of the buoy (inertia, stiffness and wave damping), or by using the machinery to get closer to the optimum trajectory. In practice we often use a combination of the two (Todalshaug, 2017).

Geometry control

Geometry control relates the first option mentioned above whereby some fundamental property of the device is physically changed as opposed to using the PTO directly. For example the spring constant of the AWS device can be changed by changing the air pressure and volume inside the submerged chamber (Polinder, Damen, & Gardner, 2004). Likewise, the sloped IPS device can change its spring constant by restraining the motion of the device to an intermediate direction between surge and heave (Payne, 2006). Altering the angle of the device varies the natural frequency and bandwidth of the device. The submerged pressure differential CalWave (2018) device is another interesting WEC which utilises geometry control, coming second in a recent U.S Dept. of Energy Wave Energy Prize, (2018). Another example of geometric control would be the use of ballast to change the mass of a floating structure (which also changes the draft and hydrodynamic parameters of the device) Nolan, (2006)

Complex conjugate control

Complex conjugate control relates to the other option which is to implement machinery forces for the purposes of control. The method can be accredited to Nebel (1992) who

implemented the strategy using an experimental model Salters Duck. In order to maximize wave-energy input to an oscillating body, one necessary condition is that the body's velocity should be in phase with the wave's excitation force acting on the body. This condition is automatically fulfilled at resonance, that is, if the wave frequency equals the natural frequency of the oscillating body. At resonance, the oscillator's mechanical reactance vanishes, off resonance, however, the oscillator has a finite mechanical reactance. Complex conjugate control cancels out this intrinsic reactance by using the PTO to supply external reactance of an opposite sign, thus the oscillation velocity is in phase with the excitation force (Falnes & Bjarte-larsson, 2006). This optimal control method requires advanced knowledge of the incoming wave profile as well as the requirement to input power at very high efficiency to the WEC at certain instances in time. The method simultaneously satisfies the optimum amplitude trajectory and the optimum phase condition

Latching (phase) control

Another method which seeks primarily to satisfy the optimum phase control, such the buoys velocity is in phase with the excitation force is known as latching or phase control. The principal of the method is shown in
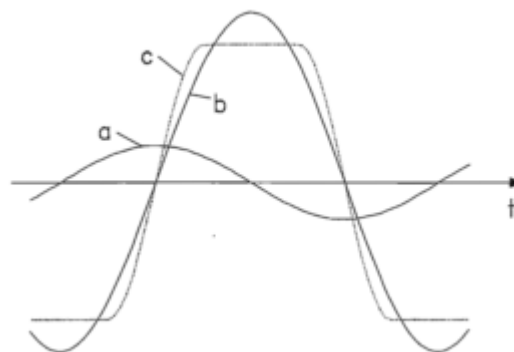
Figure 2:19: Latching principal, (a) is the wave elevation, (b) the optimum displacement of the body and (c) the actual displacement using latching. (Source Falnes (2002))

The method works by holding the device in position at certain moments during the wave cycle (when the velocity is nil) and releasing the device at a later stage such that the velocity is now in phase with the excitation force. In doing so, the amplitude of the device is increased along with power capture. The method can be accredited to Budal & Falnes (1975).

2.8 Viscous losses and vortex shedding

When a bluff cylindrical body such as a circular cylinder is moved with constant velocity normal to its axis, one might expect the resulting flow to be steady and laterally symmetrical. In fact, neither of these assumptions is correct, because of the oscillatory shedding of vortices (Newman, 1977).

Boundary layers

In 1904, Prandtl set out the basics of boundary layer theory, proposing that all viscous effects are concentrated within it (Pijush K & Iran M, 2007). The fluid in immediate contact with a solid boundary cannot move relative to that surface - the no-slip condition. The physical tangential velocity on the surface therefore must be zero (Faltinsen, 1990). This is at odds with the boundary conditions of diffraction modelling where fluid velocities tangential to surfaces are not zero. As a result of the no-slip condition, velocity gradients will be high moving outward from the surface until the velocity matches that of the free stream velocity. This layer of high velocity gradients, where viscous effects are appreciable, is known as the boundary layer.
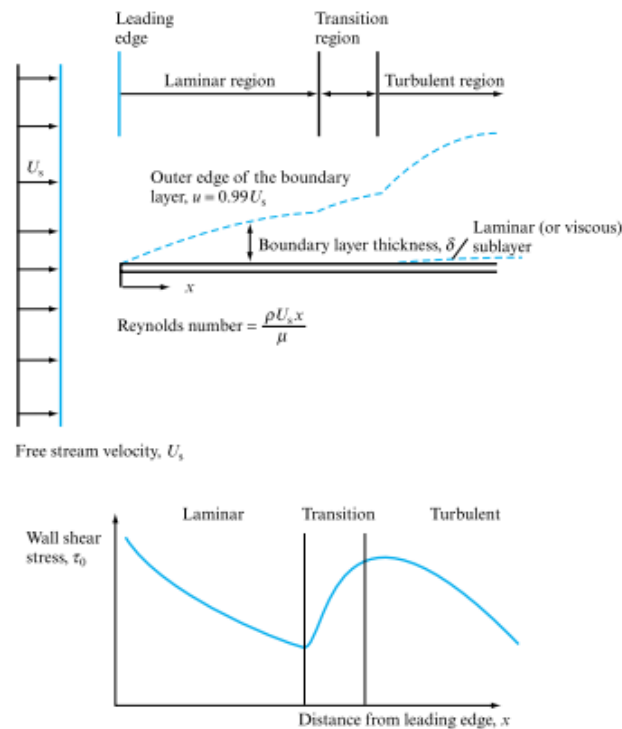
Figure 2:20; Development of the boundary layer along a flat plate, illustrating variations in layer thickness and wall shear stress (source (Douglas et al (2005))

Fluid mechanics textbooks typically explain boundary layer by depicting fluid flow over cylinders, hydrofoils or horizontal plates as depicted in the figure above. Figure 2:20 shows a steady velocity flow from the left. The horizontal velocity at the plate must be zero according to the no slip condition. This will set a region of where there exists a velocity gradient, within which viscous effects are significant. Boundary layer flow, can be laminar or turbulent, depending on the value of the Reynolds number involved. Munson et al (2009) define the boundary layer thickness as the distance from the plate at which the fluid velocity is within some arbitrary value of the upstream velocity (typically 99%).

The use of an inviscid model for the entire fluid, therefore, requires the thickness of the boundary layer to be small, such that it can be neglected. Alternatively, its thickness should be known and this region accounted for separately from the remaining flow using viscous theory. The remaining flow, adhering to the inviscid assumption, can be modelled using inviscid theory and the flow conditions at the interface between the two regions provides the boundary condition for the viscous boundary layer equations (Sykes & Thomas, 2011).

Flow separation

Under certain conditions, flow may separate from a solid boundary. The main parameters affecting this phenomenon are the fluids velocity and viscosity, the bodies shape and surface roughness, and the angle of attack between the flow and body. Sharp corners are likely to induce flow separation.

Chapter 3: Wave Basin Tests

3.1 Introduction

The Hydraulics and Maritime Research Centres (HMRC) wave basin, located at Pouladuff was originally built by Edinburgh Designs for UCC in 1993. The original paddles and driving system was in need of an overhaul. Acquiring extensive knowledge of wave basin dynamics was an essential prerequisite to the objectives of this research. At the time the basin tests (to be described in this chapter) were carried out, the final WEC concept for experimental work had not been finalised. The rationale for carrying out these tests was therefore twofold; to gain familiarity with the basin for future work, and to determine characteristics such as reflections, which would influence the decision of WEC concept for future work. For example to provide efficiency curves on an oscillating surge wave converter would require the separation of the incident wave field from reflected.

With this in mind, a comprehensive series of tests to analyse the performance of the wave basin were carried out. Both regular and irregular waves at a variety of different wave periods and wave heights were tested. The tests determined how the wave basin performs under conditions commonly used for physical modelling purposes. As a result of the work carried out, key performance parameters such as water surface elevations and reflection coefficients were obtained.

Theory on additional topics, evanescent waves, cross waves and deep water instability are briefly discussed here. These phenomena are more pertinent to the isolated topic of wave generation in a basin (the focus of this chapter). For this reason, these topics are presented here rather than in the earlier theory section.

3.2 Evanescent waves

Recalling the dispersion relationship which tells us how the relationship between frequency and the wavenumber, which out is the separation constant discussed earlier.

$$\omega^2 = gk \tanh(kd_w) \qquad \text{(3.1)}$$

However, it is possible for the wavenumber to take up imaginary values, and all solutions whether real or imaginary must be considered. Letting k=ik leads to

$$\omega^2 = -gk \tan(kd_w) \tag{3.2}$$

This equation has an infinite number of solutions which correspond with the evanescent modes. The eigenfunction expansion is a superposition of all these modes and is given by Mei et al. (2005)

$$\phi(x,z) = a_0 f_0(z) e^{\pm ikx} + \sum_{n=1}^{\infty} b_n f_n(z) e^{\mp k_n x} \begin{cases} x_+ < x < \infty \\ x_- > x > -\infty \end{cases} \tag{3.3}$$

The first term corresponds to the propagating mode, while the series terms are only of local importance and are called the evanescent modes. Evanescent waves appear on the surface as standing waves and decay in amplitude exponentially with distance away from the wavemaker. Evanescent waves can contaminate the test area in a wave tank distorting the wave field from the intended sea state; however, this is generally avoided by leaving a distance of two to three times the still water depth between the wavemaker and the test area since we know that the evanescent waves decay over distance away from the wavemaker (Keaney, 2015).

Falnes (2002) proposed that, if the wavemaker paddle profile is chosen, such that it matches the wave field velocity profile of the waves, then the evanescent waves will be cancelled out. Maguire & Ingram (2011) consider (numerically) four different wacemaker profiles for active absorption as shown in Figure 3:1.
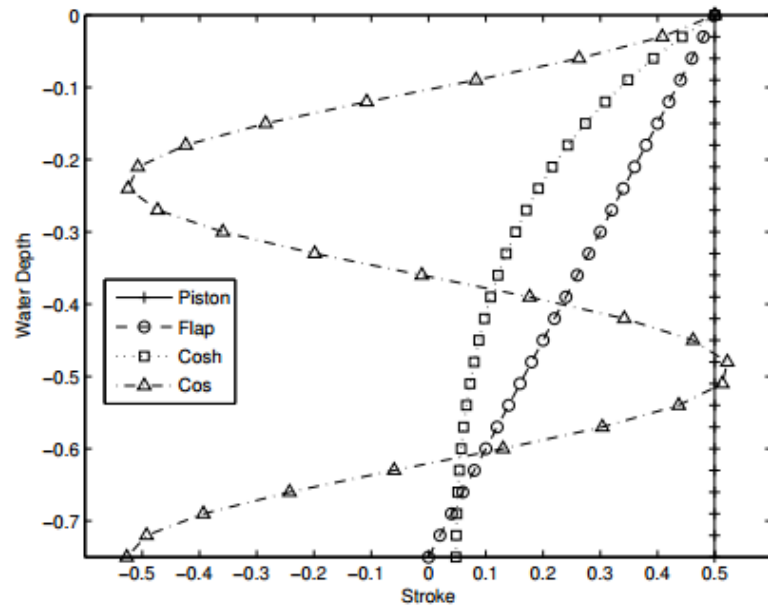
Figure 3:1: Four different wavemaker shape profiles (source Maguire & Ingram (2011))

In addition to different shape profiles, different control strategies were also considered for absorbing wavemakers; mass-spring-damping, spring-damping, mass-damping and damping. Results showed that absorption of incoming waves is sensitive to the shape, the control strategy used to implement the absorption and also the choice of tuning frequency in the control strategy. It was shown that the best absorption, at frequencies between π rad/s and 3.5π rad/s, was achieved with a hyperbolic cosine, cosh, wavemaker with control coefficients tuned to a frequency of $\omega_p = 3\pi$ using a mass-spring-damper control system.

Maguire (2011) states that the works purpose is not the recommendation of building a cosh shaped wavemaker as it would prove difficult; Rather that shaped absorbing wavemaker, however, could be used as a numerical boundary condition to deal with unwanted wave reflections in numerical wave tanks, offering an alternative to other methods that can be computationally intensive and the potential for improved results.

For further reference see Maguire (2011).

3.3 Seiche and Cross waves

Unwanted amplifications are often caused when the basin is excited at a frequency corresponding with a resonant mode dependant on the geometry of the basin. These can occur in the longitudinal and transverse directions, termed seiche and cross waves. In a similar manner to a guitar string having resonant frequencies depending on its length, so too, the seiche and cross-waves resonant frequencies are determined by basin length and width respectively. In reality the guitar string is a simpler analogy, as with a basin, water depth and indeed the amplitude and frequency of the forcing wave also play a role. Resonant modes have shape which is a function of the basin geometry, and a problem with wide basins that as the width increases; so too does room for integer number of resonant cross waves. I.e. more resonance frequencies lie within the working frequency range of the tank. The resonant modes occur for integer multiples of n and m such that the free surface elevation η takes the form below as given by Sykes & Thomas (2011).

$$\eta(x, y, t) = A_{nm} \cos\left(\frac{n\pi x}{L}\right) \cos\left(\frac{m\pi y}{W}\right) \tag{3.4}$$
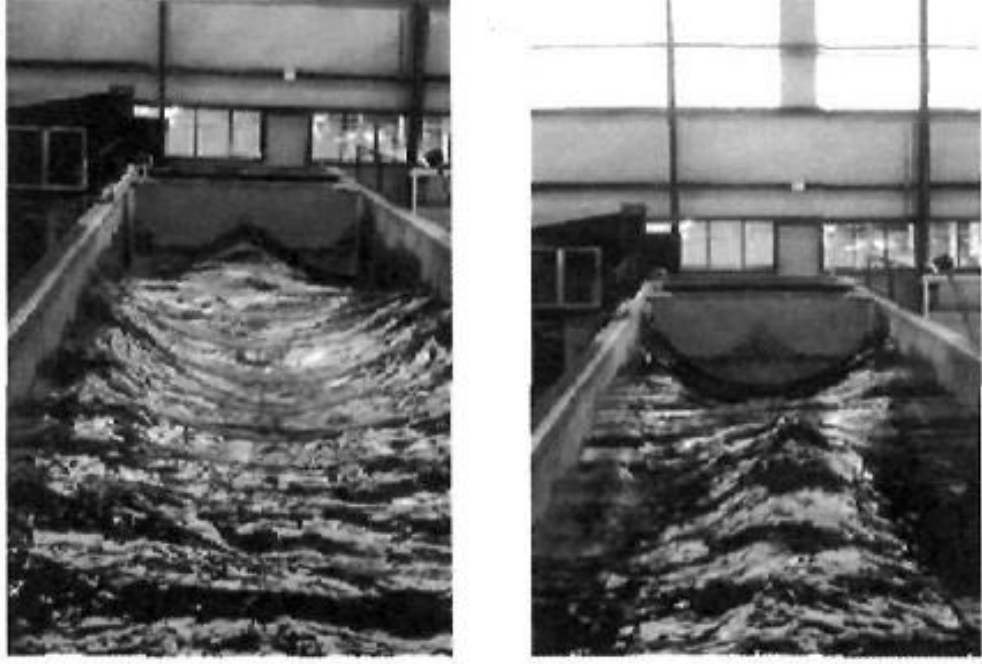
Figure 3:2: Snapshot of cross waves at two instances of time at the 2D wave channel at the O. H. Hinsdale Wave Research Laboratory (OHH-WRL), Oregon State University (source Hudspeth, 2006).

Where L and W are the x and y dimensions of the basin respectively. The associated wavenumbers are

$$k_{nm} = \sqrt{\left[\left(\frac{n\pi}{L}\right)^2 + \left(\frac{m\pi}{W}\right)^2\right]} \qquad \textbf{(3.5)}$$

Making use of the dispersion relationship, the natural periods are then given by

$$T_{nm} = \sqrt{\frac{4\pi}{g\sqrt{\frac{n^2}{L^2} + \frac{m^2}{W^2}}\ tanh\left(h\pi\sqrt{\frac{n^2}{L^2} + \frac{m^2}{W^2}}\right)}} \qquad \textbf{(3.6)}$$

Referring to the basin description sketch in Figure 3:5, the length of the basin L (x dimension) is 23.25 m while the width W (y dimension) is 17.15 m. The seiche modes will have modes m=0, n=1,2,3,… while cross waves will have the modes n = 0 m = 1, 2, 3,… The even modes correspond with a node on the centreline of the basin and the odd modes correspond with an anti-node at the same location. The water particles in the location of a node in such a

cross standing wave will move purely horizontally, while at an anti-node will move purely vertically (recall from Figure 2:7). This is also visible in Figure 3:2 where one can see an antinode at the centreline as well as at the side walls. The condition of zero horizontal velocity through the wall incrassates that an antinode be at these locations (Dean & Dalrymple, 1991). The inclusion of the incident wave train will superimpose additional dynamics to the water surface profile. The basin seiche and cross waves resonance periods are shown in Table 3-1 overleaf. It should be noted that the basin is not uniform depth, due to the sloping beach, so the values given are approximate values. A slight modification would be needed for equation (3.6), but the indicative values are deemed to be interest.

The effect of the seiche and cross waves is not only the modulation of the surface wave envelope but they also result in an (often significant) amount of residual wave energy at the conclusion of a wave run. The time taken for this energy to be dissipated before the next run can continue is known as the stilling time or stilling period. The active wave absorption system and the passive absorbing beach will absorb some of the energy in the longitudinal direction, however, the cross waves travelling between the side walls will take longer to die out. Note from the table that there are several cross wave resonance periods <=1 s. This is a well-known phenomenon for this particular basin, with periods ~1 s being regarded as particularly "noisy". These frequencies often coincide with the lower range of frequencies of interest; there is little to be done save for the advice to delay the short period tests until before lunch/coffee break to avoid the tedium of waiting!

Additional material on the theory of cross waves ca be found in Hudspeth, (2006) and Ibrahim (2005).

Table 3-1: Wave basin seiche and cross waves resonance periods

	$T_{n,0}$	$T_{0,m}$
1	14.891	11.012
2	7.513	5.596
3	5.081	3.826
4	3.885	2.965
5	3.181	2.464
6	2.722	2.139
7	2.401	1.914
8	2.166	1.748
9	1.987	1.621
10	1.846	1.521
11	1.732	1.439
12	1.638	1.370
13	1.559	1.311
14	1.492	1.260
15	1.434	1.215
16	1.383	1.175
17	1.337	1.139
18	1.296	1.106
19	1.259	1.076
20	1.226	1.049
21	1.195	1.023
22	1.167	1.000
23	1.140	0.978
24	1.116	0.957
25	1.093	0.938
26	1.071	0.919
27	1.051	0.902
28	1.032	0.886
29	1.014	0.870
30	0.997	0.856

3.4 Deep water instability

An additional phenomenon to be aware of in the context of wave generation is known as deep water instability or Benjamin and Feir instability, that is; In deep water, a uniform train of plane waves of finite amplitude is unstable!

Mei, et al (2005) affirm that, it is common experience in the laboratory that a uniform train of relatively steep waves is difficult to maintain in a long-wave tank. This difficulty was first explained theoretically by the work of Benjamin & Feir (1967) who found that Stokes' waves were unstable to side-band disturbances, that is, disturbances whose frequencies deviated slightly from the fundamental frequency of the carrier waves.
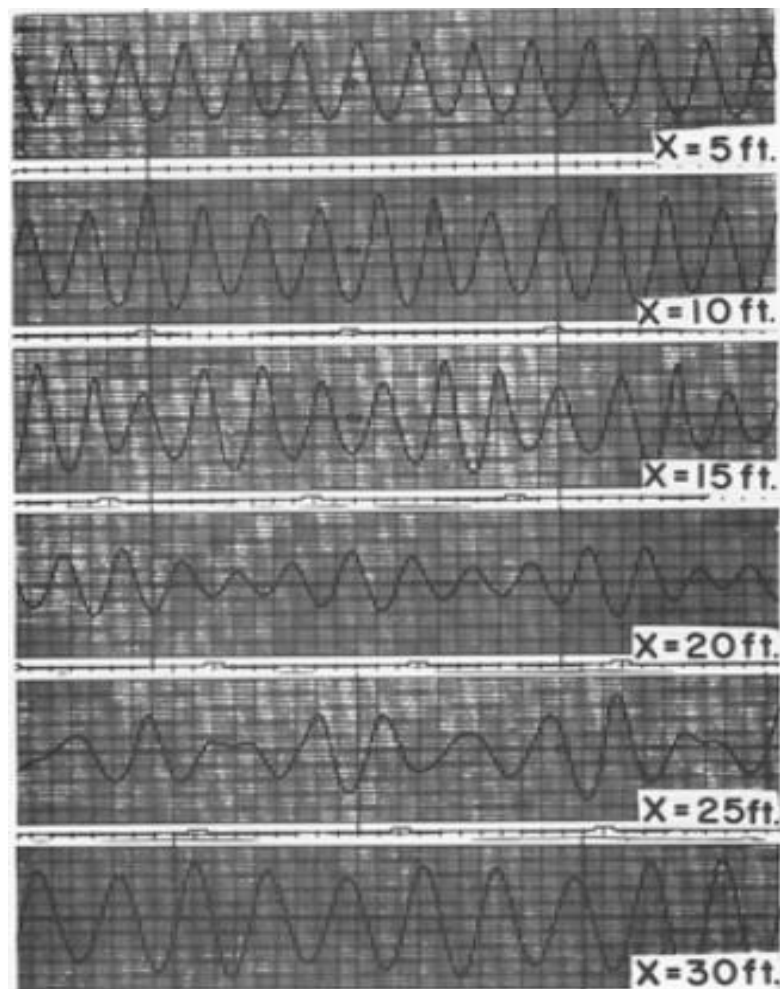
Figure 3:3: Example of the long-time evolution of an initially nonlinear wave train. Initial wave frequency is 3.6 Hz; oscillograph records shown on expanded time scale to display individual wave shapes (source Segur, 2009)

Figure 3:3 shows the evolution of an initially non-linear wave train at various locations in the tank. Note the wave shapes are not exact repetitions each modulation period, because each

modulation period does not contain the same integral number of waves. The phenomena is also known as the "sideband" instability because it manifests itself as a pair of sideband components around the carrier wave component in a power spectrum. This illustrated in Figure 3:4 showing the early stages of both the measured wave form and wave amplitude spectrum. In the figure the initial stage of "sideband" modulation instability van be clearly seen. The instability appears as a weak long wave modulation of the wave-form envelope and as a pair of sideband components centered around the carrier wave component in the spectrum.
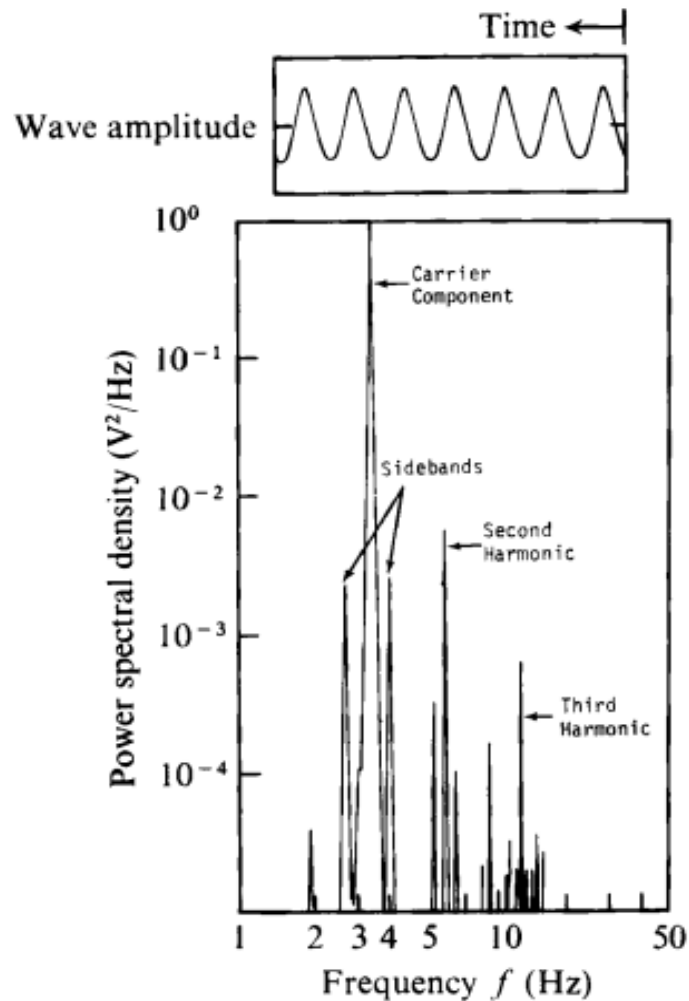
Figure 3:4: Measured wave form and wave amplitude spectrum showing initial stage of "sideband" modulation instability (source Yuen & Lake, 1982)

The fact that the uniform wave train is unstable to long-wave perturbations was first established by Lighthill (1965) but his results were confined to infinitely long perturbations (Yuen & Lake, 1982). A physical explanation of this side-band instability has been given by Lighthill (1978); Consider a Stokes wavetrain with a slowly modulated envelope. The crests

near a peak of the envelope are faster than those on either side of the peak and, therefore, tend to shorten the waves ahead and lengthen the waves behind. Now the group velocity in deep water is larger for longer waves. The rate of energy transport is lower in front and higher behind, hence accumulation occurs near the envelope peak, whose height must increase. Similarly, the trough of the envelope will tend to decrease, resulting in instability.

Numerical theories on the formation of deep water instability relate to the relatively advanced topic of solutions to the non-linear Schrodinger equation and are beyond the scope of this work. For further reference see Mei, et al (2005) and the review paper by Yuen & Lake (1982).

3.5 Basin description

The internal dimensions of the wave basin are approximately 23.25 m long - from the front face of the wavemaker paddles to the back wall - by 17.15 m wide - measured between the inner surfaces of the side walls-. Additionally, at an approximate distance of 14.25 m downstream from the wavemaker front, the wave basin floor forms a sloping beach section of slope 1:10 resulting in a plan view length of 5 m.

The depth of the wave basin before the slope section is maintained at 1 m. Consequently, the basin depth at the opposite wall to the wavemaker (after the slope section) is nominally 0.5 m. Two rows of baskets containing mesh absorbing plastic are situated along the back wall with the purpose of minimising the amount of reflected waves within the basin. These baskets (triangular in plan) are approximately 0.64m wide and 1.16m long. Both an instrument carriage and pedestrian bridge span the width of the basin and can by rolled longitudinally down the basin as they are mounted on tracks.

The wave generation system is comprised of forty flap type paddles hinged at 300mm above the basin floor, with each paddle element having a horizontal spacing of 0.425m. Each paddle is individually driven by an electrical motor connected to a series of belts and pulleys. The wave generator also utilises an active absorption system whereby wave fields incident upon a particular paddle are sensed by a dynamic force transducer located on the upper segment of the panel; this adjusts the driving signal to the paddles so that any incoming waves are absorbed and do not return into the generated wave field. The wavemaker paddles, driving software and active absorption system were all pioneered at the University of Edinburgh and

Edinburgh designs (a company which stemmed from the university) (Bolton King & Rogers, 1997).

The coordinate system of the wave generator is as follows;

- x-axis is perpendicular to the paddle face
- y-axis is parallel to the paddle face
- z-axis is perpendicular to the still water surface and positive upwards.

3.6 Equipment used

Several pieces of equipment are required in order to measure and record the water surface elevation height at different areas of the basin. The main equipment used is as follows;

3.6.1 Resistance wave gauges

Data were collected by means of wire probes (resistance wave gauges) situated on an instrument carriage spanning the width of the basin. These probes manufactured by Churchill Controls Ltd, (2018) consist of two wires approximately 500mm long and 1.5mm thick with a spacing of 12.5mm. The water depth can be inferred on the principle that the measured conductance is proportional to the length of wire beneath the water surface. The conductance can be measured by applying a high frequency AC-voltage signal across the wires to energise the gauges. The current is proportional to the probe immersion as long as the water conductivity remains the same. Water conductivity changes with temperature and concentration levels of dissolved salts. The system is fully analogue and simply gives a voltage output proportional to wave height. Each probe is energised at a user selectable frequency set by jumpers on the circuit board; the options are 4, 5, 6, 7, 8 and 10KHz. Crosstalk is avoided by energising the closest probes with very different frequencies and really only becomes a potential problem when the probe spacing is less than 10mm. A meniscus tends to form on the rods at the air-water interface, leading to measurement errors which can be significant when measuring small amplitude waves (H.-T. Liu, Katsaros, & Weissman, 1982). If the gauges are cleaned before use then for most amplitudes the meniscus on the rods can be assumed to remain the same shape as the waves rise and fall. However, the curvature of the meniscus is reduced slightly as the water reaches its highest point creating noticeable effects when the waves are very small (Skyner, 1987).

0.425m Paddle Element Spacing

Paddle Hinge Distance

0.3m

0.5m

5m

1 m

0.5m

4m

14.25m

z

x

y

Wave Paddles

Instrument Carriage

23.25m

Sloping Beach Section

Mesh Absorbers

17.15m

94
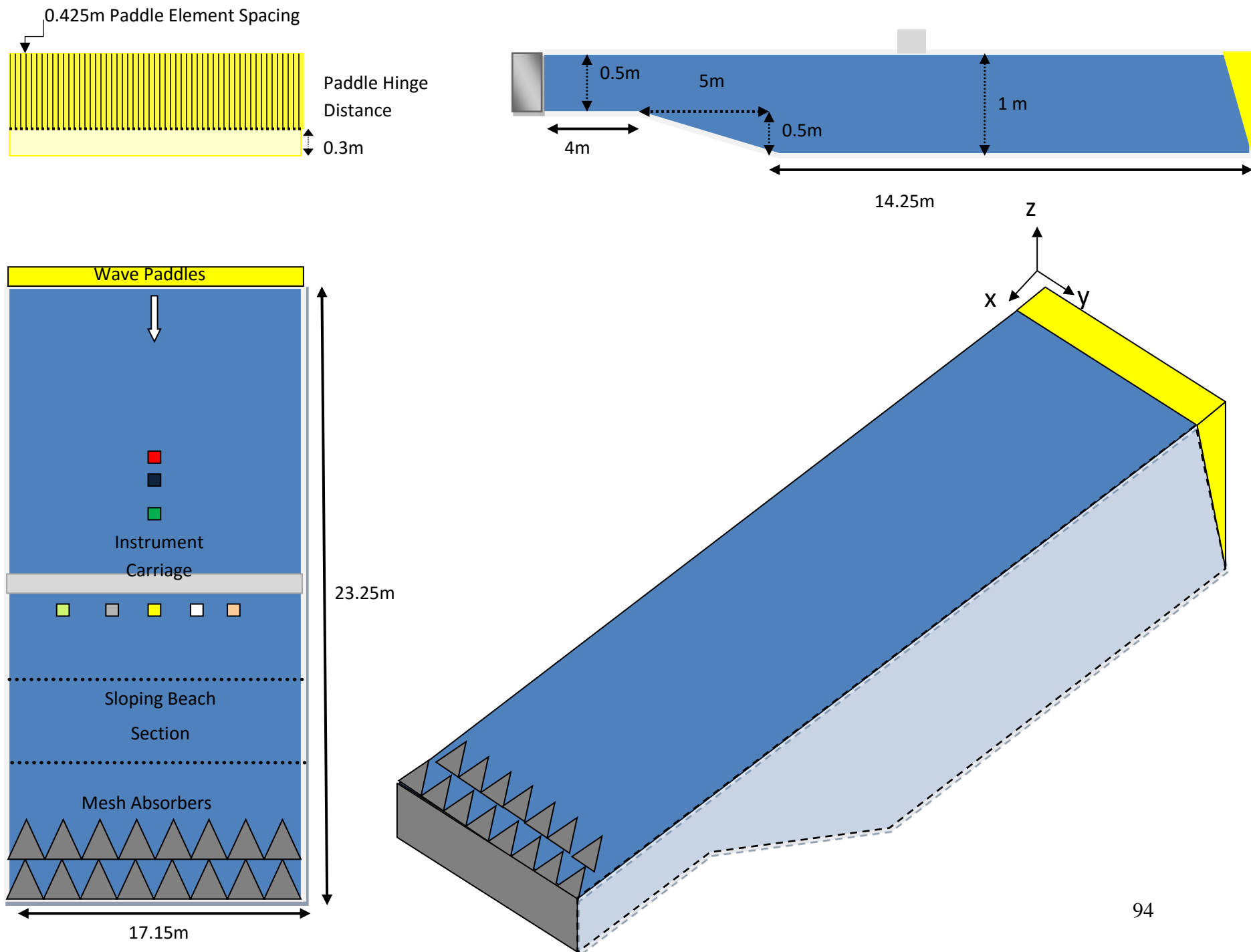
Figure 3:5: Basin dimensions, and probe layout (coloured squares left hand figure)

3.6.2 Calibrated probe holder

The probe holder comprises of a movable vertical bar carrying the probe held in a laboratory type clamp. The bar has a series of holes accurately drilled 10mm apart through which a retaining pin is inserted, allowing for ease of calibration since the submersion level of the probe can be altered a known distance and the resulting voltage output recorded. The wave probe calibration procedure is to initially take the voltage reading at still water level. Subsequently the probe is moved up and down by known distances and re clamped using the probe holder. The new Voltage level is recorded and the procedure is repeated, taking the voltage reading at each position. The slope of the plot is then used such that a given Voltage can be converted into an equivalent displacement reading. In some basin facilities, several probes can be hooked up to an actuator system, which can the move all the probes simultaneously. This is useful as it speeds up the calibration process.
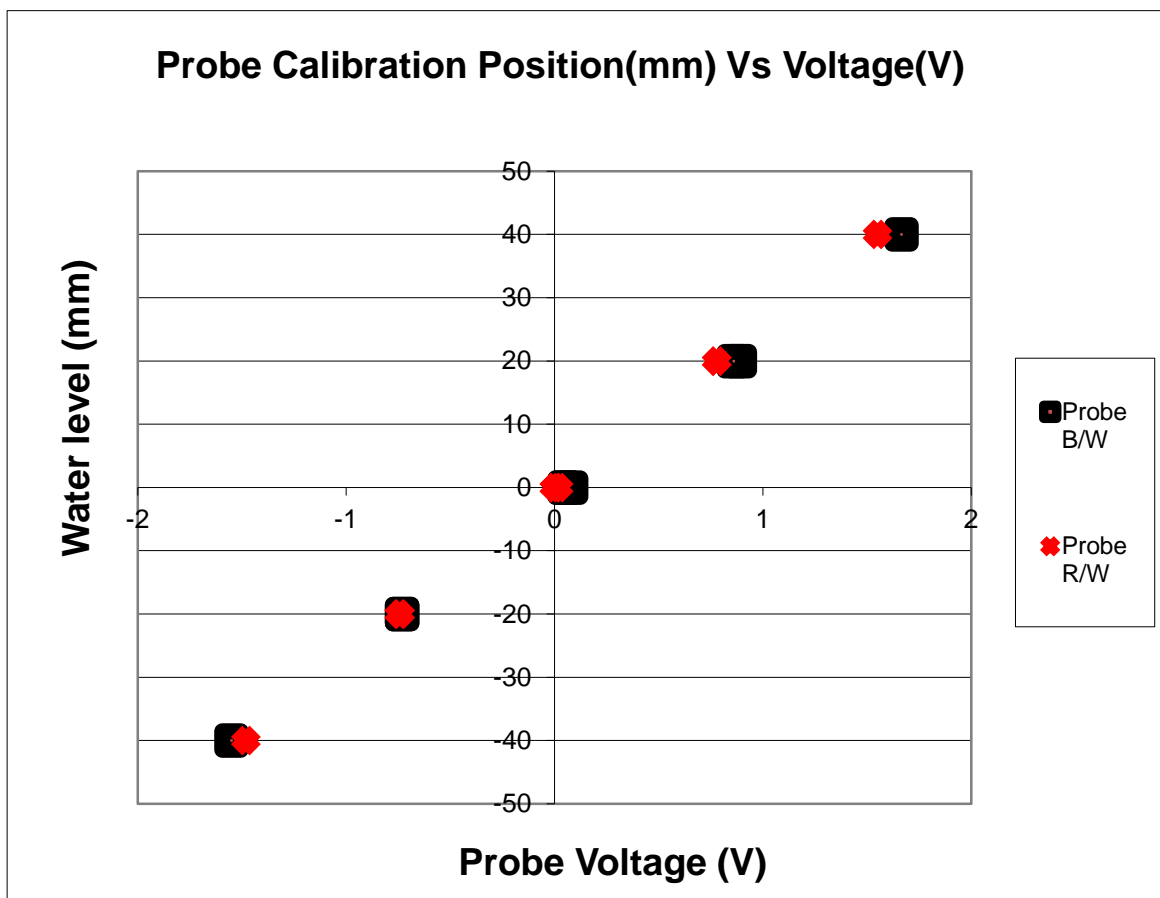
Figure 3:6: Sample wave calibration plot

3.6.3 Wave monitor module

The module is cable connected to the probe and provides output signals to a computer via Microlink 3000 using an I.E.E.E-488 interface (a link that allows communication in both directions between PC and Microlink). These signals then enable parameters such as wave height, frequency and profile to be observed.

The module contains a high frequency oscillator to energise the probe and a sensing amplifier which measures the voltage drop produced by the probe current across a pair of series resistors.

3.7 Water surface envelopes

When a fraction of the incident wave field is reflected by the beach, a partial standing wave is created, with antinodes at the points where incident and reflected wave fields combine and nodes where they detract from one another.
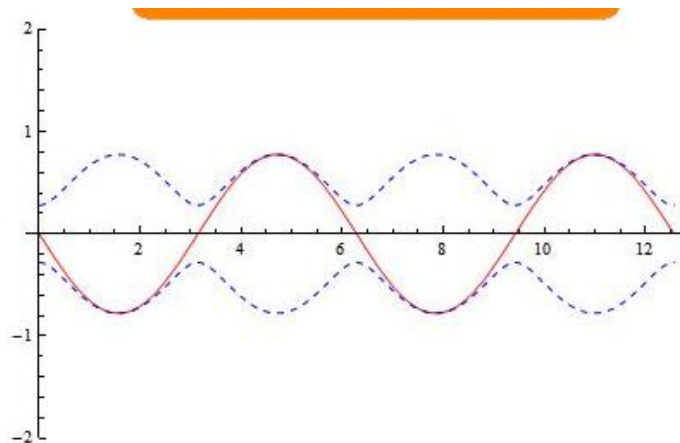
Figure 3:7: Example of partial standing wave surface envelope

A series of tests was conducted in order to gauge the water surface envelope along the direction of wave propagation and traversely across the wave basin. Resistive wave gauges were mounted on the instrument carriage at distances of 6, 8, 9 (the centre of the basin), 10 & 12 meters from the cabin wall. An additional three probes were placed on a cantilever strut along the centreline of the basin. (The probe set-up used is illustrated in Figure 3:5).

96

3.8 Testing procedure

The wave basin was graduated in 50mm spacings longitudinally as illustrated in Figure 3:8.

Figure 3:8: Wave Basin with instrument carriage

Initially the carriage was placed a distance of 1.7m away from the wavemaker paddles. The wavemaker was then started up and after allowing sufficient time for the waves to be refleced from the beach and again from the paddles (i.e. a steady state testing regeime) the wave height was recorded at the initial location. The amount of time for this to occur could be calculated using the group velocity. Since the total length of tests was quite long anyway, such precision was not saught and it was decided to err on the side of caution and allow additional time before beginning recording. After a certain period of time (typically enough for ten waves to have passed), the carriage is moved on to the next longitudinal spacing. While the carriage is in transit and for a certain amount of time after reaching the next position (the carriage will be oscillating), the data being recorded by the wave probes are not of much use and are therefore considered 'bad' data. In order to distinquish between moments when the carriage is in

position and at rest (i.e., 'good' data) and moments when the carriage is in transit or oscillating at a fixed position ('bad' data), a simple on/off switch is used. During the periods where the data are considered bad the switch is off and has an output of 0 volts. Conversely, when the conditions for accurate data logging are met the switch is flicked on and the output is 22 volts. Figure 3:9 below shows a sample of wave height data collected using the switch system. In the early stages of the figure the switch is on and data from this position will be labelled 'good'. The switch is turned off and the bridge is being moved to the next position. The most significant variation in amplitude as a result of bridge vibration is visible ~33 seconds. A waiting period ensues (perhaps overly cautious in this particular example) before the switch is turned back on to label data at the next position as 'good'. In the post processing stages, only the data with the switch on is used for data analysis.
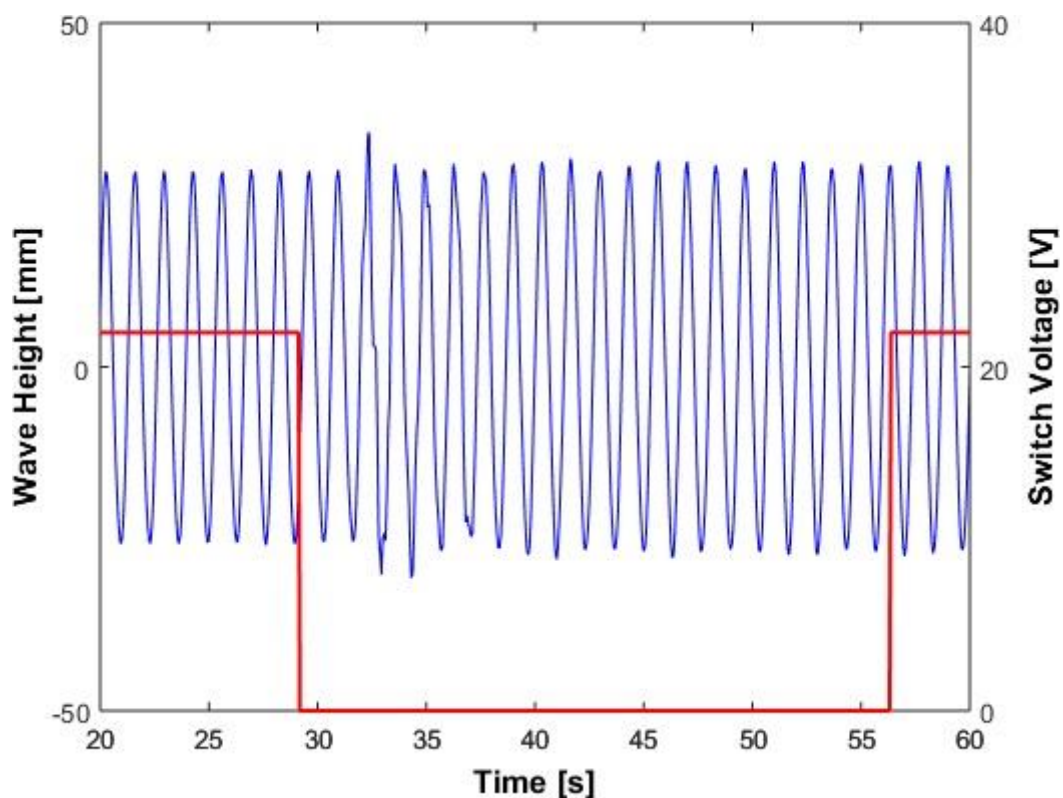
Figure 3:9: Example of data collected with on/off switch

Data were recorded at several intervals (as per Table 3-2 overleaf) up to a distance of 13m from the paddles. The interval spacing was chosen so that there would be a larger number of points for the shorter period waves, which also have shorter wavelengths, thereby furnishing a finer resolution for the surface envelopes.

98

Table 3-2: Regular wave test parameters

Period (s)	Gain Setting		Spacing (m)	Wavelength (m)
0.695	32	64	0.05	0.75
0.8	32	64	0.05	1
0.889	32	64	0.05	1.23
1	32	64	0.05	1.56
1.14	35	70	0.1	2.02
1.23	43	86	0.1	2.34
1.33	43	86	0.1	2.71
1.45	42	84	0.1	3.16
1.6	45	90	0.1	3.73
1.78	60	120	0.1	4.41
2	55	110	0.1	5.21
2.28	65	130	0.1	6.22
2.65	60	120	0.1	7.54

The tests were also conducted at two different gains in order to determine if irregularities in the water surface envelope were independent of wave height. The gain setting is a factor sent out to the paddle driver and is directly analogous to amplitude. The majority of these waves would be classed as intermediate waves.

3.9 Results

A sample result of a water surface envelope is given in Figure 3:10. The absolute variation in water surface elevation is shown for 2.66 second monochromatic waves (both the high and low gain setting are shown). The resulting surface envelope resembles a typical partial standing wave with distinct antinodes, where incident and reflected waves combine to create a larger wave, and nodes where they subtract from one another to form a smaller wave. Furthermore the nodes and antinodes are separated by a distance of approximately 1.8m which corresponds to a quarter wavelength, as is to be expected. It is also evident that the shape of the envelope is the same for both high and low gains (there is a scaling factor of two).
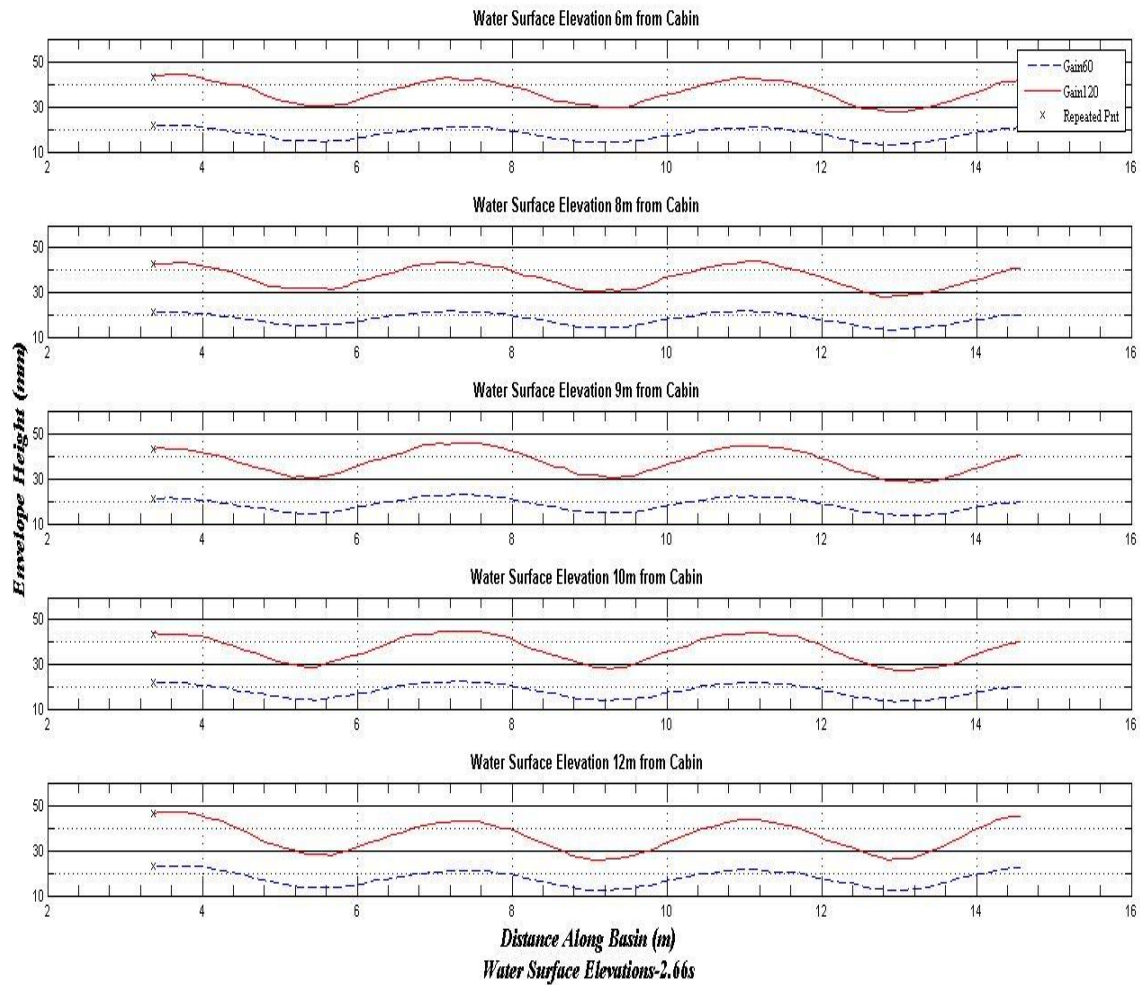
Figure 3:10: Variation in water surface elevation is shown for 2.66 second monochromatic waves

Connecting the data from the five probes placed across the basin in a linear fit, it is then possible to view a 3D representation of the surface envelope. Figure 3:11 shows the area of the basin that was used for surface envelope tests as a reminder.
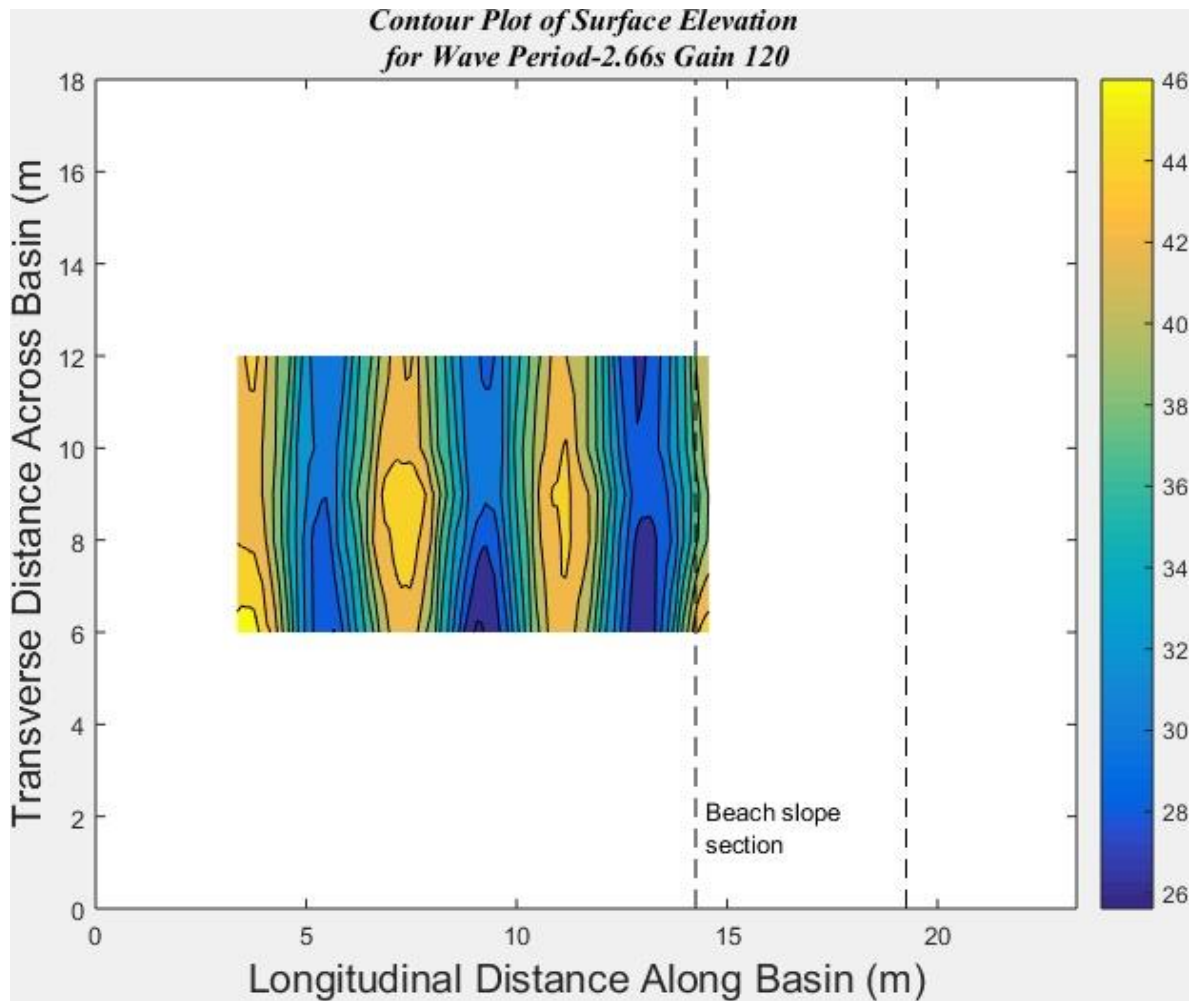
Figure 3:11: Area of the basin used for surface envelope test

Figure 3:12 &Figure 3:13 (overleaf) show contour plots of both the low and high gain tests for a 2.66s period monochromatic wave. As the basin width is roughly 18m and the probes are spaced from 6 m to 12 m, the figures give a representation of the middle third of the basin. Both plots show a typical surface envelope shape; by comparing both gain plots it is apparent that one is a scaled version of the other.
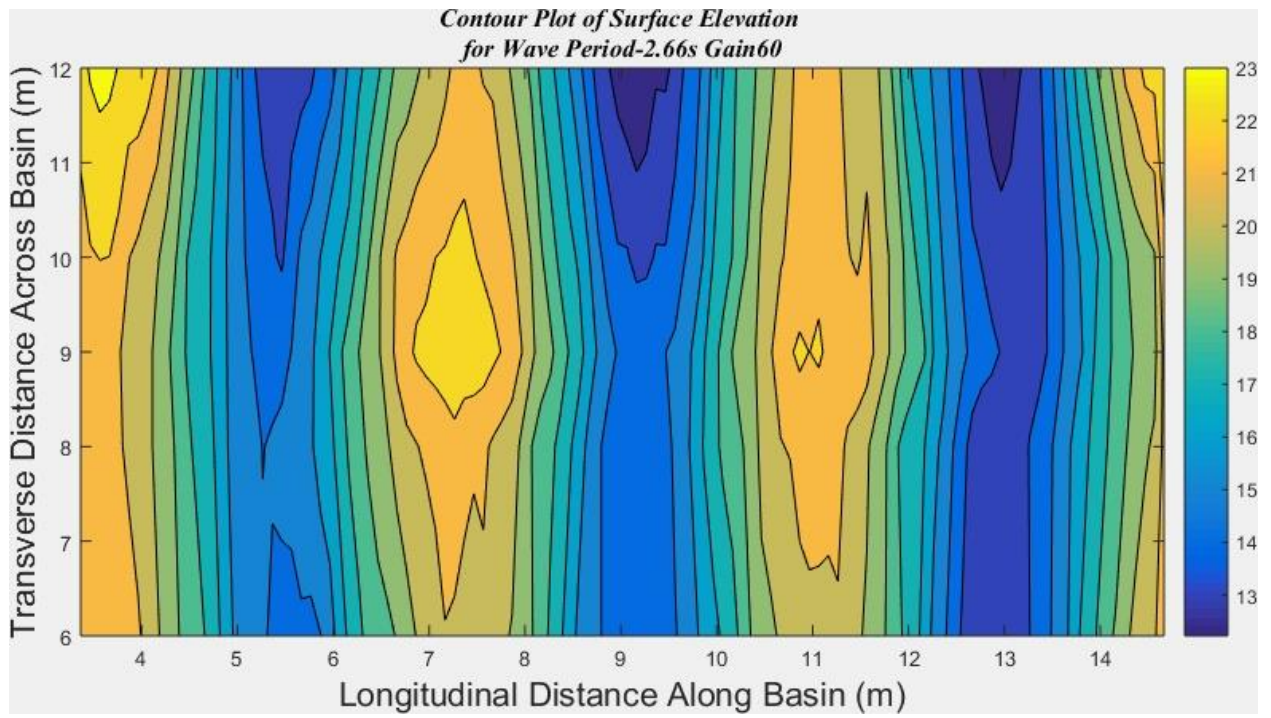
Figure 3:12: 3D surface elevation for 2.66s wave, gain 60
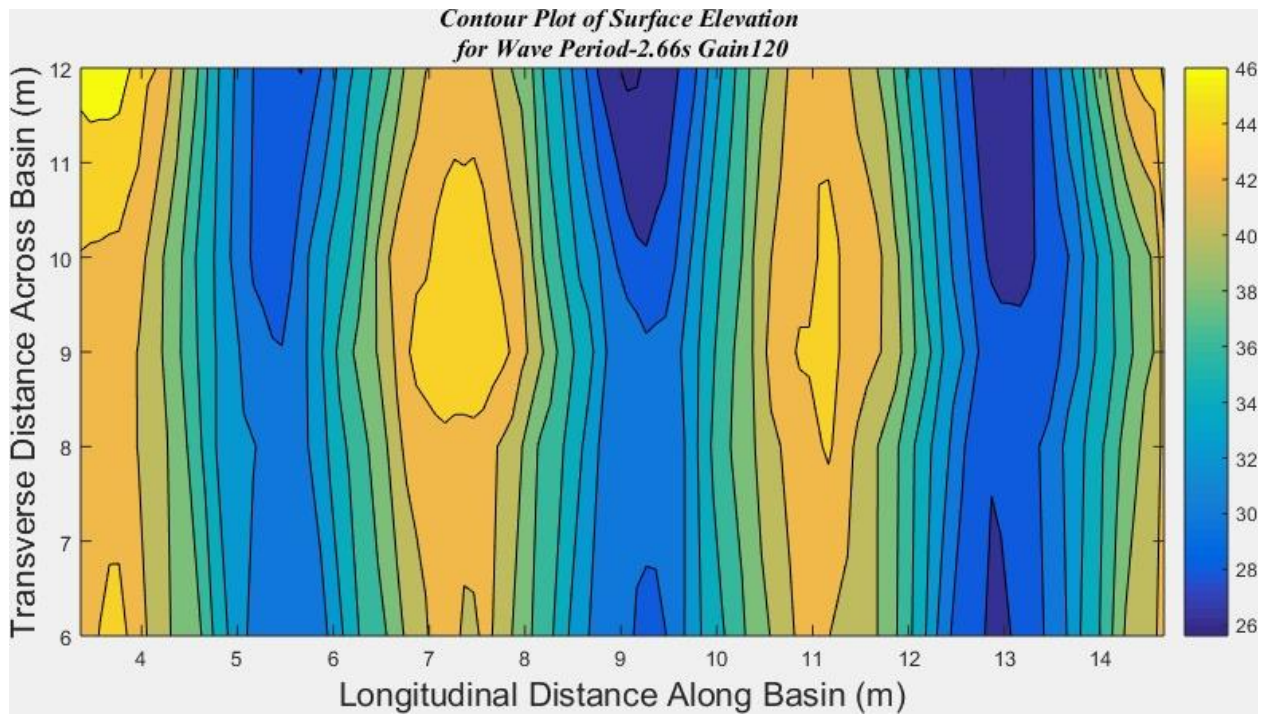
Figure 3:13: 3D surface elevation for 2.66s wave, gain 120

102

Figure 3:14 shows the envelopes for 1.45 second monochromatic waves; the partial standing wave envelope is evident but upon inspection of the 3D plots (Figure 3:16 & Figure 3:17) it can be seen that there is a greater variation in wave height across the width of the tank.
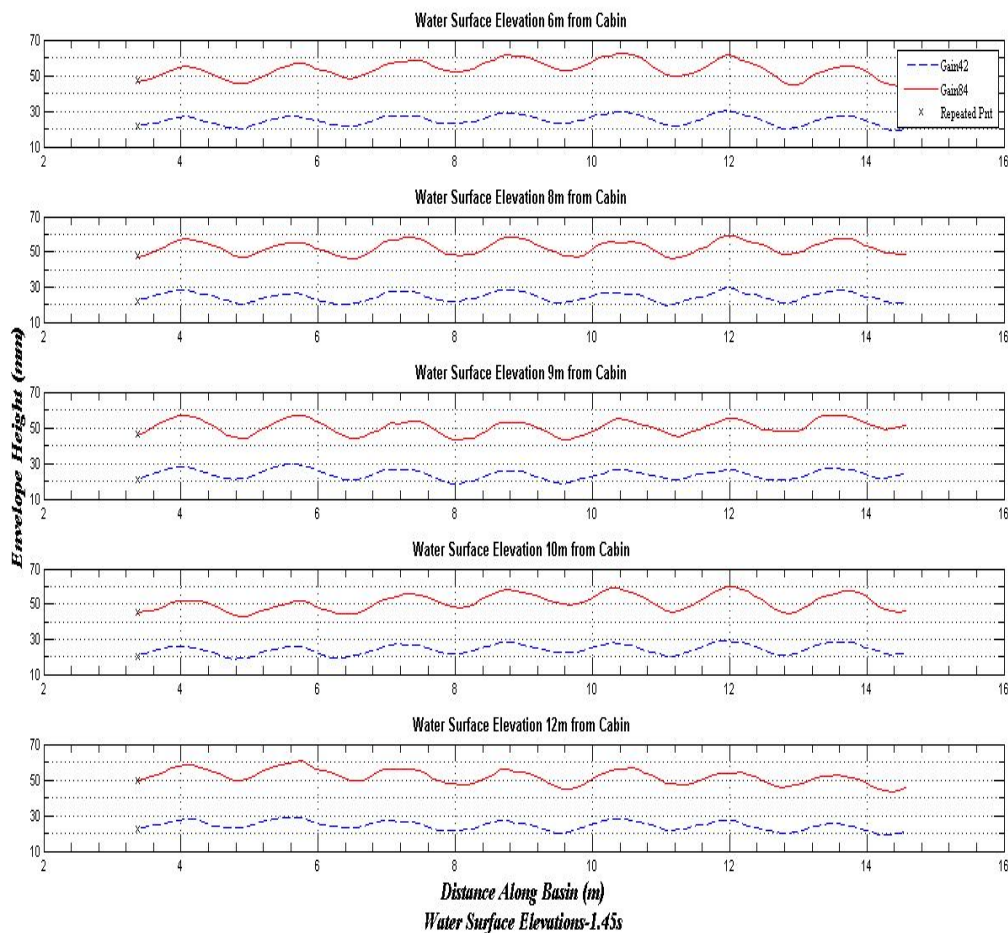
Figure 3:14: Variation in water surface elevation is shown for 1.45 second monochromatic waves

Figure 3:18 & Figure 3:19 show the longitudinal and transverse variations in surface envelope for the 0.695 s period. It can be seen that the surface envelope is more 'messy' in both the longitudinal and traverse directions for this shorter period. A full set of surface envelope data can be found in Appendix A. It is worth noting that for all frequencies tested, there exists significant variation in both longitudinal and transverse directions. This is to be expected however as when generating regular waves in an enclosed structure such as a wave basin, there will be reflections at the boundaries; where both the incident and reflected wave will be of equal frequency but the phases of the incident and reflected waves are 'locked' by the fact that they are both equal at the boundary. The name for this phenomenon is unsurprisingly known as phase locking. A consequence of this partial standing wave pattern is the

103

presence of nodes and antinodes as evidenced by the surface envelope graphs presented previously. As mentioned previously the lower period waves are also susceptible to exhibiting significant cross waves, resulting in an overall wave surface envelope which can be said to be non-homogeneous.
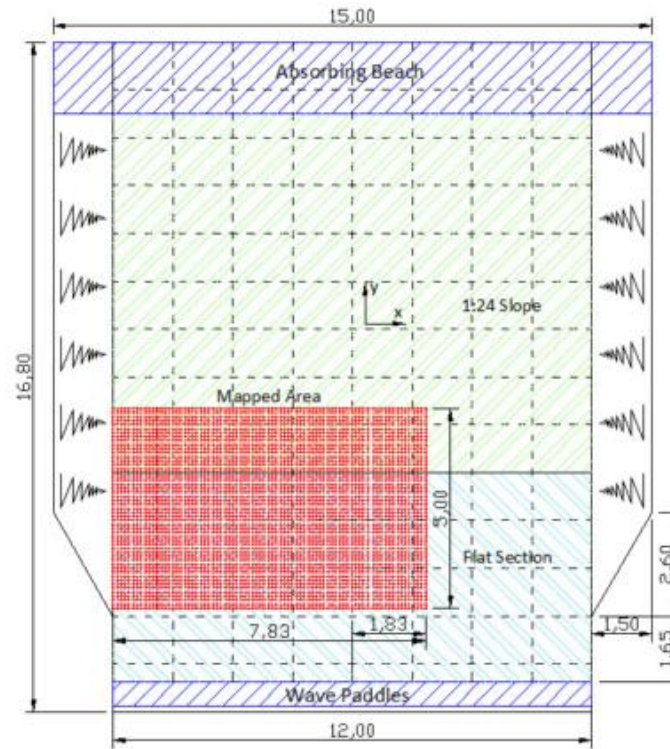
Figure 3:15: Layout of Queens University Marine Laboratory basin (dimensions in meters Boyle, Elsaesser, Folley, & Whittaker (2011)

In (Boyle et al. 2011), an investigation into wave basin homogeneity at Queens University Marine Laboratory (QUML) in Portaferry is described. Rather than examining individual wave frequencies separately, a wave packet containing 8 discrete frequencies with a range of wave amplitudes and a repeat time of 32 seconds was generated. The observed area covered a 5m x 7.8m section of the tank (see Figure 3:15) and by applying a FFT to the wave trace at each location, the amplitude of each frequency component in the wave trace could be calculated. Oscillating amplitude variation was observed at different distances from the wave paddles and was present for all frequency components. The average variation over all frequencies was ± 43%. Every basin is different; in terms of layout, depth (0.5 m at QUML) beach setup and in this particular case the presence of a steep slope, which is designed to dissipate wave energy (across the tank) by inducing wave breaking. This basin will also have different cross and seiche wave resonance frequencies
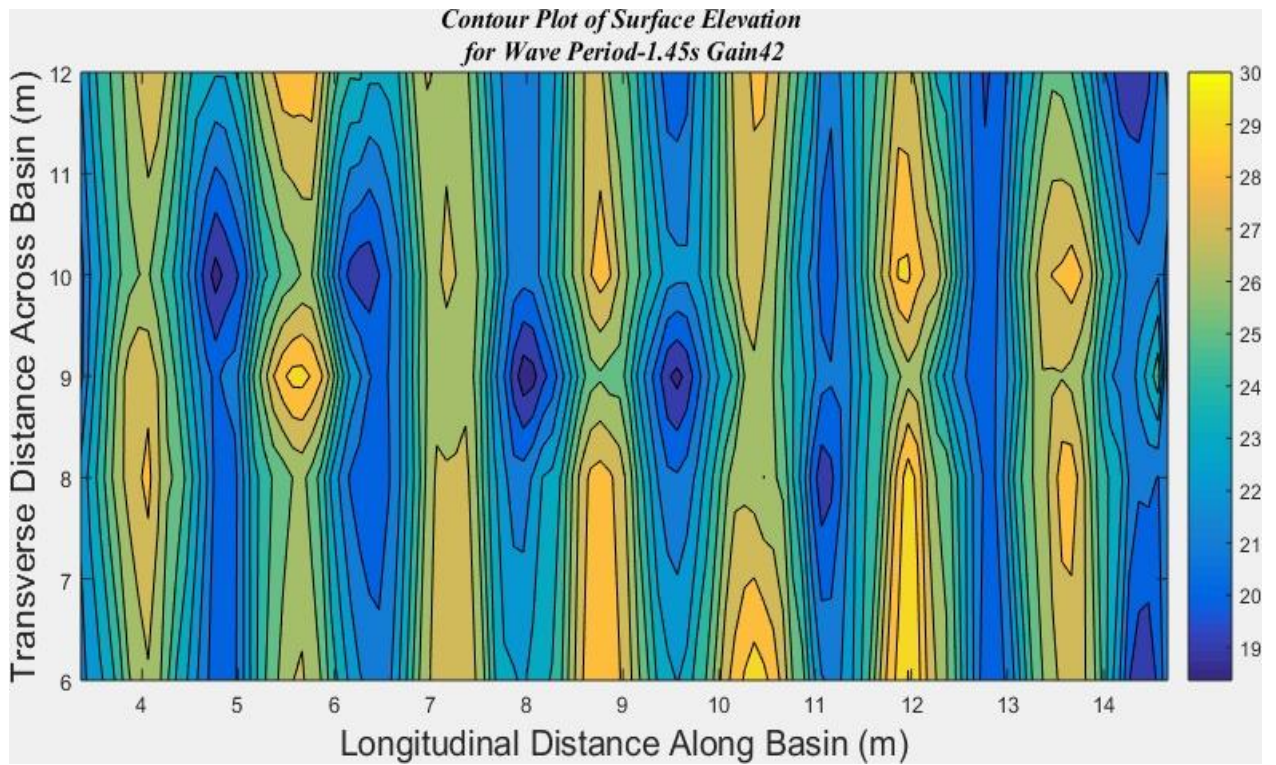
Figure 3:16: 3D surface elevation for 1.45s wave, gain 42
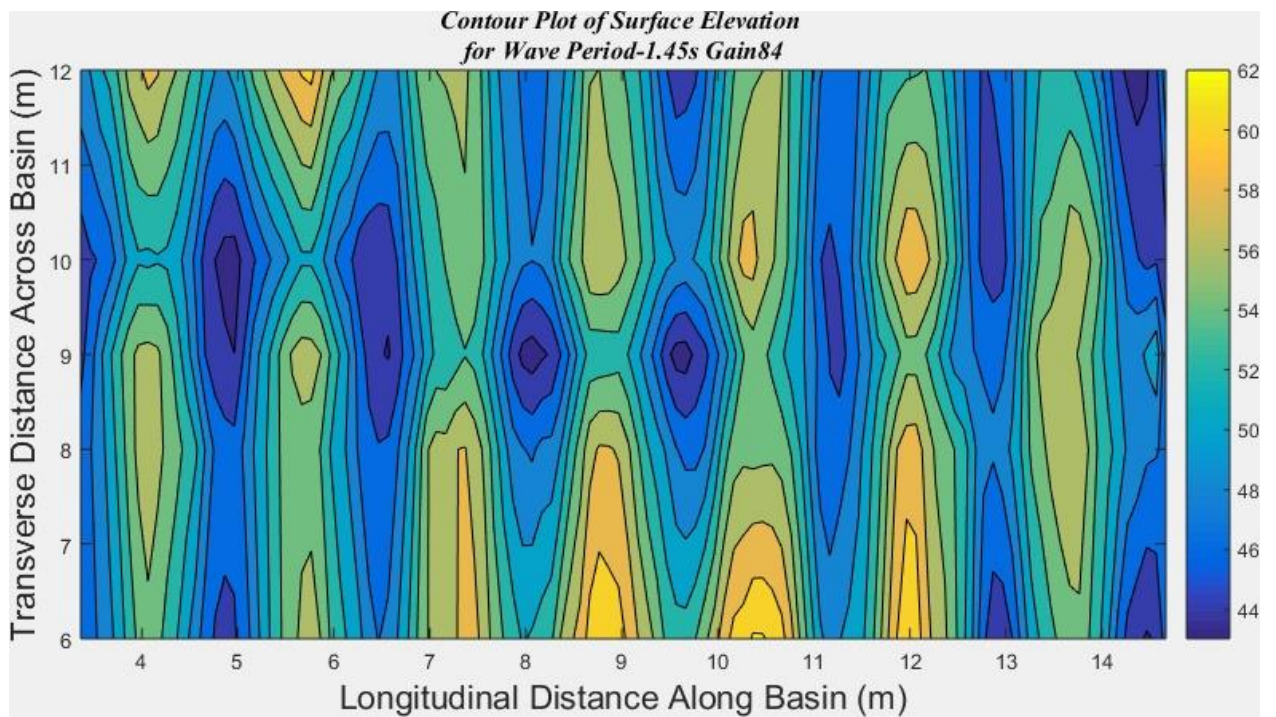
Figure 3:17: 3D surface elevation for 1.45s wave, gain 84
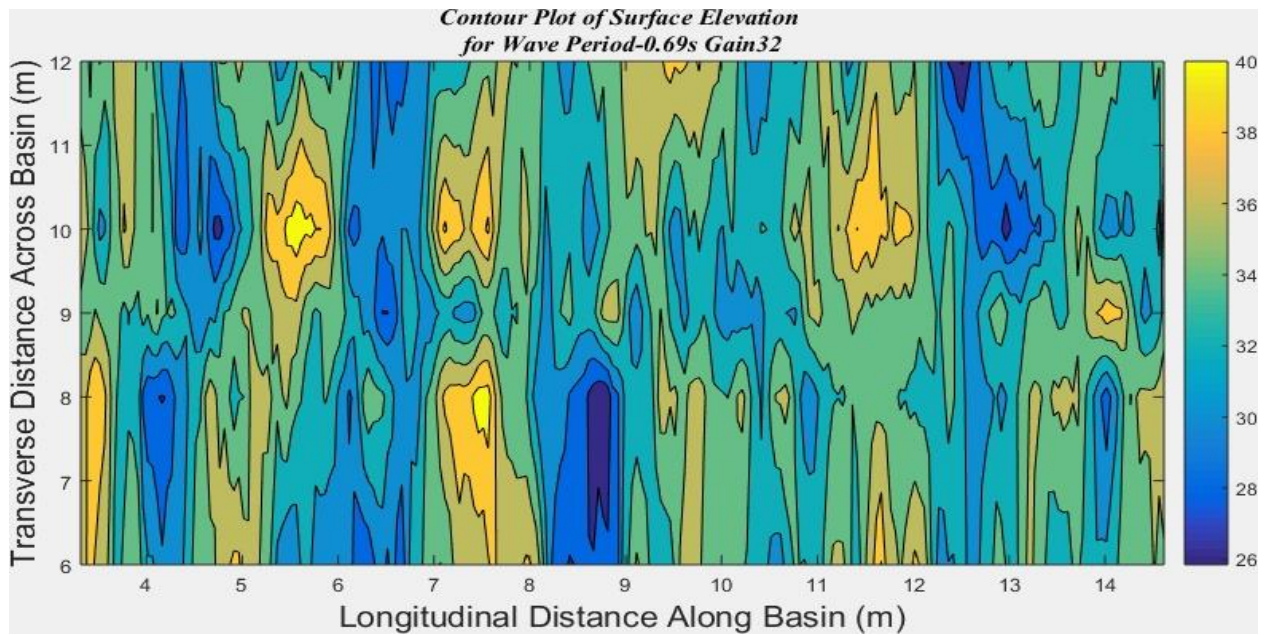
Figure 3:18: 3D surface elevation for 0.695s wave, gain 32
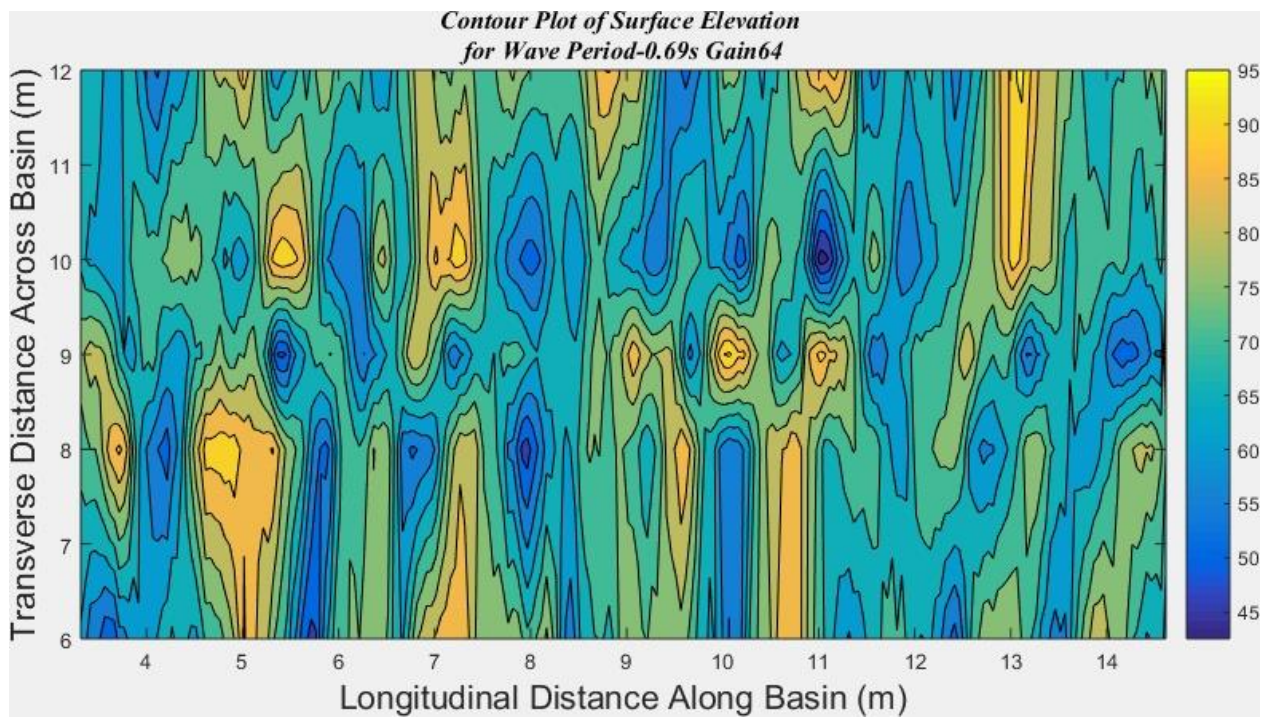
Figure 3:19: surface elevation for 0.695s wave, gain 64

Table 3-3: Summary statistics of surface height variation (low gain)

Period	Wavelength	Mean Height	Slope	Cumulative deviation	Longitudinal deviation	Traverse deviation
(s)	(m)	(mm)	-	(mm)	(mm)	(mm)
0.690	0.750	33.927	0.045	2.720	2.691	2.229
0.800	1.000	28.755	0.029	1.989	1.968	1.661
0.889	1.230	26.372	0.021	1.887	1.862	1.680
1.000	1.560	24.979	0.016	1.946	1.910	1.406
1.140	2.020	25.394	0.013	1.798	1.737	1.478
1.230	2.340	29.193	0.012	2.378	2.291	1.626
1.330	2.710	27.795	0.010	2.587	2.536	1.588
1.450	3.160	24.247	0.008	2.627	2.614	1.192
1.600	3.730	22.930	0.006	2.189	2.188	1.087
2.000	5.210	21.648	0.004	1.869	1.772	1.030
2.280	6.220	20.786	0.003	2.001	1.864	0.932
2.660	7.540	17.962	0.002	2.861	2.847	0.699

Table 3-3 & Table 3-4 show the summary statistics relating to the variation of surface envelope height throughout the basin. The mean surface height is taken from all measurement points (227 x 5=1135 points for periods ≤ 1s & 114 x 5=570 points for periods ≥1s). The cumulative deviation is then calculated for all points using this mean value. The mean of the deviation in the longitudinal direction is taken from the five individual deviations σ_{6m}, σ_{8m}, σ_{9m}, σ_{10m}, & σ_{12m}. The average value for the coefficient of variation, which is defined as the ratio of standard deviation to mean, is 9 % for both high and low gain settings. The coefficient of variation is larger for the longitudinal direction (8 % both gain settings) than the variation in the traverse direction (6 % high gain, 5 % low gain)

Table 3-4: Summary statistics of surface height variation (high gain)

Period	Wavelength	Mean Height	Slope	Cumulative deviation	Longitudinal deviation	Traverse deviation
(s)	(m)	(mm)	-	(mm)	(mm)	(mm)
0.690	0.750	71.214	0.095	9.832	9.769	9.256
0.800	1.000	61.793	0.062	7.492	7.379	6.489
0.889	1.230	55.619	0.045	4.398	4.180	4.159
1.000	1.560	51.638	0.033	3.918	3.477	3.713
1.140	2.020	52.832	0.026	3.759	3.042	3.930
1.230	2.340	61.318	0.026	4.332	3.630	4.214
1.330	2.710	58.471	0.022	4.336	3.863	3.537
1.450	3.160	51.746	0.016	4.318	4.177	2.580
1.600	3.730	49.373	0.013	3.866	3.835	2.307
1.780	4.410	57.179	0.013	3.674	3.302	3.201
2.000	5.210	45.044	0.009	3.137	2.868	2.135
2.280	6.220	43.577	0.007	4.668	4.442	1.885
2.660	7.540	36.715	0.005	5.535	5.504	1.400

3.9.1 Stability

The duration of each test was typically 2-2.5 hours, which is a considerable amount of time for the continuous running of the wave generating paddles. At the conclusion of each test, the instrument carriage was returned to the initial starting point and the data were recorded to determine the effect of continually running the basin. In the previous 2D surface envelope graphs, these repeat points are marked with an 'x'. The agreement between repeated and original elevation is very good for all frequencies.

3.10 Reflection

In many laboratory studies it is desired to separate the measured wave train into its incident and reflected wave components so that model response can be related to parameters of the incident wave field (Hughes, 1993). With this in mind, tests were carried out in order to quantify the amount of wave reflections present in the tank for different regular wave periods. Using a three probe method described by (Funke & Mansard, 1980) it is possible to separate the two wave fields provided the wave probes are separated a known distance which is based on the wavelength of the incoming wave.

Whilst many wave tank centre utilise a package called Wavelab to perform reflection analysis, this program in this facility is not available. Consequently the author modified an existing FORTRAN program into a more user-friendly Matlab graphical user interface (GUI) that performs the least squares analysis described by Mansard & Funke. This set of codes is still used by other researchers at UCCs wave making facility.

3.10.1 Regular Waves

Reflection tests were carried out at six key locations along the centreline of the tank (3.5,5,6,7,9.5 & 12 meters from the paddles) in order to examine if the amount of reflection remains constant. Only one wave run was tested for each frequency at each location. Ideally, repeat runs would be carried out, to examine any deviation in the results. The three probe Funke & Mansard (1980) method was used to determine reflection coefficients, due the recommendation from the work of (Isaacson, 1991).The percentage reflection is defined as the reflected wave height divided by the incident wave height. The same gain settings as the water surface envelope tests were used as input for the test (Table 3-2). Results are displayed in Figure 3:20 overleaf; the blue line shows the average reflection for the lower gain setting whilst the red line depicts the high gain setting. Error bars are also shown for all points indicating the amount of variation in the reflection coefficients i.e., the variation between the six measuring stations.
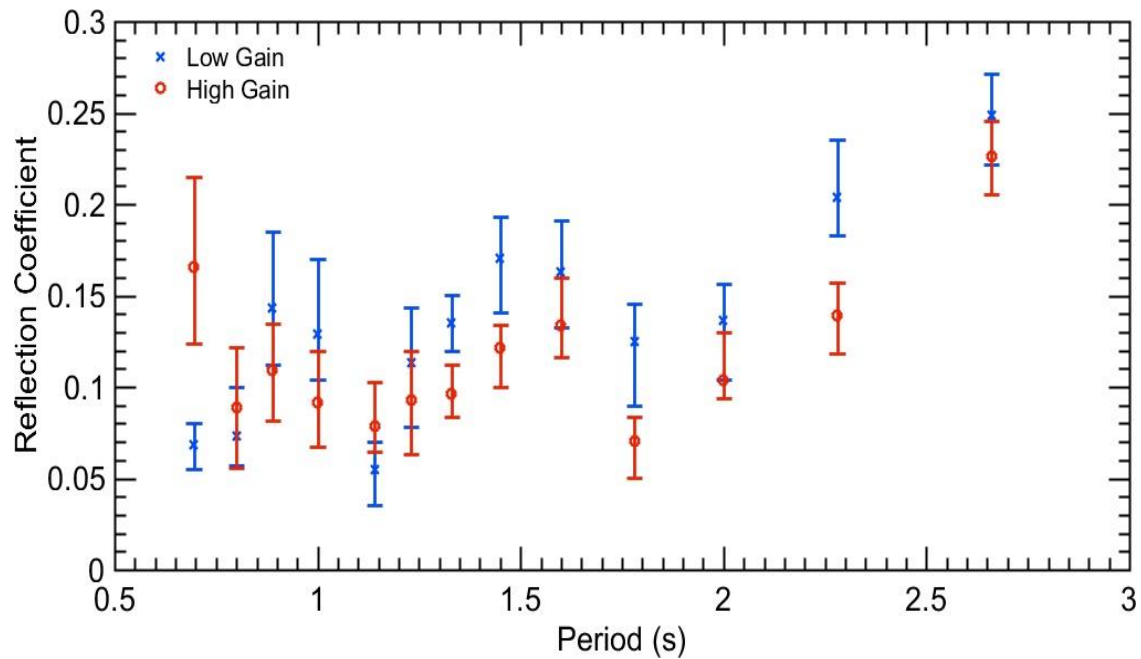
Figure 3:20: Reflection vs wave period (s)

The average amount of reflection over all periods is 10%. Typically for both gain settings the amount of reflection is lower for the shorter periods and higher for the longer periods. This is to be expected as the plastic mesh absorbers are more effective at trapping the reflections of shorter wavelengths. A point of interest is the results for the high gain 0.7 second tests, average reflection 12% with variation 7-17%. It must be noted that the analysis method is most sensitive to errors in probe spacing, and since the 0.7 s wave has the shortest wavelength any slight error in probe spacing could result in erroneous reflection coefficients. When placing the probes care must be taken to ensure that the wave gauges are in good condition prior to testing and that they're not deformed as part of the installation and calibration process. It is also essential that probe spacing be taken at the still water level. Initially the wave probes at HMRC were in poor condition due to years of continuous wear and tear. This required the purchase of new straighter probes and a stricter adherence to measuring at the water level. Despite all precautions taken, slight measuring error can never be completely discounted.
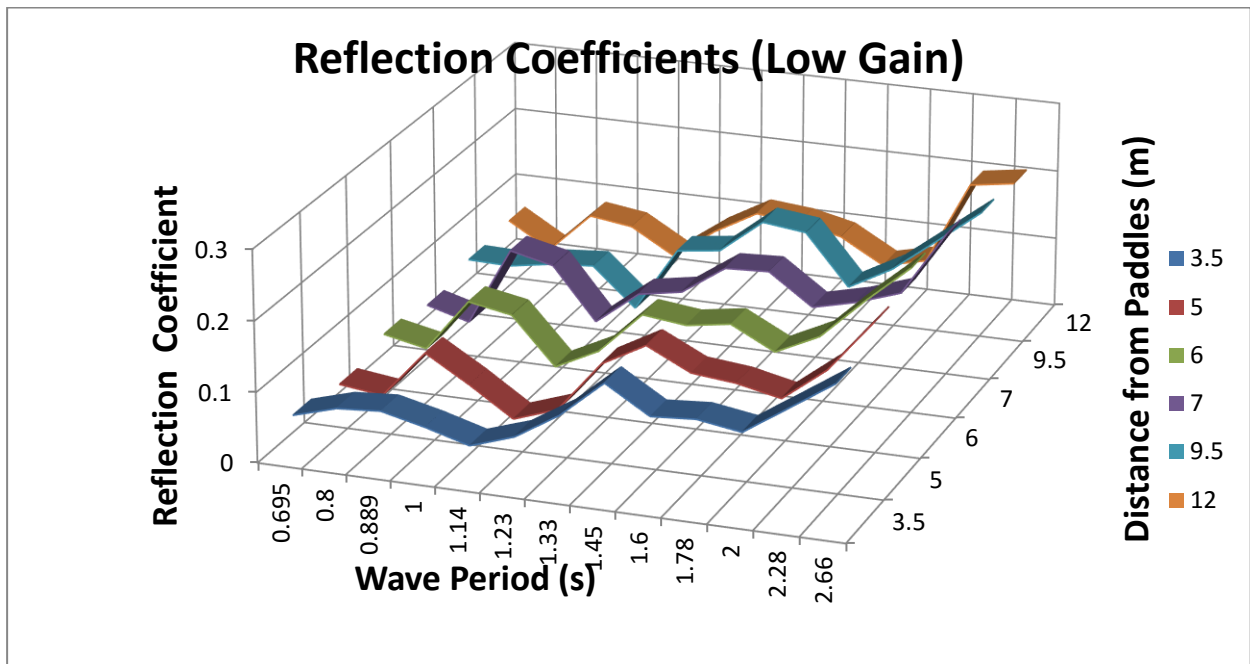
Figure 3:21: Reflection coefficient vs wave period for different longitudinal stations (low gains)
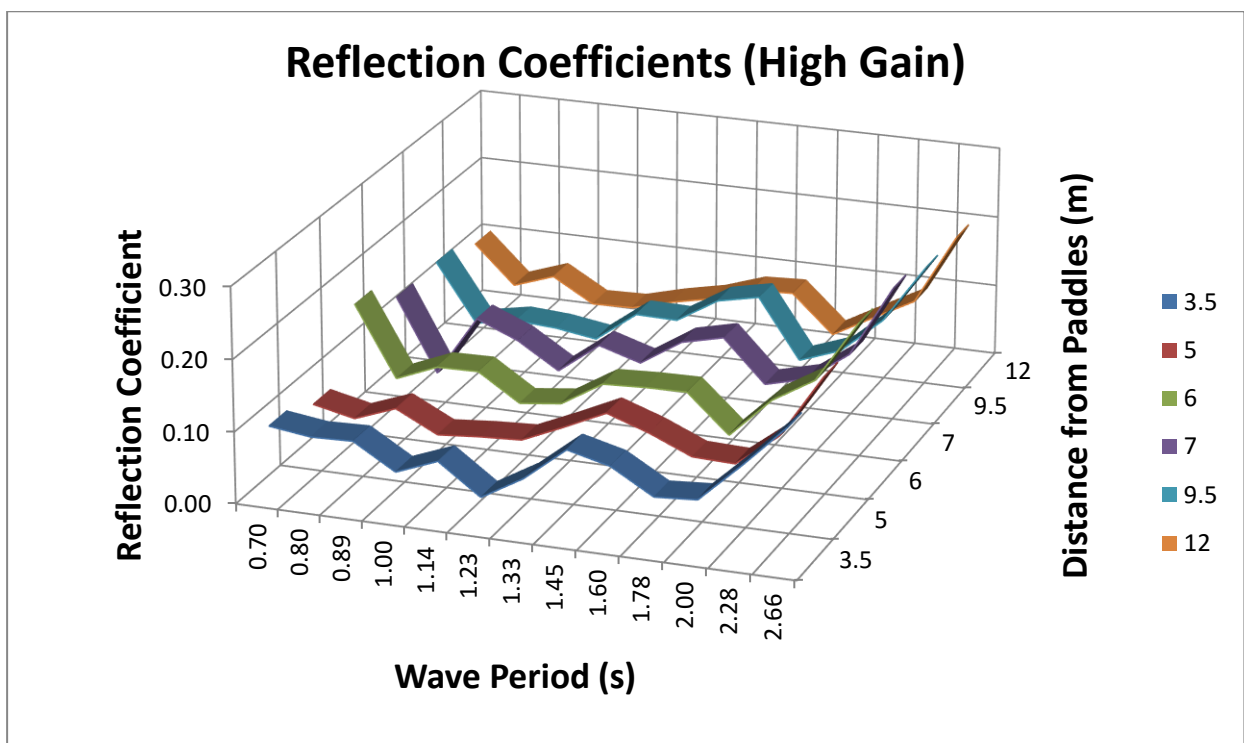
Figure 3:22: Reflection coefficient vs wave period for different longitudinal stations (high gains)

3.11   Incident & Reflected Wave Heights
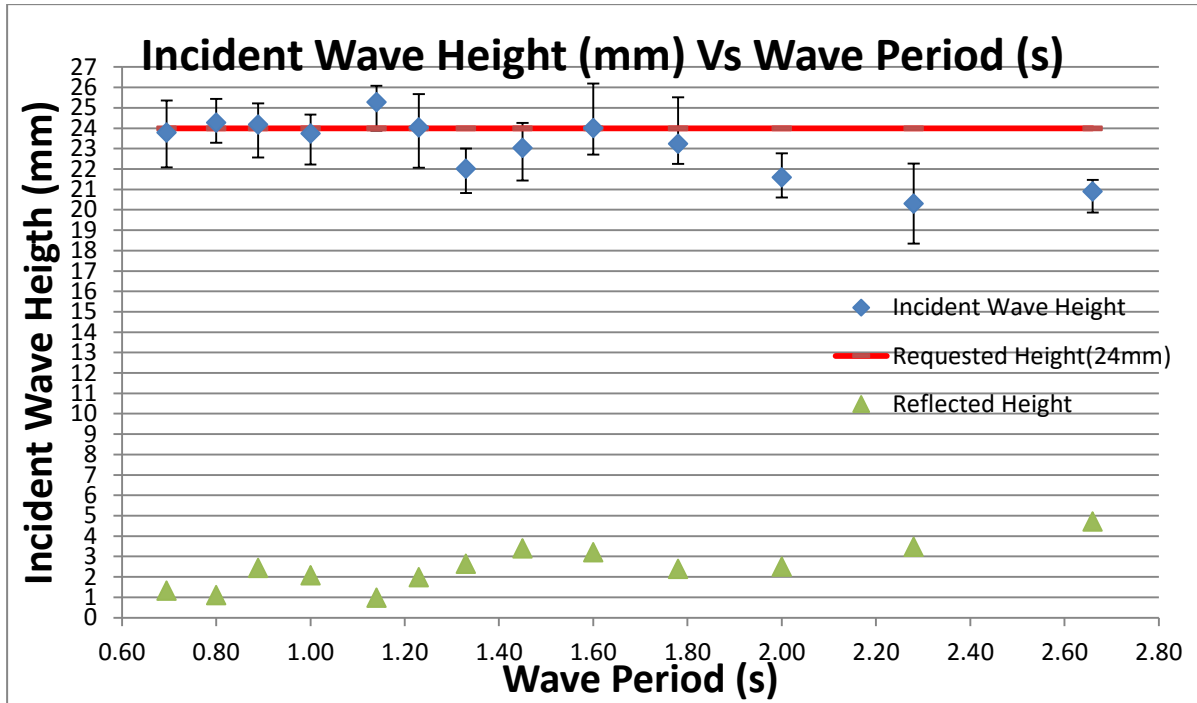
Figure 3:23: Incident & reflected wave heights for low gain settings
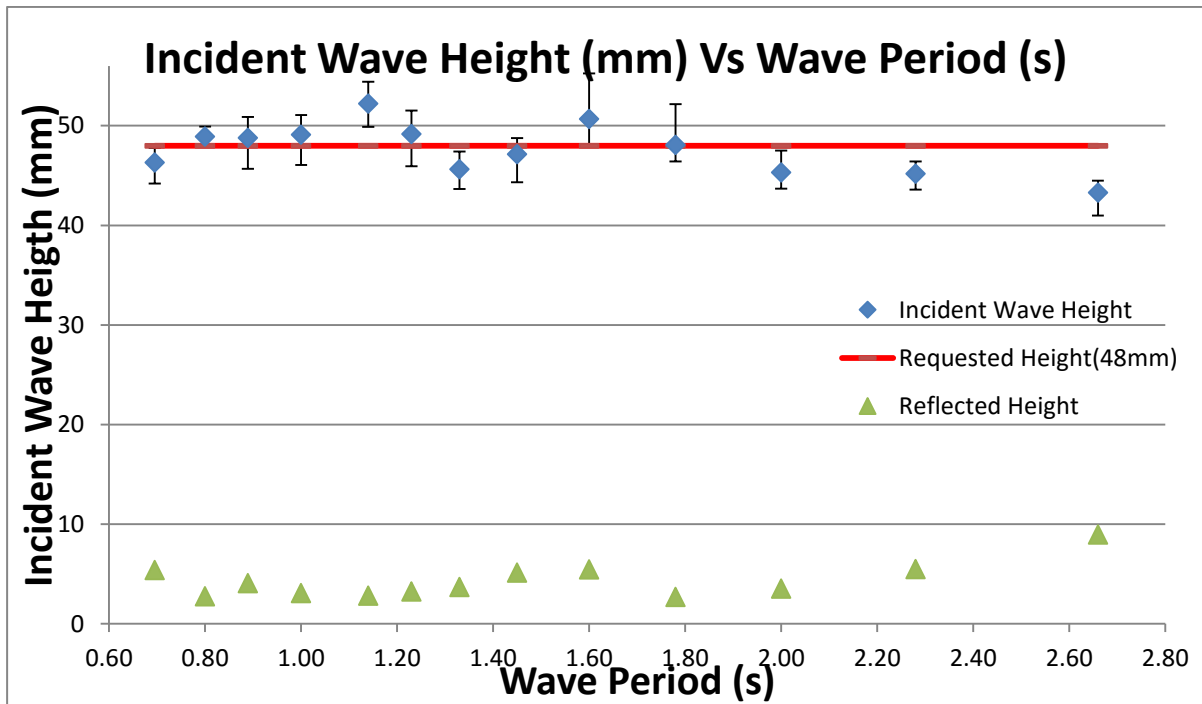
Figure 3:24: Incident & reflected wave heights for high gain settings

Figure 3:23 & Figure 3:24 show the incident & reflected wave heights for the low and high gain settings respectively. In general, there is a good agreement between the requested and the generated incident wave height. The reflected wave height increases as the period gets longer; this is mirrored in the fact that the reflection coefficient increases with increasing wave period. A problem with the Funke & Mansard method is that the formulation of the theory assumes only two dimensional (variation in z axis and propagation in x axis) linear waves. In reality waves in a basin will not be purely linear but rather will have higher harmonics present, particularly as the wave slope increases. Additional non-linearity is introduced in the form of deep water instability described previously. Lastly the 2D assumption is not truly the case either as in a basin there will be cross waves. The net effect of these non-linearities is that the measured wave heights will be different to predictions of the underlying linear theory which is assumed. Signal noise and measurement error can also affect results.

3.11.1 Healy's method

Since the surface envelope was already acquired as described in section 3.7, this data was used to estimate reflections using Healy's method for comparison purposes. Examining the nodes (H_{mins}) and antinodes (H_{maxs}) of the envelope, it is possible to infer information about the incident and reflected wave heights. The following quantities are given in terms of H_{min} and H_{max} with the last entry known as Healy's formula.

$$\frac{H_{max} + H_{min}}{2} = H_i \tag{3.7}$$

$$\frac{H_{max} - H_{min}}{2} = H_r \tag{3.8}$$

$$\frac{H_{max} - H_{min}}{H_{max} + H_{min}} = \frac{H_r}{H_i} = K_r \tag{3.9}$$

Table 3-5 & Table 3-6 show the results of the analysis of the surface envelope of the centreline probe for both the high and low gain setting. The erratic and 3 dimensional nature of the high gain, shorter period waves is evident in the higher standard deviation of reflected wave height and consequently the standard deviation of reflection coefficient. The average wave reflection coefficient found using Healy's method was 8.5 % and 10 %.

Table 3-5: Reflection results using Healy's method for high gain settings

Period (s)	mean Hi (mm)	std Hi (mm)	mean Hr (mm)	std Hr (mm)	mean Kr	std Kr
0.69	70.33	6.60	8.46	5.25	0.12	0.07
0.80	60.53	5.50	3.42	2.36	0.06	0.04
0.89	55.15	4.21	3.62	1.41	0.07	0.03
1.00	50.49	3.09	2.98	0.96	0.06	0.02
1.14	51.88	1.91	2.35	1.12	0.05	0.02
1.23	58.36	2.89	2.82	1.32	0.05	0.02
1.33	55.64	1.88	4.09	1.01	0.07	0.02
1.45	50.08	1.56	5.26	0.85	0.11	0.02
1.60	48.86	2.59	4.77	1.06	0.10	0.03
1.78	58.95	4.21	2.26	1.51	0.04	0.03
2.00	46.65	1.96	2.49	1.37	0.05	0.03
2.28	45.33	0.67	4.89	0.56	0.11	0.01
2.66	37.54	0.81	7.70	0.48	0.21	0.01

Table 3-6: Reflection results using Healy's method for low gain settings

Period (s)	mean Hi (mm)	std Hi (mm)	mean Hr (mm)	std Hr (mm)	mean Kr	std Kr
0.69	33.89	1.39	1.72	0.94	0.05	0.03
0.80	29.00	1.21	1.28	0.69	0.04	0.02
0.89	26.08	1.30	2.50	0.64	0.10	0.03
1.00	24.88	1.28	2.32	0.64	0.09	0.03
1.14	25.45	1.01	1.79	0.93	0.07	0.04
1.23	28.47	1.25	2.81	0.65	0.10	0.03
1.33	26.91	1.45	3.14	0.61	0.12	0.02
1.45	23.62	0.96	3.50	0.58	0.15	0.03
1.60	22.80	1.44	2.91	0.62	0.13	0.03
1.78	0.00	0.00	0.00	0.00	0.00	0.00
2.00	22.55	0.87	2.19	0.45	0.10	0.02
2.28	21.57	0.42	2.52	0.33	0.12	0.01
2.66	18.36	0.42	3.88	0.36	0.21	0.02

3.12   Harmonic analysis

The output from the Funke & Mansard program is both an incident and reflected wave spectra. Examining the incident wave spectra, it is possible to check for the presence of waves at frequencies other than the fundamental frequency (i.e., harmonic waves) being generated by the wavemaker. If purely linear monochromatic waves were being generated, the output of the incident spectra would be a single 'spike' at the fundamental frequency (ideally the requested frequency). The presence of amplitudes elsewhere in the incident spectra is therefore an indication of non-linearity in the incident wave. Figure 3:25 below shows a typical incident and reflected amplitude spectra for the various longitudinal stations of the basin.
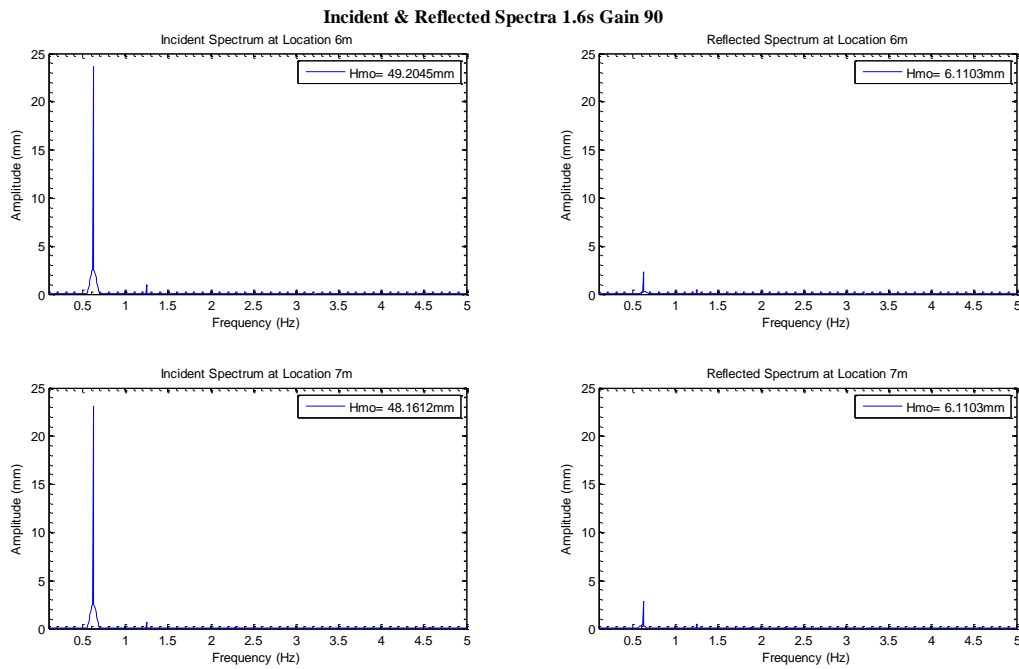
Figure 3:25: Incident & reflected spectra for 1.6 s gain = 90, locations = 6 & 7 metres from paddles

Figure 3:26 overleaf shows the ratio between 2nd & 3rd harmonics to the fundamental as a function of wave steepness (H/L). It can be seen that, in general, the amplitude of the second harmonic is less than

6% of the fundamental while the amplitude of the third harmonic is generally less than 2%. There is a trend however, for the amplitude of the higher harmonics to increase with wave steepness.
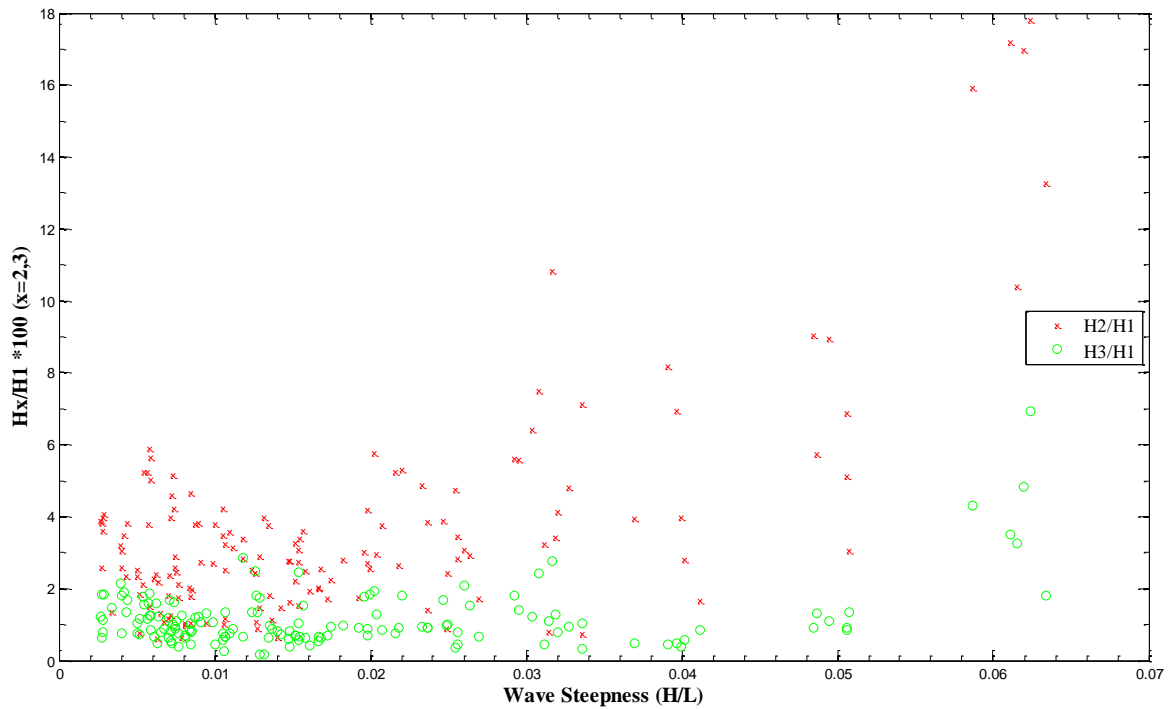
Figure 3:26: Ratio of the higher harmonics to the fundamental versus wave steepness

A 50mm wave height at 0.695s period is the steepest wave tested (see Figure 3:27 below), the higher harmonics are clearly more prominent and are a result of the 2nd or 3rd order Stoke's components of the fundamental wave.
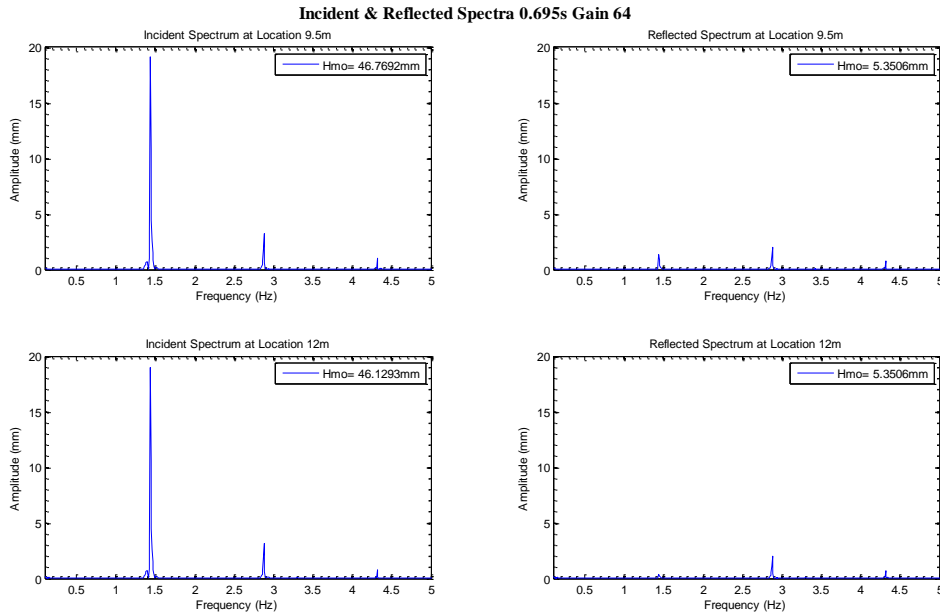
Figure 3:27: Incident & reflected spectra for 0.695 s gain = 64, locations = 9.5 & 12 metres from paddles

3.13 Multiple probe test

In autumn 2010 the wave basin at HMRC was renovated, a process which included installing new servomotors for the wave-maker paddles. Additionally, each paddle was given an optical sensor so that all 40 paddles could be aligned on start-up and during testing. Under the previous set-up, paddles could become disjointed and not move in unison. With these updates in mind, it was decided to redo the Funke & Mansard reflection tests for regular waves and also carry out irregular wave tests. Since the test plan involved different periods, wave heights, and sampling locations along the basin; and it was found from previous testing experience that changing the probe spacing after each test was a time consuming task which required a great bit of care (due the aforementioned sensitivity to erroneous probe spacing) it was decided to use several probes in order to cover all periods being tested. The solution entailed the use of 8 probes all in a parallel line to the direction of the waves. This then gave $\binom{8}{3} = 56$ possible three-probe combinations for use in the algorithm. Although the shortest wavelength requires 3 probes relatively close together and the longest wavelength needs at least 1 probe the furthest out, resulting in only a single suitable combination for these two wavelengths, intermediate wavelengths will have multiple possible combinations of probes to use, allowing for a comparison to be made. The calculation of probe spacing involved a brief foray into the mathematical programming language MATEMATICA. The original idea was to treat the probe spacing as a mini-optimisation problem, such that maximum amount of coverage could be obtained. However, with the

117

window of tank availability fast approaching a more basic graphical approach was taken, ensuring coverage for all wave runs (see Figure 3:28 and Figure 3:29).
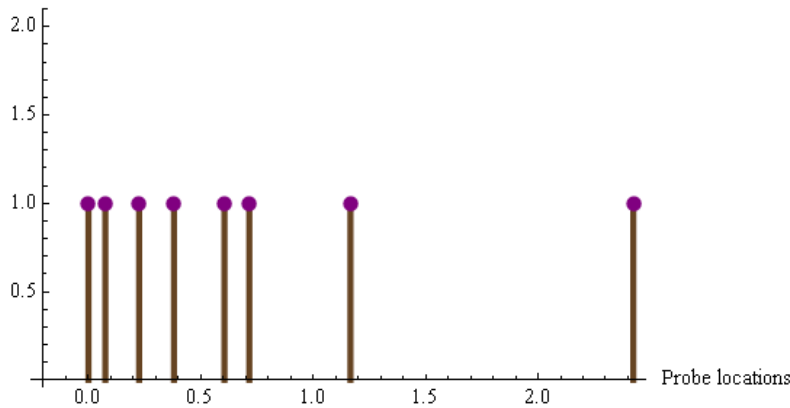
Cover[{0.00, 0.075, 0.225, 0.380, 0.605, 0.715, 1.165, 2.423}]

Figure 3:28: Developing probe spacing's (in meters) using MATHEMATICA.

B1	{{0., 0.075, 0.225}}
B2	{{0.075, 0.225, 0.38}}
B19	{{0., 0.075, 0.225}}
B3	{{0., 0.225, 0.38}, {0.225, 0.38, 0.605}, {0.225, 0.38, 0.715}}
B4	{{0., 0.225, 0.38}, {0.225, 0.38, 0.605}, {0.225, 0.38, 0.715}}
B5	{{0., 0.225, 0.38}, {0.225, 0.38, 0.605}, {0.225, 0.38, 0.715}}
B6	{{0., 0.225, 0.605}, {0., 0.225, 0.715}, {0.075, 0.38, 0.715}}
B7	{{0., 0.225, 0.605}, {0., 0.225, 0.715}, {0.075, 0.38, 0.715}}
B8	{{0., 0.225, 0.605}, {0., 0.225, 0.715}, {0.075, 0.38, 0.715}}
B16	{{0., 0.225, 0.605}, {0., 0.225, 0.715}, {0.075, 0.38, 0.715}}
B9	{{0.225, 0.605, 1.165}, {0.38, 0.605, 1.165}, {0.38, 0.715, 1.165}}
B10	{{0.225, 0.605, 1.165}, {0.38, 0.605, 1.165}, {0.38, 0.715, 1.165}}
B17	{{0.225, 0.605, 1.165}, {0.38, 0.605, 1.165}, {0.38, 0.715, 1.165}}
B18	{{0.225, 0.605, 1.165}, {0.38, 0.605, 1.165}, {0.38, 0.715, 1.165}}
B20	{{0.225, 0.605, 1.165}, {0.38, 0.605, 1.165}, {0.38, 0.715, 1.165}}
B11	{{0.075, 0.38, 1.165}, {0.075, 0.605, 1.165}, {0.225, 0.605, 1.165}, {0.225, 0.715, 1.165}}
B12	{{0.075, 0.38, 1.165}, {0.075, 0.605, 1.165}, {0.225, 0.605, 1.165}, {0.225, 0.715, 1.165}}
B13	{{0.075, 0.38, 1.165}, {0.075, 0.605, 1.165}, {0.225, 0.605, 1.165}, {0.225, 0.715, 1.165}}
B14	{{0.075, 0.38, 1.165}, {0.075, 0.605, 1.165}, {0.225, 0.605, 1.165}, {0.225, 0.715, 1.165}}
B15	{{0., 0.38, 1.165}, {0., 0.605, 1.165}}
B21	{{0.075, 0.38, 1.165}, {0.075, 0.605, 1.165}, {0.225, 0.605, 1.165}, {0.225, 0.715, 1.165}}

Figure 3:29: Wave probe spacing options for the different irregular test runs

3.13.1 Regular Waves

The same periods used in the previous examination (as given in Table 3-2) were used with two different requested wave heights of 25 & 50 mm. However the number of longitudinal stations was reduced to three being 6 ,8 &10.5 m from the paddles -the central area of the basin most often used for model

118

tests-. The results of the multiprobe reflection tests are shown in Figure 3:30(overleaf). In general the amount of reflection is lower for shorter periods, an increase in reflection exists for the mid-range periods (1.45-1.6s), while for the longer periods (>2s) there is a linear relationship with reflection levels increasing with period.
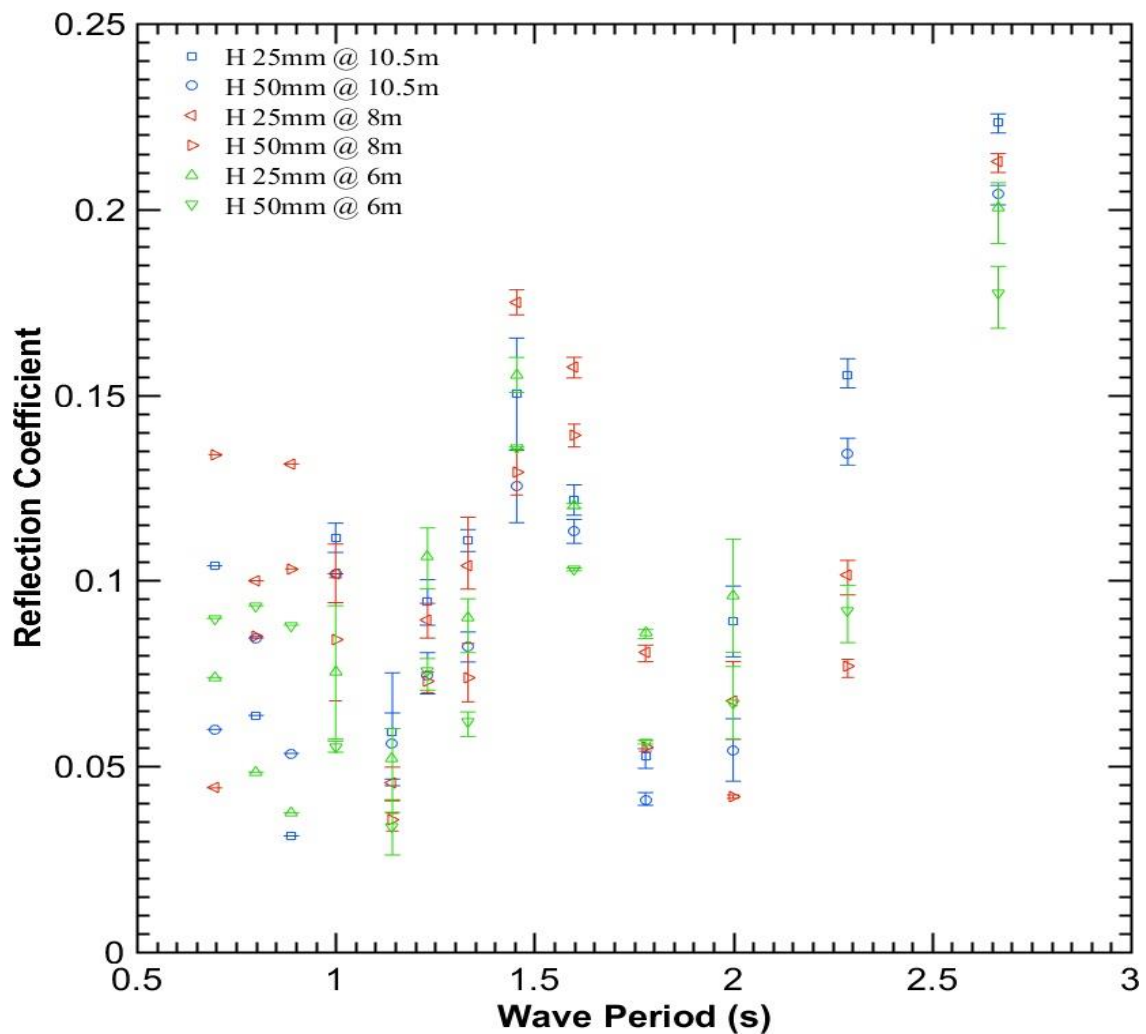
Figure 3:30: Reflection coefficient Vs wave period (s)

As a result of the work carried out, it was revealed that the basin was perhaps not operating as ideally as first thought, with reflection coefficients being particularly high (averaging 10%).

3.13.2 Irregular Waves

Twenty different Bretschneider sea states were used for the irregular wave tests. Tests were carried out at two different locations (6m &10.5m from the paddles). The repeat time of the wave series was 256 s corresponding to 8192 data points for analysis.

3.13.2.1 Irregular Wave Reflection

Figure 3:31 shows the results of the reflection analysis for the irregular wave data at a distance of 6 metres from the paddles. For the sea states where more than one combination of probes can be used, an average reflection value is given. In general the reflection coefficients are around 15%, higher coefficients are found with higher significant wave height. The highest reflection coefficients are found for the B1,B19,B2,B5 & B8 sea states which all just lie on the inside of a 1:10 steepness line. Indeed a reflection coefficient of 49% is reported for the B1 sea state however it is worth noting that;

- This sea state has the shortest peak period of 0.8s making it the most sensitive to probe spacing inaccuracies
- The method of resolving incident and reflected spectra is essentially a least squares error curve fitting exercise using linear sinusoids in both directions. The extreme steepness of this sea state would make the individual waves in the series non-linear
- The method also assumes wave propagation in 2 dimensions, whereas the real system is likely to have 3 dimensional aspects (i.e. wave propagation in more than one plane, due to the presence of cross waves)
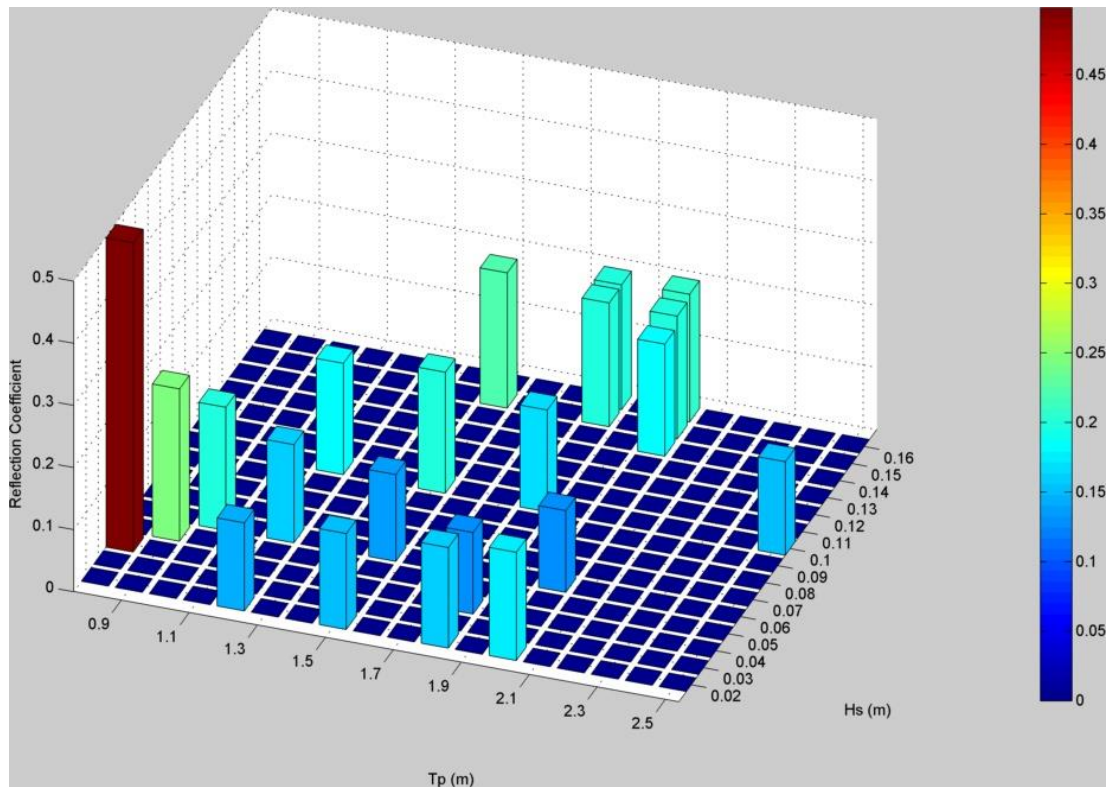
Figure 3:31: Average reflection coefficient for the different Bretschneider sea states tested @ 6m

3.14 Discussion

This spatial variation in wave elevation means one must give due care when inserting a WEC into the basin for testing purposes. In Payne (2008) the author warns that free floating devices (particularly those with slack mooring configurations) can drift away from their original positions. Although the slack mooring could hardly be blamed in such an instance for performing its functionality. The point is that the model could potentially be subjected to waves whose characteristics are different from those of the waves recorded at the original location. If the device were to drift from a 'hot spot' (antinode) to a 'cold spot' (node); this would significantly affect results. It is essential that the incoming wave envelope profile be measured at the location where the device operates. This should be measured before testing with the device out of the water.

Another concern of varying surface elevation is that if the operation of a potential WEC has any directional dependency (such as a surging or pitching device), then the surface elevation alone may not be sufficient to calculate incident wave power due to spatial variations and efforts should be taken to separate the incident and reflected parts of the wave. Indeed the basin characterisation tests

influenced the decision to select an axisymmetric point absorber type device for the experiments to follow. Such devices can absorb power indiscriminately from all directions.

Finally the non-homogeneous nature of water surface elevation in wave basins becomes a troublesome obstacle when examining WEC arrays and the interactions between neighbouring devices in an array. It would be an extremely difficult task to isolate variations related to tank inhomogeneity to that of the interaction effects from other devices (which would be an objective of such a test).

It is important that wave basins are characterised like this study, and the (Boyle et al., 2011) study in QUML, so that developers/researchers can be informed on the dynamics of the tank before carrying out a test schedule.

Chapter 4: Numerical Modelling

4.1 Introduction

Numerical modelling is a low cost and time efficient method of predicting device response to a host of different input conditions. Simulations basically invoke the use of a mathematical (or numerical) model of the system with the aid of computer software, while experimental analysis will involve measurements from physical apparatus of the real life system. Simulation results can be used to validate experimental results, but more importantly once a degree of confidence is reached in a model, it can be used to gauge the response of the device to scenarios outside of physical tests. An additional benefit of numerical modelling is the ability to simulate very large data sets which to carry out physically would be extremely time consuming, as well as expensive. A frequency domain model is first formulated which is applicable to the post transient response of the device. The model is not capable of dealing with non-linearities (in the PTO for example). Despite such a models limitations, it is often the first port of call from a modelling perspective due its ease of formulation.

Since, in practice, most converters are equipped with strongly nonlinear mechanisms, a time-domain is also described. According to Falcão (2010) time domain modelling of WECs was originally carried out in 1980 for oscillating-body converters by Jeffreys (1980), closely following the theory, based on Fourier transform techniques, developed for ship hydrodynamics by Cummins (1962). Much of this chapter is related to the necessary theory of such models. Hydrodynamic parameter results are presented which were obtained using the Boundary Element Method (BEM) WAMIT. A sanity check on the developed time domain model is carried by comparing the RAO curves to that of the frequency domain model. Blottner (1990) simply and eloquently differentiates between verification and validation of numerical models;

Verification: Solving the equations right.

Validation: Solving the right equations

The validation work is carried out in the next chapter alongside the experimental tests.

4.2 Frequency domain modelling

Recalling the equation of motion described in chapter 2 which can be found in many textbooks and papers e.g. (Pastor & Liu, 2014)

$$M\ddot{z}(\omega, t) = F_e(\omega, t) + F_{rad}(\omega, t) + F_{hyd}(\omega, t) + F_{PTO}(\omega, t) + F_{Tun}(\omega, t) \qquad \textbf{(4.1)}$$

If we assume that all the dynamic quantities vary sinusoidally with time and with angular frequency ω, then we may introduce phasors for the various quantities, i.e., the buoys velocity which we have restricted to heave motion only is given by

$$u(t) = \frac{dz}{dt} = u_{max} \cos(\omega t + \phi_u) = \Re\{U(\omega)e^{i\omega t}\} \qquad \textbf{(4.2)}$$

Where $U(\omega) = u_{max}e^{i\phi_u}$ is the velocity phasor.

By differentiation and integration respectively, we obtain the acceleration and displacement i.e.

$$a(t) = \frac{du}{dt} = -\omega u_{max} \sin(\omega t + \phi_u) = \Re\{i\omega U(\omega)e^{i\omega t}\} \qquad \textbf{(4.3)}$$

$$z(t) = \int_0^t u \, dt = \frac{u_{max}}{\omega} \sin(\omega t + \phi_u) = \Re\{\frac{U(\omega)}{i\omega}e^{i\omega t}\} \qquad \textbf{(4.4)}$$

When the radiation force is considered in the frequency domain, it can be expressed as follows

$$F_{rad}(t) = -\Big(b_{hyd}(\omega) + i\omega m_a(\omega)\Big)U(\omega) \qquad \textbf{(4.5)}$$

Where $m_a(\omega)$ and $b_{hyd}(\omega)$ are the frequency dependent added mass and damping terms respectively. Falnes (2002) notes the usefulness of using the radiation impedance Z_{rad} as is done in electrical and other oscillatory systems.

$$Z_{rad}(\omega) = b_{hyd}(\omega) + i\omega m_a(\omega) \qquad \textbf{(4.6)}$$

The hydrostatic force

$$F_{hyd}(t) = \frac{-c}{i\omega}U(\omega) \qquad \textbf{(4.7)}$$

Finally the tuning force

$$F_{Tun}(t) = i\omega m_{sup} U(\omega) \tag{4.8}$$

We also define an excitation force phasor $F_e(\omega)$ and a PTO-force phasor $F_{PTO}(\omega)$. The frequency domain equation of motion is then

$$i\omega \left(m + m_{sup} + m_a(\omega) \right) U(\omega) + b_{hyd}(\omega)U(\omega) + \frac{c}{i\omega}U(\omega) = F_e(\omega) + F_{PTO}(\omega) \tag{4.9}$$

Equation (4.9) is valid only when $F_e(t)$ and $F_{PTO}(t)$ are sinusoidal. Furthermore, the equation is only suitable for the steady state response of the system (unsuitable for transients). The limitation that $F_{PTO}(t)$ be sinusoidal means that the applied external damping must be linear i.e.

$$b_{ext} = {F_{PTO}}/{u} = constant \tag{4.10}$$

The convenience of using impedances is that it makes equation (4.9) more concise

$$(Z_{mech} + Z_{rad})U = F_e \tag{4.11}$$

Here Z_{mech} is the intrinsic or mechanical impedance of the system given be

$$Z_{mech} = b_{ext} + i\left\{ \omega(m + m_{sup}) - \frac{c}{\omega} \right\} \tag{4.12}$$

Assuming the system is linear then the post-transient response to polychromatic waves can be determined via the principle of superposition.

The hydrodynamic parameters can be obtained from boundary integral equation methods more often referred to as boundary element methods (BEM) codes such as WAMIT. The objective of WAMIT is to evaluate the unsteady hydrodynamic pressure, loads and motions of the body, as well as the pressure and velocity in the fluid domain. The flow is assumed to be potential, free of separation or lifting effects. The free-surface and body-boundary conditions are linearised and a harmonic time dependence is adopted. (WAMIT, 2014).

WAMIT consists of two subprograms: a) POTEN, which is a solver for the velocity potential accounting for radiation and diffraction and b) FORCE, which is employed for the hydrodynamic response of the structure and computes hydrodynamic coefficients, motions and first and second order forces. The following quantities can be evaluated by WAMIT: hydrostatic coefficients; added-mass $m_a(\omega)$, and

damping $b_{hyd}(\omega)$ coefficients; wave exciting force $F_e(\omega)$ and moments; motion amplitudes and phases for a freely-floating body; forces restraining a body which is freely-floating in some modes; hydrodynamic pressure and fluid velocity on the body surface and in the fluid domain; free surface elevation; all components of the drift force and moments by integration over a control surface; mean yaw moment by integration in the far field; all components of the drift force and moment by local pressure integration over the body surface and drift force and moment in bidirectional waves (Vyzikas, 2014).

The more advanced higher-order panel method, which is based on a continuous B-spline representation for the velocity potential was used. The order of the B-spline basis functions is defined by the order of the polynomial (Ku and Kv) and the number of panels (Nu and Nv). The dimension of these linear systems is denoted by NEQN (number of equations). In the low-order method NEQN is the same as the number of panels. In the higher-order method NEQN depends on the number of patches, panels, and on the order of the basis functions;

$$NEQN = \sum_{i=1}^{Np} (NU(i) + KU(i) - 1)x(NV(i) + KV(i) - 1) \qquad \textbf{(4.13)}$$

Where N_p is the total number of patches (two for these tests), NU and NV are the numbers of panels on each patch, and KU and KV are the orders of the B-splines used to represent the solution (three for these tests). According to the WAMIT user manual the higher-order method experience indicates that the convergence rate is reduced, and it is generally advisable to use the direct solver.

If the body geometry has one or two planes of symmetry, half or a quarter of its wetted surface is represented with panels, respectively. Figure 4:1 shows the quarter body representations of the cone and hemisphere buoys.
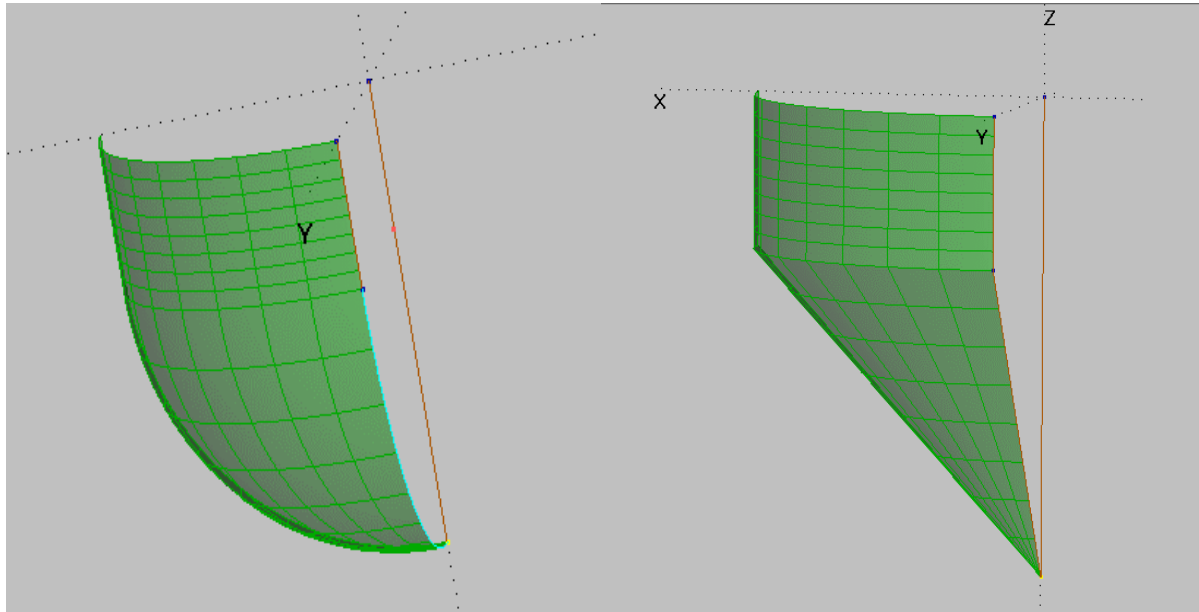
Figure 4:1: Multisurf representation of Cone-cylinder and Hemisphere-cylinder shapes
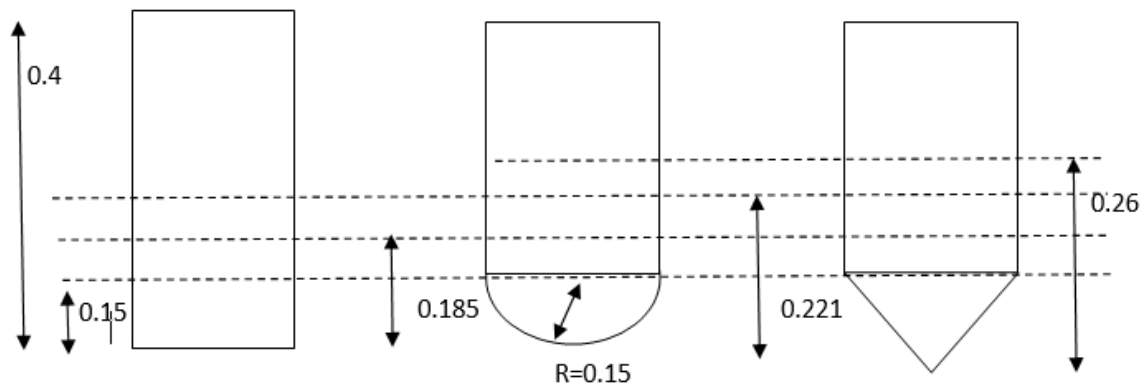
Figure 4:2: Model Scale dimensions (in meters)

Since this work is primarily interested in model scales, the dimensions of the devices as given in Figure 4:2Figure 4:2 were used an input into the numerical model. Table 4-1 lists the different order of the B-splines that was used for a convergence test.

Table 4-1: Numbers of panels on each patch and Number of Equations

Nu	Nv	NEQN
6	6	128
8	8	200
16	16	648
20	20	968
25	25	1458
30	30	2048
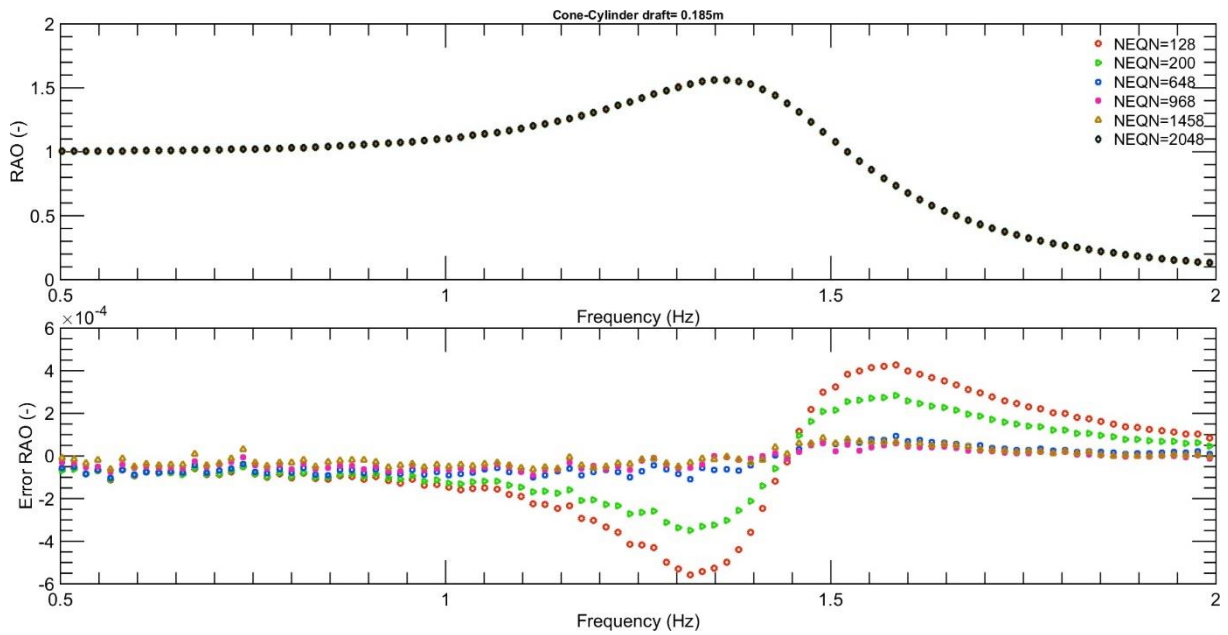
Figure 4:3: Convergence of RAO for cone-cylinder draft=185mm

Figure 4:3 depicts the results of a convergence test of response amplitude operator (RAO) for cone-cylinder draft=185mm. The lower plot shows the error between the values estimated at the highest NEQN from all other iterations. From the results it can be seen the error remains minimal for NEQN of 968 and above.

4.2.1 WAMIT Output

Figure 4:5 to Figure 4:7 show the results from WAMIT for the various buoy shapes and drafts. Figure 4:5 shows the added mass against frequency, the cylinder having much more intrinsic inertia than the cone-cylinder and hemisphere-cylinder has much more added mass. Over the typical frequency range tested in the wave basin (0.5-1.25 Hz), one sees that the smaller the draft, the larger the added mass, something which is true for all shapes tested.

Figure 4:6 shows the hydrodynamic damping versus frequency. The cone-cylinder exhibits the highest values, then the hemisphere-cylinder and then the cylinder. Invoking the adage that a good wave energy absorber should be a good wave energy maker, Figure 4:6 suggests that the cone and hemisphere would be superior to the cylinder as a wave absorber/generator. As was the case with added mass, the shallower the draft, the greater the amount of hydrodynamic damping. The somewhat less than usual added mass profile (more specifically at very low frequencies) is an artefact of the water depth (HBOT in WAMIT) of 1 m. It can therefore be considered a shallow water effect. A similar added mass profile is observable from the Wavestar device shown in (evaluated at full scale dimensions).
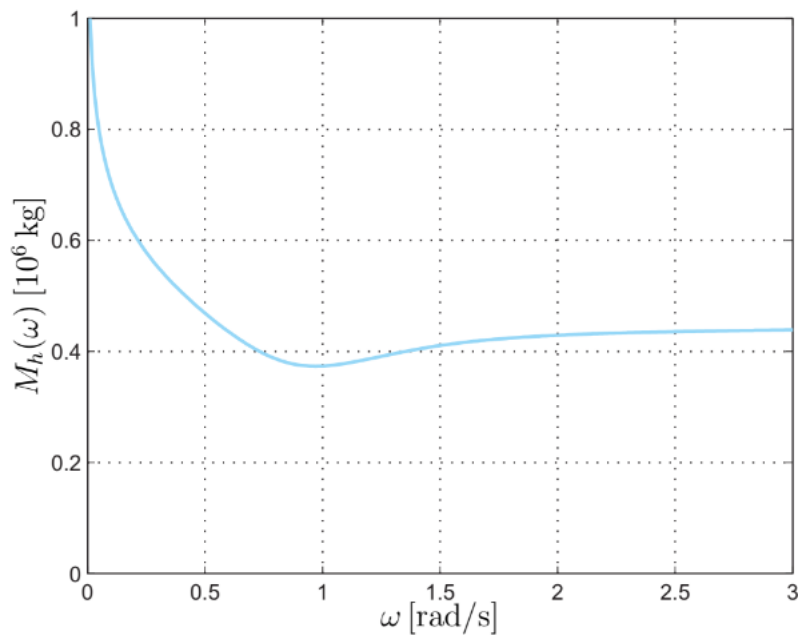
Figure 4:4: Wavestar added mass versus angular frequency (source (Nielsen et al 2012))
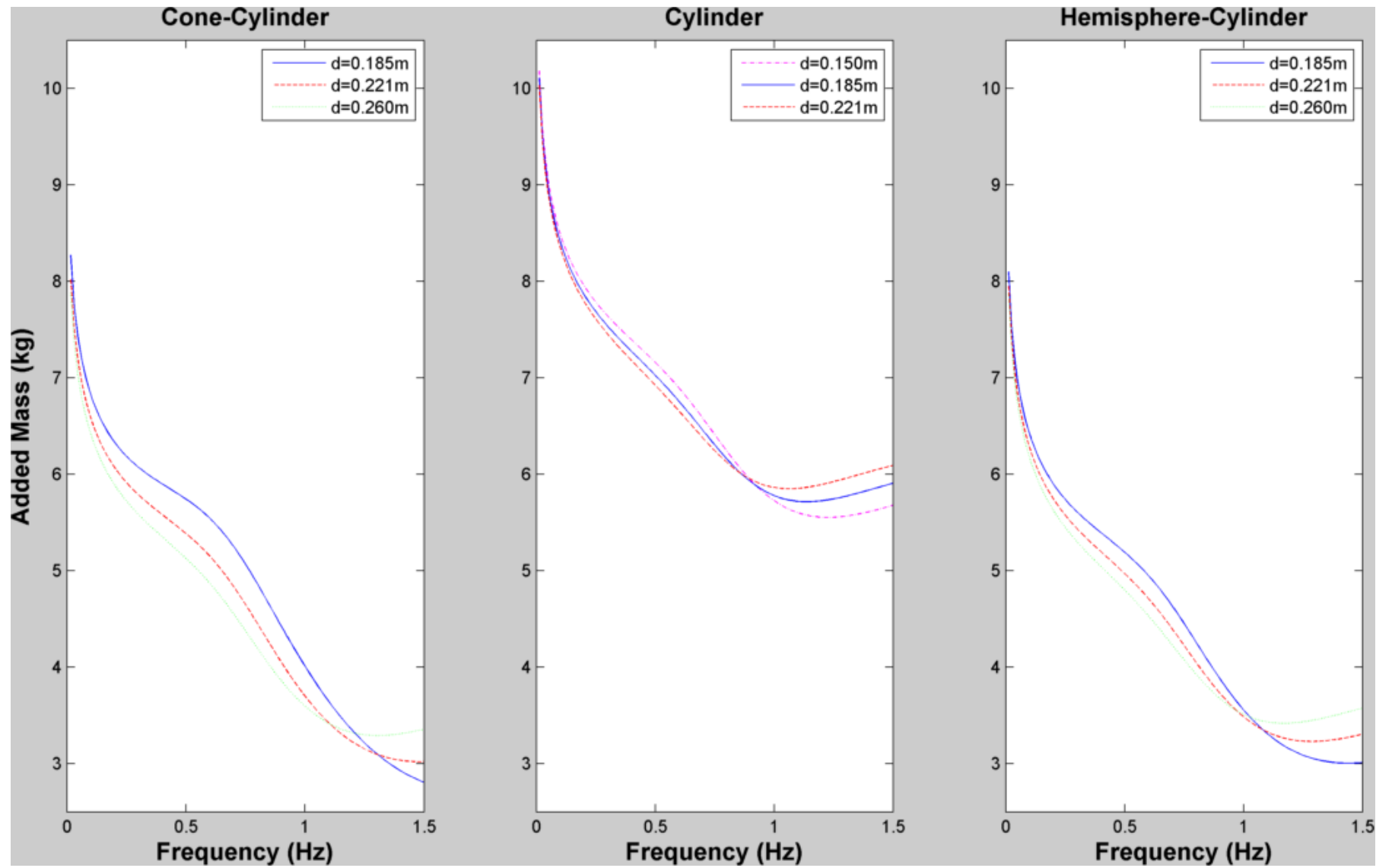
Figure 4:5: Added mass vs frequency for the cone-cylinder (left), cylinder (middle) and the hemisphere-cylinder (right)

130
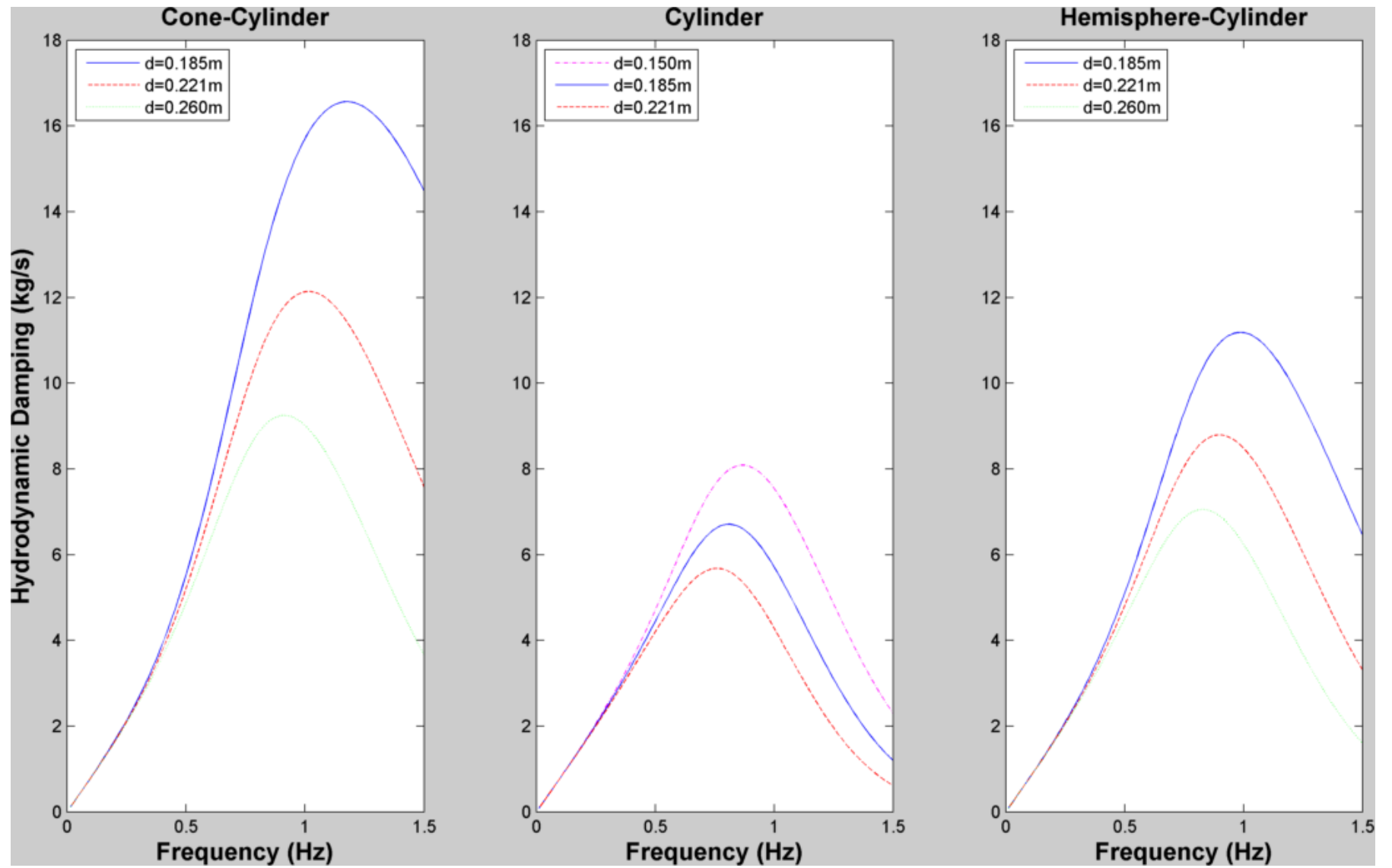
Figure 4:6: Hydrodynamic damping vs frequency for the cone-cylinder (left), cylinder (centre) and the hemisphere-cylinder (right)
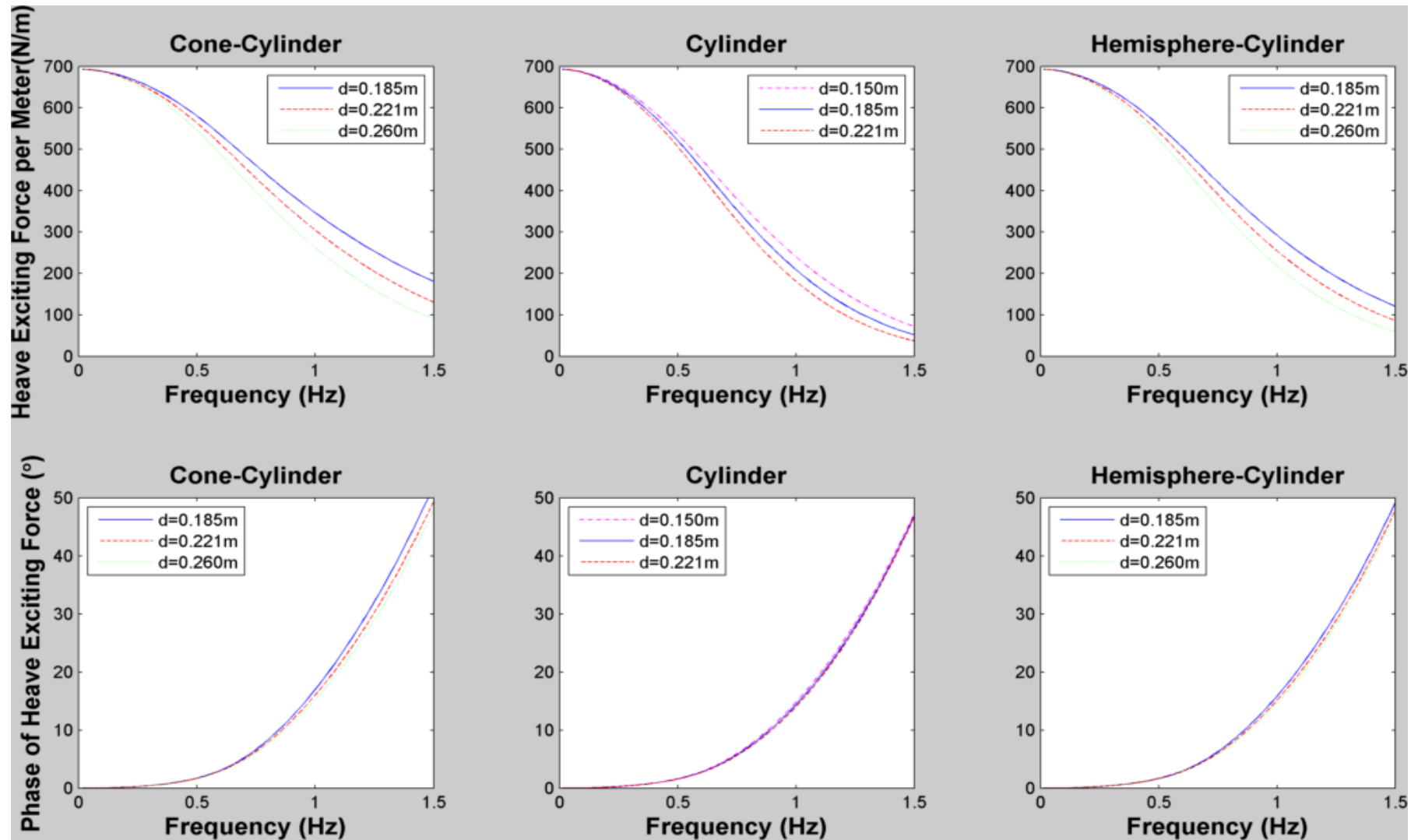
Figure 4:7: Magnitude of heave excitation force per metre wave height (upper row) and phase of excitation force (lower row) vs frequency for the cone-cylinder (left), cylinder (centre) and the hemisphere-cylinder (right)

Figure 4:7 shows the magnitude of the heave excitation force per unit wave amplitude as well as the phase of the excitation force. The phase of the excitation force is very similar over the frequency range of interest for all shapes and drafts. The zero frequency limit of the excitation force for all shapes and drafts has the roughly the same value of 693.5 (N/m). This corresponds to the hydrostatic force $\rho g A_w$ since all the buoys share the same wetted area A_w at the neutral draft position. As frequency increases then generally, the cone retains slightly higher magnitudes, followed by the hemisphere and then the cylinder. Once again the shallower drafts exhibit the larger excitation forces.

Figure 4:8 shows the RAO values for all shapes and drafts. The same colour is used for a constant draft while the cone, cylinder and hemisphere are marked with crosses, circles and squares respectively. The effect of mass is clear from the resonance frequencies, the lighter cone shaped buoys have higher natural frequencies, then the hemispheres and then the cylinders. It is interesting to note that the largest hemisphere draft of 0.26 m matches very closely the profile of the 0.21 m draft cylinder. As was noted in chapter two, most of the wave energy is at the surface (decaying with depth due to e^{-kz} term). Therefore the further the hemisphere is submerged, the closer it 'resembles' a pure cylinder to the incoming waves. Another way to look at it, is that even if the device profile has better wave making capabilities (which a cone and hemisphere do relative to a cylinder); the further you submerge this section, the more you lose this effect.
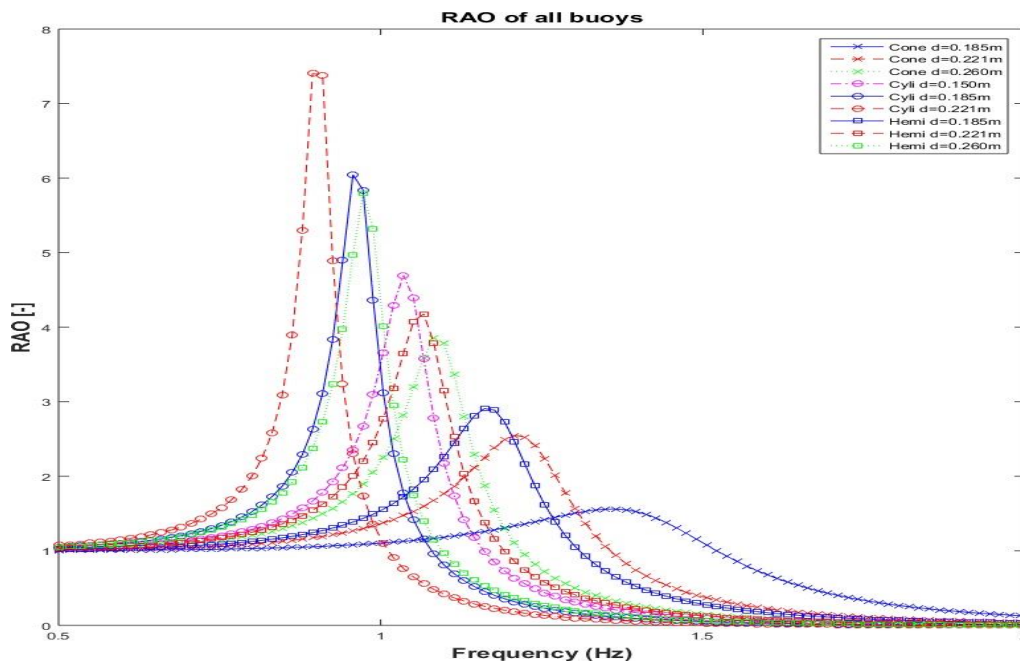
Figure 4:8: RAO vs Frequency for all shapes and drafts

4.2.2 Irregular Waves

Assuming the system is linear, the post-transient response to polychromatic waves can be determined via the principle of superposition. For this to be the case both the waves and motion response must be restricted to small amplitude, there can be no non-linearites in the system (such as friction), and the method of useful power absorption must be a linear damper. Price (2009) writes that for linear waves, the wave amplitude should be low with respect to wavelength. The hydrodynamic coefficients: exciting force, added mass and added damping; can be calculated using linear potential flow theory, which treats the waves as linear and the wetted area of the body as constant.

Since the wave elevation is assumed to be a zero-mean Gaussian process, the loads and the response are also a zero-mean Gaussian distributed process. It is then appropriate to generate spectra of loads and responses. The amplitude spectrum of buoy displacement is defined as:

$$S_z(\omega) = S_\zeta(\omega)\frac{z^2}{\zeta^2} \qquad\qquad \textbf{(4.14)}$$

A useful plot illustrating what equation (4.14) entails is given by Journée & Massie, (2001) shown in Figure 4:9. The left hand side of the figure shows the component waves and associated spectra of the incoming irregular time series. In the center the amplitude and phase transfer functions associated with the device. The component sum of each the individual response curves is shown on the right, which can then be transformed into a motion response spectrum.

Analogous to the concept of significant wave height (or amplitude) discussed in chapter 2, the significant amplitude of buoy displacement can be defined as

$$Z_{a,sig} = 2\sqrt{\int_0^\infty S_\zeta(\omega)d\omega} \qquad\qquad \textbf{(4.15)}$$

De Backer (2010) used such a statistical approach to predicting loads and motions. The author used constraints to curtail the otherwise unrestrained numerical predications of the frequency domain model.
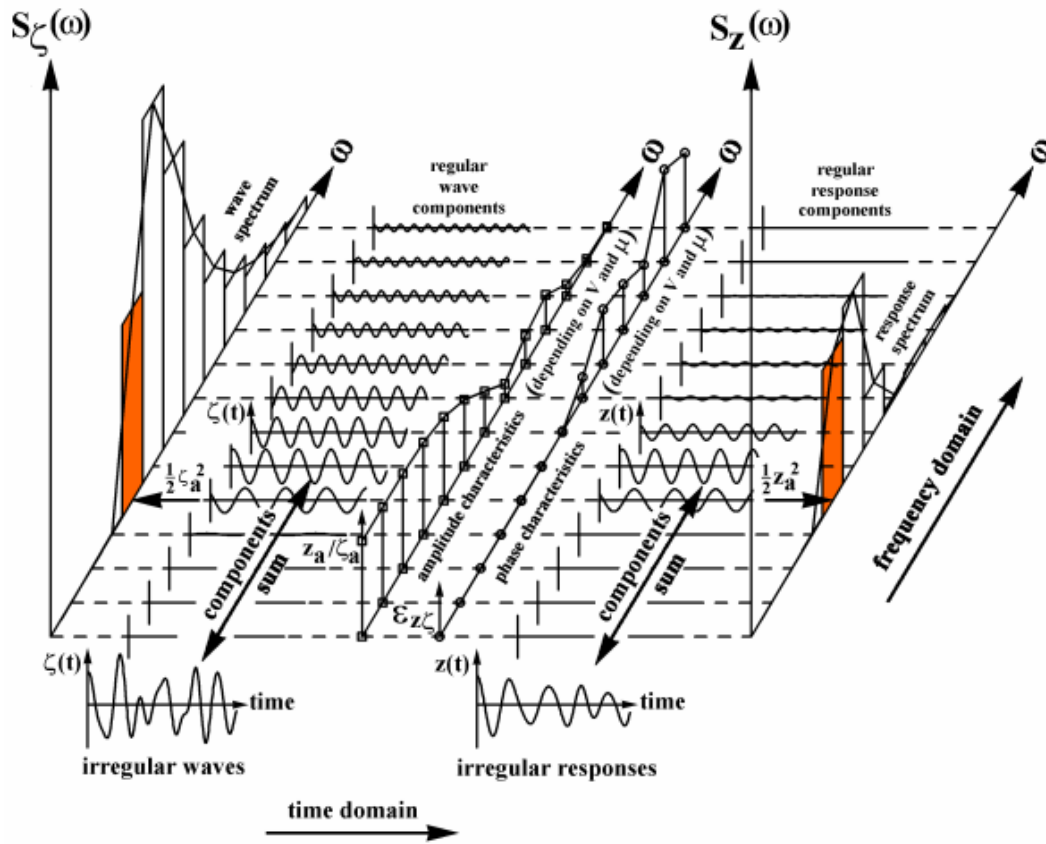
Figure 4:9: Principle of Transfer of Waves into Responses (source Journée & Massie, (2001))

Stroke Constraint

Restrictions on the buoy motion, e.g., imposed by the limited height of the hydraulic rams/ encasing platform structure can be accounted for by specifying an upper limit on the significant amplitude of floater motion.

$$Z_{a,sig} \leq Z_{a,sig\ Max}$$ (4.16)

If the incident wave spectra is suitably narrow then the wave heights will follow a Rayleigh distribution. Additionally if the WECs response to said incoming wave is linear (which is the core assumption in frequency domain modelling) the floater response will also follow a Rayleigh distribution. With this in mind assuming a Rayleigh distribution of floater motion, the probability of exceeding a is

$$P\{Z_a > limit\} = e^{-2\left(\frac{limit^2}{Z_a^{\ 2}}\right)}$$ (4.17)

135

To generate some potential figures, assuming a scaling ratio of 1:20 such that the laboratory scale diameter of 0.15m became a prototype 3 m diameter, then if a stroke amplitude limit of 2.5 m is assumed .

Selecting two arbitrary $Z_{a,sig\ Max}$ maximum significant amplitudes of 2 m and 3 m, the resulting probability of exceeding the stroke amplitude is 4.39% an 25%. Clearly the 3 m constraint is far too weak with one in four oscillations violating the imposed conditions.

Similar constraints can be for example;

Slamming Constraint

When the buoy loses contact with the water surface, it experiences a significant slamming force upon re-entry. Repeated instances of slamming reduce the lifespan of the device due to high impact forces/fatigue loading. This problem could be alleviated by an intelligent control system which predicts instances of slamming and executes measures to prevent such events.

Force Constraint

Optimal control parameters for maximum power absorption, result in very large and often unrealistic control forces. If the PTO system is required to deliver these forces then there will likely be a limit on the force that can be outputted by the PTO, certainly from a design and economic perspective.

Defining a force spectrum

$$S_F(\omega) = 2\sqrt{\int_0^\infty S_F(\omega)d\omega} \tag{4.18}$$

$$F_{a,sig} = 2\sqrt{\int_0^\infty S_F(\omega)d\omega} \tag{4.19}$$
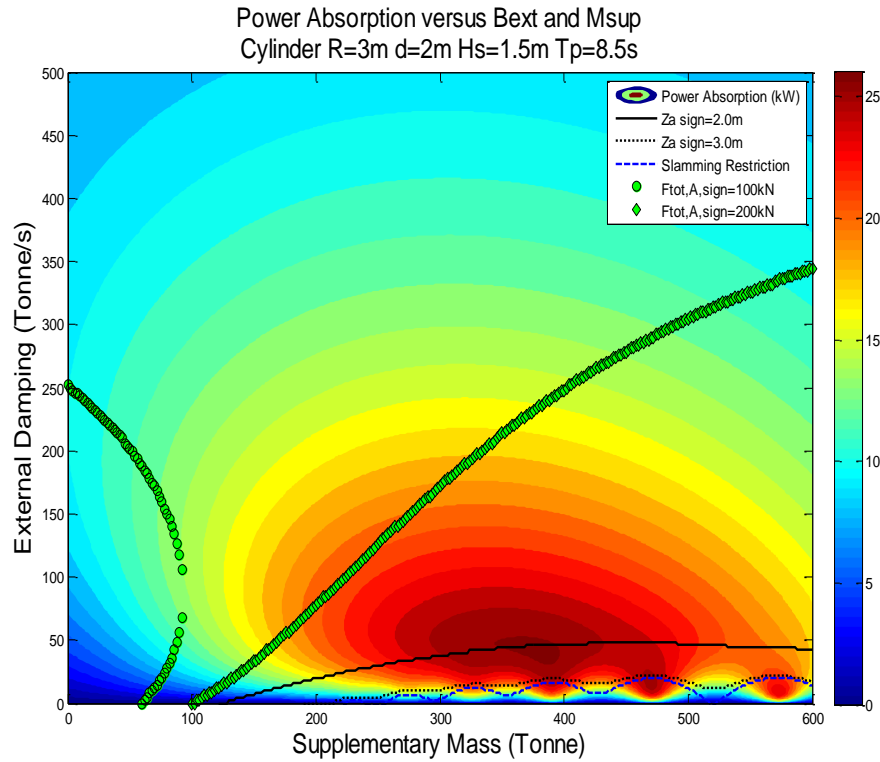
Figure 4:10: Power absorption Vs B_{ext} and M_{sup} for Cylinder shape

Although such a statistical based, frequency domain method was not preferred in this work, Figure 4:10 displays the power absorption plot with constraint curves (which is shown for illustrative purposes). Power absorption values are given for a cylinder of radius 3m and draft 2m. Incoming wave conditions are a Bretschneider spectrum with H_s of 1.5m and T_p of 8.5s. The frequency domain model will predict extremely large power absorption levels. It will also predict large (unrealistic) displacement amplitudes and control forces. The constraint curves described previously will therefore put bounds on the maximum power capture.

Whilst taking a statistical approach, which includes constraints, is useful for predicting more realistic responses and loads in the frequency domain, the inability to include transients and control inputs is a weakness of such an approach. For example, in a prototype scenario if the stroke limit is being approached, then a likely scenario will be the instantaneous increase in damping to impede the buoys displacement.

The assumption of constant wetted surface becomes increasingly inaccurate as the displacement relative to the water surface increases. Buoyancy spring is often linearised by assuming constant waterline area, an assumption that also becomes increasingly challenged for larger relative motion.

For large relative motions, in addition to the time variant/inaccurate coefficients, highly non-linear forces not included in the linear model appear and may dominate the behaviour. Price (2009) lists some of these forces including:

• Non-linear spring such as mooring, • Losses due to viscous drag, bearings and PTO, • Wave slamming, overtopping, and re-emerging,

• Restraints on displacement, forces or power capture as these reach economic or practical design limits,

• Non-linear PTO strategies, • Parasitic resonant responses in other degrees of freedom.

In order to have a numerical model which can cope with these non-linearity's and transient behaviours it is necessary to work with a time domain model.

4.3 From frequency domain to time domain

The Retardation Transfer Function (RTF) symbolised by $H(\omega)$ is defined by

$$H(\omega) = b_{hyd}(\omega) + i\omega(m_a(\omega) - m_\infty) \tag{4.20}$$

Where m_∞ is the infinite frequency added mass value. The frequency domain equation (4.9) can be rearranged to become

$$i\omega(m + m_{sup} + m_\infty)U(\omega) + H(\omega)U(\omega) + \frac{c}{i\omega}U(\omega) = F_e(\omega) + F_{PTO}(\omega) \tag{4.21}$$

Noting that the addition of the added mass at infinite frequency term with the second term in the equation; frequency domain multiplication, of the retardation function with the velocity yields the radiation force. Multiplication in the frequency domain is equivalent to convolution in the time domain. Therefore taking the inverse Fourier transform of (4.21) yields

$$(m + m_{sup} + m_\infty)\ddot{z}(t) + h(t) * \dot{z}(t) + cz(t) = F_e(t) + F_{PTO}(t) \tag{4.22}$$

138

Where $h(t)$ is the radiation impulse response function. Writing the convolution in its integral form, the time domain equation of motion takes the form of that put forward by (Cummins, 1962)

$$\left(m + m_{sup} + m_\infty\right)\ddot{z}(t) + \int_0^\infty h(\tau)\dot{z}(t-\tau)d\tau + cz(t) = f_e(t) + f_{PTO}(t) \qquad \textbf{(4.23)}$$

Ogilve (1964) carried out an extension to the work of Cummins by taking the Fourier transform of equation (4.23), determining the relationship between the frequency dependent added mass and damping parameters and the time domain convolution term.

$$m_a(\omega) = m_\infty - \frac{1}{\omega}\int_0^\infty h(t)\sin(\omega t)dt \qquad \textbf{(4.24)}$$

$$b_{hyd}(\omega) = \int_0^\infty h(t)\cos(\omega t)dt \qquad \textbf{(4.25)}$$

$$h(t) = \begin{cases} \dfrac{2}{\pi}\displaystyle\int_0^\infty b_{hyd}(\omega)\cos(\omega t)d\omega & \text{if } t \geq 0 \\ 0 & \text{if } t \leq 0 \end{cases} \qquad \textbf{(4.26)}$$

4.3.1 Parametric model approximation of the radiation integral term

The convolution term in the equation of motion must be computed at each time step, something that is cumbersome from a numerical simulation point of view and inconvenient from a control system analysis point of view. As convolution is a linear operation, it can be represented by a linear ordinary differential equation, i.e., the convolution product can be replaced by a state space model (Perez & Fossen, 2008b)

.

$$\dot{x}_r(t) = A_r x_r(t) + B_r \dot{z}_r(t) \qquad \textbf{(4.27)}$$

$$\int_0^\infty h(\tau)\dot{z}(t-\tau)d\tau \approx C_r x_r(t) \qquad \textbf{(4.28)}$$

One of the advantages of state-space models is that they possess the Markov property, which guarantees that any future state of the system depends only on the present value of the system states.

As a consequence, no past information needs to be stored by contrast with the convolution method, as all the memory effect is contained in the state vector x_r (Jonkman, Duarte, Alves, & Sarmento, 2013). There are many different methods of achieving the state space approximation using system identification techniques (essentially curve fitting exercises). Attempting to find a linear state space model which has the same characteristics as the retardation function as given in equation (4.10) is known as frequency domain identification. Alternatively, by taking the inverse Fourier transform of the retardation function or by using equation (4.26) directly to determine the impulse response of the radiation system, it is possible to find a system which shares the same impulse response. This approach is known as time domain identification.

4.3.1.1 Complex curve fitting

This section discusses fitting a rational transfer function to the hydrodynamic coefficients used in the frequency domain. The frequency-domain identification method consists of finding the polynomial coefficients that allow representing the RTF as a rational function (see Ricci, 2016). Specifically, we consider

$$\widehat{H}(s,\theta) = \frac{P(s,\theta)}{Q(s,\theta)} = \frac{p_m s^m + p_{m-1} s^{m-1} + \cdots + p_0}{s^n + q_{n-1} s^{n-1} + \cdots + q_0} \tag{4.29}$$

Where s is the usual Laplace transform variable and θ is the vector of parameters
$[p_m, \ldots, p_0, q_{n-1,\ldots,}q_0]^T$
By restricting s to take only imaginary values, $i\omega$, the frequency response of the model is obtained via

$$\Re\left\{\frac{P(i\omega,\theta)}{Q(i\omega,\theta)}\right\} = \widehat{b}_{hyd}(\omega) \tag{4.30}$$

$$\Im\left\{\frac{P(i\omega,\theta)}{Q(i\omega,\theta)}\right\} = \omega(\widehat{m}_a(\omega) - m_\infty) \tag{4.31}$$

Where $\widehat{b}_{hyd}$ and $\widehat{m}_a(\omega)$ are the model approximations of the hydrodynamic damping and added mass respectively.

An important aspect of constructing a parametric model is that it must possess certain properties in order to be physically relevant. The implications or constraints on the parametric model arise from the underlying hydrodynamics, and thorough reviews can be found in (Unneland, 2007) as well as multiple papers from Perez & Fossen (2008, 2008a). A brief summary will be listed here.

4.3.1.2 Low-frequency asymptotic value

A structure cannot radiate waves at zero frequency, meaning that

$$\lim_{\omega \to 0} H(\omega) = 0 \tag{4.32}$$

The implication of this is that the model have a zero at $\omega = 0$, which in turn requires p_0 to be zero.

4.3.1.3 High-frequency asymptotic value

The high frequency limit of the damping is zero as the body oscillations do not generate any water waves at infinite frequency, and thus cannot carry energy away to infinity. Faltinsen (1990) notes that the linearised free surface boundary condition (evaluated at z=0) shows that the velocity cannot be both vertical and horizontal components at the free surface.

$$\lim_{\omega \to \infty} H(\omega) = 0 \tag{4.33}$$

The imaginary part of the retardation function equation (4.24) tends to zero due to the Riemann-Lebesque lemma.

$$\lim_{\omega \to \infty} \omega(m_a(\omega) - m_\infty) = \lim_{\omega \to \infty} \int_0^\infty -h(t)\sin(\omega t)dt = 0 \tag{4.34}$$

This means that the model transfer function must be strictly proper, meaning that, the degree of the denominator must be greater than that of the numerator.

4.3.1.4 Initial time value

The initial value of the impulse response must not be zero and is in fact related to the area under the damping curve.

$$\lim_{t \to 0} h(t) = \lim_{t \to 0} \frac{2}{\pi} \int_0^\infty b_{hyd}(\omega)\cos(\omega t)d\omega = \frac{2}{\pi} \int_0^\infty b_{hyd}(\omega)d\omega \neq 0 \tag{4.35}$$

Using the initial value theorem

$$\lim_{t \to 0} h(t) = \lim_{s \to \infty} sH(s) = \lim_{s \to \infty} s\frac{P(s)}{Q(s)} = \frac{p_m s^{m+1}}{s^n} \tag{4.36}$$

Therefore, if the limit above is to have a finite value, the relative degree of the transfer function must be one ($n = m + 1$). The minimum order transfer function is therefore second order.

4.3.1.5 Final time value

$$\lim_{t\to\infty} h(t) = \lim_{t\to 0} \frac{2}{\pi} \int_0^\infty b_{hyd}(\omega)\cos(\omega t)d\omega = 0 \qquad \textbf{(4.37)}$$

Once again the Riemann-Lebesque lemma is invoked to show that as time goes to infinity, the impulse response tends to zero. This property is known as the bounded input bounded output (BIBO) stability criterion and it means that the poles and zeros of the transfer function must lie in the left hand s plane.

4.3.1.6 Passivity

A system is said to be passive if it can store and dissipate energy but not generate energy. A consequence of this condition is that the damping cannot have negative values. Hence

$$\Re\{H(i\omega, \theta)\} = b_{hyd}(\omega) \geq 0 \qquad \textbf{(4.38)}$$

4.3.1.7 Frequency domain identification

The parameter estimation problem can be formulated as a least squares complex curve fitting problem using the model estimates and the non-parametric data $H(i\omega_l)$ obtained from WAMIT evaluated over a finite number of frequencies $l = 1, \dots, N$ ($N = 256$ in this study).

$$\theta = \arg\min_\theta \sum_l \omega_l (\epsilon_l^* \epsilon_l) \qquad \textbf{(4.39)}$$

Where ω_l are the weighting coefficients, chosen so that certain frequency ranges can be prioritised and

$$\epsilon_l = H(i\omega_l) - \frac{P(i\omega_l, \theta)}{Q(i\omega_l, \theta)} \qquad \textbf{(4.40)}$$

McCabe et al. (2005) proposed the use of the Matlab function *invfreqs* to solve the least squares problem. The routine uses the method of Levy (1959) to linearise the problem:

$$\theta' = \arg\min_\theta \sum_l \omega_l'(\epsilon_l'^* \epsilon_l') \qquad \textbf{(4.41)}$$

$$\epsilon_l' = Q(i\omega_l, \theta)\epsilon_l = Q(i\omega_l, \theta)H(i\omega_l) - P(i\omega_l, \theta) \qquad \textbf{(4.42)}$$

4.3.1.8 Time domain identification

The impulse response can alternatively be used to fit a model for the radiation force. The impulse response can be obtained by an IFFT of the retardation function or by using equation (4.26) which would entail an integration method (such as trapezoidal integration) of the hydrodynamic damping values obtained from WAMIT.

One time domain method is the Matlab function *prony* which is based on a method of fitting the impulse response with a series of exponential functions.

$$h(t) = \sum_{i=1}^{N_e} \alpha_i e^{\beta_i t} \qquad\qquad \textbf{(4.43)}$$

Where N_e is the number of exponentials used in the fitting process. The method takes its name from Gaspard Riche de Prony and has been developed from a wave energy perspective by (Clément, 1995), Duclos et al. (2000) at the Ecole Centrale de Nantes.

Another time domain method is the Hankel Singular Value Decomposition (HSVD) based on the work of (Kung, 1978) and was put forward as means of identifying the radiation force of marine structures by (Kristiansen & Egeland, 2003).

A difficulty with time domain identification methods is that they use the frequency domain values from WAMIT as a starting point. Since values from WAMIT will only have been evaluated up to a certain frequency (the maximum frequency is related to the size of the panels used in the BEM method), a distortion effect will be introduced (recall that the initial value of the impulse response is related to the entire area under the damping curve). In effect the numerically produced damping curve can be thought of as the real damping filtered with a rectangular filter up to the maximum (distortion) frequency. This problem can be somewhat alleviated by extrapolating the data towards the high frequency tail using an exponential function as in (Kurniawan, Todalshaug, & Moan, 2011).

In a comparative study by (Jonkman et al., 2013), four different methods of system identification (invfreqs, FDI Toolbox, Prony's method and HSVD) were compared for different 6-degree-of-freedom floating platforms of varying hydrodynamic complexity A reproduction of results from this paper is given in Figure 4:11. The plot shows the number of states (y-axis) required to achieve different levels of fit (R^2 on the x-axis) for the four methods. The models under consideration are two different type of floating offshore wind (FOW) platform; a relatively simple spar type, and a semisubmersible type. Observing the figure it is evident that the frequency-domain method using the (FDI) toolbox and the

time-domain method based on the HSVD realization method offered the best quality fit using the smallest number of states.
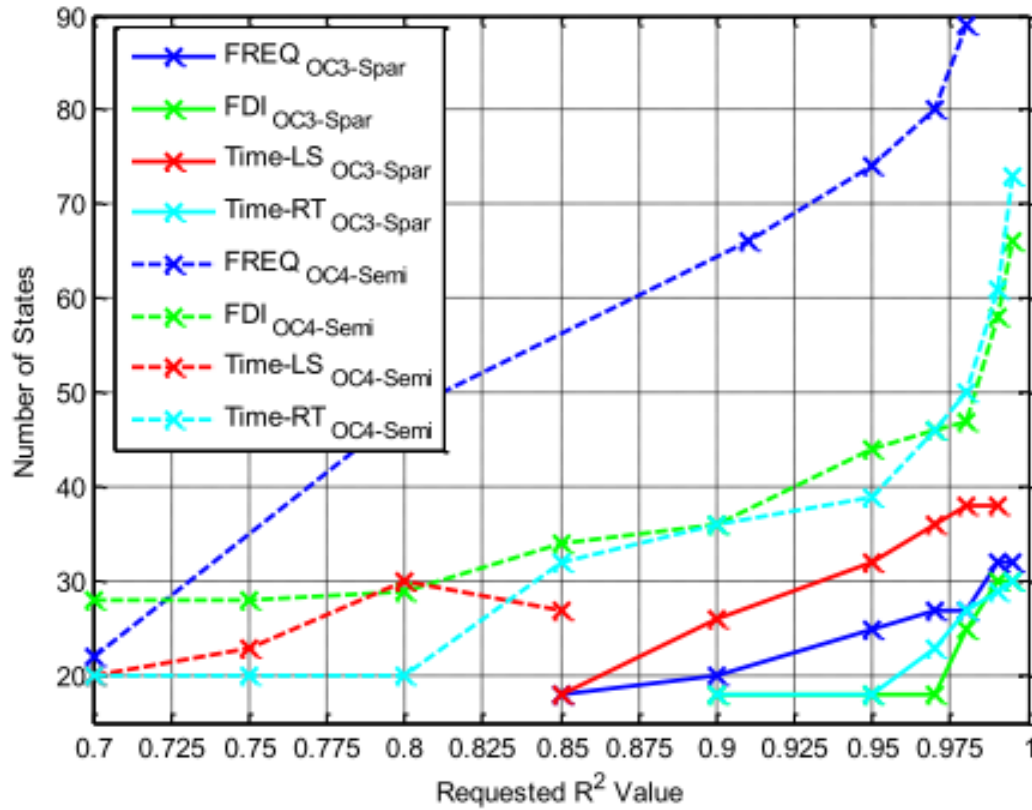
Figure 4:11: Reproduction of results from (Jonkman et al., 2013). R^2 values are plotted for four different types of fit. Two frequency domain based methods (FREQ in blue and FDI in green) and two time domain based methods (Prony red and HSVD cyan) are compared for two different 6-DOF floating wind turbine models; A Spar (solid lines) & a Semisubmersible (dashed lines).

Although the single degree of freedom case in this study makes a simpler problem the FDI Toolbox compiled by Perez & Fossen (2009) is preferred as it adds prior knowledge stemming from the hydrodynamics of the model.

4.4 Sample results

The magnitude of the non-parametric retardation function, for the cone-cylinder shaped buoy of draft 260 mm, which is obtained using values from WAMIT is shown in Figure 4:12 alongside the fifth order fitted function obtained using the FDI toolbox. The fit agreement is very good with an R^2 value of 0.998. The error between WAMIT values and fitted values is plotted on the right-hand axis of each plot. Figure 4:13 Figure 4:14 show the original and fitted curves of the hydrodynamic damping and added mass

respectively. As to be expected from such a relatively large number of states used in the approximation, the fitting agreement is good.
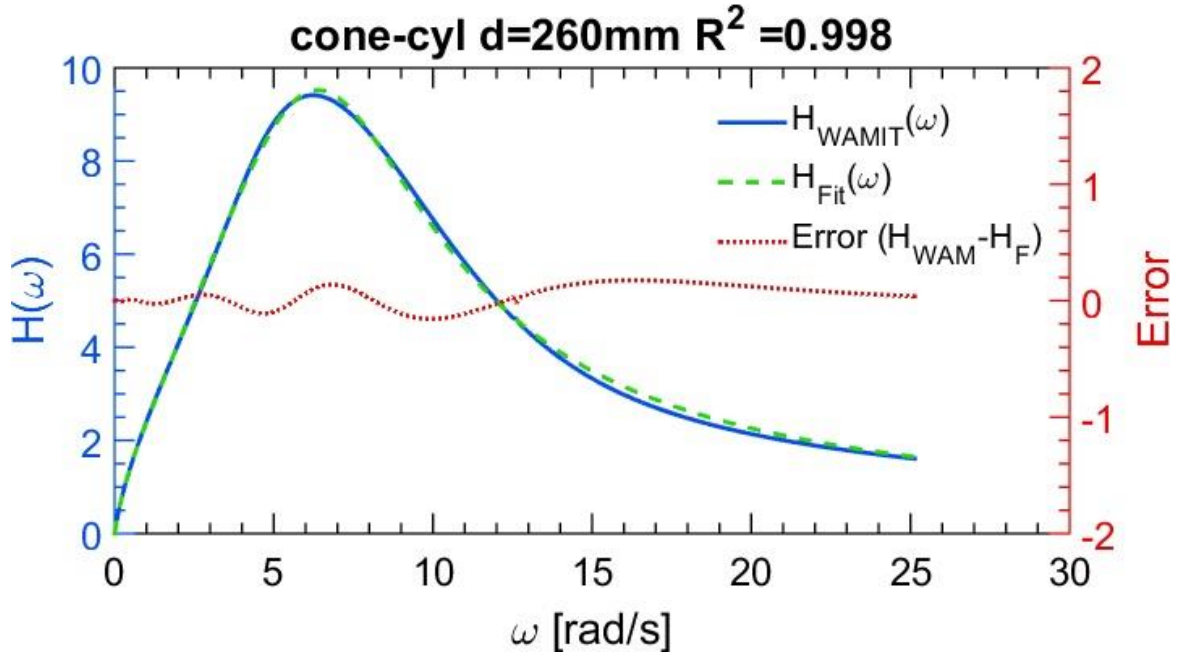
Figure 4:12: Magnitude of the Retardation function, WAMIT values and 5th order fit using FDI toolbox
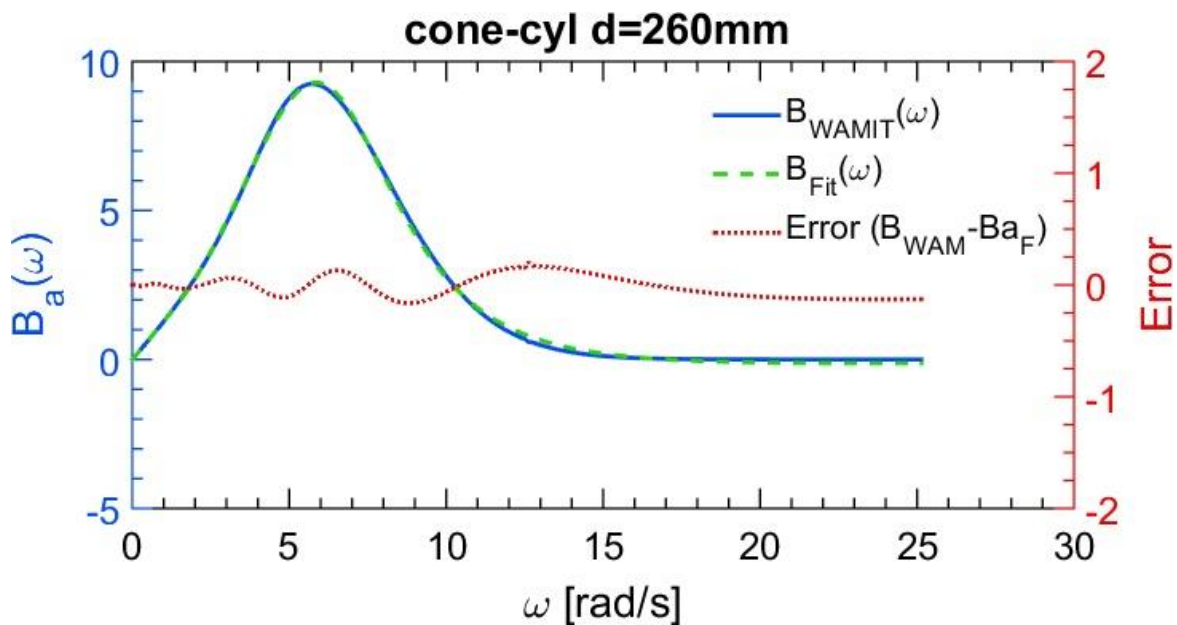
Figure 4:13: Hydrodynamic damping, WAMIT values and 5th order fit using FDI toolbox
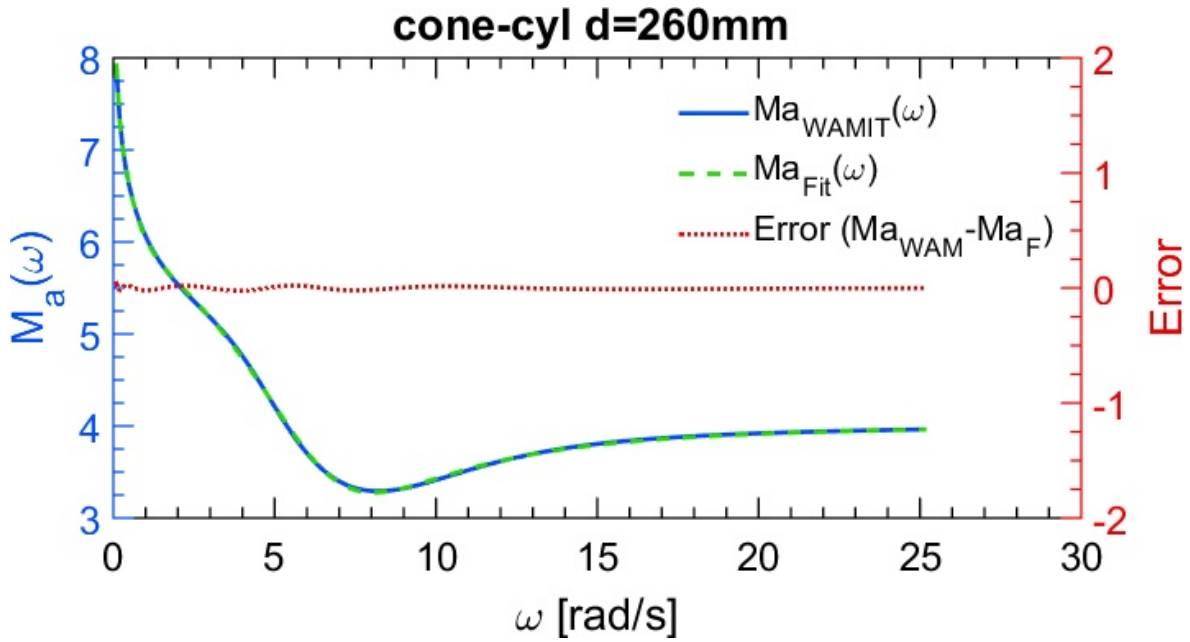
Figure 4:14: Added Mass, WAMIT values and 5th order fit using FDI toolbox

4.4.1 Simulink model

Simulink, developed by MathWorks, provides an interactive, graphical environment for modeling, simulating and analyzing dynamical systems. Its primary interface is a graphical block diagramming tool and a customizable set of block libraries. Examples of commonly used blocks are integrators, gain and summation blocks all of which are depicted in Figure 4:15: The figure can be thought of as a block diagram representation of the time domain based physical equation (4.23) described previously.

The summation block takes all the relevant forces as inputs and outputs (after multiplication with the mass gain block) the acceleration (labelled x'' in the figure).

The integrator is the most basic for modelling dynamical systems, taking the acceleration signal as input and outputting the velocity. This velocity signal is then used to as input to the state space block to determine the radiation force as described in the previous sections. The velocity signal is also used for the power capture, which can be resistive damping, Coulomb damping or other non-linear approaches. The ability to model non-linear methods of power extraction is an advantage of the time domain numerical model over the frequency domain one.

146

The second integration block takes velocity as input and outputs the position of the device. The position signal is then used to determine the hydraulic restoring force.

Figure 4:15: Simulink model including state space representation of radiation force. The input to the model is the excitation force, which is prepared separately before each simulation. The excitation force can be determined in two possible ways; the preferred method used here is to obtain the spectral information of the incident wave, multiply this by the force transfer function obtained using WAMIT (see Figure 4:7), and then perform an inverse Fourier Transform on the result to obtain the force signal. Alternatively, the excitation force impulse response can be used to perform convolution with the wave elevation signal to obtain the excitation force.

Simulations are carried out using both linear damping and Coulomb damping for the PTO force. Chapter 6: discusses these simulations along with experimental results.
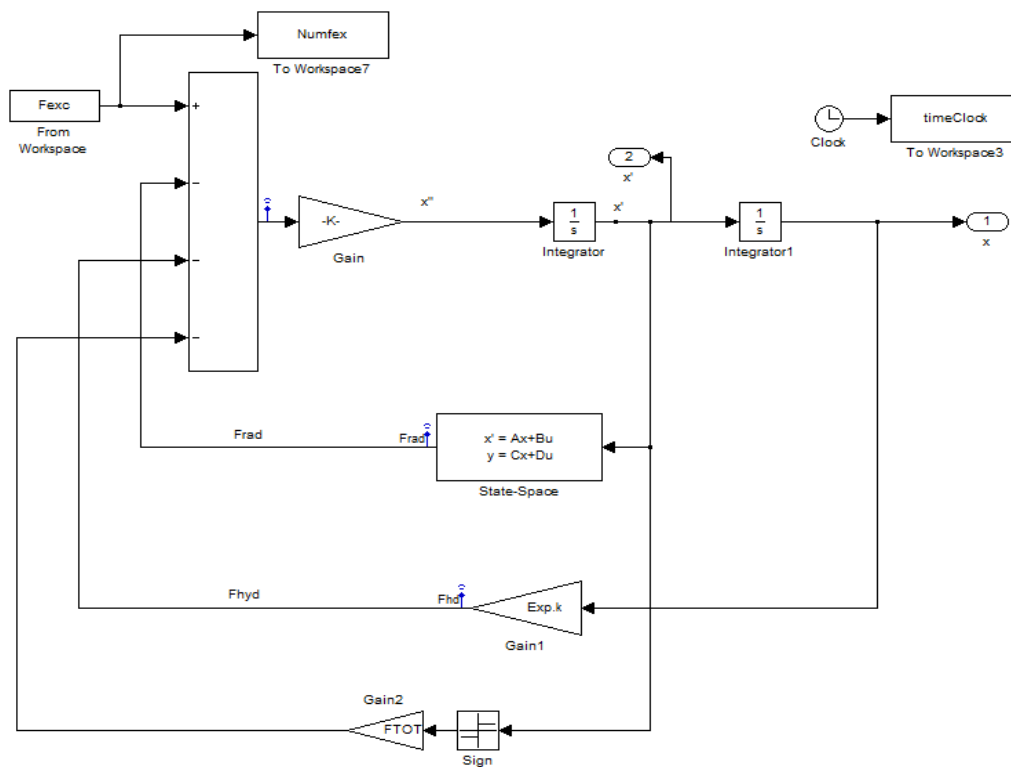

Figure 4:15: Simulink model including state space representation of radiation force

Now that the time domain model is assembled, including an approximation of the radiation force, it could be validated against the radiation forces produced by using only the frequency domain procedures. However, since the floater displacement response is usually of more interest than radiation forces, a natural validation check at this stage is to compare predicted floater responses using both frequency and time domain methods.

Figure 4:16 shows such a comparison of RAOs obtained using both methods. The RAO has been calculated using the time domain model at 256 separate frequencies ranging from 0 to 4 Hz. Simulations are run for 600s with a sampling time step of 0.05s. Curves for all three shapes with a constant draft of 221 mm are plotted, with RAO results being plotted on the left hand y-axis and the difference between both methods being plotted on the right hand y-axis. The agreement between the curves for all shapes is good with the main difference being close to the resonance zone. Referring back to Figure 4:12 it can be seen that although the fit of the retardation function is very close, there is some error near resonance.

Figure 4:16 evaluates the RAOs with both the supplementary mass and external damping settings set to zero. As a result of this the rankings of highest RAO observed; cylinder hemisphere-cylinder and cone-cylinder are merely an artefact of the buoys intrinsic mass and hence the natural frequency. Upon tweaking the supplementary mass and external damping parameters towards the optimum setting, the superior excitation force and hydrodynamic damping of the lighter buoys can be exploited.

4.4.1.1 Effect of using a linear spring term in numerical model

Recall from chapter 2 that the hydrostatic restoring force F_{hyd} is equal to the Archimedes force F_{Arch} minus the gravitational force F_g:

$$F_{hyd} = \rho g V(t) - mg \qquad \textbf{(4.44)}$$

Assuming the heave excursions are small then the hydrostatic force can be approximated by

$$F_{hyd} = -cz \qquad \textbf{(4.45)}$$

Where c is the hydrostatic spring constant. $\rho g A_w$, with A_w being the waterline area.
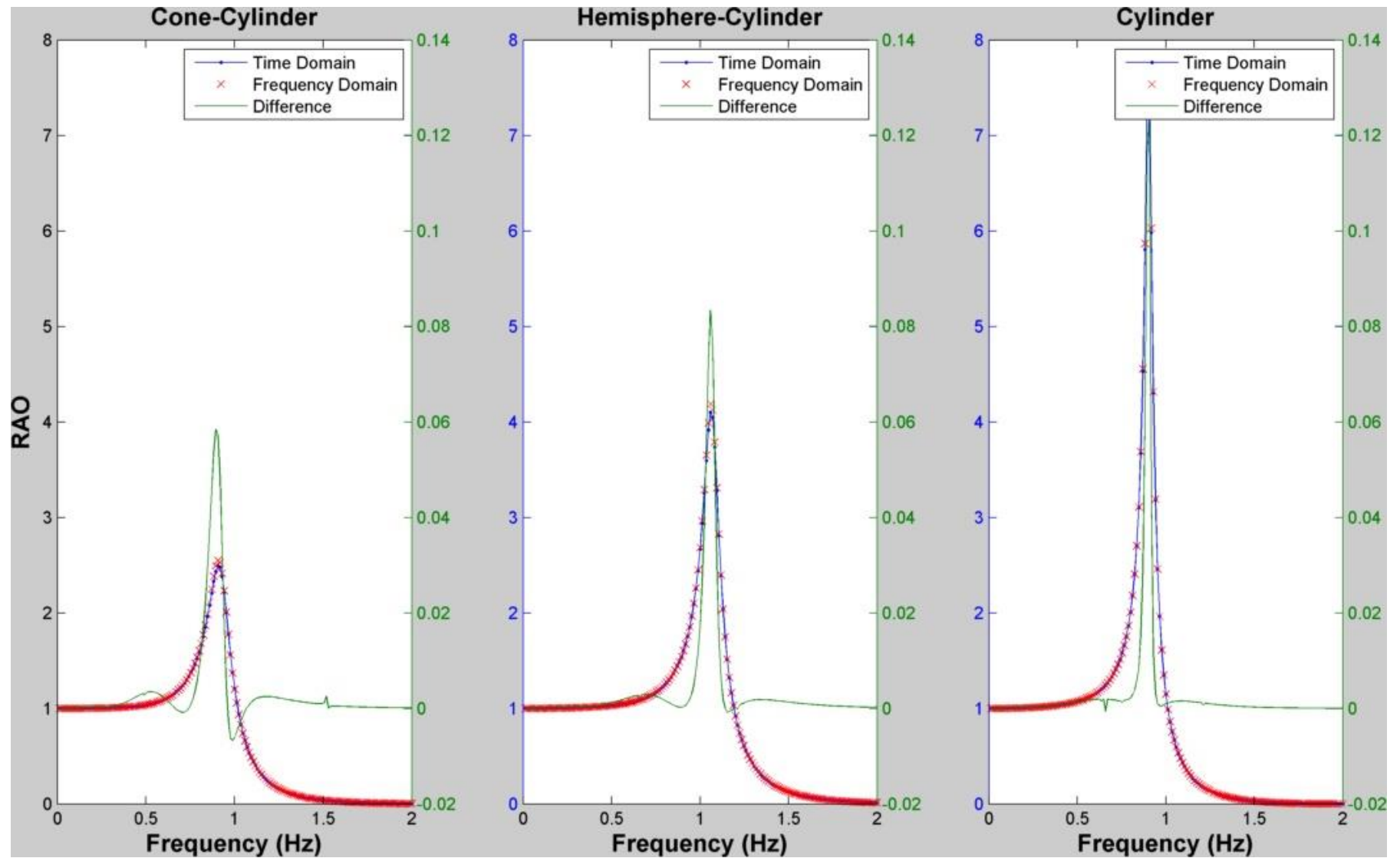
Figure 4:16: Comparison of time domain and frequency domain RAO

The use of a constant spring term is permissible for a cylinder shape buoy except for two possible scenarios (illustrated in Figure 4:17 below): the first being where the buoy has fully emerged from the surface of the water, in which case the restoring force will be comprised solely of the buoys own weight; the second is whereby the buoy becomes submerged to a depth greater than the freeboard of the device.
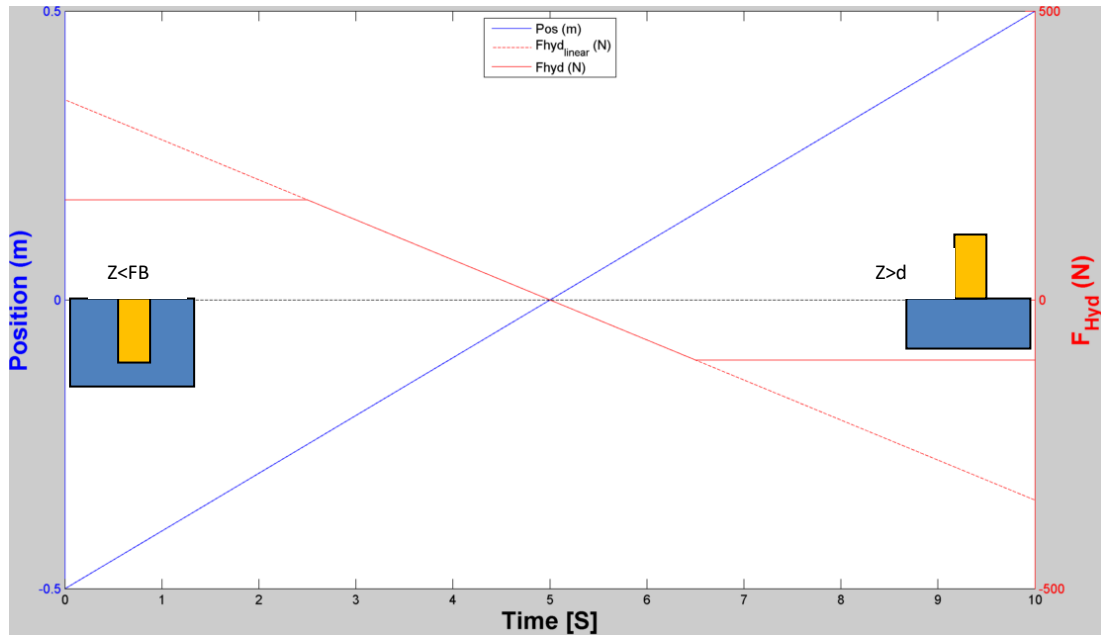
Figure 4:17: Hydrostatic restoring force for the cylinder shape buoy

Using a linear spring term, the magnitude of restoring force would increase with submerged depth (dashed red line) when, in reality, the hydrostatic restoring force would be limited: that limit being the additional buoyancy force given by the now submerged freeboard.

If a linear spring term is used for the cone-cylinder and hemisphere-cylinder shaped buoys, then the numerical model will overestimate device performance, especially near the resonance zone.

Clearly a more sophisticated approach to estimating the hydrostatic restoring force for the cone-cylinder and hemisphere-cylinder would be to calculate the instantaneous submerged volume which can then be used to calculate the buoyancy force. Determining the total submerged volume becomes a problem of finding the volume of cylindrical section and additional conical or hemispherical section.
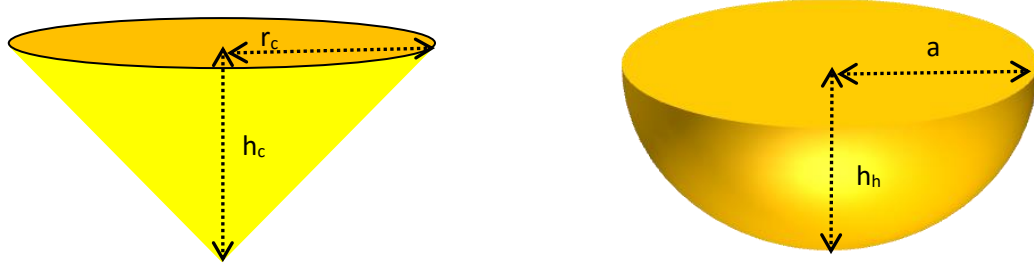
Figure 4:18: Cone and spherical cap

The volume of the cone is given by,

$$V_c = \frac{1}{3}\pi r_c^2 h_c = \frac{1}{3}\pi h_c^3 \tag{4.46}$$

Since the cone extends an angle of 90° meaning $h_c = r_c$.

As the volume of the hemisphere section changes with depth the immersed volume is that of a spherical cap (a portion of a sphere cut off by a plane) given by,

$$V_{cap} = \frac{\pi h_h}{6}\left(3a^2 + h_h^2\right) \tag{4.47}$$

Here a is the radius of the base of the cap, and h_h is the height of the cap. When the height and radius of the spherical cap are equal to the initial radius R, then the volume of the hemisphere is

$$V_h = \frac{2\pi}{3}R^2 \tag{4.48}$$

It may be of interest to note that for the same radius and height, the volume ratios of the cone, hemisphere and cylinder are 1/3, 2/3 and 3/3 respectively.

The spherical cap radius a is related to the initial radius of the hemisphere R by

$$a = \sqrt{2Rh_h - h_h^2} \qquad\qquad\text{(4.49)}$$

Thus the volume can expressed in terms of known parameters h_h and R as

$$V_h = \frac{\pi}{6}\left(6Rh_h^2 - 2h_h^3\right) \qquad\qquad\text{(4.50)}$$

A schematic of the Simulink block code used to estimate the instantaneous volume of the cone-cylinder and hemisphere-cylinder is given in Figure 4:19 & Figure 4:20 respectively.
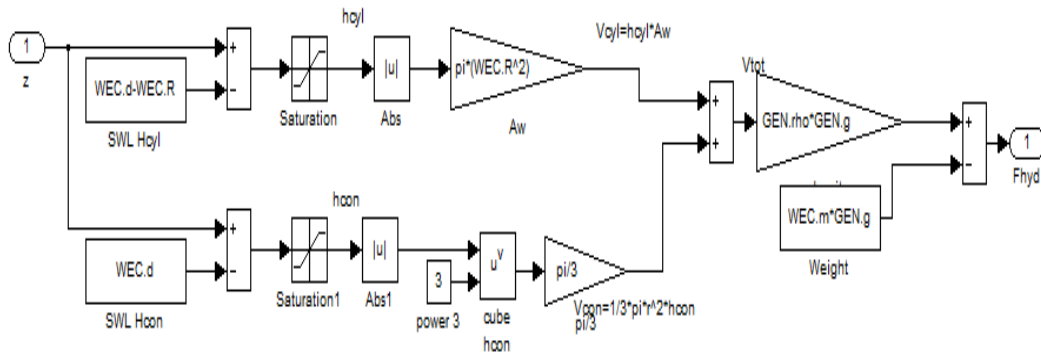
Figure 4:19: Hydrostatic restoring force for the cone-cylinder shaped buoy
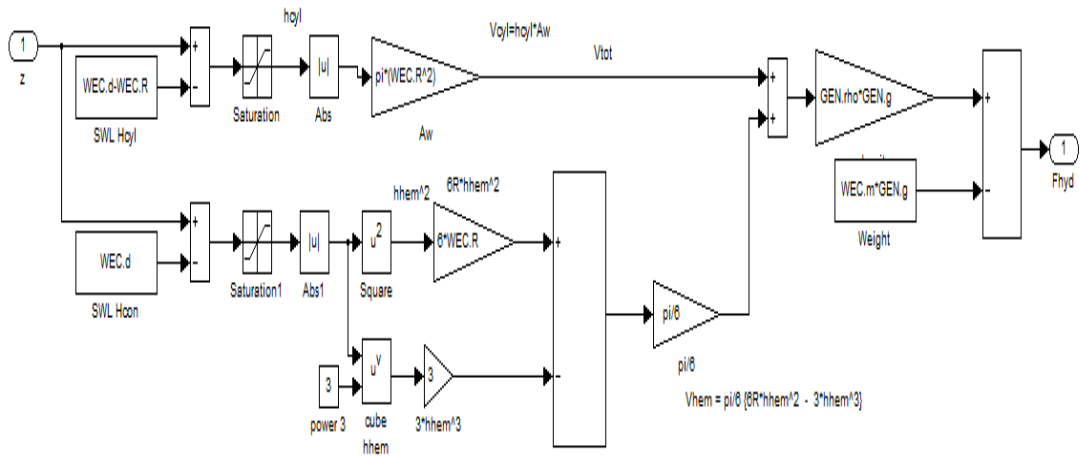
Figure 4:20: Hydrostatic restoring force for the hemisphere-cylinder shaped buoy

Chapter 5: Experimental setup

5.1 Introduction

As a result of the review of existing lab scale PTO systems (Chapter 1) It was decided that a simple point absorber constrained to heave motions only, would provide a good case study for examining details such as excitation forces, response amplitudes and power absorption. The model set-up is not intended to replicate any existing WEC device but rather as means of more general theoretical research.
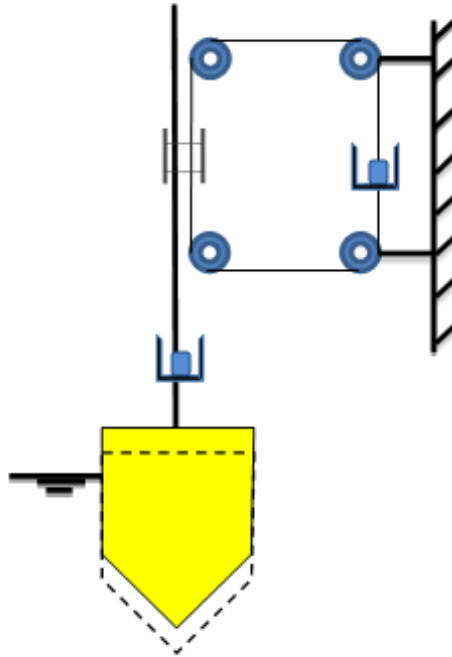
Figure 5:1: Sketch of Model Rig

5.2 Rig components

The experimental test rig is comprised of several different parts each of which is now discussed briefly under separate headings.

Frame

The outer frame of the rig was assembled from a 40cmx40cm modular aluminium profile. The purpose of the frame is to provide a fixed structure about which the wave buoy can oscillate. All subsequent parts are also mounted directly or indirectly on the frame.
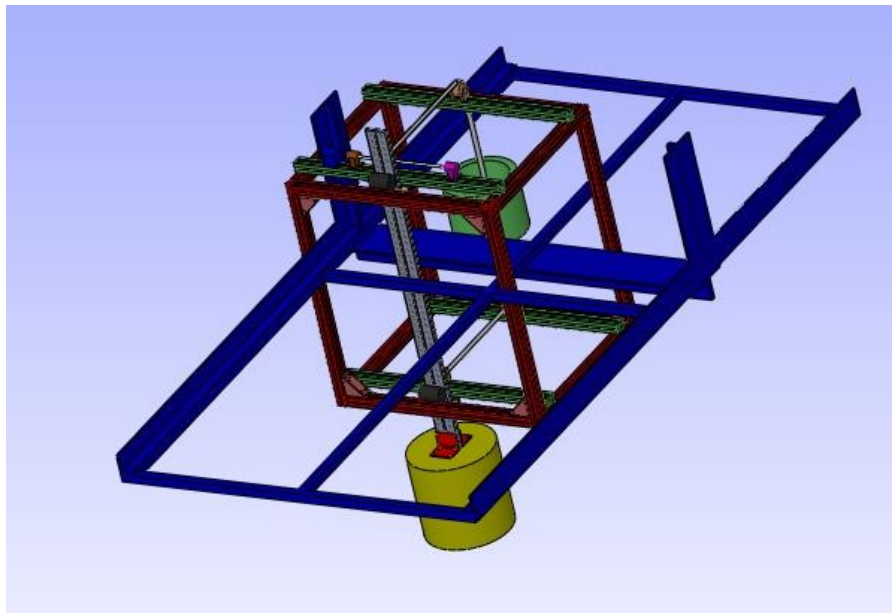
Figure 5:2: Solidworks design of the experimental rig

Buoys

Three different buoy shapes were used for the experiments. The first buoy constructed was a simple right cylinder made out of Kingspan 100mm thick insulation material. The individual sections of insulation are held together by using threaded bars protruding through the centre, in order to compress them between a thin 5mm base plate and a 10mm Perspex top plate {Figure 5:3 (b)}. Two other buoys formed a right cylinder with conical and hemispherical ends. These were made from a thicker (150mm) and denser polyurethane material as it was more suitable for the necessary machining. The buoys are made of an open cell material and as a results will take on water during experiments in the tank. Consequently the draft was

closely monitered before each experiment. Since all the buoys required significant ballast to achiev desired draft; the correct dratt was achieved through the removal of weights to ensure consistency between tests.

The cone and hemisphere shapes were made using a computer numerical controlled (CNC) milling machine. A plastic insert maintaining the shape of the respective buoys forms the end of the buoy (more prominent in Figure 5:3 (a)), through which a 10mm diameter threaded bar holds the individual pieces together. It was decided to use a 90 degree angle cone for ease of machining even though a more rounded section would reduce slamming and vortex shedding as the buoy enters the water.

| (a) | (b) | (c) |
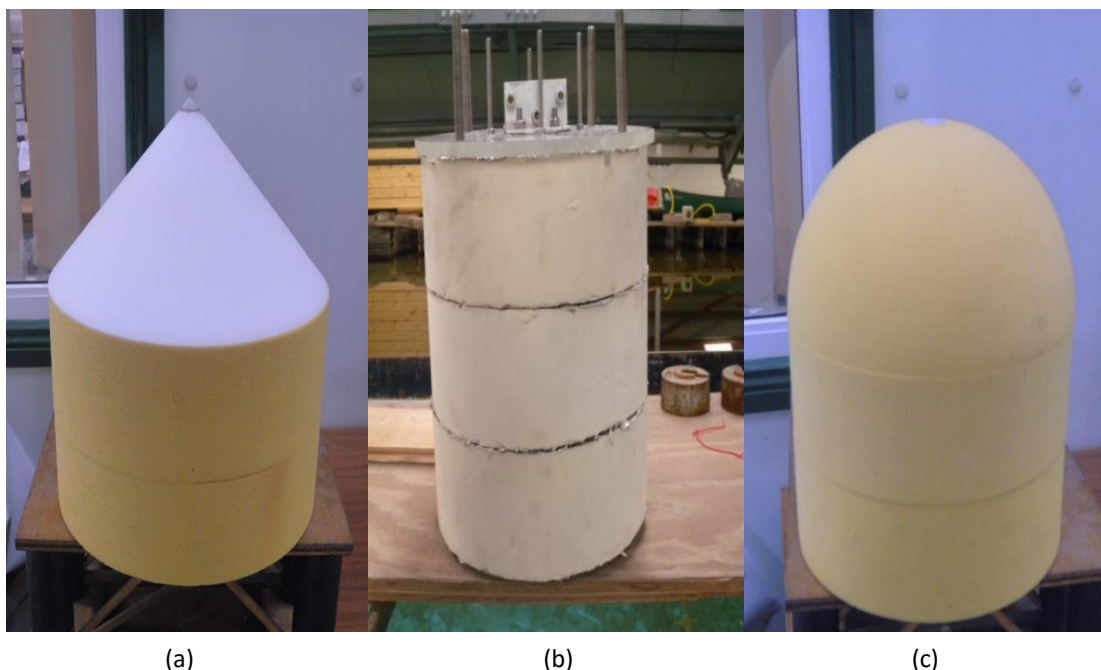
Figure 5:3: Different buoy shapes used: (a) cone-cylinder (b) cylinder (c) hemisphere-cylinder

Buoy top-plate

The same 10mm thick Perspex circular top plate section (Figure 5:4 below) was used for all buoys. It acts as a terminus for the threaded bar pieces as well as a mount for the bracket which connects the buoy to the vertical guiding rod. It also contains four larger bolts on which weights can be added in order to change the mass (and hence the draft) of the buoy.

Figure 5:4: Buoy top-plate and guiding rod

Buoy drafts

Table 5-1 below lists the different draft and mass for each buoy shape tested.

Table 5-1: Different buoy drafts & masses tested

Draft (m)	Cylinder Mass (kg)	Cone-Cylinder Mass (kg)	Hemisphere-Cylinder Mass (kg)
0.15	10.60	⍰	⍰
0.185	13.08	6.01	9.54
0.221	15.62	8.55	12.09
0.26	⍰	11.31	14.84

Guiding rail

An aluminium bar is used as a guiding rail to ensure the buoys motion is constrained to heaving only between the rollers.

Rollers

There are a total of eight roller bearings to restrict the motion of the device. Four rollers prevent the swaying motion of the device and another four prevent the surging motion of the buoy. One of the sway rollers is grooved (visible in Figure 5:6 overleaf) so as to not impede the motion of the belt.

Figure 5:5: Rollers and guiding rod

Belt and pulley system

The guiding rod is connected to a toothed belt which turns one driving pulley and three idlers. The other end of the belt is fastened to the counterweight bin.

Counterweight bin

A steel container (Figure 5:7) was used is a counterweight bin. By adding weight to the buoy and counterweight bin simultaneously, the total mass of the oscillating system can be increased without changing the draft of the buoy. This has the effect of changing the natural frequency of the device.

Torque sensor and encoder

An ETH Messtechnik gmbh DRFL-I type torque transducer was used (see Figure 5:8). The shaft of the sensor is fixed in the chasing between two ball bearings. To measure the torque, it causes a proportional bending of the shaft (within the elastic range) and this is measured with applied strain gauges. The strain gauges are connected as a wheatstone bridge. The transducer measures clockwise as well as counter clockwise torque, with clockwise torque having positive output. The sensor has its own encoder built in to measure rotation speed and angle deflection.
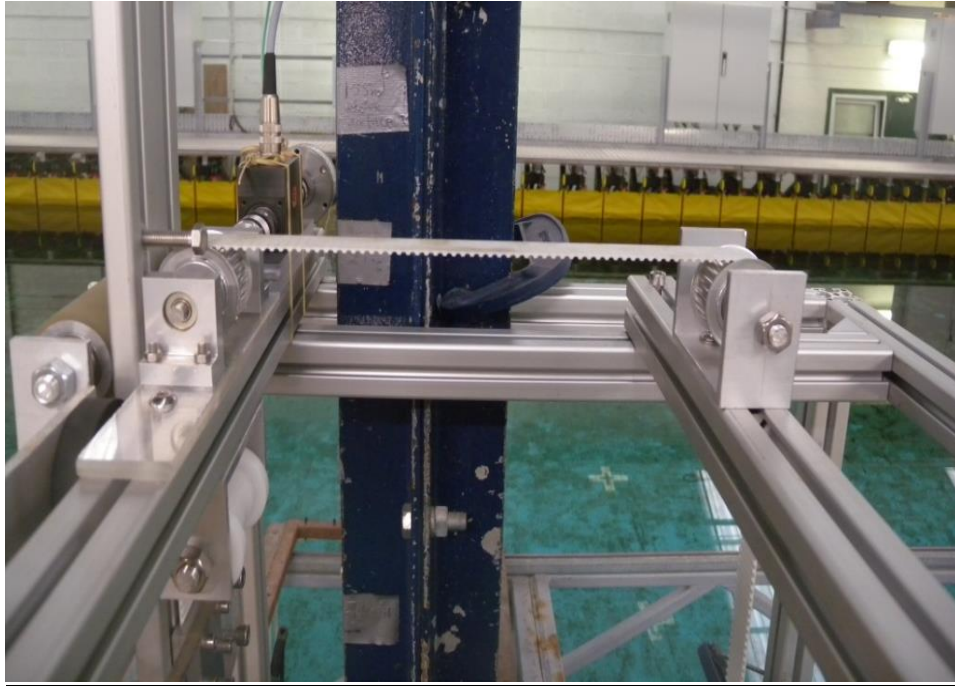
Figure 5:6: Belt and pulley system

Figure 5:7: Counterweight bin
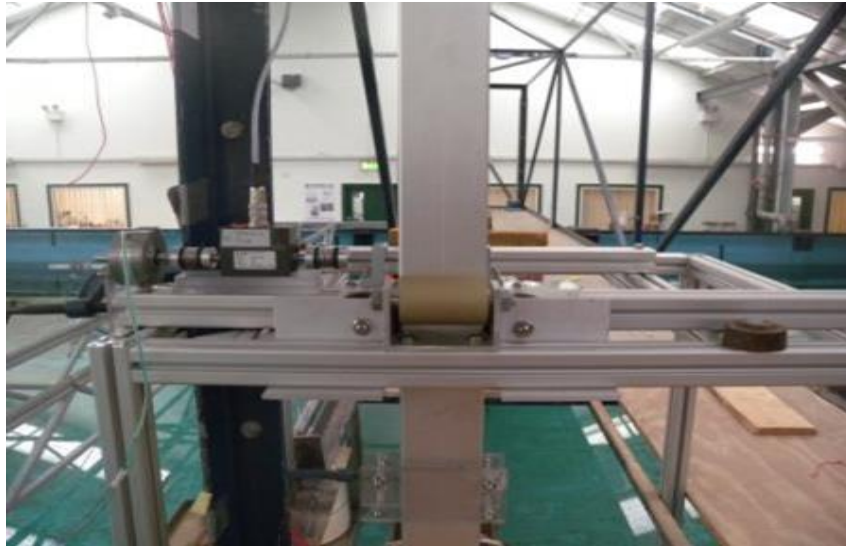
Figure 5:8: PTO coupled to torque transducer

Power Take Off mechanism

A magnetic particle brake was used as the power take off mechanism for the experiments. The brake is comprised of an output disk/shaft which does not touch the outer body. The gap between the shaft and body is filled with a fine, dry stainless steel powder. The powder is free flowing, until a magnetic field is applied from the coil. The powder particles form chains along the magnetic field lines linking the disk to the body. The torque is proportional to the magnetic field strength, and therefore to the applied D.C. input current. If the load torque is less than the output torque, the shaft won't rotate. When the load torque is increased, the brake will slip smoothly at the torque level set by the coil input current.

Since friction is underlies the internal braking process of the particle brake, the resulting force signal resembles Coloumb damping, or square wave damping as shown in Figure 5:9: Braking torque as a function of voltage
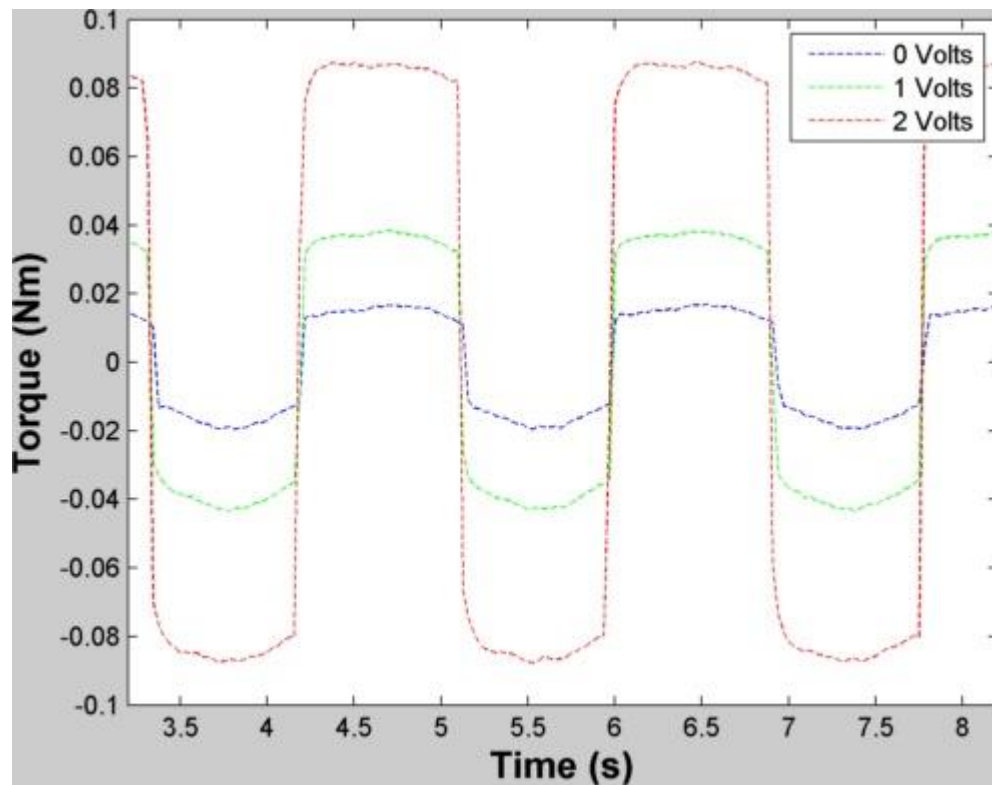
Figure 5:9: Braking torque as a function of voltage
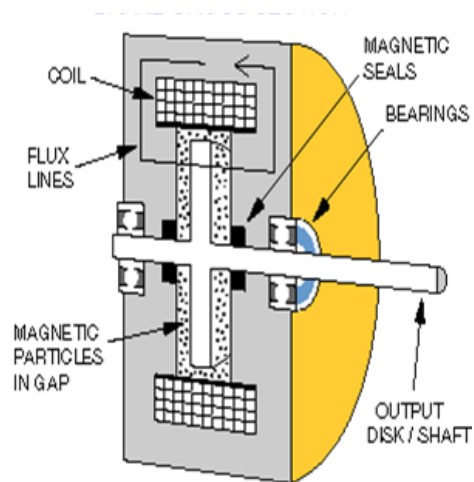
**Figure 5:10: Brake cross-section ("Placid Industries Magnetic Particle Brakes - Home page,"
2017)**
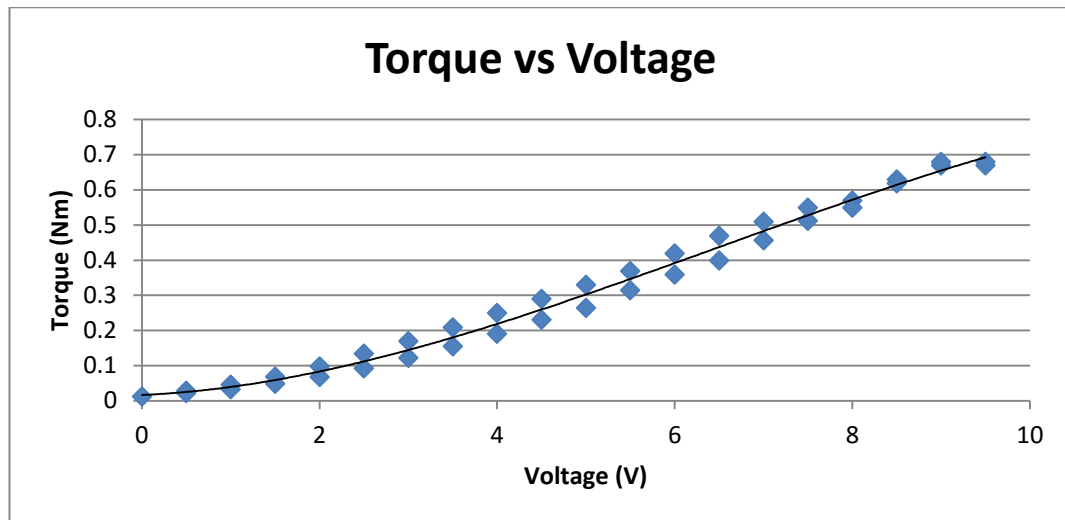
Figure 5:11: Brake torque hysteresis

The brake exhibits some hysteresis. Figure 5:11 above shows the result of increasing the voltage from zero to a maximum 10 Volts, and then decreasing the input voltage from maximum to zero. Two different curves are graphed, with the second one illustrating a higher torque.

Prior to assembly, the rig design was created using Solidworks to allow the following constraints to be taken into consideration:

- The height of the frame (and guiding bar) to be sufficient to allow the free movement of the buoy. (Knowledge of the typical incoming wave heights and an estimation of the response amplitude operator (RAO) of the buoy provide a useful aid in determining this design factor)
- The length of the frame to be adequate to allow secure clamping to the pre-existing bridge which spans the wave basin
- The width of the frame to be enough to allow the counterweight bin to move without clipping a central flange of the bridge (the modular nature of the frame eases this design worry).
- To ensure correct alignment of the shaft, driving pulley, couplings, torque sensor and brake.
- To guarantee adequate length of toothed belt.

5.3 Free response tests

A series of tests were carried out with the buoy decoupled from the timing belt. A hemisphere cylinder buoy with a draft of 221mm was used for the tests. The buoy is still constrained to heave motions between the rollers but since the buoy is not connected to the timing belt (and the encoder), a new system of measurement was required to measure the motion of the buoy.

5.3.1 Codamotion

Codamotion is an optical 3D movement analysis system which measures the locations of active markers with high resolution and accuracy. A marker was placed on the floater to measure its displacement response to the waves. Both measurement systems are to begin recording by the same trigger command. Before commencing the tests, it was necessary to validate the output of the new measuring system. A calibration test involving the use of both the optical encoder and the coda motion tracking device was carried out, the result of which is shown in Figure 5:12 below. It is evident that there is very good agreement between the two measuring systems. It is interesting to note that the maximum error (plotted on right-hand y-axis) of ±1 mm occurs near the zero crossings. There is a phase difference of 2.7 º between the two methods of displacement sensors.
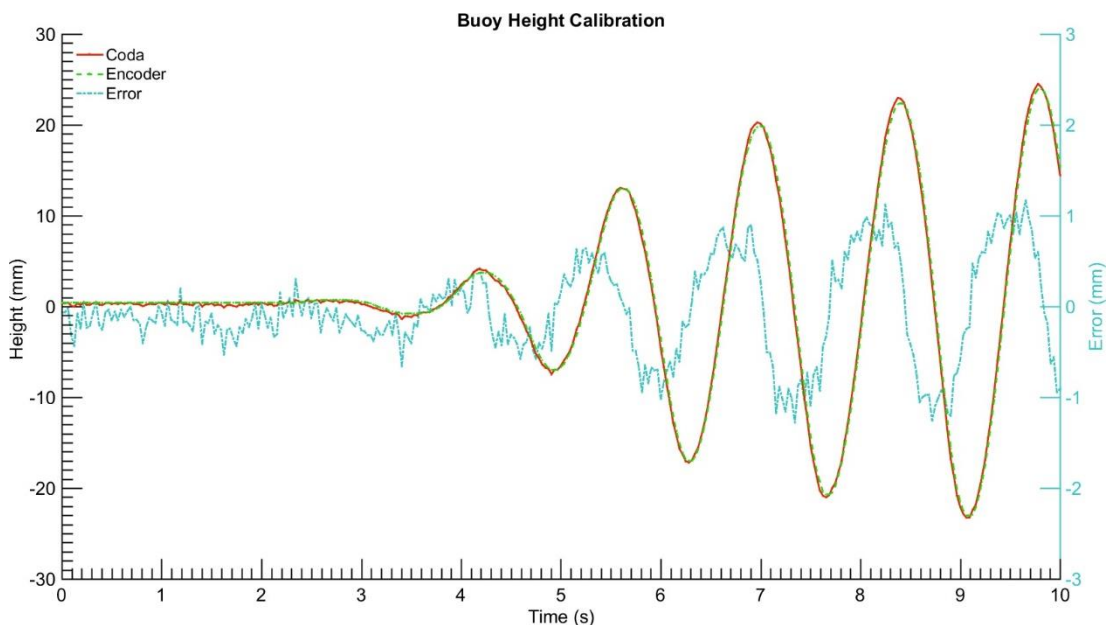

Figure 5:12: Coda motion calibration

5.3.2 Linearity tests

Figure 5:13 shows the result of linearity tests carried out for five different frequencies. The upper graph plots the amplitude of heave motion against wave amplitude while the lower graph plots the phase difference in degrees between the motion of the buoy and the wave. No filtering was applied to the signals before performing the DFT.
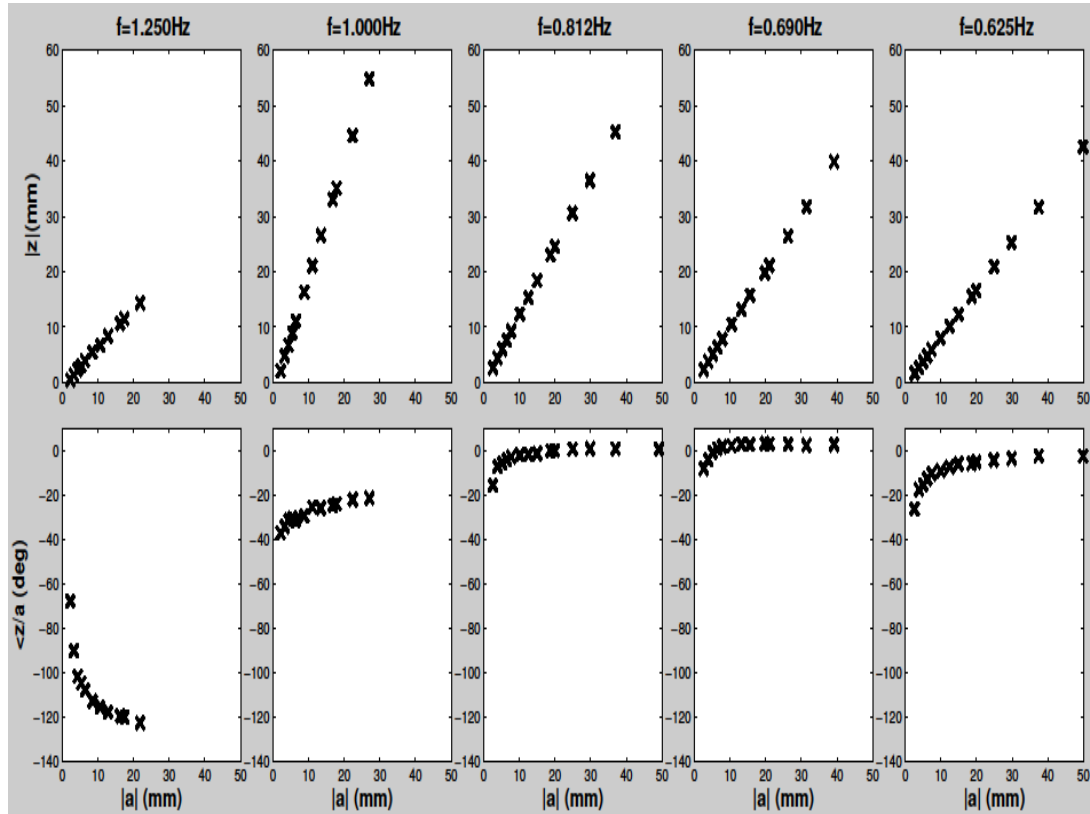
Figure 5:13: Linearity tests showing amplitude |z| and phase <z of heave motion versus wave amplitude for different frequencies

Looking at the amplitude plots, one observes good linearity for all frequencies with lines of fit for slope |z/a| of 0.65, 2, 1.2, 1.0 and 0.83 corresponding to the frequencies 1.25, 1.0, 0.812, 0.690 and 0.625 Hz, respectively. The ratio |z/a| is known as the Response Amplitude Operator (RAO). It should be noted that for all frequencies tested, when the wave amplitude is small (|a|<8mm), the resulting RAOs are slightly less than the figures reported above. An explanation for this is that two wire sensors can be inaccurate for small waves and also the static friction or stiction of the rig is more likely to be prevalent when the wave amplitude is small. There is some variation in the phase shift between the buoy and the wave motion, as

also occurred in (Bjarte-larsson & Falnes, 2006). The variation is particularly evident for the 1.25Hz test and predominantly occurs when wave amplitudes are small. However, in such cases, both the wave and buoy motion signals are quite noisy and again the effect of stiction cannot be ignored. A motor or linear actuator would be able to compensate for stiction by adding the amount of stiction into the system in a feed-forward loop as described in Rohrig & Jochheim (2001).

5.3.3 Resonance frequency

Figure 5:14 shows the results of testing carried out in order to find the resonance frequency of the buoy. Examining the phase results in Figure 5:13 it is noted that the results deviate less once the amplitude is greater than 8 mm. Since test frequencies for the RAO plot including relatively high frequencies, a test amplitude of 12 mm was selected as a happy medium to avoid overly steep waves for the short period waves, whilst having relatively large enough amplitude to avoid the phase uncertainties described previously. Each run lasted 93.75 seconds, of which the final 32 seconds were selected for analysis as this ensures the reflected wave has travelled from the beach to the paddles.
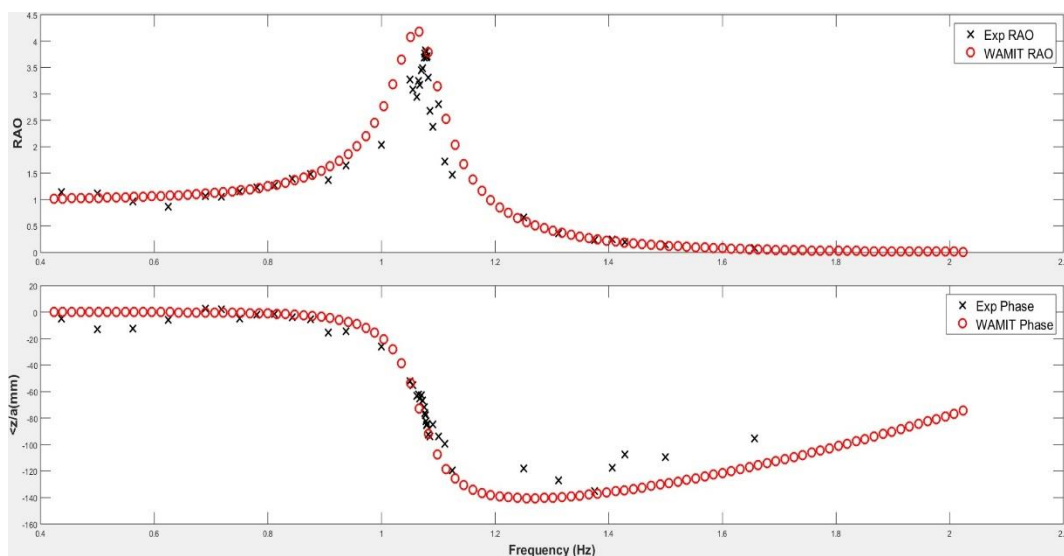

Figure 5:14: RAO vs frequency (upper plot) and phase shift between heave position and wave (lower plot).

The sampling frequency was 32 Hz, yielding 1024 data points for the FFT algorithm. For the most part wave frequencies were chosen which were an integer multiple of 1/32Hz. For frequencies where this condition was not met, the sampling duration was chosen so as to contain an integer number of wave cycles. This prevents spectral leakage and erroneous phase results. In Figure 5:14 an experimental resonance peak is visible at f=1.077Hz with a corresponding phase lag of 78°. The WAMIT resonance peak occurs at a slightly lower value of 1.067 Hz, implying that the numerically modelled buoy may be slightly heavier than the experimental one. A disparity between measured buoy radius and its numerical counterpart would affect both the spring term (numerator) and the inertia (denominator) of the peak frequency equation ($\omega_n = \sqrt{k/m}$). More probable is that a slight error in measured draft has occurred, as this is a more difficult quantity to reliably ascertain experimentally. For the cone and cylinder shapes buoys a draft test could be carried out by raising the device until it just pierces the water surface. The amount of travel can then be recorded by the encoder. This test proved to be more difficult with the hemisphere due to the curvature of the device. A second visual check is to draw marker lines at the desired level, but errors could occur both where the line is marked and when trying to visually check that the waterline is level with said mark.

Figure 5:15 shows the result of running different wave heights at the resonant frequency. The upper plot shows the measured floater response amplitude against wave amplitude. The points line up closely to the green line of best fit. Residual error between measured data and line of best fit is shown in the middle plot, where it is evident by the absolute error of ~1 mm that agreement is good. Finally, the lower plot shows the different in phase angle between floater and wave. Choosing those tests where the wave amplitude, |a|>8mm gives an average RAO of 3.88±0.1 and phase of 81.7±2.8°. This phase is the phase difference between the buoy motion and the wave elevation signal; for the numerical peak resonance frequency, the phase difference between the displacement and the force is 90°.
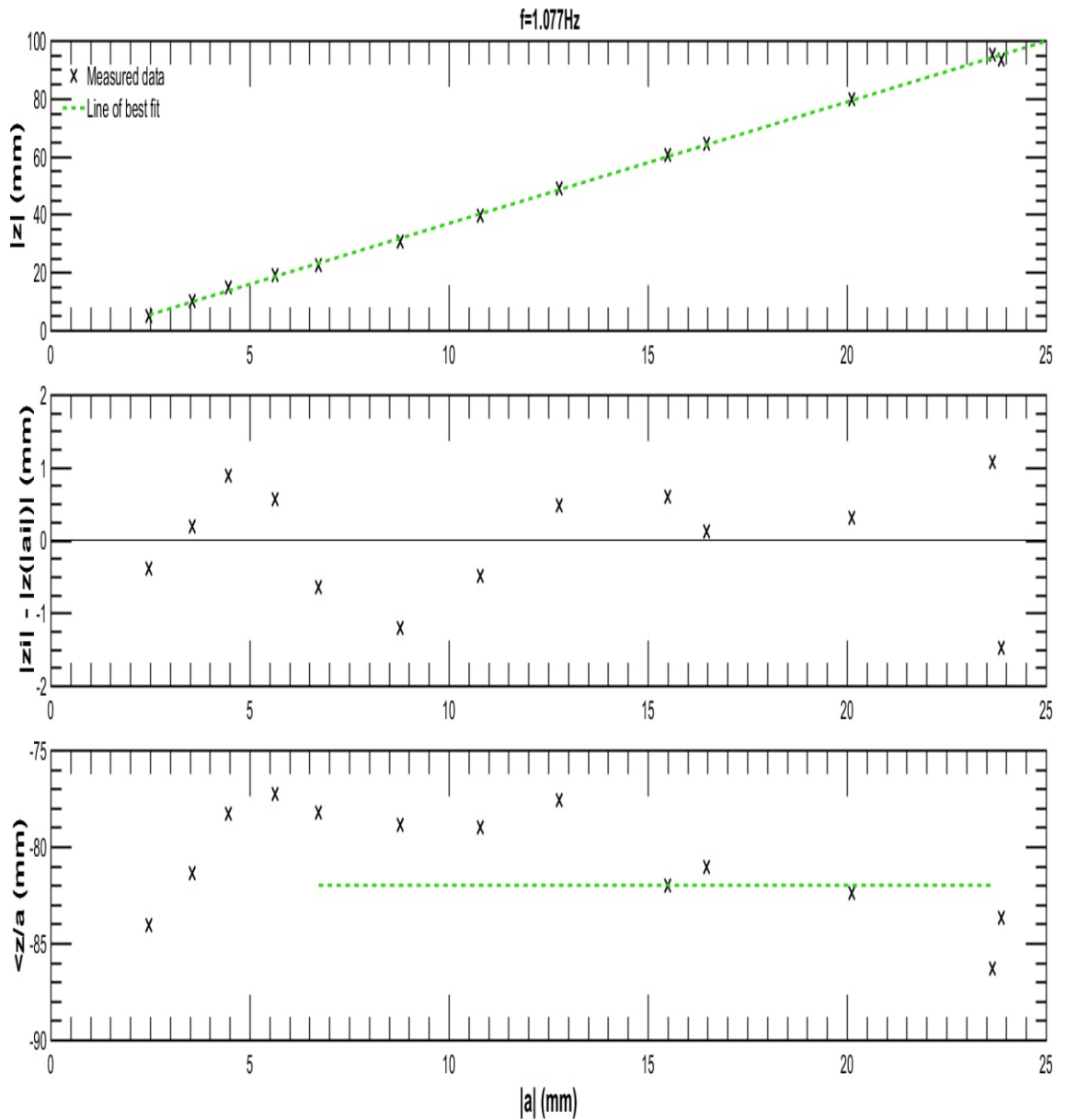
Figure 5:15: Linearity tests at the resonance frequency f=1.077Hz

5.4 Forced oscillation tests

Haskind and Rieman in 1946 developed a forced oscillation experimental method with a ship model at zero forward speed to obtain its hydrodynamic characteristics. (Lin, 1999). In this method, a scale model was forced to carry out harmonic oscillatory motion within water initially at rest through known amplitudes and frequencies. Several other experimental studies have carried out forced oscillation tests.

According to (Falnes, 2003) the forced oscillation problem can be thought of a simple dynamic system with the external force F(t) as input and the velocity u(t) as output. Recalling the concept of mechanical impedance (the transfer function between force and velocity) laid out in chapter two.

$$Z = \frac{\hat{F}}{\hat{u}}$$ (5.1)

Where Z is a complex function of (ω)

$$Z = Z(\omega) = R + iX$$ (5.2)

The impedance can be separated into its real and imaginary components. The real part represents the hydrodynamic damping and is in phase with the velocity.

$$R = Z \cos(\varphi)$$ (5.3)

The imaginary part accounts for inertia and hydrostatic spring terms, and has a resultant vector ninety degrees out of phase with the velocity. When the oscillation frequency is much less than the natural frequency the spring term dominates and the force is in phase with the displacement. If on the other hand the oscillation frequency is much greater than the natural frequency the inertia term dominates and the force is in phase with the acceleration.

$$X = Z \sin(\varphi)$$ (5.4)

The frequency dependant added mass can be extracted from the imaginary part of the impedance by

$$M_a(\omega) = (X - M.\omega - {}^C/_\omega)/\omega$$ (5.5)

With this in mind it, was decided to carry out forced oscillation tests in an attempt to experimentally determine values of added mass and hydrodynamic damping. A linear rig, typically used for OWC experiments in HMRC, was used to drive the device in still water. The set-up used is shown in Figure 5:16 below. The linear rig is mounted to the upper supports of the blue bridge spanning the width of the basin. The experimental rig occupies its regular position on the centreline of the basin.
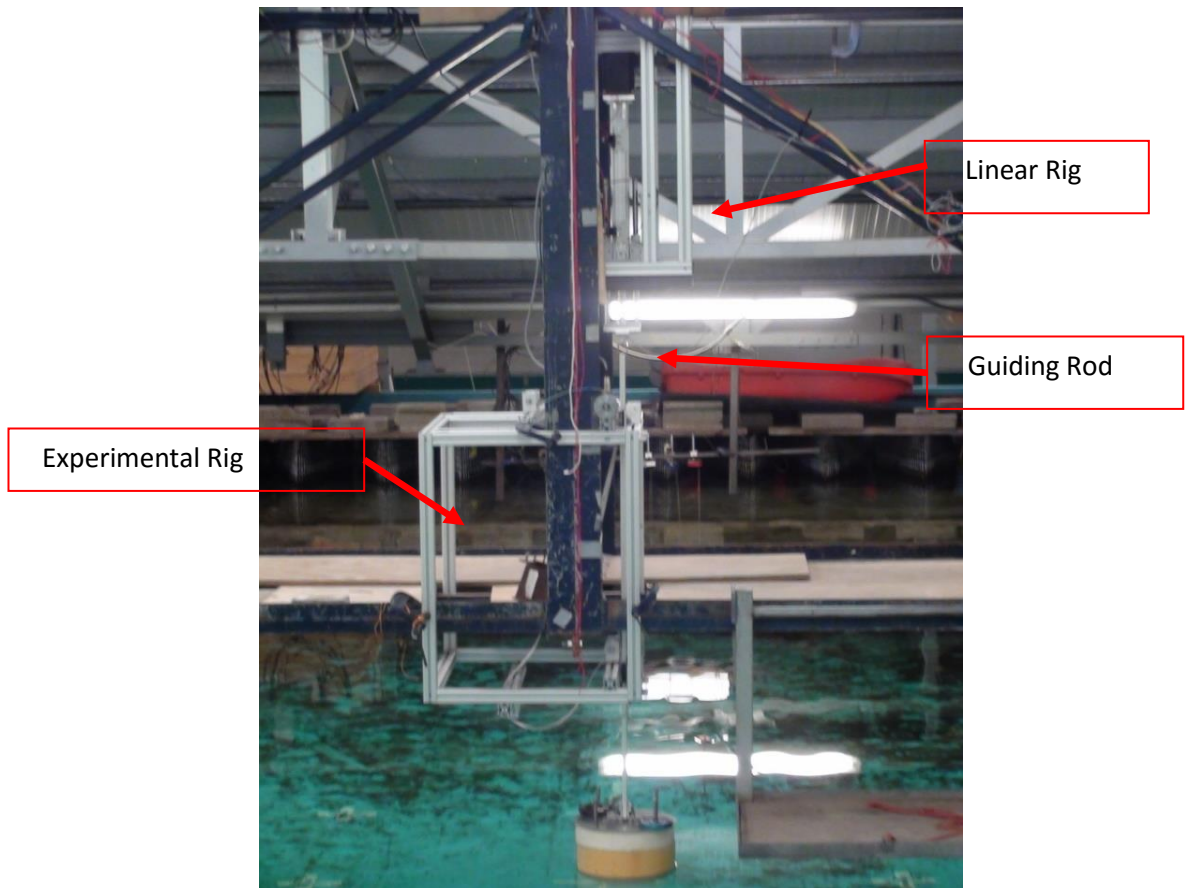
Figure 5:16: Test set-up for forced oscillation tests

The linear rig is connected to the guiding rod of the experimental rig as depicted in Figure 5:17. A load cell interposes the piston head of the linear rig and the experimental guiding rod so the force delivered to the buoy can be measured. The guiding bar is disconnected from the timing belt and pulleys for the forced oscillation tests, however, the bar does retain contact with the rollers to ensure movement is in the heave direction.

Figure 5:17: Connection between linear and experimental rigs

Figure 5:18: Linear rig components

5.4.1 Linear rig components
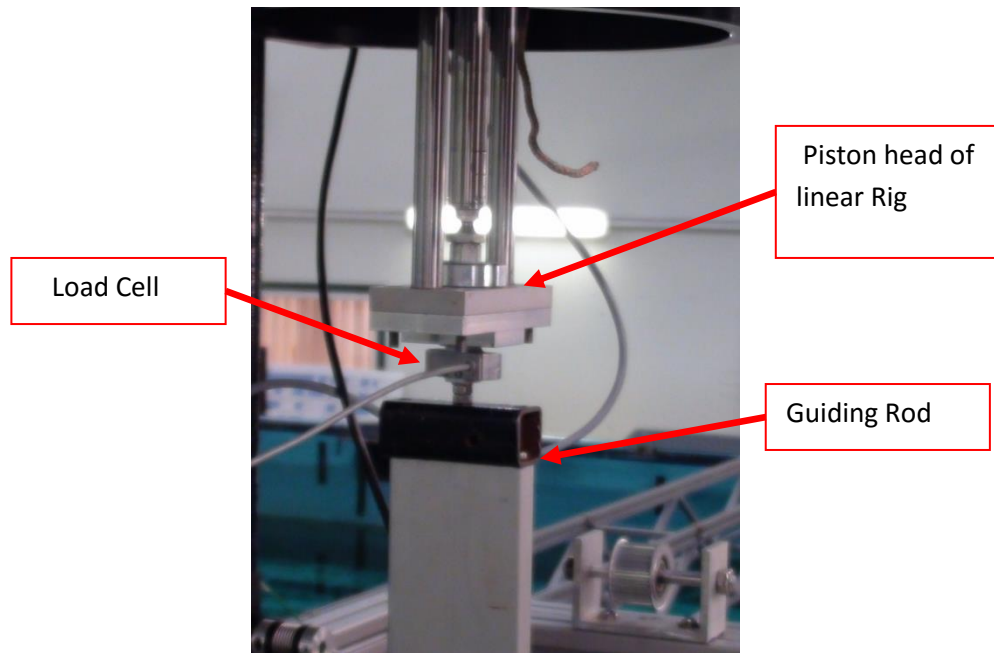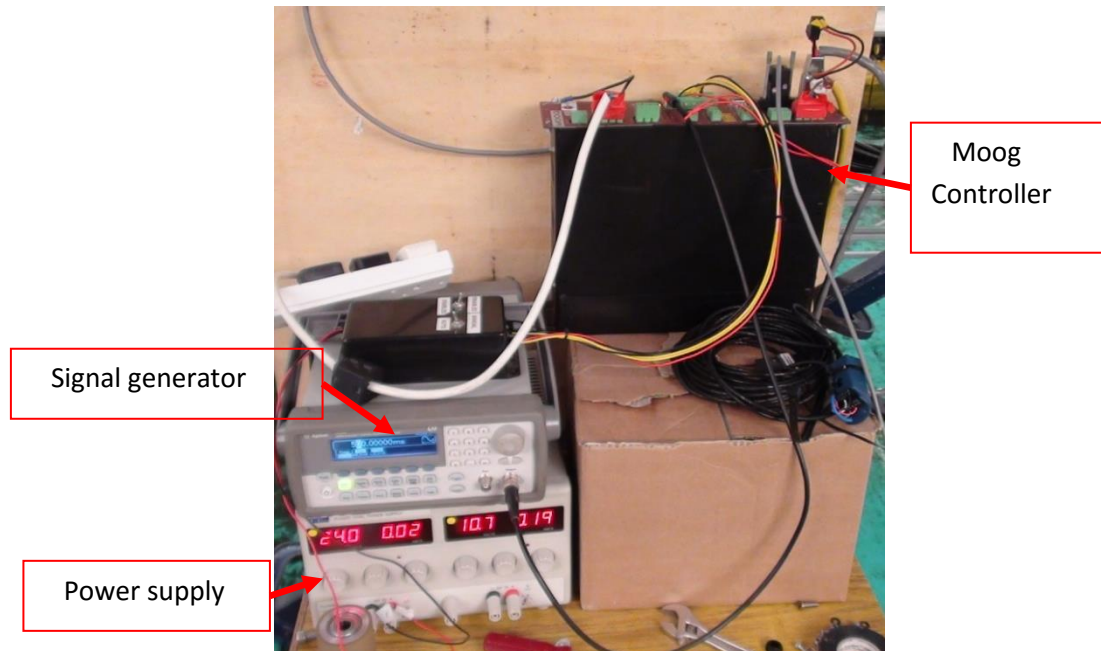
The driving motor behind the linear rig uses a lead screw to convert rotary motion into linear motion. Various components associated with the linear rig are displayed in Figure 5:18. The motor is controlled by a MOOG T200 servo drive. A signal generator is used to input the desired monochromatic frequencies tested. The motor exhibits a linear relationship between stroke height and voltage supplied as depicted in Figure 5:19.
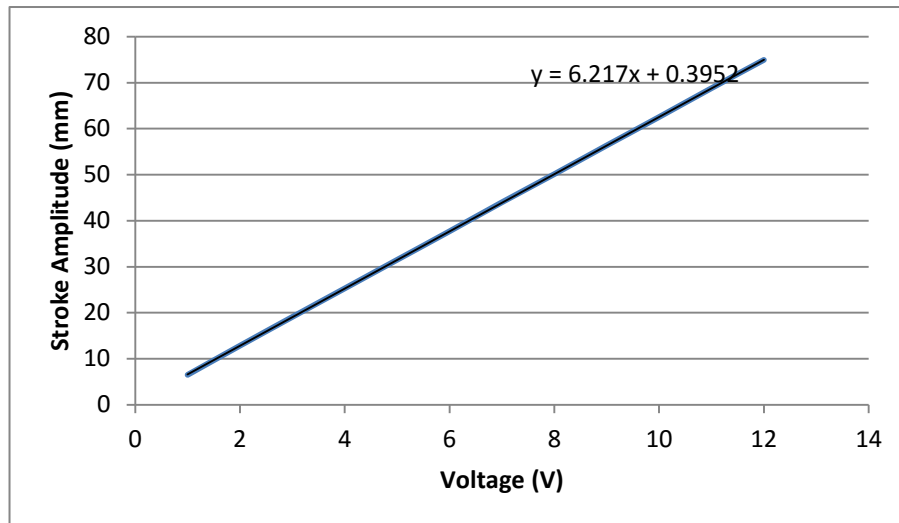

Figure 5:19: Stroke height as function of voltage

The linear rig measures position via a resolver. The resolver was calibrated with the encoder as shown in Figure 5:21 the agreement between the two measuring devices is excellent.
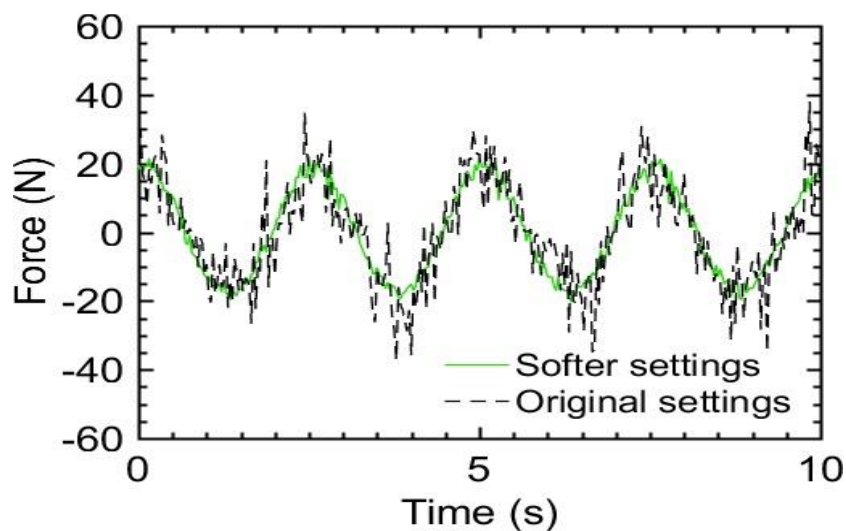

Figure 5:20: Load cell signal from original and softer controller settings
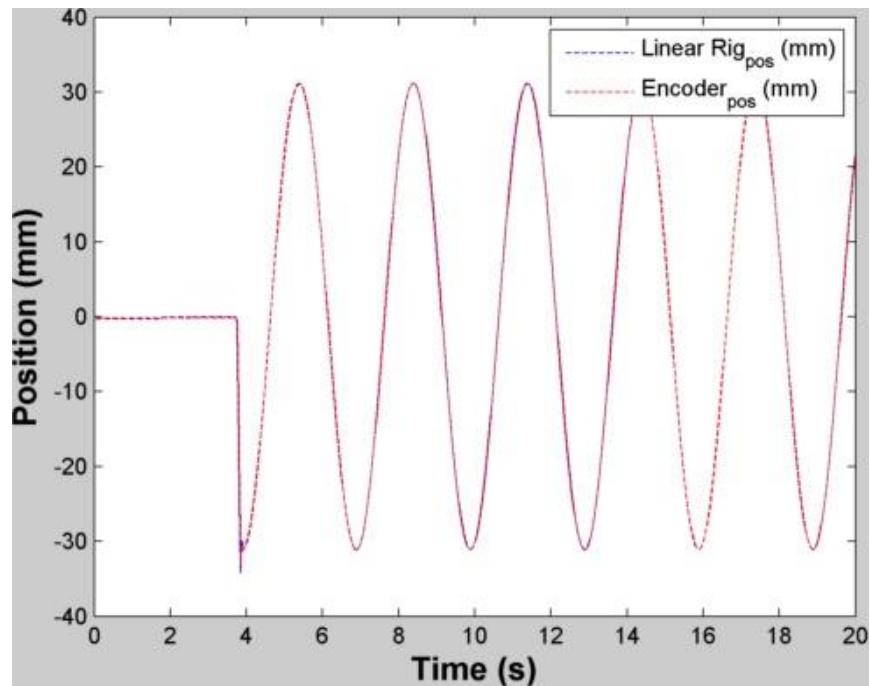
Figure 5:21: Position measured from linear rig resolver and encoder

5.4.2 Load cell calibration

Good experimental practice dictates that physical instruments should be calibrated prior to use. ITTC (2014) guidelines for force calibrations, recommend that load cells are generally performed under static conditions, in the dry using traceable masses. The load cell was calibrated by hanging known weights from the end of the load cell. It's then possible to convert the load cells voltage (V) to mass (grams). Figure 5:22 below shows the results of two load cell calibrations. In the first test (blue line), the motor is switched off and the usual calibration procedure of incrementally adding weights is carried out. The second test (red line), the motor is switched on and the weights are removed one by one. It is clear that the output signal is very noisy when the motor is switched on compared to when it is switched off. The culprit for this noise is not electrical but rather mechanical vibration. As the motor attempts to hold its position, it constantly exerts a force, transmitted internally through the ball and lead screw into the piston in order to achieve this goal. The constant (audible) vibrations are transferred through the load cell, leading to the signal produced in Figure 5:22 (red line).
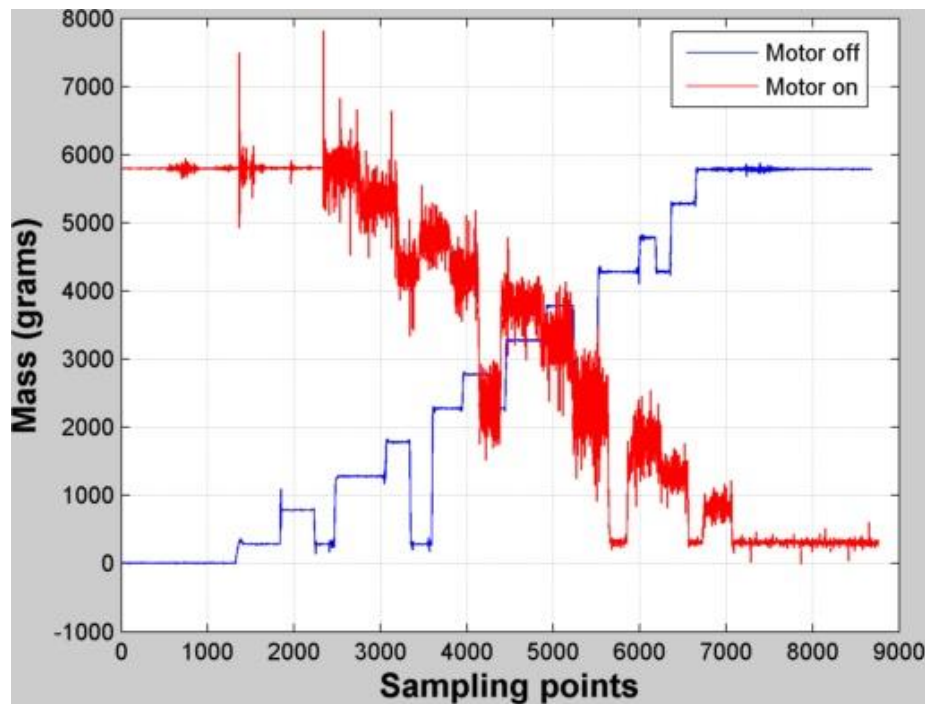
Figure 5:22: Load cell calibration

A low pass filter would remove some of the high frequency oscillations, however, to due concerns of phase modulation this approach was not taken. A smoother signal was instead sought by altering the linear rigs control parameters, resulting in a slightly 'softer' response, without compromising the positional control of the rig see Figure 5:20. However, while some improvement was found, the measured force signal remained noisy due to mechanical vibration.

5.4.3 Testing procedure

Tests were carried out for the cone-cylinder and hemisphere cylinder buoy shapes. For each shape and draft tested, three different stroke heights (15, 30 & 60 mm respectively) were tested. All data were recorded at 32 Hz, and the sampling duration for each frequency tested was 35 seconds, allowing for at least 1024 points to be used for analysis purposes...

5.4.4 Results

In the following section, results are plotted for hydrodynamic damping and added mass obtained from the forced oscillation tests. Numerically approximated values using WAMIT are also plotted for comparison purposes. The natural frequency can be determined from

observing the frequency at which the reactive part of the impudence vanishes and values are also compared to experimental predictions.

5.4.4.1 Hydrodynamic damping and assed mass

Figure 5:23 through to Figure 5:28 show the results of the impedance tests for the shapes and drafts tested. The hydrodynamic damping which represents the real part of the impedance is shown in the upper section of the figures. Experimentally determined results for the three different stroke heights used are plotted alongside the numerical results predicted by WAMIT for comparison purposes.

The agreement between numerical and experimental results is poorest at low frequencies, with the majority of tests showing negative hydrodynamic damping values for frequencies below 0.5 Hz. The reason for this is that the phase of the measured impedance for the lower frequencies tend to lie just within the third quadrant (i.e. -91°, -92°) whereas the theoretical phase asymptotically approaches   -90° since for low frequencies the spring term dominates and the force is in phase with the displacement. The deviation between the different experimental stroke heights is also largest for the low frequencies but since the magnitude of the impedance is largest at these frequencies, any error in phase will propagate through. For example, in Figure 5:27, which shows the data for the cone-cylinder with a draft of 221 mm, when the forcing frequency is 0.25 Hz, for a stroke height of 30 mm the phase of the impedance is -89.3° yielding a damping value of 5.3 kg/s. When the stroke height is increased to 120 mm, the measured impedance phase is -91.5° giving a damping value of -11.8 kg/s. The phase value predicted by WAMIT for that shape and frequency is -89.7° which would give a damping value of 2.1 kg/s. WAMIT assumes an inviscid fluid and a constant water plane area. Additionally WAMIT would not take vortex shedding into account. It is therefore reasonable to assume there would be slight differences between physical and numerical results.

The agreement between numerical and physical damping results improves for the middle range frequencies tested, with damping values slowly increasing, then reaching a peak value before dropping off again. In general, experimental damping values are higher than those predicted numerically, however mechanical friction in the guide bearings is not taken into account and this would result in higher values being reported.

The high frequency experimental damping values do not decay at the same rate as the numerical, where similar to the low frequency scenario the magnitude of the impedances are similar but differences in the phases exist. The numerically predicted phase asymptotically approaches 90° in phase with the acceleration since the inertia terms dominates the impedance. For the experimental tests the velocity does lag the force but not quite to the same extent predicted by the numerical model. The poor quality (noisy) force signal is likely to influence the measured phase and as mentioned previously slight deviations in phase can affect the real part of the impedance particularity when the modulus (absolute value) of the impedance is large. Additionally as the forcing frequency increases so should the sampling frequency so that the resolution (number of samples per cycle) remains the same for each frequency.

The experimentally determined and numerically predicted added mass is plotted in the lower section of each plot in Figure 5:23 through to Figure 5:28. As with the hydrodynamic damping, the agreement between the two methods is poor initially for the low frequencies but improves significantly as frequency increases. The scatter visible in physically determined results is a disappointing consequence of the mechanical vibration. As a result of this feature confidence in results is poor for the extremities of the frequencies tested. I.e. when the magnitude of the impedance is large, both at low frequencies with a large spring term and high frequencies with a large inertia term. When the magnitude of the impedance reduces, agreement improves but, the effect of friction is not taken into account. Overall results can be considered disappointing in what is an otherwise very useful experimental procedure to carry out. Determination of added mass and damping values is extremely useful as they determine a devices radiation capabilities. This in turns reveals the power absorption capabilities since the ability to absorb power depends on the devices radiated wave interfering with the incident wave. The results plotted highlight the tremendous benefit towards utilising a more advanced PTO capable of driving the buoy at small model scales, such as a linear actuator.
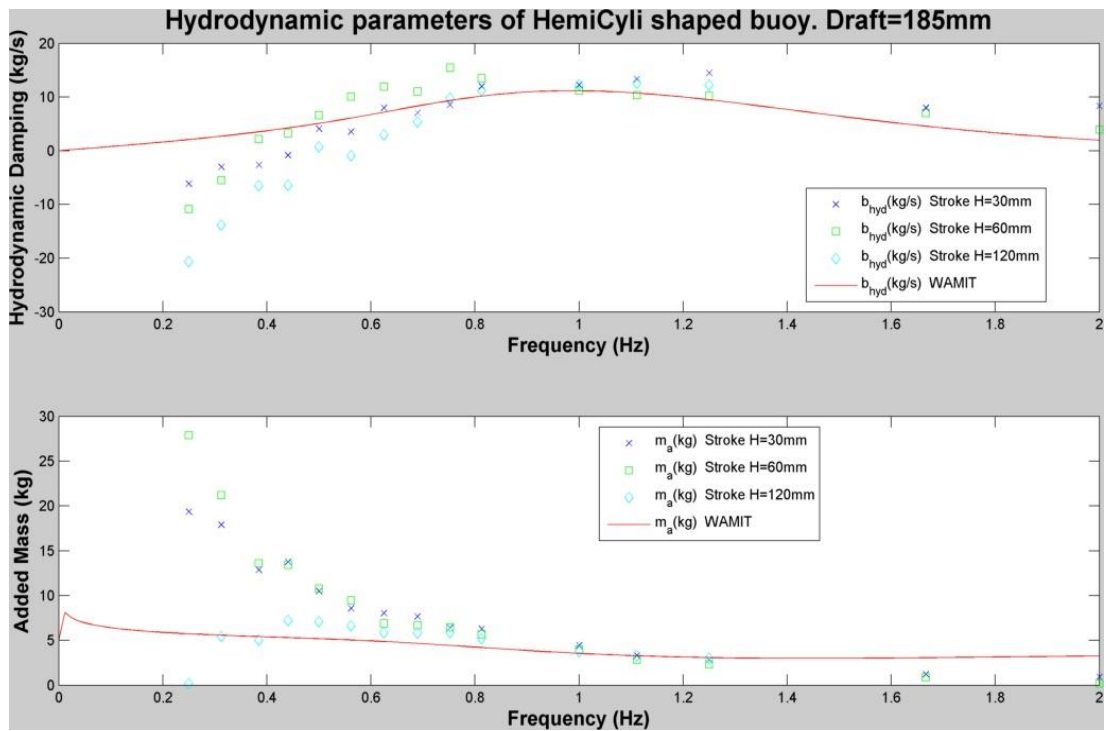
174

Figure 5:23: Hydrodynamic damping and added mass for hemisphere-cylinder draft=185mm
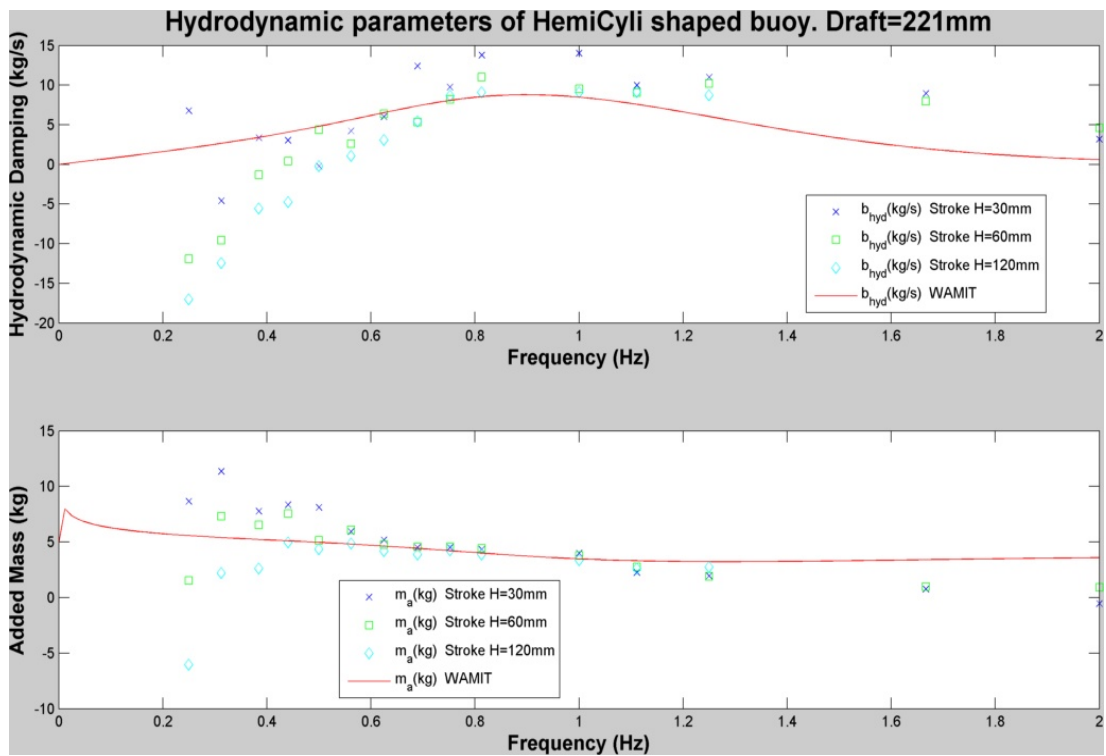

Figure 5:24: Hydrodynamic damping and added mass for hemisphere-cylinder draft=221mm
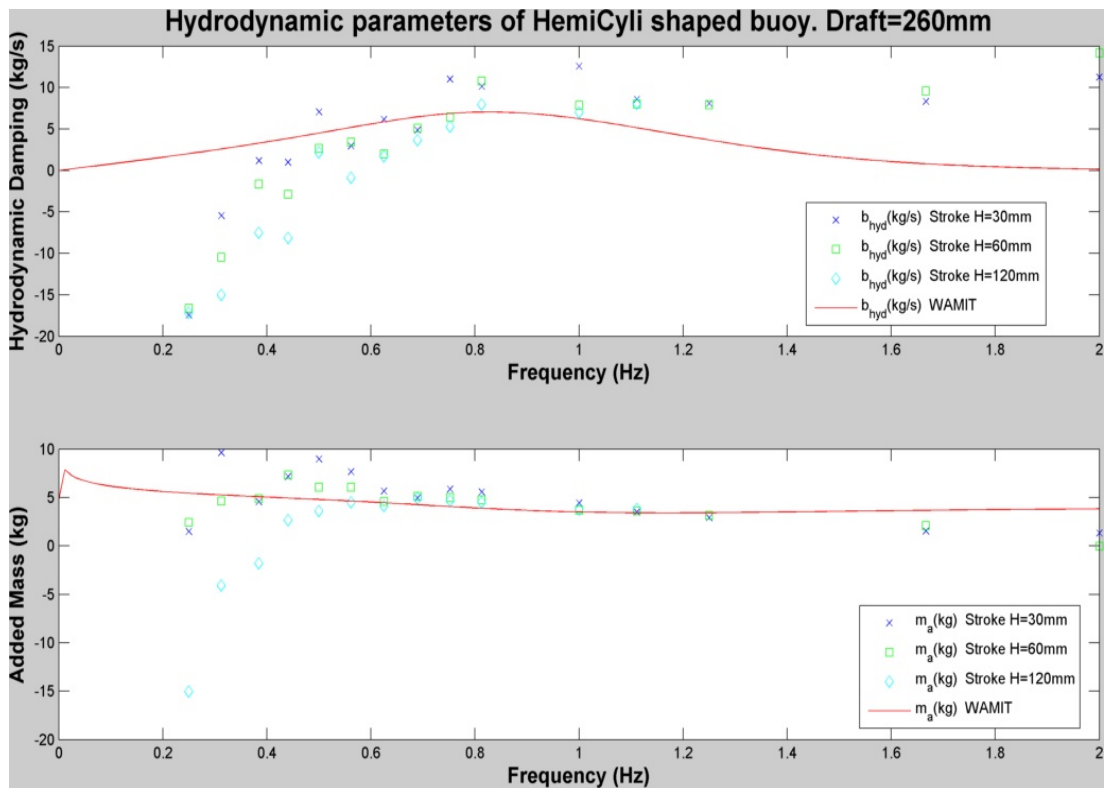
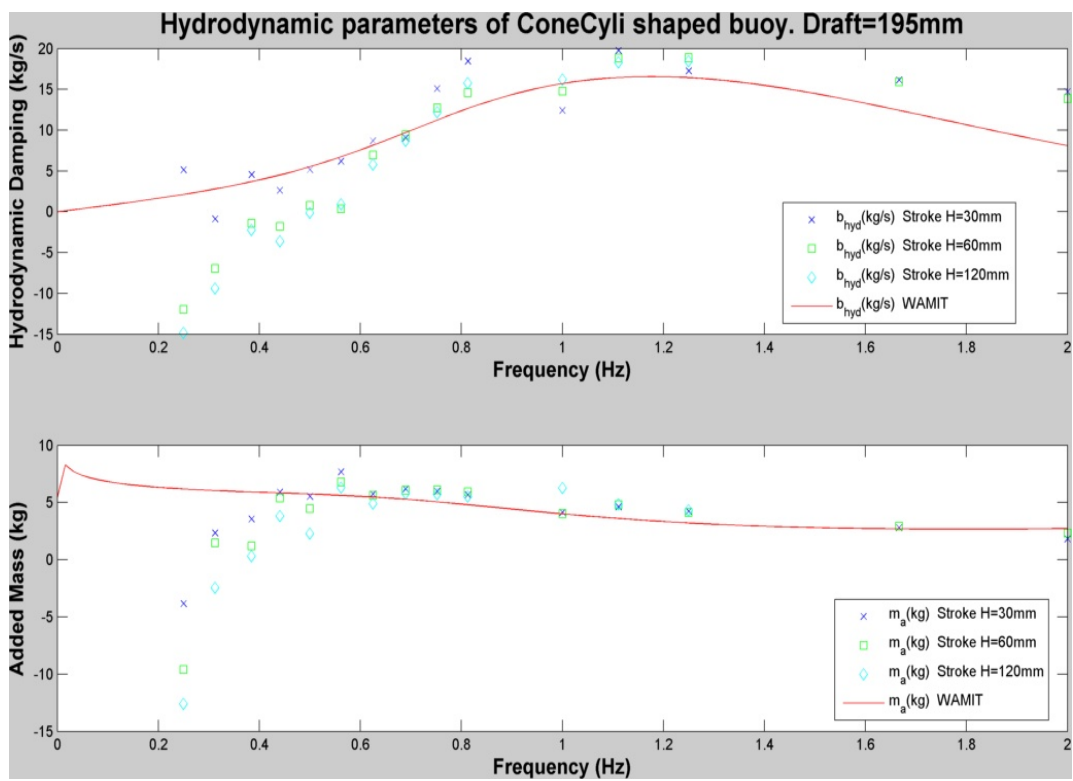**Figure 5:25: Hydrodynamic damping and added mass for hemisphere-cylinder draft=260mm**

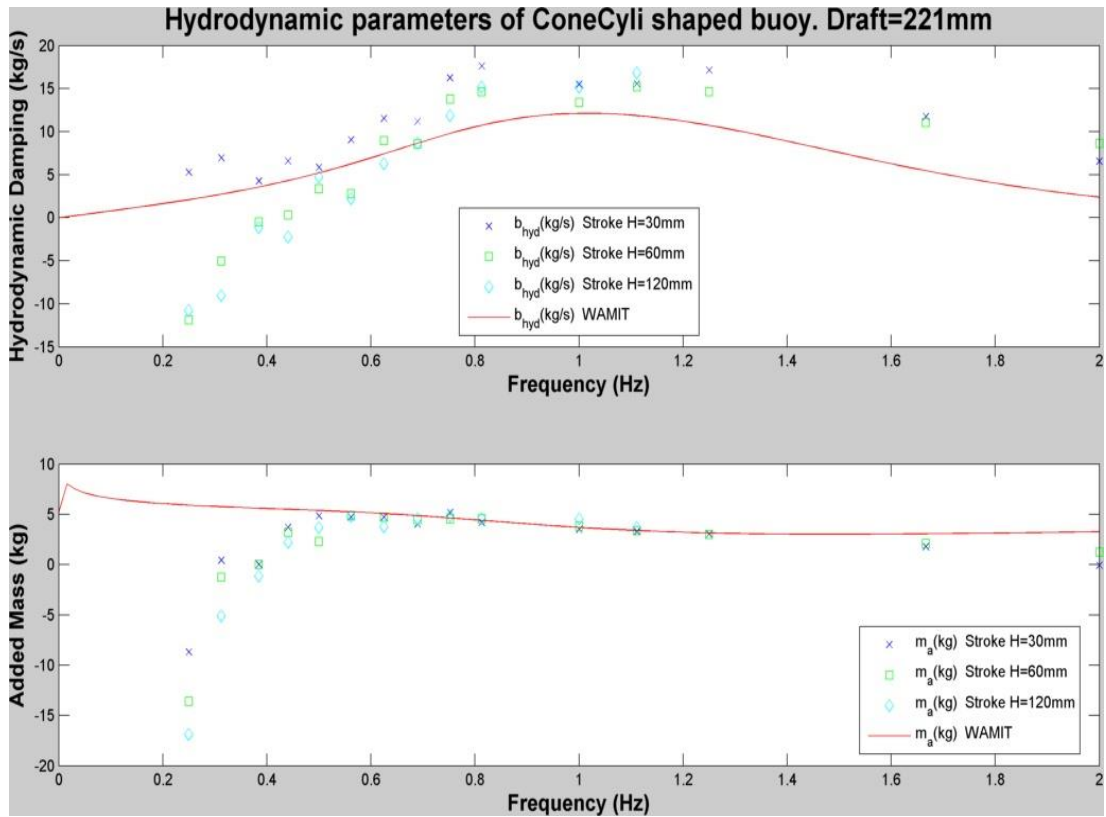**Figure 5:26: Hydrodynamic damping and added mass for cone-cylinder draft=195mm**

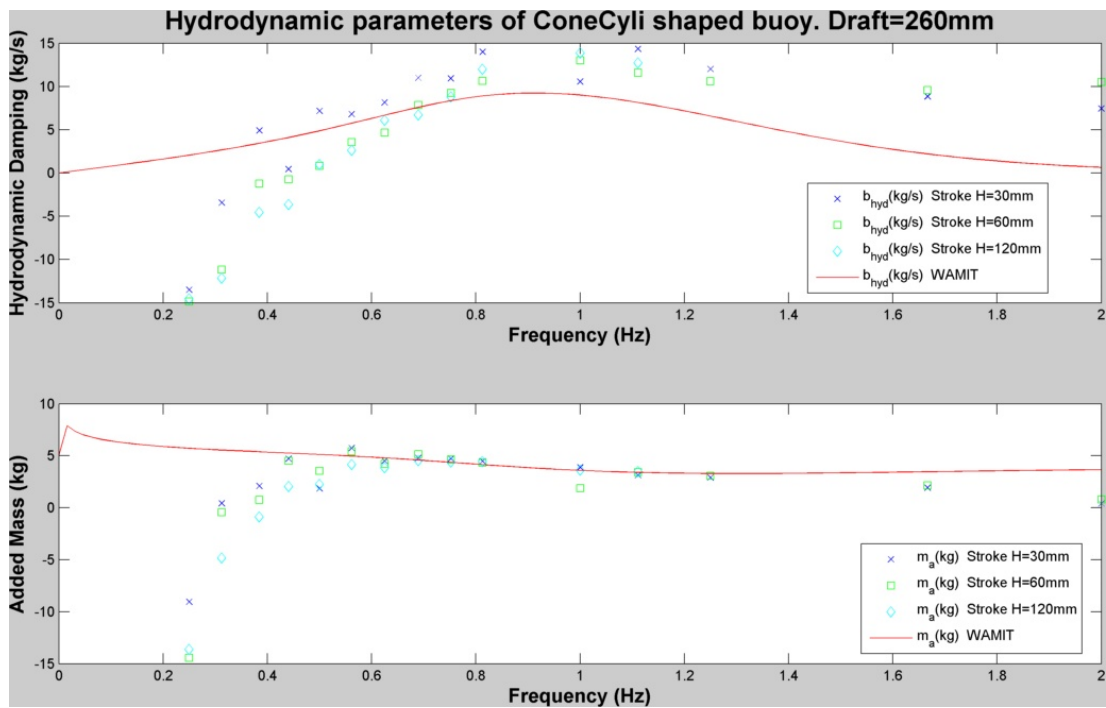**Figure 5:27: Hydrodynamic damping and added mass for cone-cylinder draft=221mm**

Figure 5:28: Hydrodynamic damping and added mass for cone-cylinder draft=260mm

5.4.4.2 Natural frequency

By examining the imaginary part of the impedance (reactance) it is possible to determine the natural frequency of a given buoy shape and draft. When the inertia and spring terms balance each out the reactance vanishes. The frequency at which this occurs is known as the natural frequency.

Figure 5:29 shows the imaginary part of the impedance for the hemisphere-cylinder shaped buoy. The top plot is for a draft of 185 mm, the middle plot is 221 mm and the lower plot is for 260 mm. The low frequency reactance is similar for all three drafts, since the spring term dominates at low frequencies and the spring term is related to the cross-sectional area which is the same for all three drafts. At the high frequency end, the reactance is determined by the inertia of the buoy. At the highest frequency tested (0.5 Hz) the magnitude of the reactance is the least for the buoy with the shallowest draft and increases as the draft increases and the buoy has more intrinsic inertia.

A sixth degree polynomial was fitted to the experimental data so that the frequency at which the reactance was zero could be determined.

Table 5-2 gives the natural frequency (and natural period) results for the hemisphere-cylinder shaped buoy. The inclusion of both period and frequency is not intended to insult the reader by presuming the task of inversion too difficult; rather as an acknowledgment that researchers tend to work in units that they are most familiar with. Some think in seconds, some in Hertz, others in angular frequency and some a combination of all three depending on the task at hand. There is good agreement between the values obtained for each stroke height and, as expected, the natural frequency decrease with draft. Figure 5:30 shows the reactance for the cone-cylinder shaped buoy. The top plot is for a draft of 195 mm, the middle plot is 221 mm and the lower plot is for 260 mm.

Table 5-2: Natural Frequency data for the hemisphere-cylinder shaped buoy

Draft (mm)	Stroke Height (mm)	fn_Exp (Hz)	fn_WAM (Hz)	Tn_Exp (s)	Tn_WAM (s)
	30	1.177	1.175	0.850	0.851
185	60	1.179	1.175	0.848	0.851
	120	1.179	1.175	0.848	0.851
	30	1.083	1.066	0.923	0.938
221	60	1.075	1.066	0.931	0.938
	120	1.075	1.066	0.930	0.938
	30	0.946	0.977	1.057	1.023
260	60	0.965	0.977	1.036	1.023
	120	0.963	0.977	1.038	1.023

Table 5-3: Natural Frequency data for the cone-cylinder shaped buoy

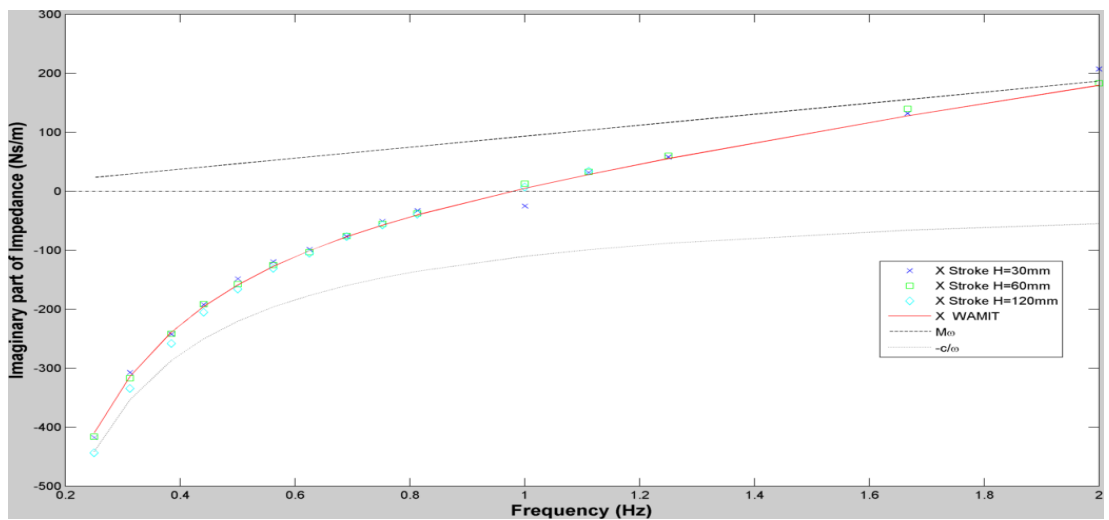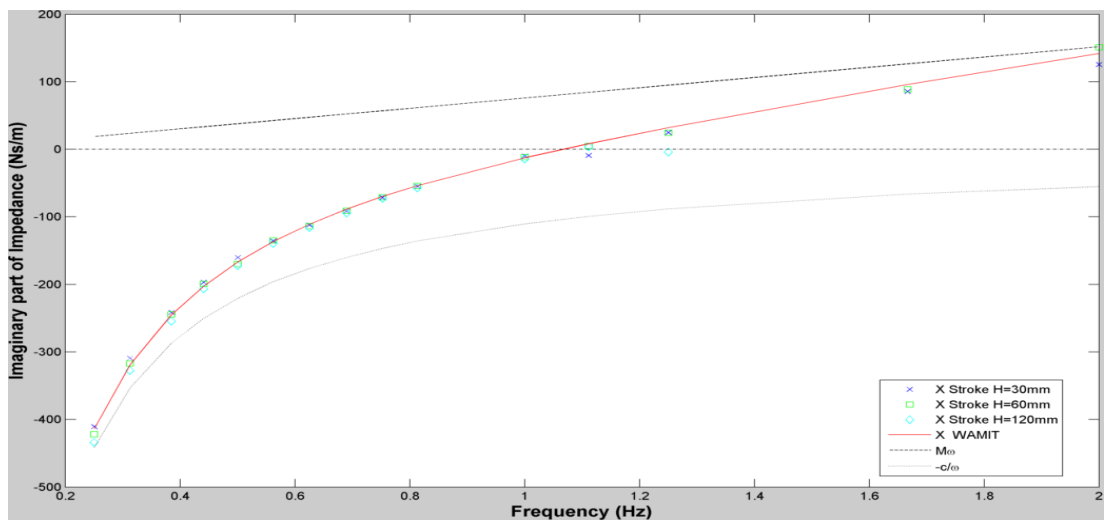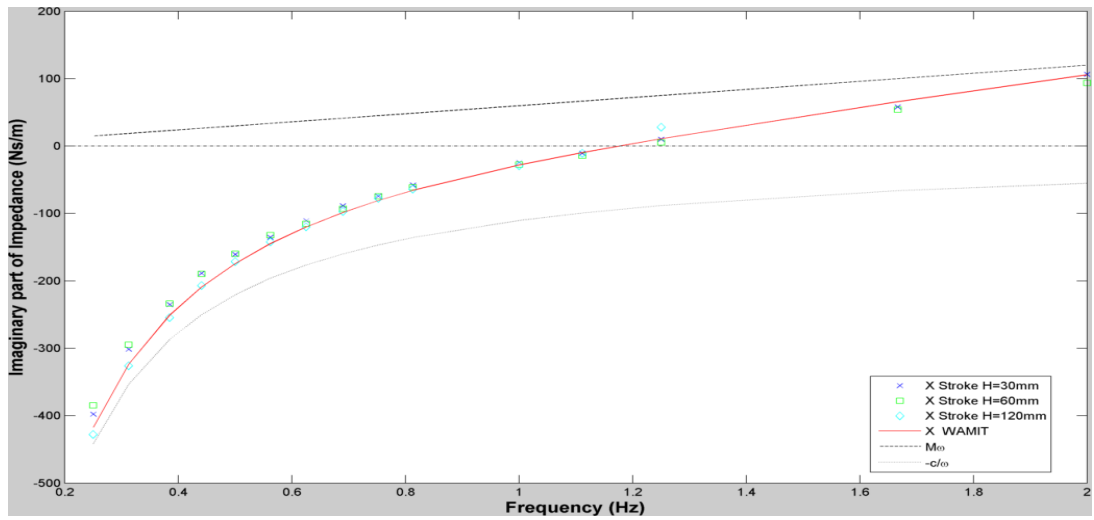| Draft (mm)	Stroke Height (mm)	fn_Exp (Hz)	fn_WAM (Hz)	Tn_Exp (s)	Tn_WAM (s)
	30	1.316	1.405	0.760	0.712
195	60	×	1.405	×	0.712
	120	×	1.405	×	0.712
	30	1.229	1.223	0.814	0.818
221	60	1.233	1.223	0.811	0.818
	120	×	1.233	×	0.818
	30	1.093	1.092	0.915	0.916
260	60	1.116	1.092	0.896	0.916
	120	1.091	1.092	0.917	0.916

Figure 5:29: Imaginary part of impedance for Hemisphere-Cylinder shaped buoy, draft=185mm (top) draft=221mm (middle) draft=260mm (bottom)
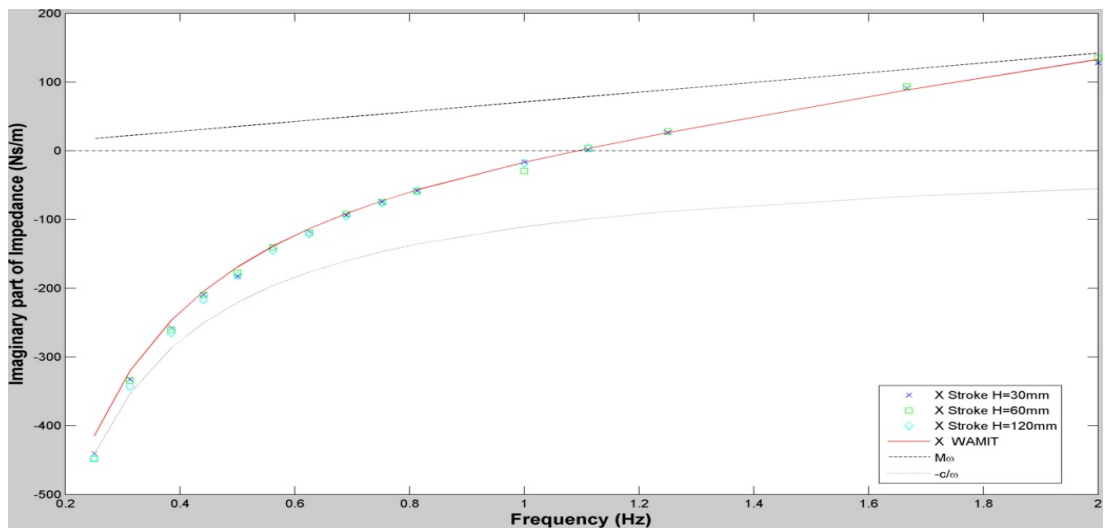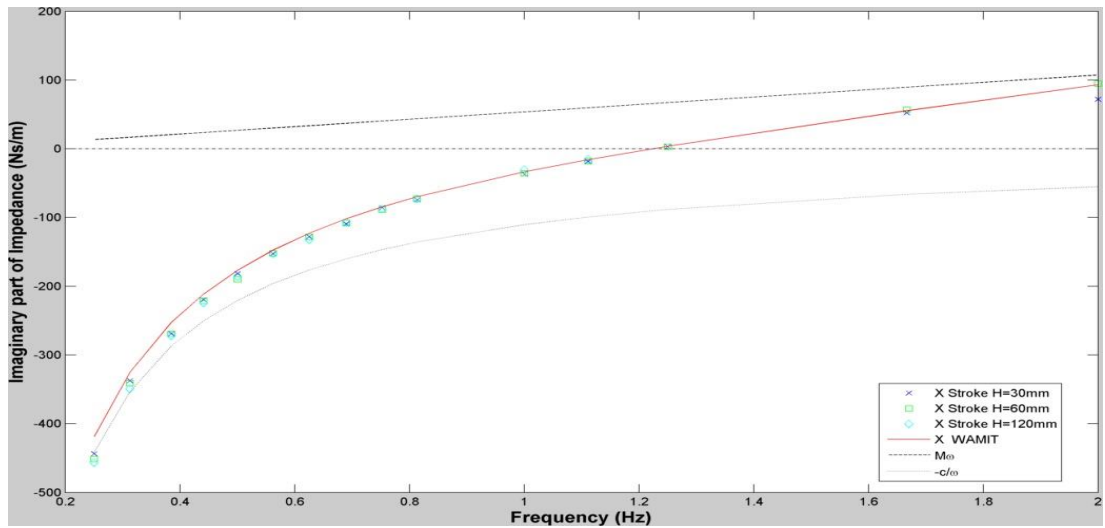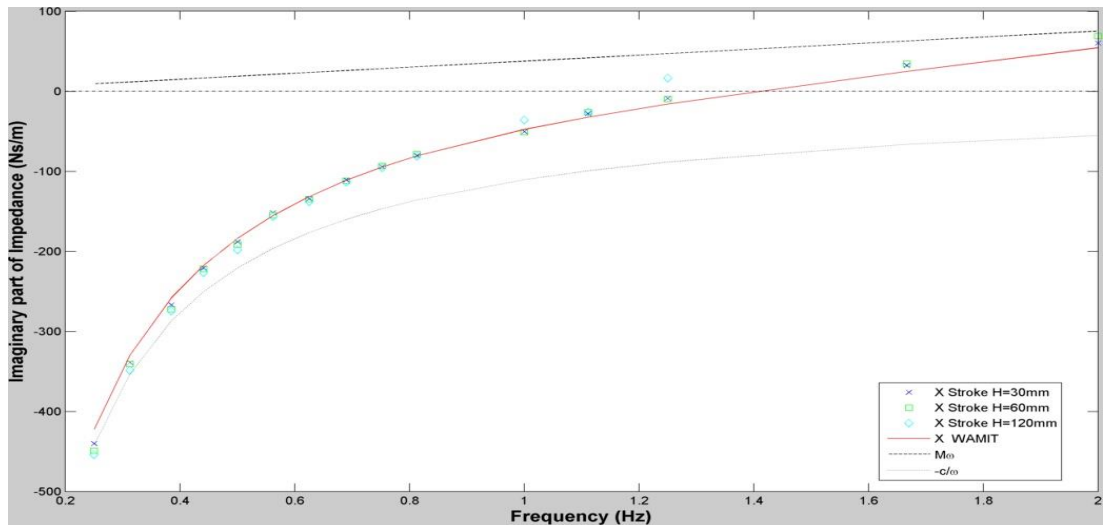
Figure 5:30: Imaginary part of impedance for Cone-Cylinder shaped buoy, draft=195mm (top) draft=221mm (middle) draft=260mm (bottom)

Once again, the natural frequency of the buoy can be interpolated from the experimental data yielding the results shown in Table 5-3.

The higher natural frequencies for the cone in comparison to the hemisphere indicate the cone is much lighter. High frequency tests at a large stroke height were avoided as they induced a resonance response in the supporting bridge structure, hence the natural frequency was not found for some scenarios.

5.1 Heave exciting wave forces

To calculate the heave excitation forces, the buoy is held fixed at still water level during regular wave tests of varying frequency. In doing this it is possible to measure the total exciting force on the buoy for a range of different frequencies. Recalling form the theory section 2.5.2 that the exciting force is comprised of two parts; the incident or Froude-Krylov force and the diffraction force. The Froude-Krylov force is the result of integrating the pressure field of the undisturbed fluid acting over the wetted surface of the body. The diffraction forces is related to the disturbance felt by the wave field due to the presence of the floating body.

It is then possible to compare experimental results with numerically predicted values. In order to hold the buoy fixed it is necessary to either externally clamp the device or better yet apply sufficient damping force through the PTO mechanism. By sending the maximum voltage to the brake, the braking force is sufficient to prevent movement of the buoy for the range of periods tested -1.23, 1.33, 1.45, 1.6, 1.78, 2 and 2.27s-. This is a beneficial characteristic of the PTO mechanism selected. Tests were carried out on three different buoy shapes and for each shape three different drafts were tested.

The total wave excitation force consists of the force (torque) measured by the torque sensor as well the contribution of the internal friction of the system. Figure 5:31 shows the results of the heave excitation test for the different shapes and drafts tested. The numerical results from WAMIT are given as excitation force per meter wave amplitude (N/m). Accordingly the experimental forces obtained for each frequency are divided by the wave amplitude at that frequency. The fundamental harmonic of the force signal is used and the wave amplitude is achieved by placing a wave probe at the centre of the buoy location and running the waves with no model in the water. For each shape tested, larger excitation forces are achieved with

a shallower draft. The zero frequency limit of the excitation force is equal to the hydrostatic spring value as the cylindrical section of three shapes is the same. As the frequency increases the effect of buoy shape becomes apparent {Looking at either the blue lines (draft =185mm) or the red lines (draft=221mm)} as the cone values remain the highest followed by the hemisphere and then the cylinder. As the input wave frequency increases above 0.6 Hz the experimental values begin to exceed their numerical counterparts for all configurations tested. This can be attributed to increasing non-linearity of the wave profile with increasing wave steepness due to the relatively large wave amplitudes tested, of approximately 80 mm.
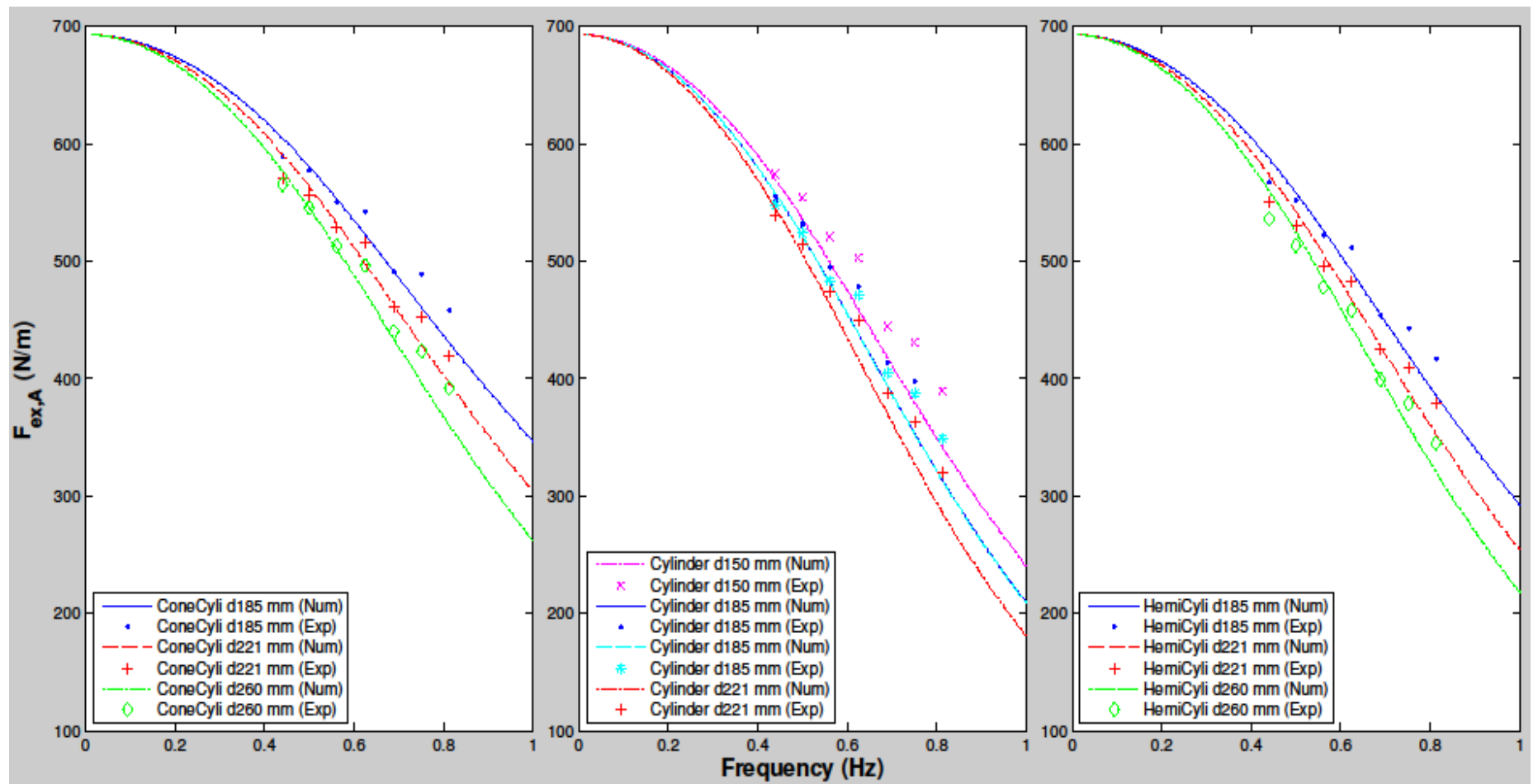
Figure 5:31: Experimental and numerical heave excitation force (per meter wave amplitude) for all shapes and drafts tested

5.2 Power absorption tests

5.2.1 Regular waves

Figure 5:33 overleaf gives the testing plan for power absorption tests carried out for regular waves. The first variable parameter is buoy shape, with three different shapes tested. For each shape, three separate drafts were tested, and for each draft setting, a number of different supplementary mass configurations were also tested. For a given shape, draft and supplementary mass configuration, five different regular waves were used. Finally for each period, four to five different external damping values were applied. The damping applied for the following series of tests was of a constant force. According to Price, (2009) the Oyster device uses a constant PTO force as an operational design choice to reduce the capital costs and complexity of the system. Murtagh & Walsh (2015) also suggest that a Coulomb damping strategy would have economic advantages over purely linear damping. The is because with Coulomb damping, the magnitude of the maxima of forces in any sea state is lower than in the linear case, along with higher transmission velocities in the Coulomb damping case. This would result in cheaper PTO expenditure. Although the authors acknowledge that the higher velocities come at the cost of larger stroke lengths compared to the linear damping strategy; which is naturally more problematic when it comes to PTO endstop constraints.

Table 5-4 below shows the wave height and periods used for regular wave testing. The wave height is determined by removing the buoy from the water and placing a resistance probe at the centerline location.

Table 5-4: Regular wave characteristics

Period (s)	Height (m)
1.23	0.099
1.33	0.09
1.45	0.101
1.6	0.084
1.78	0.094

The measured wave profile with no device in the water is used as input for the numerical model.
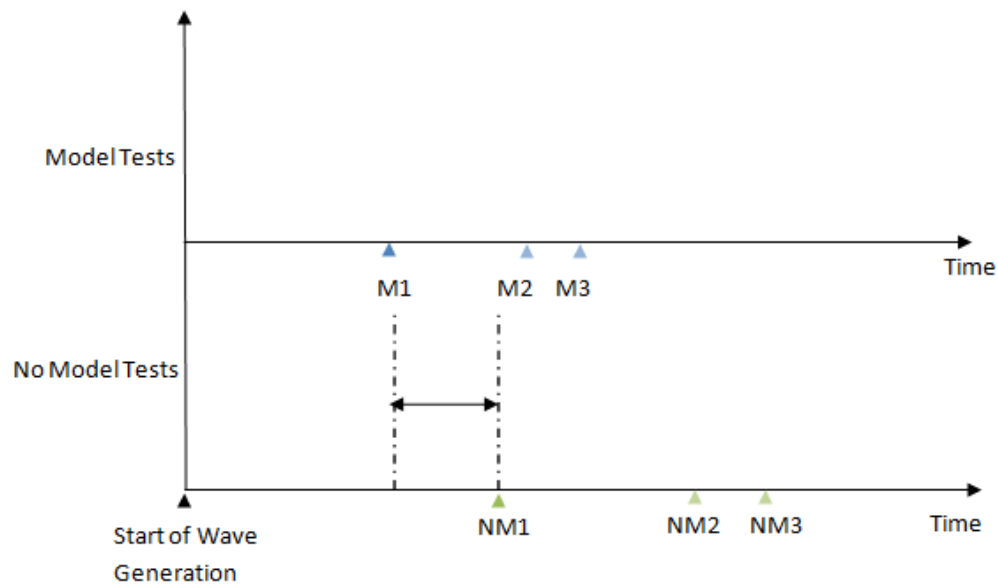

Figure 5:32: schematic indicating the different phase shift between no-model and model tests.

Unfortunately wave generation and data acquisition are achieved using different computers i.e., non-synchronous. The operator first begins the wave generation on one computer, then begins recording data on a second computer. No-model tests and model tests can therefore begin at various different times. The "no-model" wave profile is shifted (as shown in Figure 5:32) to ensure a correct phase is maintained for the numerical simulation. The effectiveness of this approach is illustrated in Figure 5:34. Regular wave tests are run for 93.75 s and all data is sampled at 32Hz. Only the final 32 s of data are used for a comparison between numerical and physical results. The numerical model is started an additional 32 seconds earlier to ensure any transients associated with the initial conditions are removed and a steady state is reached.
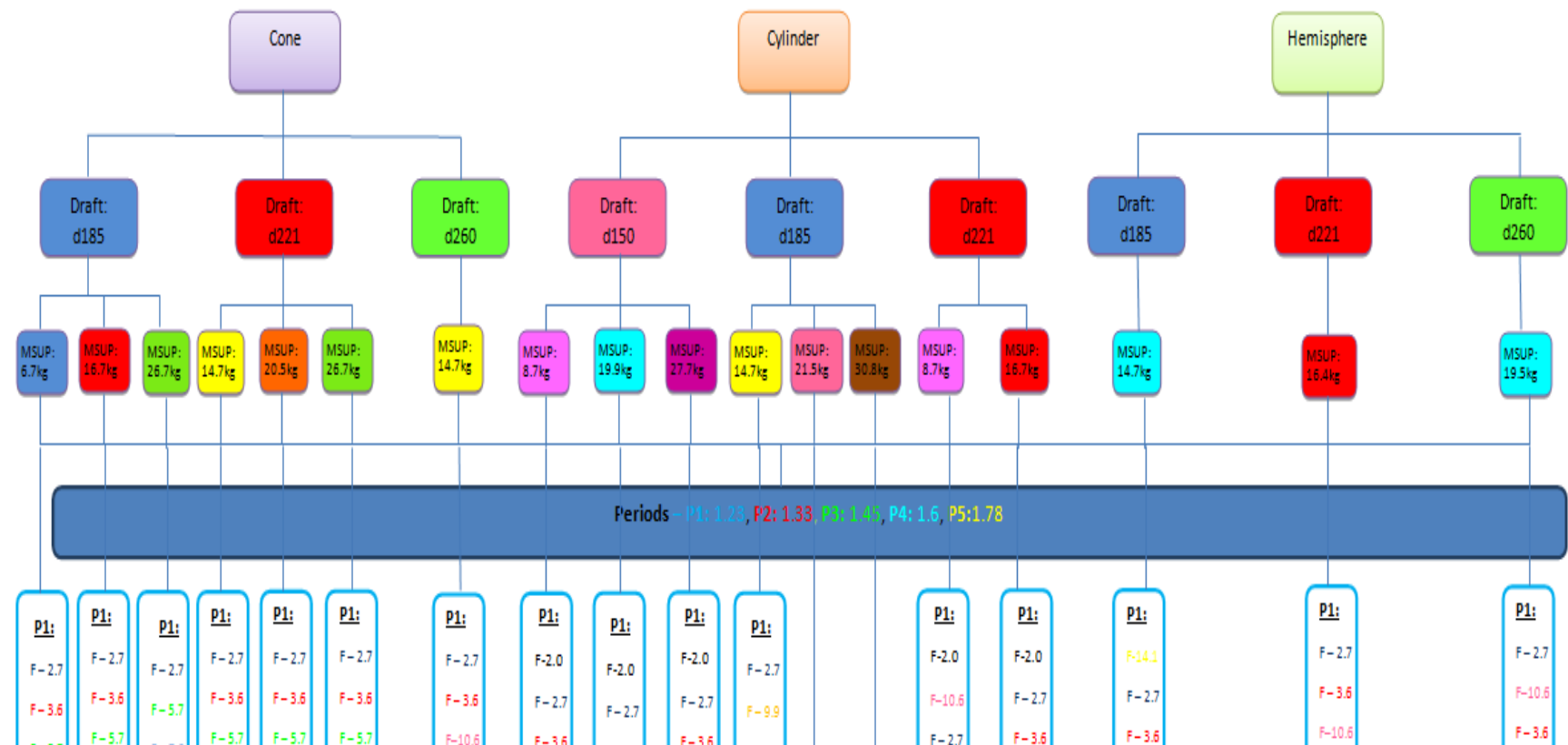
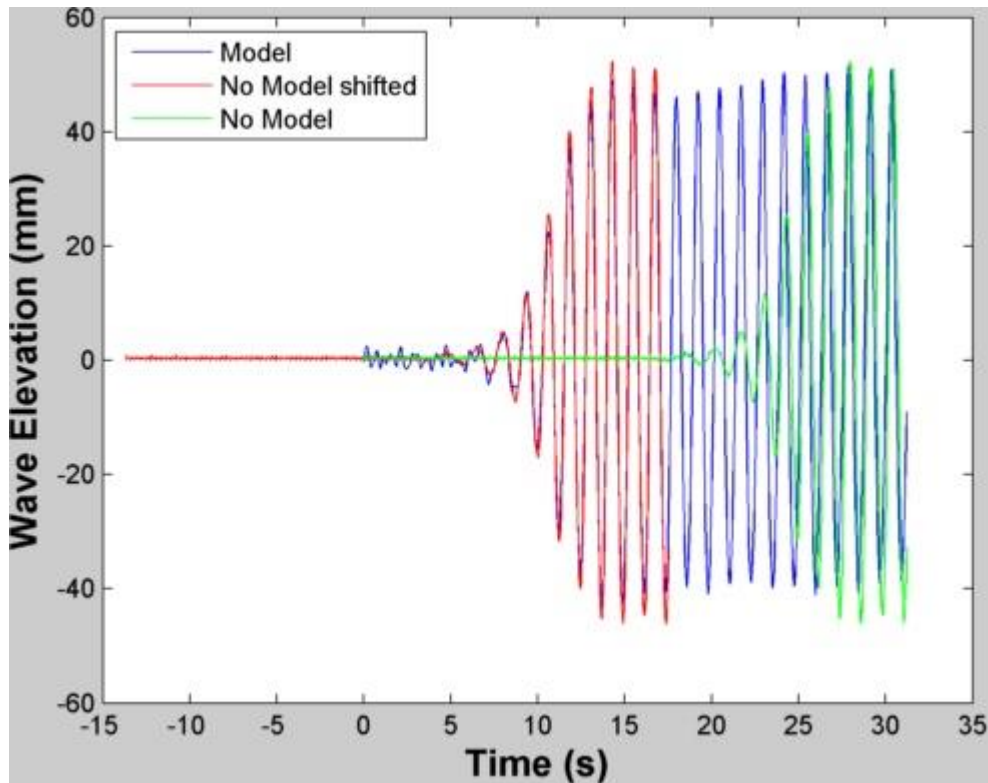**Figure 5:33: Regular wave test plan**

Figure 5:34: Example of phase shifting the incoming wave

Figure 5:35 (overleaf) shows the response of a cylinder shape buoy with a draft of 185mm to an incoming regular wave of height 94mm and period 1.78 seconds. The applied damping force from the brake is 3.9 N (excluding the friction force). The supplementary mass for this test is 14.7 kg resulting in a tuning ratio T/T_n = 127%. As a result of this tuning the buoy response lags that of the wave and there is also some amplification of the buoy height compared to the wave height (RAO=1.46). The numerical model matches the experimental result quite well for this test set-up.

The central graph shows the measured damping force and buoy velocity -note the separate y-axis-, the damping is in the form of a square wave whose sign is proportional to the that of the velocity. The lower plot shows the time series of the experimental and numerical power absorption. The measured experimental average power over the comparison period is 0.925 W, while the numerical average is 1.05. The ratio of maximum power to average power is roughly 1.6. Performing a spectral analysis on both experimental and numerical position signal reveals there is 4.8 º phase difference.
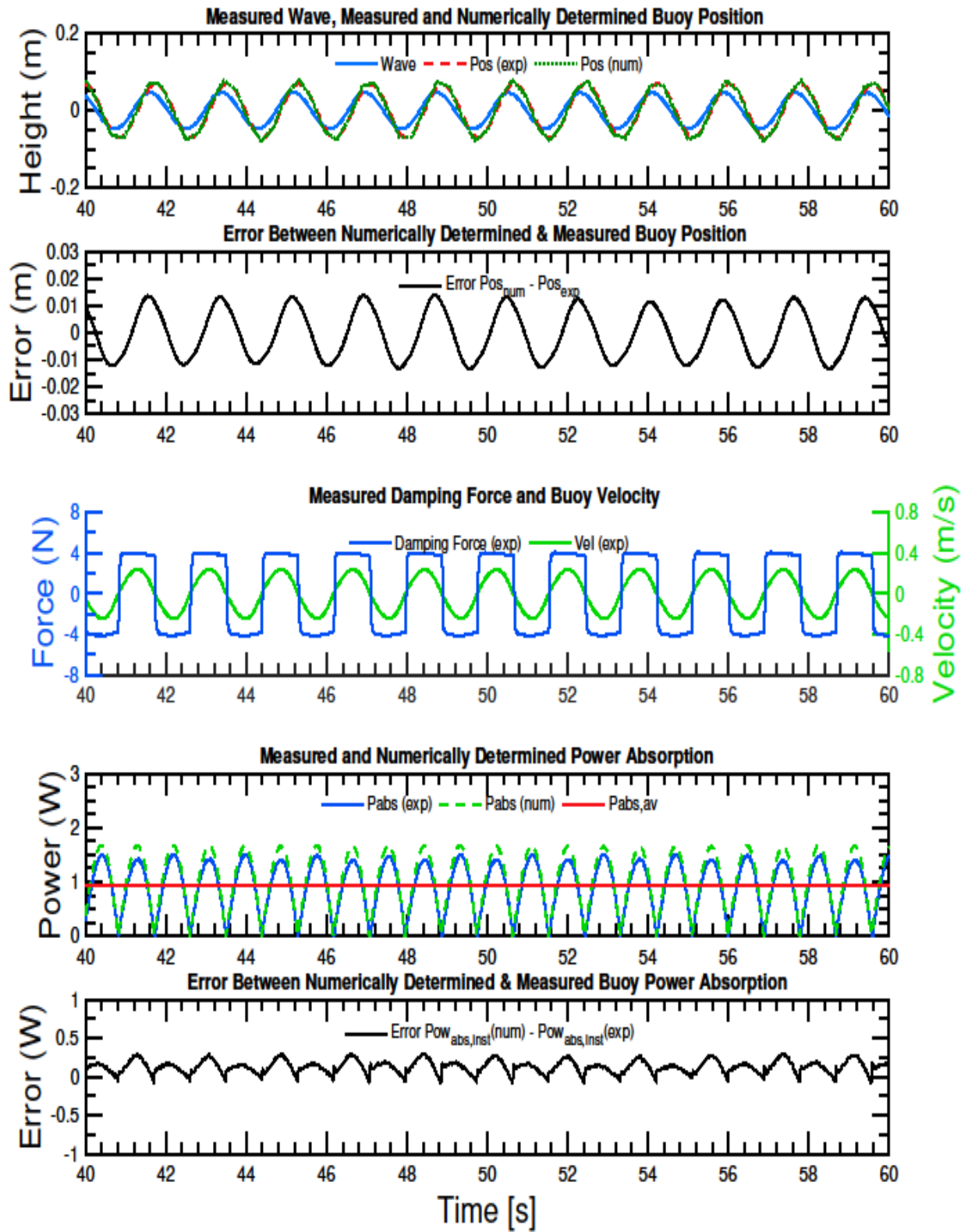
189

Figure 5:35: Experimental and numerical results for cylinder shape, draft=185mm, Msup=14.7kg, $F_{d,A}$ =3.9 N, for wave H= 94mm, T=1.78s
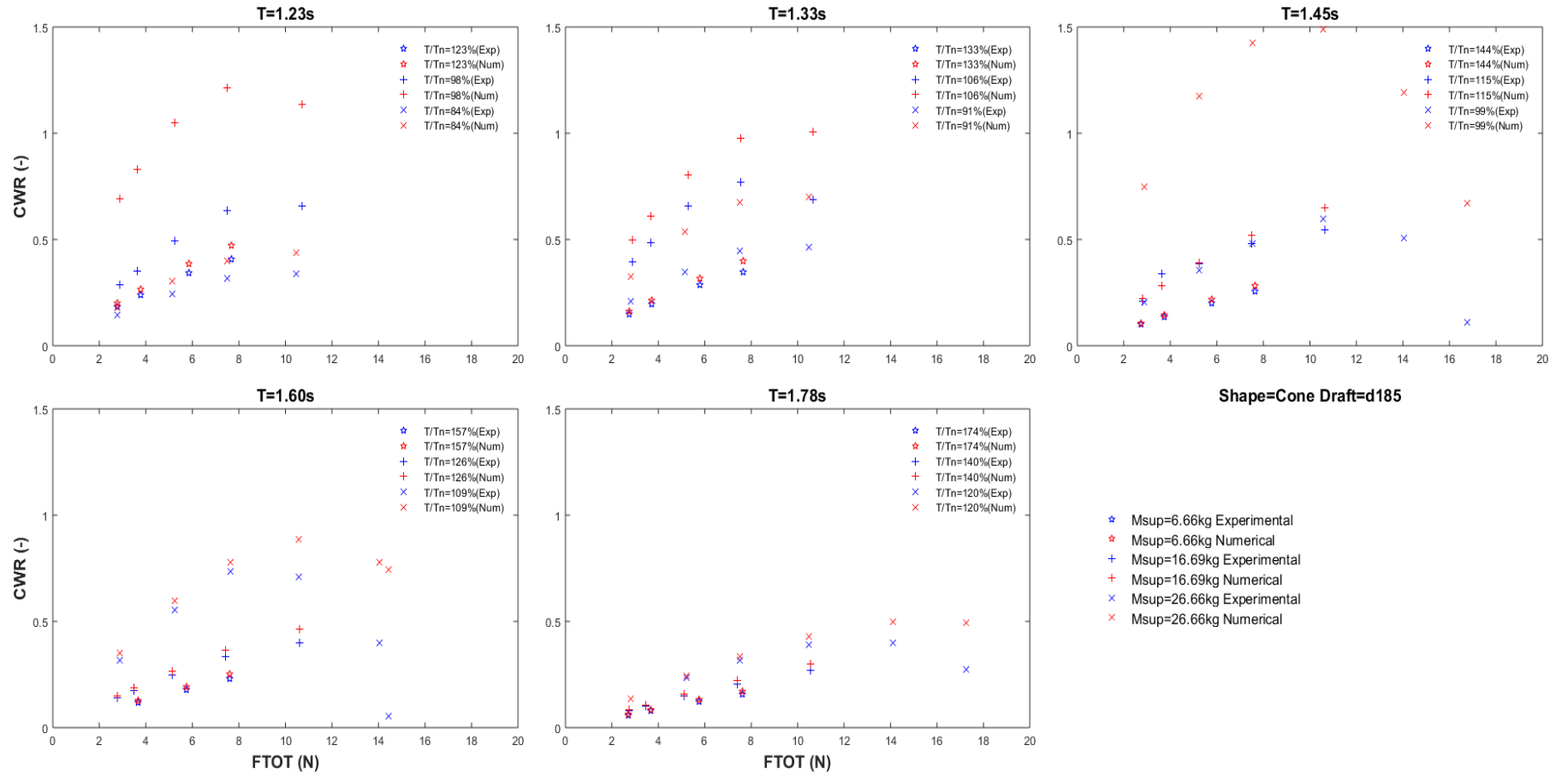
Figure 5:36: Capture width ratio vs total damping force for different periods and supplementary masses. Cone-cylinder shape buoy draft 185mm

Figure 5:36 plots the power absorption capture width ratio (CWR) against the total damping force (applied force plus friction force) for the cone-cylinder shape buoy with draft equal to 185mm. Recall the formula for CWR was given in chapter 2. Tests were carried out for three separate supplementary masses with five different periods tested for each supplementary mass set-up.

The 'star' marker signifies the results of the smallest supplementary mass M_{sup}=6.7kg, with blue depicting the experimental results and red showing the numerical results. For this set-up the natural period is approximately equal to 1s, hence all five tested periods are greater than the natural period. The correspondence between physical and experimental results is very good particularly for the higher periods. There is some drift between the results for the 1.23s and 1.33s tests as the damping force is increased, with the numerical model predicting better efficiencies than those achieved in reality.

The '+' marker show the results of the second set-up, where the supplementary mass has been increased to 16.7kg. The tuning effect of the added mass can clearly be seen in the results for the 1.23s test, as, at this period the buoy is now almost at resonance (T/T_n=98%). The increase in buoy velocity associated with operating at resonance means that for the same damping force, more power can be produced leading to higher absorption efficiencies than those achieved with the lower supplementary mass ('star' marker). From a validation viewpoint, the shifting towards resonance is bad, as near resonance, the fundamental assumptions of linear theory, which form the basis of the numerical model, break down. This is evident in the large discrepancy between the numerical and physical results for the 1.23s test and also the 1.33s test which is also very close to resonance. The point absorber effect whereby capture width ratios greater than 1 are attainable can be seen in the numerical predictions. However, the maximum CWRs observed from experimental results are between 0.6-0.7. When examining the M_{sup}=16.7kg set-up it is interesting to note that the numerical model predicts the highest CWR of 1.21 when the incoming wave period is 1.23s (T/T_n=98%), while the highest experimental CWR of 0.76 is achieved at the larger period of 1.33s (T/T_n=106%). It seems likely that the natural period for that set-up is closer to 1.33s. The added mass at the exciting frequency is used in the calculation of the natural period and since the value used was the value taken from WAMIT, any error in this value will propagate. However, the reason for the discrepancy lies in the method of calculating the natural period using a constant hydrostatic spring term ($c \approx 693$ N/m). In reality, the wetted area A_w of both

the cone and hemisphere-cylinders will vary with draft. Finally, it is worth noting from the results that the CWRs suffer a drop off when the tuning ratio is on the 'wrong side' of 100%, i.e., the exciting period is less than the natural period.

The agreement between experimental and physical results becomes better as the period is increased and the buoy is operating further from resonance. The 'x' markers show the results of the test runs where the supplementary mass is equal to 26.7kg. A consequence of this additional mass is that the natural period is now approximately 1.45s. An increase in efficiency is achieved for 1.78s and 1.6s tests as these periods are now closer to resonance. However, the opposite is true for the 1.33s and 1.23s tests. These periods are now further away from resonance than previously ('+' markers), indeed for the 1.23s test the detuning effect is such that the CWR is even less than that of the 6.7kg supplementary mass set-up. The effect that the different tuning ratios have on both the amplitude and phase of the buoy response is illustrated in Figure 5:37 below.
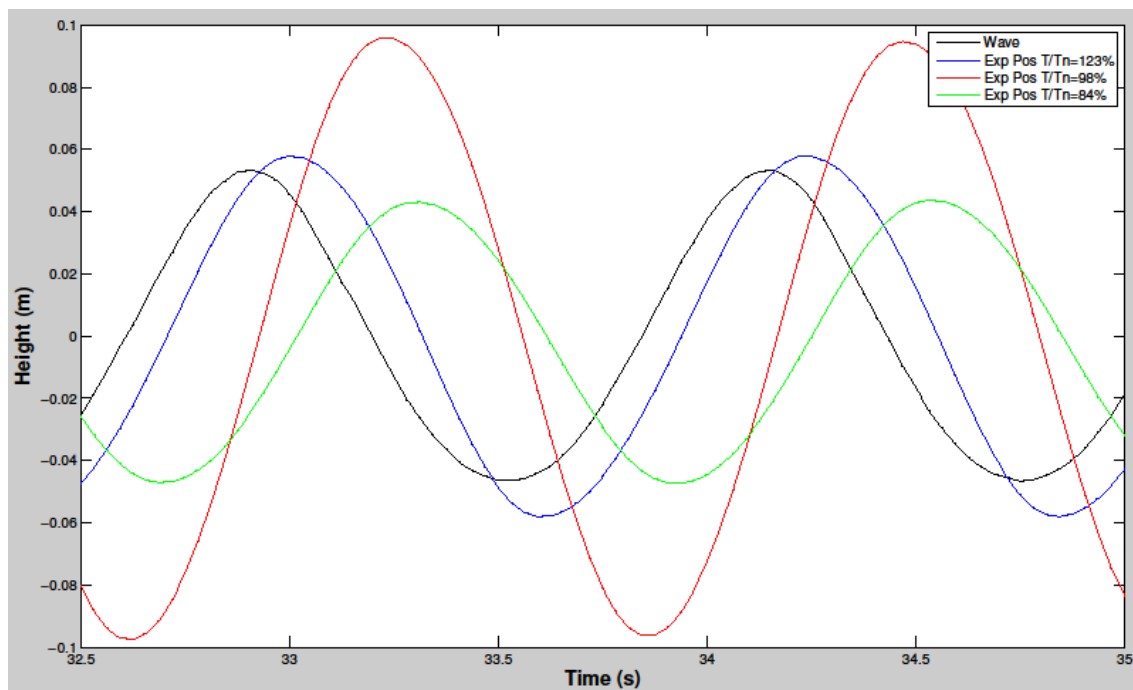

Figure 5:37: Effect of supplementary mass on the cone-cylinder shape buoy response.
Draft = 185mm, wave height=100mm, period=1.23s, total damping force=7.5 N

193

The graph shows the response of the cone-cylinder buoy with draft equal to 185mm to regular waves of height 100mm and period 1.23s, for three different supplementary masses. The total damping force was 7.5 N for each test. The first mass set-up corresponds to a tuning ratio of $T/T_n=123\%$; the buoy lags the wave and the RAO is slightly greater than 1. When the buoy is tuned closer to resonance the response of the buoy increases to nearly twice the wave amplitude, and the phase lag between the buoy and the wave is nearly 90°. An additional increase of mass shifts the phase lag even further and the amplitude of the buoy motion is now less than that of the wave, a significant de-tuning effect.

The increase in supplementary mass has the same effect as if the device exhibited higher hydrodynamic added mass (m_a). They have the same effect since they are both inertial terms. If we think in terms of phasors as we did for the impedance (forced oscillation) tests. Whereby spring terms (displacement), resistive terms (velocity) and inertia terms (acceleration) will each extend a 90 degree angle between them, on a polar plot. Adding inertia will increase the reactive part of the impedance, pulling the devices velocity phasor closer to the heave excitation force phasor. Indeed the velocity phasor of the red curve in Figure 5:37 would be very close to heave excitation force phasor. We have induced resonance, and in doing so can yield improved power capture. The further increase in inertia, increases the reactance too much, such that the velocity phasor has been drawn away from the heave excitation force phasor.

5.2.1.1 Effect of varying supplementary mass

The tuning effect of varying the supplementary mass is further illustrated in Figure 5:38 below, which plots CWR against period for the cylinder shape buoy, at a draft of 150mm. Three different supplementary masses were tested for this shape and draft with the total applied damping for all tests being 5.74 N. For the tests where M_{sup}=8.69 kg (asterisks marker), the highest efficiencies (both numerical and experimental) are seen when the incident wave has a period of 1.23 s. Increasing the supplementary mass to 19.96kg (diamond marker) shifts the peak to approximately 1.45s, while a further increase to 27.66kg (triangle marker) moves the natural period to roughly 1.6s. The disparity between numerical and physical results near the resonance zone is apparent for all three mass set-ups.
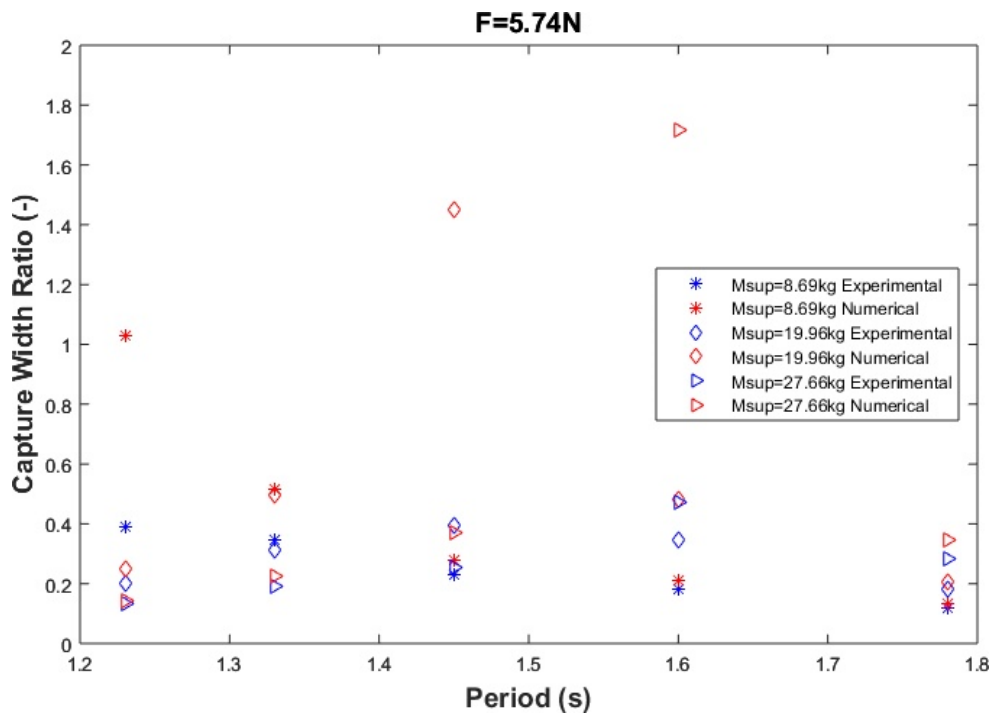

Figure 5:38: Efficiency vs period for varying supplementary mass M_{sup}. Cylinder shaped buoy, draft=150mm, F_{Tot} = 5.74 N.
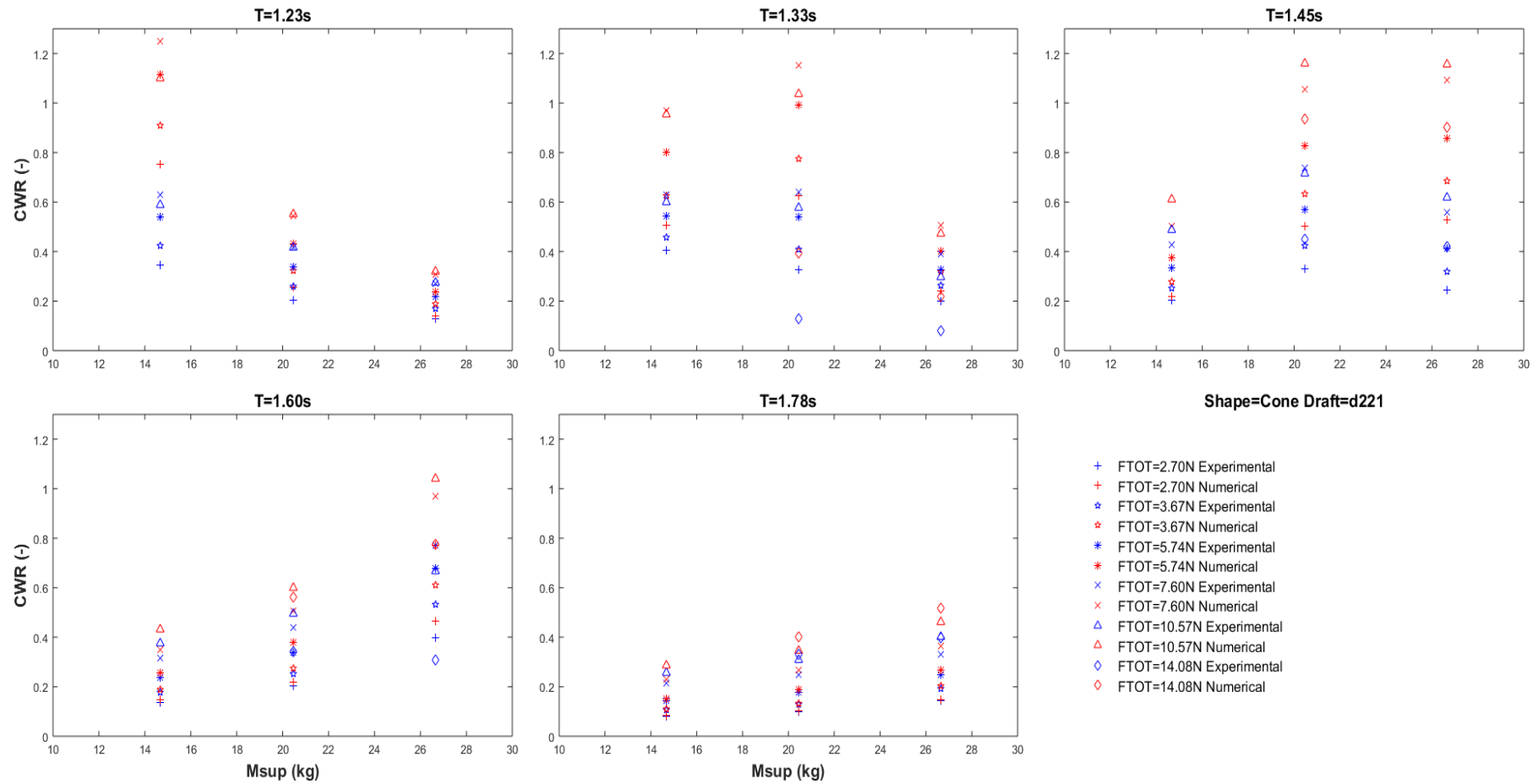
Figure 5:39: CWR vs supplementary mass for different input wave periods and varying damping forces. Cone-cylinder shape buoy draft = 221mm.

The effect of varying the supplementary mass to tune for different incoming wave periods is illustrated in Figure 5:39, giving data for the cone-cylinder shape buoy of draft 221 mm. Beginning with the top left-hand subplot, which is for a wave period of 1.23s, it can be seen that, with an additional mass of 14.7kg, the buoy is well tuned for the period with experimental CWRs ranging from 0.35-0.6 depending on the value of damping applied. A further increase in mass however, tunes the buoy towards higher periods meaning that the efficiency decreases as extra mass is added for the same period of 1.23s.

Examining the top right-hand figure for a wave period of 1.45s, it can be seen that the initial mass of 14.7kg is not the optimum set-up for this frequency. It has already established that this mass is better for the lower period of 1.23s. Increasing the supplementary mass to 20.5kg gives improved CWRs of up to 0.73. A further increase in mass de-tunes the buoy slightly with the heaviest mass of 26.7kg shifting the resonance period of the buoy towards 1.6s (lower left-hand plot).

Looking at the longest period of 1.78s (lower right-hand plot), it can be seen that while increasing the mass does increase the efficiency, an optimum value is not reached as was achieved for the other wave periods. In order to achieve an optimum, even more additional mass is required, which gives an indication of the large tuning forces required for longer period waves. While the CWRs are lower for the longest period, the available power in the waves does increase with period (for the same wave height), meaning that overall energy yield could potentially be increased by targeting the longer period waves. Ultimately, such a strategy will depend upon the design capabilities of the PTO and the cost/reward ratio from an economic standpoint.

Referring back to Figure 5:38 it can be seen that the CWR increases with period in accordance with point absorber theory as discussed in chapter 2, since

$$CWR_{max} = \frac{L}{2\pi D}$$ (5.6)

The experimental increase in CWR with additional mass is less pronounced than the numerical predictions, with the numerical simulations predicting far greater gains. Although the method of tuning the device for this study involving the use of mass either side of a toothed belt and pulley is purely meant for research purposes. By looking at Table 5-5 one can get a sense of how infeasible, certainly impractical it would be to scale up this set-up. If

the prototype scaling factor were equal to 50, so that the diameter of the full scale device would be 15 m, then every kilogram of mass added at laboratory scale is equivalent to a considerable 125 tonnes at full scale.

Table 5-5: Factors of scale

	Lab	Scale Factor = 20	Scale Factor =50
Mass (kg)	1	8,000	125,000
Force (N)	1	8,000	125,000
Diameter (m)	0.3	6	15

Even if external mass is not a viable option for a full scale device, Figure 5:40.to Figure 5:42, indicate the large tuning forces required to alter the natural period of the cylinder shape buoy with a draft of 150 mm. The figures show the tuning forces for three different supplementary masses, blue line M_{sup}=8.69 kg, red line M_{sup}=19.96 kg, green line M_{sup}=27.66 kg. The total damping force for all three mass set-ups is 5.74N.

Figure 5:40 shows the tuning and damping forces when the incoming wave has a period of 1.23 s and a height of 98mm. The amplitude of the tuning force is 18.33 N and the average absorbed power is 1.46 W. In Figure 5:41, the supplementary mass has been increased to 19.96 kg, the forces and power absorbed for a wave period of 1.45s and height of 100 mm is shown.
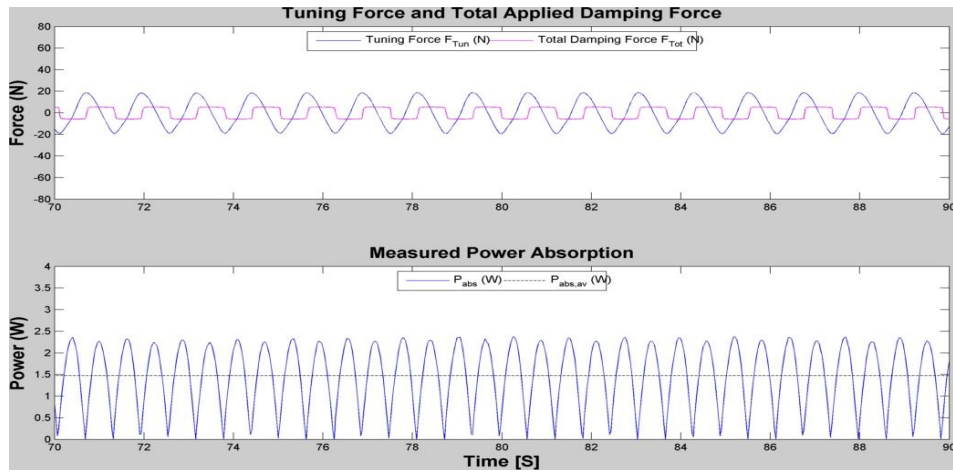
Figure 5:40: Power and forces for cylinder d=150mm M$_{sup}$=8.7kg H=98mm T=1.23s F$_{Tot}$=5.7N
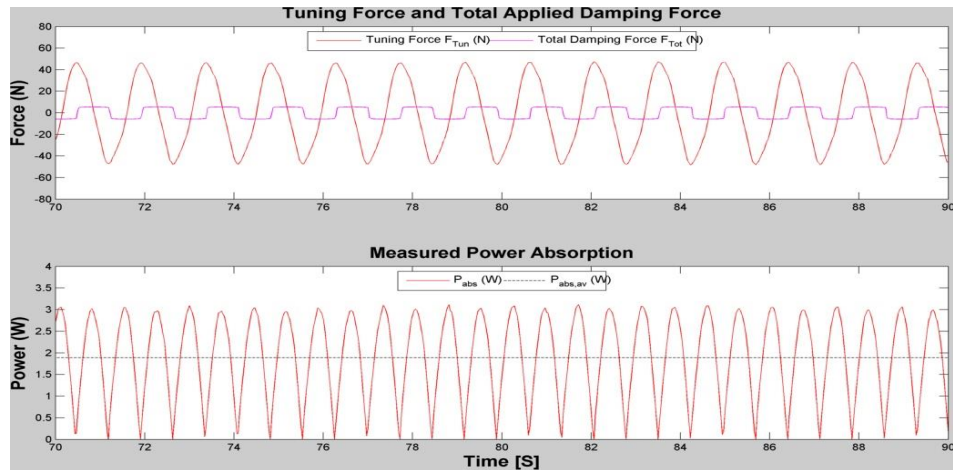
Figure 5:41: Power and forces for cylinder d=150mm M$_{sup}$=19kg H=100mm T=1.45s F$_{Tot}$=5.7N
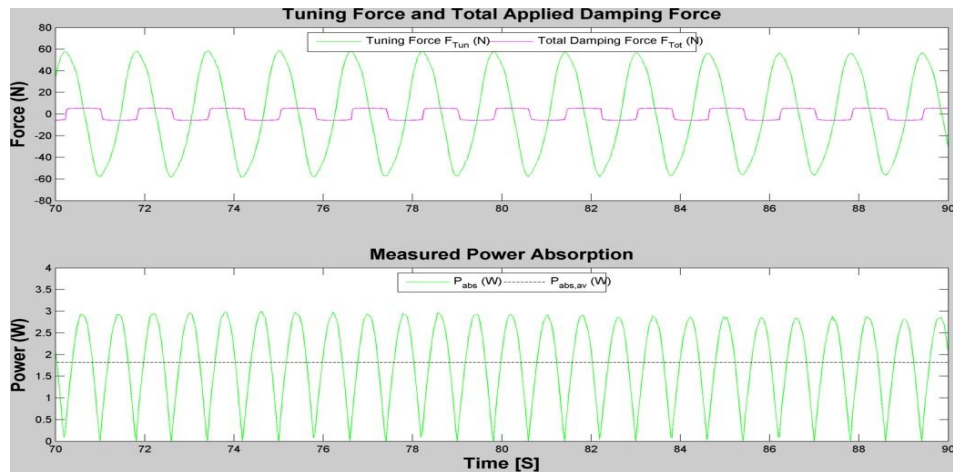
Figure 5:42: Power and forces for cylinder d=150mm M$_{sup}$=27.6kg H=84mm T=1.6s F$_{Tot}$=5.7N

199

The amplitude of the tuning force has increased to 47N while the average absorbed power is 1.88 W. Finally, Figure 5:42 shows the results for a wave period of 1.6s and height of 84 mm. The amplitude of the tuning force is 57N and average absorbed power is 1.81W. Even though the absorbed power has decreased slightly (by 0.07W), the wave height for this period is smaller, then the amount of available power delivered to the buoy is also reduced, meaning that while the absorbed power may have decreased the absorption efficiency has increased. A tuning force amplitude of 57 N is ten times larger than the total damping force. If these forces are to come from the PTO system, for example, then it represents a considerable design problem. If the device were scaled up by a factor of 50, then this tuning force would be 7.1 MN at prototype scale.

Intuitively for the same diameter and draft, the cylinder buoy will be heavier than the hemisphere-cylinder and cone-cylinder (exact buoy masses shown in Table 5-1). This coupled with the fact that over the frequency range of interest, the cylinder has slightly higher added mass values than the cone-cylinder and hemisphere-cylinder (as can be observed in Figure 4:5 of chapter 4) means that of the three shapes investigated, the cylinder is actually the easiest to tune. Conversely, the devices with lower initial inertia (the hemisphere-cylinder and particularly the cone-cylinder) will require larger tuning forces.

5.2.1.2 Effect of varying damping force

The effect of varying the total damping force for a given shape, draft and tuning ratio is illustrated in Figure 5:43. The addition of 19.46 kg of supplementary mass has shifted the natural period to approximately 1.48s which is reflected in the fact that the peaks of both numerical and experimental efficiency occur near this period. Initially as the damping force is gradually increased (from 2.7 N up to 7.6 N) an increase in efficiency is observed for all periods. A further increase in damping (10.5 N triangle marker) however worsens the CWR in the region of the peak period and particularly for the lower periods (T<T_n). The applied damping is too severe, restricting the motion and hence the power capture of the device. Interestingly for the 1.78s wave the CWR is actually increased, the reason being there is more input power from the waves so the device is not over-damped for this period. However, by

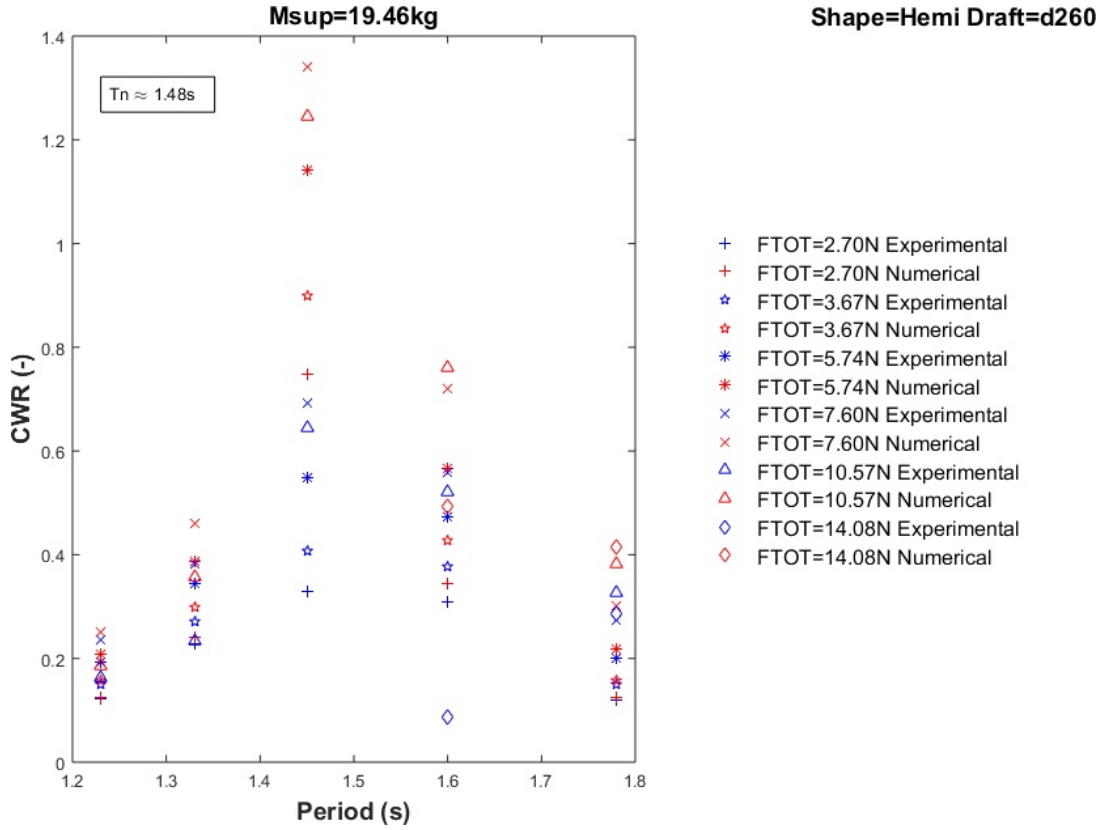further increasing the damping (14 N diamond marker) a reduction in efficiency is once again evident.

Figure 5:43: Efficiency vs period for varying total damping force F$_{Tot}$. Hemisphere-cylinder shaped buoy, draft=260mm, M$_{sup}$ = 19.46 kg.

5.2.1.3 Effect of using a linear spring term in the numerical model

If a linear spring term is used for the cone-cylinder and hemisphere-cylinder shaped buoys, then the numerical model will overestimate device performance, especially near the resonance zone as is illustrated in Figure 5:44 below. The figure shows both numerical and experimental CWR against T/T$_n$ ratio for the cone-cylinder shaped buoy, draft equal to 185 mm. The supplementary mass for this set up was M$_{sup}$=26.66 kg making the input wave of 1.45 s very close to the natural period. Indeed the numerical model indicates a maximum

CWR at this period for all the different damping set-ups tested. The linear spring term is the main contributor to this peak as it ramps up the hydrostatic force.
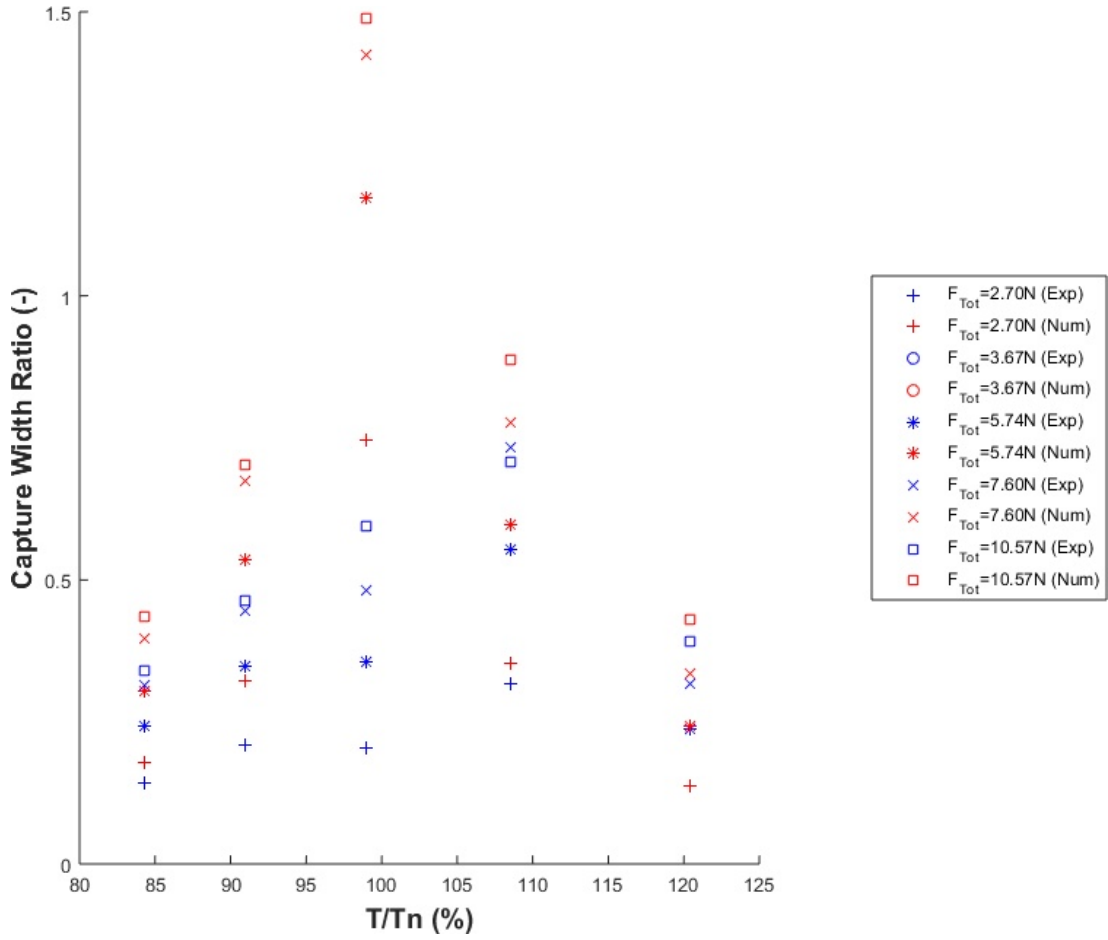

Figure 5:44: Numerical and experimental efficiency Vs T/T$_n$ ratio for cone-cylinder shaped buoy, draft 185mm. M$_{sup}$=26.66kg, linear spring term c=693 N/m.

The peak in numerical CWR is not reflected in the experimental results, as in reality the large heave excursions associated with operating near the resonance zone result in a changing of wetted area which in turn reduces the hydrostatic restoring force. The peak experimental CWR therefore occurs at a larger period. Intuitively this problem is worsened for smaller drafts and applied damping force when incoming waves lift the conical section of the buoy from the water. Conversely, increasing the draft and the damping lessens the effect as the excursions of the buoy are now more likely to be in a range where the wetted area remains cylindrical as is shown in Figure 5:45 (which plots the numerical and experimental CWR against T/Tn ratio for the hemisphere-cylinder shaped buoy, with a larger draft of 260mm). With 19.46 kg of additional mass, the natural period is again close to the 1.45s. On this

occasion, the peak CWR for both numerical and experimental cases match up owing to the increased immersion depth.
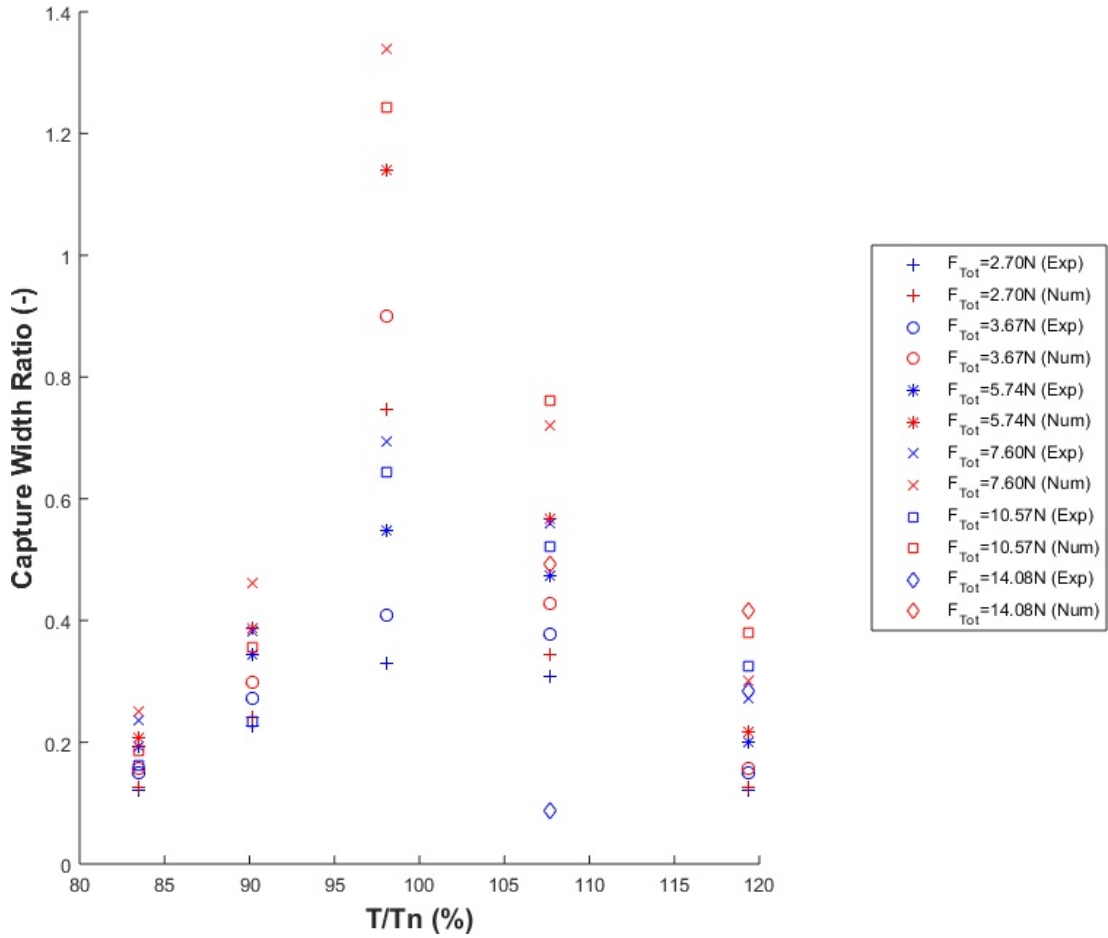

Figure 5:45: Numerical and experimental efficiency vs T/Tn ratio for hemisphere-cylinder shaped buoy, draft 260mm. Msup=19.46kg, linear spring term c=693 N/m

The implementation of a non-linear buoyancy force (which requires that the wetted area is calculated at each time) yielded the alternative numerical CWR curves displayed in Figure 5:46. It plots the numerical and experimental CWR against T/Tn ratio for the cone-cylinder with the same parameters as Figure 5:44 (d=185 mm. M_{sup}= 26.66 kg).

Both numerical and experimental CWR exhibit their maximum values at the same T/T_n ratio. It must be stated that even though this peak ratio is greater than 100%, the T_n used in the calculation is merely a 'reported' or 'estimated' value since it uses the still water wetted area in its derivation. Contrasting this figure with that of Figure 5:44, the spurious peak in

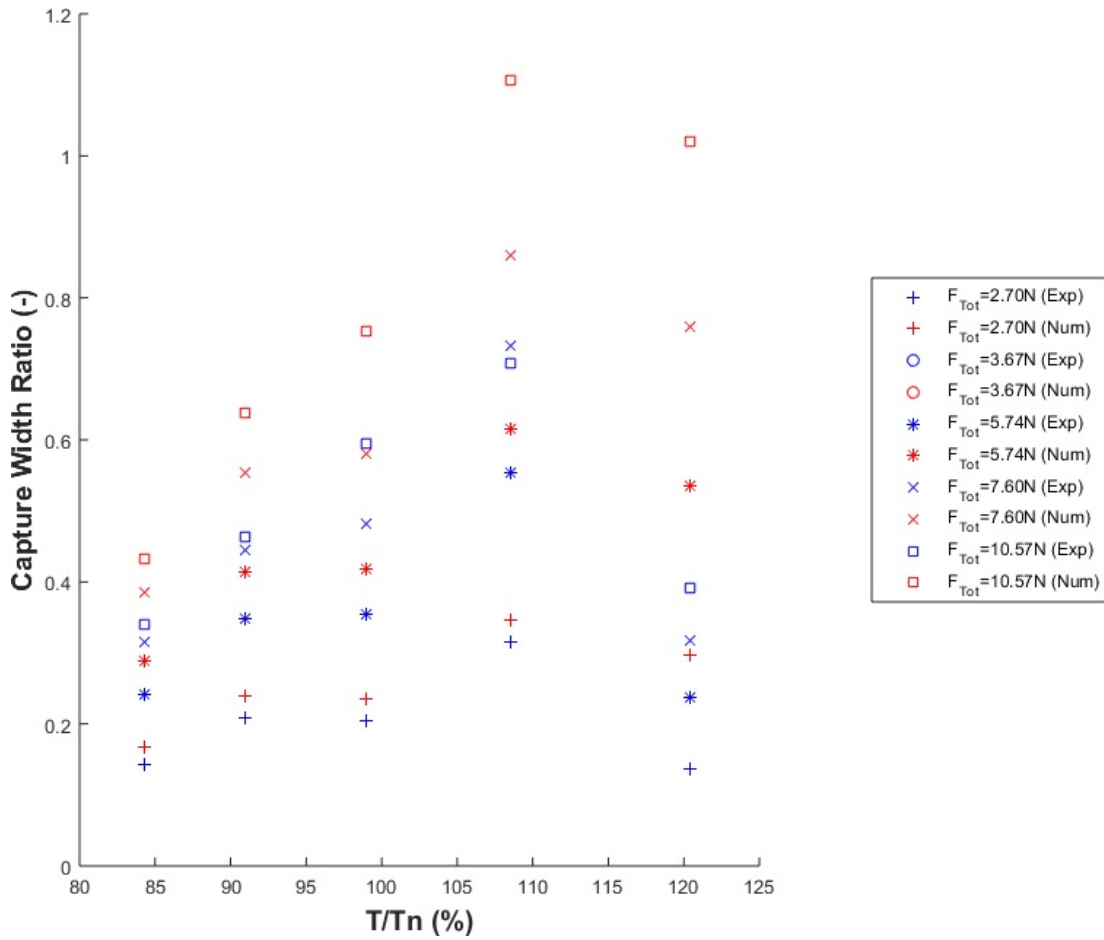numerical CWR at the T/T_n =100% mark is eradicated due to the more sophisticated numerical model.

Figure 5:46: Numerical and experimental efficiency vs T/T_n ratio for cone-cylinder shaped buoy, draft 185mm. M_{sup}=26.66kg.

Additional regular wave plots are given in Appendix B.1, while section 6.7 comments on accuracy of fit between numerically and experimentally achieved results.

5.2.2 Irregular waves

The Bretschneider spectrum is useful for fully developed conditions that exist in deep water where the sea-state and the local winds are in equilibrium and is generally considered to be representative of conditions off the Irish west coast (Holmes and Barret 2007).When

requesting an irregular Bretcshneider wave series the tester has two inputs available, peak period T_p and zero order spectral moment m_0.

The spectral moment was chosen such that

$$m_0 = \left(\frac{H_\sigma}{4}\right)^2 \tag{5.7}$$

With H_σ being close approximation to H_{m0} (strictly speaking $H_{m0} = 4.004\sqrt{m_0}$ (Goda, 2000)). Table 5-6 below shows the wave height and peak periods used for irregular wave testing. As was the case for the regular waves, wave height is determined by removing the buoy from the water and placing a resistance probe at the centreline location. Irregular wave runs were recorded for 256 s with a sampling rate of 32 Hz yielding 8192 data points for analysis. The sampling run would suggest that approximately 150-200 waves were used for each sea state depending on the peak period. This is less than the recommended amount that sampling theory suggests appropriate (approximately 1000 waves), however, due to the number of tests runs this would prove too prohibitive from a time perspective. For each of the tested sea states, the same sequence of waves used for each run. This was achieved by retaining the same random phase seed sent out to the wavemaker.

Table 5-6: Irregular wave characteristics

Requested		Generated	
Tp(s)	Hσ (m)	Tp(s)	Hσ (m)
1.20	0.060	1.23	0.068
1.40	0.060	1.52	0.071
1.60	0.060	1.55	0.071
1.80	0.060	1.67	0.071
1.60	0.100	1.55	0.113
1.80	0.100	1.78	0.119

Figure 5:47 shows the variance spectra of the different input sea-states. A 9-point moving average has been applied to the raw spectra in order to obtain smoother results.
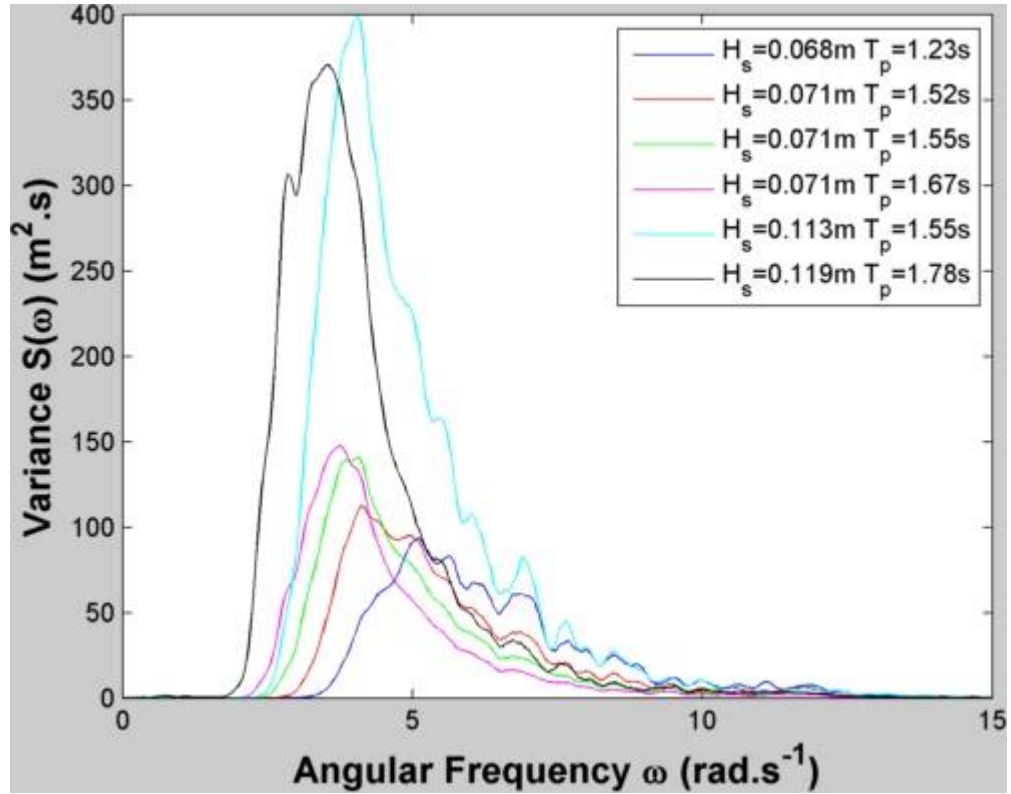

Figure 5:47: Variance spectra for Bretschneider input sea-states

Figure 5:48 shows the response of a cone-cylinder shape buoy with a draft of 185mm to an irregular wave of Hs 100mm and period 1.6 seconds. The applied damping force from the brake is 3.9 N (excluding the friction force). The supplementary mass for this test is 6.7 kg. The agreement between numerically and experimentally determined floater position is very good.
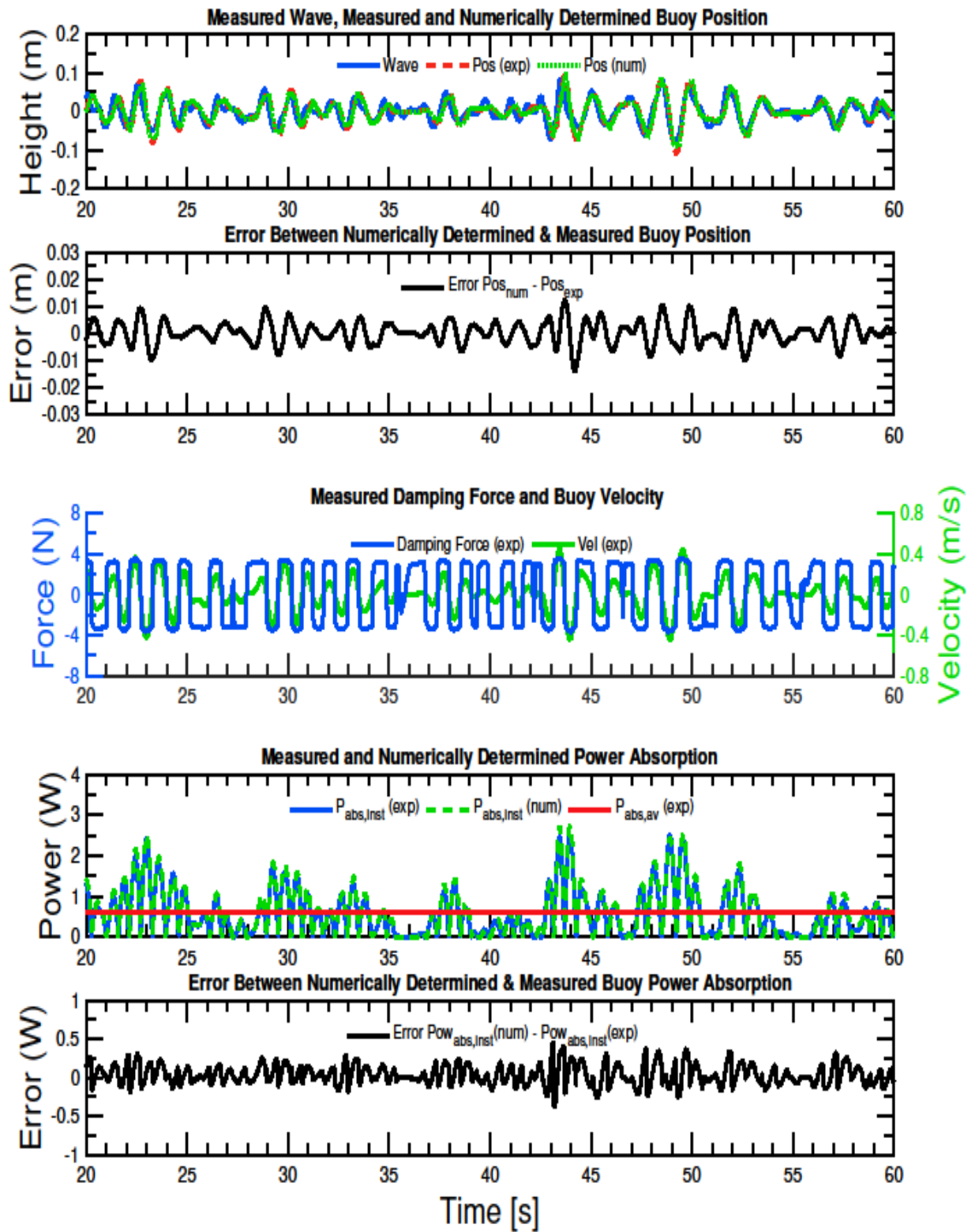
Figure 5:48: Experimentally and numerically determined data for cone-cylinder buoy, draft=185mm, M_sup=6.7kg, requested wave Hs=0.1m, Tp=1.6s.
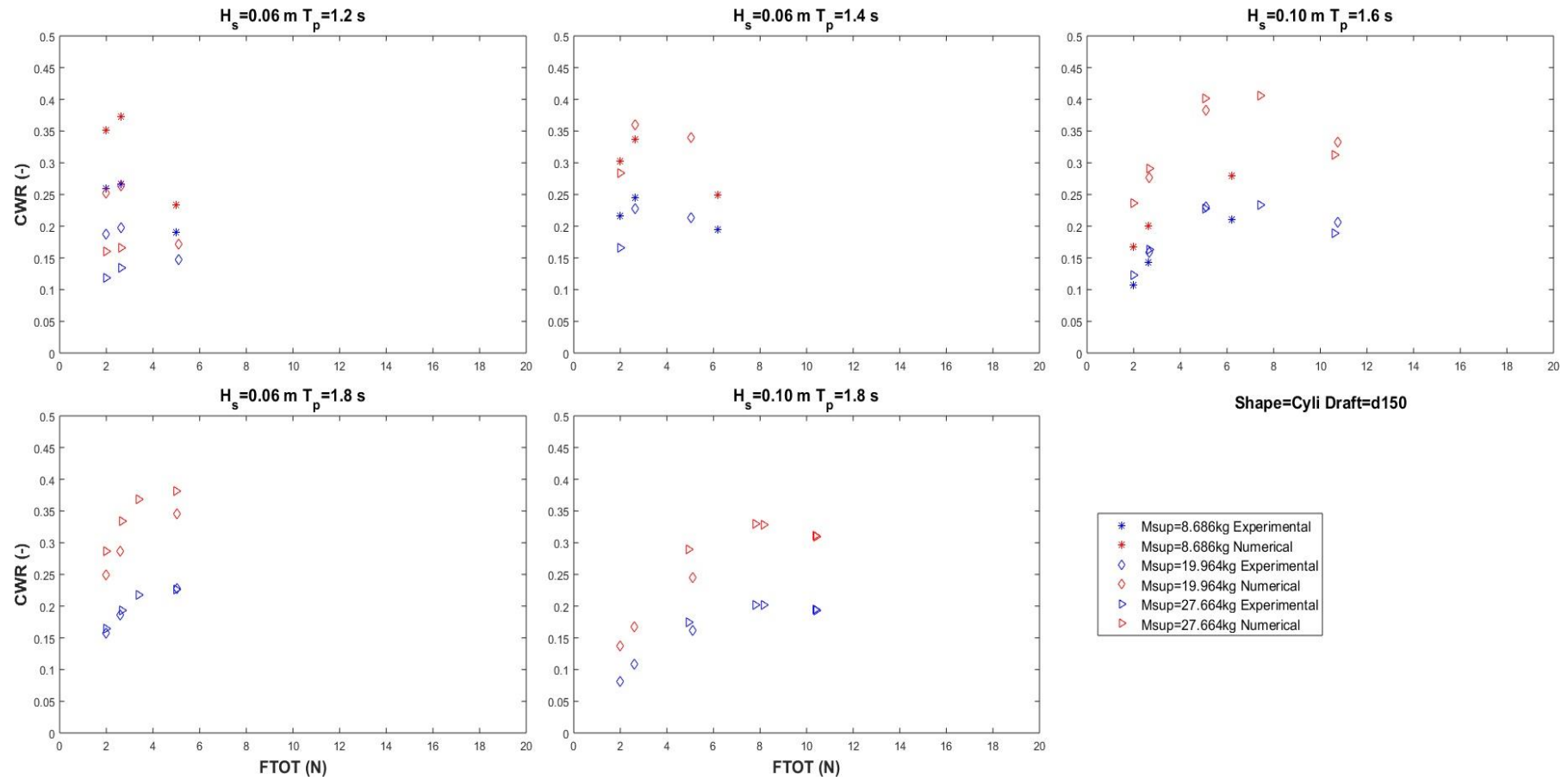
Figure 5:49: CWR vs damping force for constant sea state with varying supplementary mass. Cylinder shape, draft=150mm

208

Figure 5:49 plots summary results for Cylinder shape, of draft=150mm subjected to irregular waves. The plots show CWR vs damping for each sea-state with varying supplementary mass. The effect of increasing the damping force can be seen in most plots, with CWR rising to a maximum. The variation of additional mass from 8.7kg to 19.9kg and 27.6kg has different effects for different sea-states. For a peak period of 1.2 s it has a negative effect decreasing the CWR as the extra weight tunes the buoy towards higher periods. Increasing 8.9kg to 19.9kg results in a slight increase in CWR observed for the Tp=1.6s data set. However, a further increase to 27.6kg does not result in a significant increase in capture yield.

For a full scale device this last increase in inertia would constitute a significant waste of power put into the system, since the additional tuning force delivered by the PTO is not rewarded with increased energy yield. Adding energy in this 'blind' fashion –i.e., without regard for the time domain information of the incident wave- only tunes the buoy to a narrow range of frequencies. Tuning towards the peak frequency is clearly not the optimal control strategy, but it does demonstrate the potential for increased energy yield if a more advance control technique is adopted.

The agreement between numerically and experimentally determined results is better than for the regular wave tests. This can be attributed to an aggregation effect, as, for the majority of frequencies contained within the input spectrum, the buoy is away from resonance.

Additional irregular wave plots are given in Appendix B.2, while section 6.7 comments on accuracy of fit between numerical and physical results.

5.3 Comparison of numerical and physical results

In this section the experimental values of power absorption are compared with the numerically predicated values. Maximum experimental CWR quoted come from the summary results of the test plan laid out in Figure 5:33. That is to say results are given for certain total damping values only. If additional damping values were tested for each setup such, so as to effectively seek out the optimum each time; one would expect higher CWRs. Refer to section 6.3.3 for an optimisation study in regular waves for example. The purpose of this section is to observe general trends in power absorption between the different shapes and drafts and more so, to compare experimental results with those predicted from the linear model described in Chapter 4:.

5.3.1 Regular waves

Figure 5:50, Figure 5:51, Figure 5:52 show the summary results of the maximum CWRs achieved (both physically and numerically) as a function of T/Tn ratio for all configurations. The results presented are for regular waves and using a linear hydrostatic spring term in the numerical model. The highest experimental CWRs are observed for the cone shaped buoy with a maximum value of 0.77. The CWRs for the hemisphere are slightly smaller with a maximum of 0.69. The cylinder buoy exhibits the lowest CWRs with a maximum value of 0.54.

The rankings of most efficient shaped buoys are in accordance with the hydrodynamic parameters produced in section 4.2.1. The high efficiencies of the cone and hemisphere buoys arise from the fact that they have higher values of hydrodynamic damping over the frequency range of interest. This means that are capable of radiating larger waves to 'interfere' or 'destruct' the incident wave field, which is a necessary condition for larger power absorption.

Two different measures are taken to account for the difference between numerical and experimental results. The absolute error is given by

$$\varepsilon = |E - N| \qquad \textbf{(5.8)}$$

Where ε is the absolute error, E the experimental value under consideration and N the numerical value. The Relative Percentage Error (RPE) is given by

$$RPE = \frac{|E - N|}{E} x\ 100\% \qquad \textbf{(5.9)}$$

The RPE can be error prone if the experimental value is zero (or close to it), however this is not expected to be a problem with the comparison data chosen.

Summary error results are presented in Table 5-7 &

Table 5-8. The mean error for all ratios tested, as well as the error for regions inside and outside the resonance zone (arbitrarily picked as $\frac{T}{T_n} = 100 \pm 10$ %) are presented.
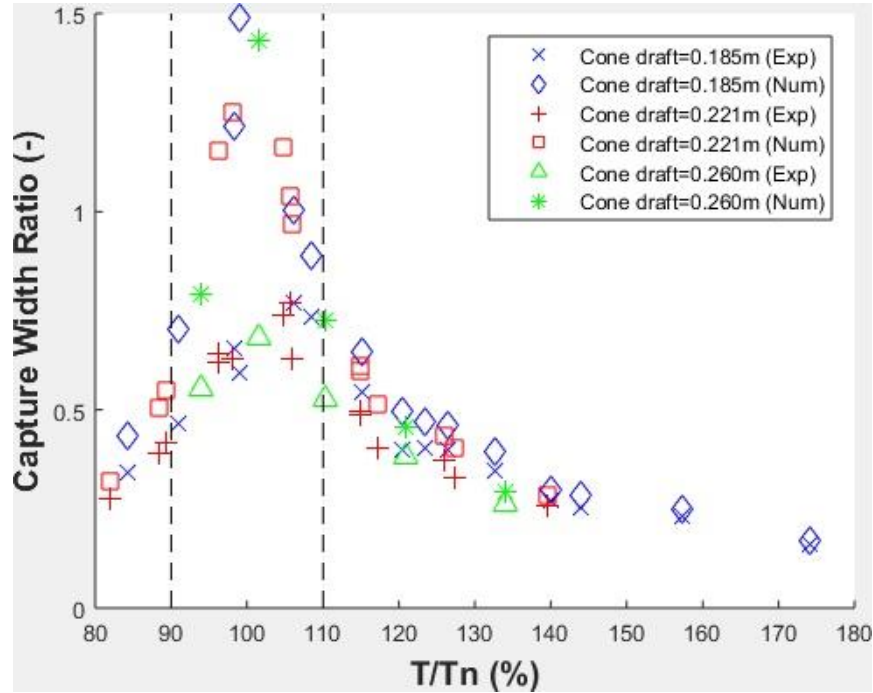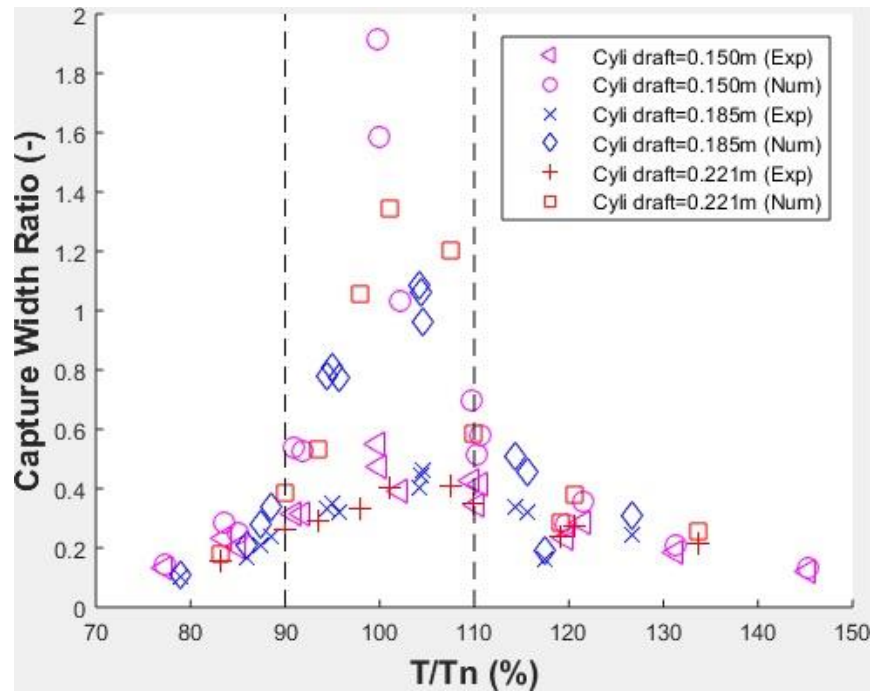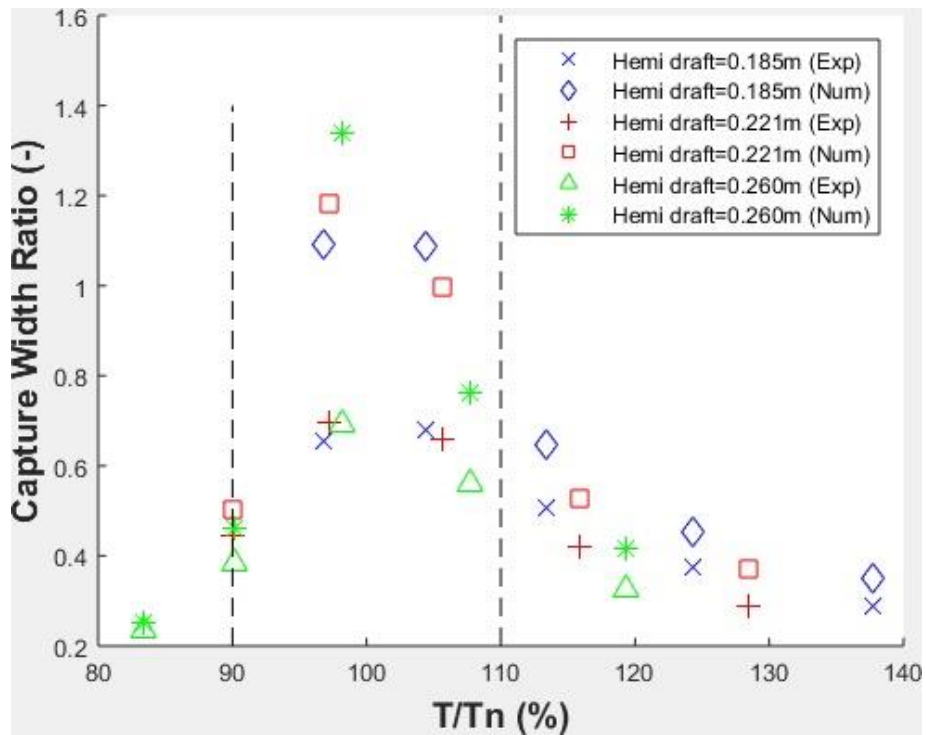

Figure 5:50: Comparison of maximum efficiencies achieved as a function of T/Tn ratio for the cone-cylinder shaped buoy.

The average absolute errors for the cone, hemisphere and cylinder are 16, 15 and 20 %, respectively. The first column of the table is the mean of all values. The second column focuses in on the region near resonance (a somewhat arbitrary value of $\pm 10\%$ of T_n was chosen). Finally the third column represents the region outside the resonance zone. The disparity between numerical and physical results is greatest for T/Tn ratios of 100 ± 10 %, with the level of error rising to 37, 25 and 41%, for the cone hemisphere and cylinder, rspectively. Away from resonance the correlation between methods is much better with an average difference of just over 4 % for each of the shapes tested.
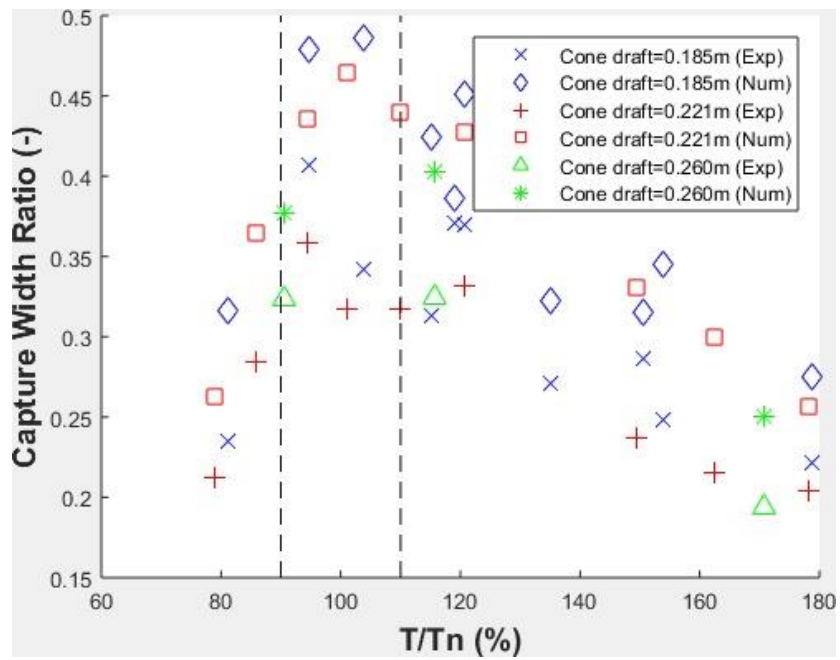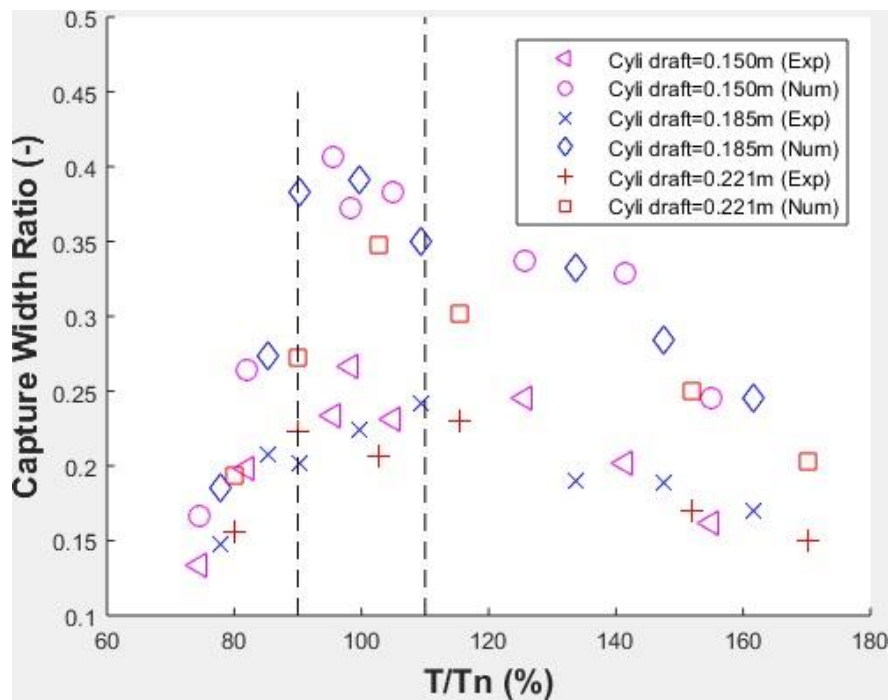
Figure 5:51: Comparison of maximum efficiencies achieved as a function of T/Tn ratio for the cylinder shaped buoy.

Figure 5:52: Comparison of maximum efficiencies achieved as a function of T/Tn ratio for the hemisphere-cylinder shaped buoy.

Table 5-7: Absolute error percentages for the different configurations in regular waves.

Cone	draft (m)	mean	+-10% of T_n	Outside
	0.185	13.8	35.0	3.1
	0.221	17.2	35.4	5.1
	0.26	19.4	41.2	4.8
Cylinder	0.15	20.9	46.7	3.7
	0.185	19.3	37.9	5.4
	0.221	20.9	38.4	3.4
Hemisphere	0.185	15.1	29.6	5.3
	0.221	15.1	21.3	5.6
	0.26	16.5	25.7	2.7

Table 5-8: RPE values for the different configurations in regular waves.

Cone	draft (m)	mean	+-10% of T_n	Outside
	0.185	39.0	93.6	11.7
	0.221	42.4	77.9	18.7
	0.26	40.8	81.7	13.6
Cylinder	0.15	68.1	142.2	18.8
	0.185	77.0	144.2	26.7
	0.221	80.5	141.6	19.4
Hemisphere	0.185	38.7	72.6	16.2
	0.221	56.9	80.1	22.0
	0.26	49.6	75.3	11.2

Table 5-8 tells a similar story with mean values of 40, 48 and 75 % for the cone hemisphere and cylinder, respectively. Outside of the resonance zone, these figures drop to 14, 16 and 21 respectively, which can be considered a reasonable trade-off between accuracy of results and ease of creation of the underlying numerical model. Close to resonance, the linear model is ill-suited to predicting the behaviour of the WEC in regular waves with RPE levels of 84, 76 and 142 % for the cone hemisphere and cylinder, respectively.

The large amplitude motions of the device when tuned towards resonance violate the underlying assumptions of linear theory. In experimental tests energy is lost to the fluid in the form of drag friction and vortex shedding, features which are not present in the numerical model. The cylinder shape buoy, having the roughest overall surface and edges, losses the most energy in this fashion.

5.3.2 Irregular waves

Figure 5:53 Figure 5:55 show the summary results of the maximum CWRs achieved as a function of T/Tn ratio for all configurations in irregular waves.

The highest experimental CWRs are observed for the cone shaped buoy with a maximum value of 0.4. The CWRs for the hemisphere are slightly smaller with a maximum of 0.36, while cylinder buoy exhibits the lowest CWRs with a maximum value of 0.26.

The average absolute errors for the cone, hemisphere and cylinder are 6, 8 and 6 %, respectively. There is less variation between average figures outside the 100% ±10% ratio.

Figure 5:53: Comparison of maximum efficiencies achieved as a function of T/Tn ratio for the cone-cylinder shaped buoy

Figure 5:54: Comparison of maximum efficiencies achieved as a function of T/Tn ratio for the cylinder shaped buoy
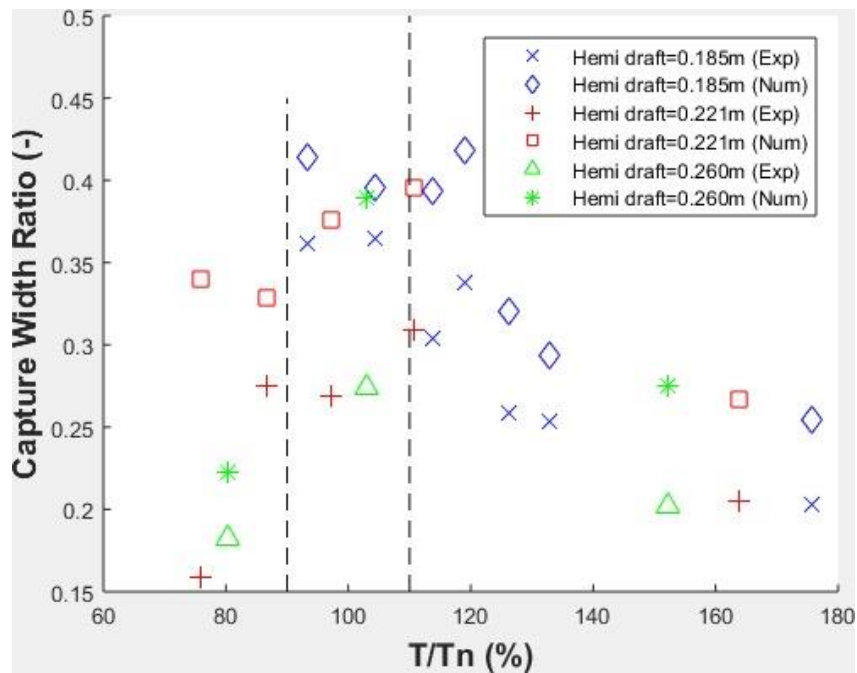
Figure 5:55: Comparison of maximum efficiencies achieved as a function of T/Tn ratio for the hemi-cylinder shaped buoy

Table 5-9: ABS error values for the different configurations in irregular waves

Cone	draft (m)	mean	+-10% of T_n	Outside
	0.185	5.9	9.1	5.1
	0.221	7.7	10.0	6.5
	0.26	4.8	3.5	5.4
Cylinder	0.15	8.5	11.1	7.0
	0.185	9.1	11.5	7.6
	0.221	6.3	11.0	5.4
Hemisphere	0.185	4.9	4.9	4.9
	0.221	7.8	9.8	7.3
	0.26	6.5	9.2	5.2

Table 5-10: RPE values for the different configurations in irregular waves

	draft (m)	mean	+-10% of T_n	Outside
	0.185	22.1	29.1	20.4
Cone	0.221	30.9	34.8	29.0
	0.26	20.1	11.8	24.3
Cylinder	0.15	47.4	56.0	42.3
	0.185	50.3	61.0	43.9
	0.221	38.0	61.5	33.3
Hemisphere	0.185	19.0	15.8	20.3
	0.221	41.8	37.7	42.8
	0.26	31.2	38.1	27.7

5.4 Chapter discussion

An observer may note the unlikelihood of such a system ever being implemented particularly when taking into account the Froude scaling effect of mass described earlier in this work. However the physical setup shown is the mechanical equivalent to the sub-optimal control method, constant coefficient reactive control.

Fc=McZ''(t)+Bcz'(t)+KcZ(t), where control spring Kc is not used but control inertia is a constant. When the controller force is written like this the vast amount of force required to tune the device becomes a little abstract. In fact when PTO efficiency is consider it is even worse.

Justifiable criticisms relating to impracticalities and inefficiencies, of such a physical system should also be aimed at the more abstract form of constant coefficient reactive control.

The linear theory based numerical model gives poor predictions when control forces are induced. Regular wave simulations are particularly poor with the model missing the

resonance frequency of the real cone/hemisphere device an interesting result. The linear numerical model is a hybrid containing the wave generating capabilities of a cone/ (hemisphere) and the spring stiffness of a cylinder. Results indicate that when control forces are involved with a buoy of varying surface profile, the (linear) natural frequency becomes somewhat of a poor metric. This is because the spring terms will vary with displacement. Added mass is also a frequency dependant parameter.

To achieve better results a more advanced nonlinear numerical model would be necessary. An interesting study by Giorgi & Ringwood, (2017) revealed that nonlinear forces show different relevance in heaving point absorbers (HPAs) and oscillating wave surge converter (OWSCs). Viscous drag effects in HPAs are small compared to the other forces, while they are significant in OWSCs. The most important hydrodynamic force in HPAs is the nonlinear FK force, while diffraction and radiation are relatively small. Moreover, the dynamic FK force is the main wave excitation mechanism in HPAs. Consequently, the relevance of nonlinear FK forces in HPAs appears to be considerably larger than the viscous drag force, since FK forces cover 81–96% of the total hydrodynamic force. Such percentages remain consistent for different wave heights and periods.

Viscous effects and vortex shedding would also need to be consider for a more complete numerical model. The large buoy motions, induced by the control forces would result in these effects taking place in the physical model, at the interface between buoy and fluid. The world is not linear, water is not dry and the actual hydrodynamics show little regard for ones simplifying assumptions.

Chapter 6: Control experiments

The following section describes measures undertaken to maximise the power output from the WECs. A description of the control method used to reliably vary the voltage signal to the brake is described. The initial purpose of this is to alter the intrinsic square wave damping force exhibited by the brake. Continually altering the resistance force at each time interval allows for a control force that is proportional to the velocity of the device (linear damping). The ability to actively change the damping in real time is a very useful feature of the PTO particularly for the relatively small scale of physical modelling described in this thesis.

As an attempt to illustrate the usefulness of such a feature; a procedure is described whereby the linear damping ratio is continually altered throughout an irregular wave run. Wavelet analysis of the incoming wave signal is used as input the controller, to search temporal variations in peak period. This method is in contrast with the far more common practice of selecting a single damping value for the entire wave run. This optimised constant damping value is also sought for the same setup.

6.1 Proportional Integral control of the brake

The resisting brake force for test results reported in chapter 6 was a square wave with constant amplitude whose sign is the same as the sign of velocity of the rotating shaft on which the brake is mounted. In order to achieve a braking force which changes in real time so that it is proportional to the velocity of the buoy such that.

$$F_{brake} = b_{brake}\dot{z}$$

(6.1)

It is necessary to implement some form of control on the braking force as the schematic below shows.
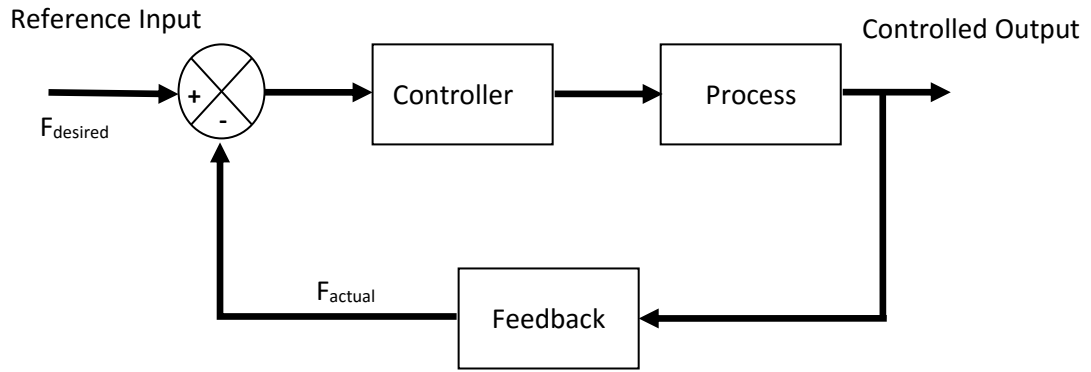
Figure 6:1: Control block diagram

At each time interval the desired braking force F_{des} can be obtained by multiplying the buoys velocity (measured by the encoder) with a user-defined damping coefficient b_{brake}. The controller can then utilise the error signal between the desired force and the actual force (measured by the torque sensor) to manipulate the voltage supplied to the brake so as to coerce the actual force supplied by the brake to the reference/desired force.

Common control methodologies include;

- Proportional (P)
- Proportional Integral (PI)
- Proportional Integral Derivative (PID)

The equation for a PID controller is

$$u(t) = K_p e(t) + K_i \int_0^t e(\tau)d\,\tau + K_d \frac{de}{dt} \qquad (6.2)$$

Where u(t) is commonly used in control theory for the controller output. the measured error between desired and actual value is e(t) and the different K terms represent constants as follows (Mude & Sahu, 2012)

Proportional (P) control uses only the proportional term K_p to control the system. This can cause problems, as, if the proportional gain is too high, the system can become unstable, In contrast, a small gain results in a small output response to a large input error, and a less

responsive or less sensitive controller. If the proportional gain is too low, the control action may be too small when responding to system disturbances.

PID control adds a derivative term, the derivative of the process error is calculated by determining the slope of the error over time and multiplying this rate of change by the derivative gain K_d. The magnitude of the contribution of the derivative term to the overall control action is termed the derivative gain, K_d. A problem with the derivative term is that it amplifies higher frequency measurement or process noise that can cause large amounts of change in the output.

The lack of derivative action may make the system more stable in the steady state when dealing with noisy data. This is because derivative action is more sensitive to higher-frequency terms in the inputs. Signal noise is a common feature of physical measurement devices. It was decided therefore to use a proportional integral (PI) controller to achieve this goal. PI controllers utilise the error signal e(t) between desired and actual signal such that the output of the controller u(t) is defined by

$$u(t) = K_p e(t) + K_i \int_0^t e(\tau) d\tau \qquad (6.3)$$

Where K_p is the proportional gain and K_i is the integral gain. The choice of tuning parameters K_p & K_i will affect the performance of the controller. The proportional term produces an output value that is proportional to the current error value. Having too a large gain value and the system can become unstable while if the gain is too low the response of the control can be insufficient. Additionally if a proportional term is used on its own (a proportional controller), then there will be an amount of steady state error or offset (since a non-zero error is required for the controller). This steady state error can be diminished by adding an integral term.

The integrand in the second term of equation (6.3) means that a record of the error, or how long and how far the measured variable has been from the reference point over time is considered. . The integral term accelerates the movement of the process towards the reference point and eliminates the residual steady-state error mentioned previously. As the integral term has a 'memory' of accumulated errors it can lead to overshoot of the reference value and also tends to increase the oscillatory nature of the process response.

Because the two tuning parameters interact with each other, it can be challenging to arrive at "best" tuning values. There are several tuning methods available, a common and effect one being the Ziegler-Nichols method.

6.1.1 Ziegler-Nichols method of controller tuning

The Ziegler-Nichols method of tuning a PI controller entails

- firstly using only the proportional gain (K_i is set to zero)
- finding the value of K_p such that the system is oscillatory {this gain setting is then denoted K_u the ultimate gain setting (see Figure 6:2)}
- The period of oscillation of the response is noted and termed P_u
- Now using the values obtained for K_u & P_u set the control parameters according to Table 6-1.
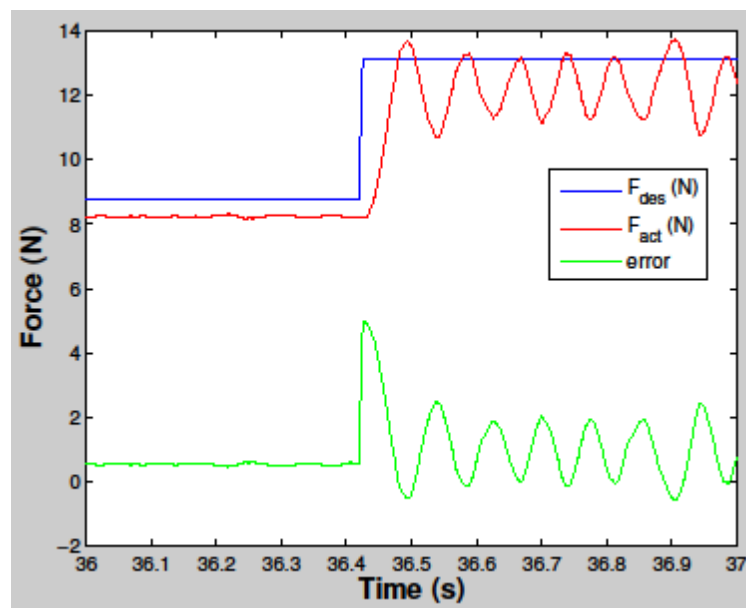
Figure 6:2: Closed loop step response Kp=16 Ki=0

Table 6-1: Ziegler-Nichols tuning recommendations

Controller Type	Kp	Ki	Kd
P	0.5Ku	-	-
PI	0.45Ku	1.2Kp/Pu	-
PID	0.6Ku	2Kp/Pu	KpPu/8

Thus the Ziegler-Nichols method of tuning first pushes the controller to the brink of stability and then chooses more stable proportional constants. Using this method the PI gain settings of $K_p=7.2$ and $K_i=115$ were chosen.

As a result of the controller tuning, the applied damping force is roughly linear -see Figure 6:3- as opposed to the square wave Coulomb damping previously. . One unavoidable feature of the brakes damping profile is that the applied damping force can never be completely zero. The reason for this is even when zero volts is sent to the brake there will exist a minimum residual force (approximately 1 N) due to frictional effects of the shaft turning in the housing. As a result of this there is a square wave portion in the force signal as the velocity approaches zero. It must be remembered also that the frictional force necessary to move the rollers and pulleys does not get accounted for in the force (torque) measured by the torque transducer. So even though the damping force from the brake can be said to be roughly linear, this force must be combined with the friction force (a sine wave built on top of a square wave) to yield the total damping force.
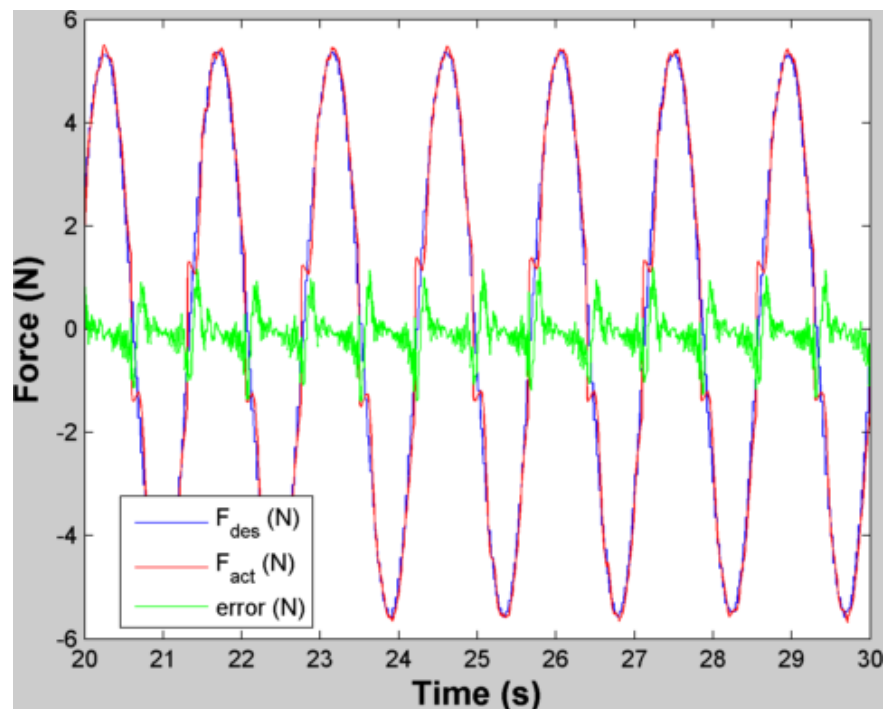
Figure 6:3: Linear damping force as a result of controller tuning

6.2 Latching

Attempts at applying the latching control technique devolved by (Lopes, Todalshaug, et al., 2009) are described in the following section. During preliminary tests it was found that the placid industries B6 brake had insufficient force capabilities to perform the task. At maximum voltage supplied to the brake, its maximum braking torque is 0.7 N which corresponds to approximately 32 N. Although this force was sufficient for the majority of heave excitation tests (requiring the buoy be held fixed as the waves traversed the buoy), since latching requires the buoy to be held at instances where the velocity vanishes; it was found that the maximum braking force was incapable of dealing with the large gravity/buoyancy forces associated with holding the buoy above/below the water.

A larger B15 brake was used which has a higher torque capacity of 1.7 N but a slightly slower response time was used for the latching experiments. At the moment the velocity vanishes the maximum voltage is sent to the brake in order to latch the buoy.

As for when to unlatch the buoy, the target is to obtain maximum oscillation velocity at the instant of maximum excitation force (Falnes & Lillebekken, 2003). Another strategy implemented by Lopes et al., (2009) is not to focus on phase-matching the peaks, but rather to ensure that the oscillator will always move in the direction of the excitation force when released ensuring power will always flow from the sea into the absorber (as long as the wave frequency is less than the natural frequency). This is achieved by releasing the oscillator at the instant when the excitation force changes direction (i.e. changes sign).

During the heave excitation tests, it was found that the force lagged the wave by a small amount (<10°) for the frequency range of interest. Therefore, as a rough estimate the excitation force was assumed to coincide with the wave height. A wave probe in line with the centre of the buoy was used to determine the release or unlatch moment (at the zero crossings of the wave elevation).
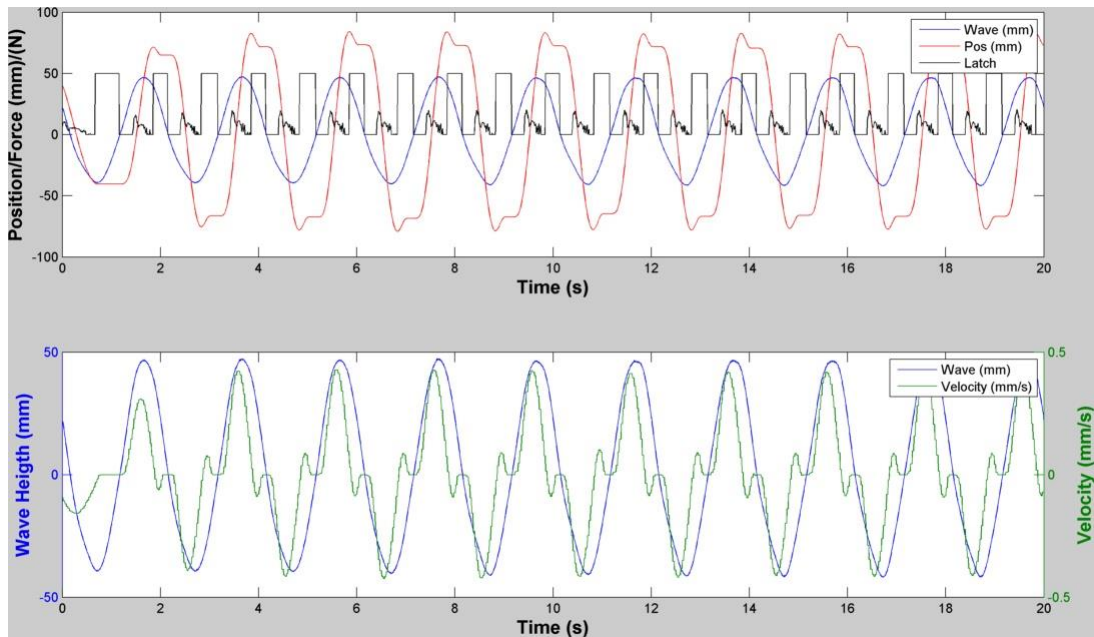
Figure 6:4: Latching of cylinder draft=100mm wave height=80mm wave period=2.0s

Figure 6:4 shows the results for an incident wave of 85 mm and period of 2 seconds. Some amplification of the buoys position is evident in the figure as, at the very beginning of the run the buoy position is just lagging the wave height with an approximate 1:1 height ratio, after the latching technique is applied the buoy displacement increases. The lower section of the figure plots the wave height and buoy velocity. The reason for the improvement in the RAO can be seen as the two signals are much closer in phase than initially. It is interesting to note that at the moment when the latch signal is sent out the buoy continues to slip, this phenomenon is looked at in finer detail in Figure 6:5 which looks at one cycle of the test with wave elevation and force plotted on the left hand axis and buoy velocity plotted on the right hand axis.

Observing Figure 6:5, it can be seen that the velocity vanishes when the buoy position is at a maximum (or minimum height). At such an instance the maximum voltage is sent out to the brake (marked with magenta x symbol). The brake cannot supply the maximum force instantaneously however, and the resisting force must ramp up at a steady rate (relating to the working physical process of the brake, i.e., the changing magnetic field causing the powder to cluster together increasing the frictional resistance of the brake), the braking force (N) is represented by the cyan line and is plotted on the left-hand x-axis. Since the required amount of force to maintain the buoys position is not being met, the buoy will continue to

225

slip until this is no longer the case. Once the requisite amount of force is supplied, the buoy will remain latched in a constant position.
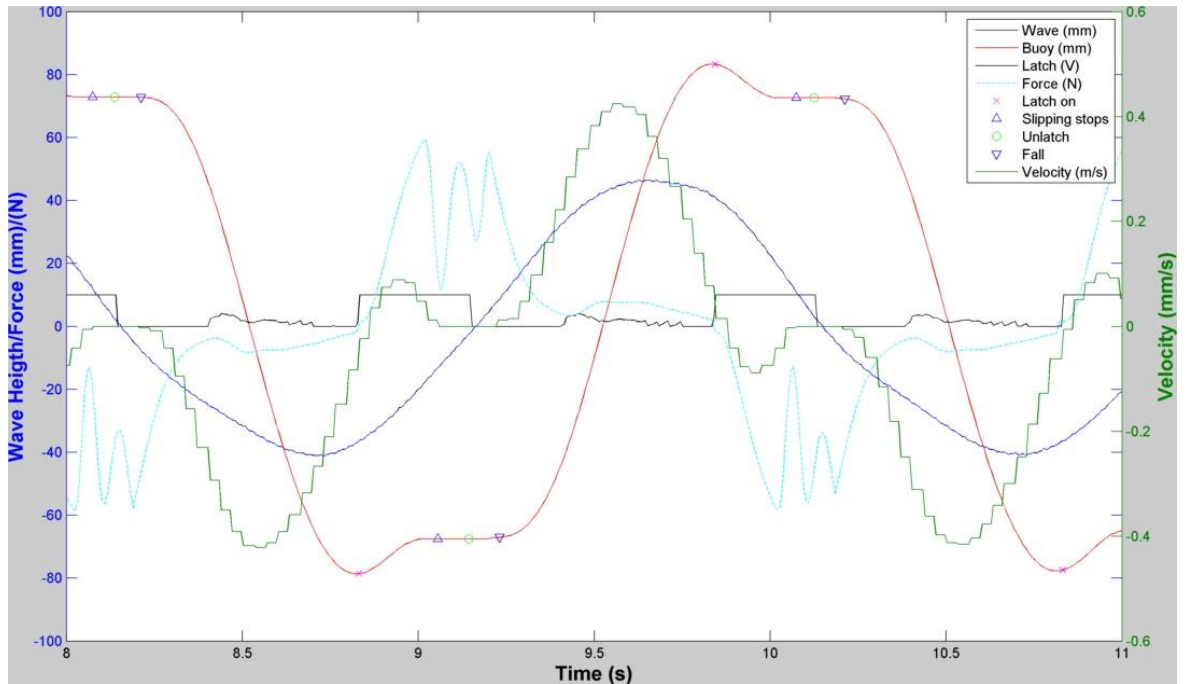
Figure 6:5: Close up of latching of cylinder d=100mm H=85mm T=2.0s

Examining the force signal during the period when the buoy remains latched it is clear than some transient oscillatory behaviour is present. The reason for this is that when latching, the buoy position is at a maximum, the velocity is (ideally) zero and hence the normal resisting force will be approximately zero. However the acceleration will be non-zero (actually at maximum value of opposite sign to the position). As a result of applying the maximum braking, the force will go through a transient process, oscillating (at a period relating to the inherent stiffness of the system) about a value required to hold the buoy in position (ignoring the variation in exciting force and radiation force).

During the latched part of the cycle, the force signal behaves like a free oscillator as is evident in Figure 6:6, where the buoy remains latched for more than one wave cycle. Observing the force, the transient effects associated with a free oscillator are clearly visible during moments of latching. The transient effects remain for approximately one quarter of a cycle after which time the signal takes on the steady state form associated with a forced oscillator. Note also the proximity in phase between wave elevation and wave force signal.
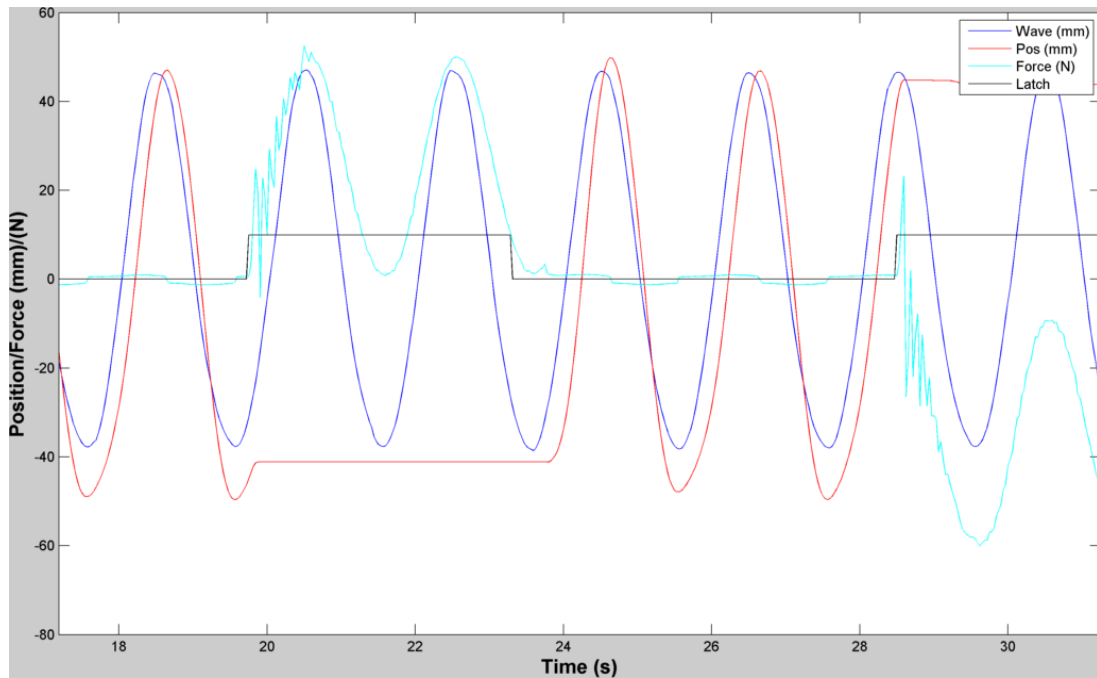
Figure 6:6: Transient effect in torque signal

In latching experiments using OWC's this transient behaviour is observable in the pressure signal as a result of sudden valve closure (the oscillations an effect of air elasticity). During the latched part of the cycle, the inner free surface of the water column will tend to behave as a free oscillator about an initial position (Lopes, Todalshaug, et al., 2009).

Returning to Figure 6:5 it can be seen that the moment of unlatching occurs when the wave elevation changes sign. Once again, however, there is a process delay between the signal of unlatching and the time when the buoy actually begins to fall. This delay is due to the time it takes for the brake to release and also the amount of inherent stiction the buoy must overcome. As a result of the delay time necessary for the buoy to fall, a similar delay factor had to be introduced to the Labview VI to prevent successive moments of unlatching and re-latching (since the condition for latching is zero velocity which is the case for a period of time after unlatching).

In order to address the slipping of the buoy at the moment of latching, it is necessary to begin the braking process at an advanced instance of time. A consequence of this, however, is that applied resistance during the power capture phase of the cycle is much larger than would normally be the case. This, in turn, affects the motion of the buoy, reducing the RAO

227

significantly (due to excessive damping). Figure 6:7 is an example of applying the braking earlier in the cycle for the same regular wave of height 85 mm and 2 s period.
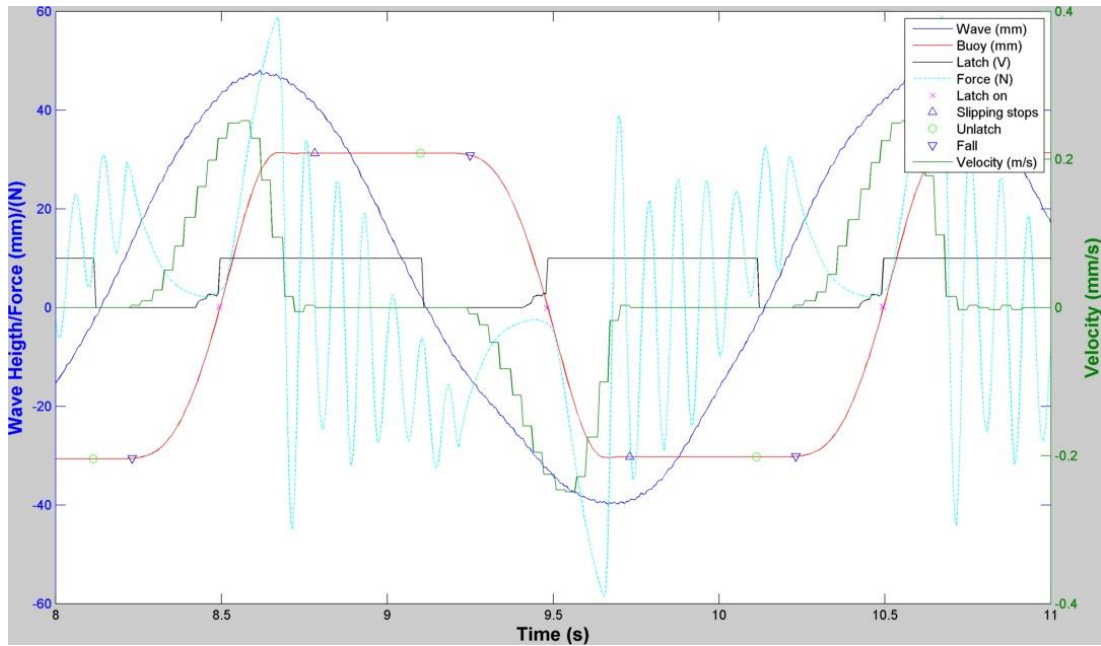
Figure 6:7: Latching earlier in the cycle. H=85mm T=2s

In order to eradicate the slipping, the braking process must begin much earlier than the ideal instance, when the velocity is zero. In fact in Figure 6:7 the braking is applied at the instance when the velocity is at a maximum. As a result of this excessive damping during the power capturing period of the latching cycle the motion of the buoy is reduced along with the capture efficiency.

A series of tests were carried out in regular waves; varying parameters were wave height, wave period and the instance in the cycle when the braking was applied. Initially the intention was to use the velocity signal to predict the future instance when the velocity would vanish, and then use this time as a variable of when to apply braking. However due to the poor quality quantisation effect of the velocity signal, this proved difficult so instead an absolute velocity threshold (termed velocity trigger) was used whereby braking would begin once the velocity slowed to a user defined amount.
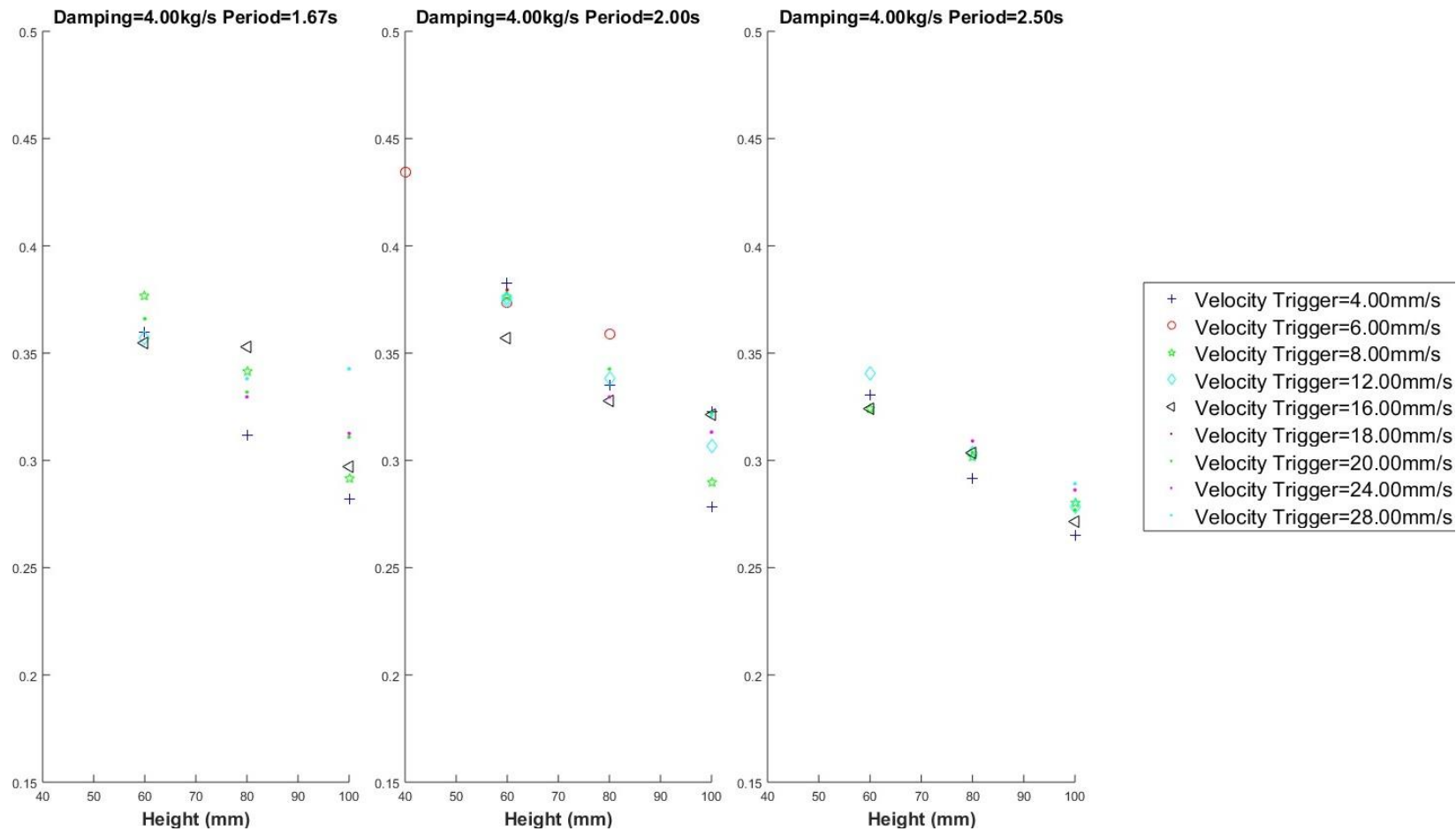
Figure 6:8: Efficiency Vs height for a constant period. Varying velocity triggers.
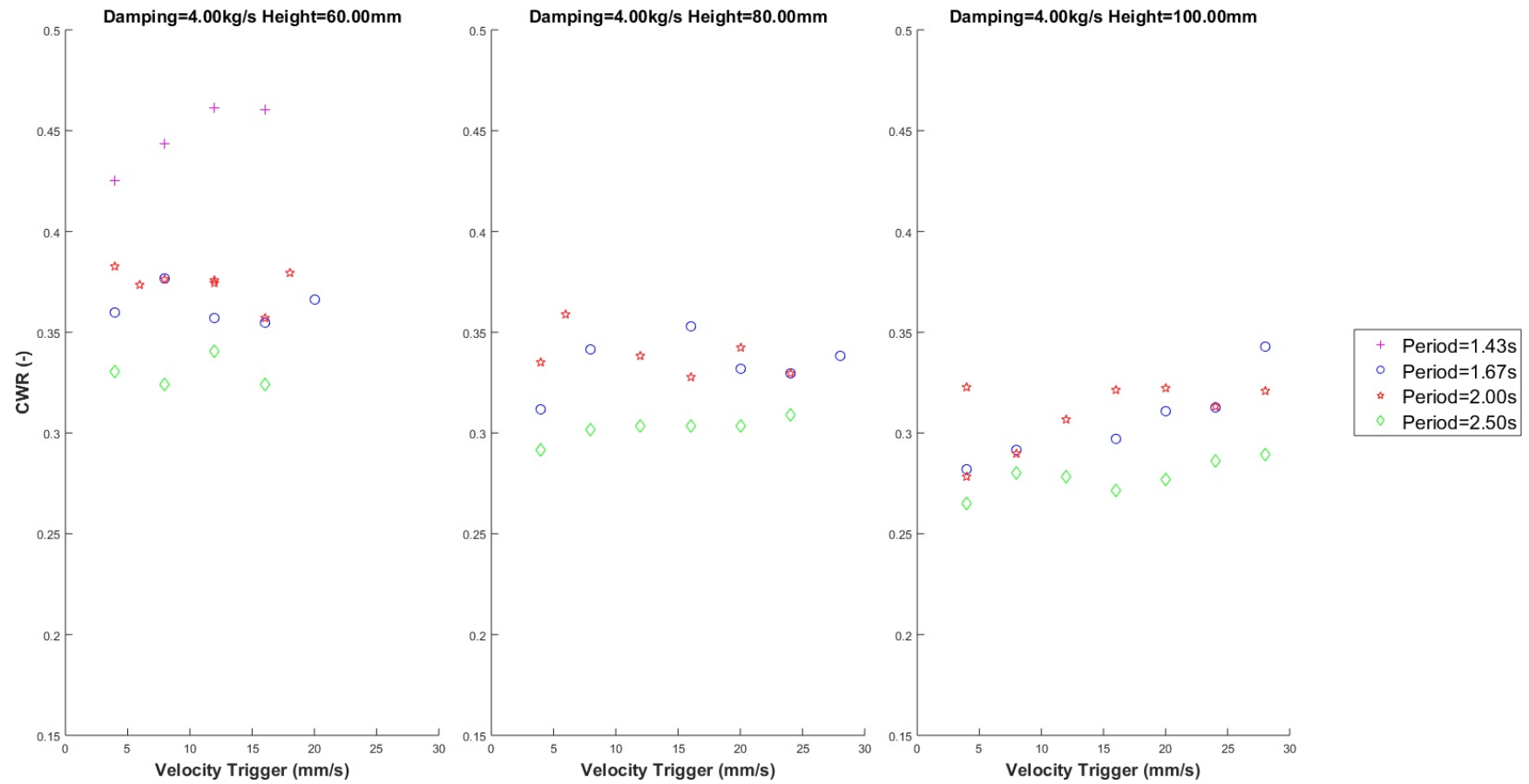
Figure 6:9: : Power Absorption Efficiency Vs Velocity Trigger for different wave heights (60mm left 80mm centre and 100mm right) and periods

230
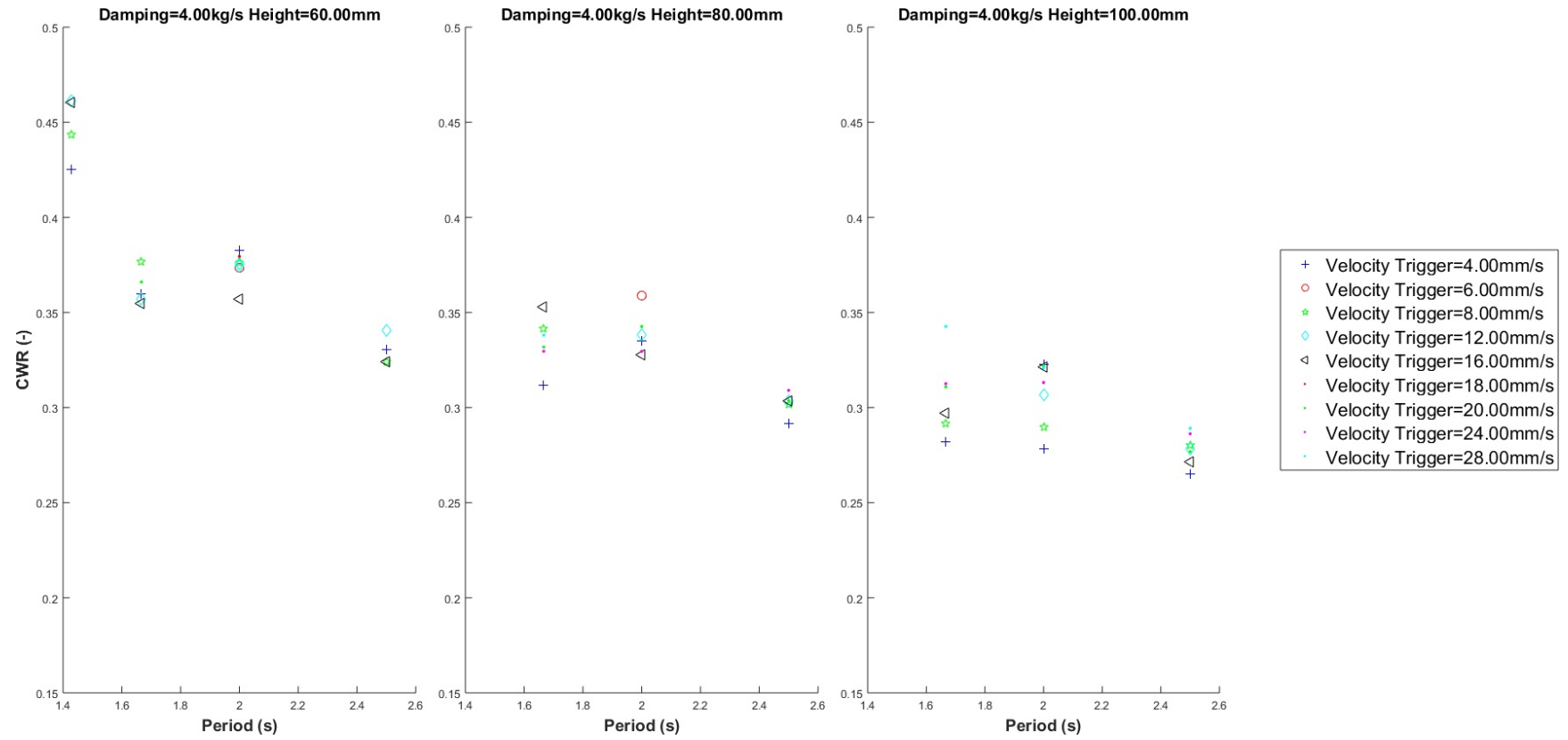
Figure 6:10: Power Absorption Efficiency Vs Wave Period for different wave heights and velocity triggers.
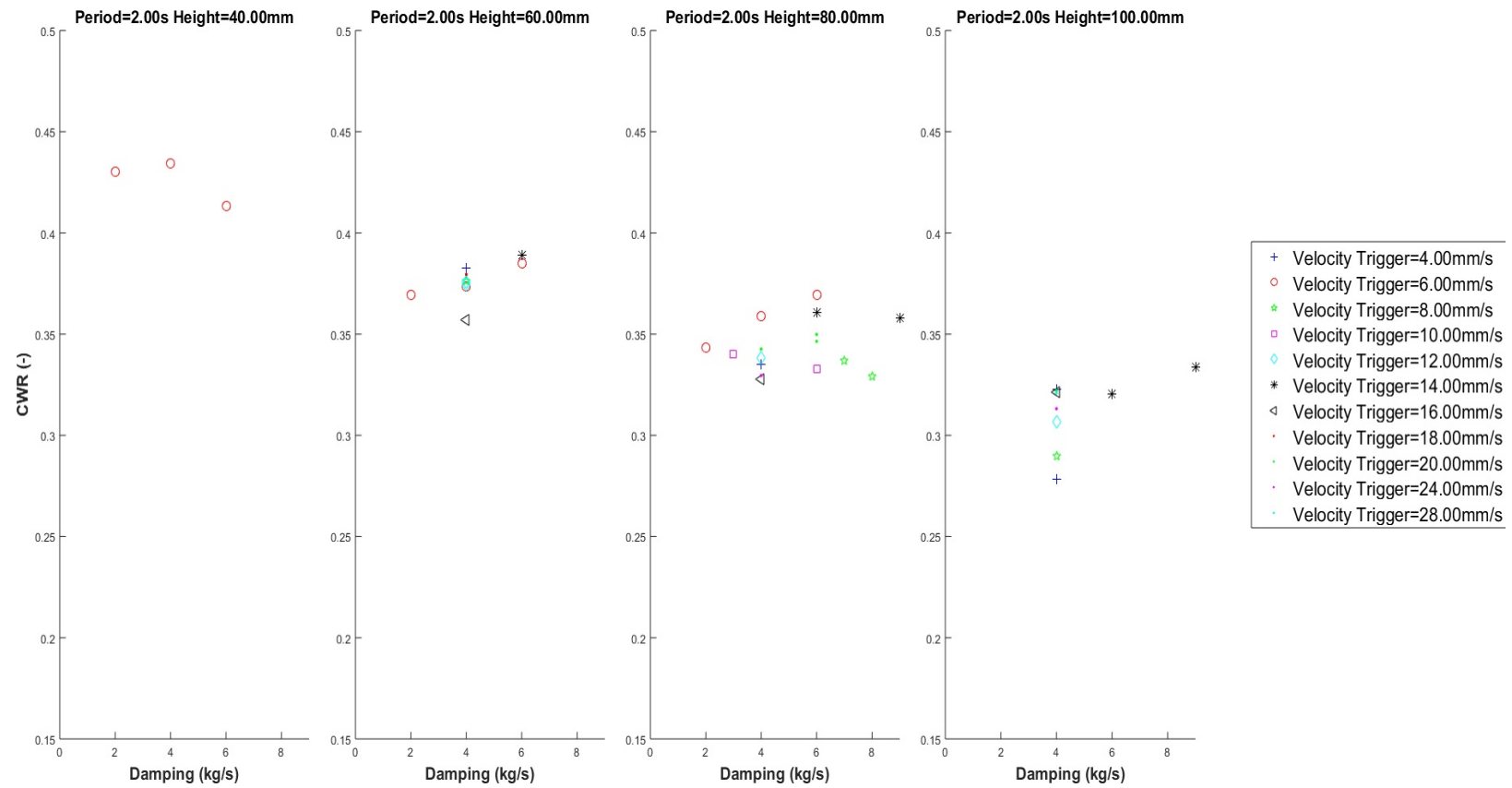
Figure 6:11: Efficiency Vs damping coefficient for wave period= 2 s.

Figure 6:8 graphs the power capture efficiency versus wave height for a constant wave period. It is clear that for all periods tested there is a linear inverse relationship between efficiency and wave height, with the smaller wave height tests exhibiting a higher efficiency than the larger wave heights. This is as expected due to the fact that the lower wave heights will require a smaller 'latching' force. As the required force decreases so too does the response time it takes for the frictional brake to attain this force. i.e. the frictional brake will better approach an ideal latch mechanism as the force decreases.

Figure 6:9 graphs the power capture efficiency versus velocity trigger for a constant wave height and different wave periods. The purpose of latching the buoy at an earlier instant in time is to prevent the buoy slipping, thereby leading to a greater travel distance between successive maxima/minima. This tactic is most successful for the H=60mm, T=1.43s wave (magenta line left hand plot). The slightly increased RAO, as a result of earlier braking, results in slightly increased capture. In general, the effect of earlier braking is marginal with the exception of the 100mm wave heights (right hand plot) which exhibit a trend of slightly higher efficiencies with increased velocity threshold. If the braking is initiated while the velocity is still ascending -as is the case with Figure 6:7- then both RAO and efficiency are affected negatively.

Figure 6:10 shows the power capture efficiency versus wave period for a constant wave height. It can be seen that there is a drop off in efficiency as the period increases. This is most likely due to insufficient damping for the larger periods. Figure 6:11 shows the influence of damping coefficient on power absorption efficiency for the 2-second wave period.

The damping coefficient for the previous tests was 4 kg/s, which is close to optimum for the lower wave height of 40 mm, however, Figure 6:11 indicates that a slightly higher efficiency could be obtained by increasing the damping as the wave height increases. Note that the damping coefficient is only applied during the intervals between unlatching and re-latching. During the period of latching or 'heavy braking', the maximum resistance is applied, resulting in the damping over the whole cycle being non-linear. Additionally, the power generated during the 'heavy braking' phase is included in the capture efficiency, if this heavy braking were applied by a separate mechanism other than the regular PTO, then capture efficiency would be even worse, (i.e., if the power from this phase were not included in the energy yield).

Overall, the efficiency results of the regular wave latching experiments can be considered poor, failing to reap the ideal benefits of such a strategy. The reason for this is that in the experiments carried out the PTO strategy was not 'latching' but rather 'heavy braking'. The process time of the brake makes it unsuitable to apply the latching strategy resulting in poor power performance. A latch has to be operated very rapidly to reduce the time for which partly engaged brake pads are slipping with a large force. This difficulty would vanish immediately if the power take-off used a ram feeding appropriate hydraulics. Friction brakes would be even worse for slowing a wave device already in motion (Salter, Taylor, & Caldwell, 2002).

Latching and reactive control and are both control strategies which are interesting to understand and observe in practical application. However, while they can be readily applied in a laboratory environment; full scale application in a real sea environment with realistic machinery and equipment is extremely difficult. Therefore even though one could assume a priori that the brake would be a poor mechanism to apply the latching technique. The reasons for failure, i.e. the requirement of extremely large forces instantaneously is applicable to full scale devices and should serve as a warning as to the feasibility of latching itself.

Similar comments relating to a strategy that can be applied in a lab but not in reality apply to complex conjugate control which is the focus of Prices thesis (2009). Although the PTO mechanism used here is not suitable to investigate such a strategy due to the inability to add energy to the system. This strategy faces a couple of problems; firstly for the strategy to work it is necessary to have future knowledge of the incoming waves (graphically depicted appropriately by a crystal ball in Prices work). Realistic displacement constraints are another limiting factor, as the control strategy may require motions larger than what is permissible by the machinery of the device. PTO efficiency is also a major sticking point for as it acts as a double tax; affecting not only the power absorption phase but more crucially the reactive power phase (see Genest et al (2014) for example). Parts of the wave cycle that require power to be supplied to the system will mean the PTO will have to draw additional power than the desired amount due to PTO inefficiencies. Will these efficiencies be the same

for both the resistive and reactive parts or will the reactive part have a lower efficiency? A useful analogy of bi-directional power flow, is that it's like pushing a shopping trolling; relatively easy to push but very difficult to pull. These are all crucial obstacles to the successful implementation of this control method.

Additionally in the authors opinion it's worthwhile to highlight the good as well as the bad features of the brake. Despite a certain reticence to using proverbs in scientific work, the quote "Look at what you've got and make the best of it. It is better to light a candle than to curse the darkness" seems appropriate.

The results of these tests while revealing disappointing performance should ward off any future researchers from heading down what is a research cul de sac.

6.3 Real time variation of damping

An experimental investigation into varying the damping coefficient from the brake in real time in order to maximise the power capture for a particular buoy set-up was carried out. The hemisphere-cylinder buoy with draft of 221 mm was chosen for the tests. The supplementary mass was 9.4kg. Due to time constraints only the hemisphere shape was used for the experiments.

6.3.1 Constant damping coefficient

Before ascertaining whether varying the damping mid experiment would increase power capture it was necessary to determine the maximum power capture achievable using a constant damping coefficient.

Figure 6:12 shows the average power capture calculated with and without the contribution of friction for several different damping coefficients. The maximum power achieved is 0.8 W for an applied damping value of 35 kg/s. This power capture was be used as a benchmark to determine if any improvement could be achieved. By contrasting the power capture calculated with and without the influence of friction, the non-linear dynamics of the scenario are apparent. The contribution of 'friction power' is greater at lower damping values since the associated buoy velocities are greater. This phenomenon creates a disparity between the peak of measured power (no friction) and actual power (with friction).
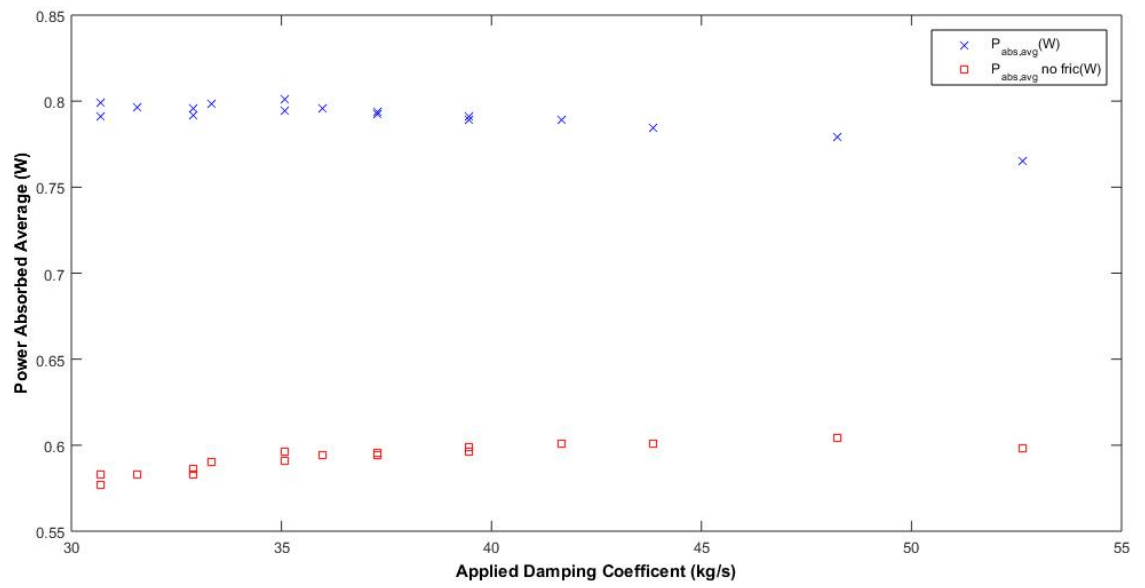
Figure 6:12: Average power absorption (W) Vs applied damping coefficient (kg/s).
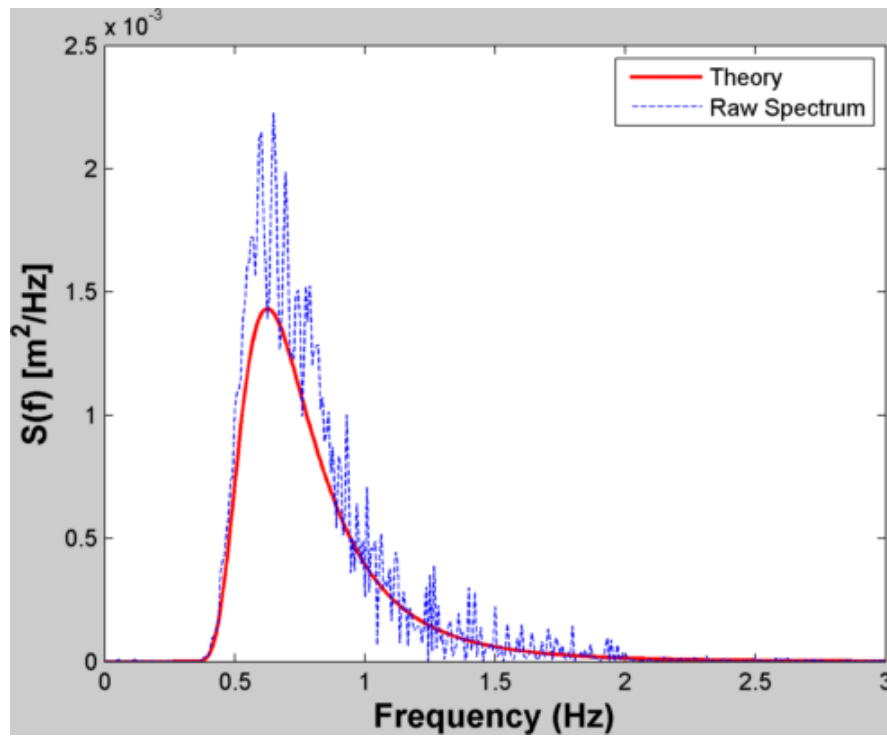
Figure 6:13: Theoretical and experimental Bretschneider spectrum Hs=0.1m, Tp=1.6s.

The input wave conditions for all tests was an irregular Bretschneider sea state H_s = 0.1 m, T_p = 1.6 s as shown in Figure 6:13. The repeat time for the wave record was shorter at 128 s as opposed to 256 s used in previous tests.

The trouble with setting a damping coefficient based on a spectral statistic, such as peak period T_p, is that temporal changes in the wave height record are concealed. In a study on the suitability of using wind wave frequency spectra (P. C. Liu, 2000), the author states that wave frequency spectrum simply cannot provide spectral information on actions occurring at any specific time of interest within the time series.

If a spectrum is broad-banded or exhibits a certain degree of groupiness (wave groups occurring over relatively short time scales) then certain events which may warrant a change in resistive damping, to maximize power capture, may be missed.

6.3.2 Wavelet Analysis

One method of examining the temporal changes in the wave envelope is to apply a wavelet analysis on the incoming wave profile to examine changes in T_p over time.
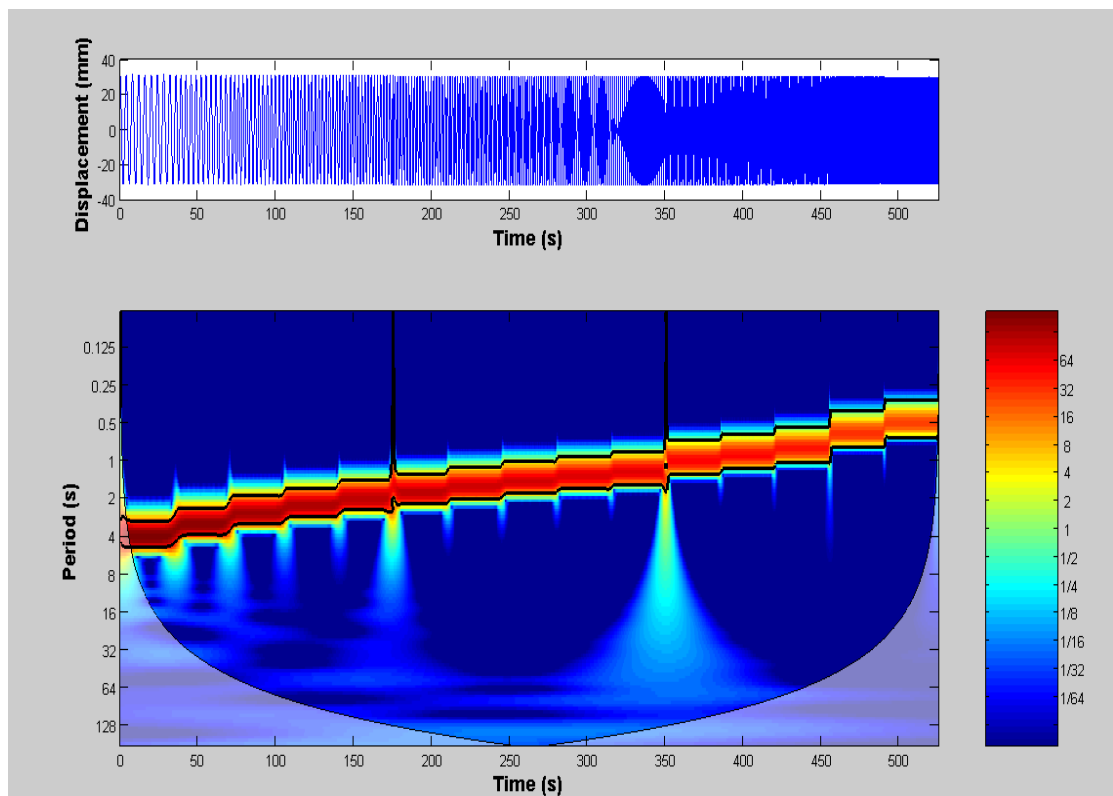
Figure 6:14: Wavelet power spectrum of buoy displacement during impedance test

237

An example of a wavelet transform is shown in Figure 6:14. The displacement of the linear rig (upper plot) during the previous impedance tests is used for analysis. The displacement signal above is called a chirp signal. A chirp is a signal in which the frequency increases (up-chirp) or decreases (down-chirp) with time. In the forced oscillation tests, the device was driven at a one frequency for a certain length of time before moving up to next frequency, and so on. The transition in period from 4 s to 0.5 s is clearly visible in the wavelet plot (lower plot). Only five frequencies were tested per record, to minimise wave reflections off the side walls .The reason for the two discontinuities at 175 s and 350 s is that the displacement time series is actually three separate forced oscillation tests spliced together. This signal shows the usefulness of wavelet analysis in determining temporal shifts in the frequency composition of a signal. If the signal in Figure 6:14 was a wave elevation time series (although a heavily contrived scenario), then one can appreciate, that the temporal information is far superior to a wave energy spectrum, in this case.
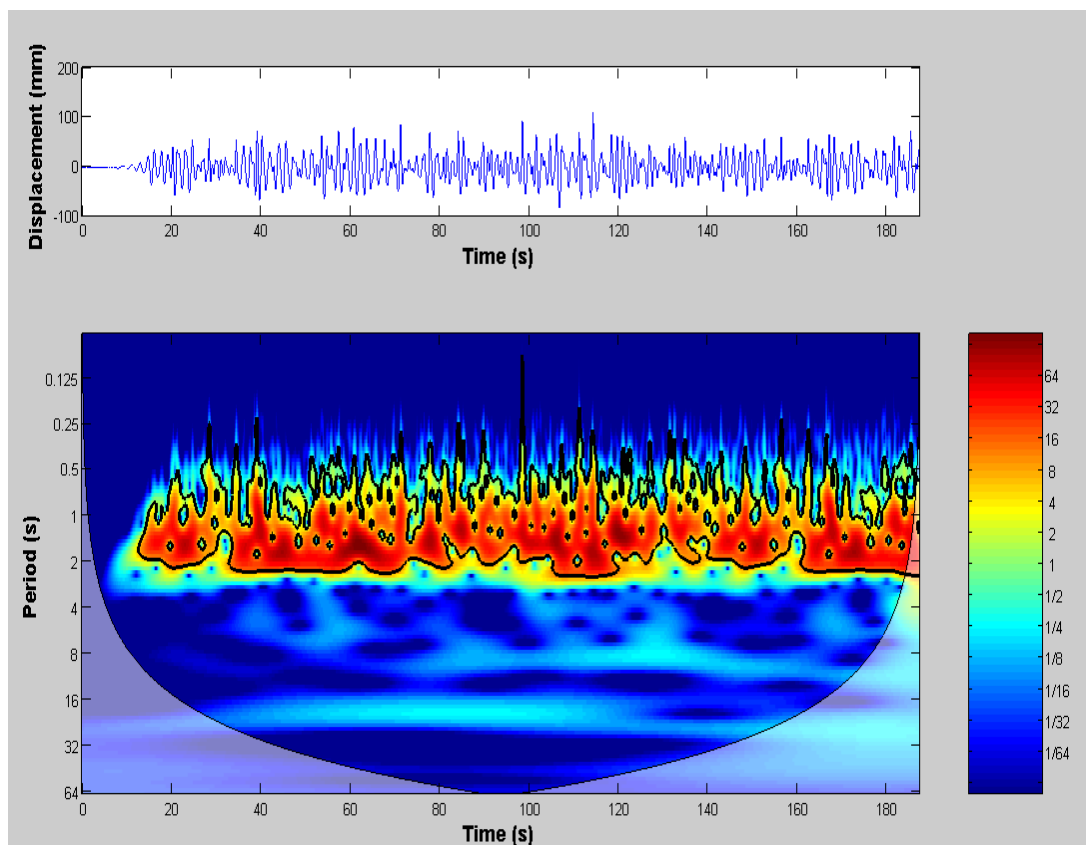
Figure 6:15: Wavelet power spectrum of input Bretschneider spectrum Hs=0.1m, Tp=1.6s

Figure 6:15 shows the incoming wave profile of the Bretschneider sea state Hs = 0.1 m, Tp = 1.6s (upper plot) and the corresponding wavelet transform in the lower plot. The wave elevation record was obtained by removing the buoy from the water and placing a wave probe at the centre of the buoy location. The variance spectrum in Figure 6:13 was obtained from the time series above.

The repeat time of the wave time series is 128 s. The wave record above is 187.5 s in duration which encapsulates the initial build up time for the wave to reach the wave probe (the wavelet plot shows almost no energy during this phase) as well as some time after the wave record has been completed. The wave envelope pattern can be seen to repeat itself in both the elevation record and the wavelet graph which illustrates the good repeatability of the wave basin.

6.3.3 Optimised damping in regular waves

In order to determine the optimum damping value for each frequency, a series of regular wave tests were carried out. A total of 28 different frequencies, ranging from 0.8 s to 2.46 s were tested. For each frequency tested, a number of different damping coefficients were trialed. Due to the large volume of tests carried out, the duration of each test was a relatively short at 18.75 s. The requested wave height was 80 mm for each frequency. The generated wave height varied but as the objective of the tests was to find an optimum damping value, the variation in wave height was not a major concern so long as it was accounted for in terms of efficiency.

Figure 6:16 plots the results of the regular wave optimization tests for the hemisphere-cylinder of draft 221 mm. The graph shows power absorption efficiency as a function of wave frequency (Hz) and applied damping coefficient (kg/s). For each individual frequency tested, as the damping is increased from zero the efficiency will rise to a maximum point. Further increases in damping however will result in the buoy being over-damped and the efficiency will drop as a consequence. The overall cumulative effect of the individual frequency tests is that the graph resembles a hill with its peak located at the natural frequency of the buoy and with the optimum applied damping value. A peak value of 108 % efficiency occurs for a frequency of 0.847 Hz (1.18 s). An efficiency value greater than 100% is an indication of the point absorber effect described in chapter 2.
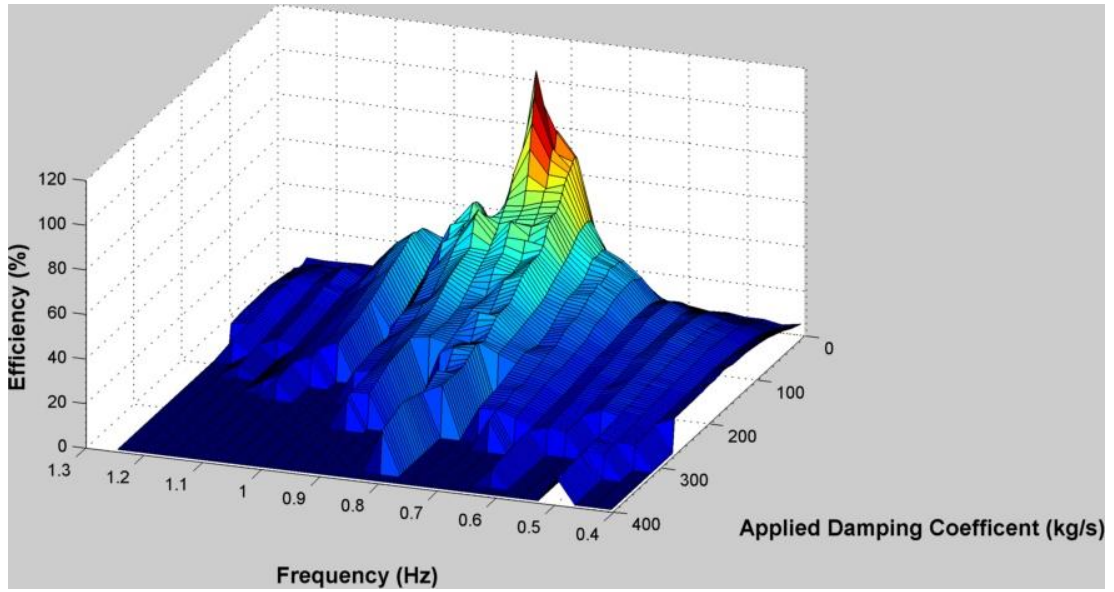
Figure 6:16: Power absorption efficiency as a function of wave frequency (Hz) and applied damping coefficient (kg/s)
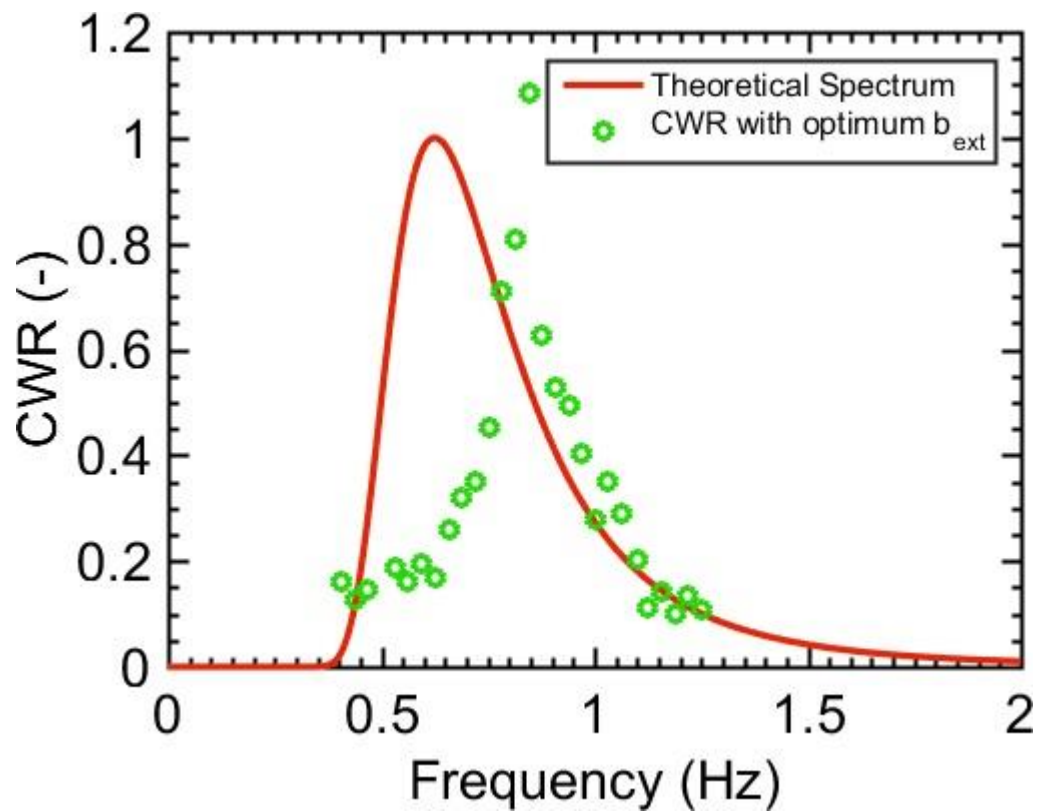
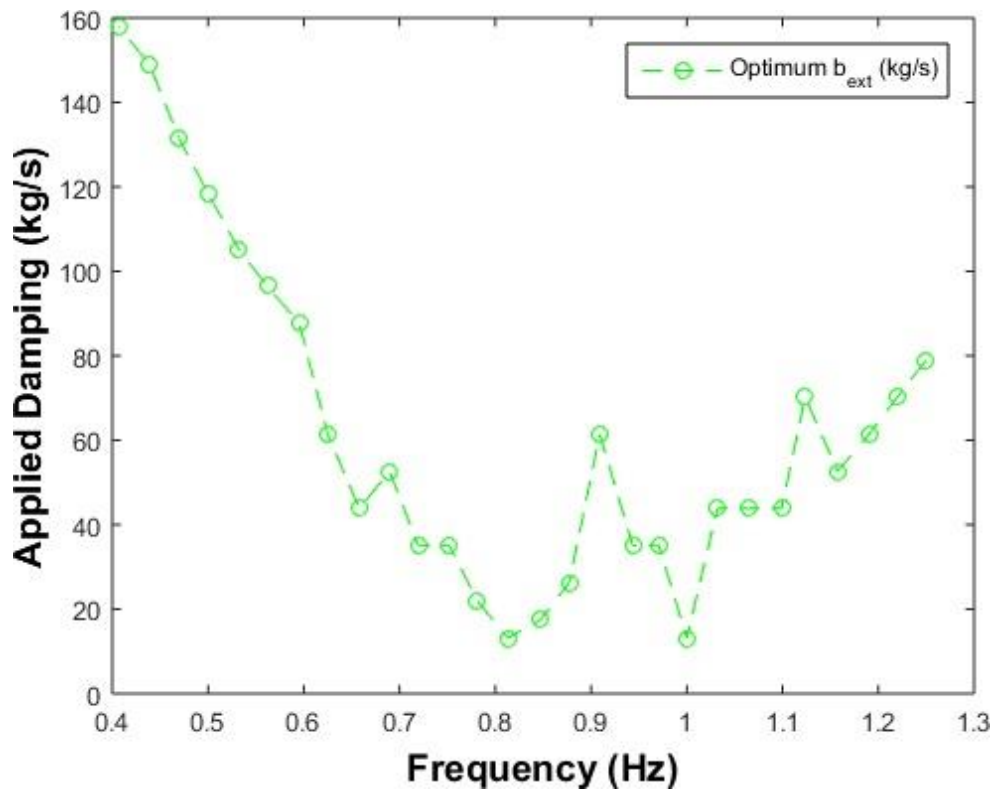**Figure 6:17: CWR curve using the optimised damping value at each frequency. Hemisphere-cylinder buoy draft=221mm, Msup=9.4kg. Requested wave height was 80mm.**

Figure 6:17 shows the capture width ratio values achieved when the optimised damping value is selected at each frequency. The CWR curve has a relatively narrow peak with dropping off either side of the peak frequency. The theoretical input spectrum used in the irregular tests (H_s=0.1m T_p=1.6s) is included here merely for comparison purposes. The spectrum is scaled to fit the CWR axis such that the peak energy density value is unity.

 Clearly, there is a disparity between the peak in CWR and the peak in the input spectrum, with the majority of the delivered power being below the peak experimental frequency. However, although the efficiency of this device set-up may be poor for long period waves, since the longer period waves are associated with more energy, meaning the total absorbed power (which is the overall objective) could potentially increase if these waves were targeted.

The disparity between spectral peaks indicates that, this buoy set up is not optimal for the incoming wave conditions. Improvement in performance would be expected if additional supplementary mass were added, shifting the peak efficiency to coincide with peak frequency of the wave. The hypothetical scenario being studied assumes however, that no more mass can be added. The reasons for this could be ascribed to a constraint on the amount of force which can be applied. The aim therefore is to achieve addition absorption through real time alteration of the damping force alone. The wavelet analysis will seek to isolate moments during the wave run, when the damping value could be changed. Ideally then, one could achieve higher absorption levels, compared to the scenario of using a constant damping value for the entire test run. Garcia-rosa et al (2017) describe a similar real-time passive control based approach using the Hilbert-Huang transform (HHT). The work is done using a numerical model whereby PTO damping is time-varying and tuned to the instantaneous frequency of the wave excitation force. The instantaneous frequency is calculated by using the HHT, an analysis method for nonlinear and non-stationary signals that relies on the local characteristic time-scale of the signal. For the studied sea states, an average energy improvement of 15%, and 29%, is obtained for the proposed control when it is compared with the constant damping respectively tuned at the energy, and the peak frequency of the wave spectrum. The author was unaware of the method (HHT) and the research was carried out after the author's time.

Figure 6:18: Optimised damping value for each regular frequency. Hemisphere-cylinder buoy draft=221mm, M_{sup}=9.4kg. Requested wave height was 80mm.

Figure 6:18 shows the optimum experimentally determined damping values for this particular hemisphere-cylinder buoy set-up in regular waves. The shape of the curve can be related to the impedance tests carried out previously. The optimum damping value at each frequency is theoretically the absolute value of the impedance at each frequency. Recalling that at low frequencies the impedance is largest due to the large hydrostatic spring term, thus a large damping value should be applied for low frequency waves. The damping curve decays until it reaches its lowest value at the natural frequency of 0.847 Hz. At this frequency the buoys velocity is in phase with the excitation force and the optimal applied damping value should be set to match the hydrodynamic damping value. A possible explanation for the outliers is that cross waves, or reflections of the devices' radiated waves off the side walls, created an interference pattern. This would alter the total wave elevated height at the buoys location.

The damping values in Figure 6:18 will be utilised in the control strategy of changing the damping value in accordance with changes in the instantaneous peak frequency as determined by the wavelet analysis. In order to ensure that the same section of the incoming wave was used for each test, it was decided to use a trigger point based on the incoming wave height. A wave probe in line with the centre of the device but with approximately 3m lateral distance between the probe and device was used. It was observed that after the initial small waves to reach the probe a wave height of approximately 40mm occurred. This then became the target value for which to synchronise the tests. The wave probe elevation for several different test is given in the figure below. As one might expect when targeting an absolute threshold value (or a zero crossing for that matter), the start point is not always exactly the same. There will therefore be a slight phase difference in some the estimates but this was considered acceptable for the series of tests. The repeatability of the incident wave train is once again observed.
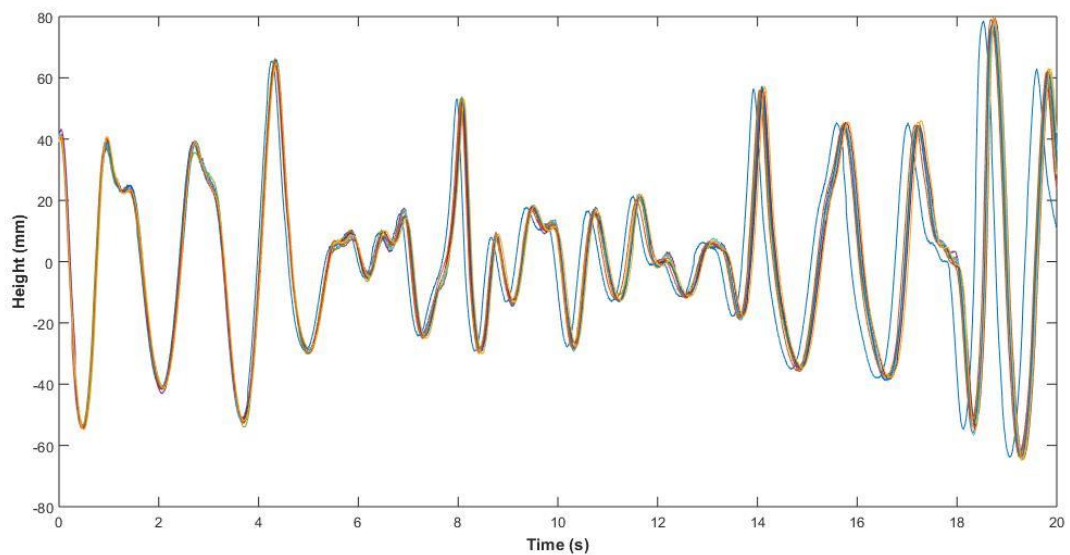
Figure 6:19: Initial absolute wave height trigger value used for all tests
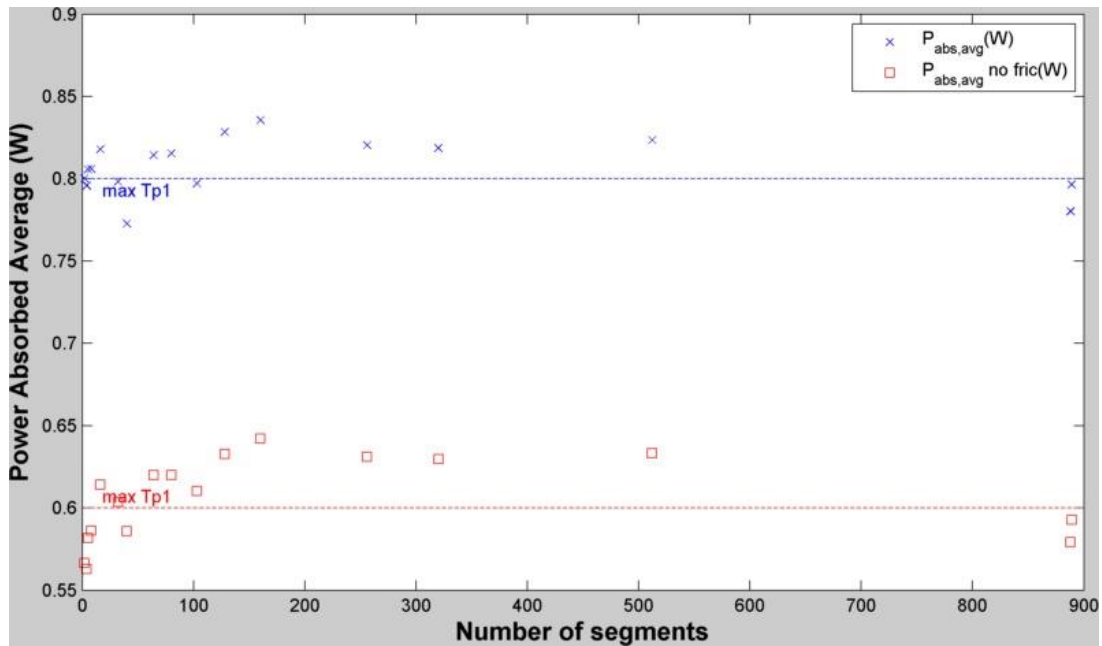
Figure 6:20: Power absorbed

Figure 6:20 shows the power absorption results against the number of segments the time series is split into. For each segment of the time series, the average T_p is determined from the wavelet analysis and the optimum damping value for this T_p was determined by the regular wave tests. While some improvement was found the gains could be considered marginal. A maximum power of 0.84W was found by breaking the time series into 160 seconds. This contrasts with the optimal value of a single damping value of 0.8W. It is interesting to note that the 160 segments roughly corresponds with the number of waves. The author was under time pressure for these tests and as a result no repeat tests were carried out. It would also be worthwhile to carry out the tests for a much greater number of waves to gather more confidence in results.

Due to the nonlinear nature of the inherent friction in the system, the damping can never truly go below a certain amount. It is therefore likely that the device is overdamped for the smaller waves. While the author thinks some further improvement to this method is possible, it would be most interesting to implement this method for double peaked spectra.

244

6.4 Discussion

A problem occurs when real sea states are represented with select spectral parameters. Barrett et al. (2009) showed that many sea states with similar values of wave height and period display distinctly different spectral shapes and that this variability is significant in the context of the performance of WECs. Barrett et al. (2008) also showed that different power levels are produced by a WEC for the same summary statistics due to this spectral variability from the analysis of concurrent wave and device output data collected during sea trials of the OE Buoy device in Galway Bay. Sea states with spectral peak closely matches the devices response peak were found (as one would expect) to perform well, however, when the resonant peak of the device falls within the valley of so called twin peaked spectra the resulting power production was observed to diminish to as low as 5% of its expected value. Twin peak spectra can occur when there exists both low frequency swell components as well as higher frequencies from local wind disturbances. Guedes Soares (1984) reports that an overall average of 22% of bimodal spectra occur in the North Atlantic.

The point being that if one limits the number of parameters used to describe the sea state, then one can lose vital information on some fundamental characteristics of the incoming wave train. Many authors suggest that H_{m0} and T_e alone are insufficient to fully predict device output and propose that other parameters, such as spectral bandwidth, mean direction at peak frequency and the directional spreading, also be included (Kerbiriou et al, (2007) and Saulnier et al., (2011)). It is proposed by the author that wavelet analysis could led to improved capture performance from a purely passive PTO. Of particular interest would be to apply the technique to twin peak spectra and compare results with the single damping value based on peak period.

The crux of the problem is that to tune the device such that the optimum frequency of the device is closer to the peak frequency of the incoming wave requires a frequency domain approach of introducing large spring or mass forces. The optimum wave to wave control of the device however must have a time domain control algorithm. Such an algorithm will inevitable require accurate information on the future wave elevation profile, the likelihood of this is the sixty four thousand dollar question.

The requirement of knowledge of the time varying frequency characteristics of the wave is less onerous compared to say complex conjugate controls need for the entire wave profile.

Wave prediction methods are beyond the scope of this work, yet the author must acknowledge, that the assumption that such time-varying spectral information could be achieved by an upstream probe is somewhat "hand wavy". In fact the accurate mapping of surface elevations from two different locations in space could be considered one the most challenging tasks in wave energy.

Svendsen (2005) succinctly discusses this issue; One of the most important features of linear problems is that solutions can be superimposed: If A and B each are solutions then A + B and A – B are also solutions to the problem. However, adding solutions that are waves of simple sinusoidal shape can lead to solutions of any shape (as in Fourier series). Therefore, a corollary to this is that the equations for linear waves support waves of any shape. Or in other words, **the linear wave theory cannot predict the shape of the waves**. This fundamental fact is often overlooked. In order to extract information about the wave motion that includes results about the wave shape (that is the phase variation), it is necessary to include the nonlinear terms we disregarded to obtain the linear form of the equations.

Chapter 7: Conclusion/Recommendations

7.1 Discussion and conclusion

A large amount of work is described in this thesis, undertaking a basin characteristics study, developing and testing a physical rig from scratch, becoming familiar with numerical modelling and control of WECs. Additionally familiarity has been gained with a wide variety of programs, Matlab, Simulink, Solidworks, Labview and WAMIT.

A study on the reflective characteristics (Chapter 3:) of the wave basin at the HMRC was carried out using regular and irregular waves. For regular waves, two different methods of establishing the amount of reflection were used: Healy's method, which requires the wave height envelope along the length of the tank, and the Funke and Mansard method, respectively. The results produced by all three methods were in agreement with each other with only slight deviation in values. The average reflection coefficient found in the wave basin was 10 %, as revealed in section 3.9.

The reflection curve along the tank was found to be similar for both a high and low gain setting, indicating that reflections are independent of wave height. The reflection coefficient was found to vary with wave period, with larger wave periods exhibiting larger reflections. This was as expected, as the beach becomes less effective at absorbing waves as the wavelength (wave period) increases. Additionally, the reflection coefficient was found to vary with position within the basin for all three methods tested. This is attributed to the variation in the water surface envelope both along and across the basin which was evident fromm the contour plots (section 3.7).

The surface envelope tests revealed variations in wave height, in both the longitudinal and traverse directions. The average value for the coefficient of variation is 9 %, with 8% in the longitudinal direction and 5-6 % in the traverse direction, as shown in section 4.6. The values are very similar for both the high and low gain settings tested.

This wave activity in the transverse direction is an artefact of generating waves within a confined structure but it significant for studies of wave energy converters. For the majority of periods, the magnitude of cross waves are relatively small compared to the main longitudinal wave, resulting in fairly similar wave height envelopes being produced across

the basin. Periods below 1 second exhibit more activity in the traverse direction, resulting in more random wave envelopes across the basin. This is a known issue for the wave basin at HMRC and such a phenomenon has been observed when previous test studies were carried out.

The active absorption aspect of the wave-maker was observed to perform very well, with no significant re-reflection. This is best observed in the repeatability of the irregular wave trains. The efficacy of the active absorption is apparent also in the regular wave surface envelope tests, where the same wave height was recorded at a location at the beginning and end of tests lasting 2 plus hours

Analysis of the incident wave train with respect to harmonics was presented in section 3.12. In general, the amplitude of the second harmonic is less than 6% of the fundamental and similarly the third harmonic is generally less than 2%. However, these figures rise with increasing wave steepness. The lower period waves exhibit second harmonic components in the resulting spectra.

A numerical model has been created Chapter 4: for a generic point absorber device constrained to move in heave motions only. Three different shapes: a simple right cylinder, a cone-cylinder and a hemisphere cylinder have been considered. For each shape, three different drafts have also been evaluated. Multisurf was used to specify the geometry of each buoy, as input to WAMIT, which in turn produces the frequency dependent parameters of added mass, hydrodynamic damping, as well as, excitation force and phase (section 4.2.1). These parameters are necessary to solve the equation of motion of the point absorber. A frequency domain model was created using MATLAB to predict the responses and power absorption of the floaters. A more sophisticated time domain model was also created (4.3) using Simulink, which is capable of dealing with non-linear PTO forces, as well as to account for the instantaneous hydrodynamic spring force (a weakness of the frequency domain model).

Part of the time domain model involved approximating the convolution term in the time domain equation of motion with a dedicated state space approximation. The FDI toolbox was used to produce fifth order fitting approximations which produced fits of very high agreement with only slight disparity near the resonance frequency (4.3.1.8). As a calibration check, the RAOs were calculated for all shapes using the time domain model and compared

to the frequency domain results. Agreement was very good with only slight deviation near the resonance frequency as was shown in section 5.3.2.

An experimental model set-up was successfully designed using Solidworks (Chapter 5:) to ensure the rig could be attached to the bridge spanning the wave basin. Model assembly included the procurement of sensors, rig frame, pulleys and timing belt, as well as the assembly of said components(5.2). Different shaped floaters were constructed in-house. A primary objective of the model rig was to find a PTO system which could operate effectively at the typically low energy levels associated with the model scale. It was found that a magnetic particle brake could adequately handle the low speed and torque requirements associated with testing at small scale. The relatively low cost of the brake is seen as a benefit. The PTO was well suited for providing resistive damping, with enough torque to adequately carry out excitation force tests (5.1). The PTO was not suitable for carrying out latching tests. The reason for this is that latching requires a very large force (proportional to the buoyancy force) instantaneously. The brake was not up to this task, in terms of response time and total torque capacity. The results highlight however the extremely demanding rigours that latching puts on a PTO system, this brings the technique into question for full scale PTO systems also.

Forced oscillation tests were carried out using a linear rig to determine the hydrodynamic coefficients of the buoys. Unfortunately, mechanical vibrations in the experiment made it difficult to establish accurate phase shifts between force and velocity signals for some frequencies. For the frequency range of interest (0.5-1 Hz, there is reasonable agreement between numerical and physical results, where the difference can be reasonably attributed to mechanical friction and viscous losses in the fluid (5.4).

Power absorption tests were carried out in both regular (5.2.1) and irregular (5.2.2) waves. In regular waves an interesting result was that for the cone and hemisphere shape buoys, the linear model misestimates the resonance peak. This because the large amplitude motions result in these profiles having a restoring spring term that is proportional to its draft. The use of non-linear restoring force improved numerical predictions for these tests, with both experimental and numerical resonance peaks matching (5.2.1.3). For regular waves, maximum experimental capture width ratios of 0.77, 0.69 and 0.54 were observed for the cone, hemisphere and cylinder, respectively. The figures for irregular waves (5.3.1) were

lower at 0.40,0. 36 and 0.26, respectively (5.3.2). The rankings of most efficient shaped buoys are in accordance with the hydrodynamic parameters produced in section (4.2.1)

Separate indictors of error between numerical and physical results are presented in (5.3). For regular waves the average absolute errors for the cone, hemisphere and cylinder are 16, 15 and 20 %, respectively. These figures rise to 37, 25 and 41%, within 10% of a T/Tn ratio of 100%, indicating that numerical model results are poor near the resonance frequency. Away from resonance, the correlation between methods is much better with an average difference of just over 4 % for each of the shapes tested. For irregular waves, the average absolute errors for the cone, hemisphere and cylinder were 6, 8 and 6 %, respectively. These figures vary less with T/Tn ratio (5.3).

A PI controller was successfully implemented using LabVIEW in order to achieve linear damping in the resistance force (6.1). A new method of real time damping variation is developed. The approach assumes that in upstream wave probe is capable of giving the time varying peak spectral frequency. A Morlet Wavelet is used as an analysis tool in this method (6.3.2).Power optimisation tests in regular waves were carried out for the hemisphere-cylinder of draft 221mm (6.3.3). The optimal damping value for each frequency is also used in conjunction with Wavelets analysis of time-varying peak frequency. A power absorption test on an irregular wave train was also carried out (6.3.1). The peak power from irregular waves using a constant damping value throughout the run was found to be 0.8W. The peak power obtained from averaging the peak period over the irregular wave cycle was 0.84W. While this is advantageous it is thought that the unavoidable non-linear friction element to the test setup results in overdamping for the smaller waves. It is hypothesised that the method would yield much greater gains in double peaked spectra. It is worth noting that the author's assumption of such information being available from an upstream probe has not being investigated, and the author acknowledges the tremendous difficulty associated with such a task.

7.2 Recommendations for future research

Useful experiments that could utilise the ability of the PTO to change the damping in real time, could involve nonlinear strategies, quadratic damping for example. The PTO would also be suitable for studying stroke constraint investigations. It would be interesting to refine the Wavelet method, (or used the Hilbert Huang Transform) for further experiments. These methods would be interesting to use in double peaked spectra, although the difficulty of the assumption of available wave information must be considered.

It is recommended that the lab scale model PTO resemble the prototype as closely as possible. In order to test the state of the art control algorithms/methods, it is necessary that the flow of power for the PTO system be bi-directional. For this reason, it is recommended that, where financially possible, lab scale PTO systems be as sophisticated as possible. It is recommended that the eddy current dynamometer, and particularly the linear actuator PTO systems discussed in chapter 3, would adequately meet the requirements necessary for advanced control methods. Another useful quality of the aforementioned systems is their ability to perform forced oscillation tests in order to accurately determine the hydrodynamic properties of the buoys.

It is recommended that basin characteristics be readily available to researchers, as the authors experience is that this is an arduous and time consuming task .Development of high end physical and numerical models in conjunction with implementing advanced control techniques at model scale is in general too great a burden for a single researcher to take on. Ideally one or more of these facets should be readily available to the researcher so that greater inroads could be made. If expertise in these interrelated disciplines is not available, then a collaborative project would be hugely beneficial. Another crucial element of research not covered in thesis relates to the final stage of energy conversion, i.e. grid capture of electricity. Control strategies must be developed with realistic PTO and grid constraints in mind; it is interesting to see what can be done in a laboratory, but any strategy must be transferable to the real ocean environment.

A hugely beneficial project linking all four disciplines would necessitate a high end physical model capable of implementing advance control techniques at laboratory scale. An advanced numerical model capable of dealing with the non-linear effects mentioned in this thesis could

then be used input the develop control strategies for the device. The benefit of the control algorithms could then be examined on the physical device. The Wavestar team working out of Aalborg for example have already achieved this but it is the author's opinion that every research centre (or clusters of centres) should have the capabilities to do likewise. Additionally a crucial missing element would be to link in the electrical side, using a lab which has both model generators/power systems and micro-grid emulation capabilities. In doing so it would be possible to replicate a complete wave to grid scenario closer to that of a full scale device and impose grid constraints on the model. Ideally this would be carried using an array of devices but if only a single device is available, then more "phantom" devices could be simulated using either the numerical model or better yet the physical model itself. A downside of this is that the interaction effects would also have to be simulated but it would still make for an interesting experiment.

With regards to physical model array studies, the non-homogenous nature of wave basin revealed in this study highlights the difficulties associated with such a topic. To attempt to isolate array interactions from underlying basin dynamics, not to mention device reflections from side-walls is an extremely difficult task and any researcher attempting to do so has the utmost respect from the author. In fact while the dictionary reveals that both 'experimenter' and 'experimentalist' are equally valid, the latter is surely more appropriate due to the word play connotations.

It has not escaped the author's attention that as we live in a capitalist society, "money rules the world" as it were. A realistic economic study is necessary to determine whether the benefits of control outweigh both the larger capital cost of the necessary machinery and the operational and maintenance costs associated with operating at higher energy regimes. It is the author's opinion that this studies should be carried out in parallel with control strategies and not after the fact. Clearly what the author is suggesting depends on the availability of a large interdisciplinary study. This ties in with the consensus amongst the wave energy community, that a greater amount of collaboration is necessary.

The vast amount of experimental testing carried would make an excellent source of data for advanced numerical modelling techniques. The addition of supplementary mass as a control force, had the effect of increasing response amplitudes beyond the range where linear theory is applicable. The small amplitude assumptions is at odds with the very purpose of control;

which is to increase the amplitudes of motion (more accurately power increase is the goal but rarely does one come without the other). The data form both the cone-cylinder and hemisphere cylinder shapes, make for interesting studies of Non-Linear Froude Krylov based methods. The simpler cylinder shape data is also useful as a base reference for comparison with the other shapes.

References

Babarit, A. (2017). *Ocean wave energy conversion : resource, technologies and performance*. Elsevierg.

Bailey, H. (2009). *The effect of a nonlinear Power Take Off on a Wave Energy Converter*. PhD Thesis, University of Edinburgh.

Bailey, H., & Bryden, I. (2009). The influence of a mono-directional PTO on a self-contained inertial WEC. In *EWTEC, Uppsala* (pp. 722–728).

Banasiak, R., Vantorre, M., & Verhoeven, R. (2003). Numerical and physical examination of a point absorber in heave – a feasibility study for Belgian coastal area. In *proceedings of 5th European Wave Energy Conference* (pp. 341–348).

Barrett, S. (2010). *Floating Wave Energy Converters: Wave Measurement & Analysis Techniques*. PhD Thesis, University College Cork.

Barstow, S., Mork, G., Mollison, D., & Cruz, J. (2008). The wave energy resource. In J. Cruz (Ed.), *Ocean Wave Energy* (p. 93). Springer.

Batchelor, G. K. (George K. (1999). *An introduction to fluid dynamics*. Cambridge University Press. Retrieved from https://books.google.ie/books/about/An_Introduction_to_Fluid_Dynamics.html?id=KdQQAQAAIAAJ&redir_esc=y

Benjamin, T. B., & Feir, J. E. (1967). The disintegration of wave trains on deep water Part 1. Theory. *Journal of Fluid Mechanics*, *27*(03), 417. https://doi.org/10.1017/S002211206700045X

Bjarte-larsson, T., & Falnes, J. (2006). Laboratory experiment on heaving body with hydraulic power take-off and latching control. *Ocean Engineering*, *33*(7), 847–877. https://doi.org/10.1016/j.oceaneng.2005.07.007

Blottner, F. (1990). Accurate Navier-Stokes results for the hypersonic flow over a

spherical nosetip. *Journal of Spacecraft and Rockets*, *27*(2), 113–122. https://doi.org/10.2514/3.26115

Boccotti, P. (Paolo). (2000). *Wave mechanics for ocean engineering*. Elsevier.

Bolton King, G., & Rogers, D. (1997). *Wave generation using Ocean and wave*. Edinburgh: Edinburgh Designs Ltd.

Boyle, L. O., Elsaesser, B., Folley, M., & Whittaker, T. (2011). Assessment of Wave Basin Homogeneity for Wave Energy Converter Array Studies. In *9th European Wave and Tidal Energy Conference* (pp. 2–9). Southampton, United Kingdom.

Bretschneider, C. L. (1964). *Generation of waves by wind. State of the art*. Report Presented at International Summer Course Lunteren, The Netherlands.

Brooke, J. (2003). *Wave energy conversion*. Elsevier.

Budal, K., & Falnes, J. (1975). A resonant point absorber of ocean-wave power. *Nature*, *256*(5517), 478–479. https://doi.org/10.1038/256478a0

Cahill, B. (2014). *Characteristics of the Wave Energy Resource at the Atlantic Marine Energy Test Site*. PhD thesis, University College Cork.

CalWave. (2018). Converting Waves into Electricity and Freshwater. Retrieved April 21, 2018, from http://calwave.org/

Carnegie Wave Energy. (2012). *Irish Marine Renewables Industry Association Presentation*. Dublin, Ireland: Carnegie Wave Energy Limited. Retrieved from www.carnegiewave.com

Chaplin, J. R., Heller, V., Farley, F. J. M., Hearn, G. E., & Rainey, R. C. T. (2011). *Laboratory testing the Anaconda*. *Phil. Trans. R. Soc.* Southampton, United Kingdom. https://doi.org/10.1098/rsta.2011.0256

Churchill Controls Ltd. (2018). Wave Monitor - Churchill Controls Ltd. Retrieved April 20, 2018, from http://www.churchill-controls.co.uk/all-products/level-measurement/wave-monitor/

Clancy, M., Scheer, J., O Gallachóir, B., Seai, Daly, H., Dineen, D., … Deane, J. P. (2011). *Energy Forecasts for Ireland to 2020*. Ireland. Retrieved from www.seai.ie

Clément, A. H. (1995). Identification de la Fonction de Green de l'Hydrodynamique Transitoire par des Modèles Continus. *Proc. 5èmes Journées de l'Hydrodyn*, 319–332.

Coastal engineering research cenre. (1984). *Shore Protection Manual* (Vol. IV). Washington D.C.: Prepared for DEPARTMENT OF THE ARMY US Army Corps of Engineers Washington, DC 20314.

Cooley, J. W., & Tukey, J. W. (1965). An Algorithm for the Machine Computation of the Complex Fourier Series. *Mathematics of Computation*, *19*, 297–301.

Cornett, A. M. (2008). A global wave energy resource assessment. In *International Society of Offshore and Polar Engineers* (pp. 1–9). Ottawa, Ontario, Canada.

Cummins, W. E. (1962). *The impulse response function and ship motions*. *Symposium on Ship Theory at University of Hamburg* (Vol. 57). Hamburg, Germany.

De Backer, G. (2010). *Hydrodynamic Design Optimization of Wave Energy Converters Consisting of Heaving Point Absorbers*. PhD Thesis, Ghent University.

Dean, R. G., & Dalrymple, R. A. (1991). *Water Wave Mechanics for Engineers and Scientists* (Vol. 2). WORLD SCIENTIFIC. https://doi.org/10.1142/1232

Douglas, J., Gasiorek, J., Swalfield, J., & Jack, L. (2005). *Fluid mechanics*. Pearson/Prentice Hall. Retrieved from https://books.google.ie/books/about/Fluid_Mechanics.html?id=LUMec3jraA4C&redir_esc=y

Duclos, G., Clément, A., & Chatry, G. (2001). Absorption of Outgoing Waves in a Numerical Wave Tank Using a Self Adaptive Boundary Condition. In *Int J*

Offshore Polar Engng (Vol. 11, pp. 168–175). International Society of Offshore and Polar Engineers. Retrieved from http://www.isope.org/publications/journals/ijope-11-3/ijope-11-3-p168-abst-CHK-43-Duclos.pdf

Durand, M., Babarit, A., Pettinotti, B., Quillard, O., Toularastel, J. L., & Clément, A. H. (2007). Experimental validation of the performances of the SEAREV Wave Energy Converter with real time latching control. In *European Wave and Tidal Energy Conference*. Porto.

Eagleson, P. S., Ippen, A., & Laboratory, M. I. of T. H. (1966). *Estuary and coastline hydrodynamics*. McGraw-Hill Book Co. Retrieved from https://books.google.ie/books/about/Estuary_and_coastline_hydrodynamics.html?id=mAczAAAAMAAJ&pgis=1

Edinburgh Wave Power Group. (2018). Edinburgh Wave Power Group. Retrieved April 21, 2018, from http://www.homepages.ed.ac.uk/v1ewaveg/

EMEC. (2018). Wave clients : European Marine Energy Centre. Retrieved April 17, 2018, from http://www.emec.org.uk/about-us/wave-clients/

Ernst & Young. (2013). *Rising Tide: Global trends in the emerging ocean energy market*. https://doi.org/10.4016/8324.01

Evans, D. V. (1976). A theory for wave power absorption by oscillating bodies. *Journal of Fluid Mechanics*, *77*, 1–25.

Evans, D. V. (1981). Power from water waves. *Fluid Mechanics*, 157–187.

Falcão, A. F. O. (2010). Wave energy utilization: A review of the technologies. *Renewable and Sustainable Energy Reviews*, *14*(3), 899–918. Retrieved from http://ideas.repec.org/a/eee/rensus/v14y2010i3p899-918.html

Falnes, J. (2003). *Ocean waves and Oscillating systems*. *Ocean Engineering* (Vol. 30). Cambridge, United Kingdom: Cambridge University Press. https://doi.org/10.1016/S0029-8018(02)00070-7

Falnes, J., & Bjarte-larsson, T. (2006). Theoretical and experimental investigation of wave energy conversion by a phase-controlled heaving body. *Proceedings of the Institution of Mechanical Engineers, Part M: Journal of Engineering for the Maritime Environment*, *220*(4), 175–183. https://doi.org/10.1243/14750902JEME52

Falnes, J., & Lillebekken, P. M. (2003). Budal's latching-controlled-buoy type wave-power plant. In *European Wave Energy Conference*. Trondheim, Norway.

Faltinsen, O. M. (1990). *Sea loads on ships and offshore structures*. Cambridge University Press. Retrieved from https://books.google.ie/books/about/Sea_Loads_on_Ships_and_Offshore_Structur.html?id=qZq4Rs2DZXoC&redir_esc=y

Farge, M. (1992). Wavalet transforms and their applications to turbulance. *Annual Review of Fluid Mechanics*, *24*, 395–457. https://doi.org/10.1146/annurev.fl.24.010192.002143

Feeny, B., & Liang, J.-W. (1996). A decrement method for the simultaneous estimation of Coulomb and viscous friction. *Journal of Sound and Vibration*, *195*, 149–154.

Feynman, R. (1965). The Flow of Dry Water. In *The Feynman Lectures on Physics*. Retrieved from http://www.feynmanlectures.caltech.edu/II_40.html

Flocard, F., & Finnigan, T. (2009). Experimental investigation of power capture from pitching point absorbers. In *8th European Wave and Tidal Energy Conference* (pp. 400–409). Uppsala.

Flocard, F., & Finnigan, T. (2010). Laboratory experiments on the power capture of pitching vertical cylinders in waves. *Ocean Engineering*, *37*(11–12), 989–997. https://doi.org/10.1016/j.oceaneng.2010.03.011

Funke, E. R., & Mansard, E. P. D. (1980). Measurment of incident and reflected spectra using a least squares method. *17th Internation Conference on Coastal Engineering*, 154–172.

Garcia-rosa, P. B., Kulia, G., Ringwood, J. V., & Molinas, M. (2017). Real-Time Passive Control of Wave Energy Converters Using the Hilbert-Huang Transform. *20th IFAC World Congress*, *50*.

Genest, R., Bonnefoy, F., Clément, A. H., & Babarit, A. (2014). Effect of non-ideal power take-off on the energy absorption of a reactively controlled one degree of freedom wave energy converter. *Applied Ocean Research*, *48*, 236–243. https://doi.org/10.1016/j.apor.2014.09.001

Giorgi, G., & Ringwood, J. . (2017). Comparing nonlinear hydrodynamic forces in heaving point absorbers and oscillating wave surge converters. *Journal of Ocean Engineering and Marine Energy*. https://doi.org/10.1007/s40722-017-0098-2

Goda, Y. (2000). *Random Seas and Design of Maritime Structures* (Vol. 15). WORLD SCIENTIFIC. https://doi.org/10.1142/3587

Goda, Y., & Ippen, A. (1963). *Theoretical and experimental investigation of wave energy dissipators composed of wire mesh screens*. Cambridge - Mass. Retrieved from http://www.worldcat.org/title/theoretical-and-experimental-investigation-of-wave-energy-dissipators-composed-of-wire-mesh-screens/oclc/636754373

Goda, Y., & Suzuki, Y. (1976). Estimation of incident and reflected waves in random wave experiments. *15th Coastal Engineering Conference*, 828–845.

Grinsted, A., Moore, J., & Jevrejeva, S. (2004). Application of the cross wavelet transform and wavelet coherence to geophysical time series. *Nonlinear Processes in Geophysics*, *11*, 561–566. https://doi.org/10.1002/etep

Guedes Soares, C. (1984). Representation of double-peaked sea wave spectra. *Ocean Engineering*, *11*(2), 185–207. https://doi.org/10.1016/0029-8018(84)90019-2

Guedes Soares, C., & Cherneva, Z. (2005). Spectrogram analysis of the time–frequency characteristics of ocean wind waves. *Ocean Engineering*, *32*(14–15), 1643–1663. https://doi.org/10.1016/j.oceaneng.2005.02.008

Hasselmann, K. (1973). *Measurements ofWind-Wave Growth and Swell Decay during the Joint North Sea Wave Project (JONSWAP)* (Vol. 46). Hamburg, Germany.

Heideman, M. T., Johnson, D. H., & Burrus, C. S. (1985). Gauss and the history of the fast Fourier transform. *Archive for History of Exact Sciences*, *34*(3), 265–277. https://doi.org/10.1007/BF00348431

Holmes, B., & Nielsen, K. (2010). *Guidelines for the development and testing of wave energy systems, OES IA Annex II Task 2.1. Energy*. Cork, Ireland.

Holthuijsen, L. (2007). *Waves in Oceanic and Coastal Waters*. Cambridge University Press. Retrieved from http://www.amazon.com/Waves-Oceanic-Coastal-Waters-Holthuijsen/dp/0521129958/ref=sr_1_1?s=books&ie=UTF8&qid=1429692788&sr=1-1&keywords=Waves+in+Oceanic+and+Coastal+Waters

Housner, G. W., & Hudson, D. E. (1950). *Applied Mechanics Dynamics*. London: D. Van Nostrand Company, Inc.

Hudspeth, R. T. (2006a). *Waves and wave forces on coastal and ocean structures*. Oregon State University, USA: World Scientific. Retrieved from https://books.google.ie/books/about/Waves_and_Wave_Forces_on_Coastal_and_Oce.html?id=T_ZQAAAAMAAJ&redir_esc=y

Hudspeth, R. T. (2006b). *Waves and Wave Forces on Coastal and Ocean Structures* (Vol. 21). WORLD SCIENTIFIC. https://doi.org/10.1142/5397

Hughes, S. A. (1993). Physical models and Laboratory techniques in Coastal Engineering (Advanced S). World Scientic Publishing Company.

Hwang, P. A., & Wang, D. W. (2004). Field Measurements of Duration-Limited Growth of Wind-Generated Ocean Surface Waves at Young Stage of Development*. *Journal of Physical Oceanography*, *34*(10), 2316–2326. https://doi.org/10.1175/1520-0485(2004)034<2316:FMODGO>2.0.CO;2

Ibrahim, R. A. (2005). *Liquid Sloshing Dynamics*. Cambridge: Cambridge University Press. https://doi.org/10.1017/CBO9780511536656

Ingram, D., Smith, G. H., Bittencourt, C., & Smith, H. (2011). *EquiMar: Protocols for the Equitable Assessment of Marine Energy Converters*. https://doi.org/978-0-9508920-3-0

Isaacson, M. (1991). Measurement of Regular Wave Reflection. *Journal of Waterway, Port, Coastal, and Ocean Engineering*, *117*(6), 553–569. https://doi.org/10.1061/(ASCE)0733-950X(1991)117:6(553)

ITTC. (2014). *Recommended Procedures Uncertainty Analysis Instrument Calibration*. Retrieved from https://ittc.info/media/4038/75-01-03-01.pdf

Jeffreys, E. R. (1980). Device characterisation. In B. Count (Ed.), *Power from sea waves*. London: Academic Press.

Jeffreys, H. (1925). On the Formation of Water Waves by Wind. *Proceedings of the Royal Society A: Mathematical, Physical and Engineering Sciences*, *107*(742), 189–206. https://doi.org/10.1098/rspa.1925.0015

Jonkman, J. M., Duarte, T., Alves, M., & Sarmento, A. (2013). STATE-SPACE REALIZATION OF THE WAVE-RADIATION FORCE WITHIN FAST (pp. 1–12). Nantes, France.

Journée, J. M. J., & Massie, W. W. (2001). Offshore Hydromechanics, chapter 12 wave forces on slender cylinders. *Offshore Hydromechanics, Delft University of Technology*, (January).

Keaney, I. (2015). *Evanescent Wave Reduction Using a Segmented Wavemaker in a Two Dimensional Wave Tank*. PhD Thesis, NUI Maynooth. Retrieved from http://eprints.maynoothuniversity.ie/7585/1/PhDThesis %28Iain Keaney%29.pdf

Kelly, S. (2007). *Hydrodynamic optimisation of a point wave energy converter using laboratory experiments*. Masters Thesis, University of Auckland.

Kerbiriou, M.-A., Prevosto, M., Maisondieu, C., Babarit, A., & Clément, A. (2007). INFLUENCE OF AN IMPROVED SEA-STATE DESCRIPTION ON A WAVE ENERGY CONVERTER PRODUCTION. Retrieved from http://www.ifremer.fr/web-com/mpre/omae2007/OMAE2007-29254.pdf

Kristiansen, E., & Egeland, O. (2003). Frequency dependent added mass in models for controller design for wave motion ship damping. *6th IFAC Confer- Ence on Manoeuvring and Control of Marine Craft MCMC*.

Krogstad, H. E., & Arntsen, O. (2000). *Linear wave theory*.

Kung, S. (1978). A New Identification and Model Reduction Algorithm via Singular Value Decomposition. Retrieved May 18, 2015, from http://libra.msra.cn/Publication/1992040/a-new-identification-and-model-reduction-algorithm-via-singular-value-decomposition

Kurniawan, A., Todalshaug, J. H., & Moan, T. (2011). Assessment of Time-Domain Models of Wave Energy Conversion Systems, (7491). Retrieved from http://www.ntnu.edu/documents/174596/8a074f75-91a3-490f-9770-bf3f661db05f

Le Mehaute, B. (1976). Similtude in Coastal Engineering. *Journal of the Waterways, Harbours, and Coastal Engineering Division*, *102*.

Levy, E. C. (1959). Complex-curve fitting. *IRE Transactions on Automatic Control*, *AC-4*(1), 37–43. https://doi.org/10.1109/TAC.1959.6429401

Lewis, T. (2014). *Annual Report Implementing Agreement on Ocean Energy Systems*. *Exchange Organizational Behavior Teaching Journal*. https://doi.org/10.1017/S0001972000001765

Liang, J.-W., & Feeny, B. (1998). *Identifying Coulomb and Viscous Friction from Free-Vibration Decrements*. *Nonlinear Dynamics*. Netherlands.

Lighthill, M. J. (1965). Contributions to the Theory of Waves in Non-linear Dispersive Systems. *IMA Journal of Applied Mathematics*, *1*(3), 269–306.

https://doi.org/10.1093/imamat/1.3.269

Lighthill, M. J. (1978). *Waves in fluids*. Cambridge University Press.

Lin, C.-P. (1999). *Experimental Studies Of The Hydrodynamic Characteristics Of A Sloped Wave Energy Device*. PhD Thesis, University of Edinburgh.

Liu, H.-T., Katsaros, K. B., & Weissman, M. A. (1982). Dynamic response of thin-wire wave gauges. *Journal of Geophysical Research*, *87*(C8), 5686. https://doi.org/10.1029/JC087iC08p05686

Liu, P. C. (2000). Is the wind wave frequency spectrum outdated. *Ocean Engineering*, *27*(5), 577–588. https://doi.org/10.1016/S0029-8018(98)00074-2

Lopes, M. F. P., Henriques, J. C. C., & Gato, L. M. C. (2009). Design of a non-linear power take-off simulator for model testing of rotating wave energy devices, 1–7.

Lopes, M. F. P., Todalshaug, J. H., Gomes, R. P. F., Moan, T., Gato, L. M. C., & Falcão, A. F. O. (2009). Experimental and numerical investigation of non-predictive phase-control strategies for a point-absorbing wave energy converter. *Ocean Engineering*, *36*(5), 386–402. https://doi.org/10.1016/j.oceaneng.2009.01.015

Madsen, O. S. (1971). On the generation of long waves. *Journal of Geophysical Research*, *76*(36), 8672–8683. https://doi.org/10.1029/JC076i036p08672

Maguire, A. E. (2011). *Hydrodynamics, control and numerical modelling of absorbing wavemakers*. PhD Thesis, University of Edinburgh. Retrieved from https://www.era.lib.ed.ac.uk/bitstream/handle/1842/5780/Maguire2011.pdf?sequence=2&isAllowed=y

Massel, S. R. (2001). Wavelet analysis for processing of ocean surface wave records, *28*, 957–987.

McCabe, A., Bradshaw, A., & Widden, M. B. (2005). A time-domain model of a floating body using transforms. *6th European Wave and Tidal Energy …*, (2),

281–288. Retrieved from
http://scholar.google.com/scholar?hl=en&btnG=Search&q=intitle:A+Time-
domain+model+of+a+floating+body+using+transforms#0

McCullen, P. (Marine I. (2005). *Accessible Wave Energy Resource Atlas : Ireland :
2005*. Dublin, Ireland.

Mciver, P., & Evans, D. V. (1984). The occurrence of negative added mass in free-
surface problems involving submerged oscillating bodies. *Journal of
Engineering Mathematics*, *18*(1), 7–22. https://doi.org/10.1007/BF00042895

Mei, C. C. (1976). Power extraction from water waves. *Journal of Ship Research,
Vol. 20, June 1976, p. 63-66.*, *20*, 63–66. Retrieved from
http://adsabs.harvard.edu/abs/1976JShR...20...63M

Mei, C. C. (1992). *The Applied Dynamics of Ocean Surface Waves* (Vol. 1).
WORLD SCIENTIFIC. https://doi.org/10.1142/0752

Mei, C. C., Stiassnie, M., & Yue, D. K.-P. (2005). *Theory and Applications of Ocean
Surface Waves* (Vol. 23). World Scientific. https://doi.org/10.1142/5566

Milgram, J. (1970). Active water-wave absorbers. *Journal of Fluid Mechanics*,
42(04), 845. https://doi.org/10.1017/S0022112070001635

MRFCJ. (2018). Mary Robinson Foundation – Climate Justice. Retrieved April 17,
2018, from https://www.mrfcj.org/

Mude, N., & Sahu, A. (2012). Adaptive Control Schemes For DC-DC Buck
Converter. *International Journal of Engineering Research and Applications
(IJERA) Www.Ijera.Com*, *2*(3), 463–467. Retrieved from
https://pdfs.semanticscholar.org/7602/ef06623420e9d5c3f4e41fa5475c1e6c51c
e.pdf

Munson, B., Young, D., Okiishi, T., & Huebsch, W. (2009). *Fundamentals of fluid
mechanics*. Wiley.

Murtagh, C., & Walsh, P. (2015). Wave Energy Conversion : Linear vs . Coulomb

PTO Damping Strategies. In *Proceedings of the 11th European Wave and Tidal Energy Conference* (pp. 1–9). Nantes.

Nebel, P. (1992). Maximizing the Efficiency of Wave-Energy Plant Using Complex-Conjugate Control. *Proceedings of the Institution of Mechanical Engineers, Part I: Journal of Systems and Control Engineering*, *206*(4), 225–236. https://doi.org/10.1243/PIME_PROC_1992_206_338_02

Newman, J. N. (John N. (1976). The interaction of stationary vessels with regular waves. *Proceedings of the 11th Symposium on Naval Hydrodynamics*.

Newman, J. N. (John N. (1977). *Marine hydrodynamics*. MIT Press. Retrieved from https://books.google.ie/books/about/Marine_Hydrodynamics.html?id=nj-k_lAmaBYC

Nielsen, K., Sichani, M. T., Kramer, M. M., & Kofoed, J. P. (2012). Optimal control of power outtake of wave energy point ansorbers. Aalborg.

Nolan, G. (2006). *Modelling and Optimisation of a Heaving Buoy Wave Energy Converter for Potable Water Production*. PhD Thesis, National University of Ireland.

Nolan, G., Ringwood, J. ., & Holmes, B. (2007). Short term wave energy variability off the West coast of Ireland. *Seventh European Wave and Tidal Energy Conference*, *2*(4).

OES Annual Report 2017 | OES - Ocean Energy Systems. (2017). Retrieved from https://report2017.ocean-energy-systems.org/

Ogilve, F. T. (1963). First-and second-order forces on a cylinder submerged under a free surface. *Journal of Fluid Mechanics*. Retrieved from https://www.cambridge.org/core/journals/journal-of-fluid-mechanics/article/first-and-secondorder-forces-on-a-cylinder-submerged-under-a-free-surface/FF712D39A79D4F8D8844045051B6446A

Ogilve, F. T. (1964). Recent Progress Towards the Understanding and Prediction of

Ship Motions. *Symposium on Naval Hydrodynamics*. Washington D.C.

Open University. (2018). Wave energy: Retrieved April 21, 2018, from http://www.open.edu/openlearn/ocw/mod/oucontent/view.php?id=18929&print able=1

Ouellet, Y., & Datta, I. (1986). A survey of wave absorbers. *Journal of Hydraulic Research*, *24*(4), 265–280. https://doi.org/10.1080/00221688609499305

Parish, D. (2015). A Novel Mooring Tether for Highly Dynamic Offshore Applications. Retrieved from https://ore.exeter.ac.uk/repository/handle/10871/21337

Pastor, J., & Liu, Y. (2014). Frequency and time domain modeling and power output for a heaving point absorber wave energy converter. *International Journal of Energy and Environmental Engineering*, *5*(2), 101. https://doi.org/10.1007/s40095-014-0101-9

Payne, G. (2006). *Numerical modelling of a sloped wave energy device*. *Doctor*. PhD Thesis, University of Edinburgh.

Payne, G. (2008). *Guidance for the experimental tank testing of wave energy converters*. Edinburgh.

Pecher, A., Kofoed, J. P., Espedal, J., & Hagberg, S. (2010). Results of an Experimental Study of the Langlee Wave Energy Converter. In *Power* (Vol. 7, pp. 877–885). Beijing, China: The International Society of Offshore and Polar Engineers. Retrieved from www.isope.org

Peiffer, A. (2009). *Modeling and Evaluation of a Wave-Energy Device - A Point Absorber with Linear Generator By*. University of California at Berkley.

Perez, T., & Fossen, T. I. (2008a). Joint identification of infinite-frequency added mass and fluid-memory models of marine structures. *Modeling, Identification and Control*, *29*(3), 93–102. https://doi.org/10.4173/mic.2008.3.2

Perez, T., & Fossen, T. I. (2008b). Time- vs. Frequency-domain Identification of

Parametric Radiation Force Models for Marine Structures at Zero Speed. *Modeling, Identification and Control: A Norwegian Research Bulletin*, *29*(1), 1–19. https://doi.org/10.4173/mic.2008.1.1

Perez, T., & Fossen, T. I. (2009). A Matlab Toolbox for Parametric Identification of Radiation-Force Models of Ships and Offshore Structures. *Modeling, Identification and Control: A Norwegian Research Bulletin*, *30*(1), 1–15. https://doi.org/10.4173/mic.2009.1.1

Pijush K, K., & Iran M, C. (2007). *Fluid Mechanics*. Pearson/Prentice Hall. https://doi.org/10: 0-8400-5444-0

Placid Industries Magnetic Particle Brakes - Home page. (2017). Retrieved March 7, 2014, from http://www.placidindustries.com/

Polinder, H., Damen, M. E. C., & Gardner, F. (2004). Linear PM Generator System for Wave Energy Conversion in the AWS. *IEEE Transactions on Energy Conversion*, *19*(3), 583–589. https://doi.org/10.1109/TEC.2004.827717

Price, A. (2009). *New Perspectives on Wave Energy Converter Control*. PhD Thesis, University of Edinburgh.

Randløv, P. (1996). *Final report and annexes to the Offshore wave energy converters (OWEC-1) project*.

Rapuc, S. (2012). *Main Report Numerical study of the WEPTOS Single Rotor*. Masters Thesis, Aalborg University.

Reynolds, O. (1883). An Experimental Investigation of the Circumstances Which Determine Whether the Motion of Water Shall Be Direct or Sinuous, and of the Law of Resistance in Parallel Channels. *Philosophical Transactions of the Royal Society of London*, *174*(0), 935–982. https://doi.org/10.1098/rstl.1883.0029

Ricci, P. (2016). Numerical modelling of wave energy converters : state-of-the-art techniques for single devices and arrays. In M. Folley (Ed.). Elsevier.

Rohrig, C., & Jochheim, A. (2001). Identification and compensation of force ripple in linear permanent magnet motors. In *Proceedings of the 2001 American Control Conference. (Cat. No.01CH37148)* (pp. 2161–2166 vol.3). IEEE. https://doi.org/10.1109/ACC.2001.946068

Salter, S. H. (1974). Wave power. *Nature*, *249*(5459), 720–724. https://doi.org/10.1038/249720a0

Salter, S. H. (1981). Absorbing wave-makers and wide tanks. In R. L. Wiegel (Ed.), *Proceedings of the conference on directional wave spectra application* (p. pp 182-202).

Salter, S. H. (2008). The theory behind the conversion of ocean wave energy: A review. In J. Cruz (Ed.). Springer.

Salter, S. H., Taylor, J. R. M., & Caldwell, N. J. (2002). Power conversion mechanisms for wave energy. *Proceedings of the Institution of Mechanical Engineers, Part M: Journal of Engineering for the Maritime Environment*, *216*(1), 1–27. https://doi.org/10.1243/147509002320382103

Sarpkaya, T., & Isaacson, M. (1981). *Mechanics of wave forces on offshore structures*. Van Nostrand Reinhold Co.

Saulnier, J. B., Clément, A., Falcão, A. F. O., Pontes, T., Prevosto, M., & Ricci, P. (2011). Wave groupiness and spectral bandwidth as relevant parameters for the performance assessment of wave energy converters. *Ocean Engineering*, *38*(1), 130–147. https://doi.org/10.1016/j.oceaneng.2010.10.002

Segur, H. (2009). Waves on deep water. Retrieved from https://www.whoi.edu/fileserver.do?id=136409&pt=10&p=85713

Sharkey, F. (2012). ESB's Westwave: Flagship project evaluates wave energy options. *Engineers Ireland: The Engineers Journal*, (March/Apri).

Sheng, W., Flannery, B., Lewis, A., & Alcorn, R. (2012). Experimental Studies of a Floating Cylindrical OWC WEC. In *Volume 7: Ocean Space Utilization; Ocean*

Renewable Energy (p. 169). ASME. https://doi.org/10.1115/OMAE2012-83040

Skyner, D. (1987). Edinburgh Wave Power Project Solo Duck Linear Analysis, *10*(1), 101.

Svendsen, I. (1985). Physical modelling in coastal engineering. In R. Dalrymple (Ed.). Retrieved from https://trove.nla.gov.au/work/18184062?q&versionId=21344482

Svendsen, I. A. (2005). *Introduction to Nearshore Hydrodynamics* (Vol. 24). WORLD SCIENTIFIC. https://doi.org/10.1142/5740

Sverdrup, H. U., & Munk, W. . (1947). *Wind, Sea and Swell: Theory of Relations for Forecasting*. U. S. Department of the Navy Hydrographic Office Pub.

Sykes, R. K., & Thomas, G. P. (2011). *The Hydrodynamics of an Oscillating Water Column An Investigation Using Numerical and Physical Modelling in the Faculty of Engineering , by*. University College Cork.

Taneura, K., Hadano, K., Koirala, P., Yoneyama, H., Nakano, K., & Ikegami, K. (2010). Dynamics of the Float-Counterweight Type Wave Power Generation System (Vol. 7, pp. 815–820). Beijing, China: The International Society of Offshore and Polar Engineers.

Taylor, J. R. M., & Mackay, I. (2001). The Design of an eddy current dynamometer for a free-floating sloped IPS buoy. In *Marine Renewable Energy Conference (MAREC)*. Newcastle upon Tyne, UK.

Thiebaut, F., O'Sullivan D, Kracht, P., Ceballos, S., López, J., Boake, C., … Lewis, T. (2011). Testing of a floating OWC device with movable guide vane impulse turbine power take-off. *9th European Wave and Tidal Energy Conference*.

Thomas, G. P. (2008). The theory behind the conversion of ocean wave energy: A review. In J. Cruz (Ed.), *Ocean Wave Energy*. Springer.

Thorpe, T. . (2000). The wave energy program in the UK and the European Wave Energy Network. In *4th European Wave Energy Conference*. Aalborg.

Todalshaug, J. H. (2013). Practical limits to the power that can be captured from ocean waves by oscillating bodies. *International Journal of Marine Energy*, *3–4*, e70–e81. https://doi.org/10.1016/J.IJOME.2013.11.012

Todalshaug, J. H. (2017). Hydrodynamics of WECs. In A. Pecher & J. P. Kofoed (Eds.), *Handbook of Ocean Energy*. Springer. https://doi.org/10.1007/978-3-319-39889-1_6

Todalshaug, J. H., Asgeirsson, G. S., Hjalmarsson, E., Maillet, J., Moller, P., Pires, P., … Lopes, M. F. P. (2015). Tank testing of an inherently phase controlled Wave Energy Converter . *Proceedings of the 11th European Wave and Tidal Energy Conference*, 1–9. https://doi.org/10.1016/j.ijome.2016.04.007

Torrence, C., & Compo, G. P. (1998). A practical guide to wavelet analysis. *Bams*, *79*, 61. https://doi.org/10.1175/1520-0477(1998)079<0061:APGTWA>2.0.CO;2

Tucker, M., & Pitt, E. (2001). *Waves in Ocean Engineering* (1st ed.).

Unneland, K. (2007). *Identification and Order Reduction of Radiation Force Models of Marine Structures*. PhD Thesis, Norwegian University of Science and Technology.

Vantorre, M., Banasiak, R., & Verhoeven, R. (2002). Extraction of sea wave energy : a mathematical evaluation of a point absorber in heave. In *Proceedings of the conference on advances in fluid mechanics*. Ghent University, Belgium.

Vantorre, M., Banasiak, R., & Verhoeven, R. (2004). Modelling of hydraulic performance and wave energy extraction by a point absorber in heave. *Applied Ocean Research*, *26*(1–2), 61–72. https://doi.org/10.1016/j.apor.2004.08.002

Velar, F. (2013). *PENWEST : AAU Deep Water Wave Basin Summary results of the tests*.

Villegas, C., & Schaaf, H. V. D. (2011). Implementation of a Pitch Stability Control for a Wave Energy Converter. *Proceedings of the 9th European Wave and Tidal*

Energy Conference, 1–6.

Vyzikas, T. (2014). *Application of numerical models and codes*.

WAMIT, I. (2014). WAMIT user manual 6.0, 6.4s. Retrieved from www.wamit.com

Wave Energy Prize. (2018). Wave Energy Prize. Retrieved April 21, 2018, from
https://waveenergyprize.org/teams/calwave

Weber, J., Costello, R., & Ringwood, J. . (2013). WEC Technology Performance
Levels (TPLs) - Metric for Successful Development of Economic WEC
Technology. *EWTEC 2013 Proceedings*.

Weller, S. D. (2010). *Wave energy extraction from device arrays*. PhD Thesis,
University of Manchester.

Weller, S. D., Stallard, T., & Stansby, P. K. (2011). Two-Dimensional Motions of a
Shallow Draft Wave Energy Converter Undergoing Regular Wave Excitation.
In *9th European Wave and Tidal Energy Conference*.

WikiWaves. (2018). WikiWaves. Retrieved April 19, 2018, from
https://wikiwaves.org/

Wypych, M., Le-Ngoc, L., Alexander, K., & Gardner, A. (2012). On the application
of circular–cylindrical waves to ocean wave power absorption. *Ocean
Engineering*.

Yeung, R. W., Peiffer, A., Tom, N., & Matlak, T. (2012). Design, Analysis, and
Evaluation of the UC-Berkeley Wave-Energy Extractor. *Journal of Offshore
Mechanics and Arctic Engineering*, *134*(2), 021902.
https://doi.org/10.1115/1.4004518

Yuen, H. C., & Lake, B. M. (1982). Nonlinear Dynamics of Deep-Water Gravity
Waves. *Advances in Applied Mechanics*, *22*, 67–229.
https://doi.org/10.1016/S0065-2156(08)70066-8

Zurkinden, A. S., Kramer, M. M., & Alves, M. (2012). Comparison Between

Numerical Modeling And Experimental Testing Of A Point Absorber WEC Using Linear Power Take-Off System (pp. 1–10). Rio de Janeiro, Brazil.

Appendix A Surface Envelopes
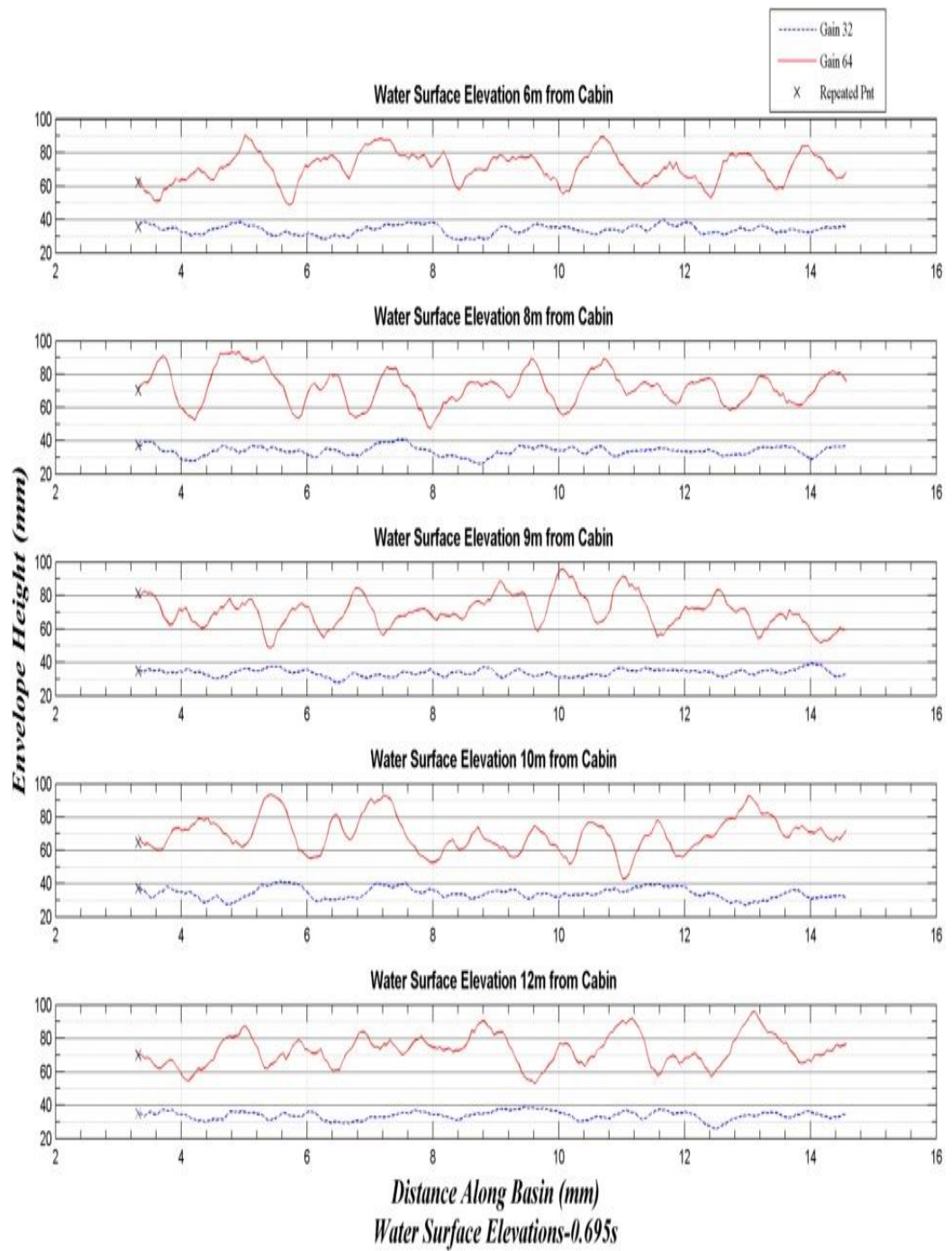
Figure A:1: Water surface envelopes for high and low gain settings, wave period=0.695s.
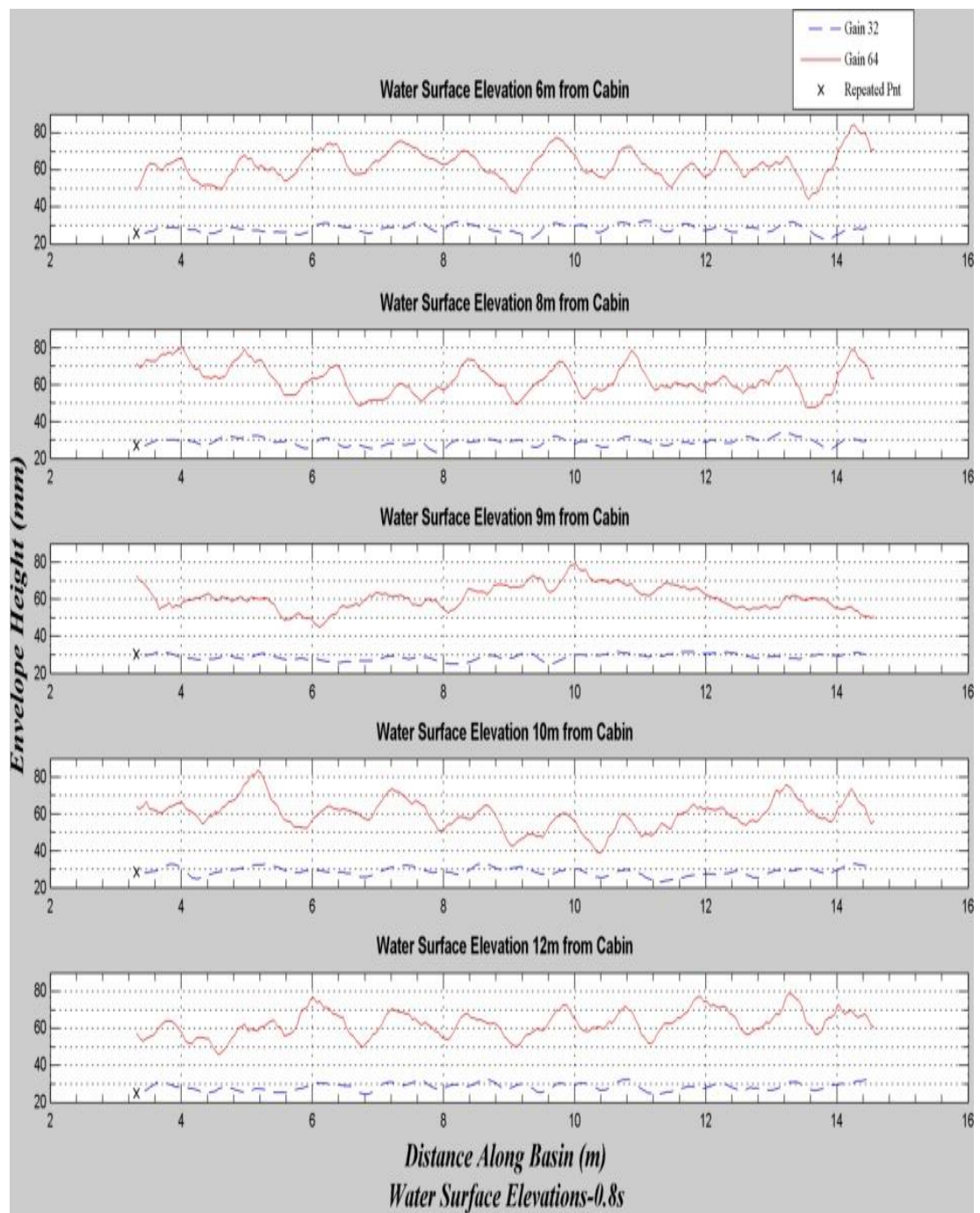
Figure A:2: Water surface envelopes for high and low gain settings, wave period=0.8s.
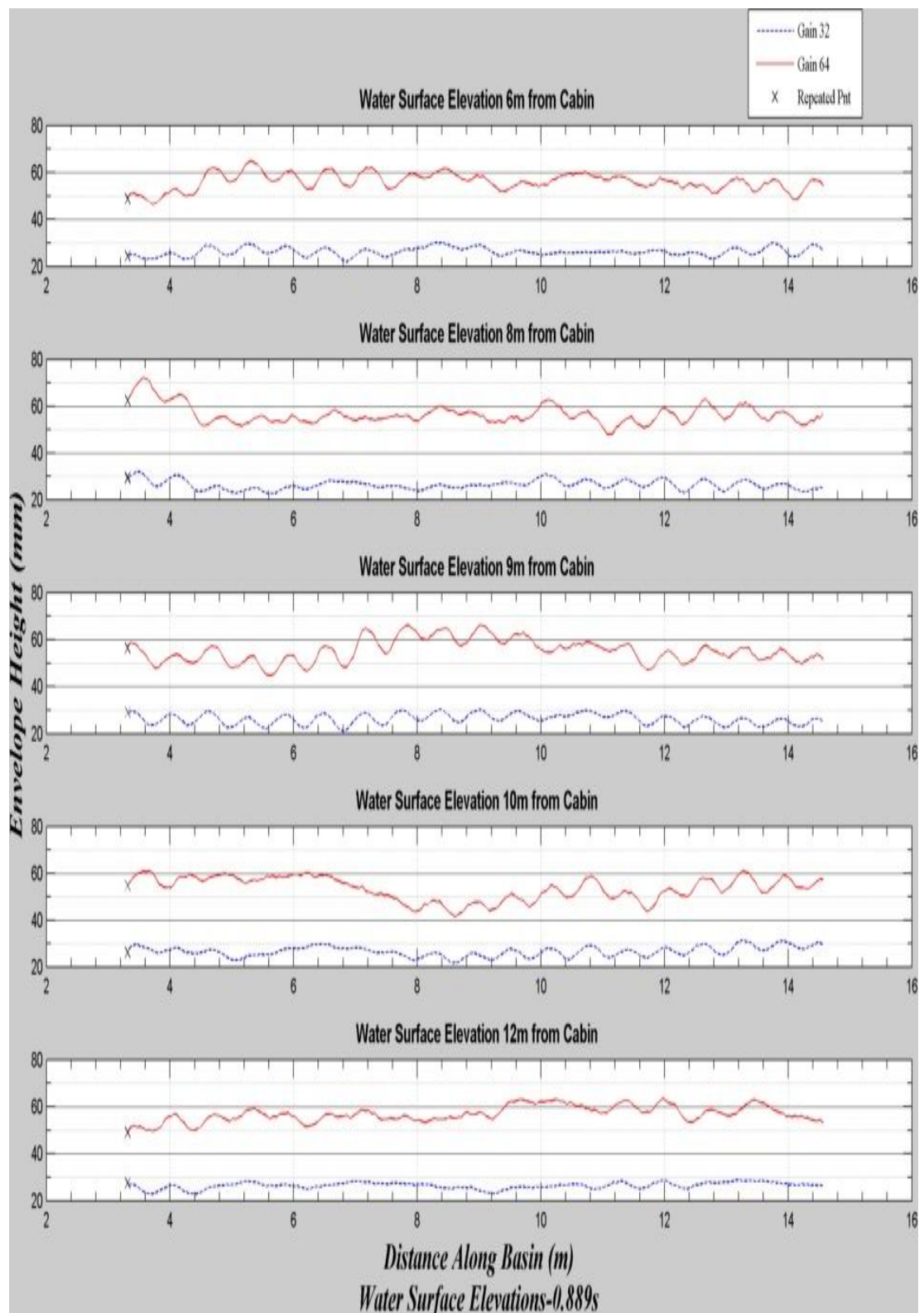
Figure A: 3: Water surface envelopes for high and low gain settings, wave period=0.889s.
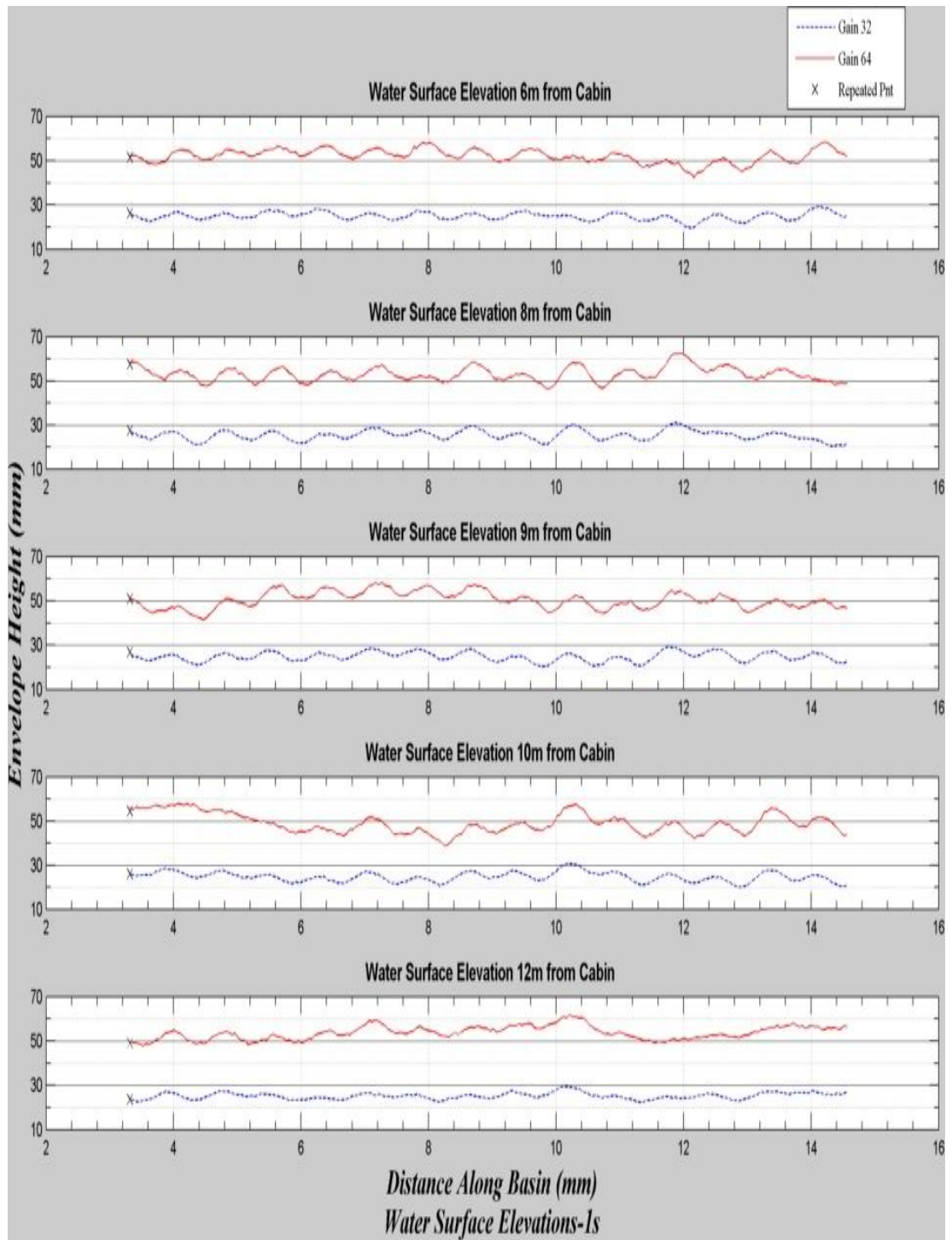
Figure A:4: Water surface envelopes for high and low gain settings, wave period=1.0.
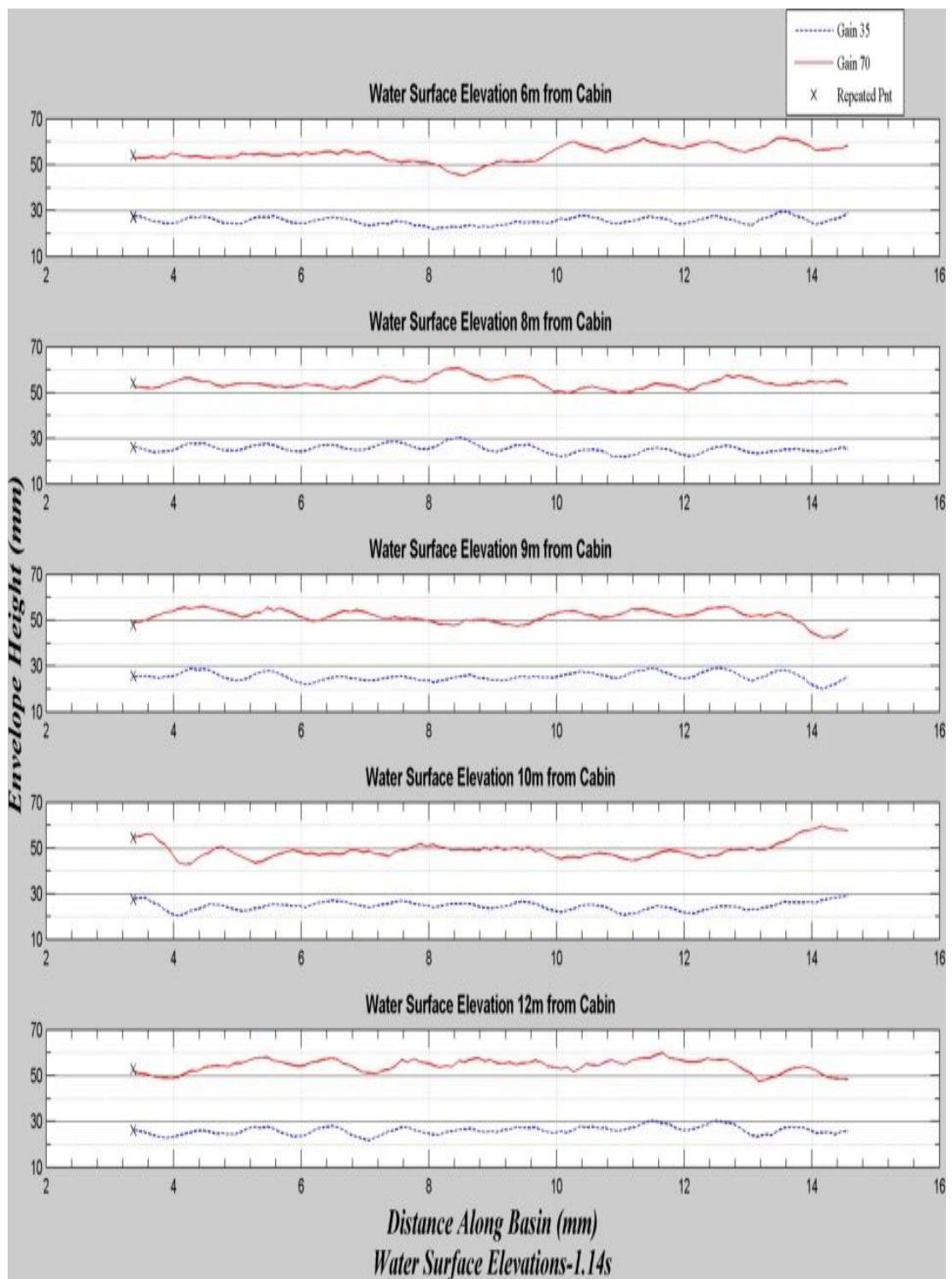
Figure A:5: Water surface envelopes for high and low gain settings, wave period=1.14s.
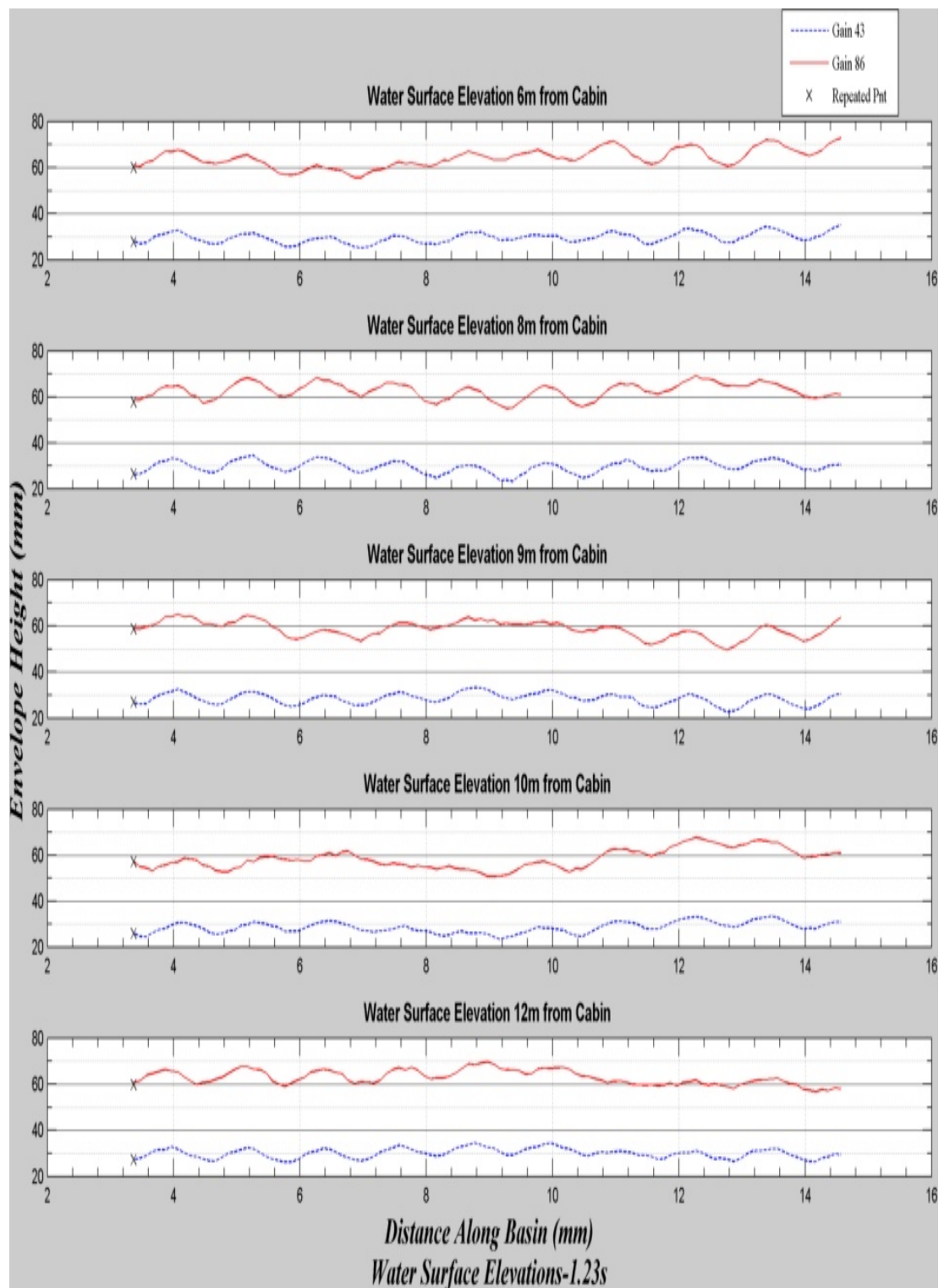
Figure A:6: Water surface envelopes for high and low gain settings, wave period=1.23s.
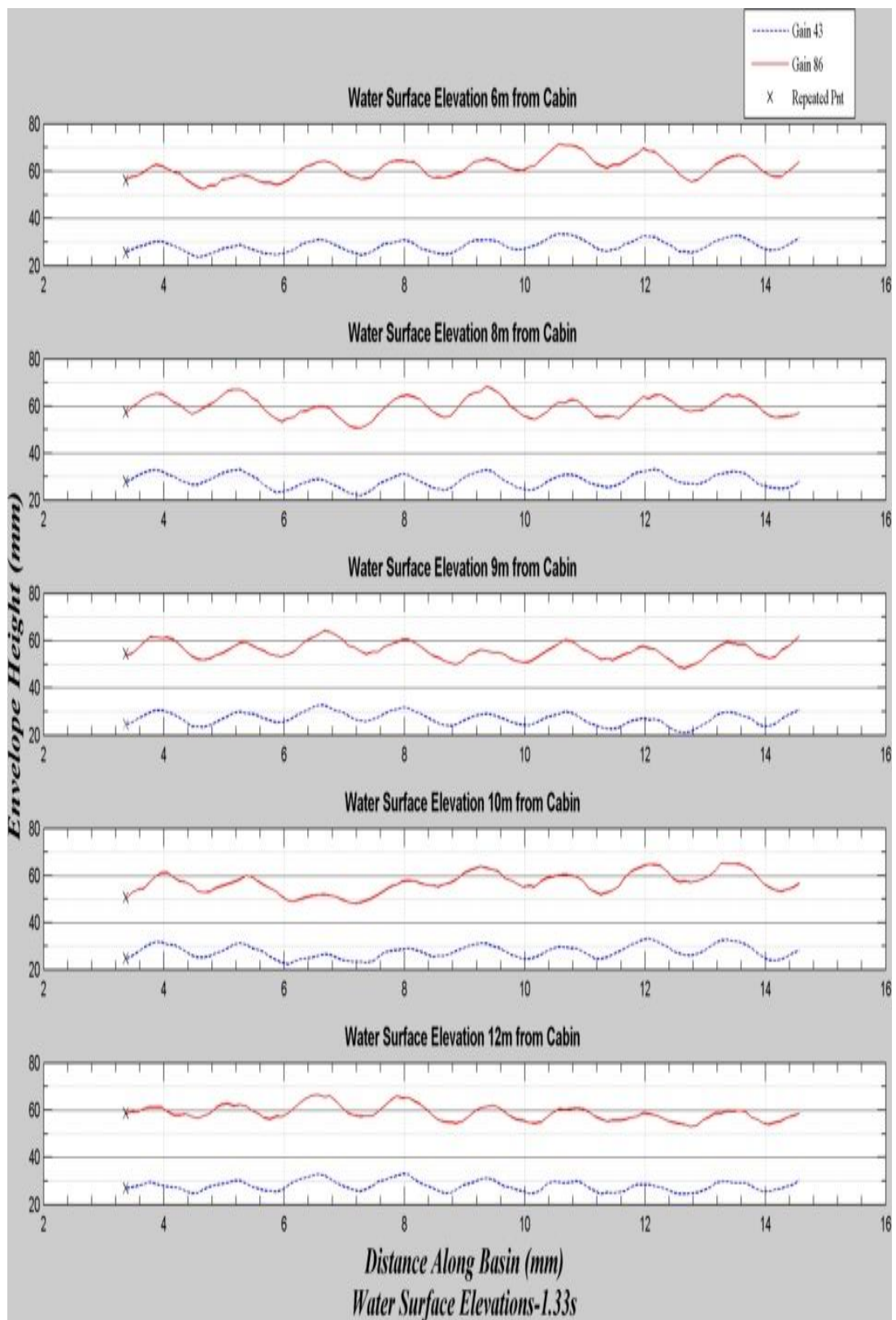
Figure A:7: Water surface envelopes for high and low gain settings, wave period=1.33s.
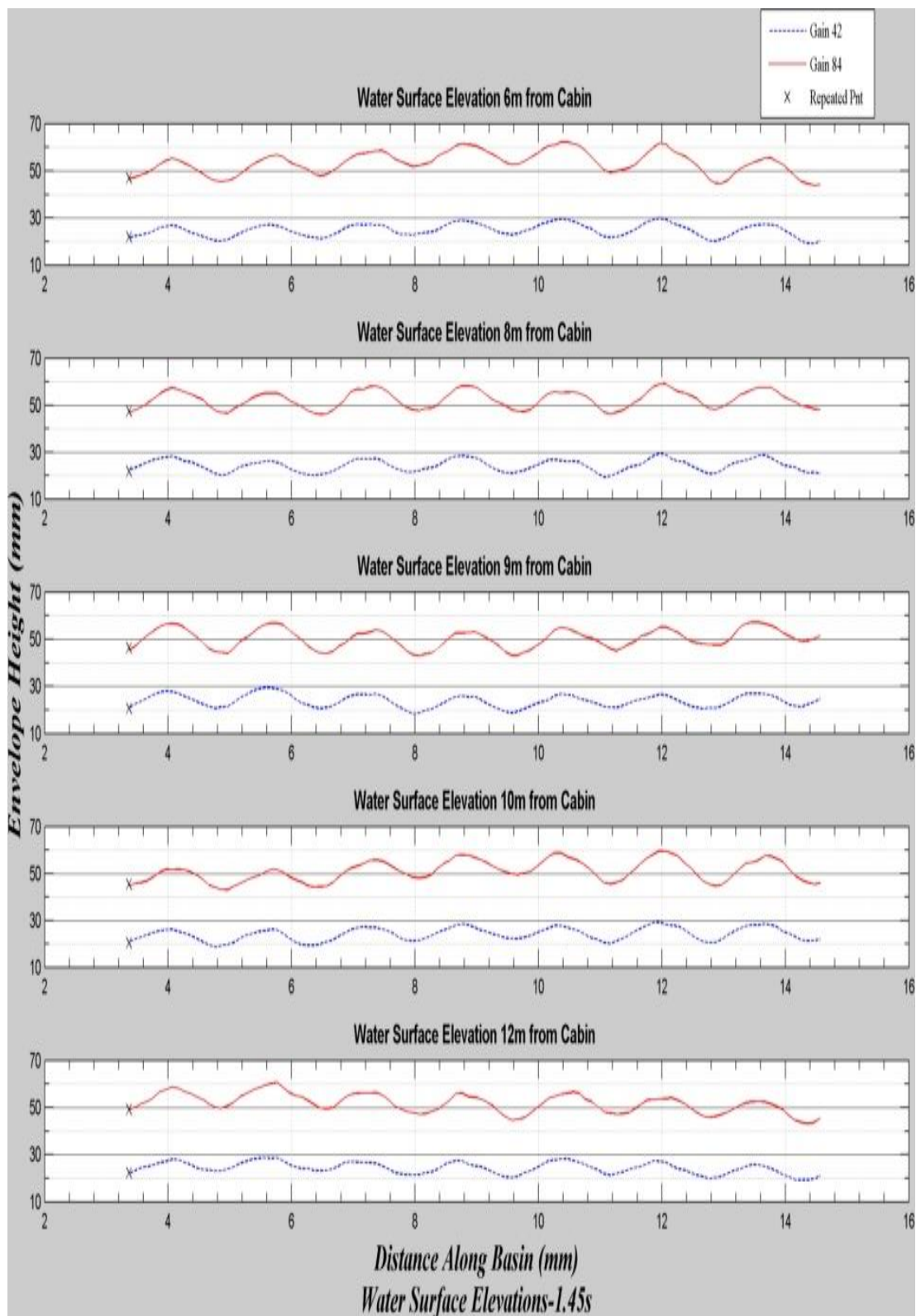
Figure A:8: Water surface envelopes for high and low gain settings, wave period=1.45s.
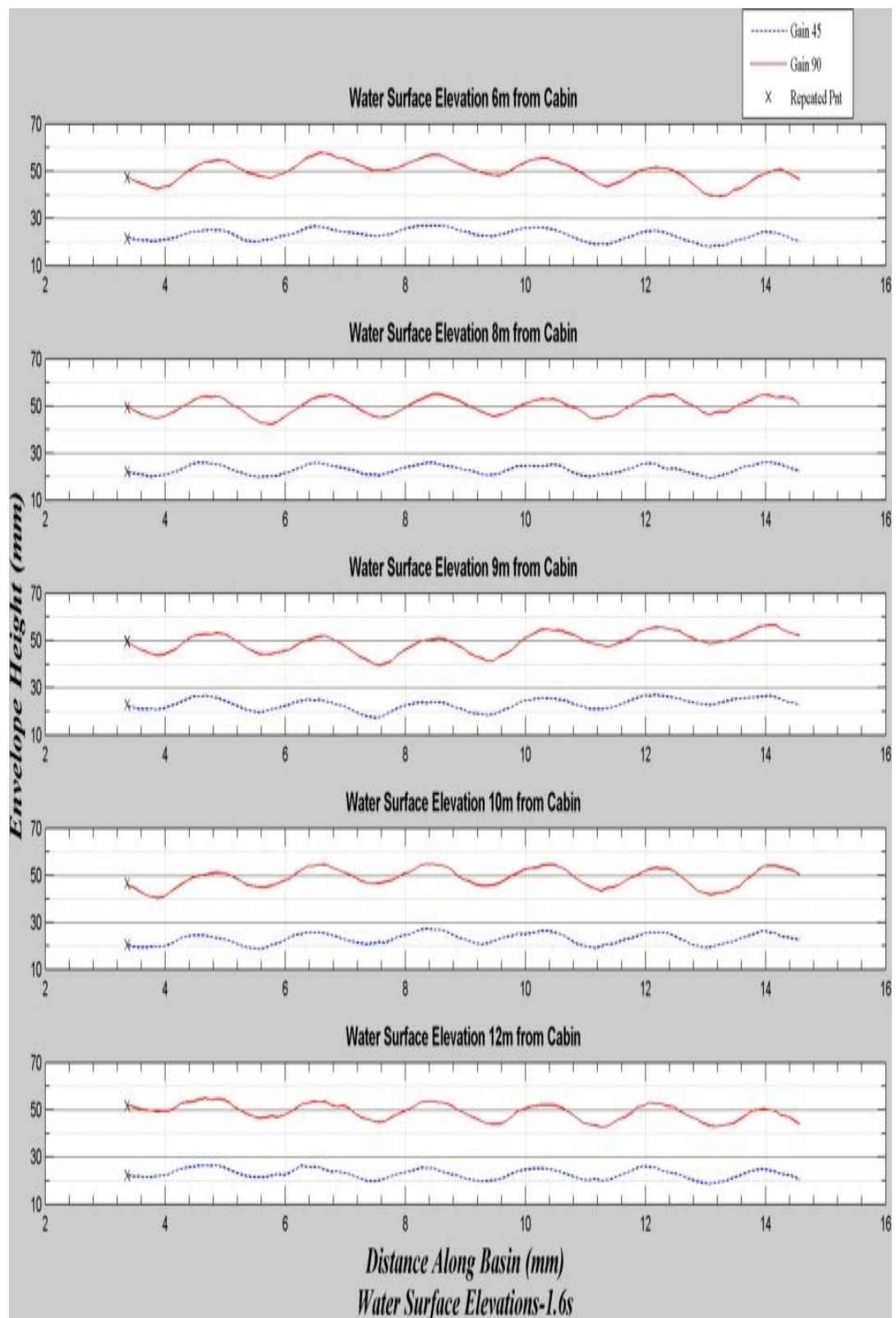
Figure A:9: Water surface envelopes for high and low gain settings, wave period=1.6s.
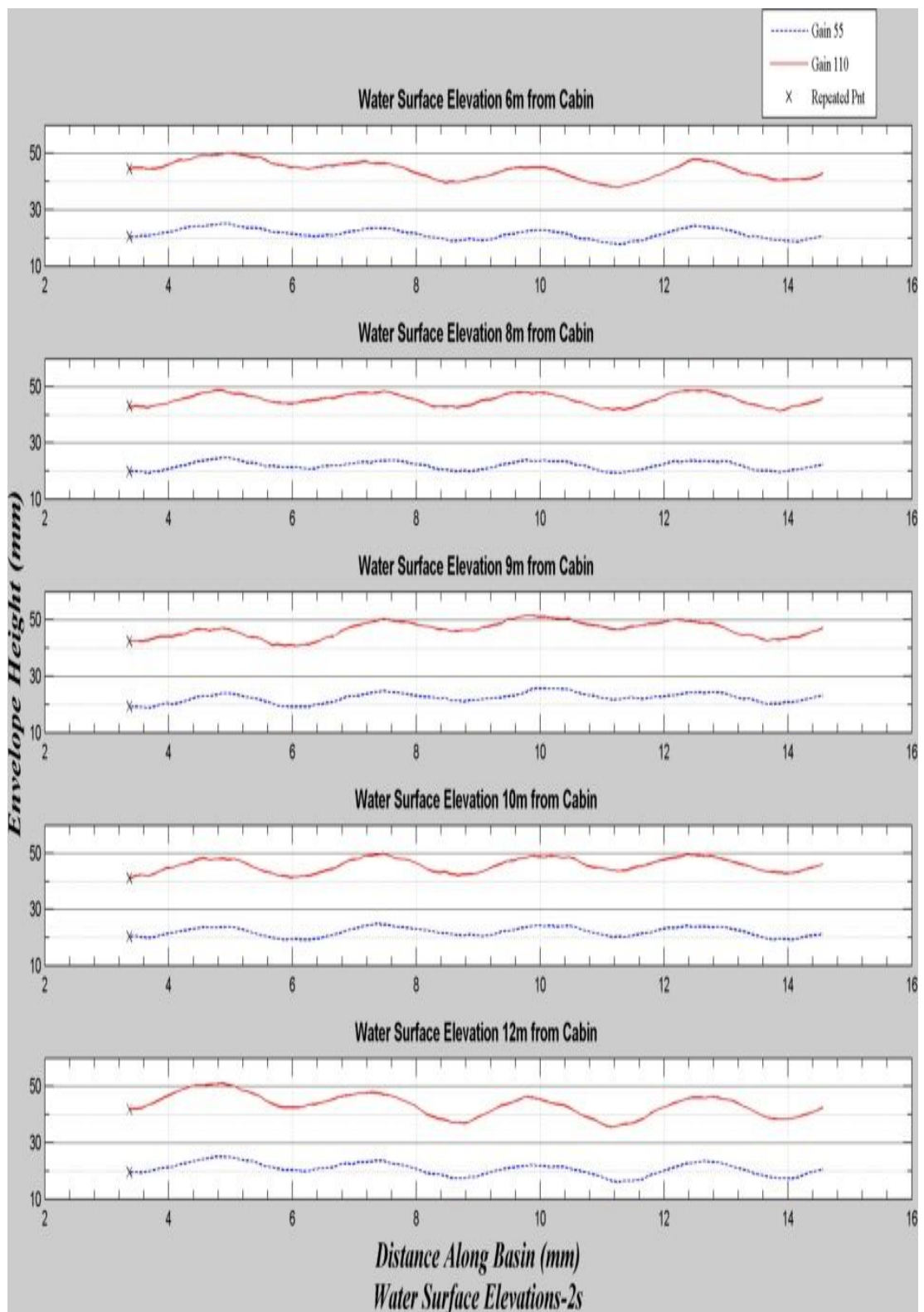
Figure A:10: Water surface envelopes for high and low gain settings, wave period=2.0s.
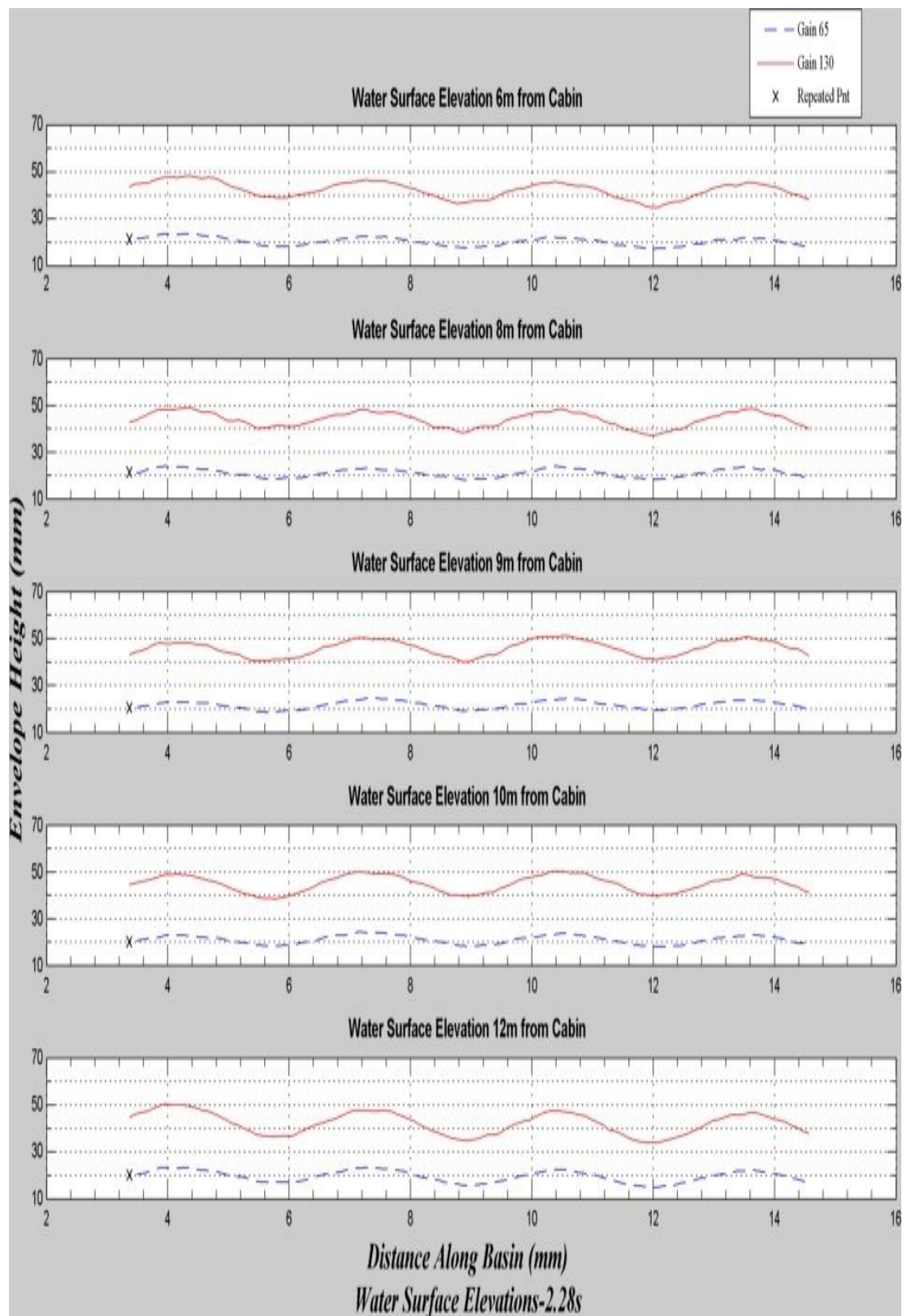
Figure A:11: Water surface envelopes for high and low gain settings, wave period=2.28s.
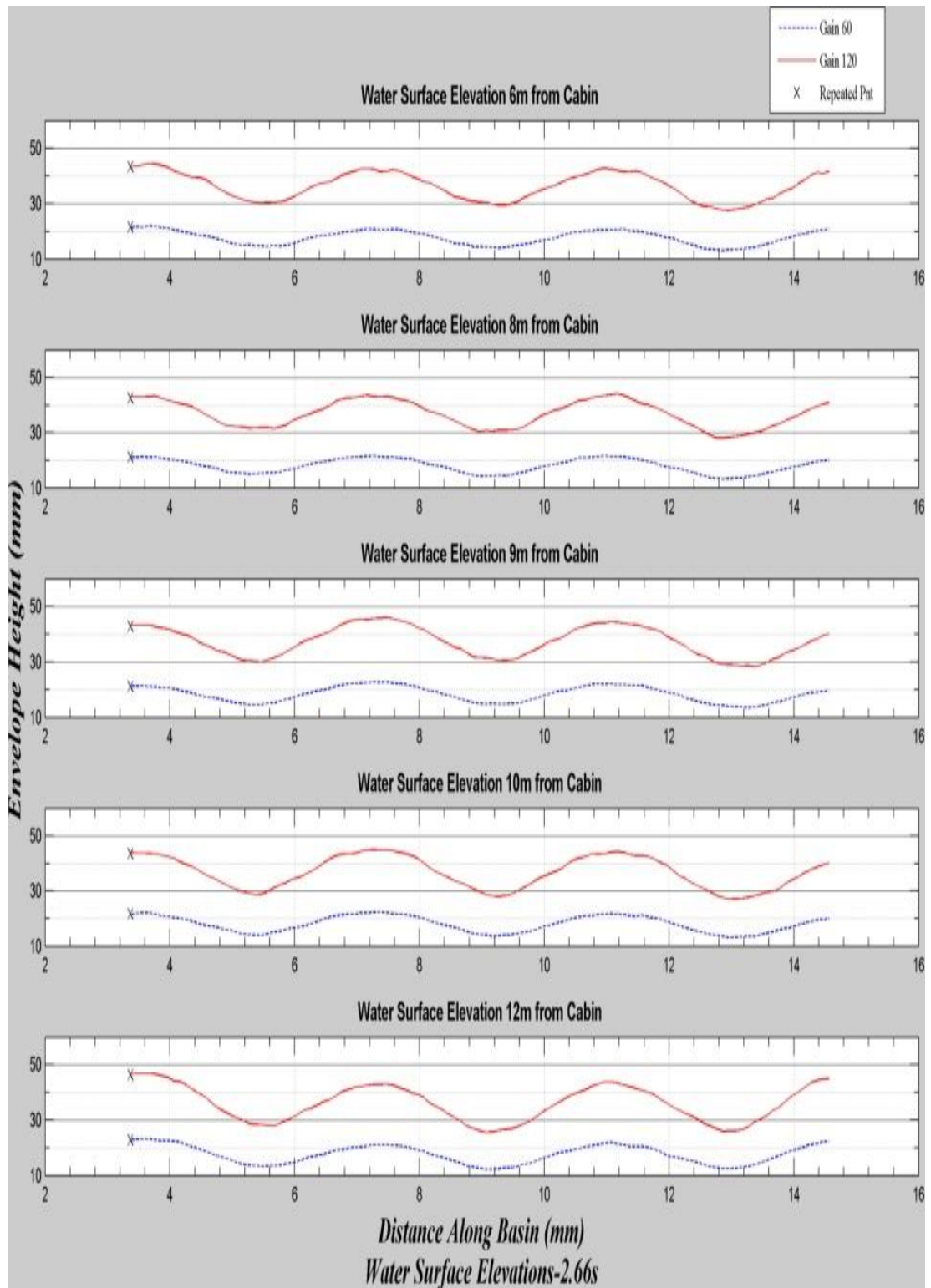
Figure A:12: Water surface envelopes for high and low gain settings, wave period=2.66s.
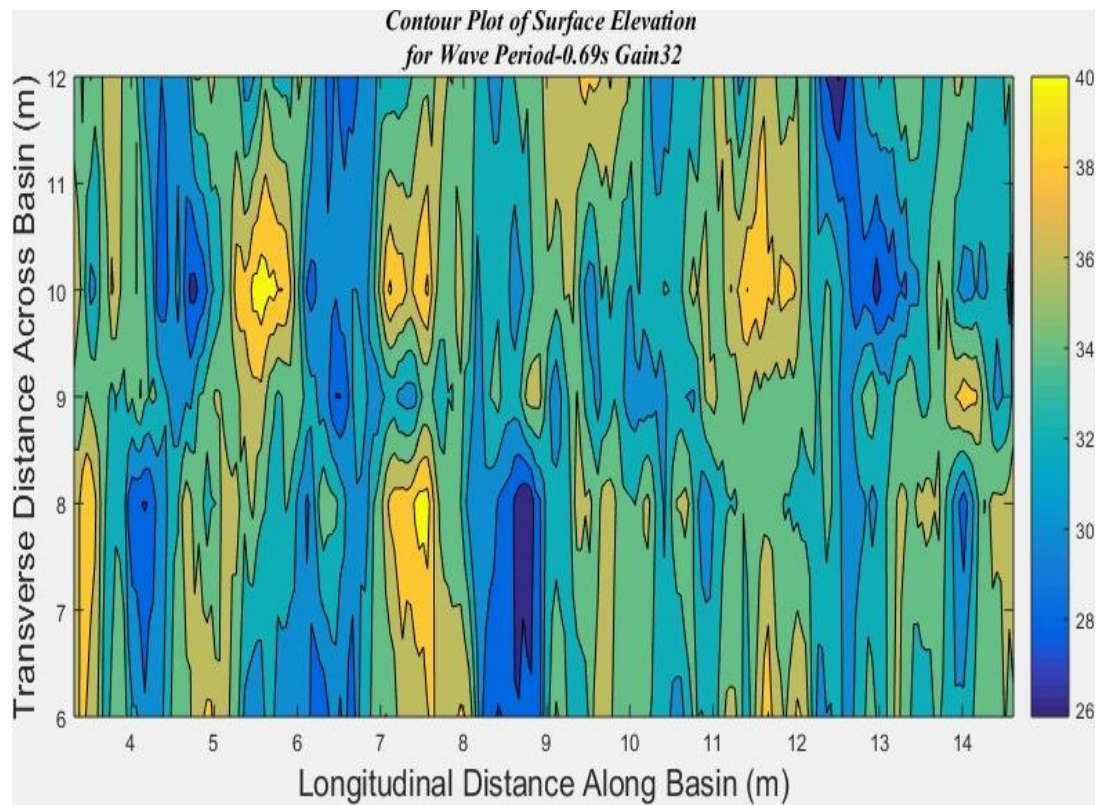
Figure A:13: 3D surface plot, low gain, wave period =0.695s
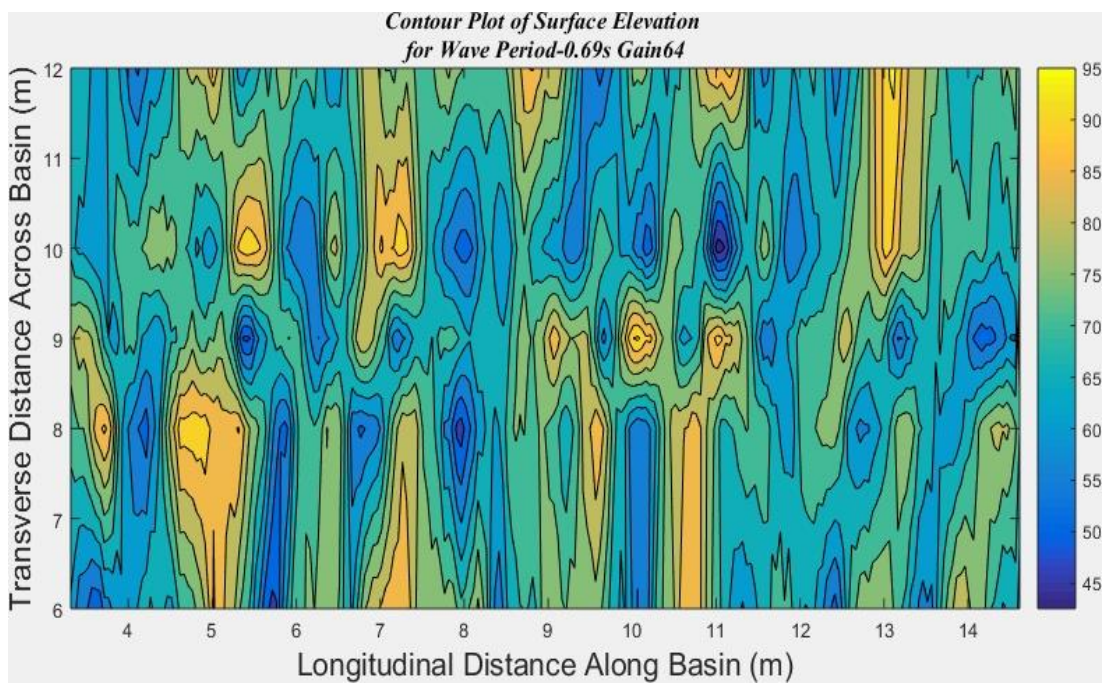
Figure A:14: 3D surface plot, high gain, wave period =0.695s
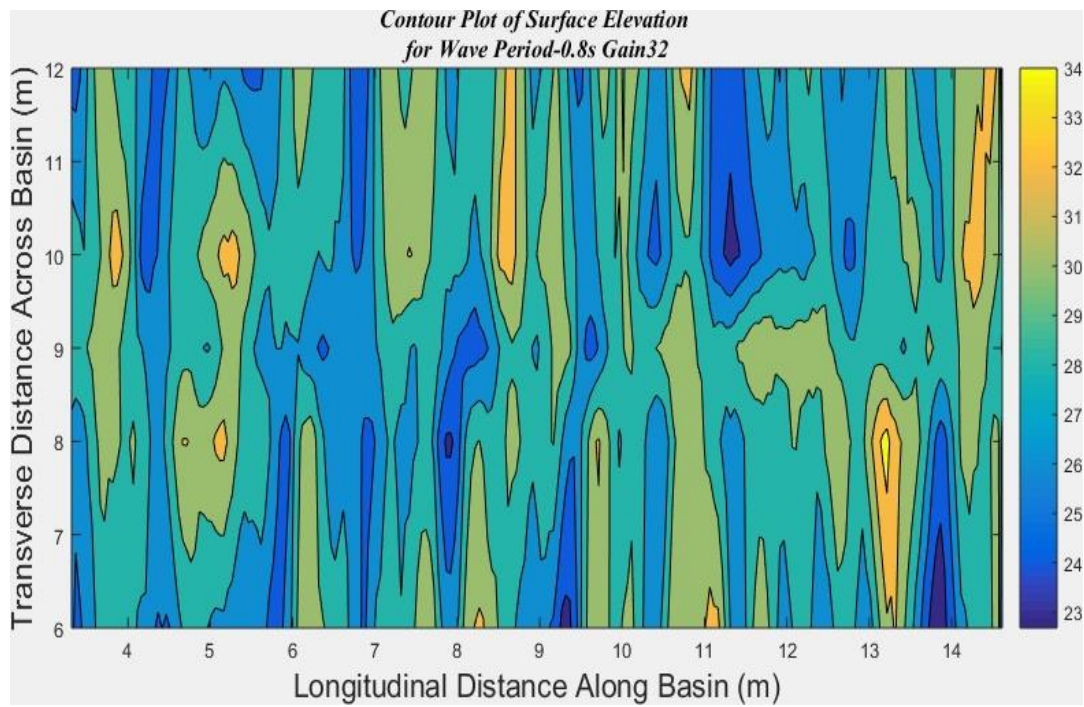
Figure A:15: 3D surface plot, low gain, wave period =0.8s
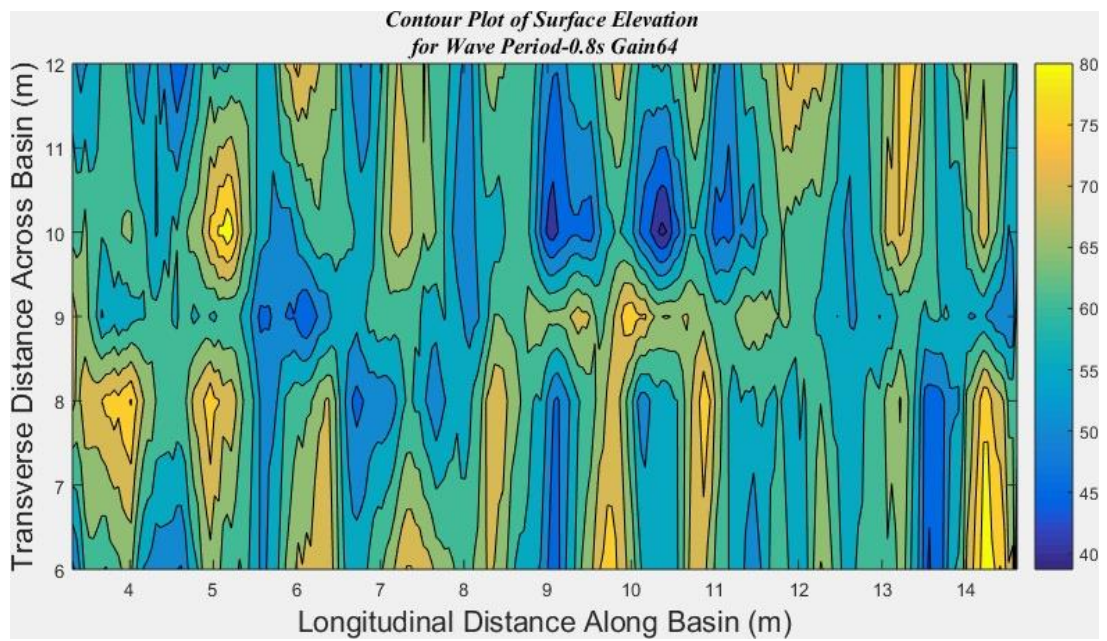
Figure A:16: 3D surface plot, high gain, wave period =0.8s
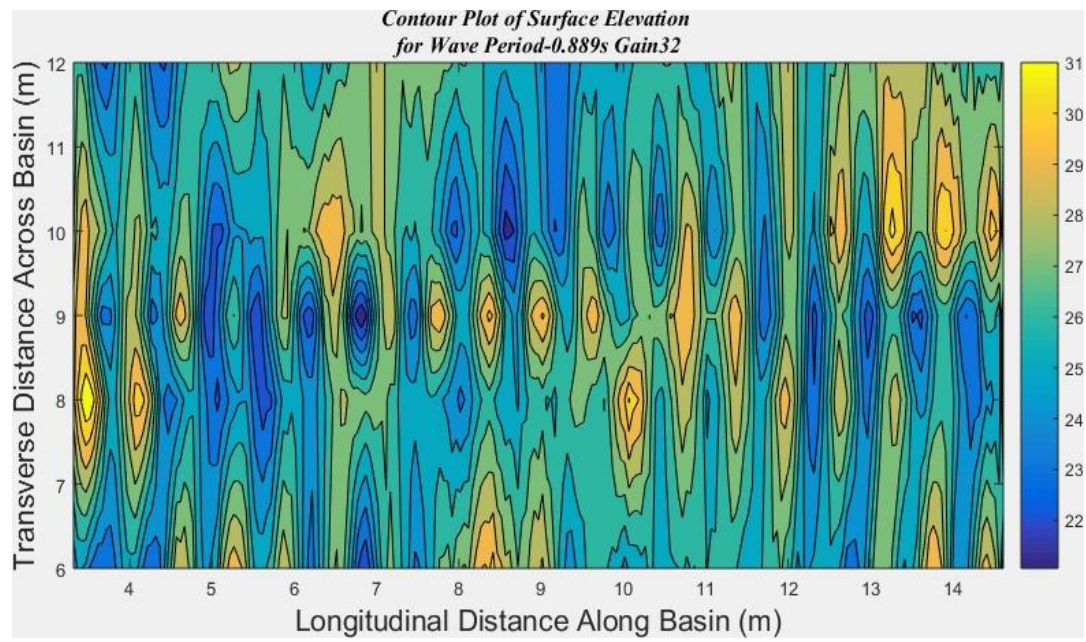
Figure A:17: 3D surface plot, low gain, wave period =0.889s
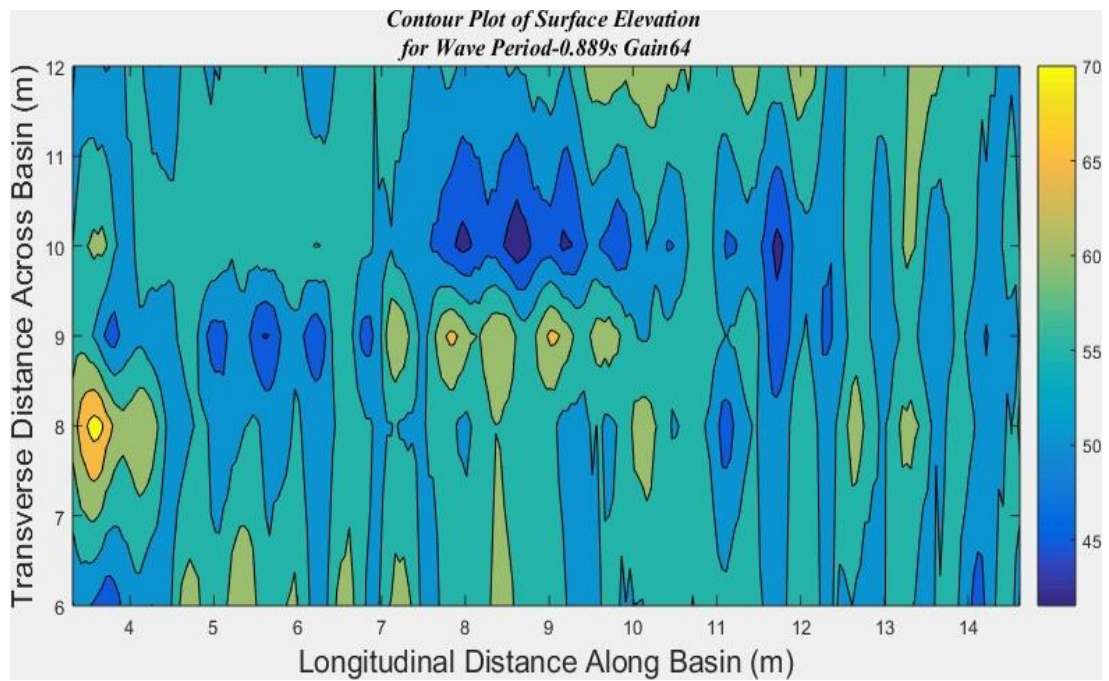
Figure A:18: 3D surface plot, high gain, wave period =0.889s
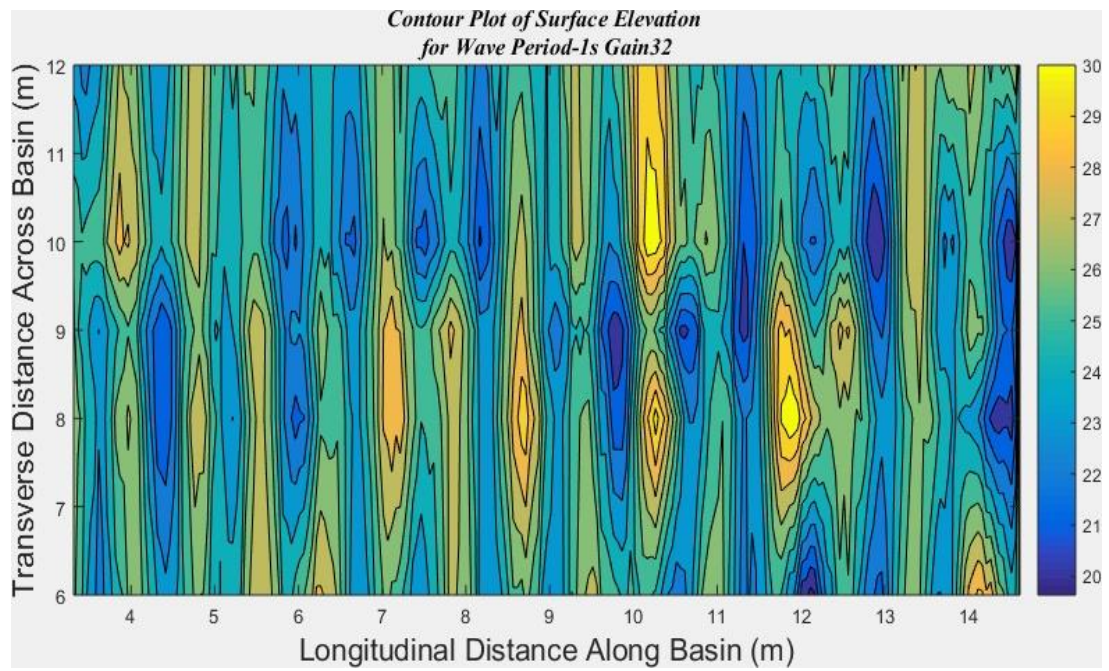
Figure A:19: 3D surface plot, low gain, wave period =1.0s
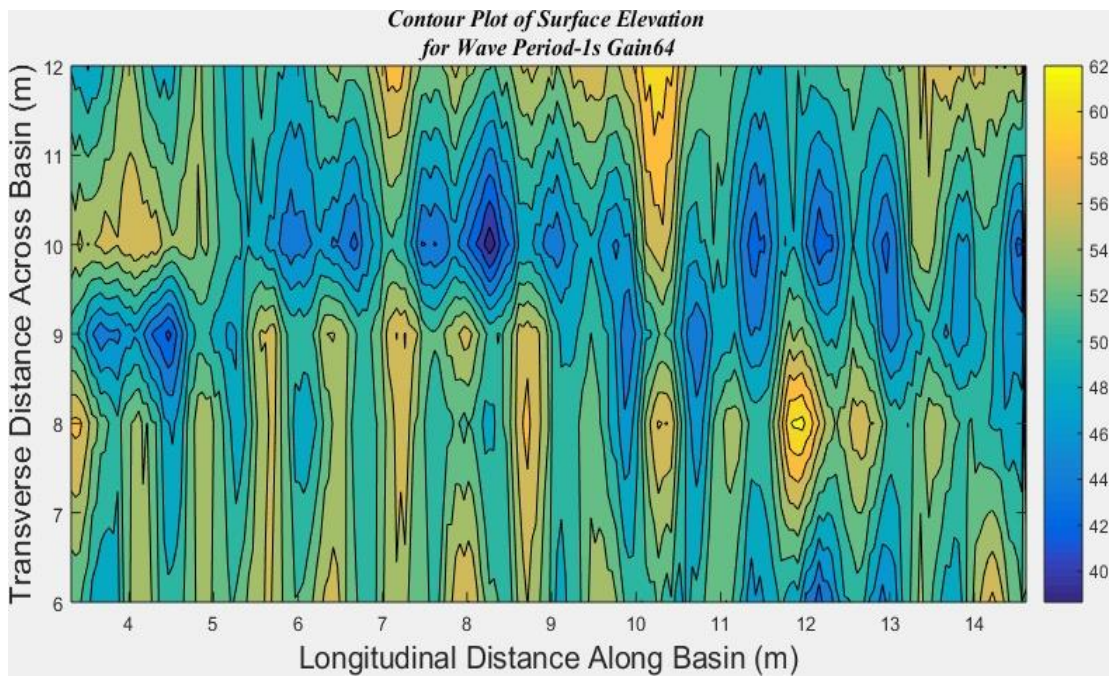
Figure A:20: 3D surface plot, high gain, wave period =1.0s
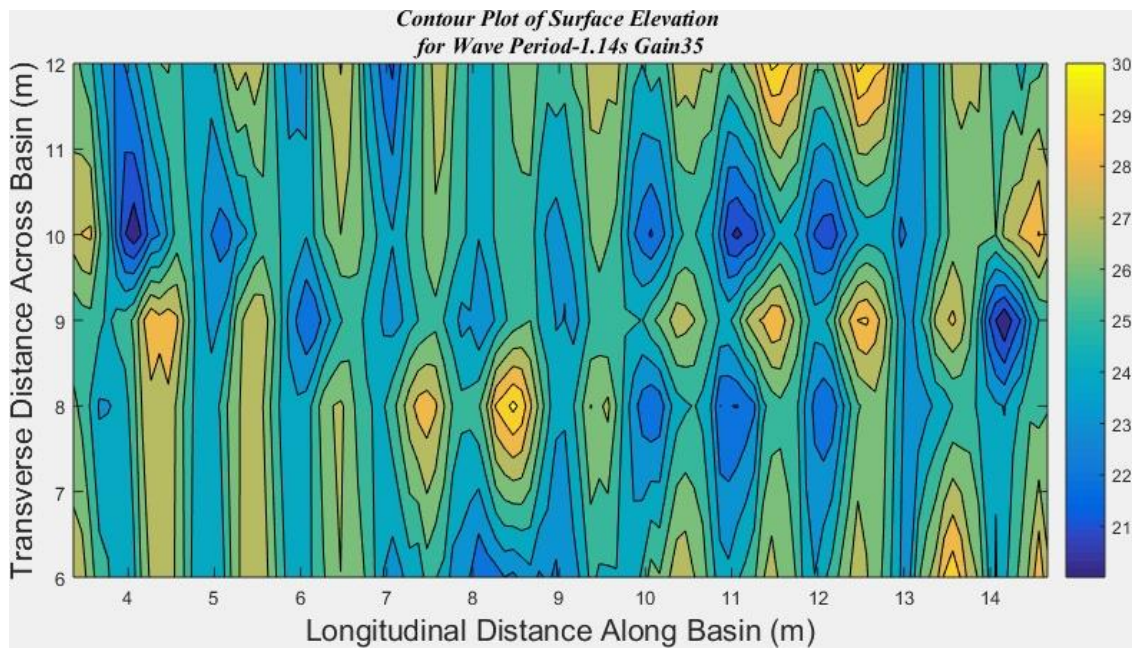
Figure A:21: 3D surface plot, low gain, wave period =1.14s
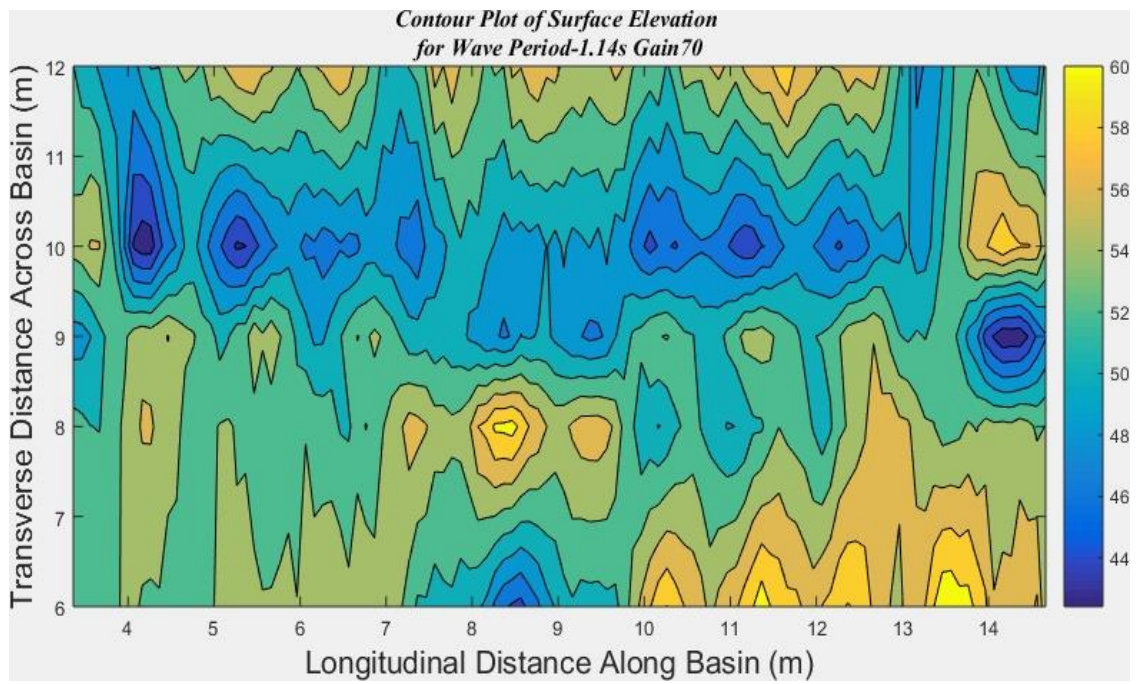
Figure A: 22: 3D surface plot, high gain, wave period =1.14s
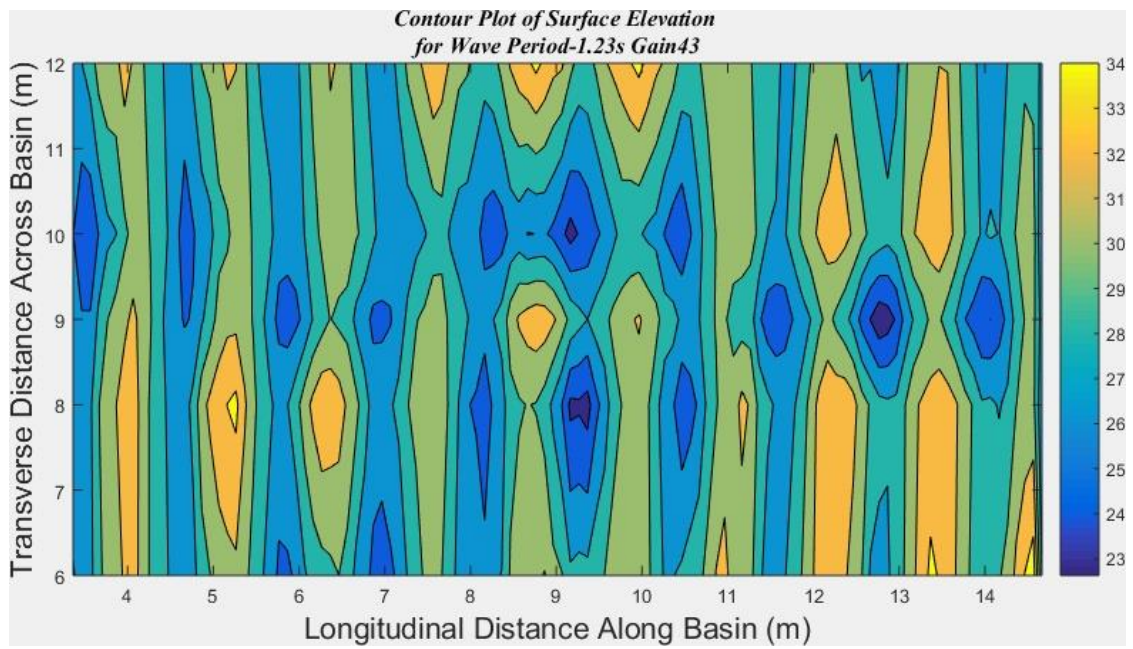
Figure A:23: 3D surface plot, low gain, wave period =1.23s
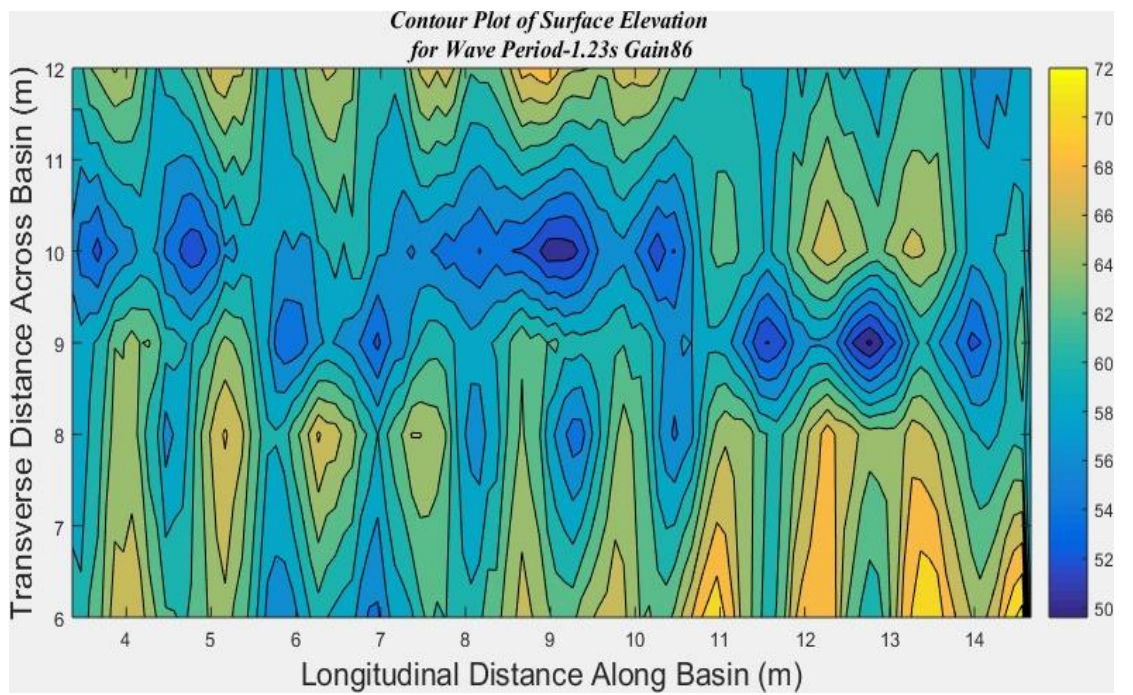
Figure A:24: 3D surface plot, high gain, wave period =1.23s
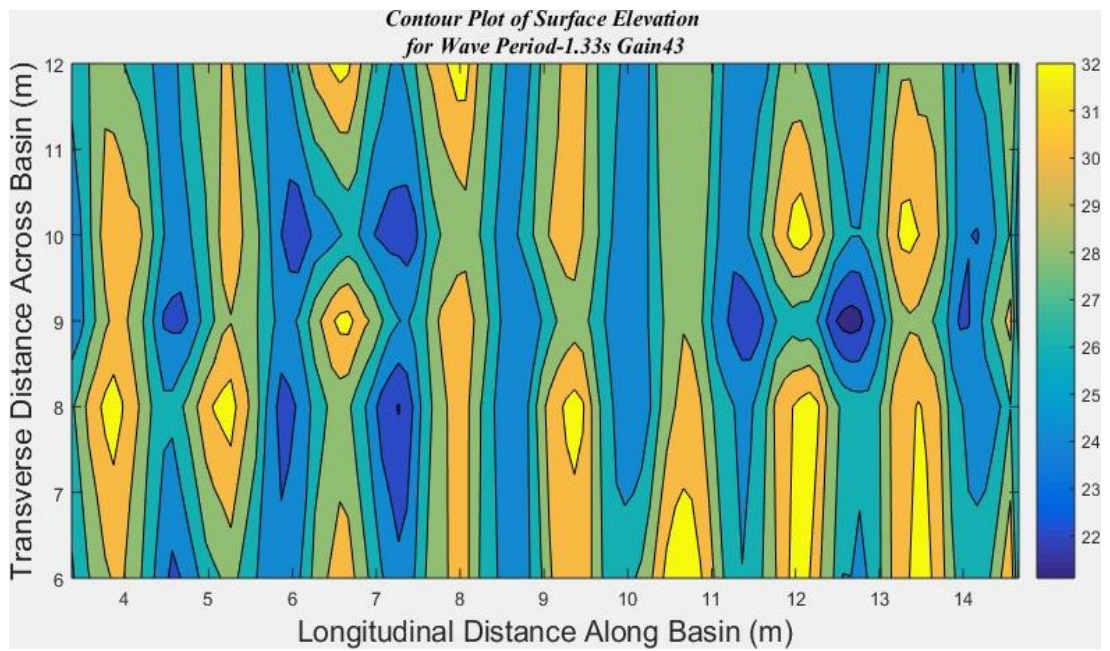
Figure A:25: 3D surface plot, low gain, wave period =1.33s
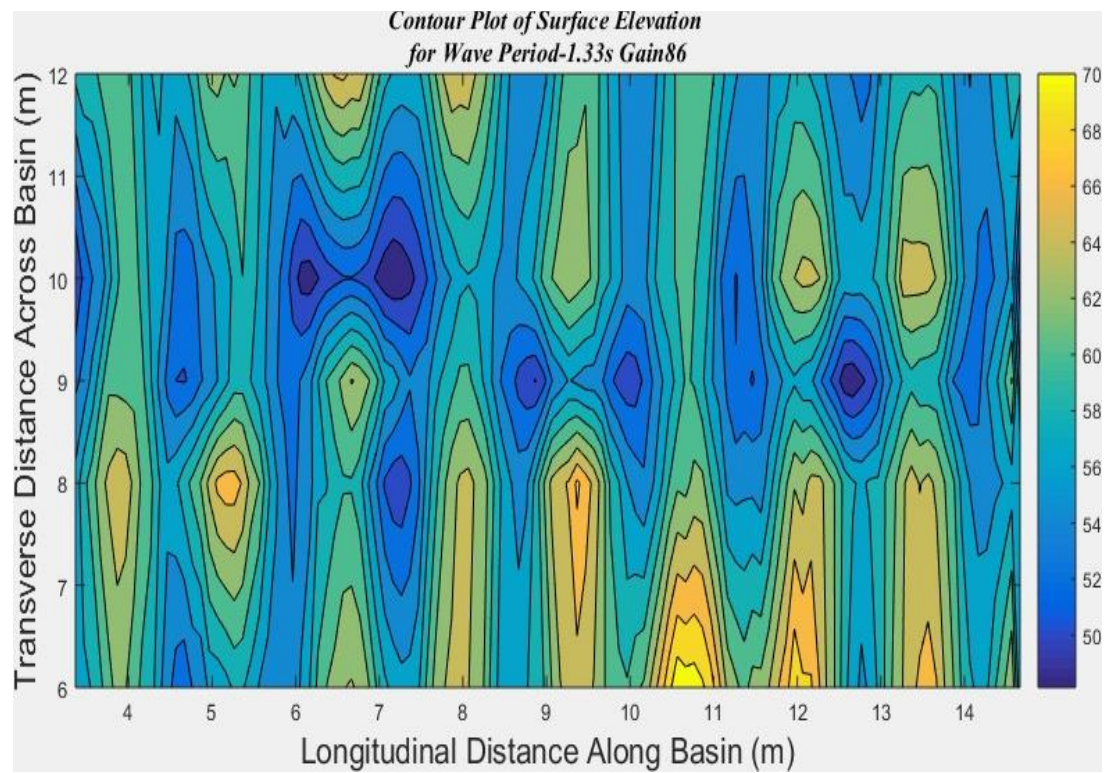
Figure A:26: 3D surface plot, high gain, wave period =1.33s
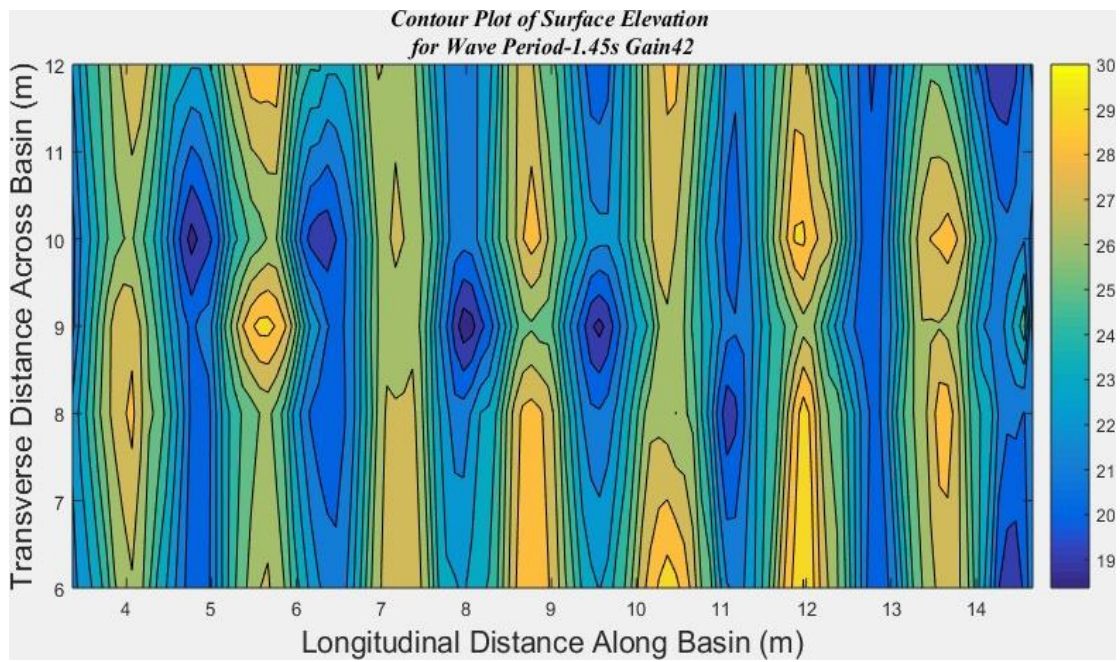
Figure A:27: 3D surface plot, low gain, wave period =1.45s
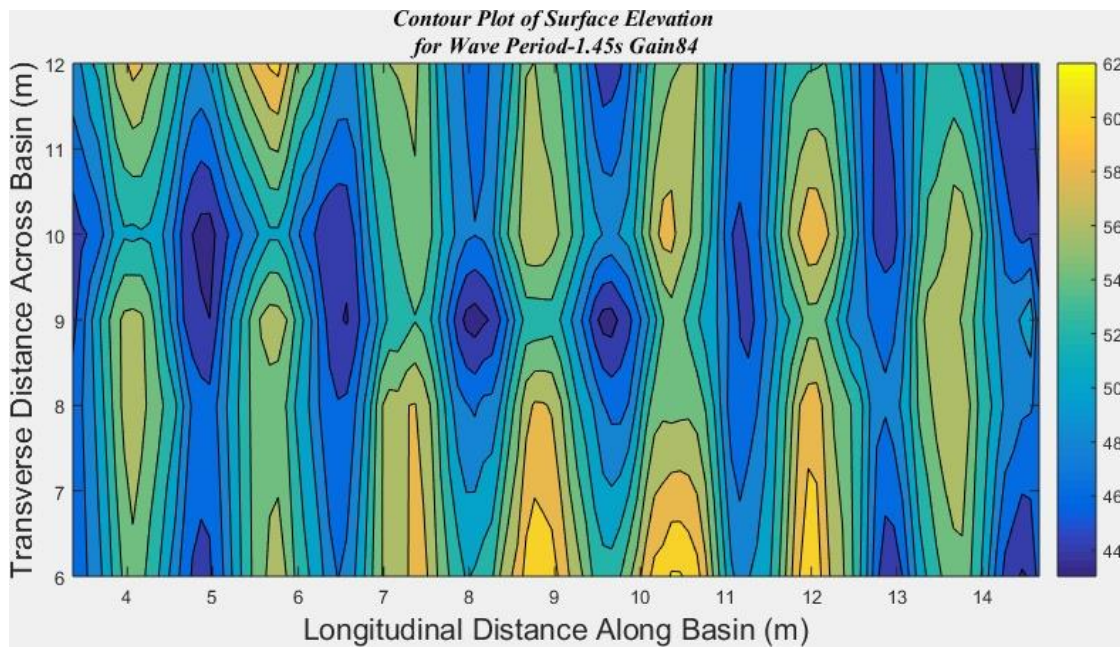
Figure A:28: 3D surface plot, high gain, wave period =1.45s
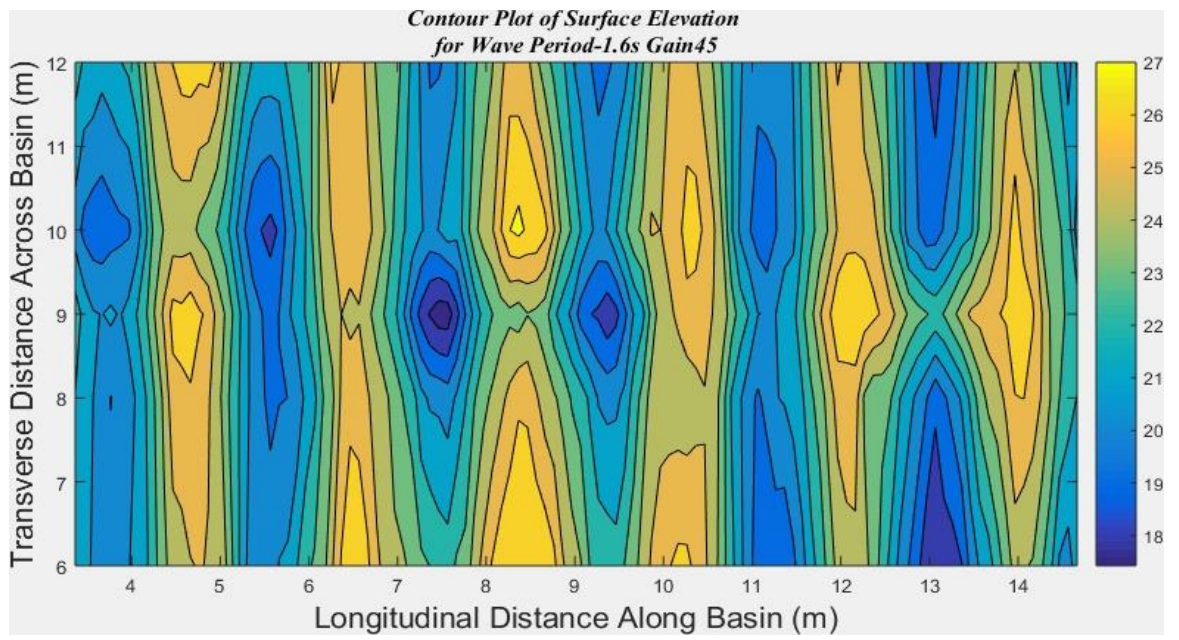
Figure A:29: 3D surface plot, low gain, wave period =1.6s
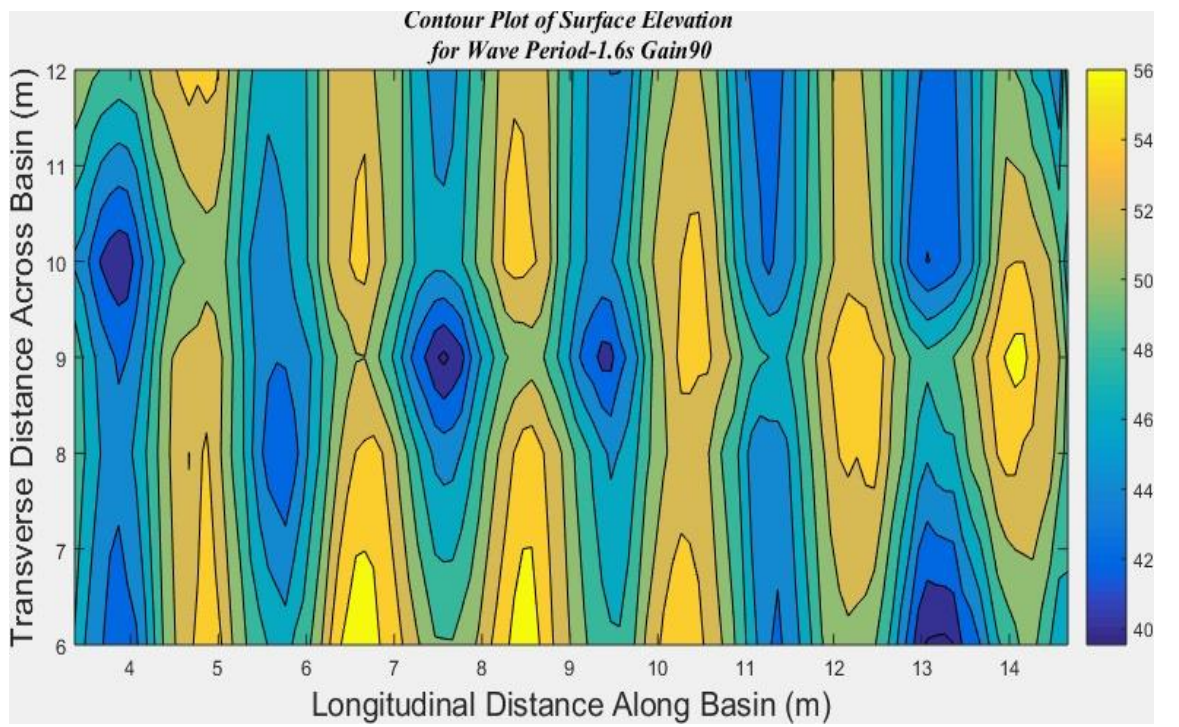
Figure A:30: 3D surface plot, high gain, wave period =1.6s
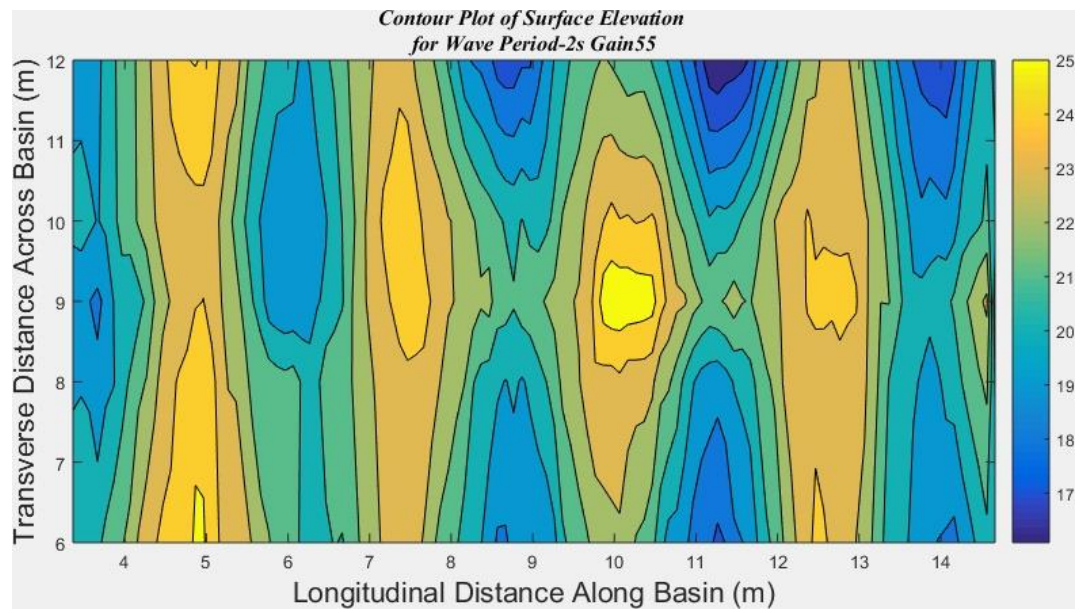
Figure A:31: 3D surface plot, low gain, wave period =2.0s
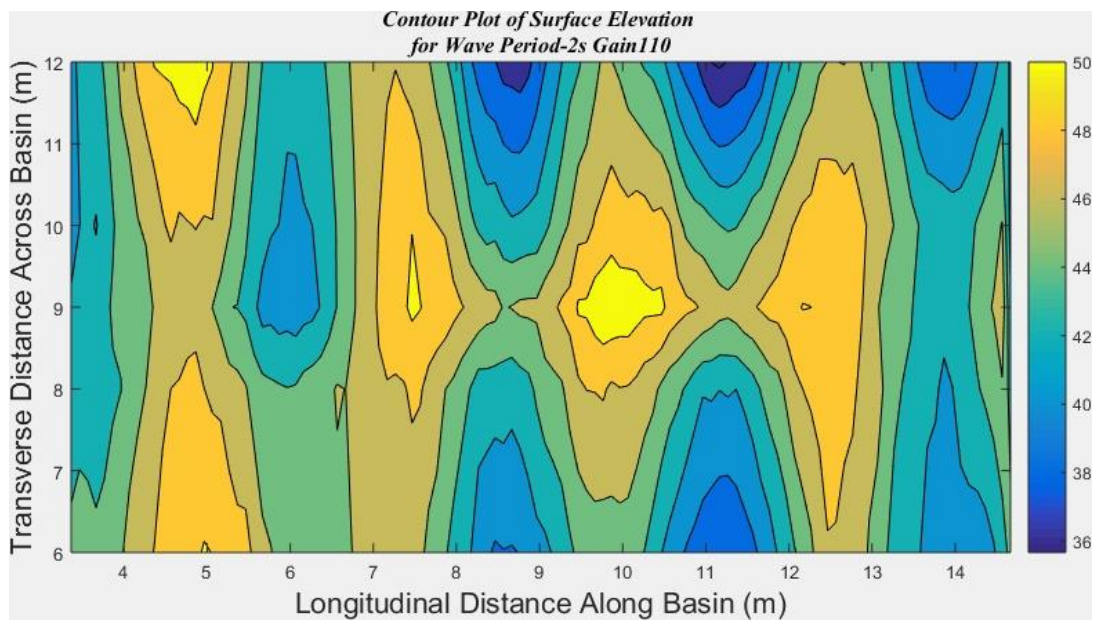
Figure A:32: 3D surface plot, high gain, wave period =2.0s

295
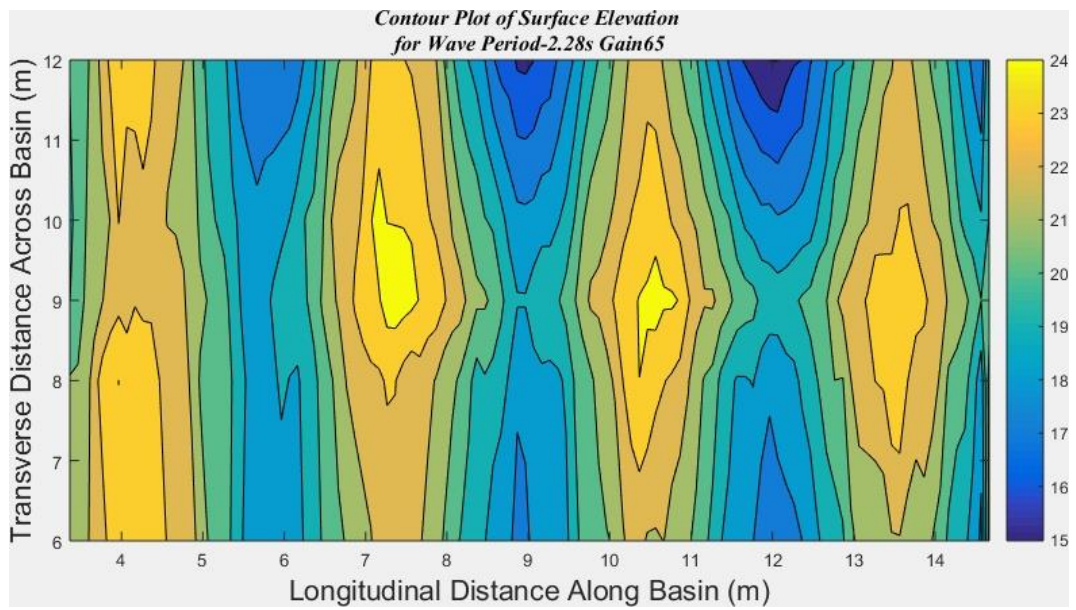
Figure A:33: 3D surface plot, low gain, wave period =2.28s
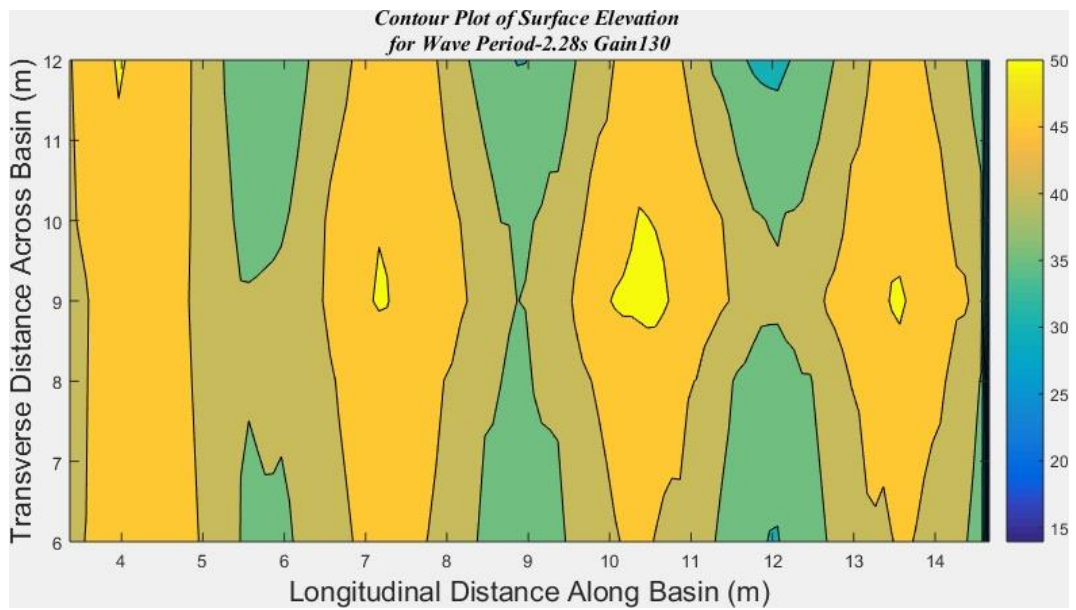
Figure A:34: 3D surface plot, high gain, wave period =2.28s
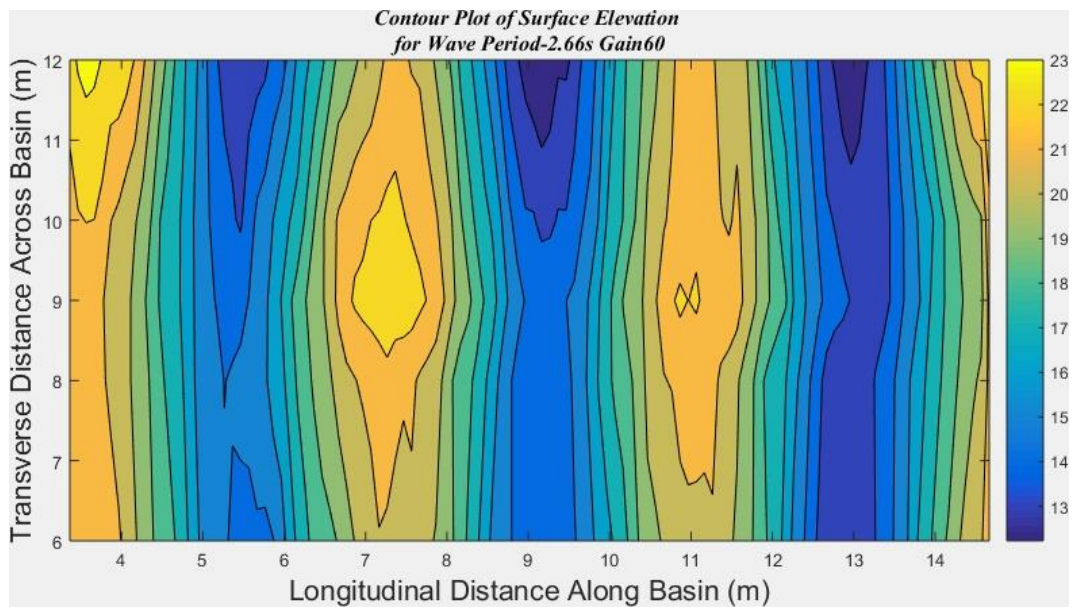
Figure A:35: 3D surface plot, low gain, wave period =2.6s
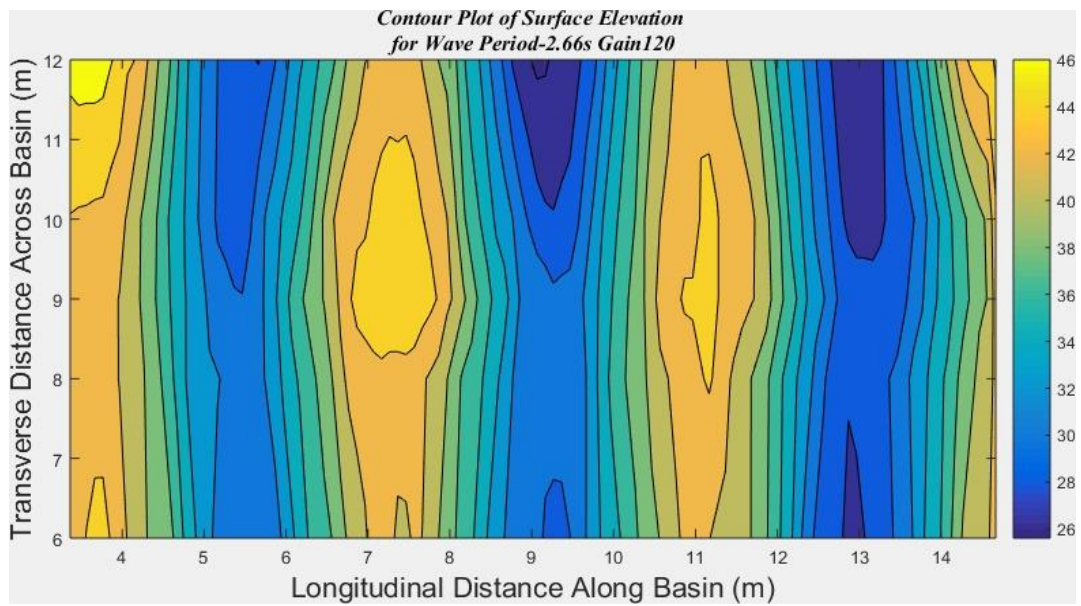
Figure A:36: 3D surface plot, high gain, wave period =2.6s

Appendix B Regular Wave Capture Width Ratios
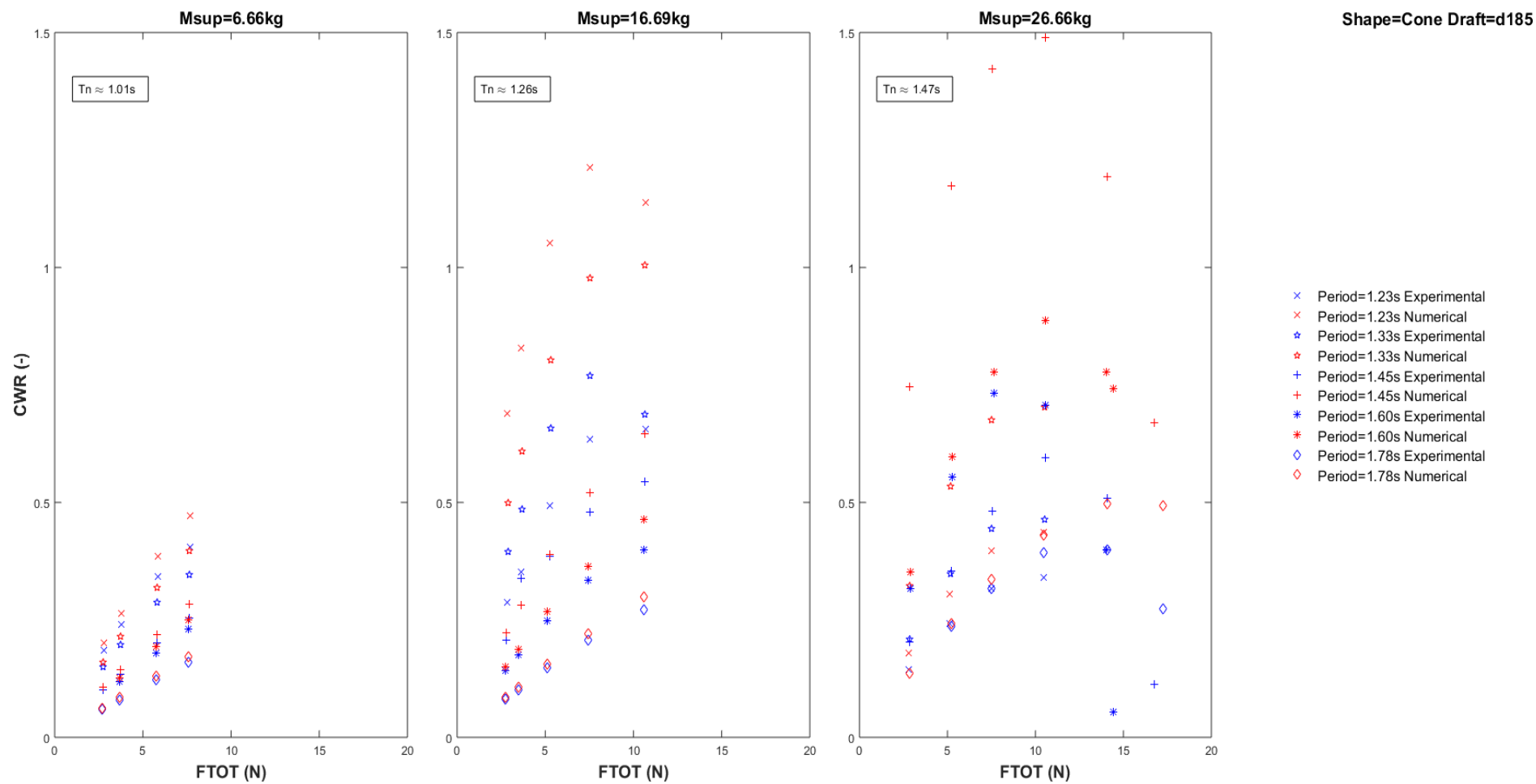
Figure B:1:Capture width ratio vs damping force for constant supplementary mass with varying wave period. Cone-cylinder shape, draft=185mm
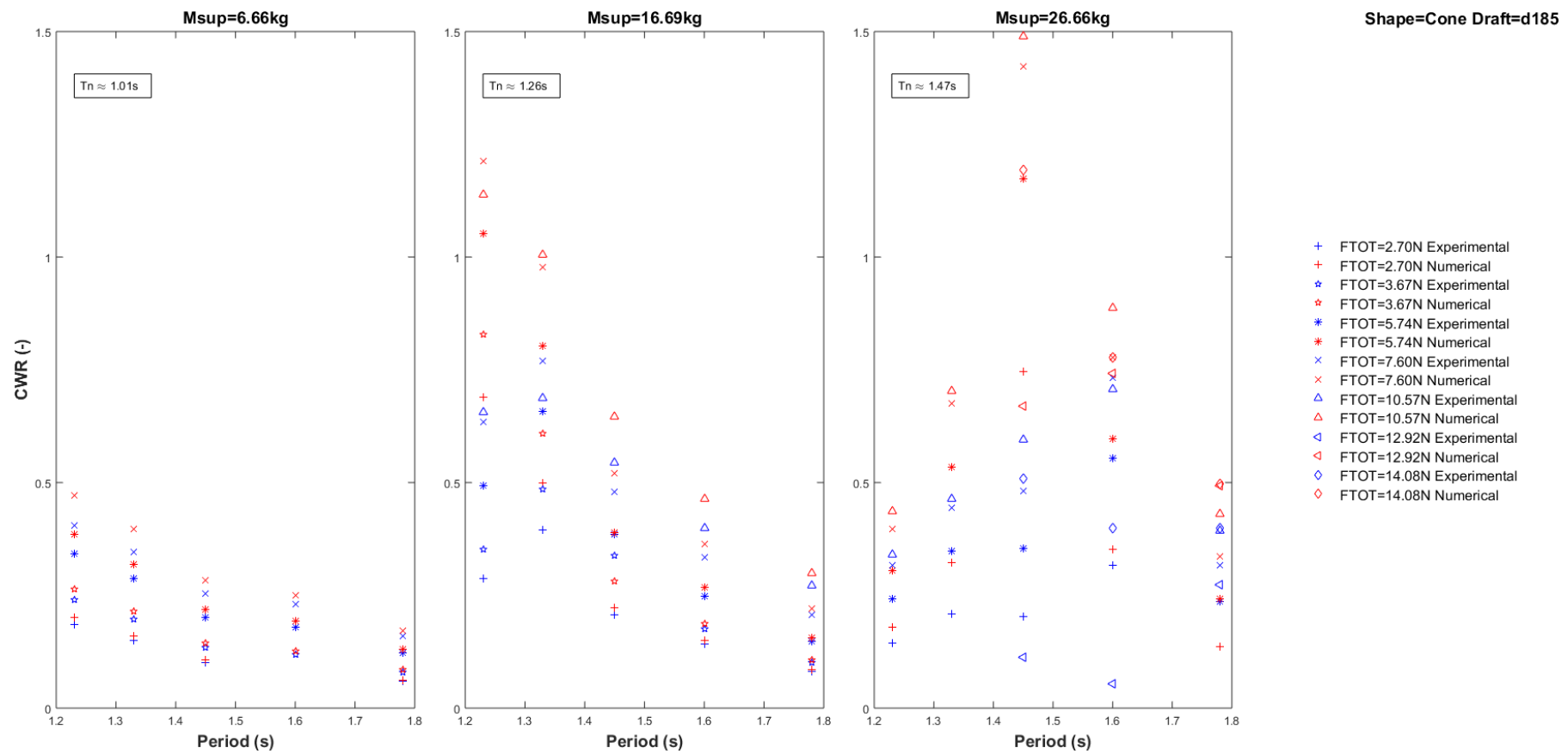
Figure B:2: Capture width ratio vs wave period for constant supplementary mass with varying damping force. Cone-cylinder shape, draft=185mm
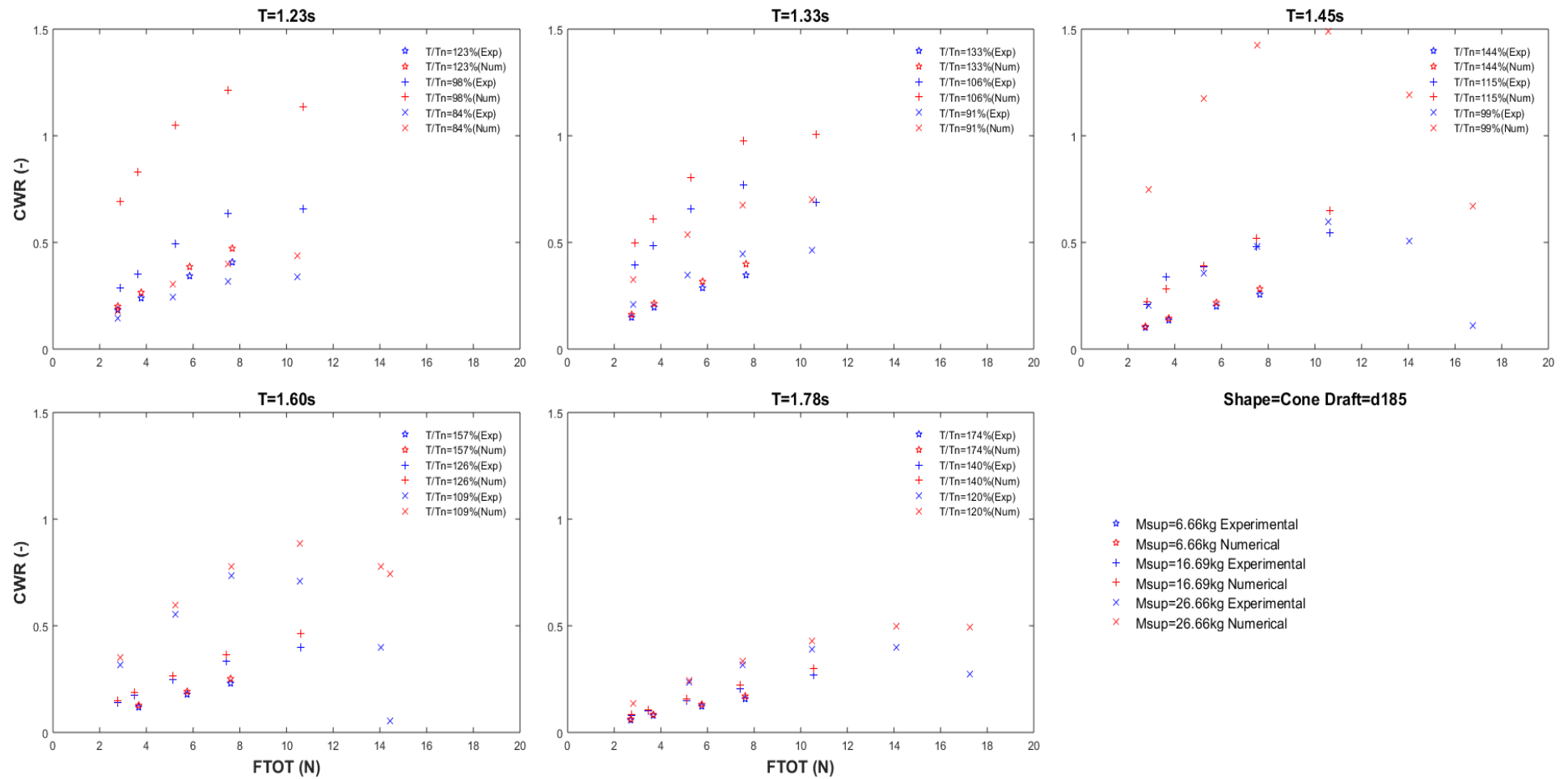
Figure B:3: Capture width ratio vs damping force for constant wave period with varying supplementary mass. Cone-cylinder shape, draft=185mm
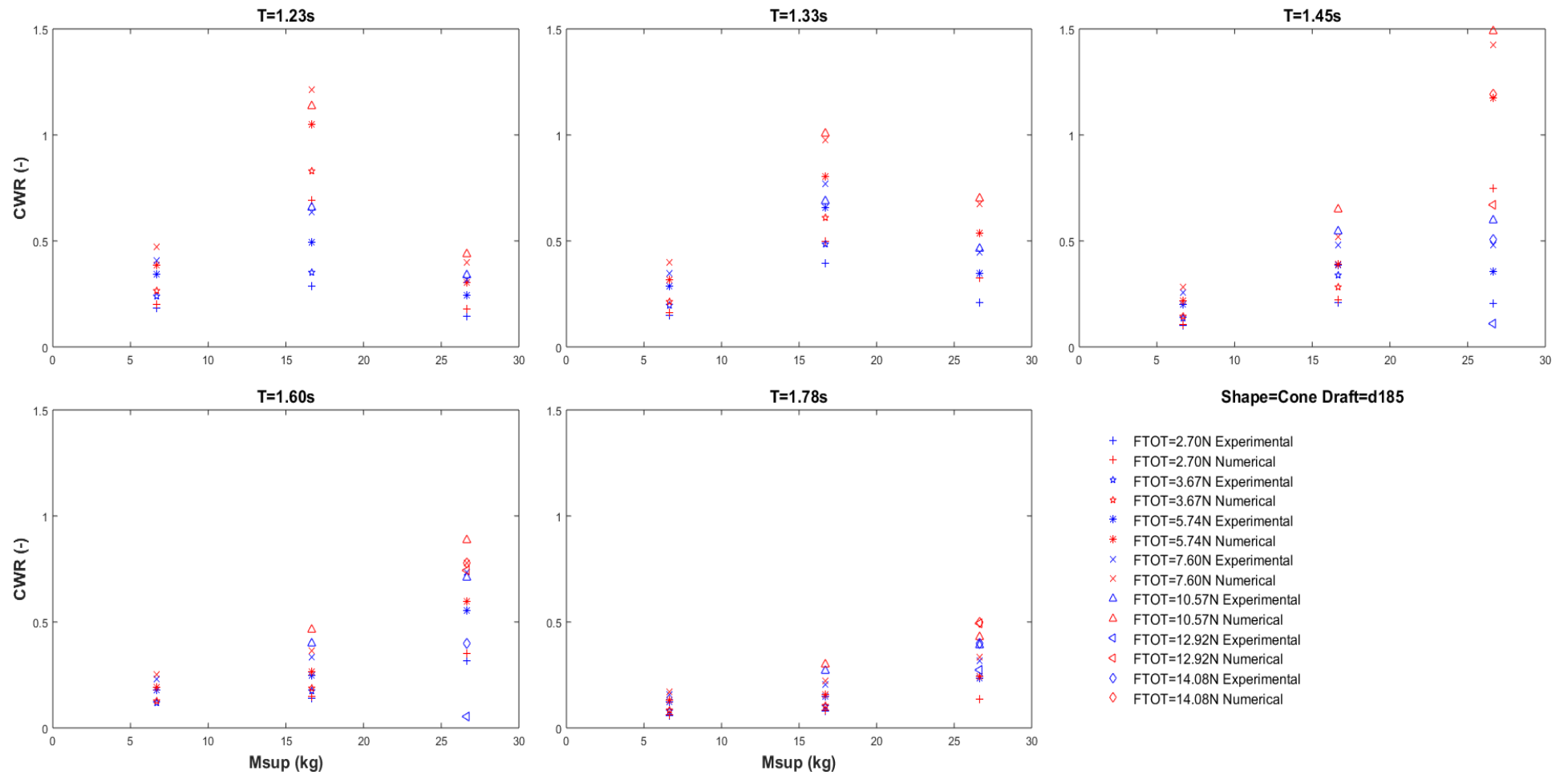
Figure B:4: Capture width ratio vs supplementary mass for constant wave period with varying damping force. Cone-cylinder shape, draft=185mm
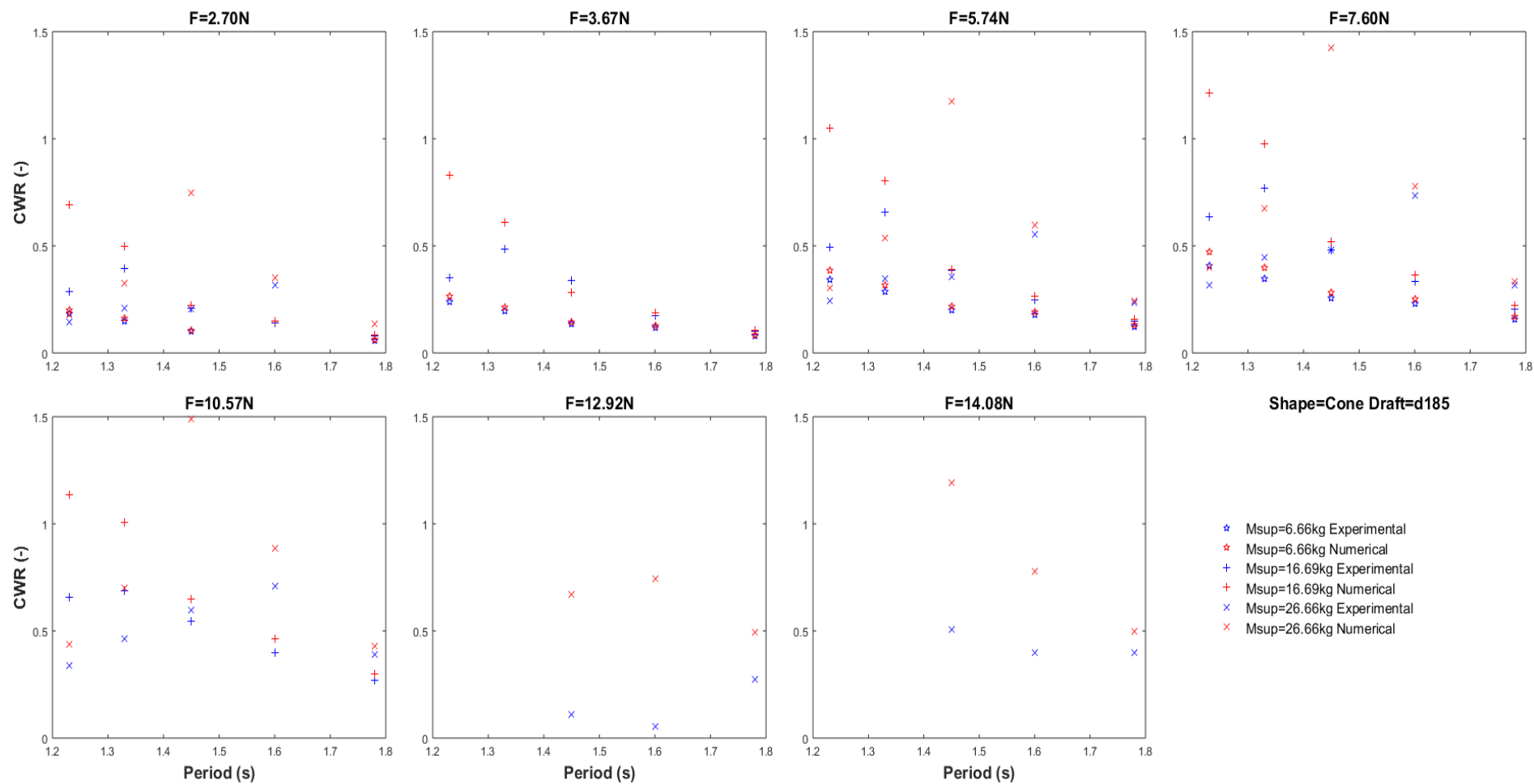
Figure B:5: Capture width ratio vs wave period for constant damping force with varying supplementary mass. Cone-cylinder shape, draft=185mm
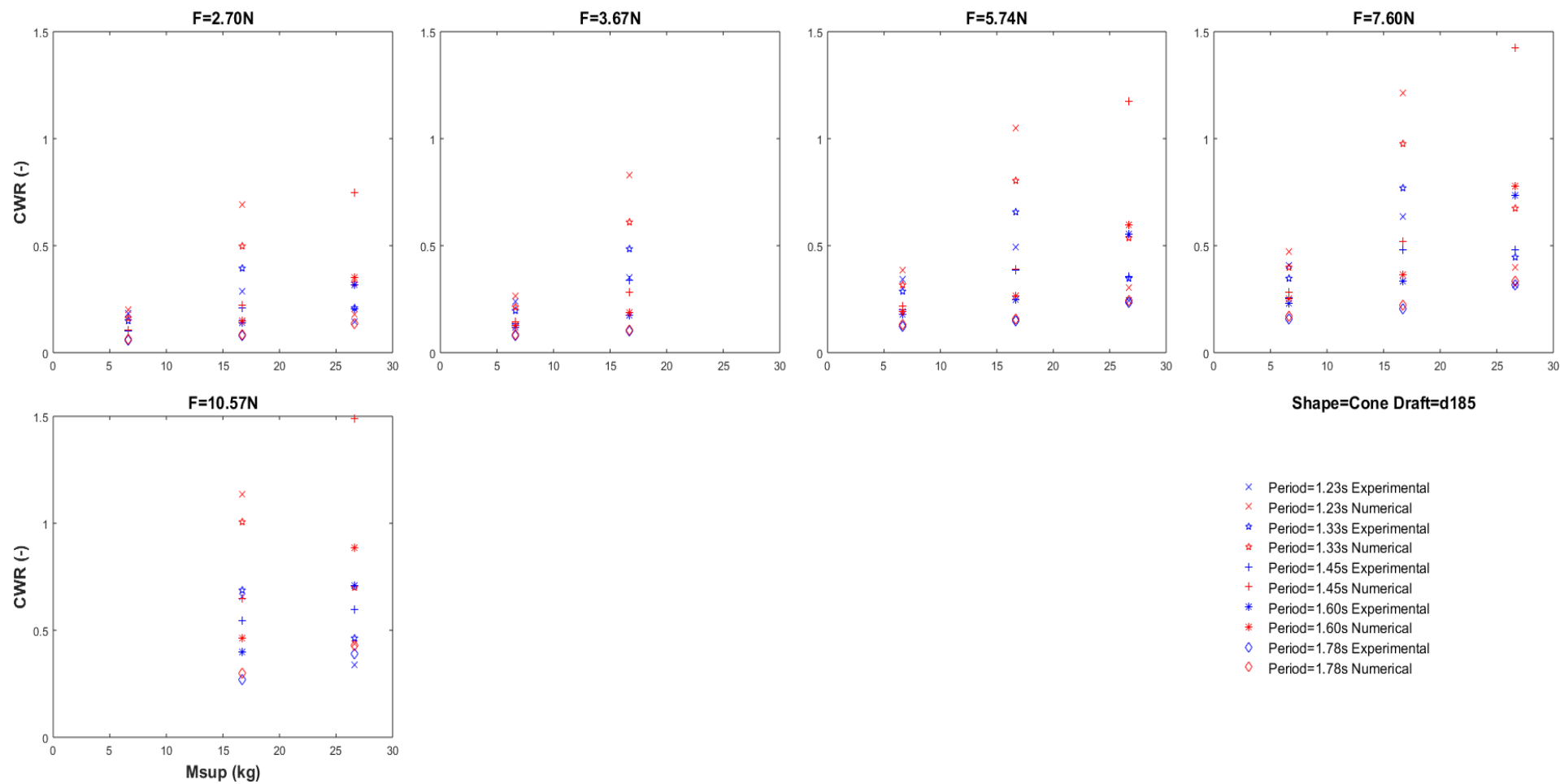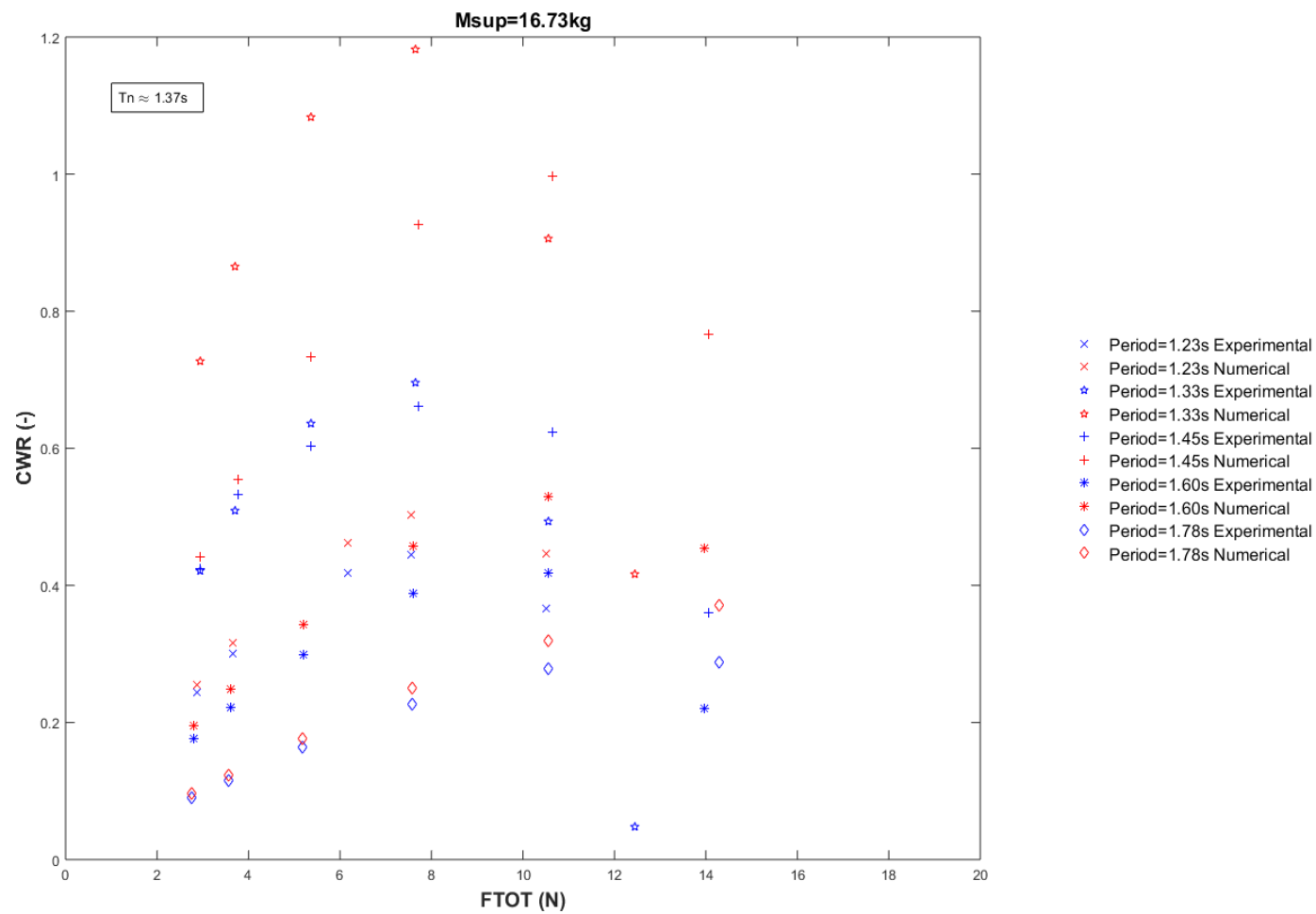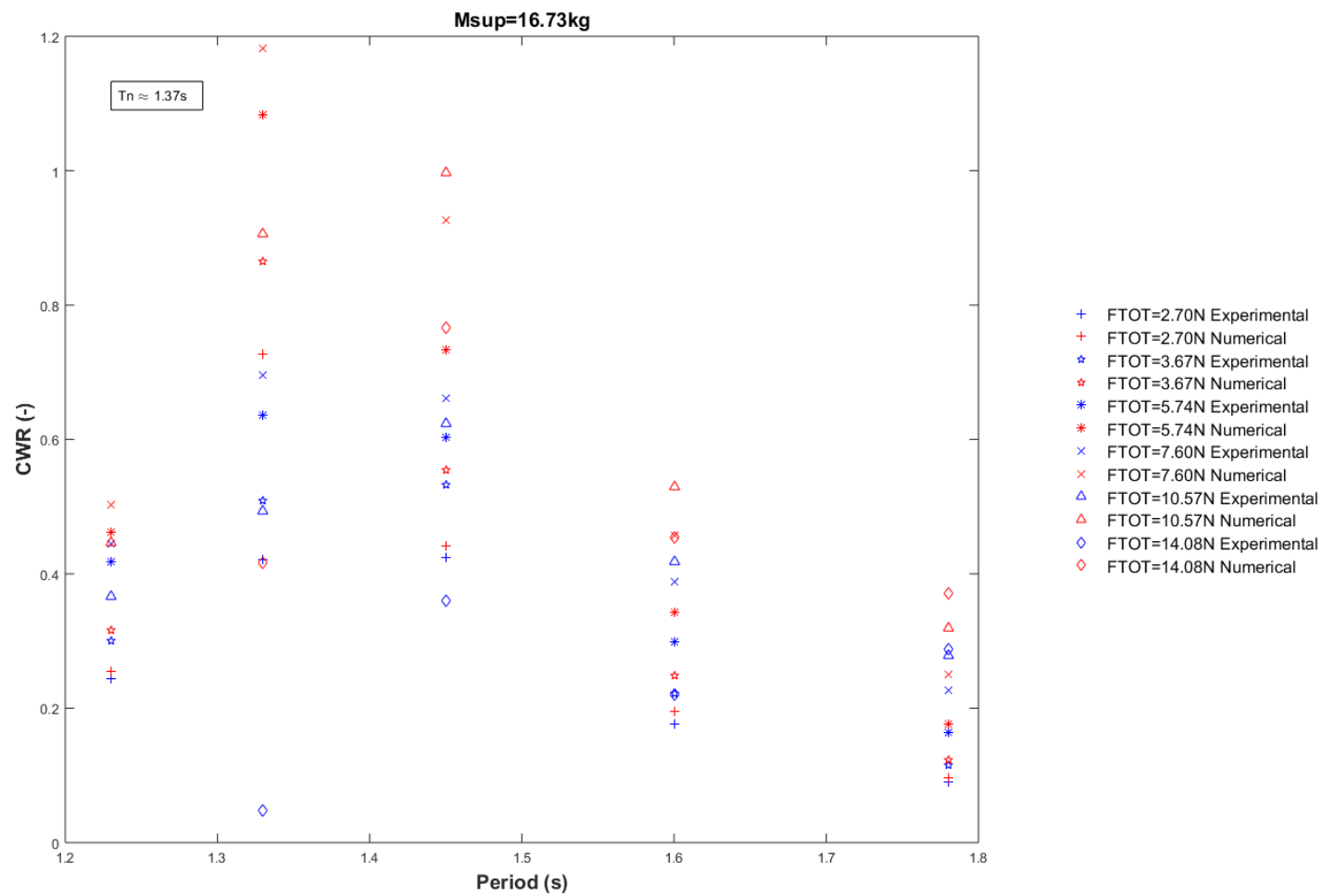
Figure B:6: Capture width ratio vs supplementary mass for constant damping force with varying wave period. Cone-cylinder shape, draft=185mm
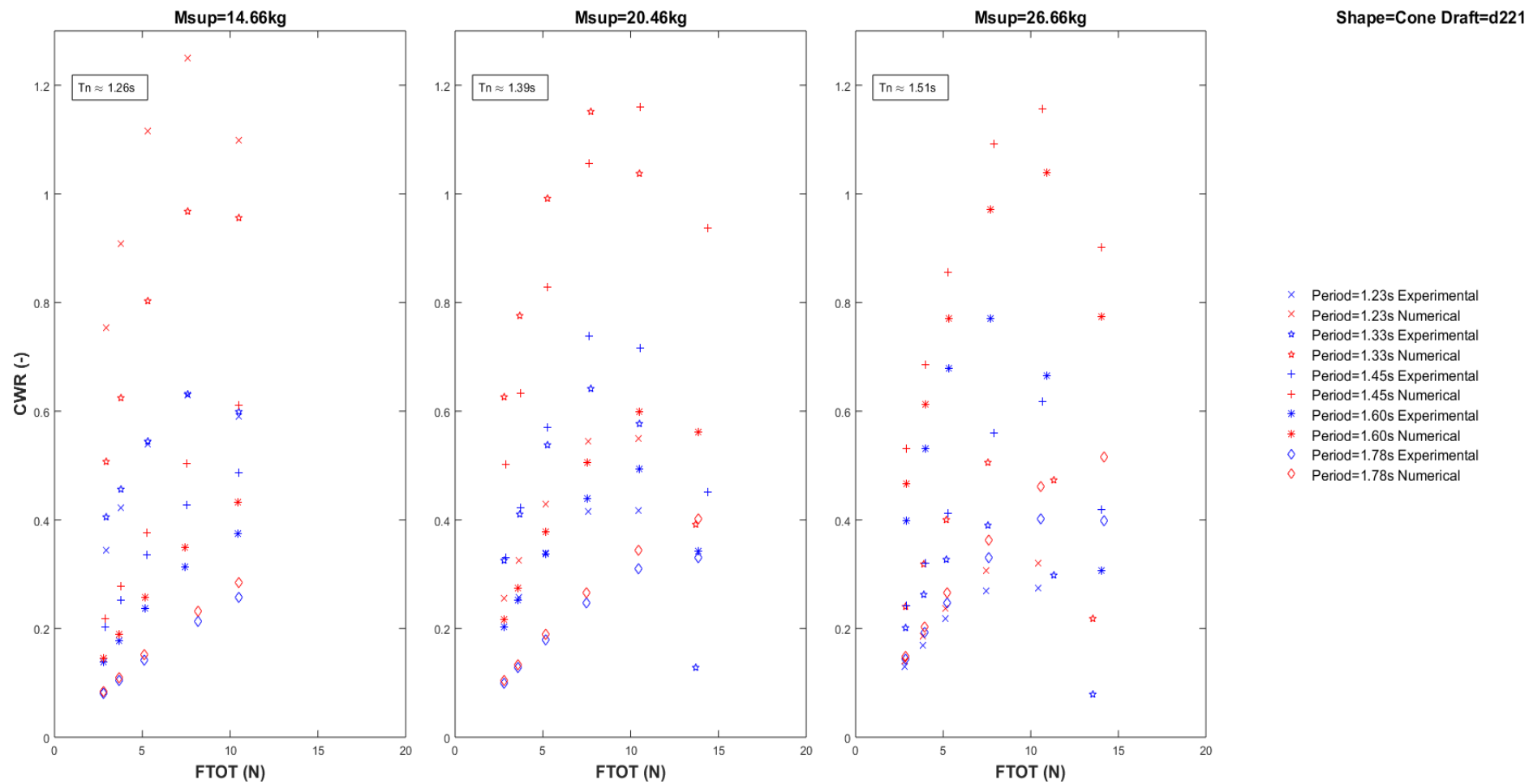
Figure B:7: Capture width ratio vs damping force for constant supplementary mass with varying wave period. Cone-cylinder shape, draft=221mm
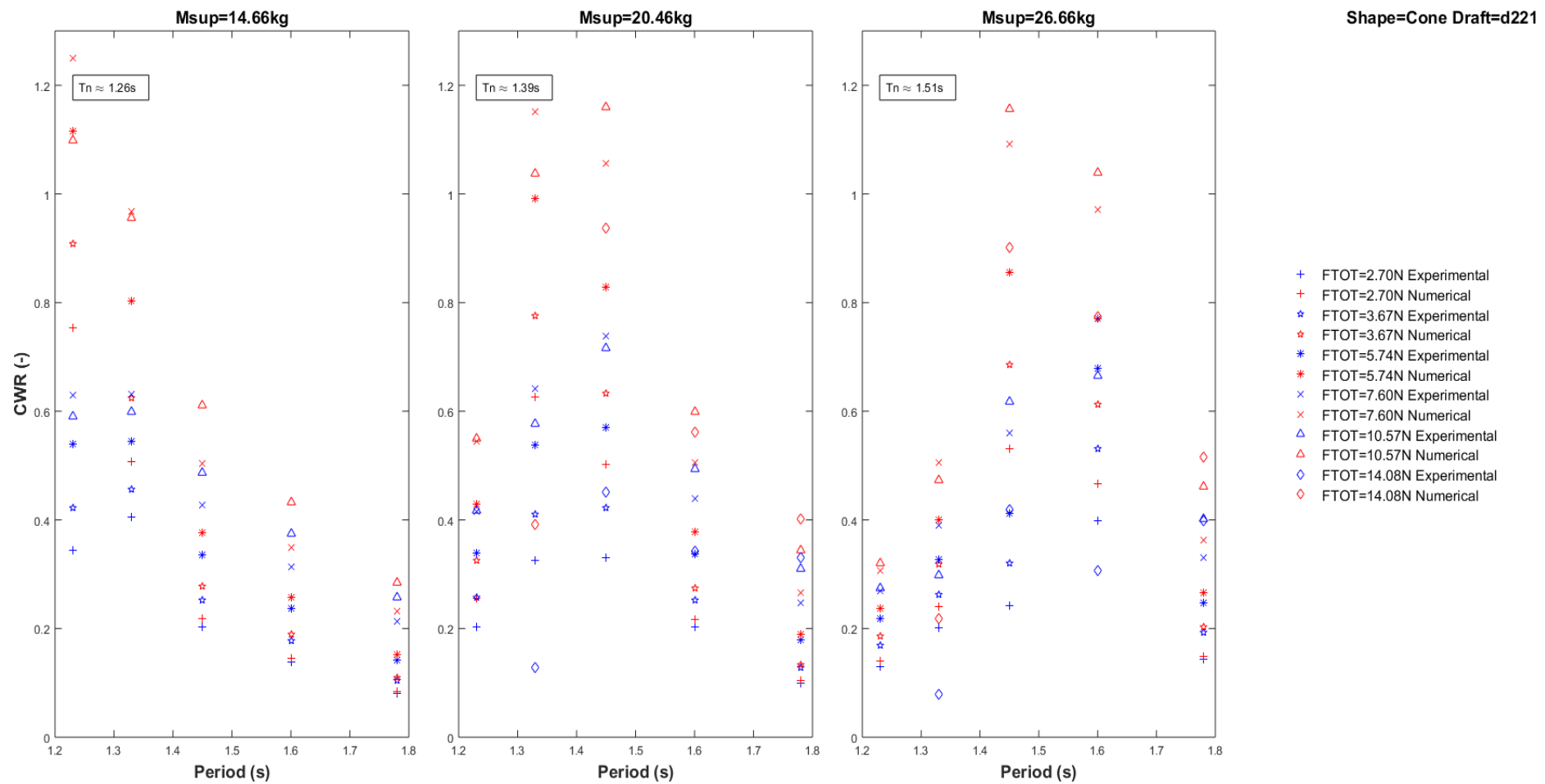
Figure B:8: Capture width ratio vs wave period for constant supplementary mass with varying damping force. Cone-cylinder shape, draft=221mm
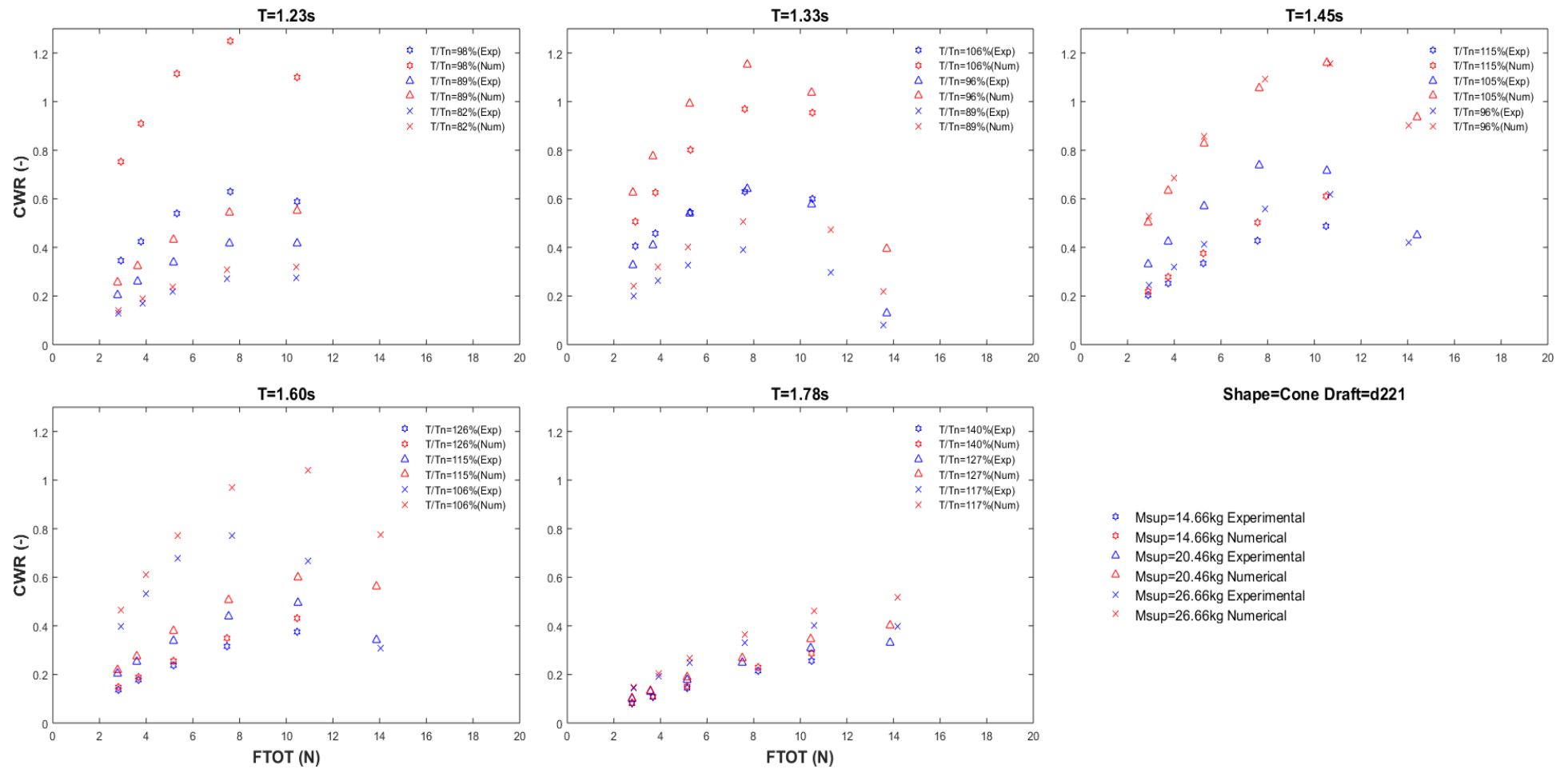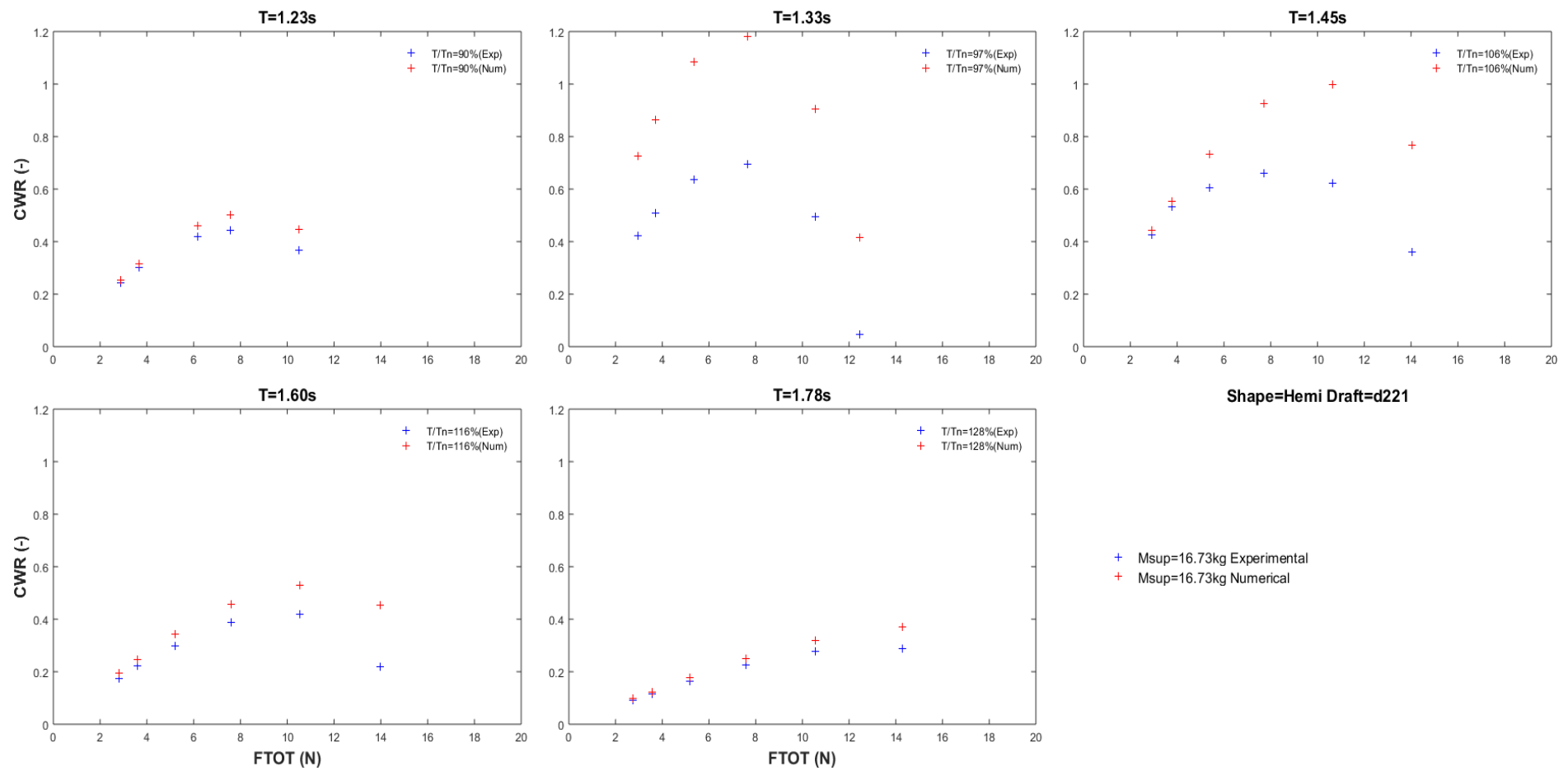
Figure B:9: Capture width ratio vs damping force for constant wave period with varying supplementary mass. Cone-cylinder shape, draft=221mm
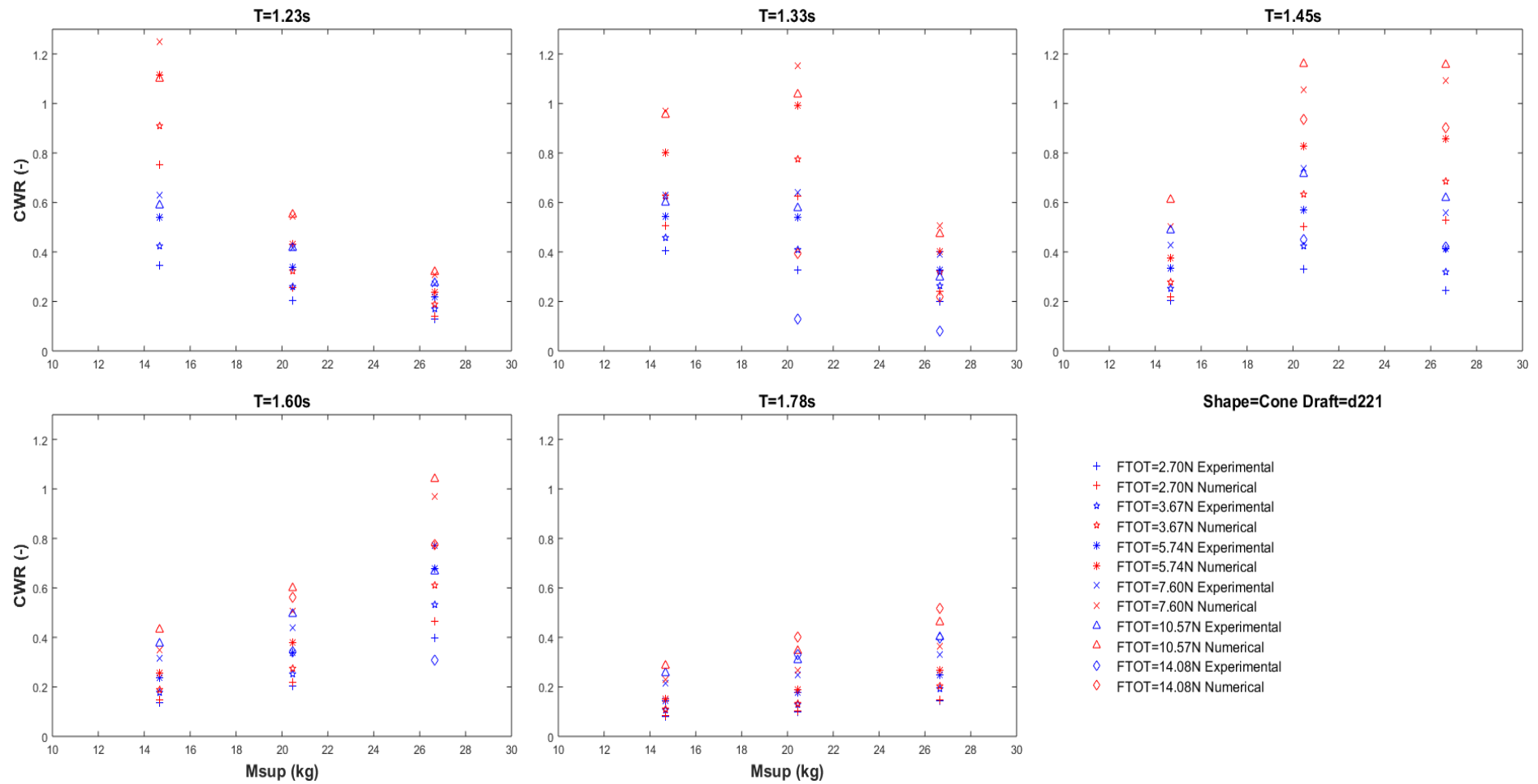
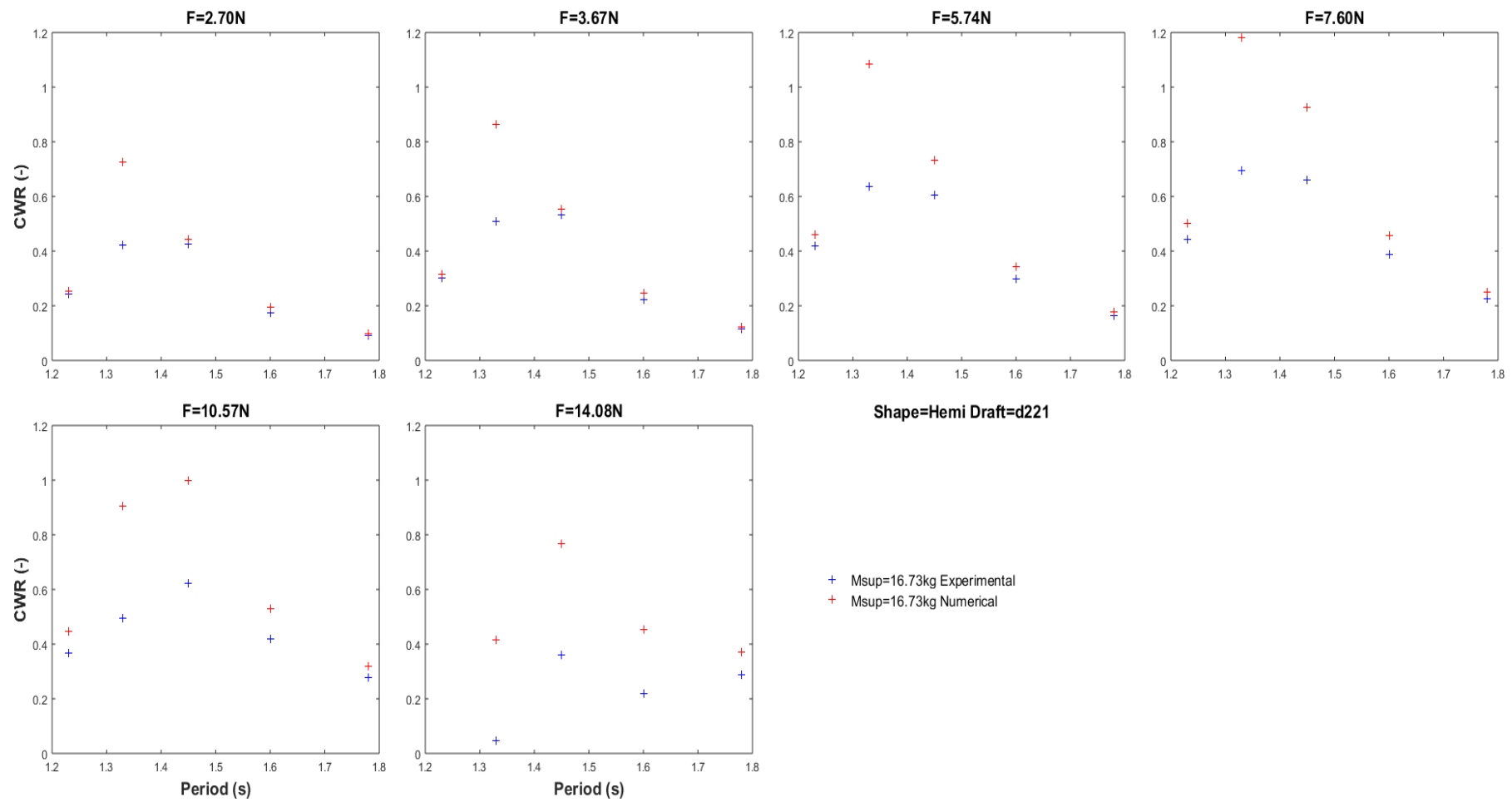**Figure B:10: Capture width ratio vs supplementary mass for constant wave period with varying damping force. Cone-cylinder shape, draft=221mm**
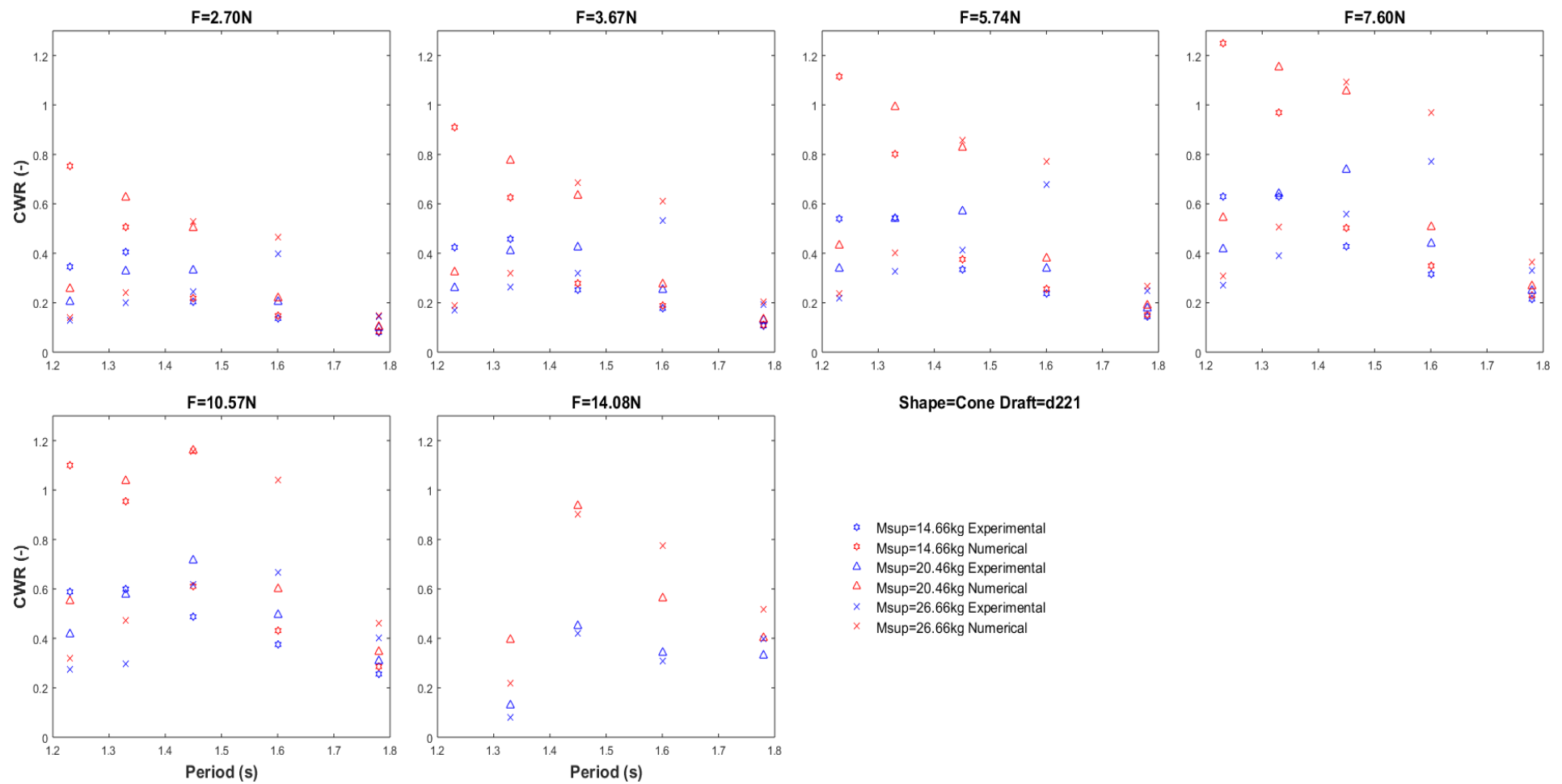
Figure B:11: Capture width ratio vs wave period for constant damping force with varying supplementary mass. Cone-cylinder shape, draft=221mm
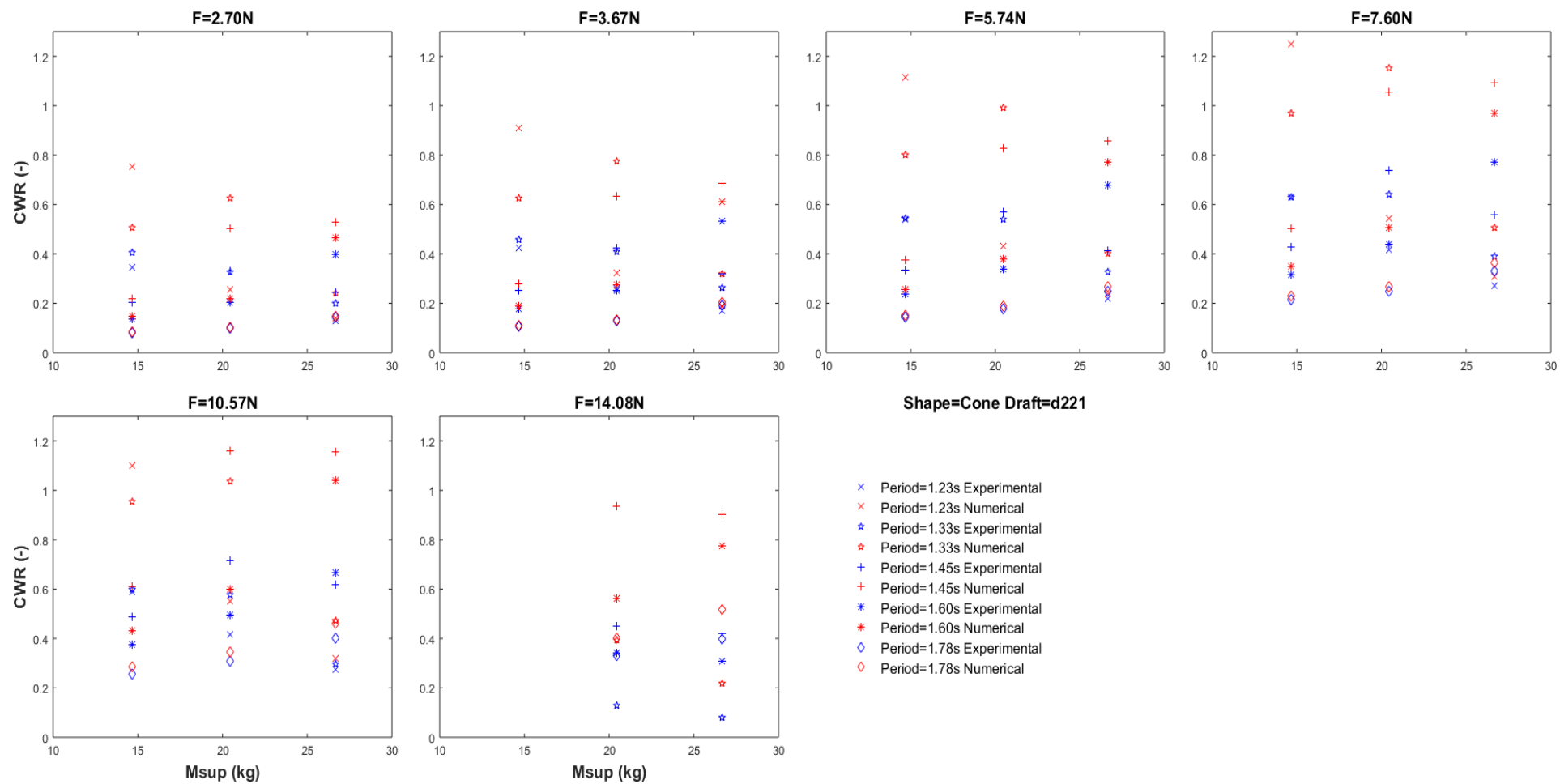
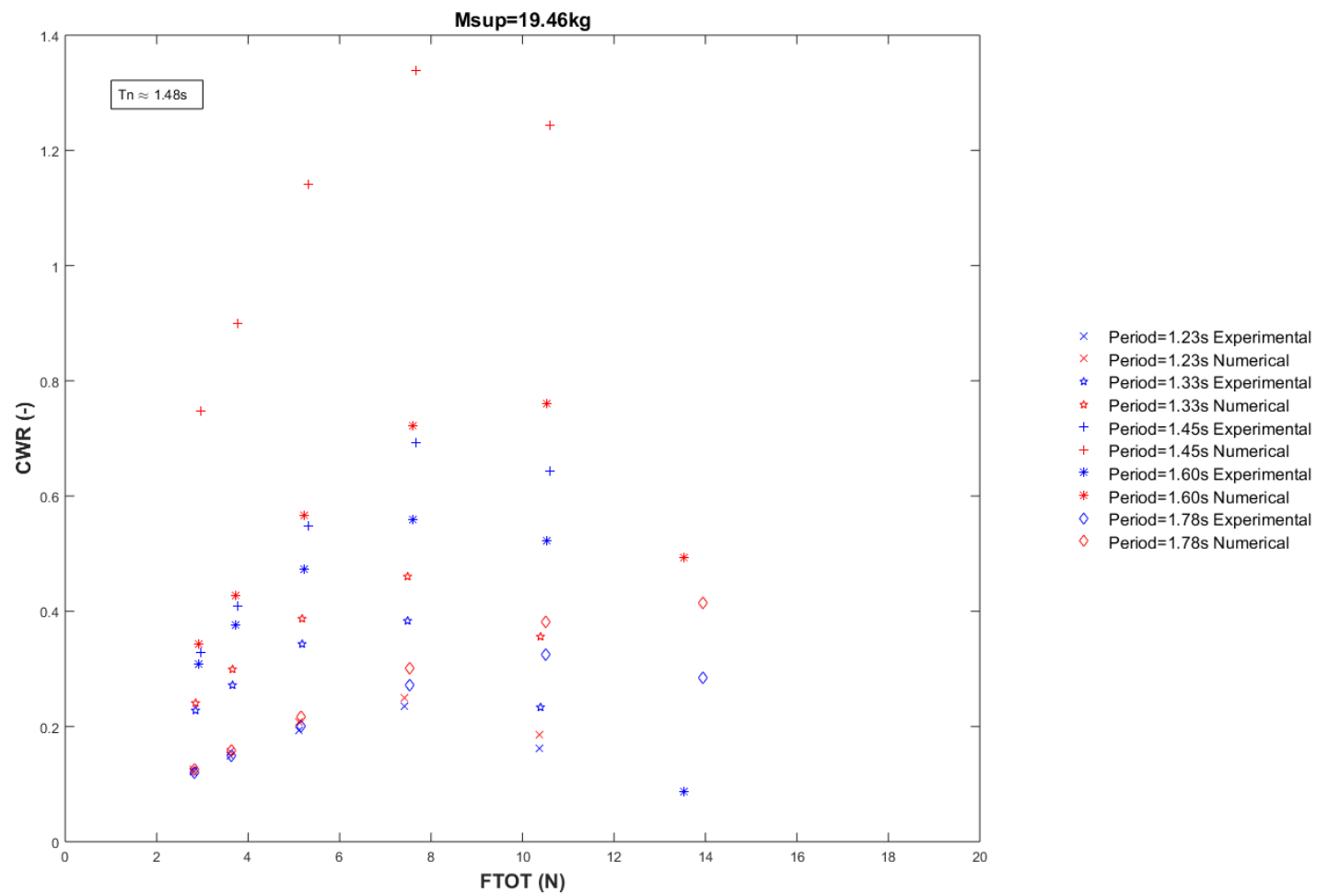**Figure B:12: Capture width ratio vs supplementary mass for constant damping force with varying wave period. Cone-cylinder shape, draft=221mm**
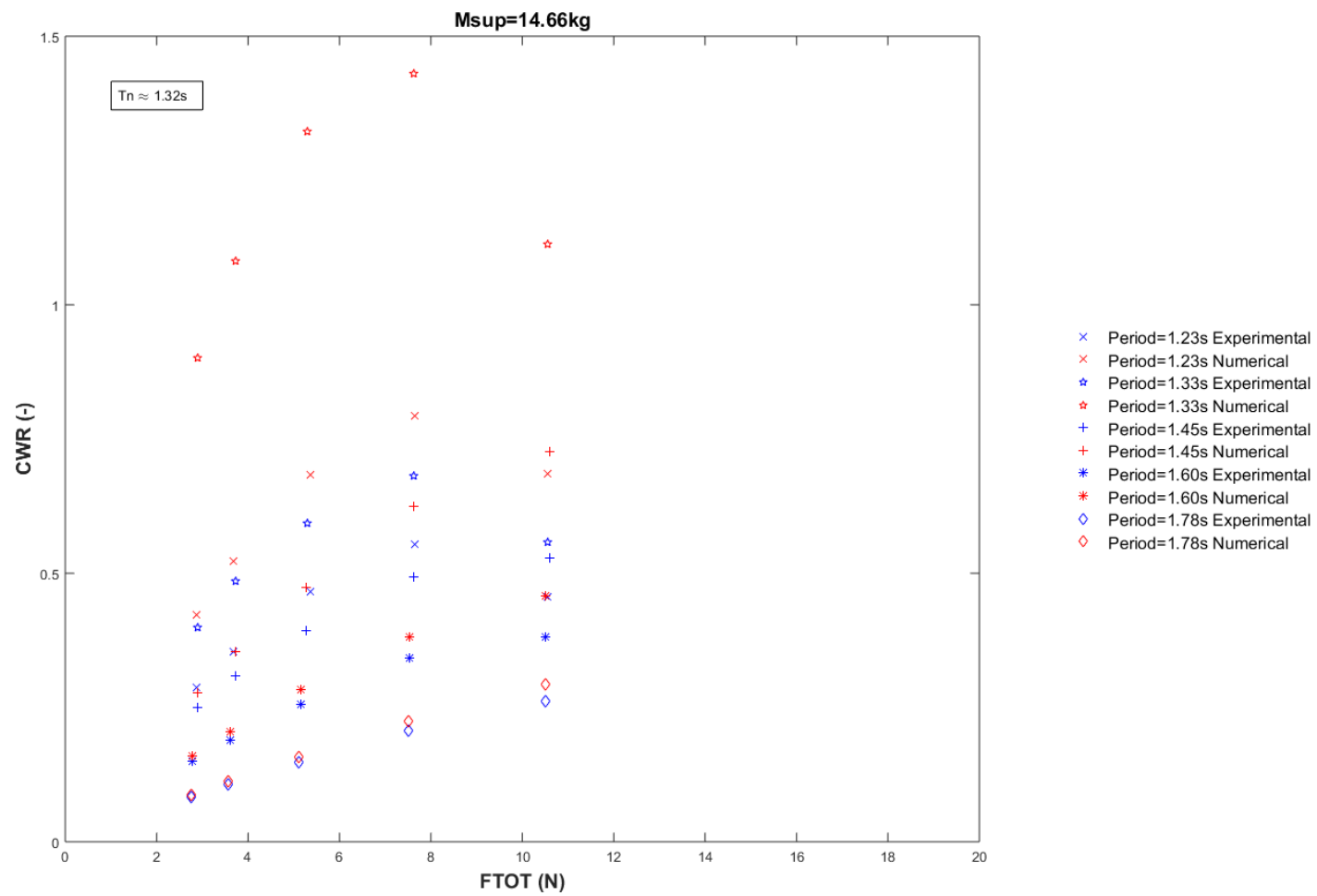
Figure B:13: Capture width ratio vs damping force for constant supplementary mass with varying wave period. Cone-cylinder shape, draft=260mm
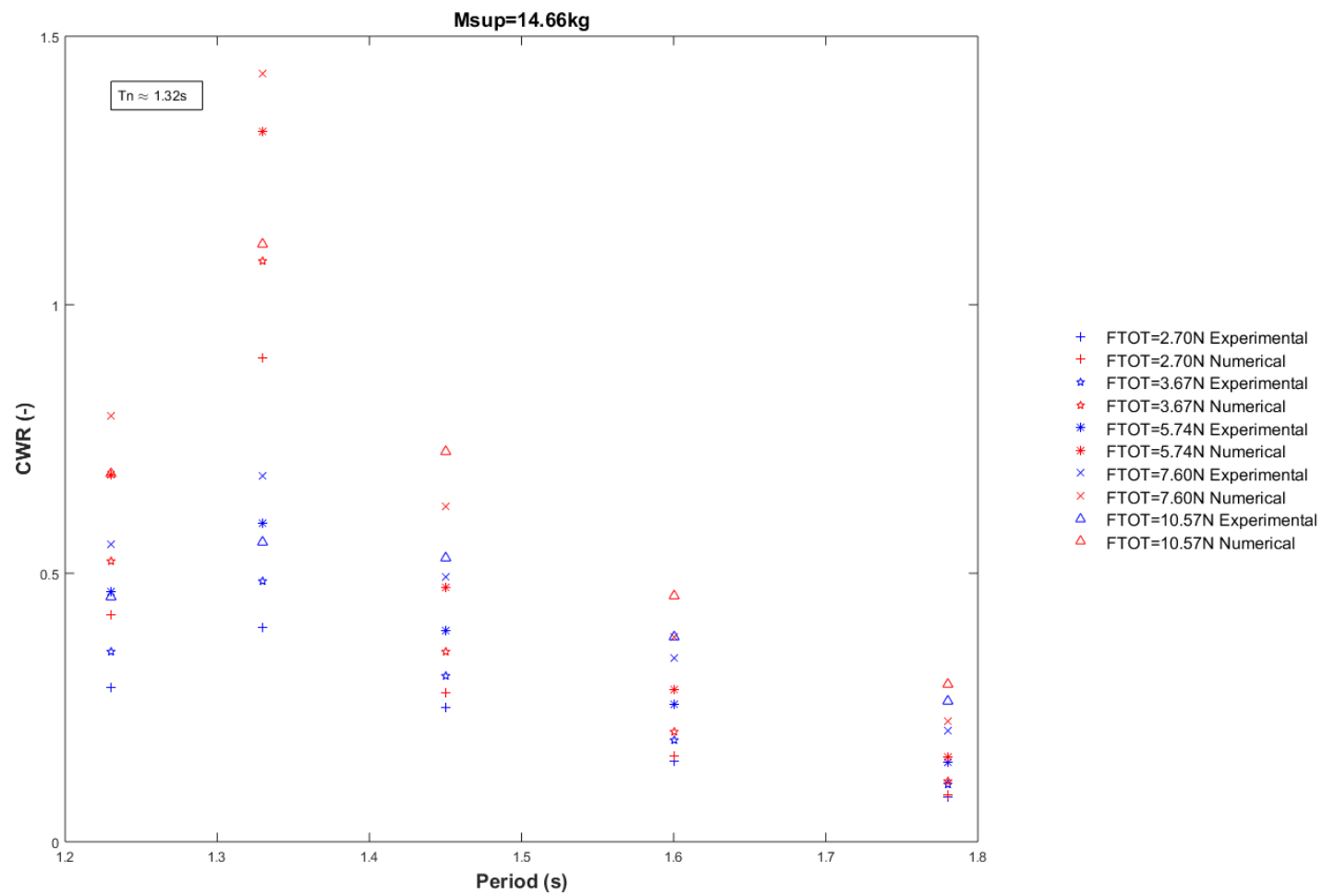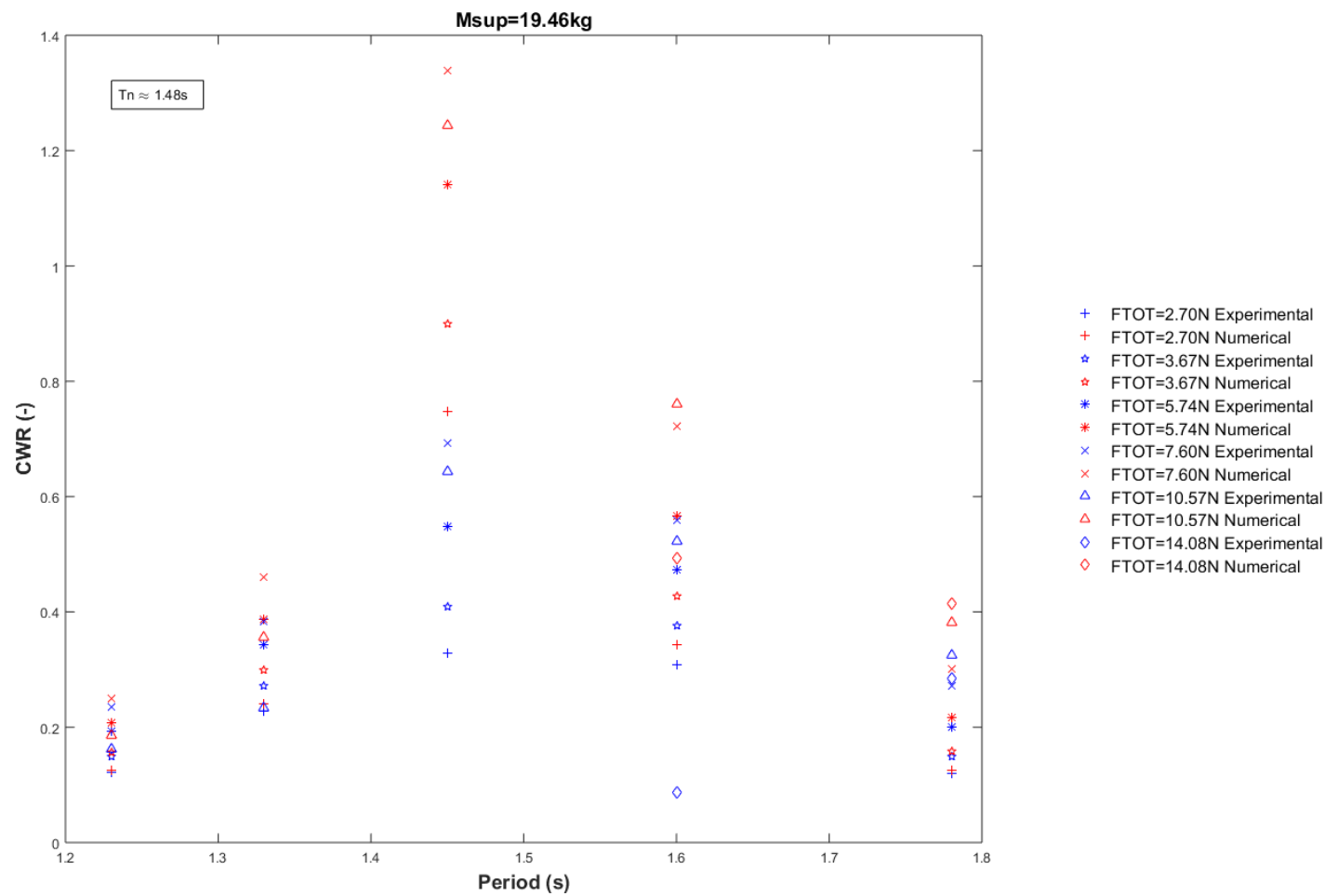
Figure B:14: Capture width ratio vs wave period for constant supplementary mass with varying damping force. Cone-cylinder shape, draft=260mm
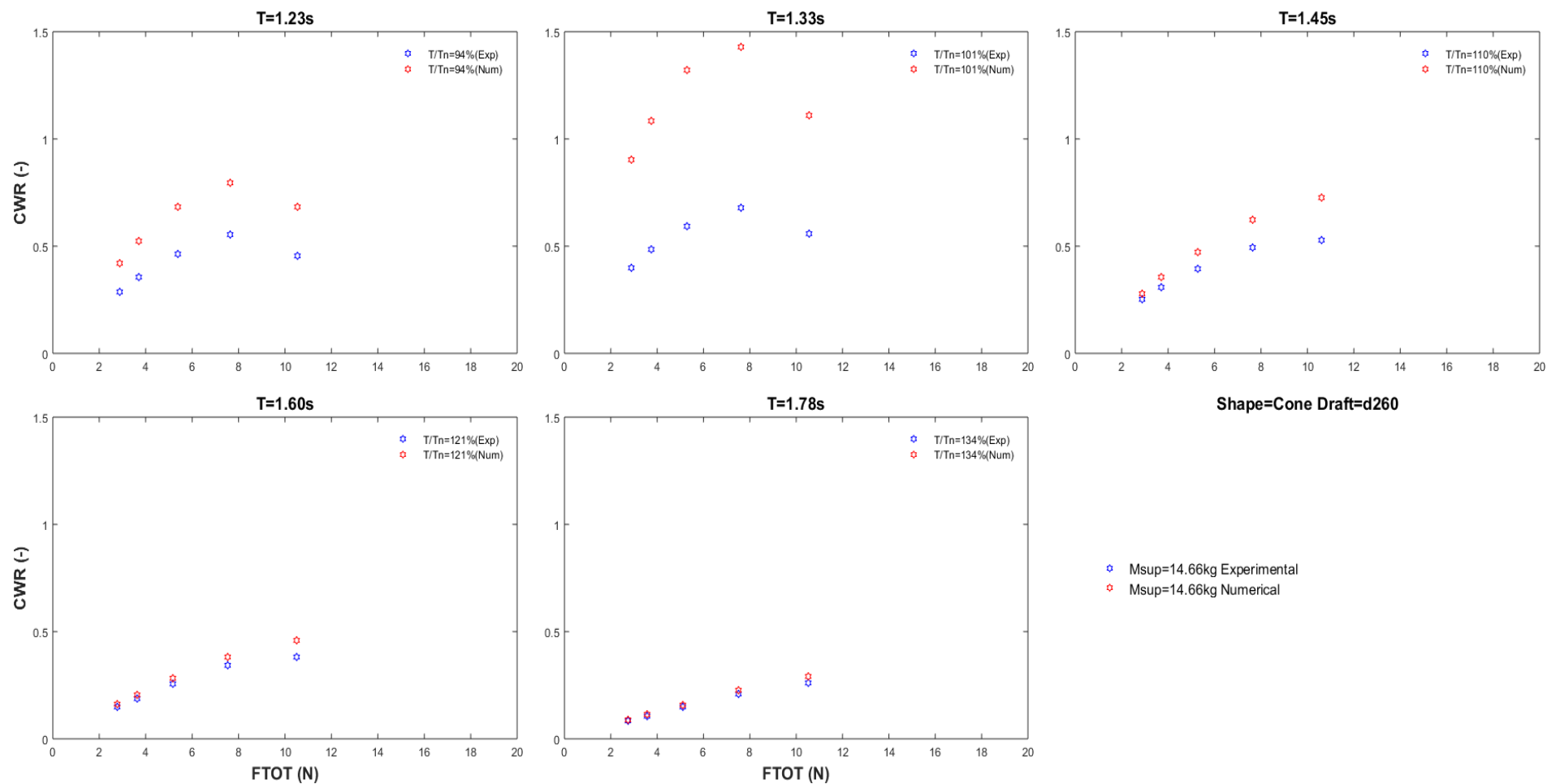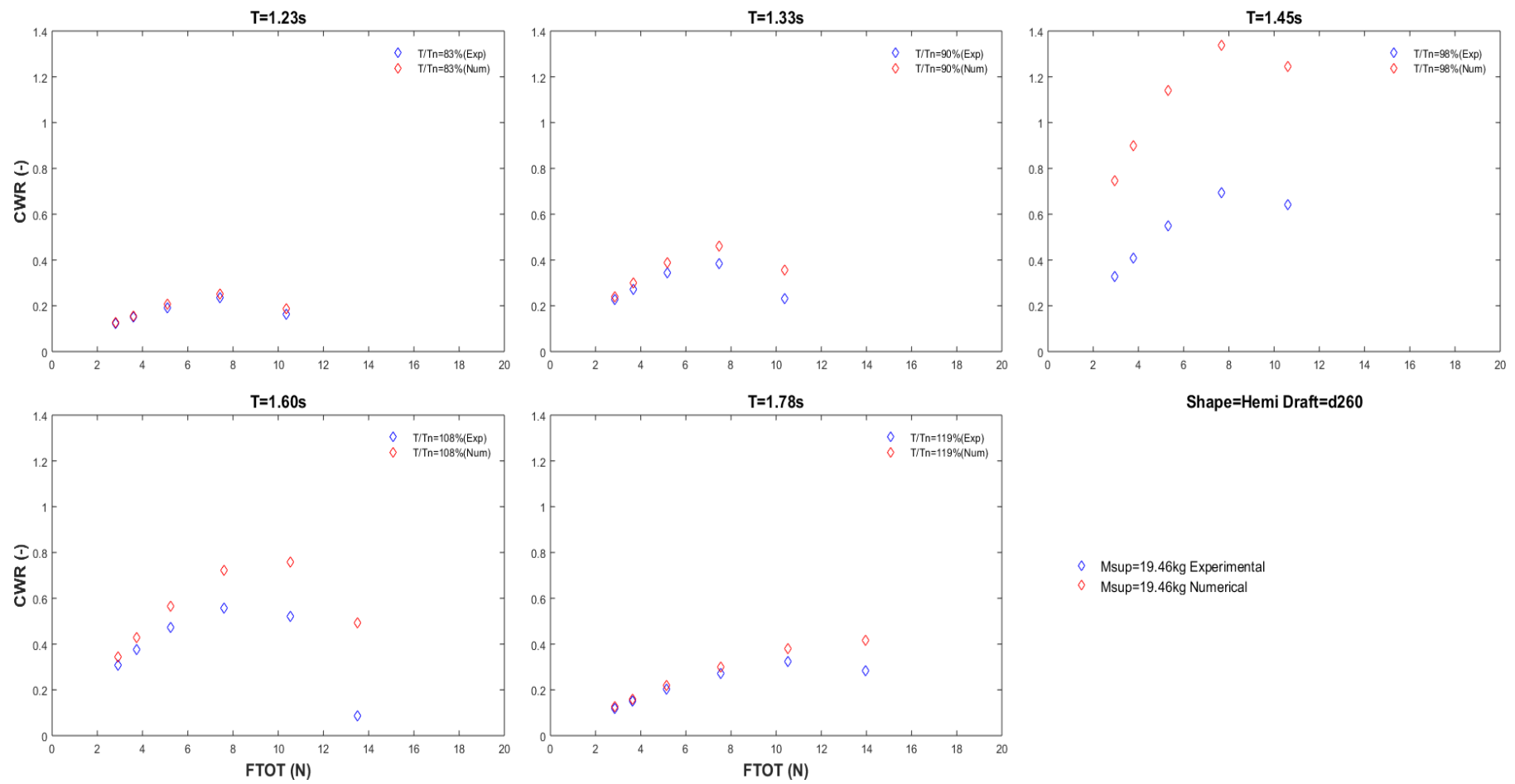
Figure B:15: Capture width ratio vs damping force for constant wave period with varying supplementary mass. Cone-cylinder shape, draft=260mm
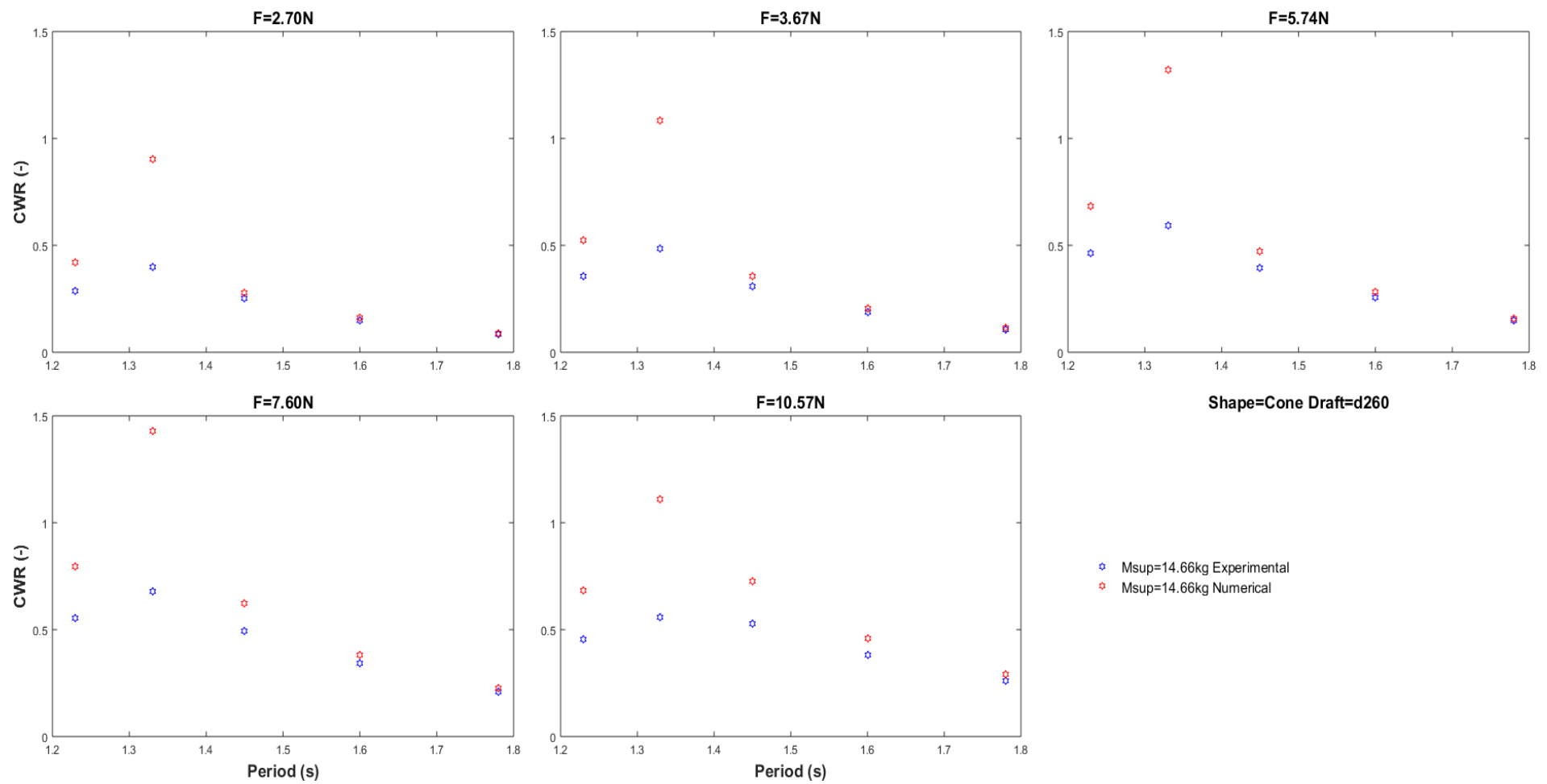
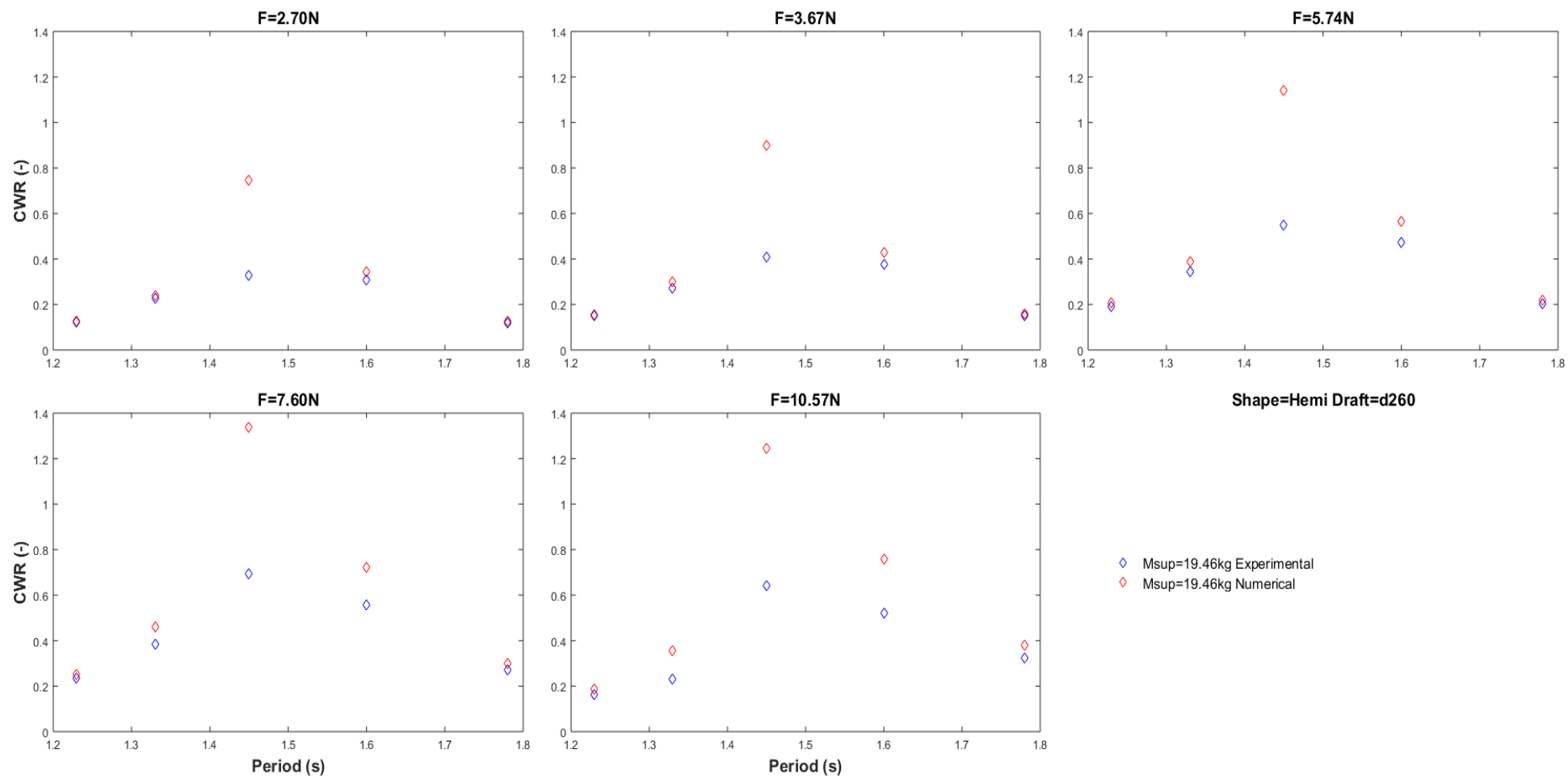**Figure B:16: Capture width ratio vs wave period for constant damping force with varying supplementary mass. Cone-cylinder shape, draft=260mm**
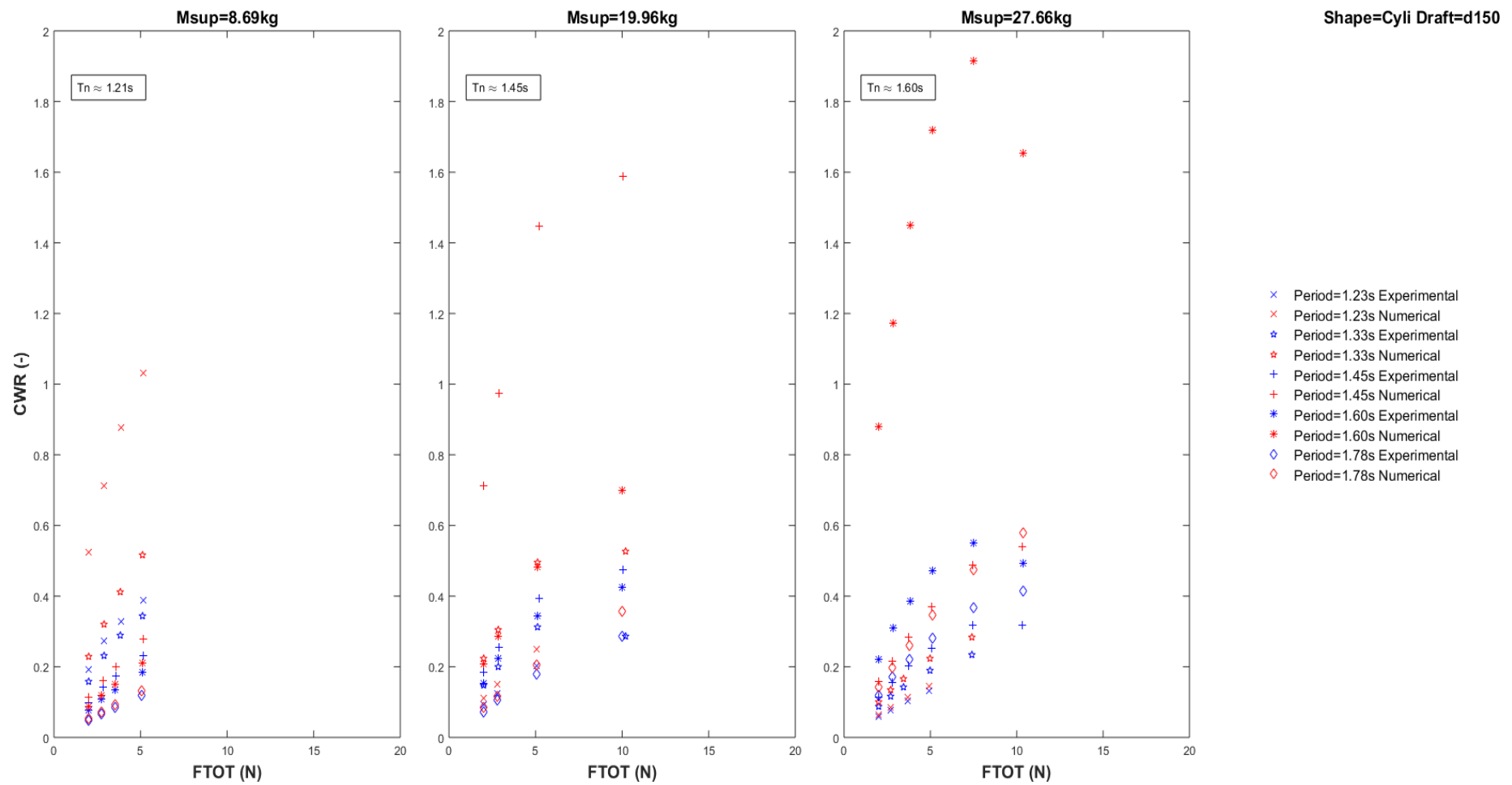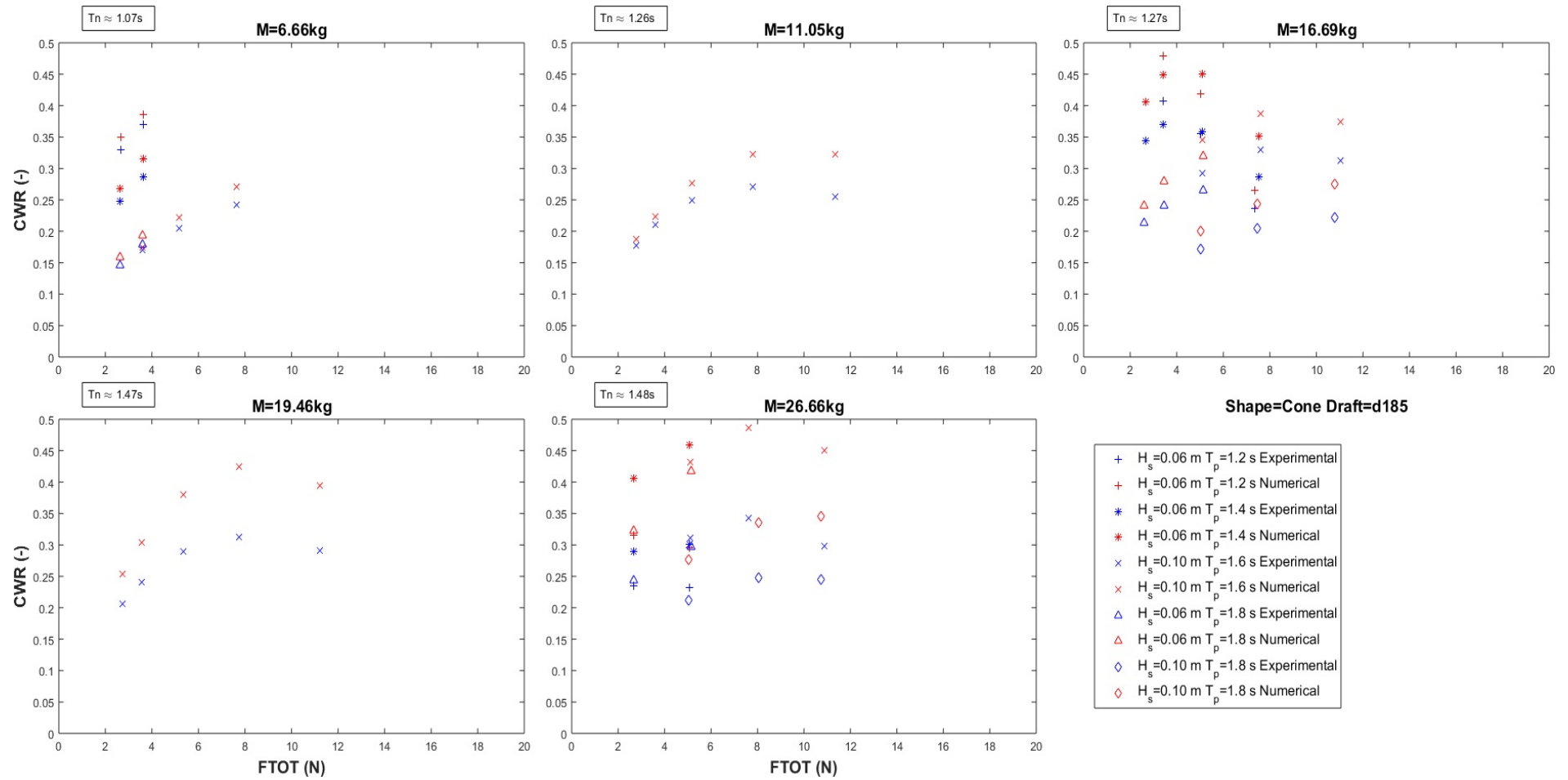
Figure B:17: Capture width ratio vs damping force for constant supplementary mass with varying wave period. Cylinder shape, draft=150mm
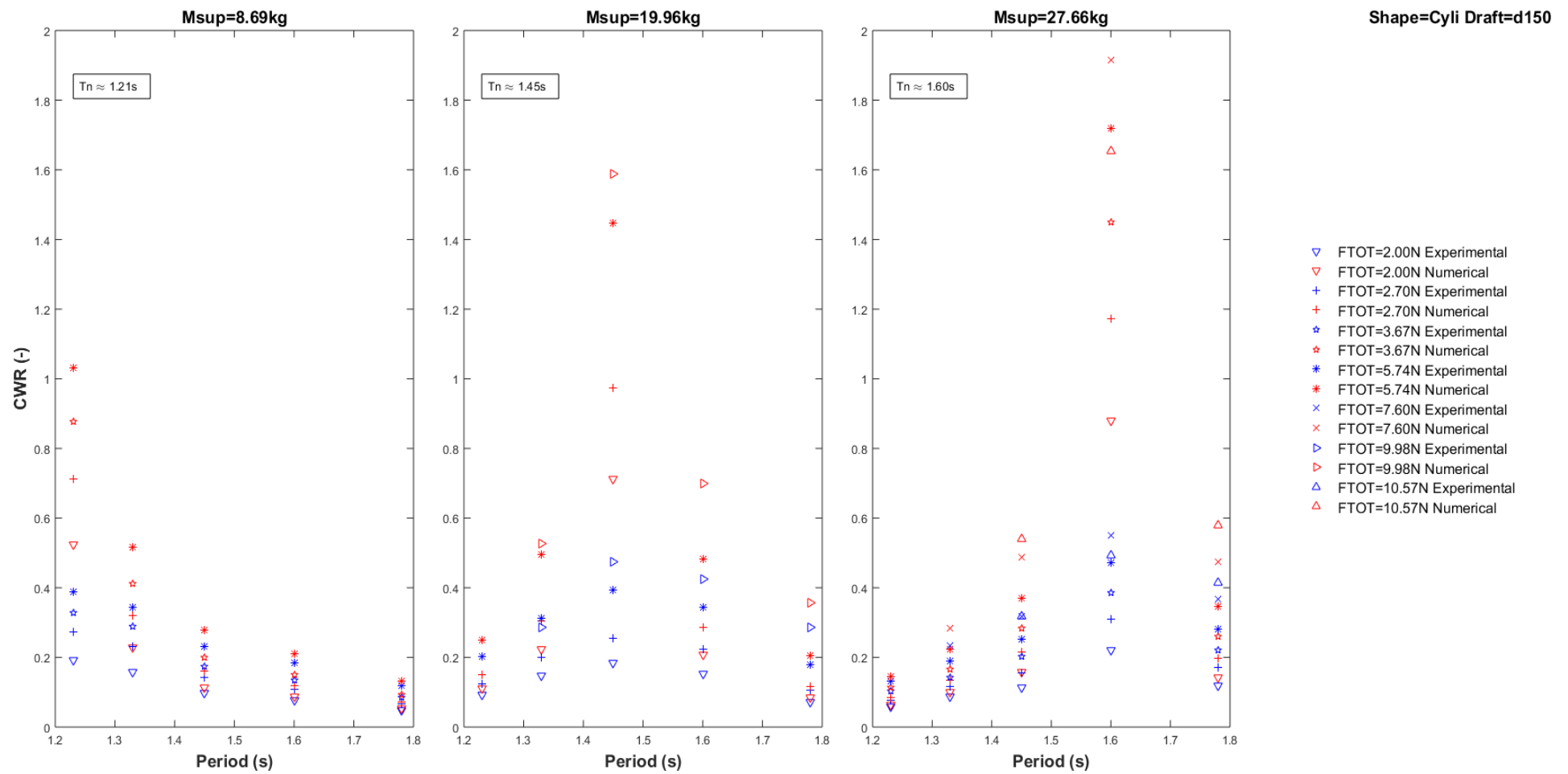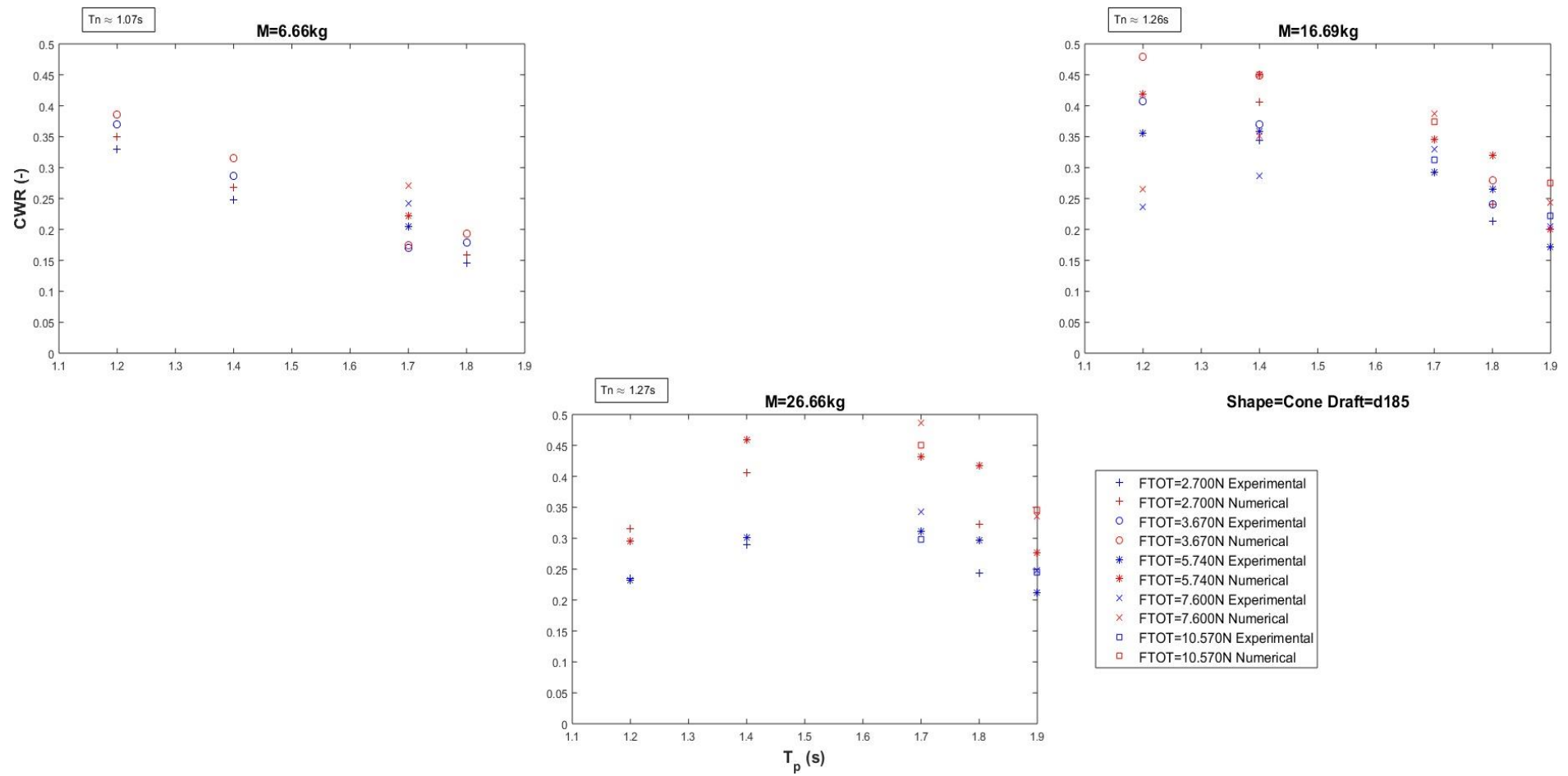
Figure B:18: Capture width ratio vs wave period for constant supplementary mass with varying damping force. Cylinder shape, draft=150mm
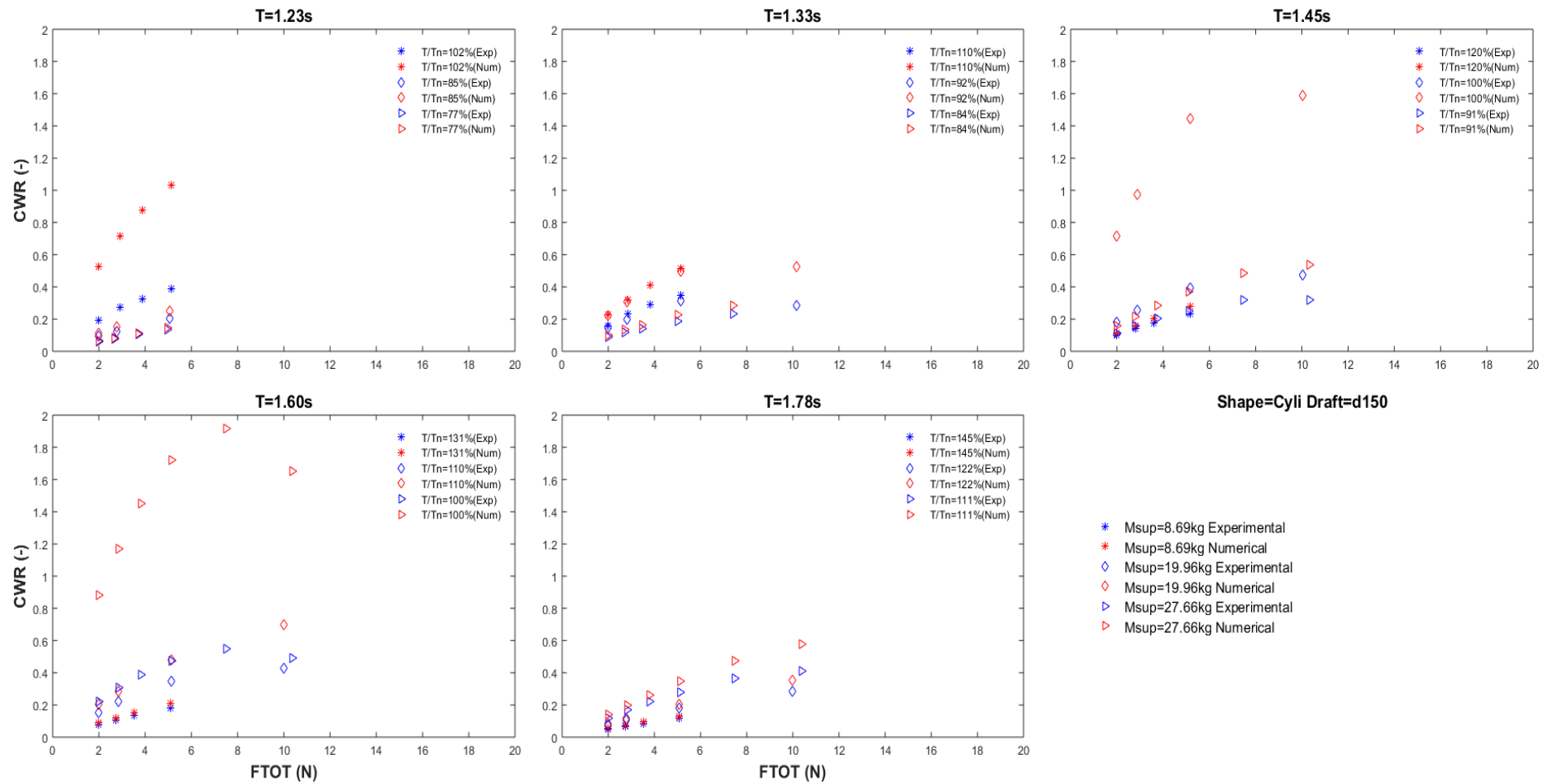
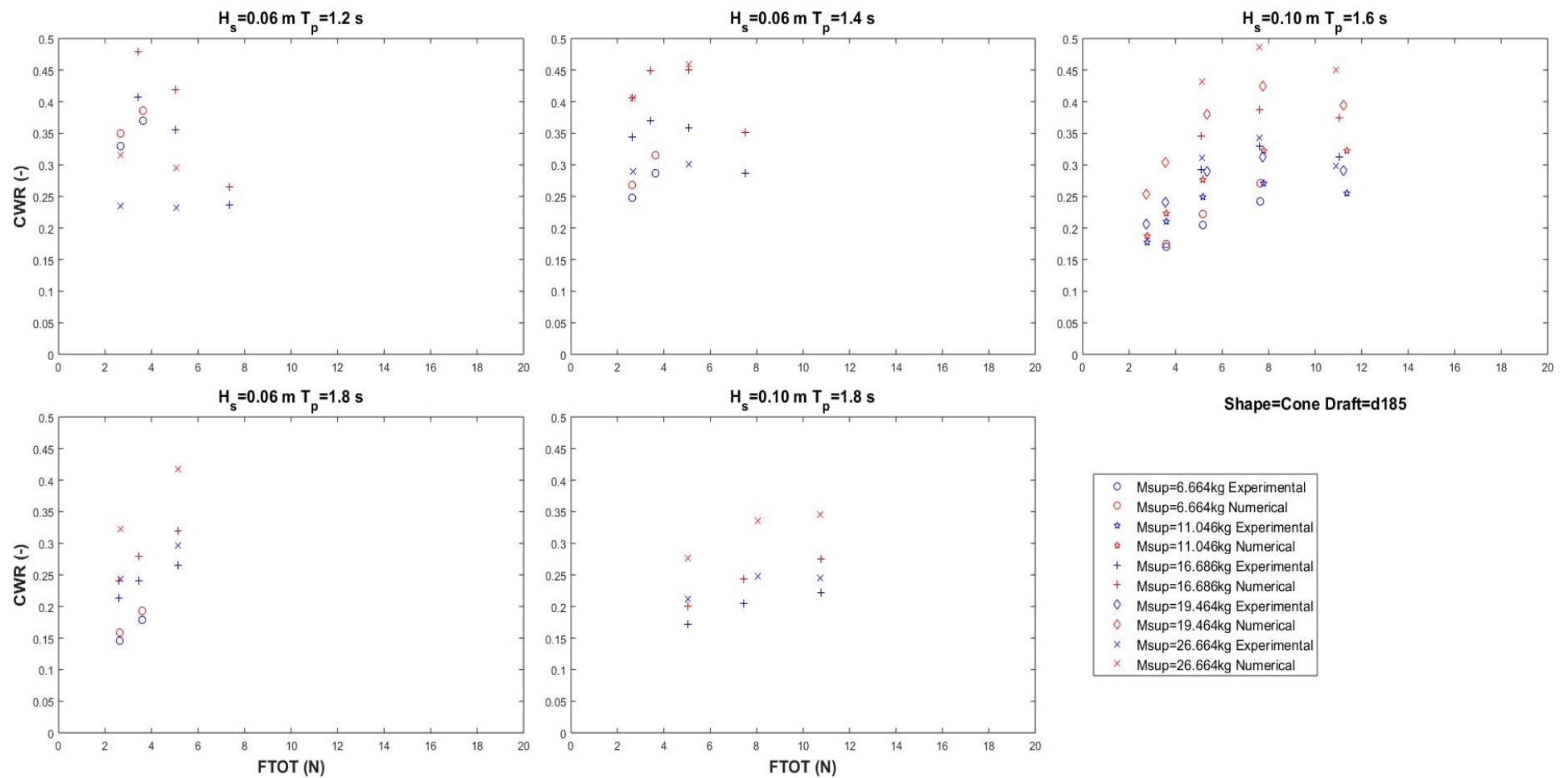**Figure B:19: Capture width ratio vs damping force for constant wave period with varying supplementary mass. Cylinder shape, draft=150mm**
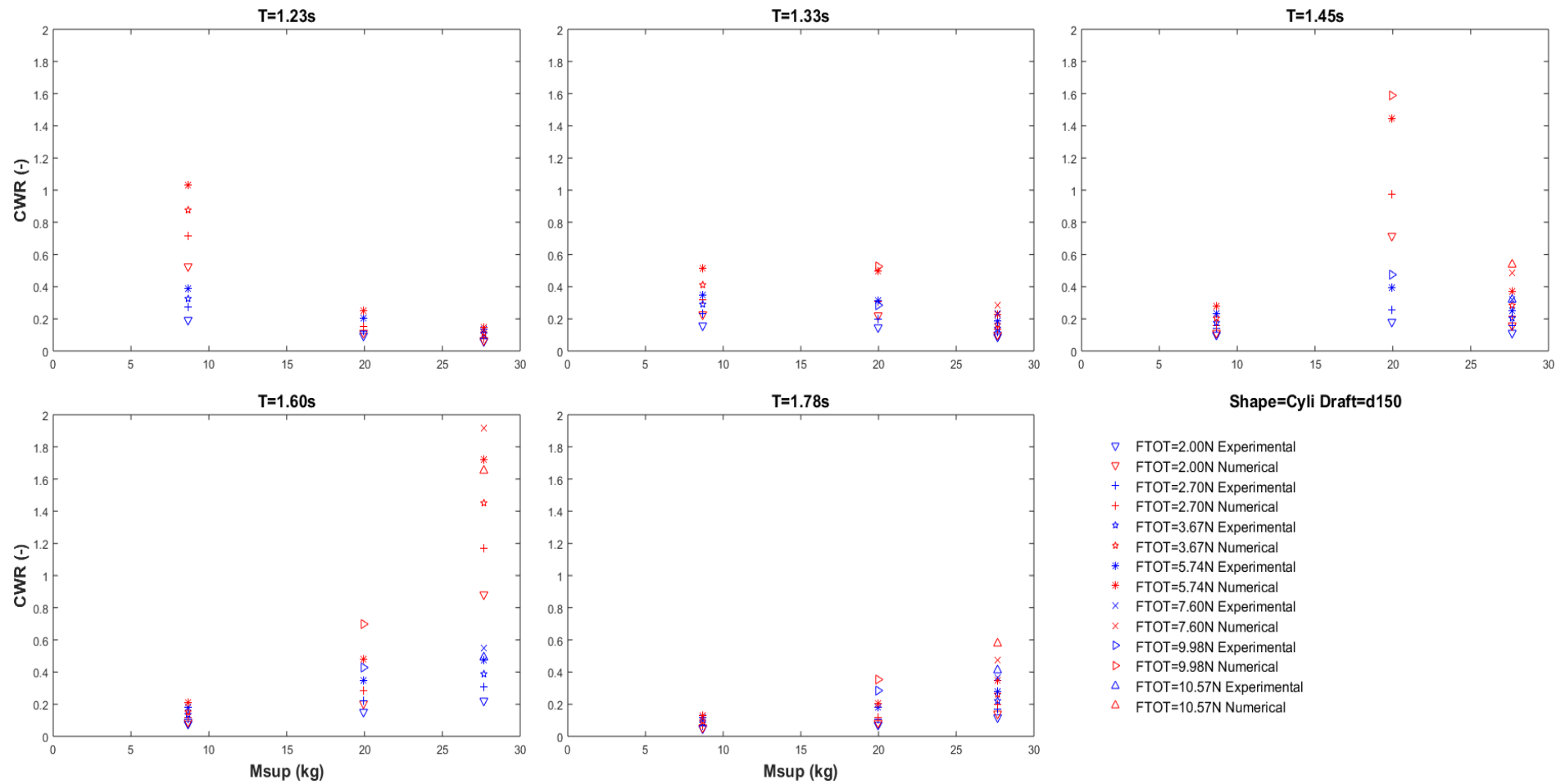
Figure B:20: Capture width ratio vs supplementary mass for constant wave period with varying damping force. Cylinder shape, draft=150mm
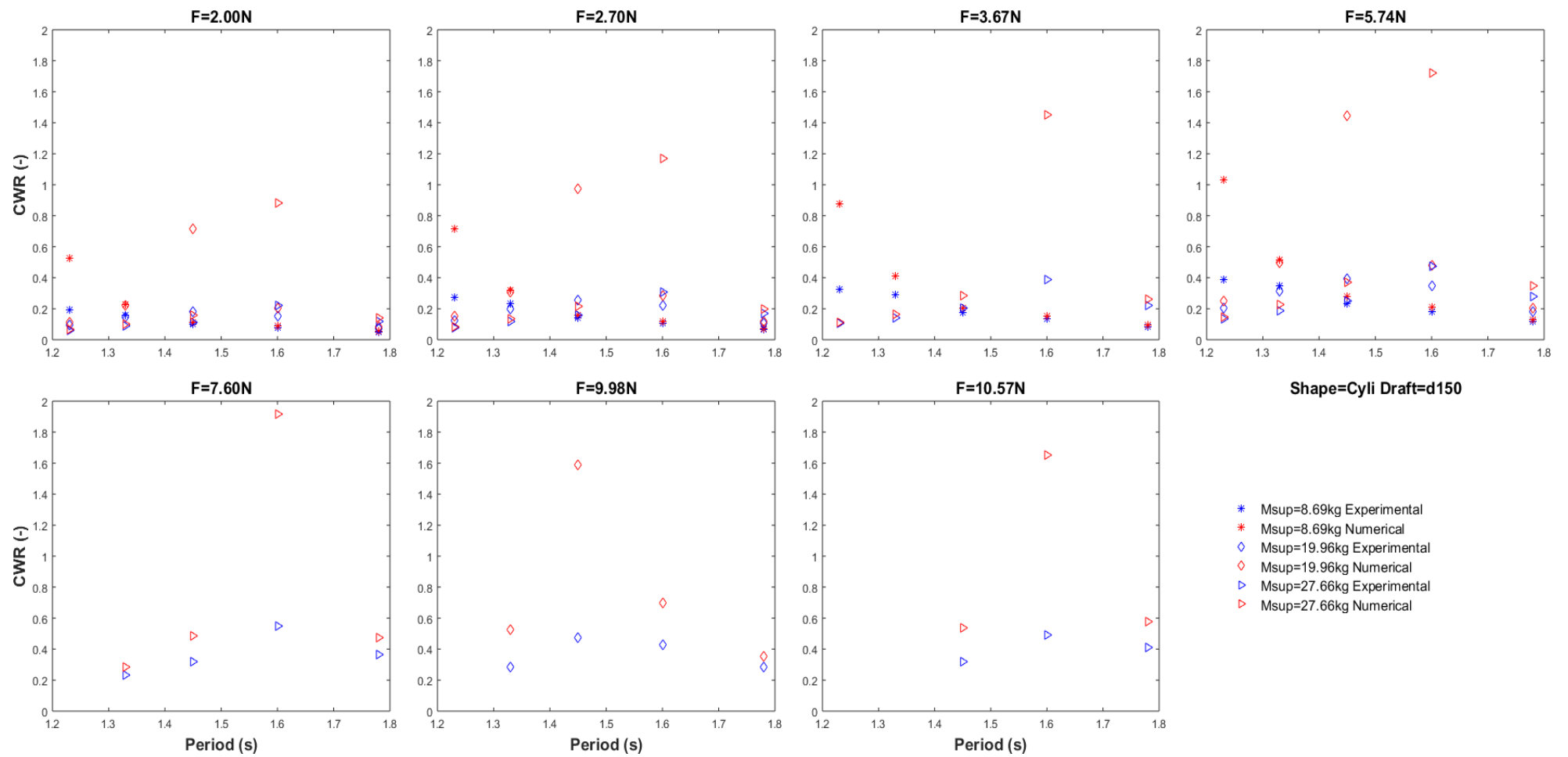
Figure B:21: Capture width ratio vs wave period for constant damping force with varying supplementary mass. Cylinder shape, draft=150mm

319
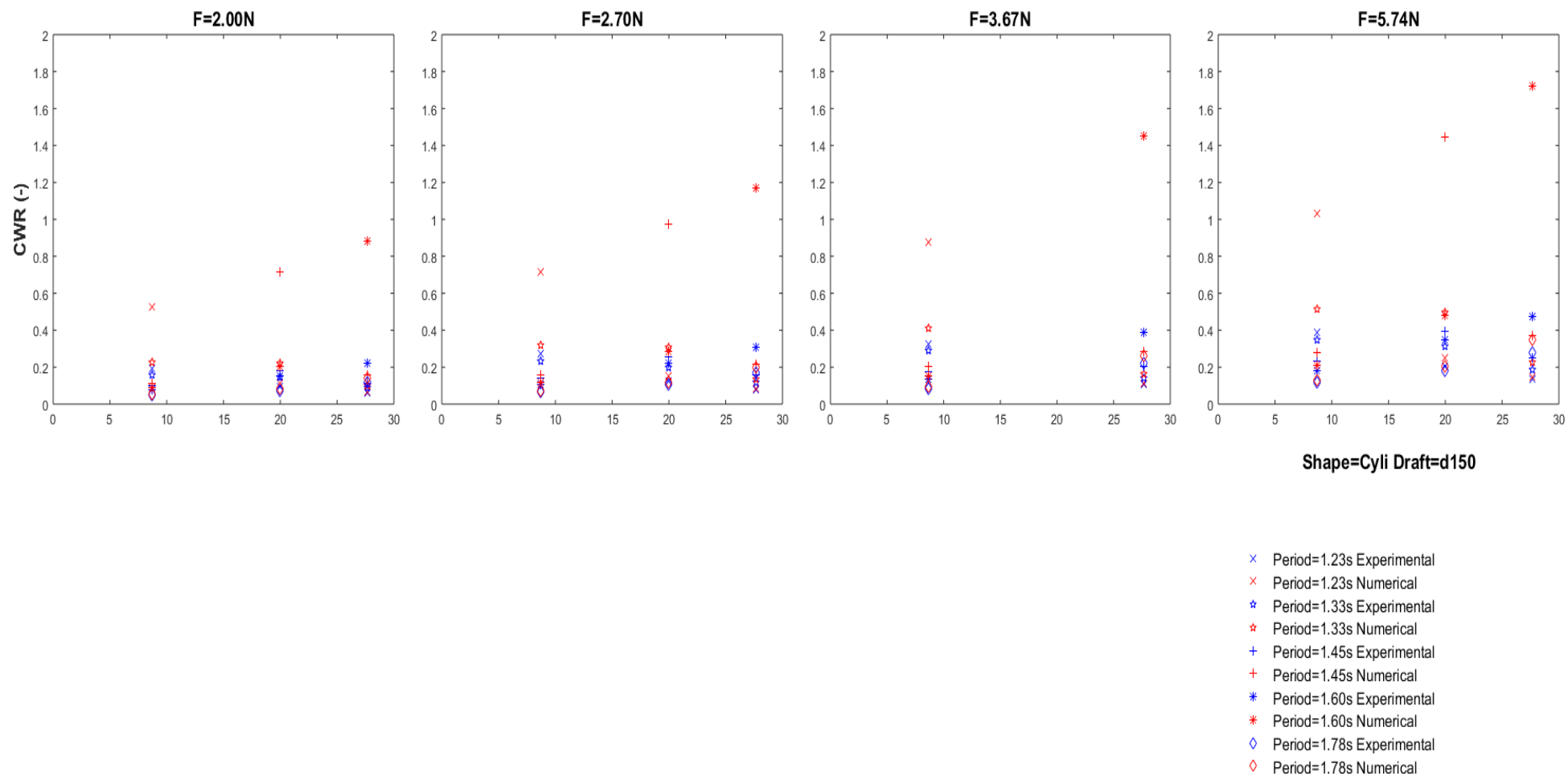
Figure B:22: Capture width ratio vs supplementary mass for constant damping force with varying wave period. Cylinder shape, draft=150mm
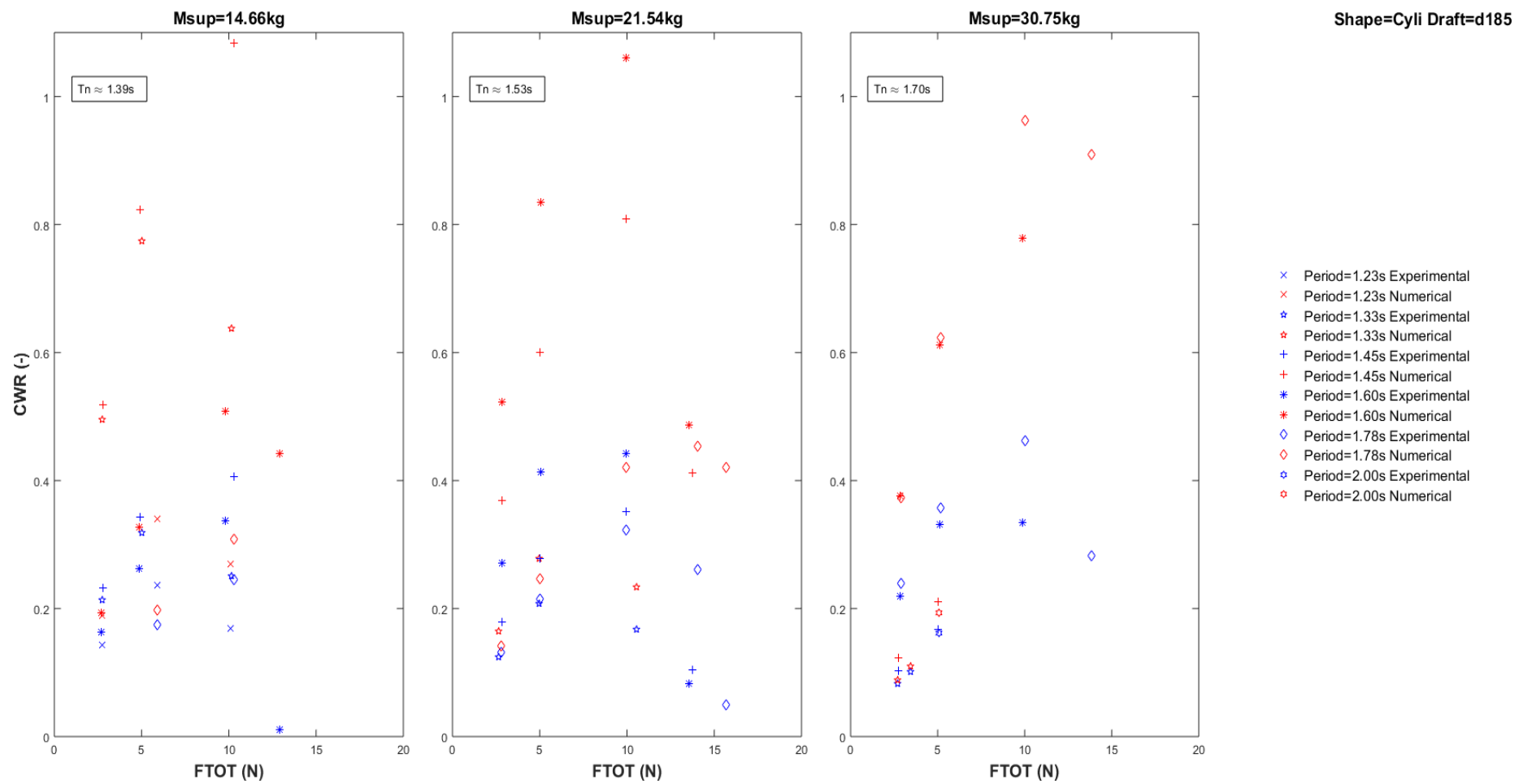
Figure B:23: Capture width ratio vs damping force for constant supplementary mass with varying wave period. Cylinder shape, draft=185mm
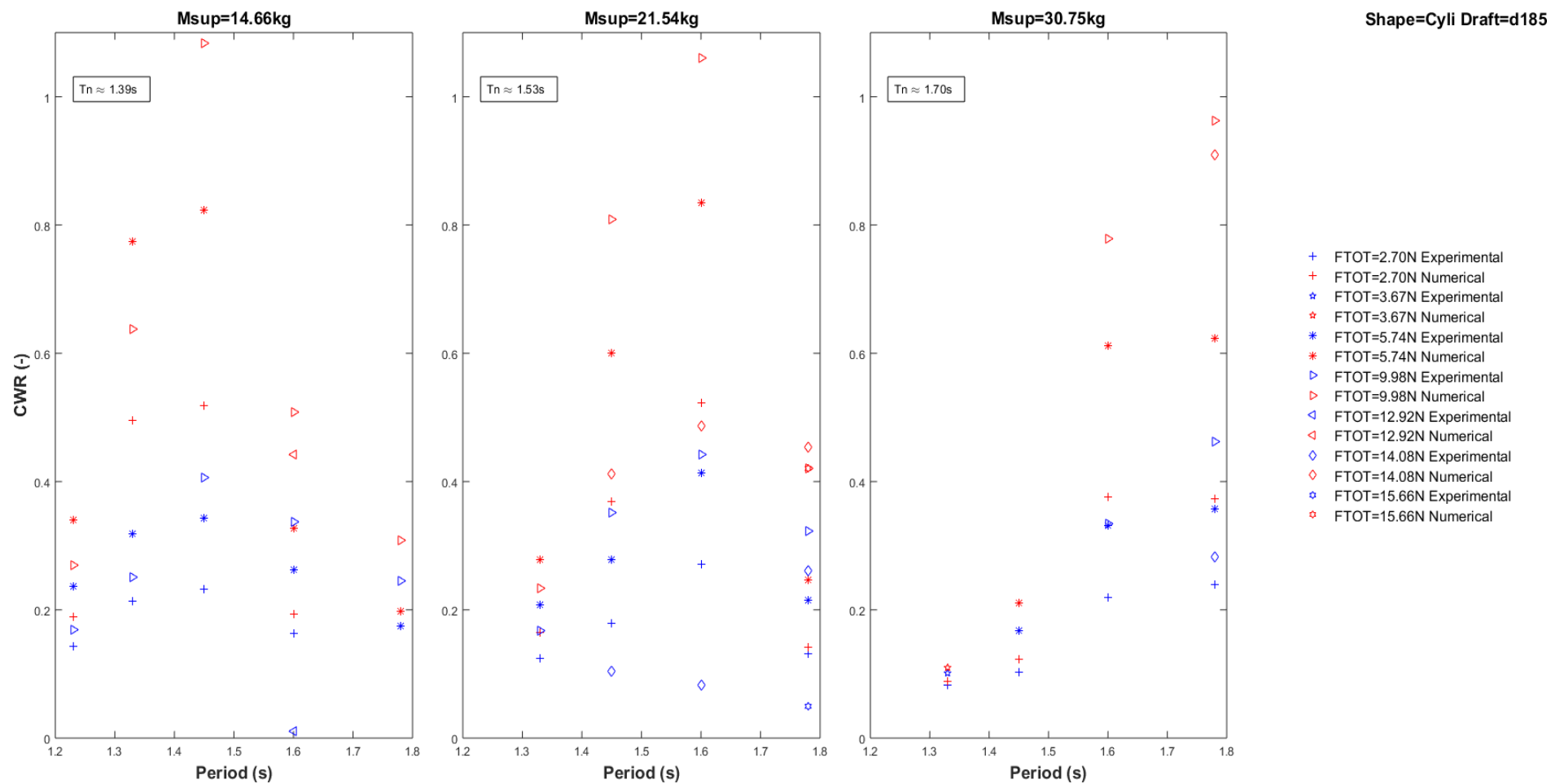
Figure B:24: Capture width ratio vs wave period for constant supplementary mass with varying damping force. Cylinder shape, draft=185mm
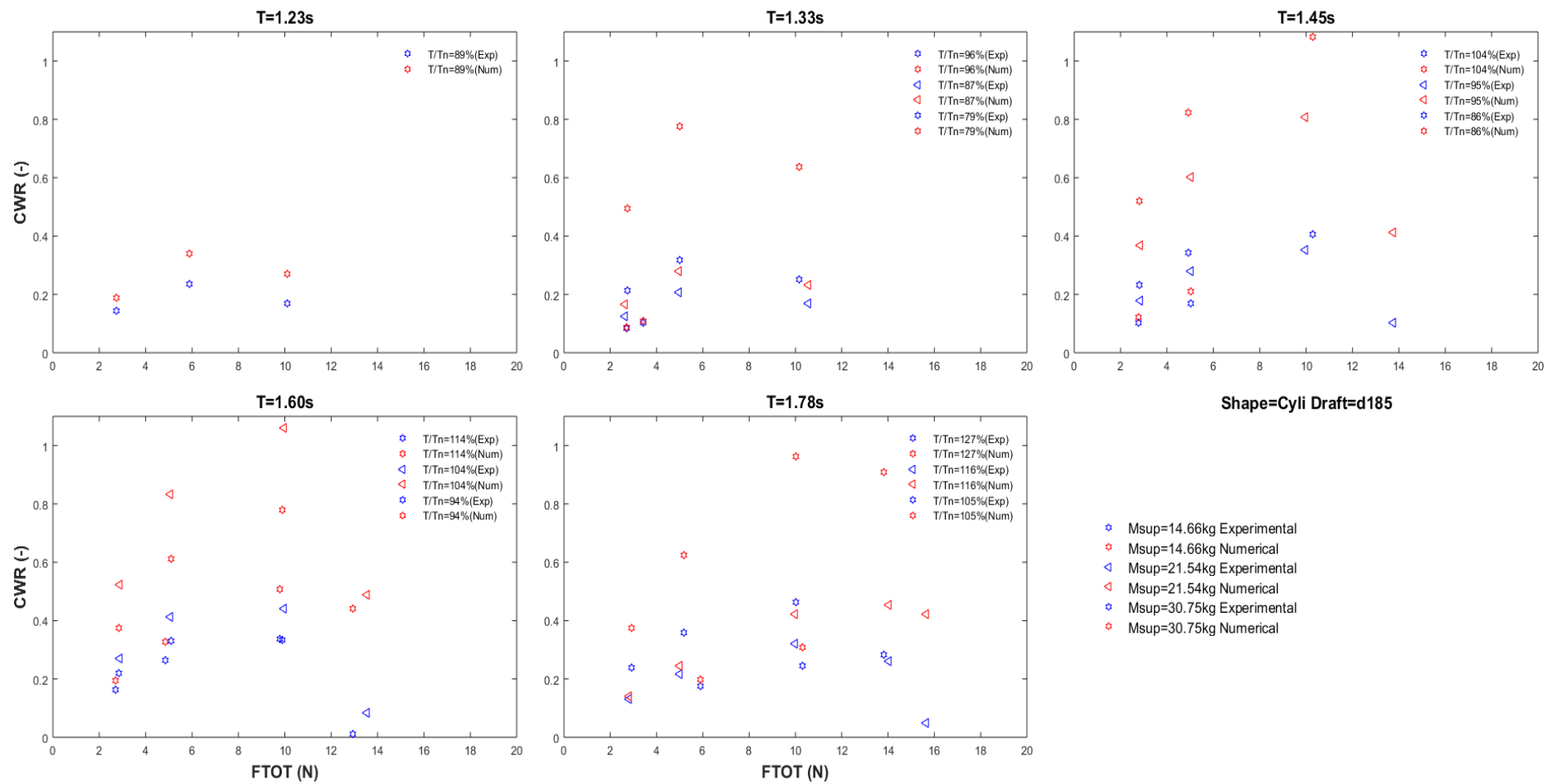
Figure B:25: Capture width ratio vs damping force for constant wave period with varying supplementary mass. Cylinder shape, draft=185mm
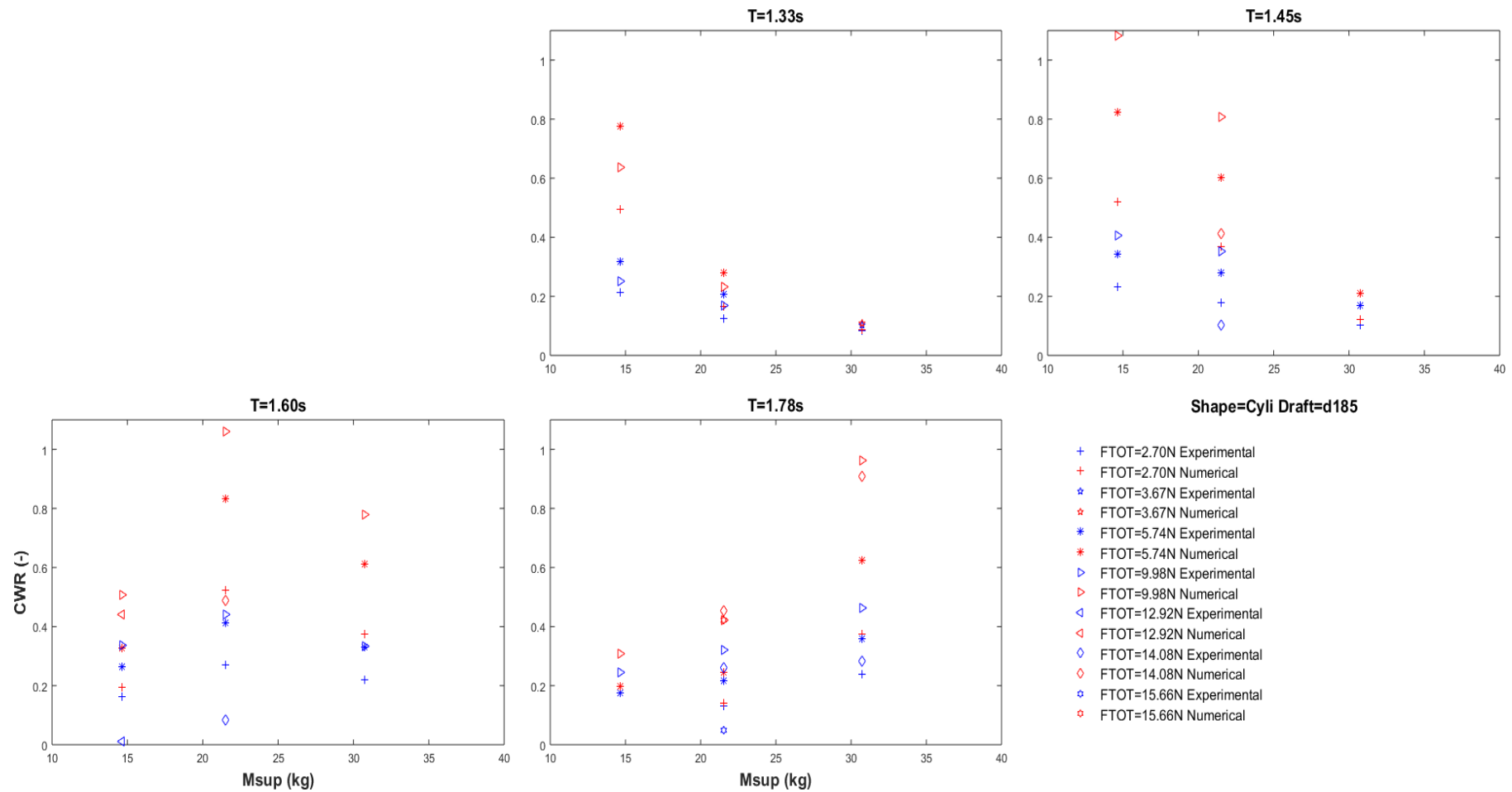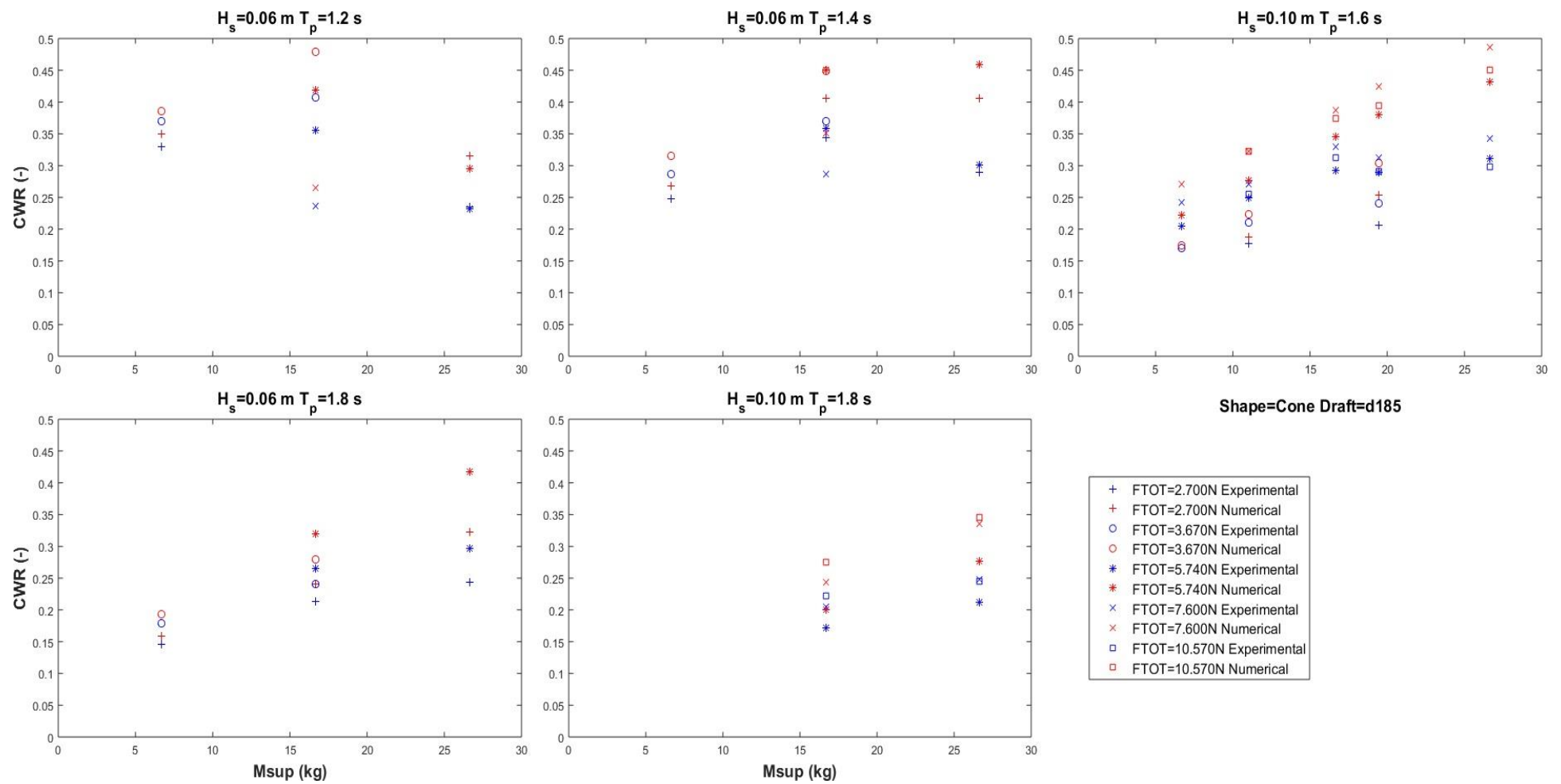
Figure B:26: Capture width ratio vs supplementary mass for constant wave period with varying damping force. Cylinder shape, draft=185mm
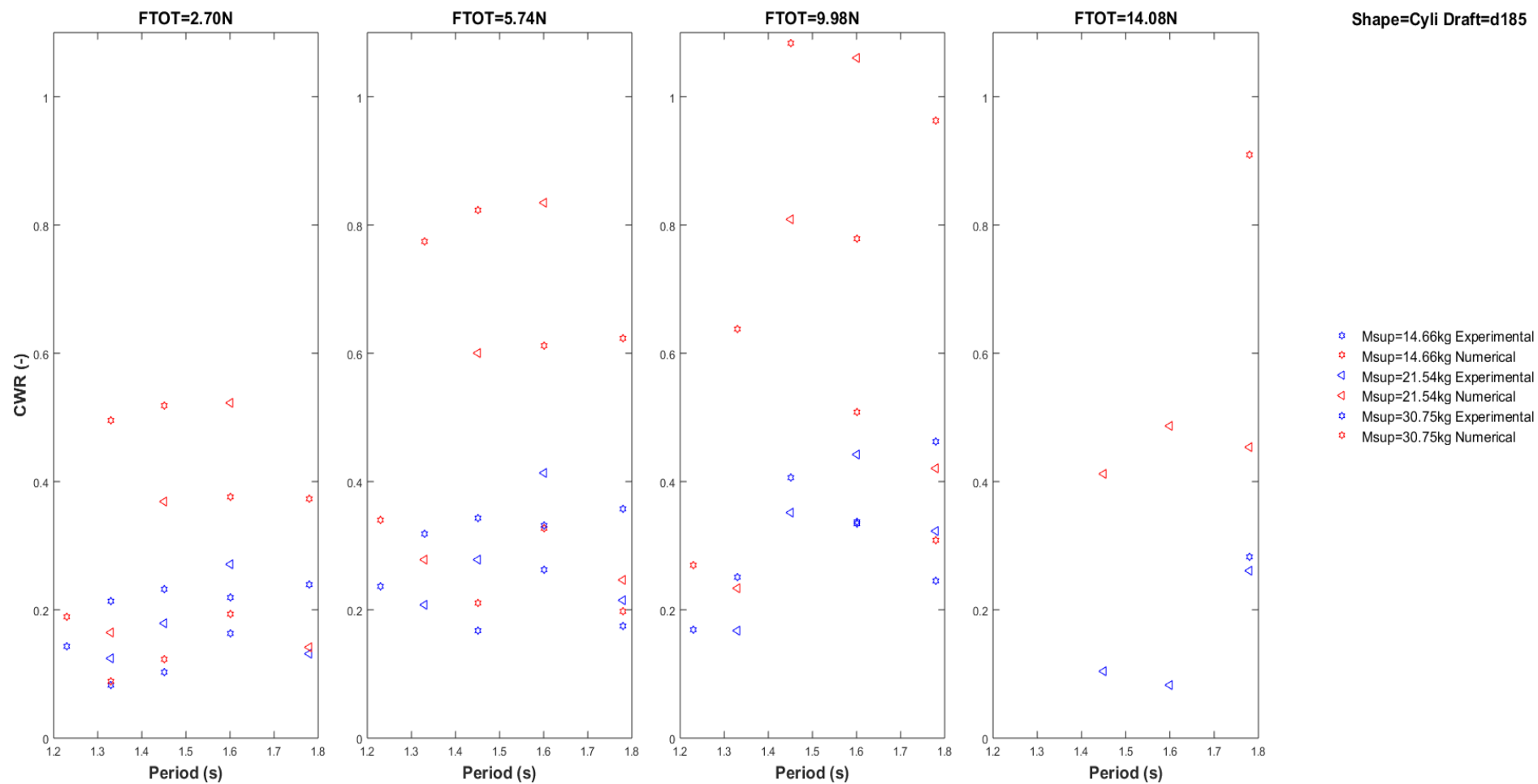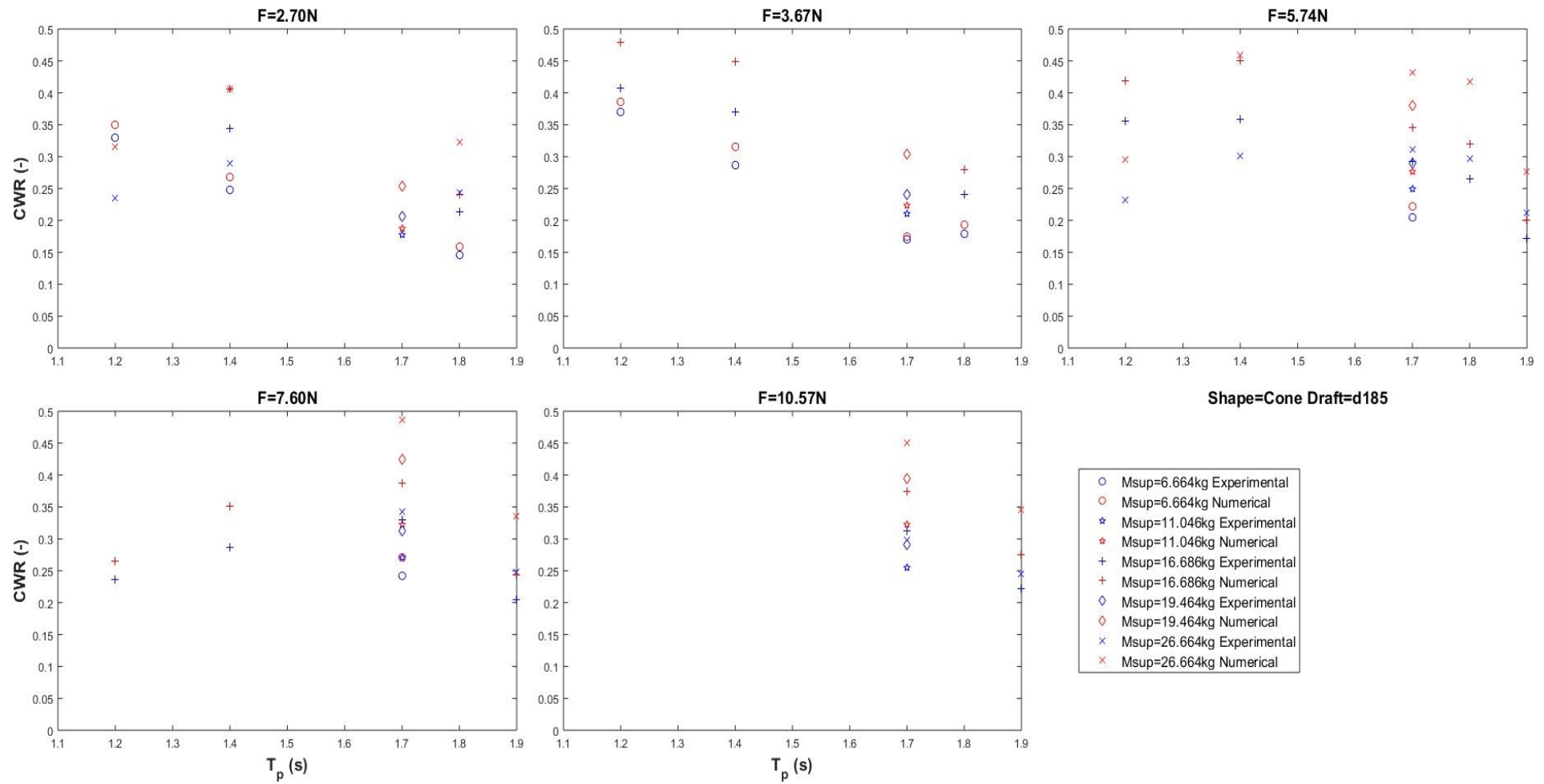
Figure B:27: Capture width ratio vs wave period for constant damping force with varying supplementary mass. Cylinder shape, draft=185mm
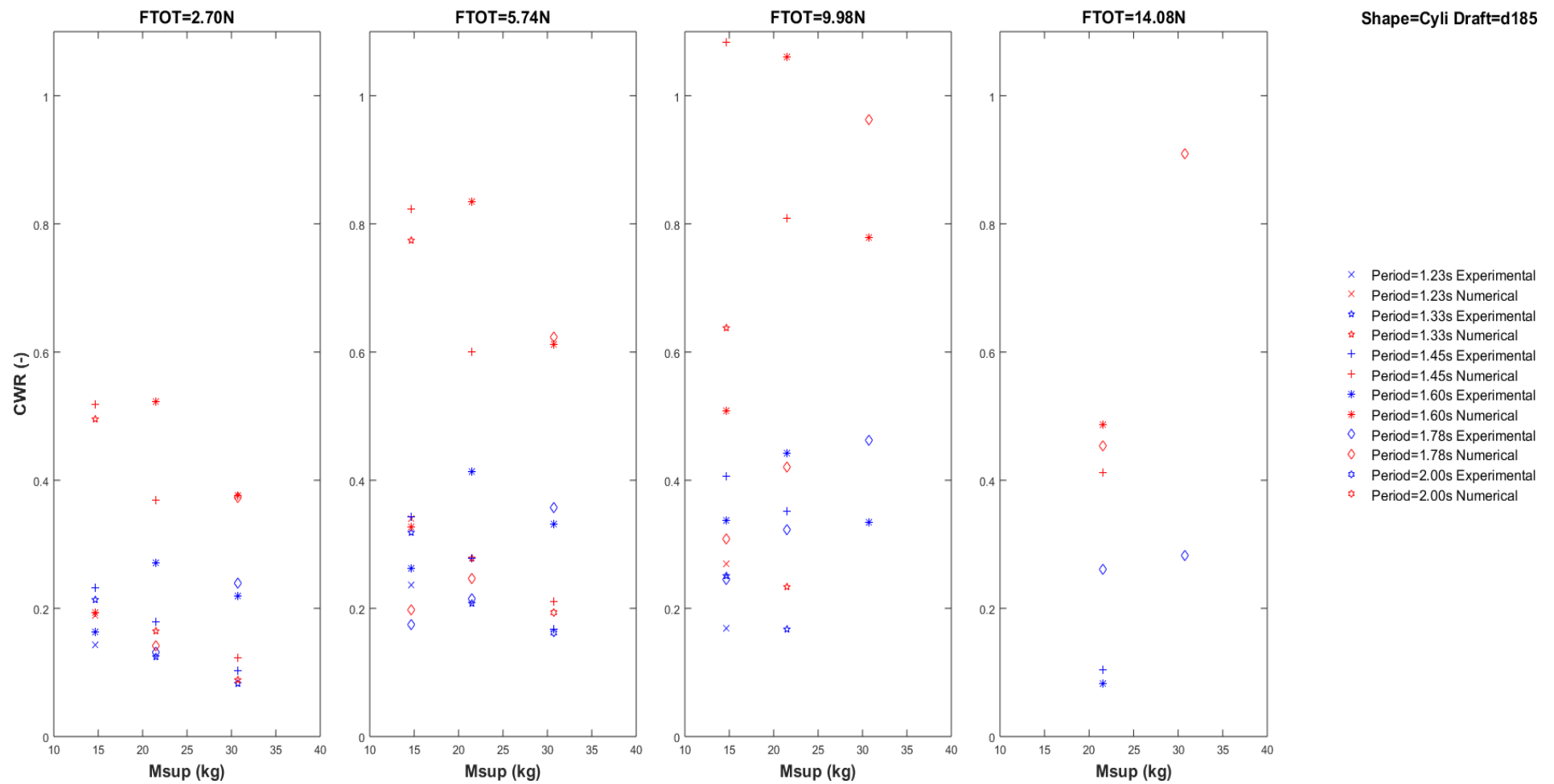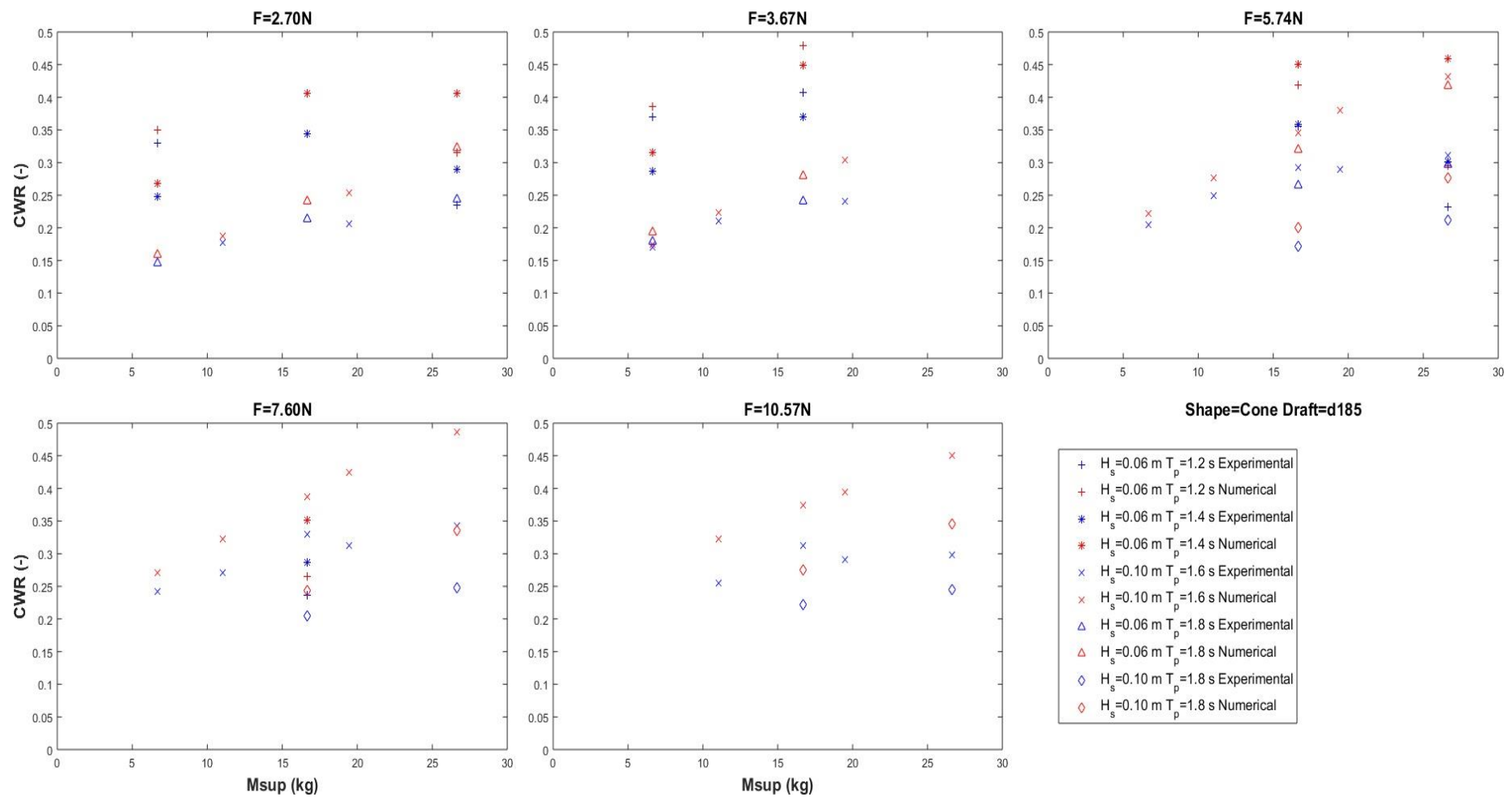
Figure B:28: Capture width ratio vs supplementary mass for constant damping force with varying wave period. Cylinder shape, draft=185mm
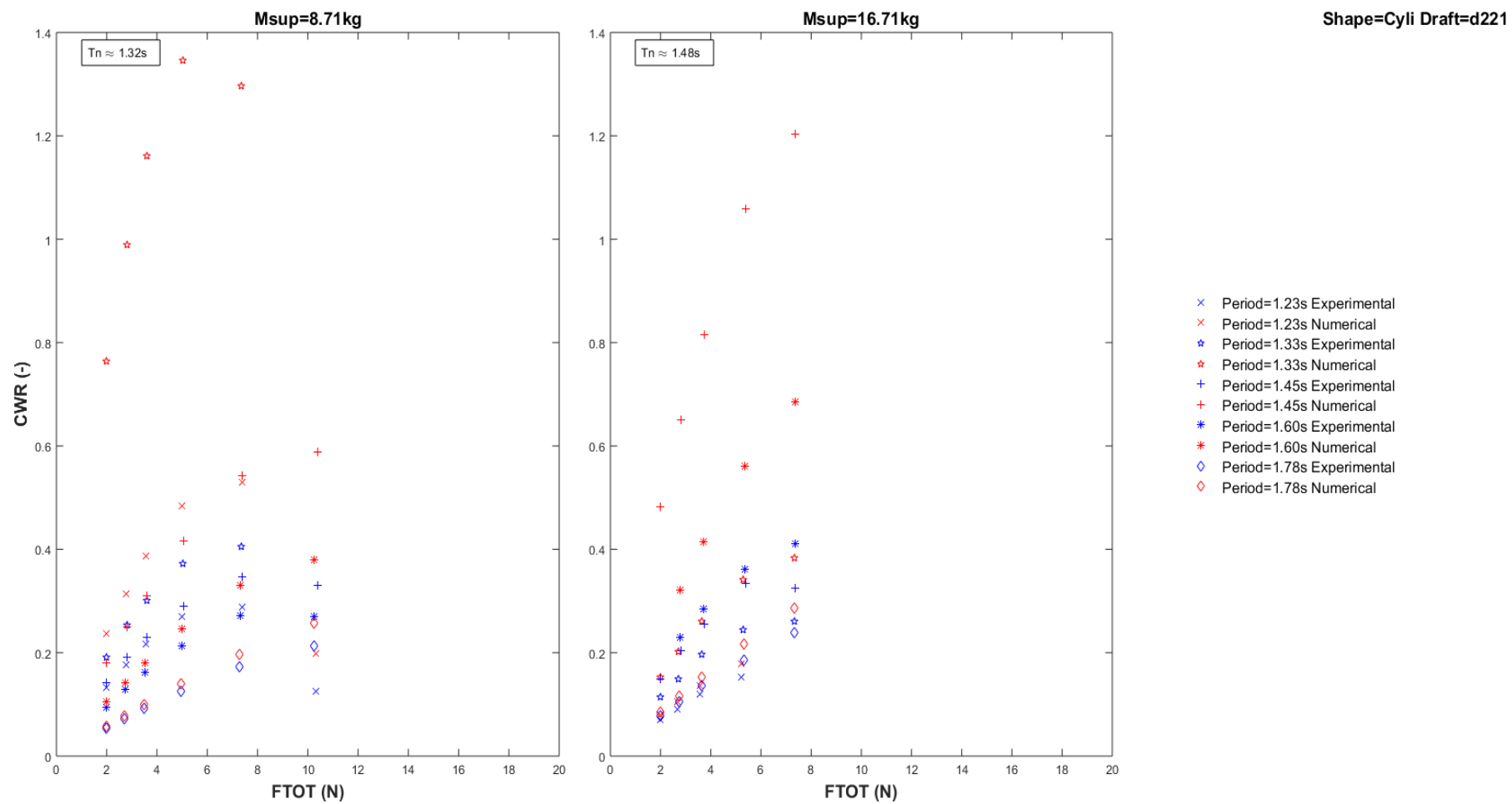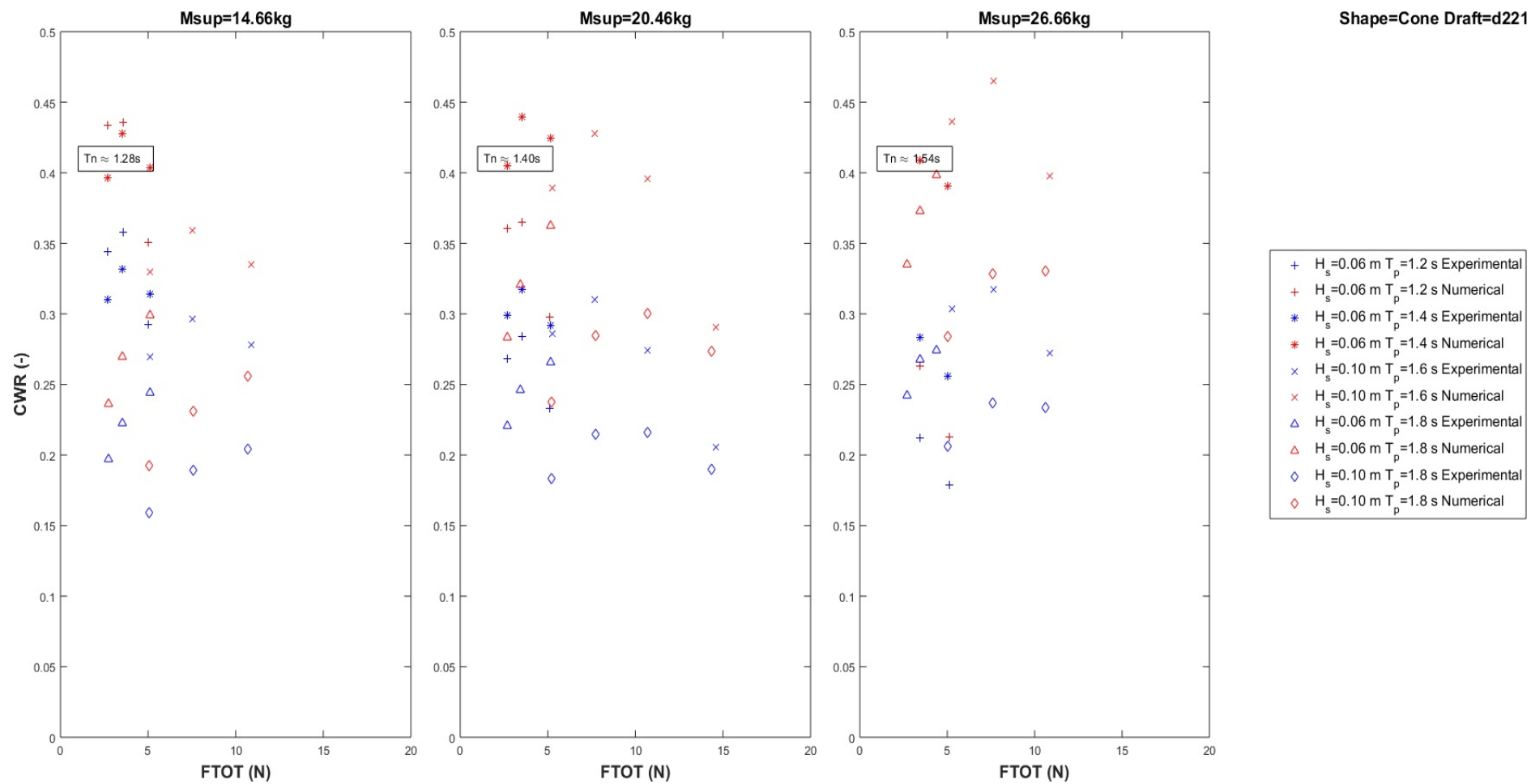
Figure B:29: Capture width ratio vs damping force for constant supplementary mass with varying wave period. Cylinder shape, draft=221mm
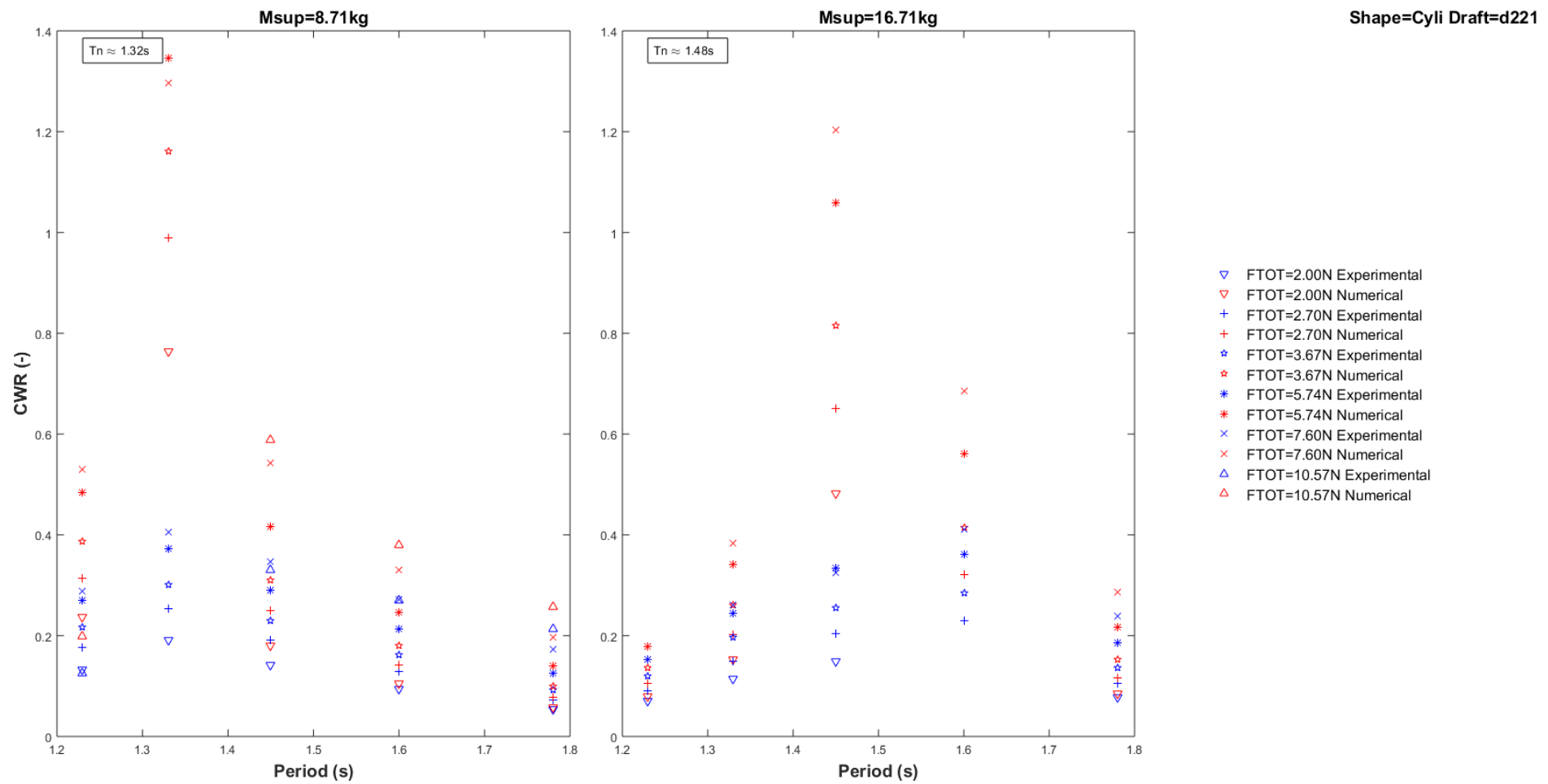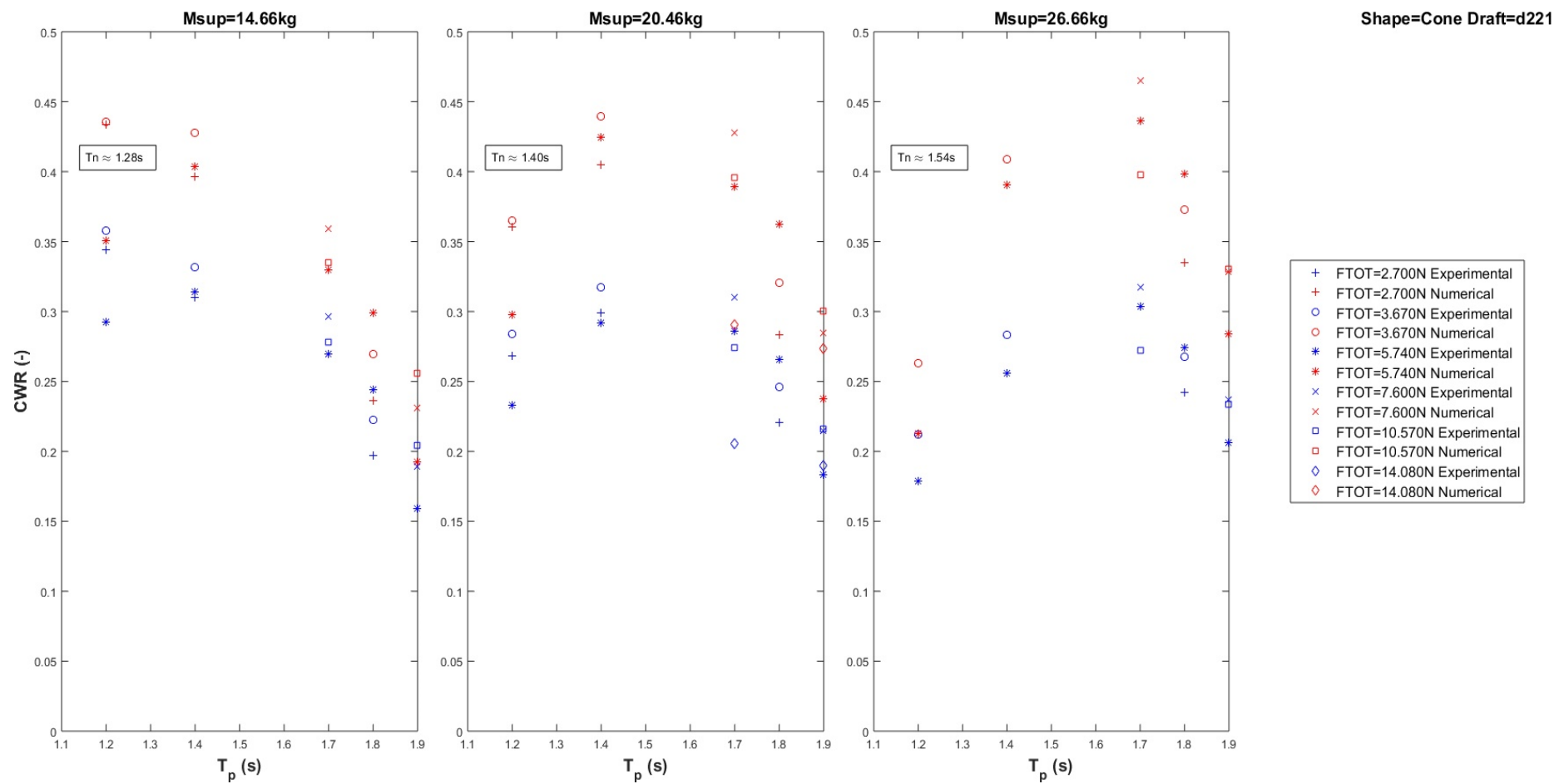
Figure B:30: Capture width ratio vs wave period for constant supplementary mass with varying damping force. Cylinder shape, draft=221mm
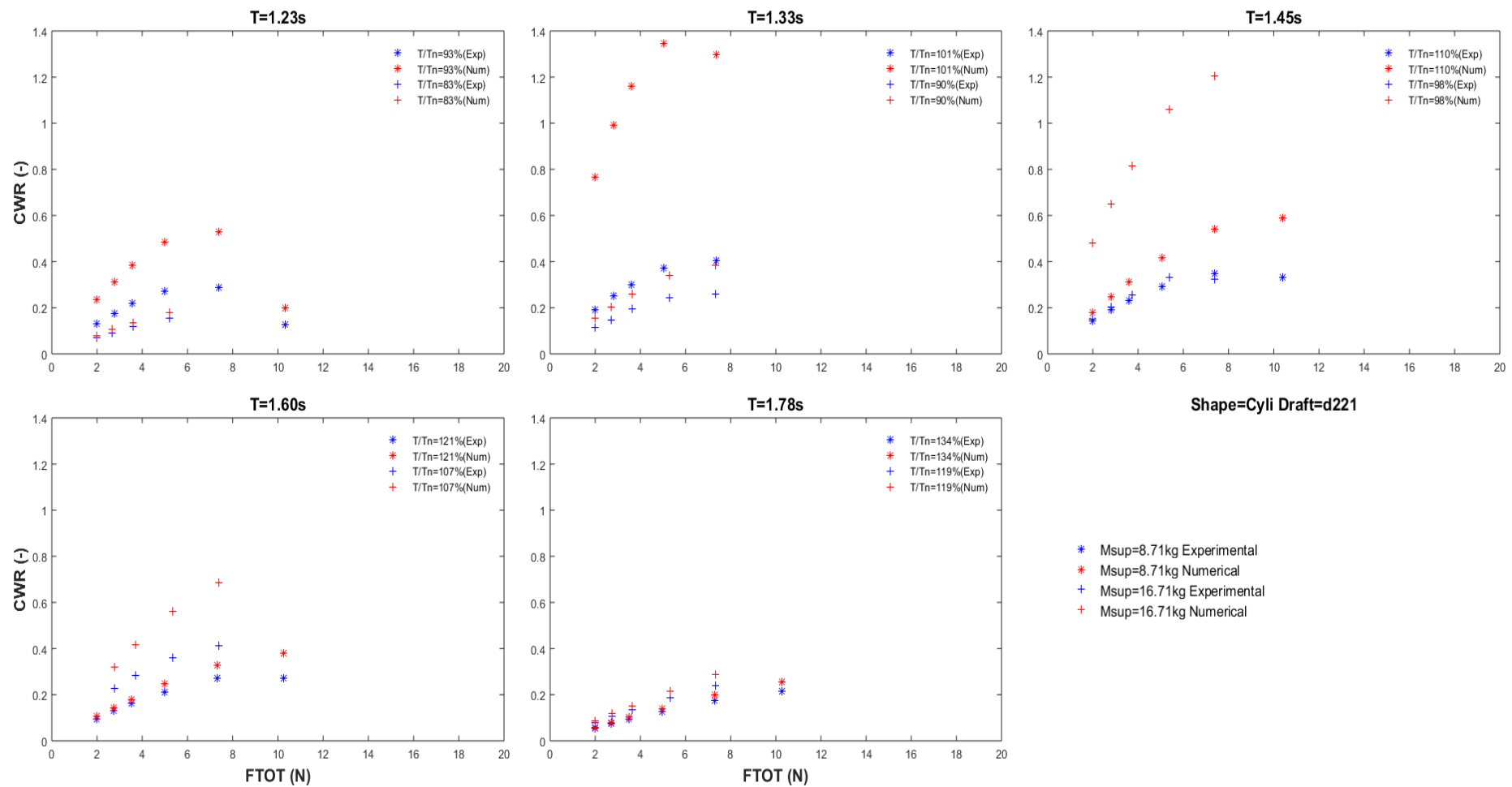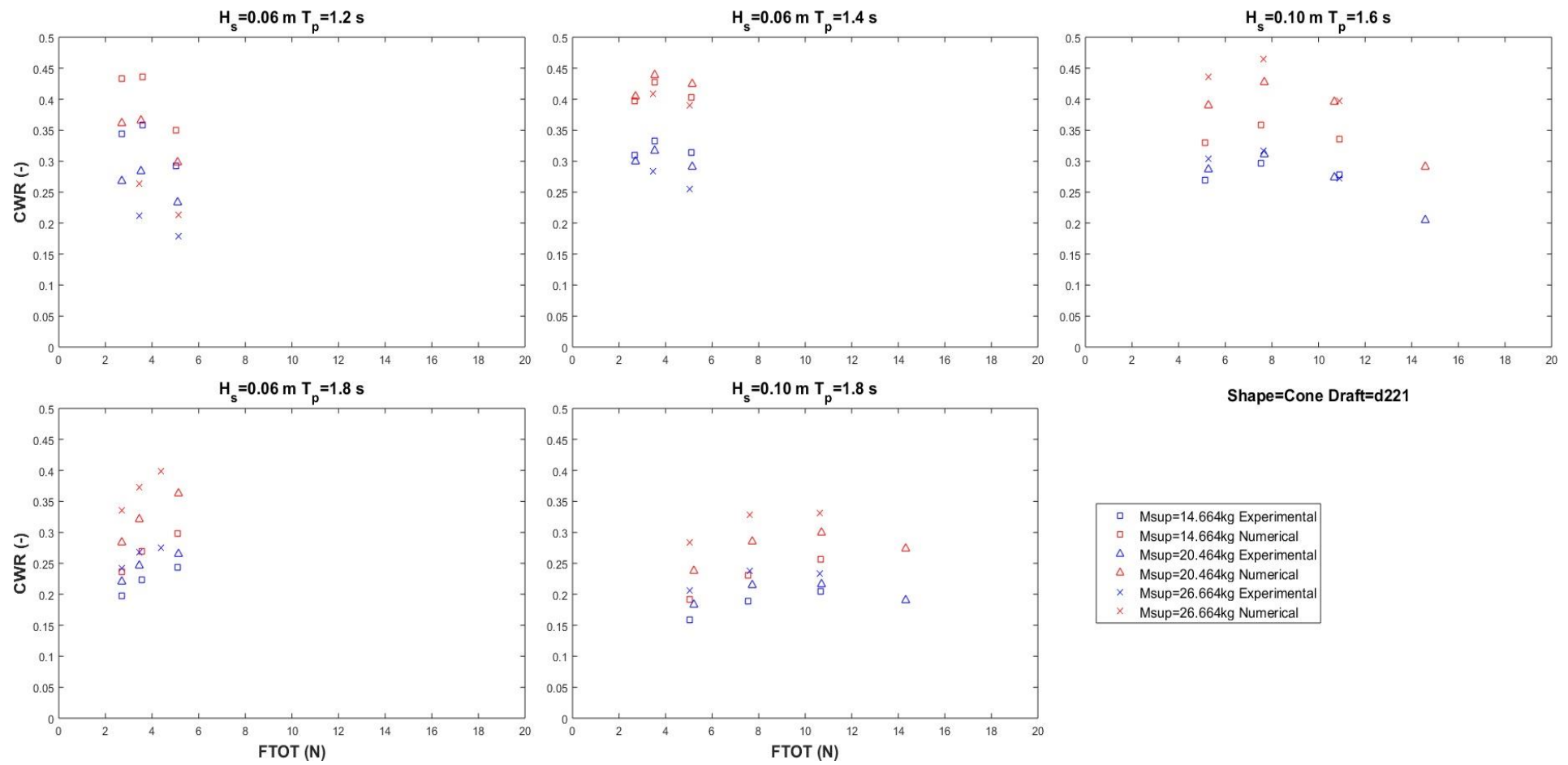
Figure B:31: Capture width ratio vs damping force for constant wave period with varying supplementary mass. Cylinder shape, draft=221mm
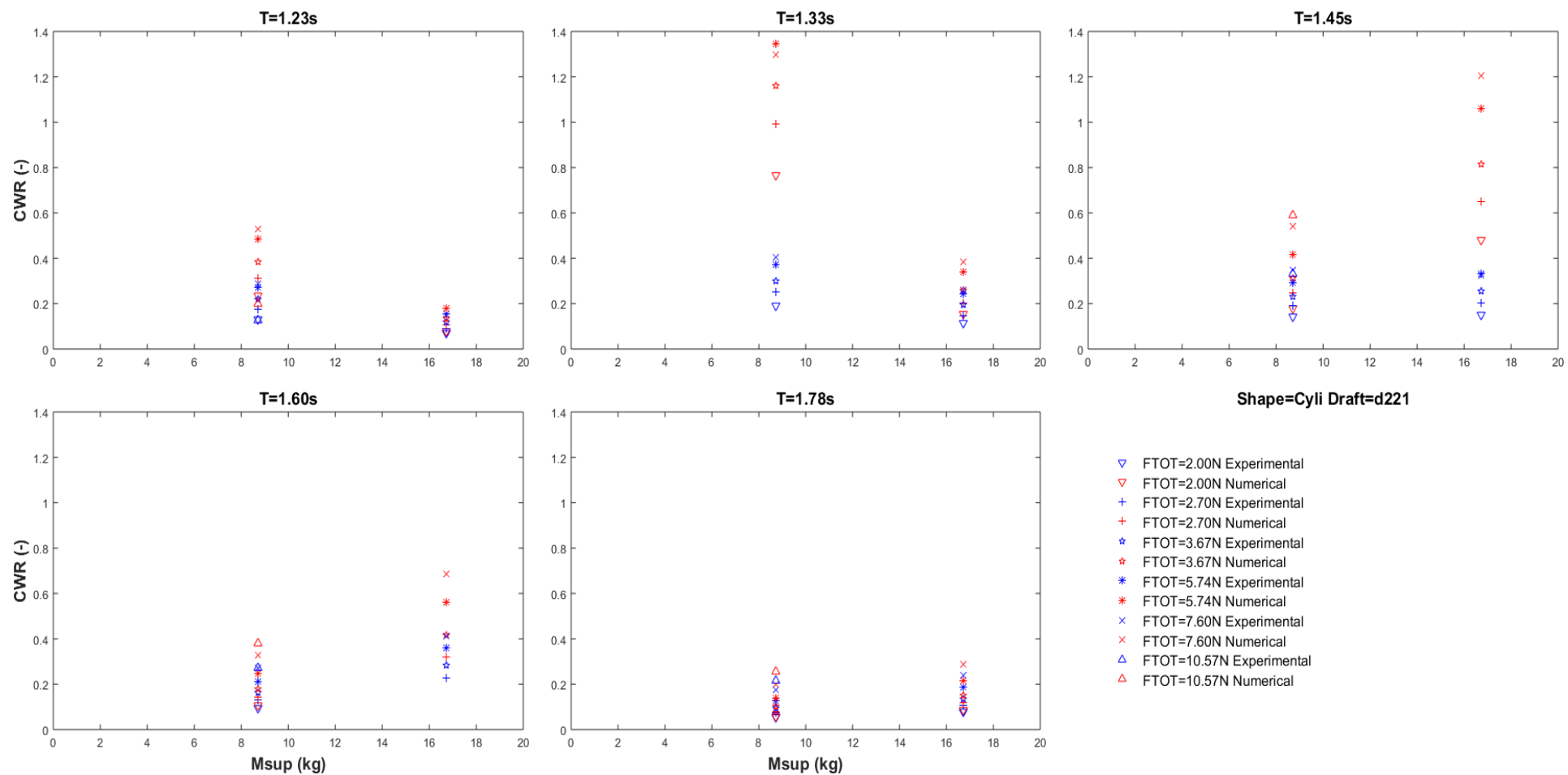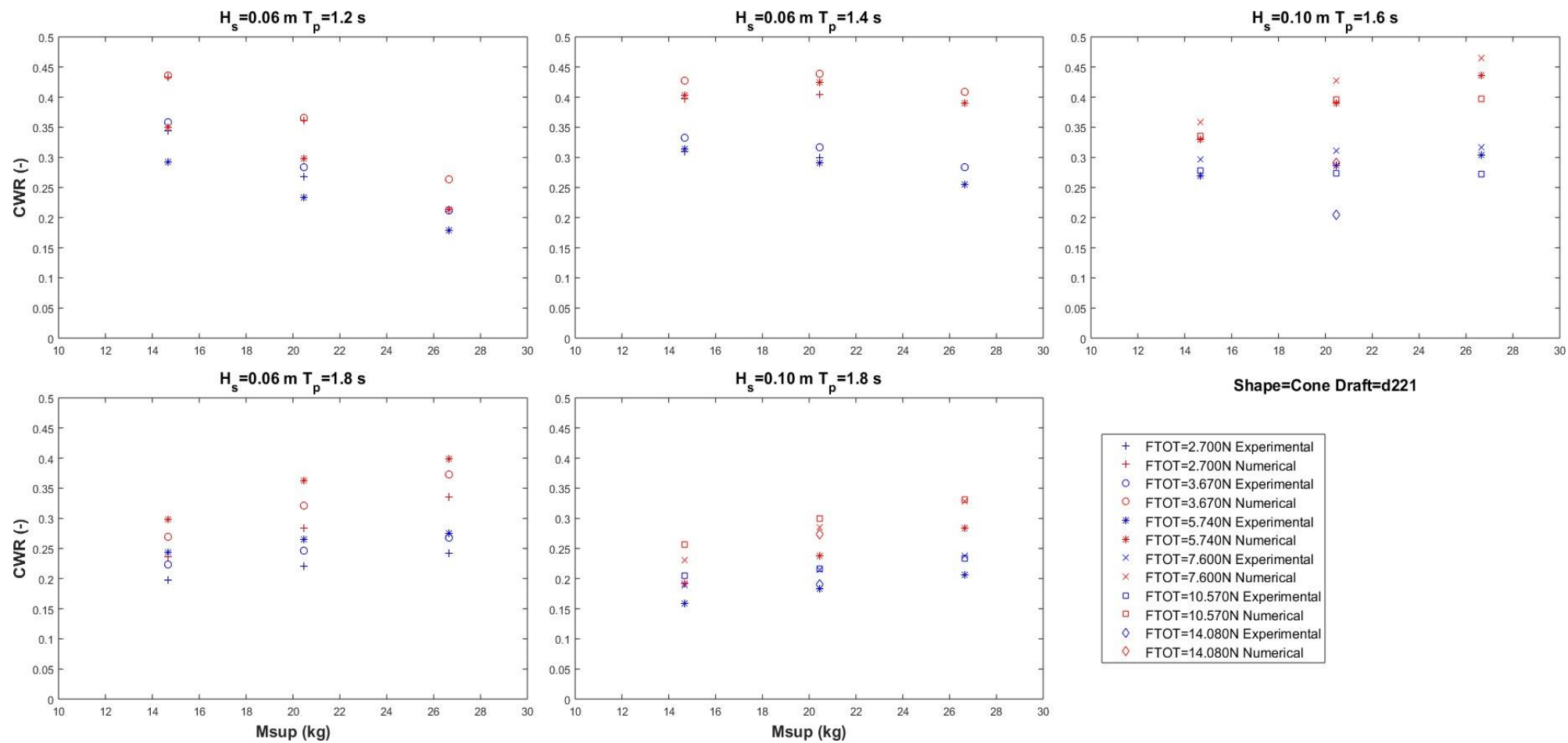
Figure B:32: Capture width ratio vs supplementary mass for constant wave period with varying damping force. Cylinder shape, draft=221mm
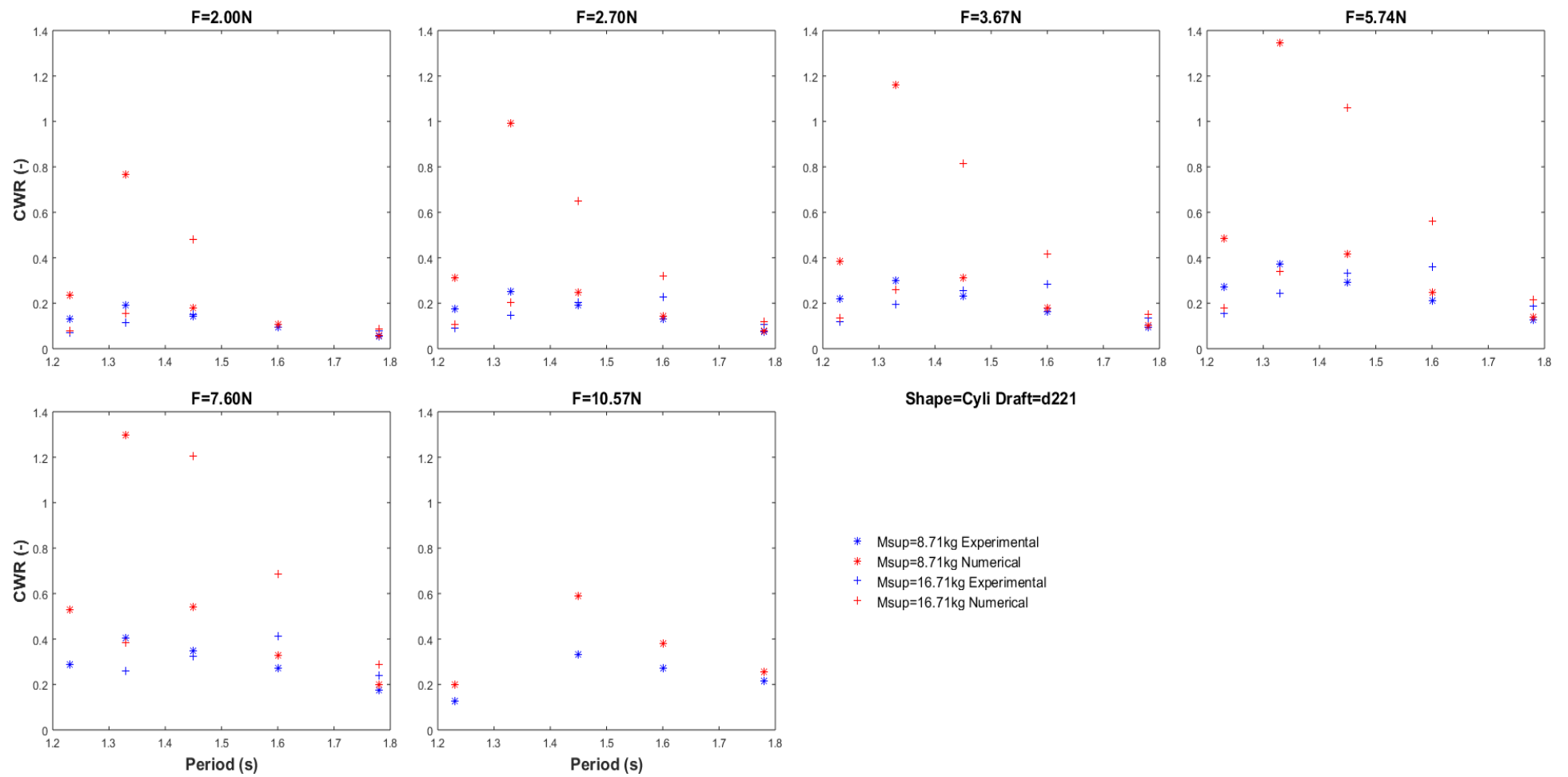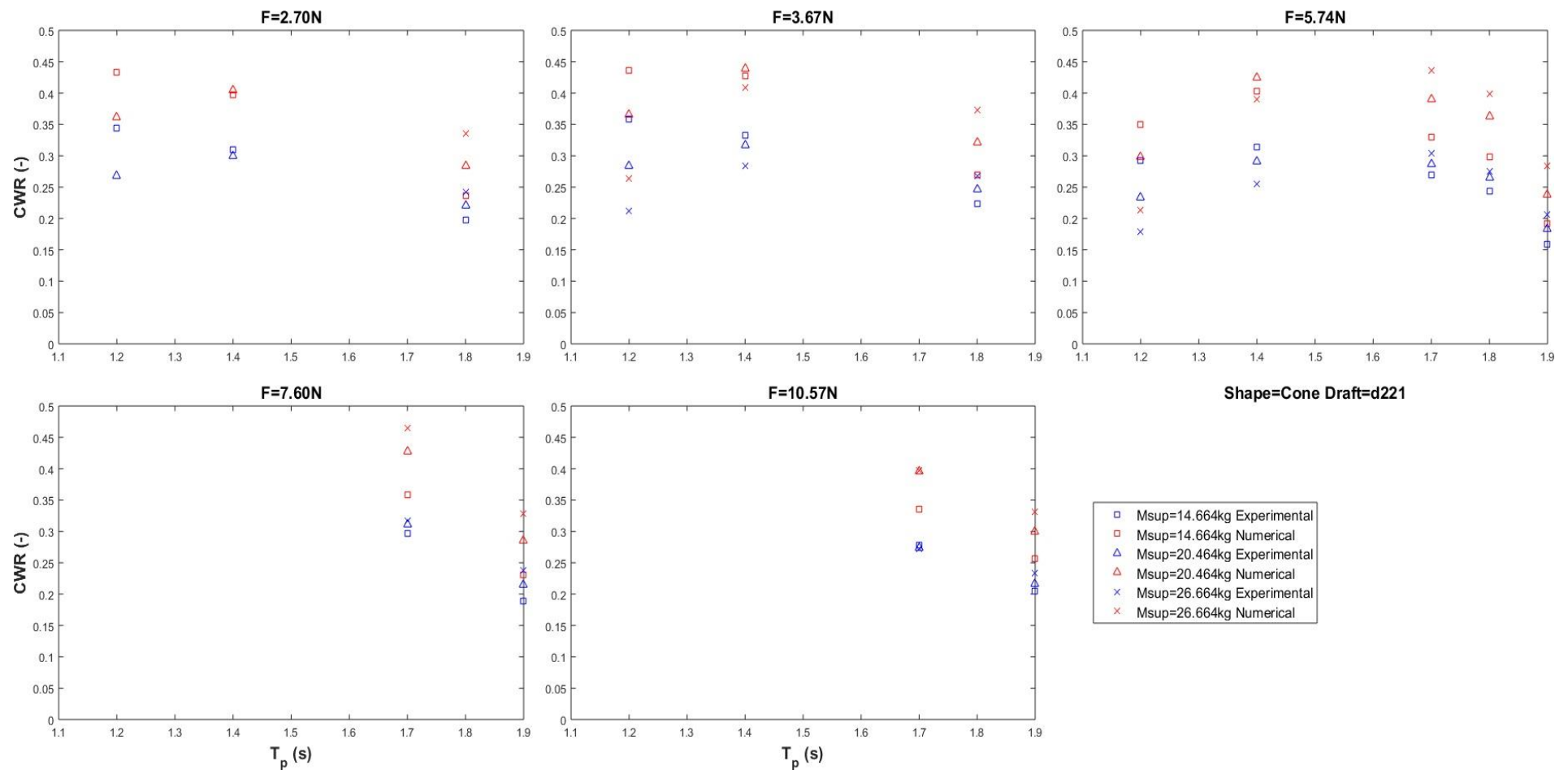
Figure B:33: Capture width ratio vs wave period for constant damping force with varying supplementary mass. Cylinder shape, draft=221mm
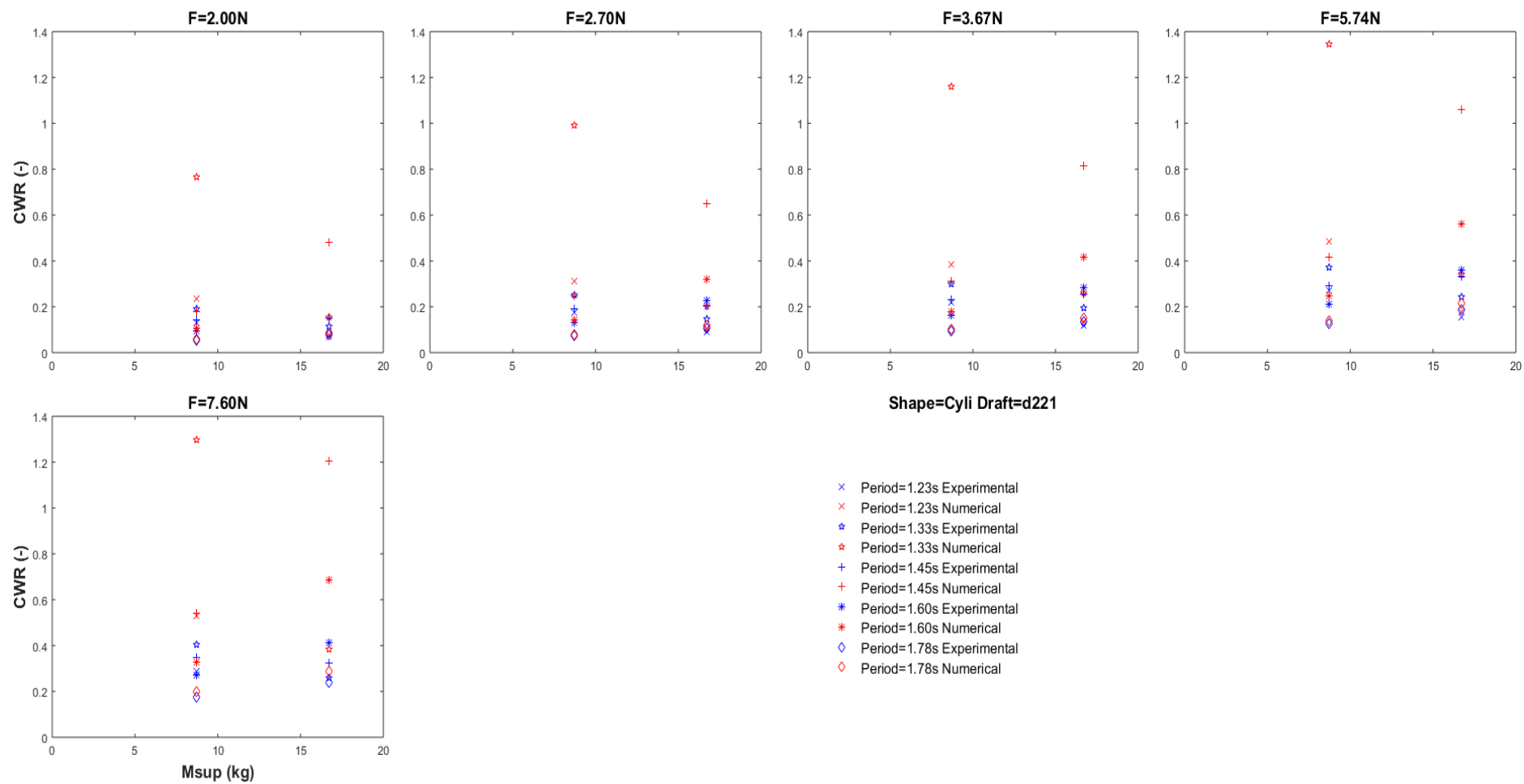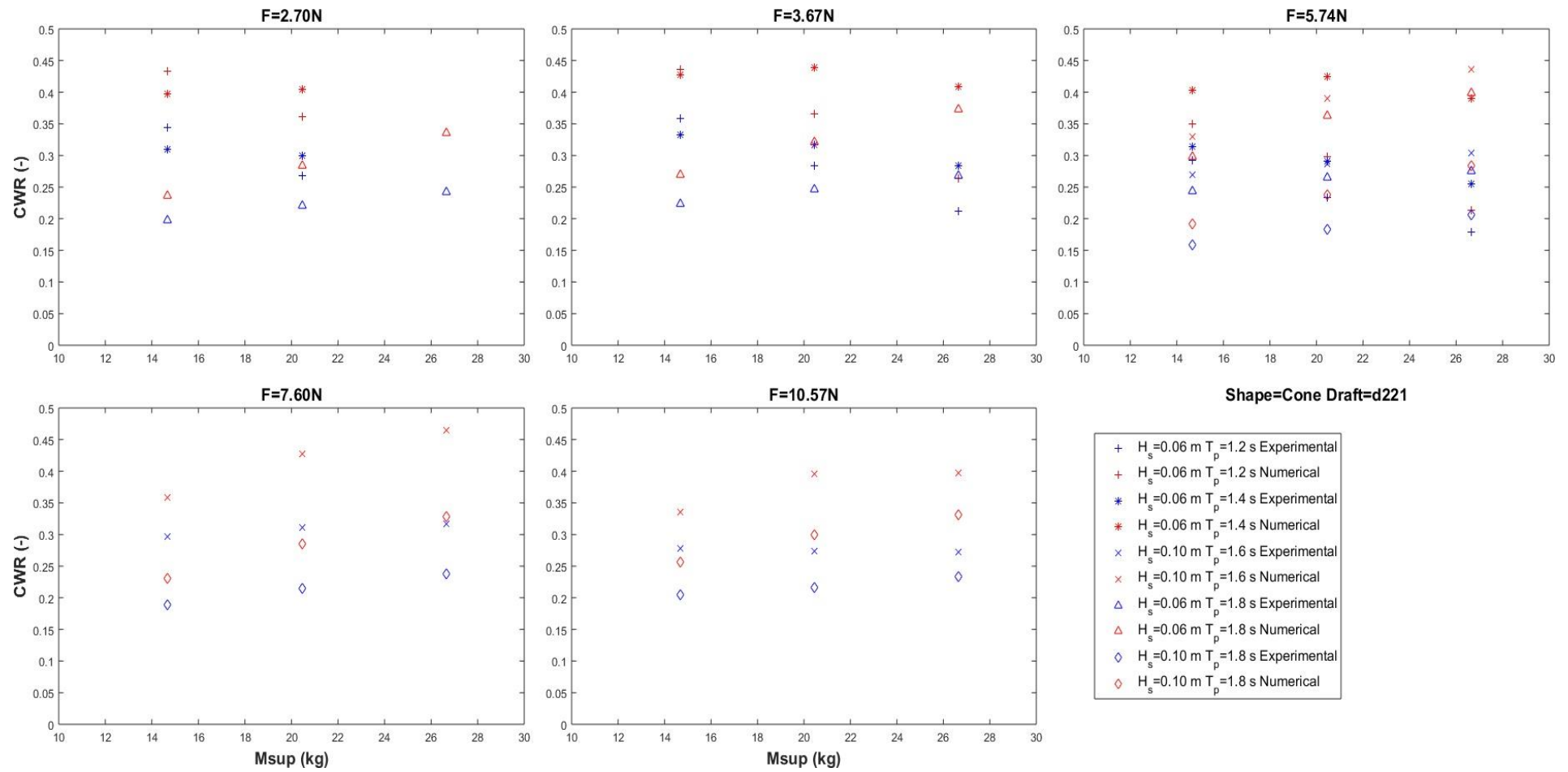
Figure B:34: Capture width ratio vs supplementary mass for constant damping force with varying wave period. Cylinder shape, draft=221mm
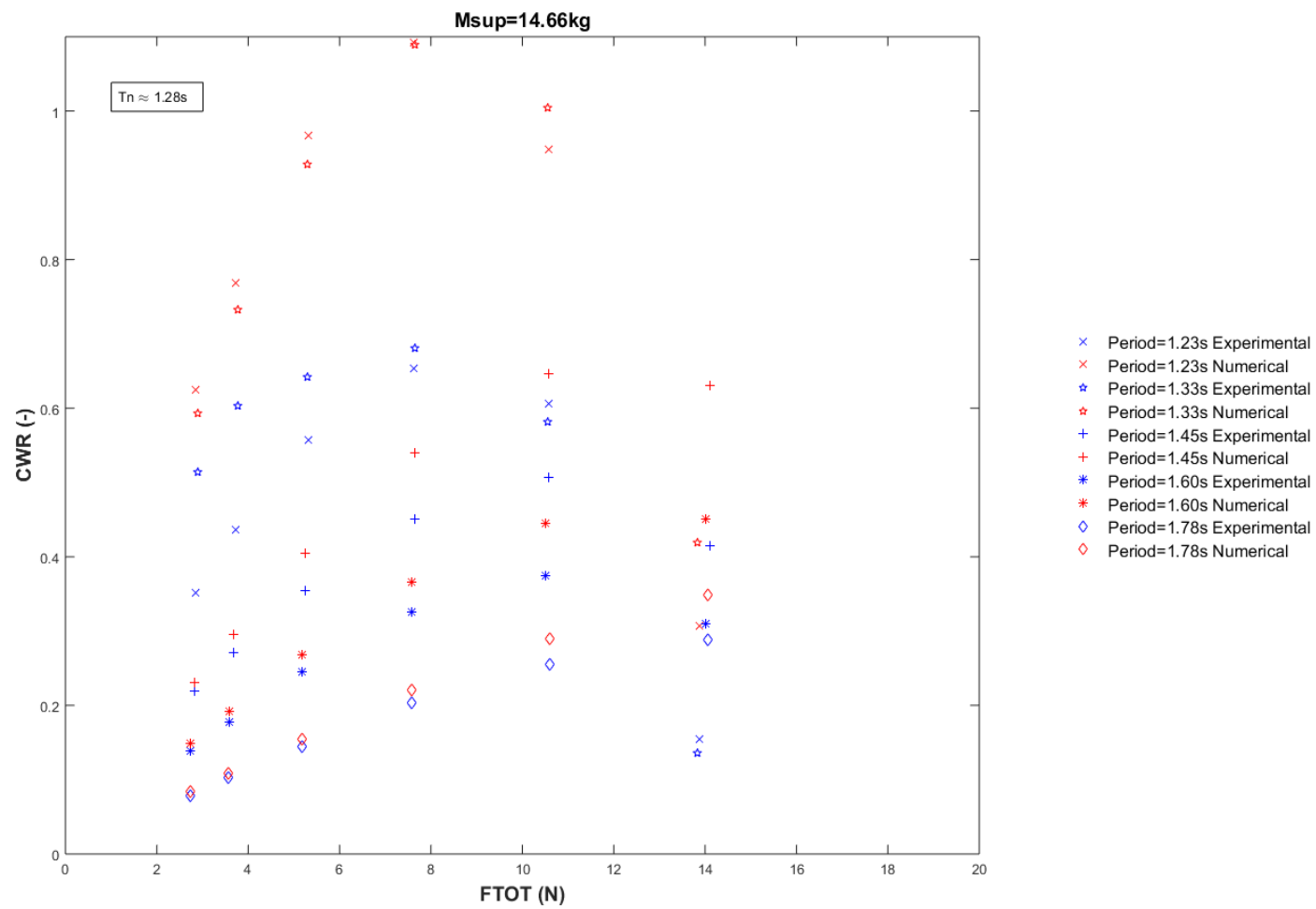
Figure B:35: Capture width ratio vs damping force for constant supplementary mass with varying wave period. Hemisphere-cylinder shape, draft=185mm
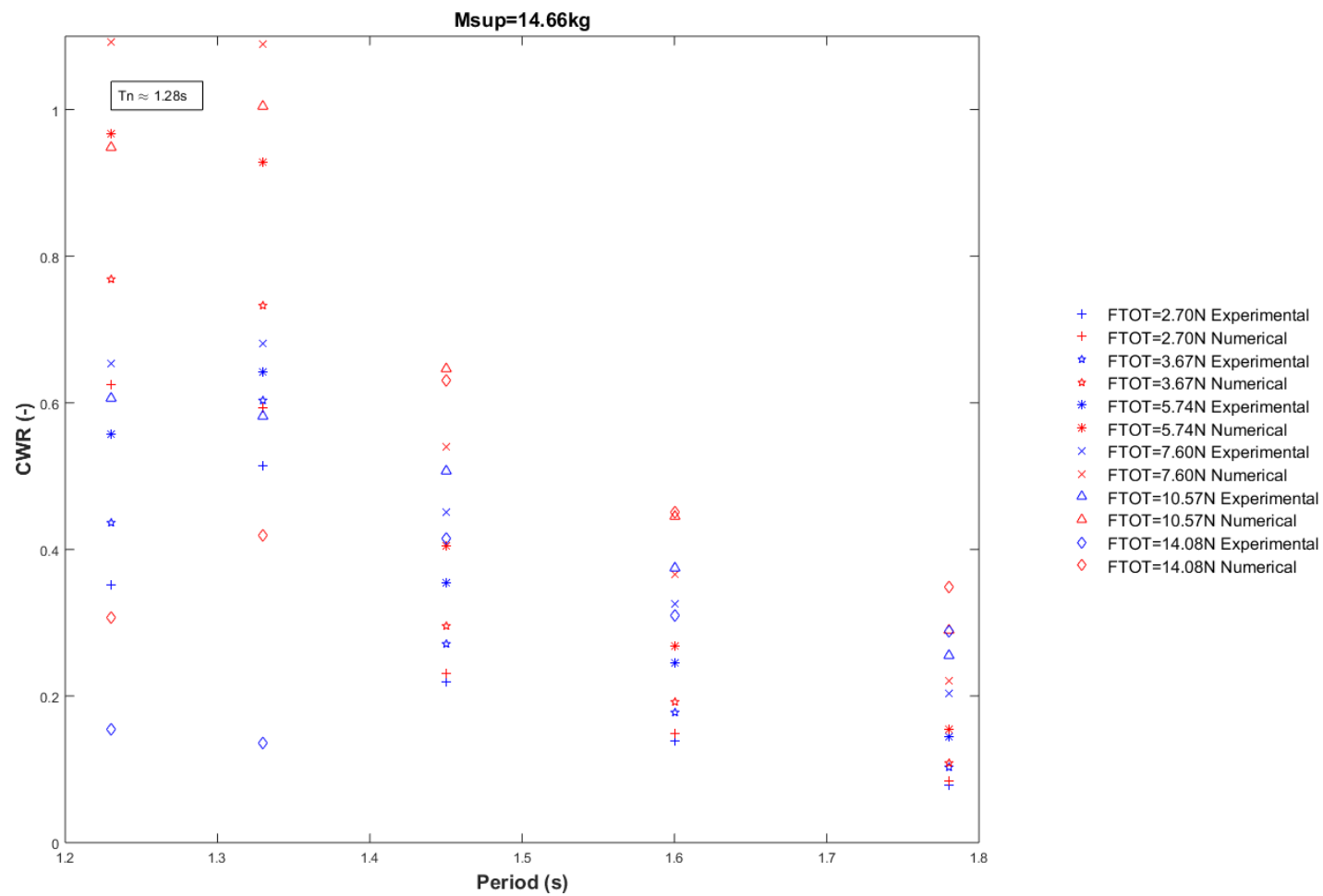
Figure B:36: Capture width ratio vs wave period for constant supplementary mass with varying damping force. Hemisphere -cylinder shape, draft=185mm
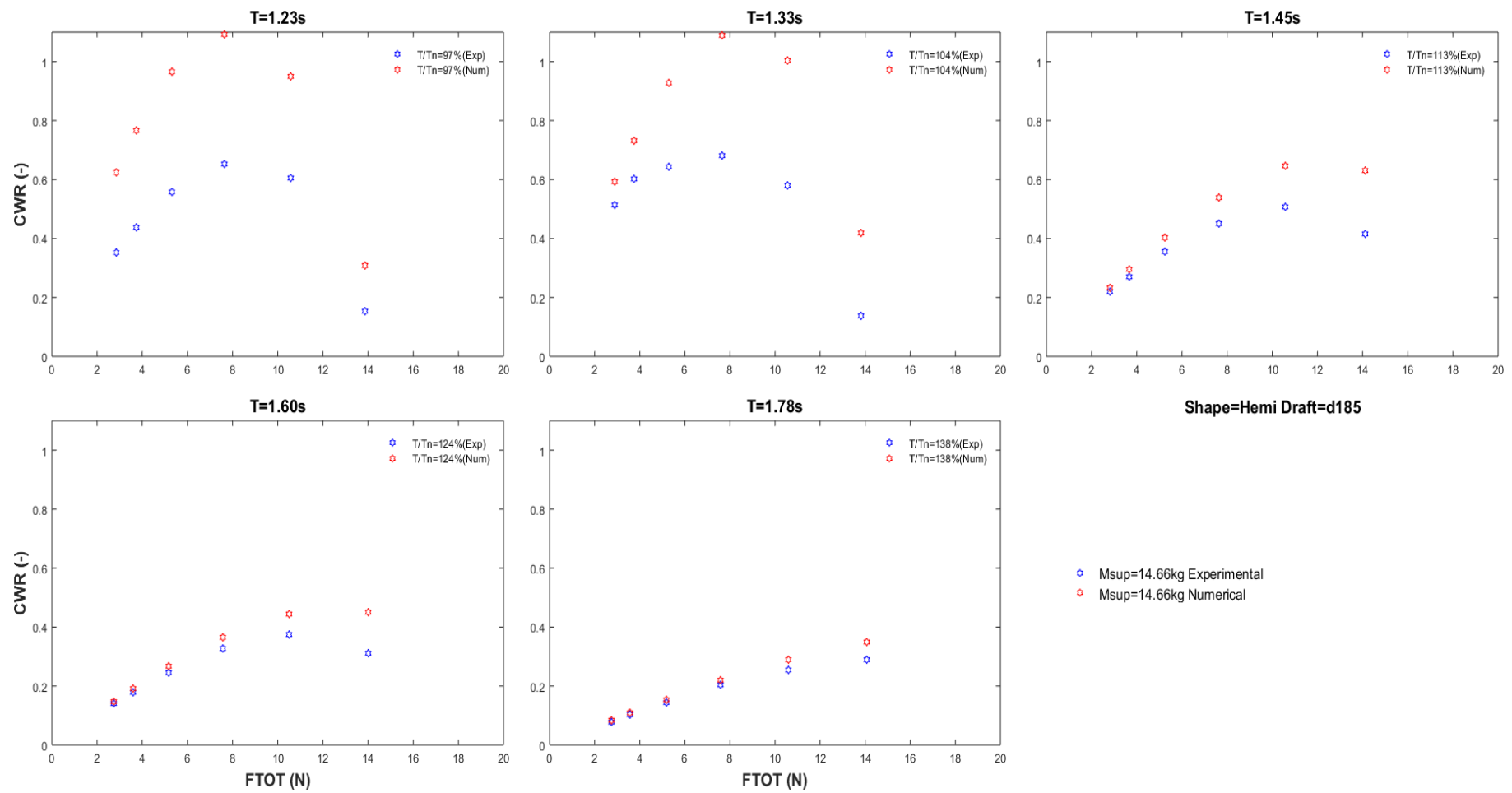
Figure B:37: Capture width ratio vs damping force for constant wave period with varying supplementary mass. Hemisphere -cylinder shape, draft=185mm

335
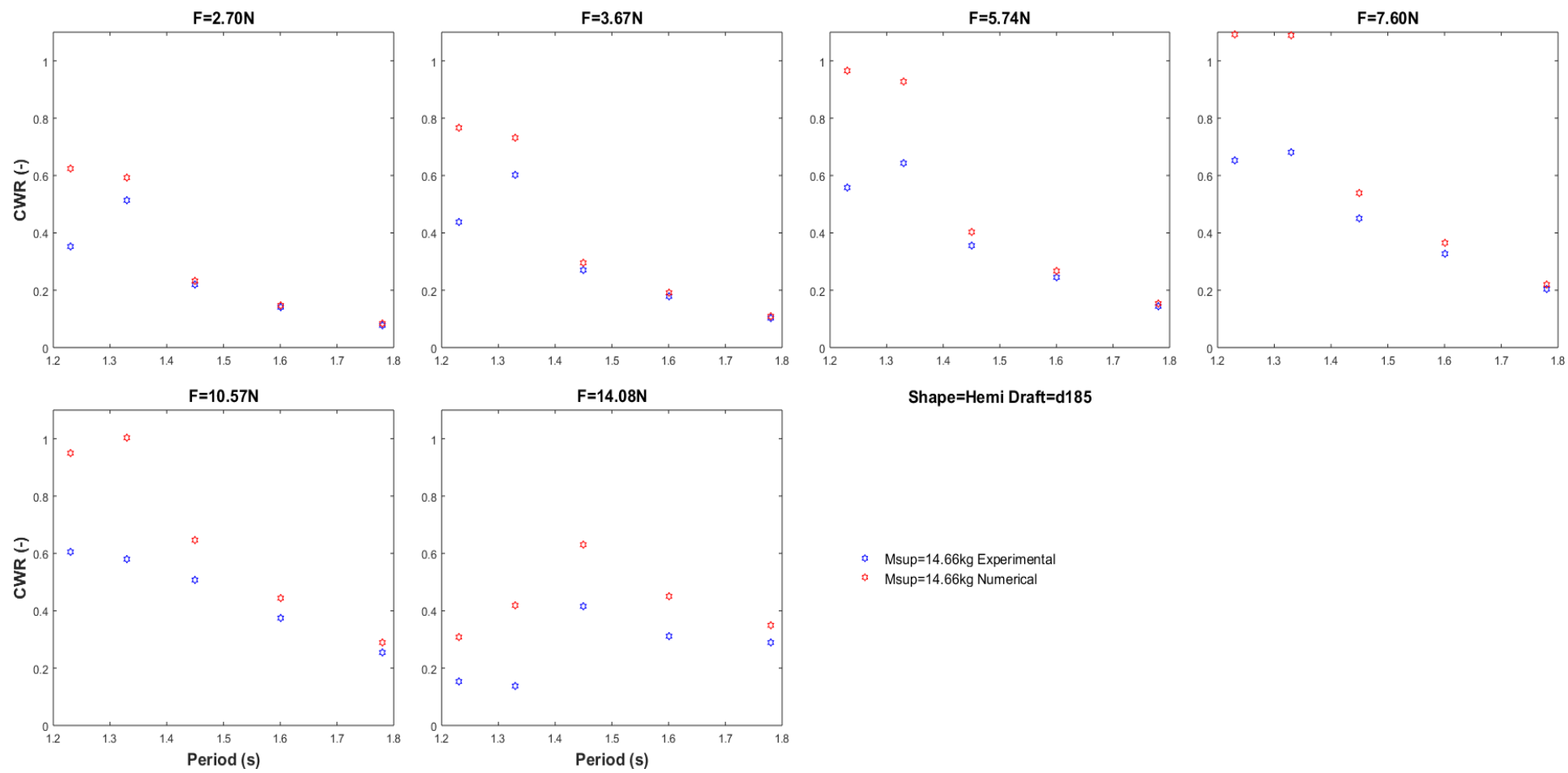
Figure B:38: Capture width ratio vs wave period for constant damping force with varying supplementary mass. Hemisphere -cylinder shape, draft=185mm

Figure B:39: Capture width ratio vs damping force for constant supplementary mass with varying wave period. Hemisphere -cylinder shape, draft=221mm
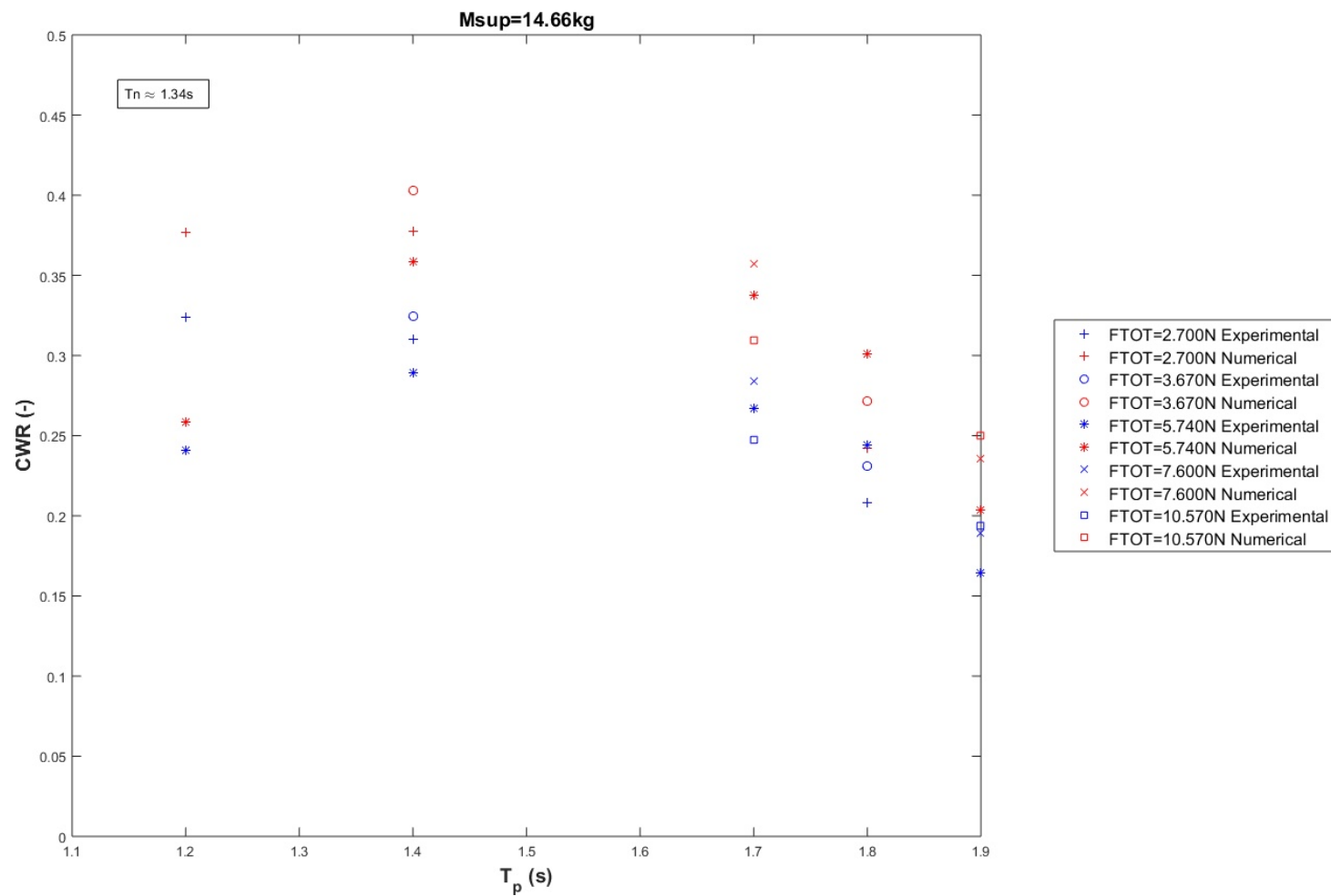
Figure B:40: Capture width ratio vs wave period for constant supplementary mass with varying damping force. Hemisphere -cylinder shape, draft=221mm
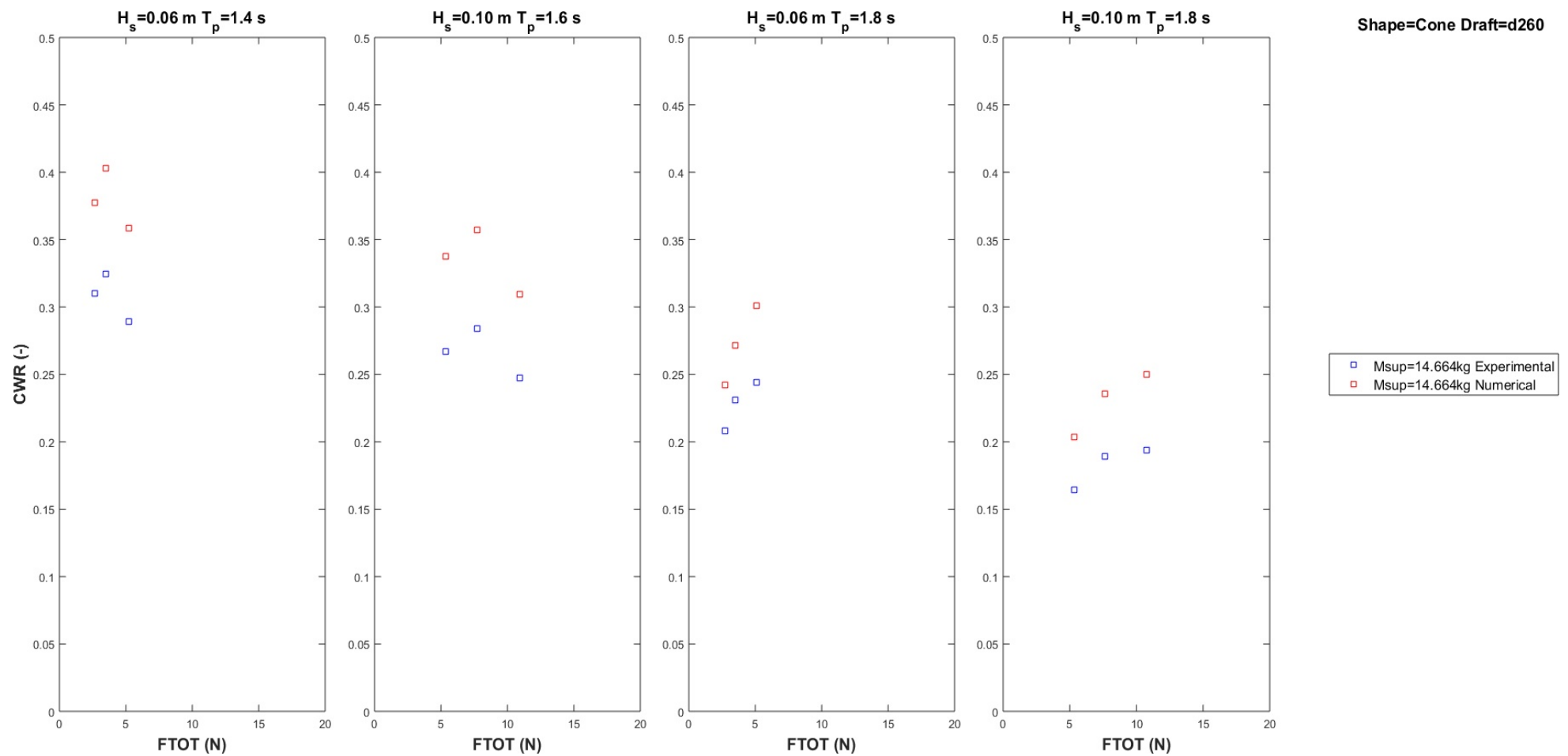
Figure B:41: Capture width ratio vs damping force for constant wave period with varying supplementary mass. Hemisphere -cylinder shape, draft=221mm
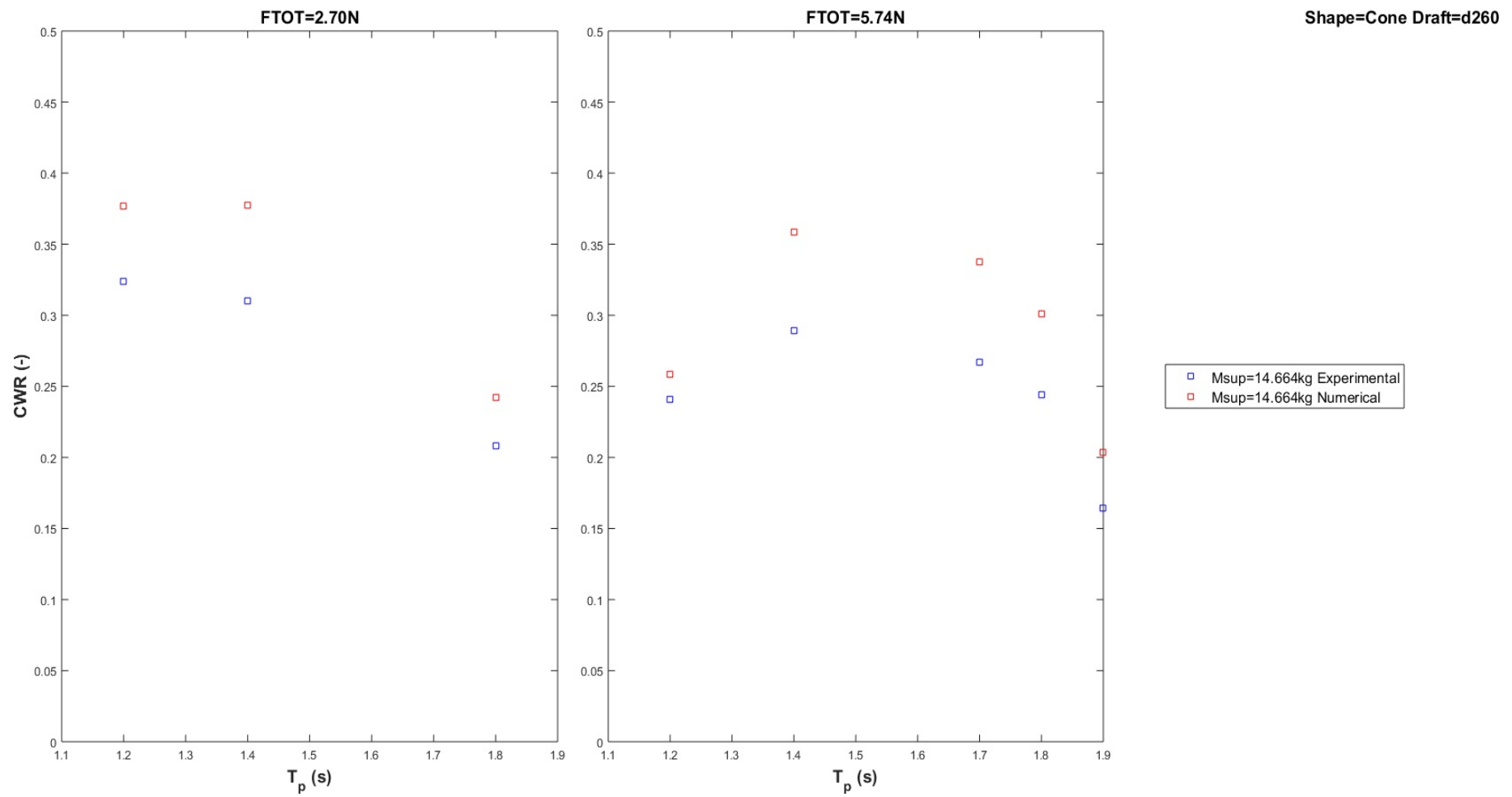
Figure B:42: Capture width ratio vs wave period for constant damping force with varying supplementary mass. Hemisphere -cylinder shape, draft=221mm

Figure B:43: Capture width ratio vs damping force for constant supplementary mass with varying wave period. Hemisphere -cylinder shape, draft=260mm

Figure B:44: Capture width ratio vs wave period for constant supplementary mass with varying damping force. Hemisphere -cylinder shape, draft=260mm

Figure B:45: Capture width ratio vs damping force for constant wave period with varying supplementary mass. Hemisphere -cylinder shape, draft=260mm

Figure B:46: Capture width ratio vs wave period for constant damping force with varying supplementary mass. Hemisphere -cylinder shape, draft=260mm
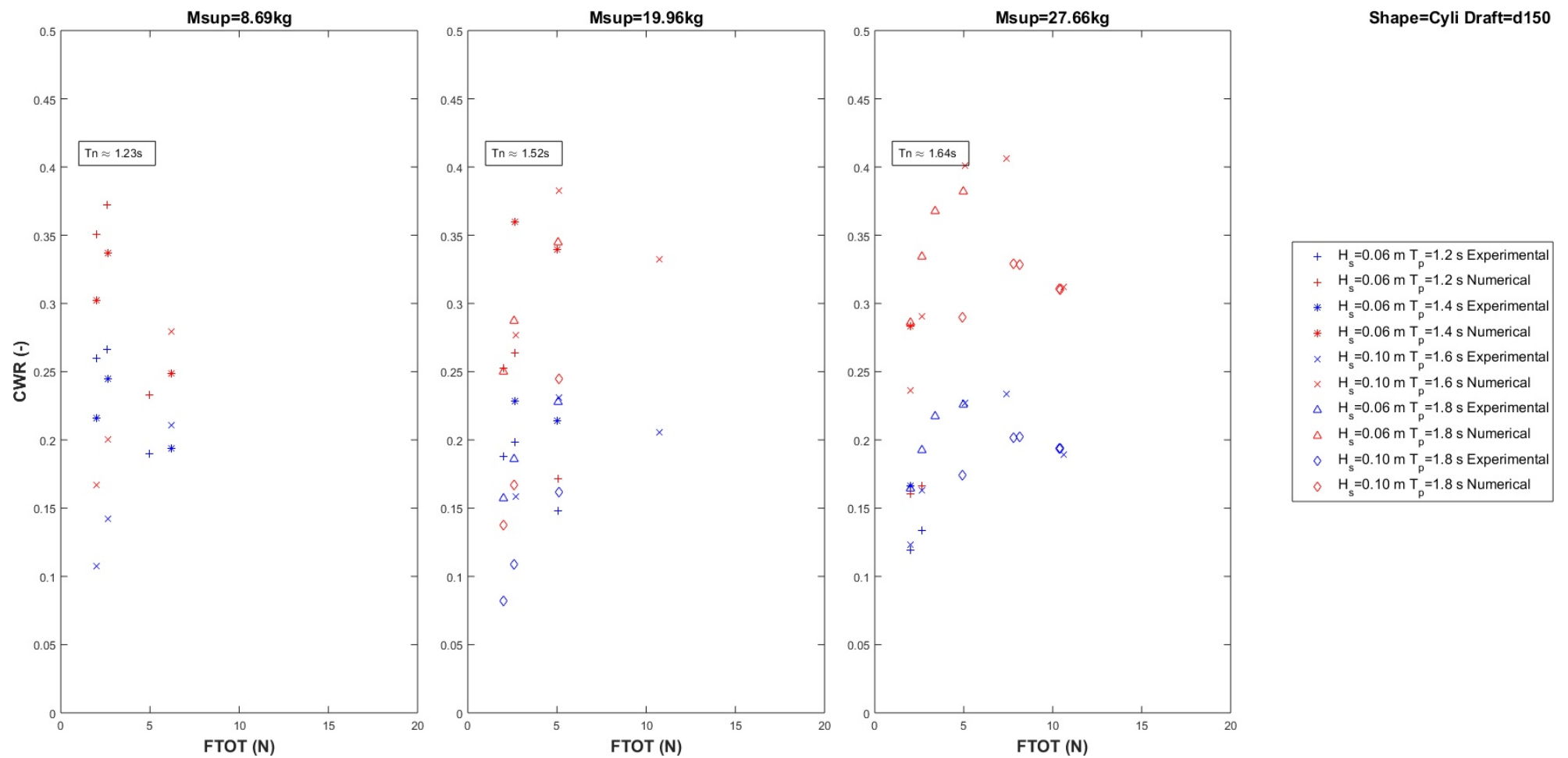
Appendix C Irregular Wave Capture Width Ratios

Figure C:1: Capture width ratio vs damping force for constant supplementary mass with varying sea state. Cone-cylinder shape, draft=185mm

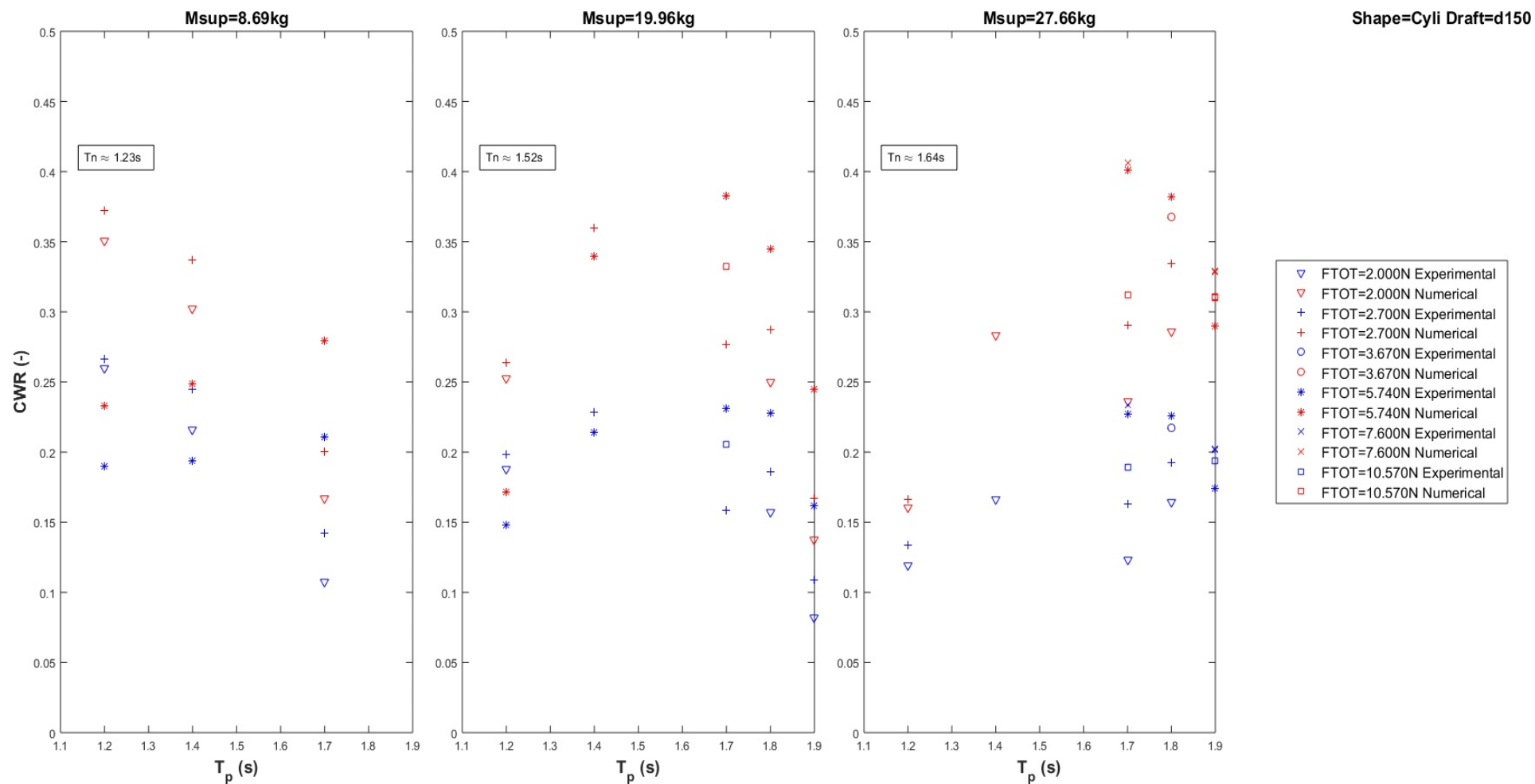**Figure C:2: Capture width ratio vs wave peak period for constant supplementary mass with varying damping force. Cone-cylinder shape, draft=185mm**
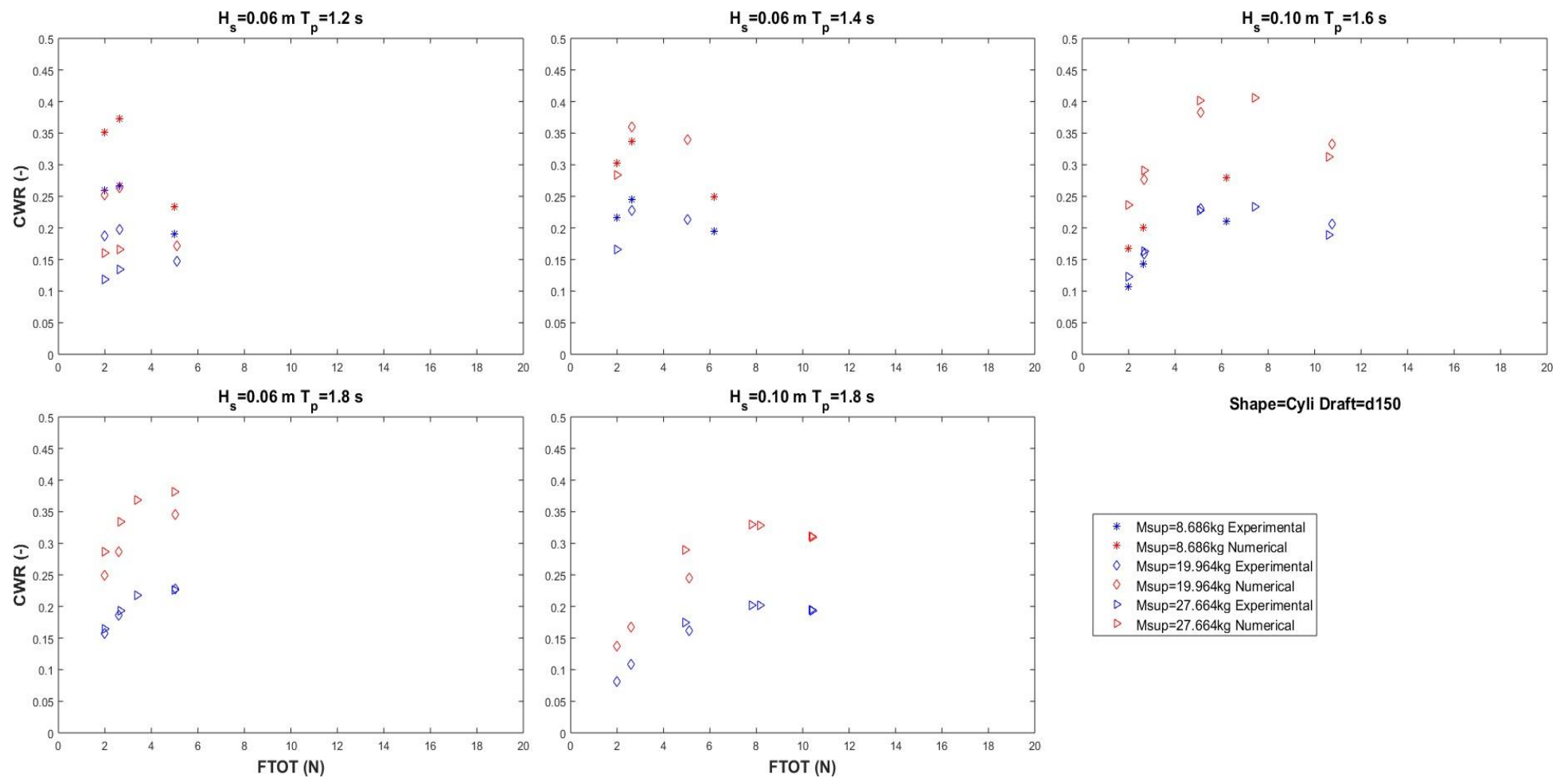
Figure C:3: Capture width ratio vs damping force for constant sea state with varying supplementary mass. Cone-cylinder shape, draft=185mm
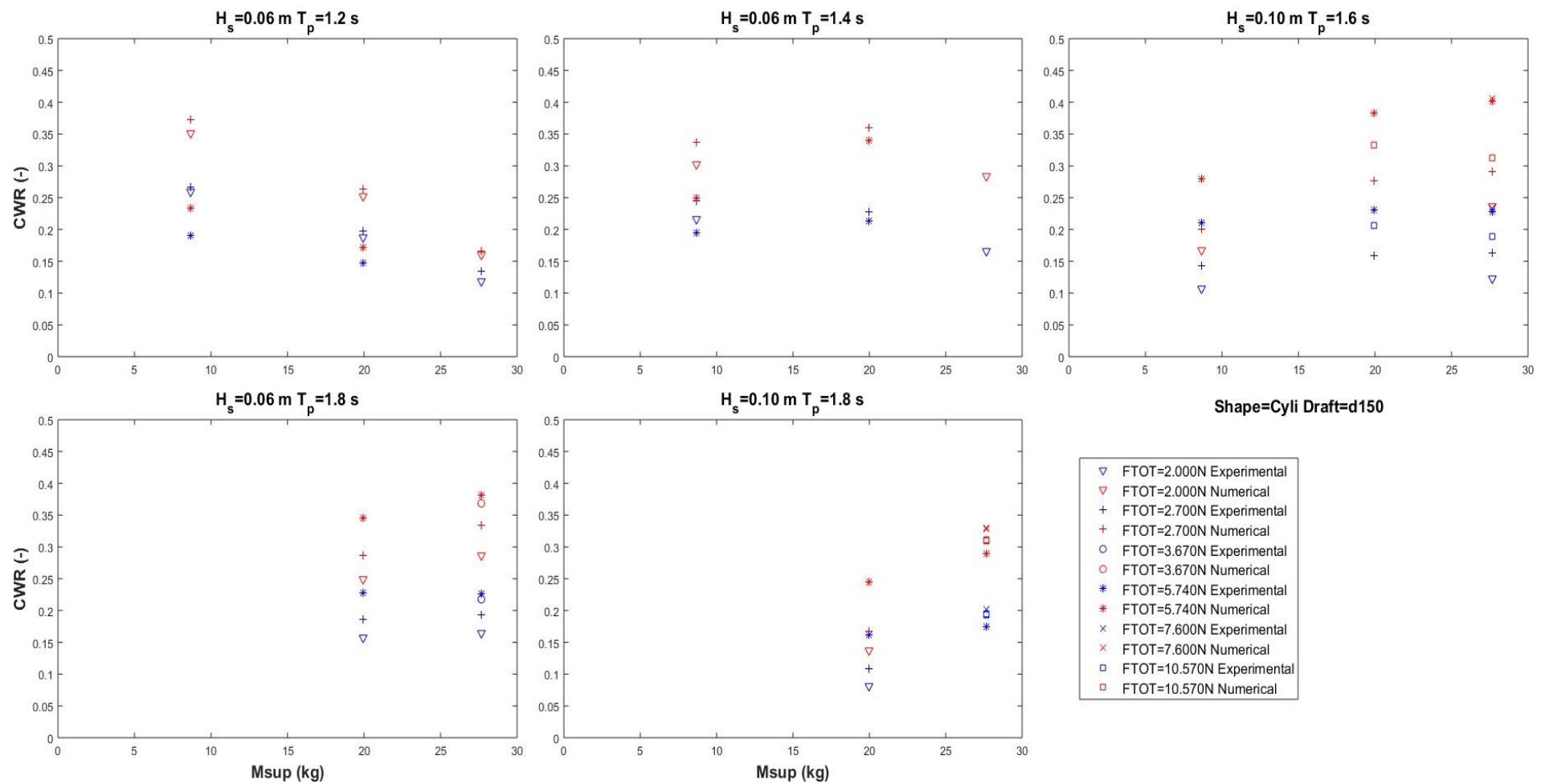
Figure C:4: Capture width ratio vs supplementary mass for constant sea state with varying damping force with. Cone-cylinder shape, draft=185mm
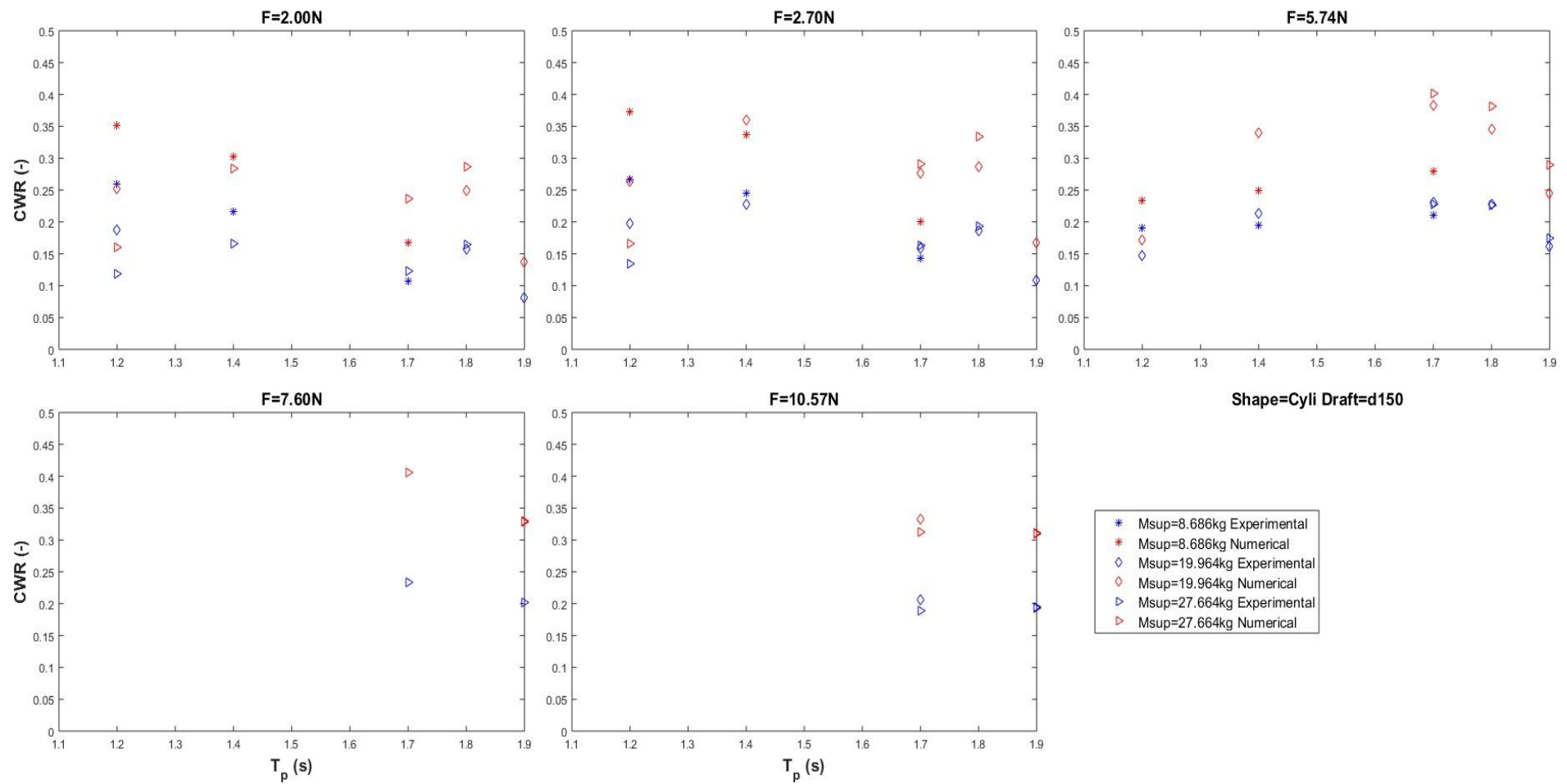
Figure C:5: Capture width ratio vs wave peak period for constant damping force with varying supplementary mass. Cone-cylinder shape, draft=185mm
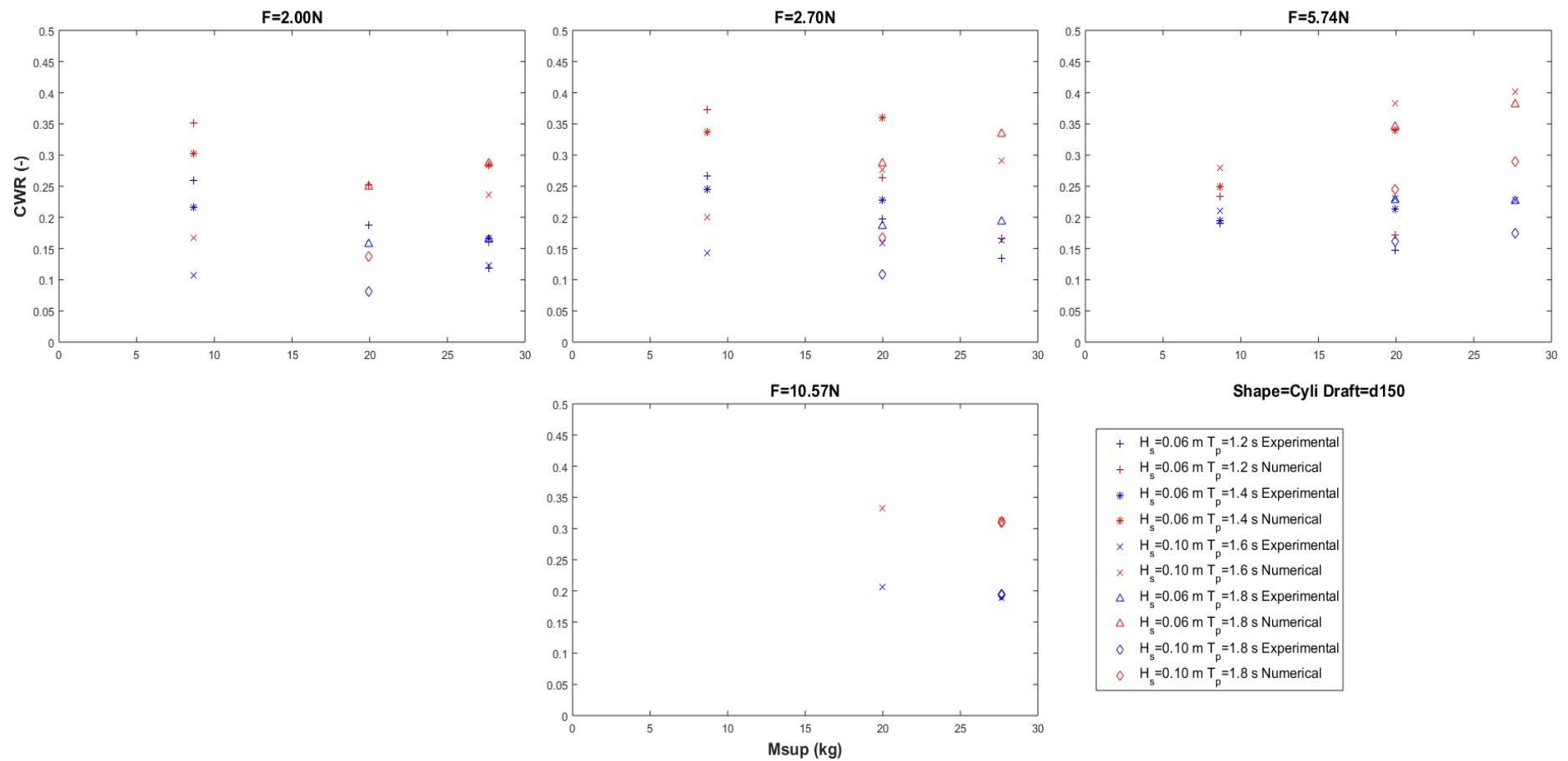
Figure C:6: Capture width ratio vs supplementary mass for constant damping force with varying sea state. Cone-cylinder shape, draft=185mm
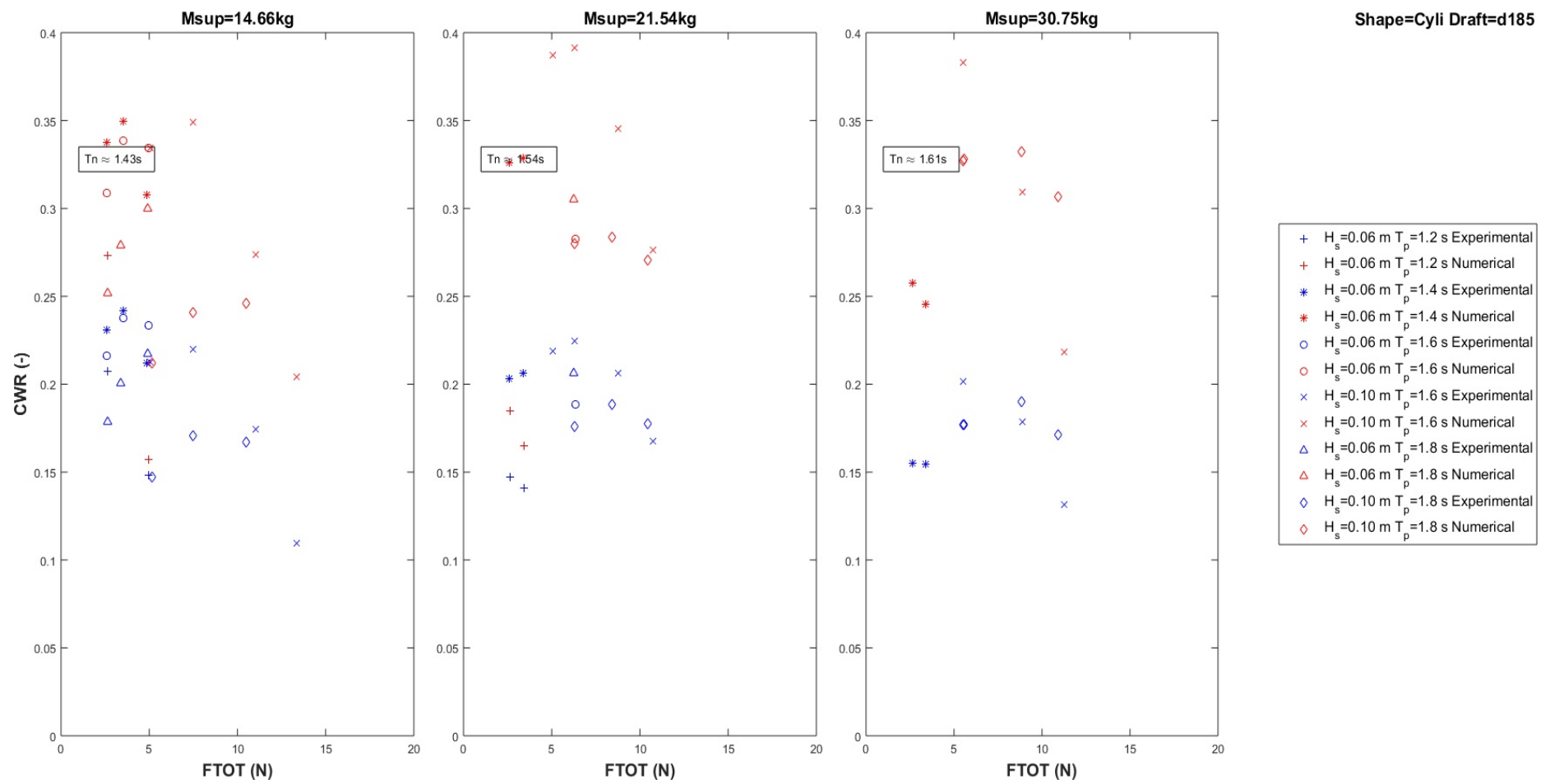
Figure C:7: Capture width ratio vs damping force for constant supplementary mass with varying sea state. Cone-cylinder shape, draft=221mm
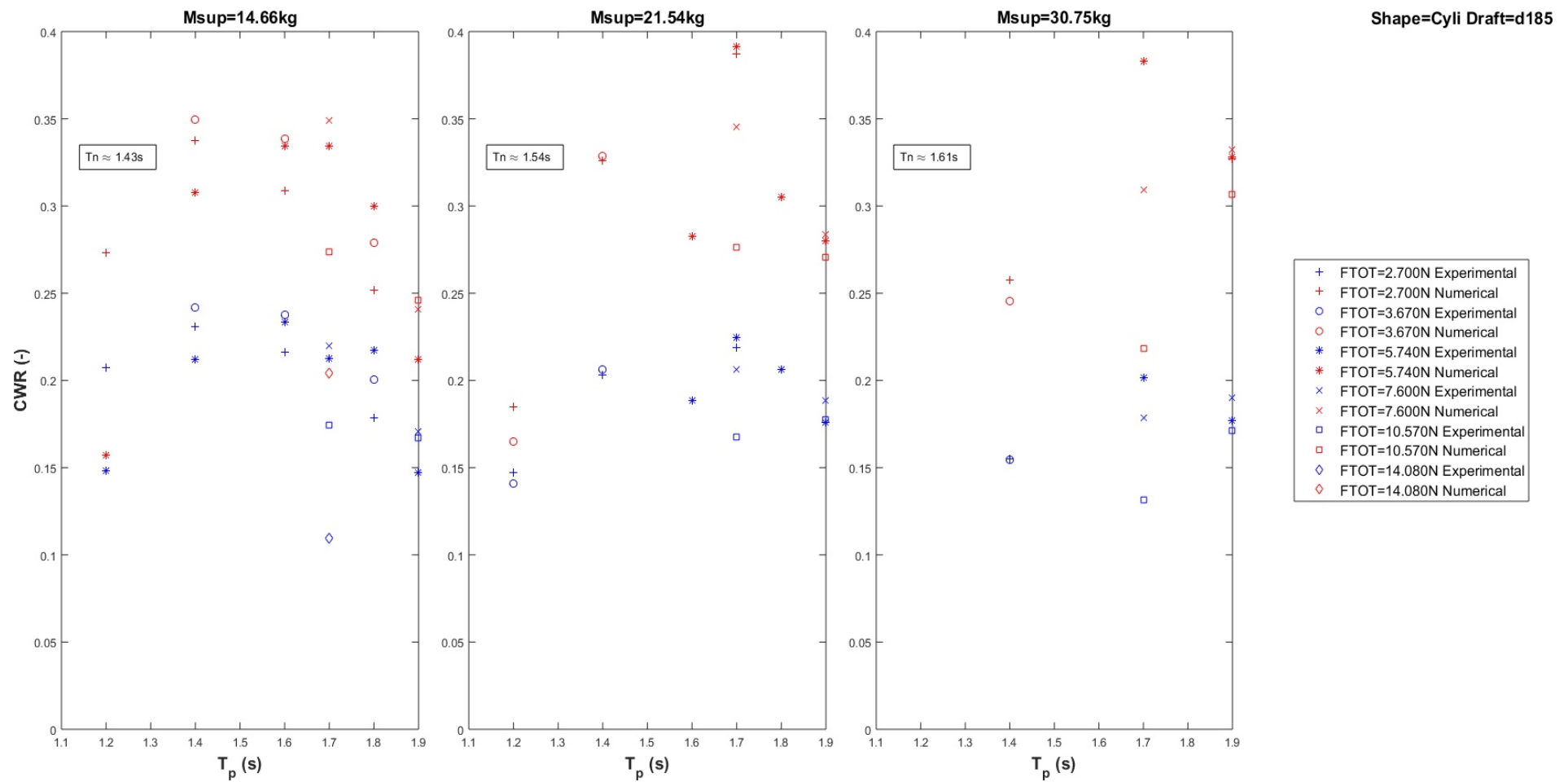
Figure C:8: Capture width ratio vs wave peak period for constant supplementary mass with varying damping force. Cone-cylinder shape, draft=221mm

Figure C:9: Capture width ratio vs damping force for constant sea state with varying supplementary mass. Cone-cylinder shape, draft=221mm

Figure C:10: Capture width ratio vs supplementary mass for constant sea state with varying damping force with. Cone-cylinder shape, draft=221mm

Figure C:11: Capture width ratio vs wave peak period for constant damping force with varying supplementary mass. Cone-cylinder shape, draft=221mm

356

Figure C:12: Capture width ratio vs supplementary mass for constant damping force with varying sea state. Cone-cylinder shape, draft=221mm

357
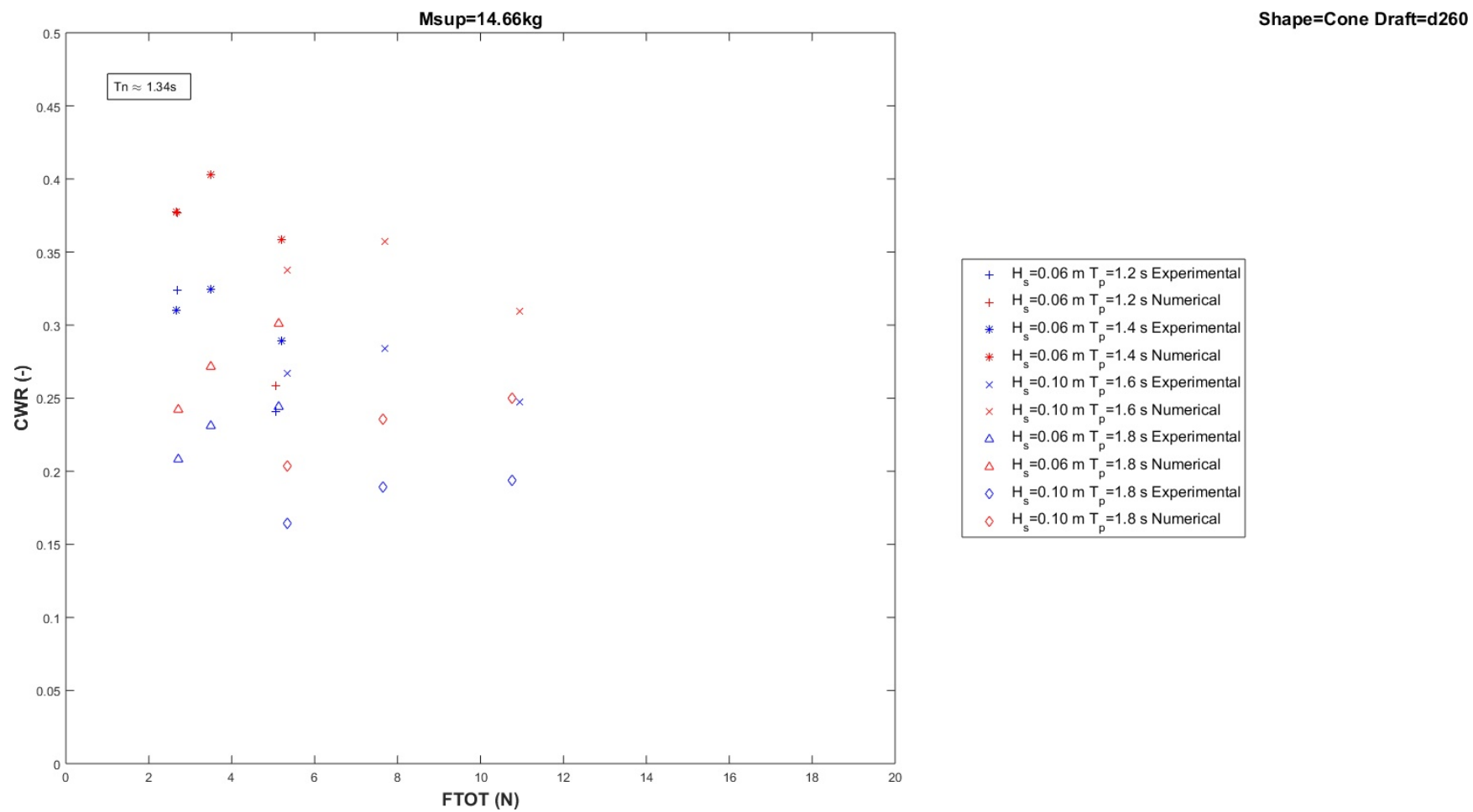
Figure C:13: Capture width ratio vs damping force for constant supplementary mass with varying sea state. Cone-cylinder shape, draft=260mm

Figure C:14: Capture width ratio vs wave peak period for constant supplementary mass with varying damping force. Cone-cylinder shape, draft=260mm
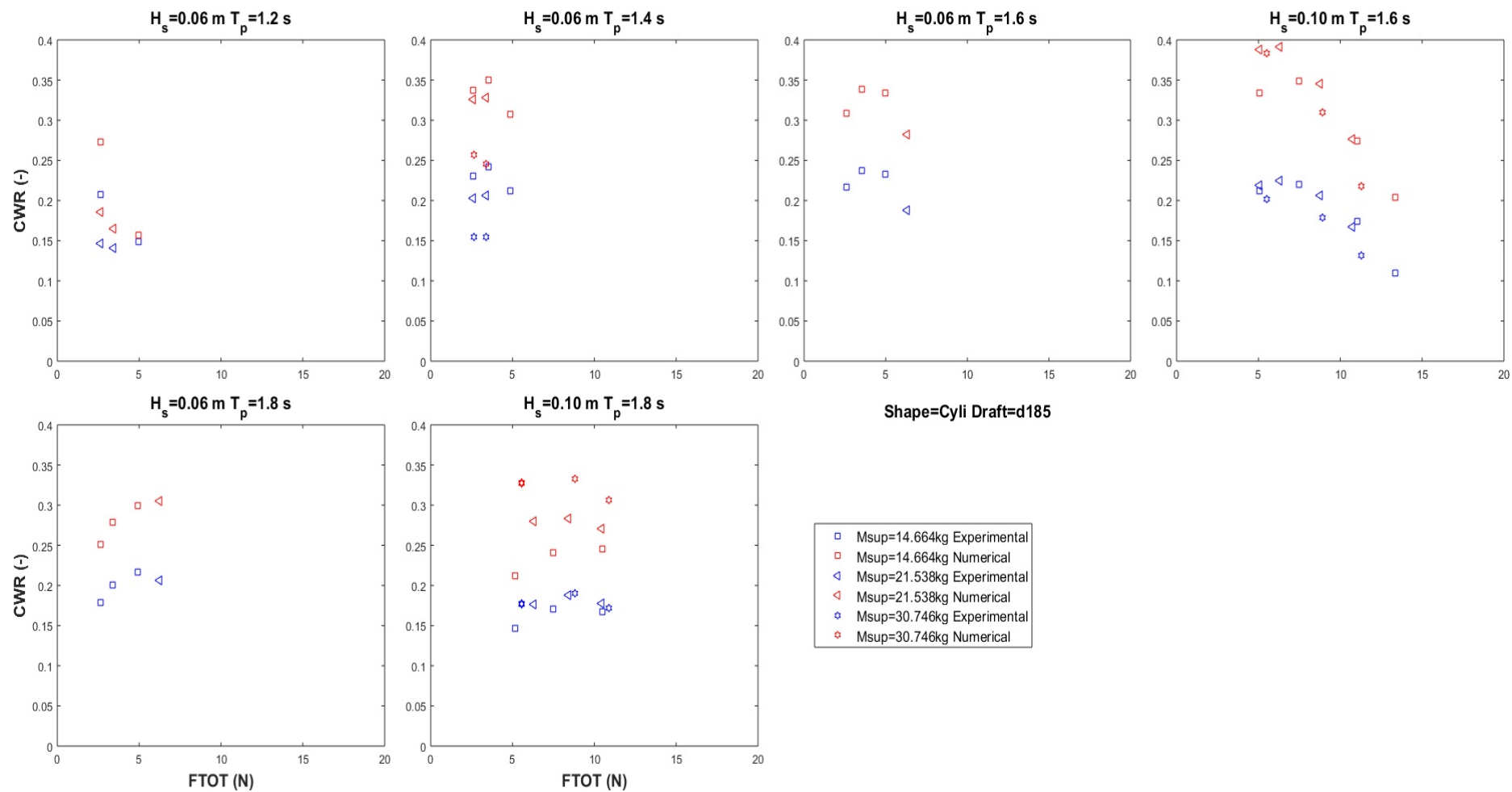
Figure C:15: Capture width ratio vs damping force for constant sea state with varying supplementary mass. Cone-cylinder shape, draft=260mm
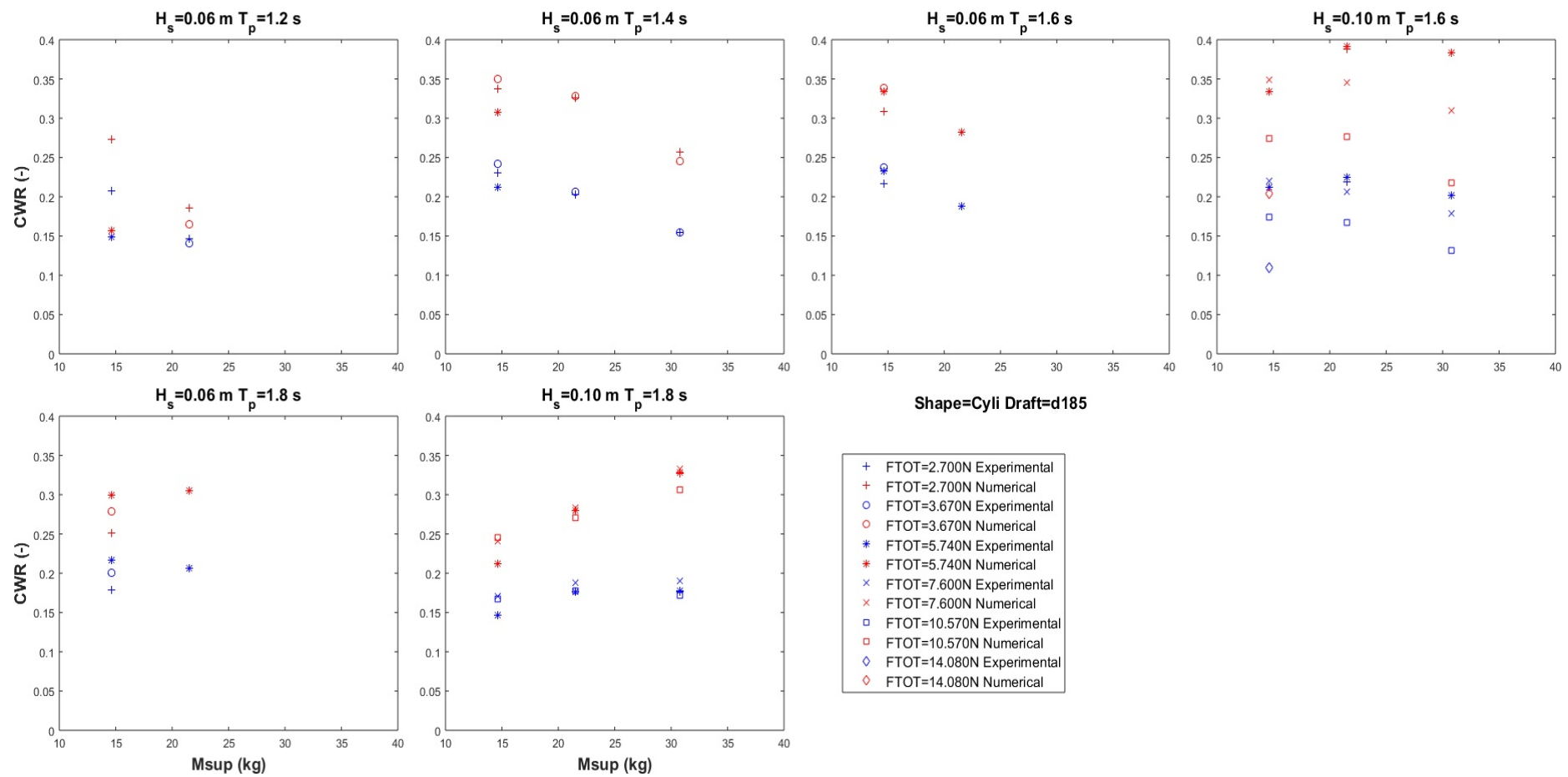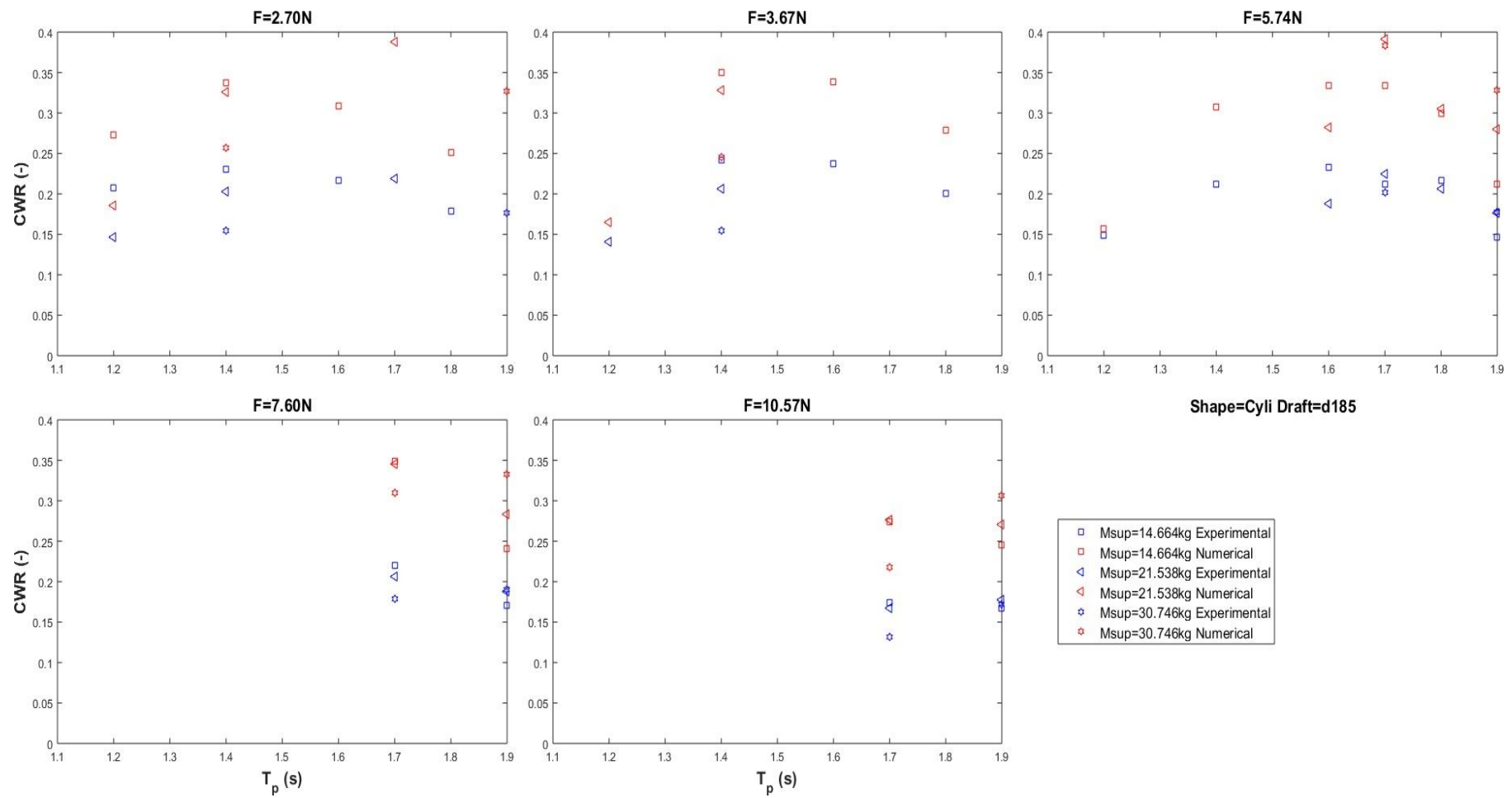
Figure C:16: Capture width ratio vs wave peak period for constant damping force with varying supplementary mass. Cone-cylinder shape, draft=260mm
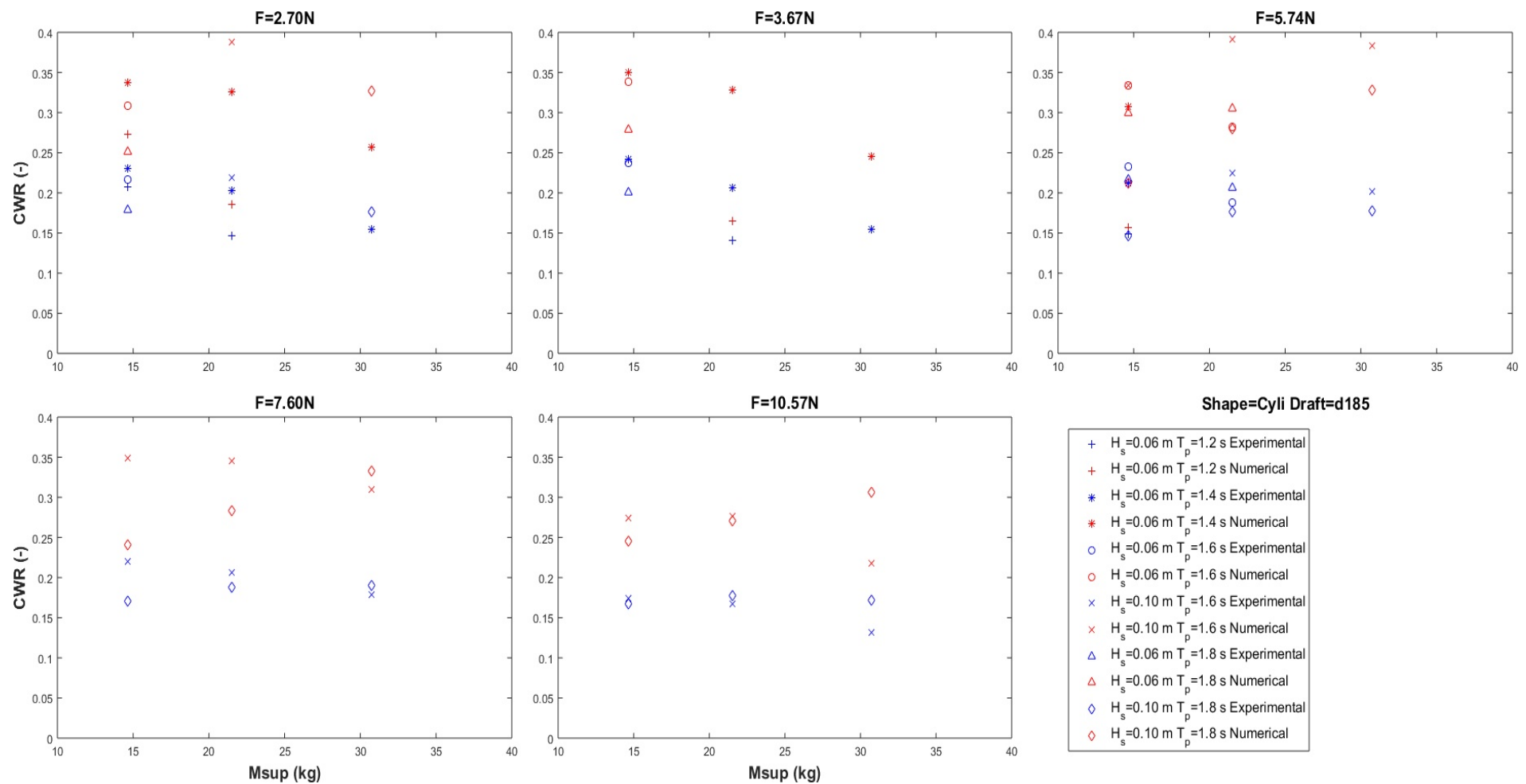
Figure C:17: Capture width ratio vs damping force for constant supplementary mass with varying sea state. Cone-cylinder shape, draft=150mm

Figure C:18: Capture width ratio vs wave peak period for constant supplementary mass with varying damping force. Cylinder shape, draft=150mm

Figure C:19: Capture width ratio vs damping force for constant sea state with varying supplementary mass. Cylinder shape, draft=150mm

Figure C:20: Capture width ratio vs supplementary mass for constant sea state with varying damping force with. Cylinder shape, draft=150mm

Figure C:21: Capture width ratio vs wave peak period for constant damping force with varying supplementary mass. Cylinder shape, draft=150mm

Figure C:22: Capture width ratio vs supplementary mass for constant damping force with varying sea state. Cylinder shape, draft=150mm
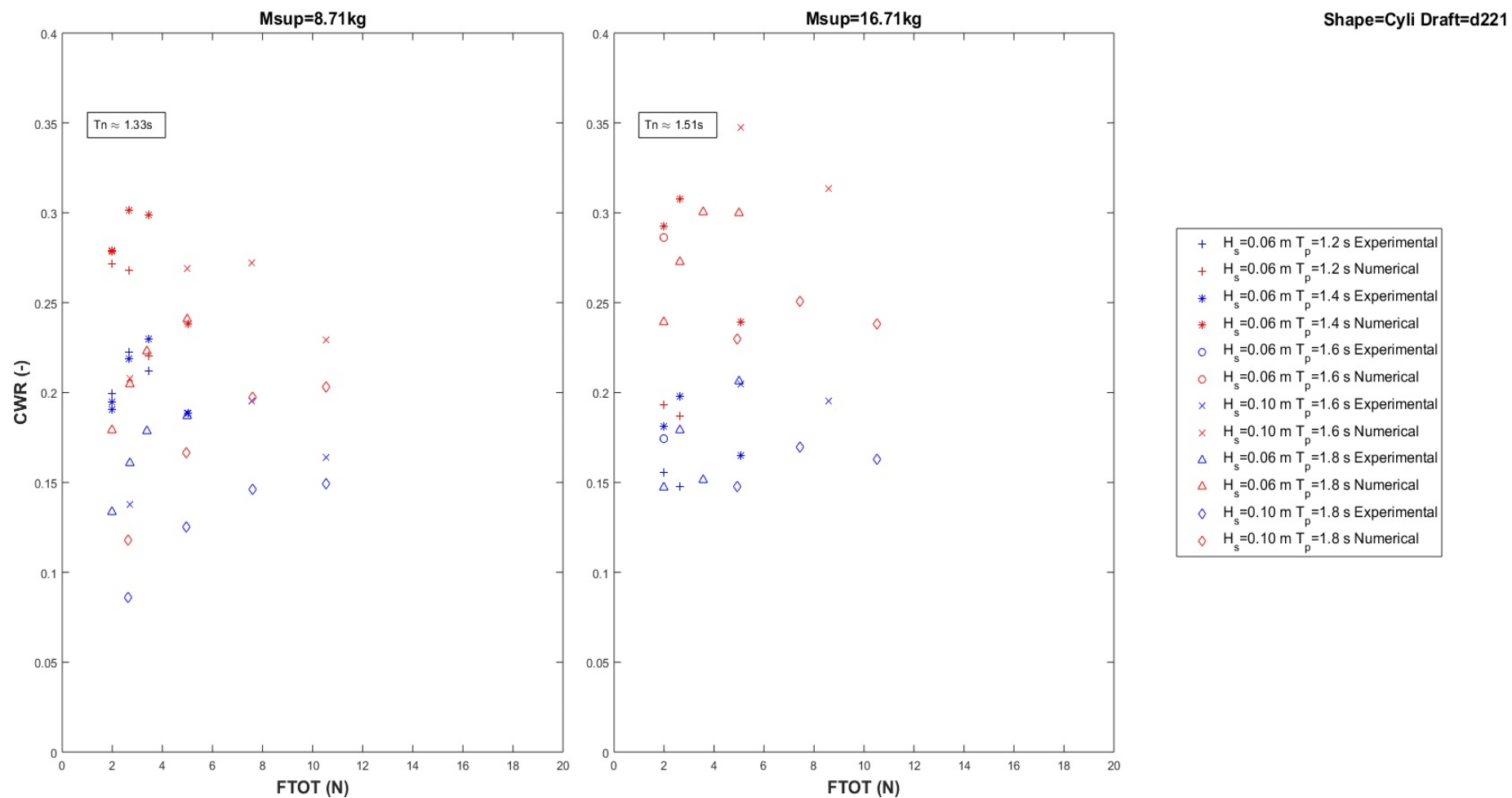
Figure C:23: Capture width ratio vs damping force for constant supplementary mass with varying sea state. Cylinder shape, draft=185mm
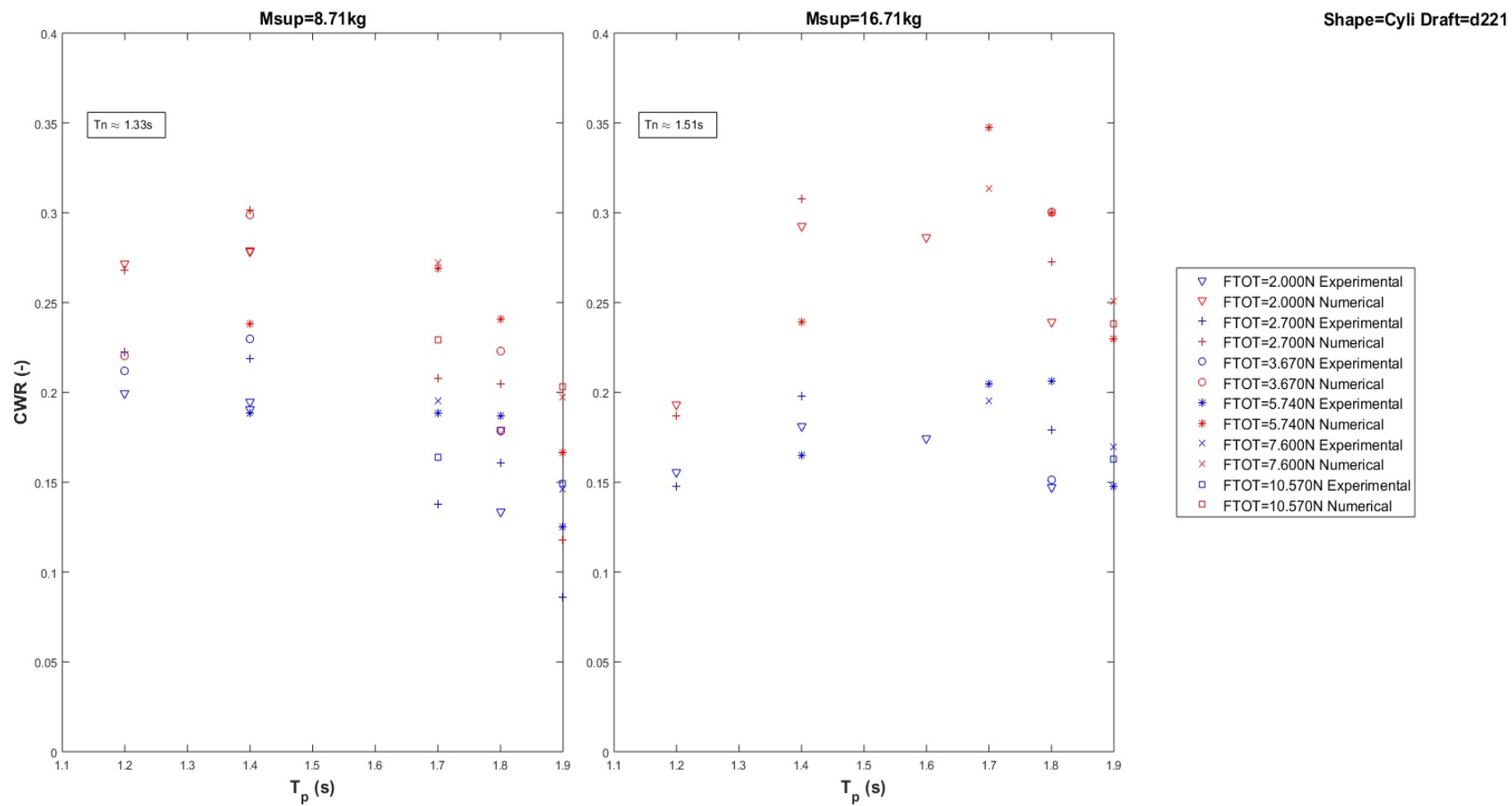
Figure C:24: Capture width ratio vs wave peak period for constant supplementary mass with varying damping force. Cylinder shape, draft=185mm
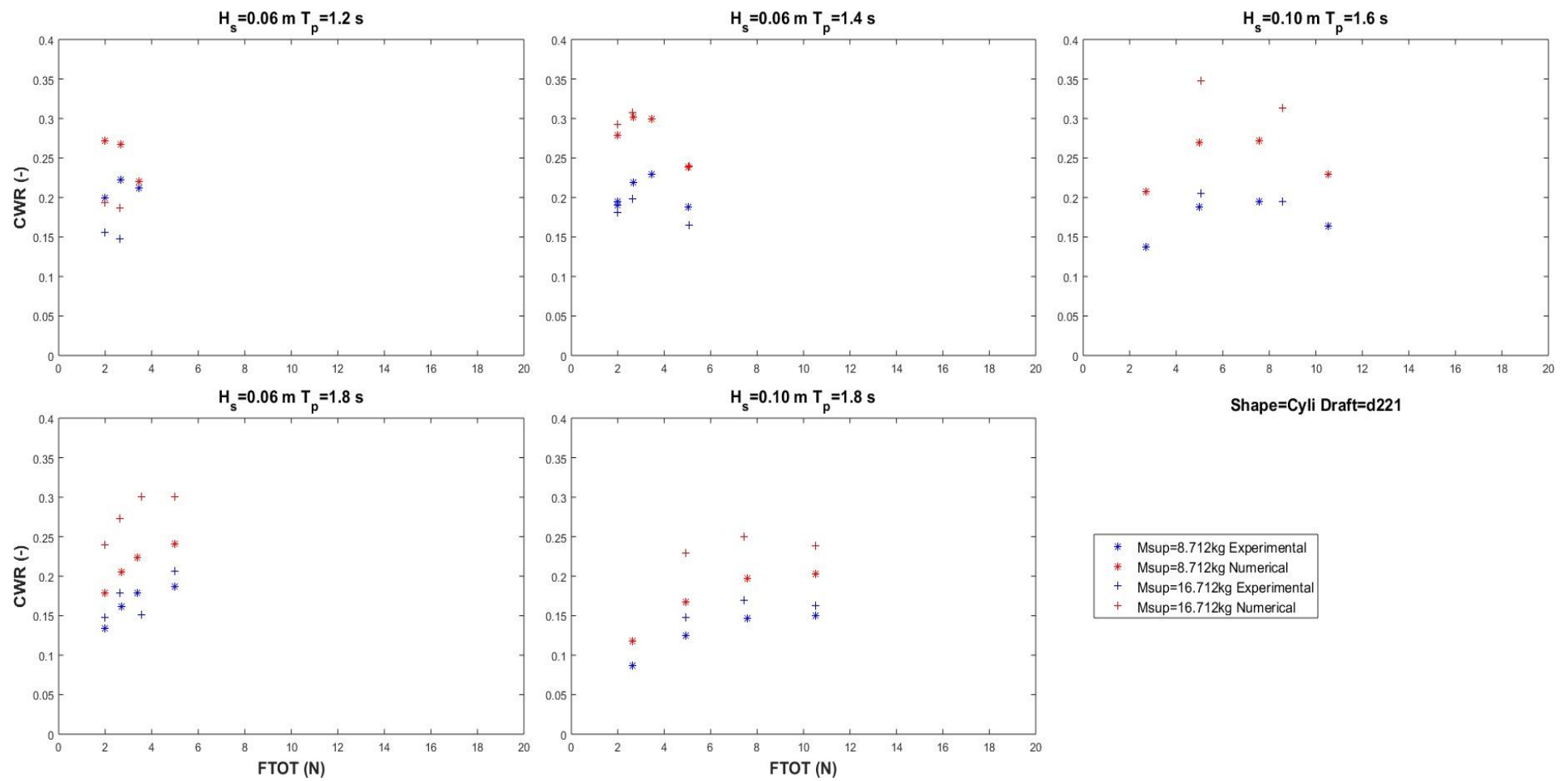
Figure C:25: Capture width ratio vs damping force for constant sea state with varying supplementary mass. Cylinder shape, draft=185mm
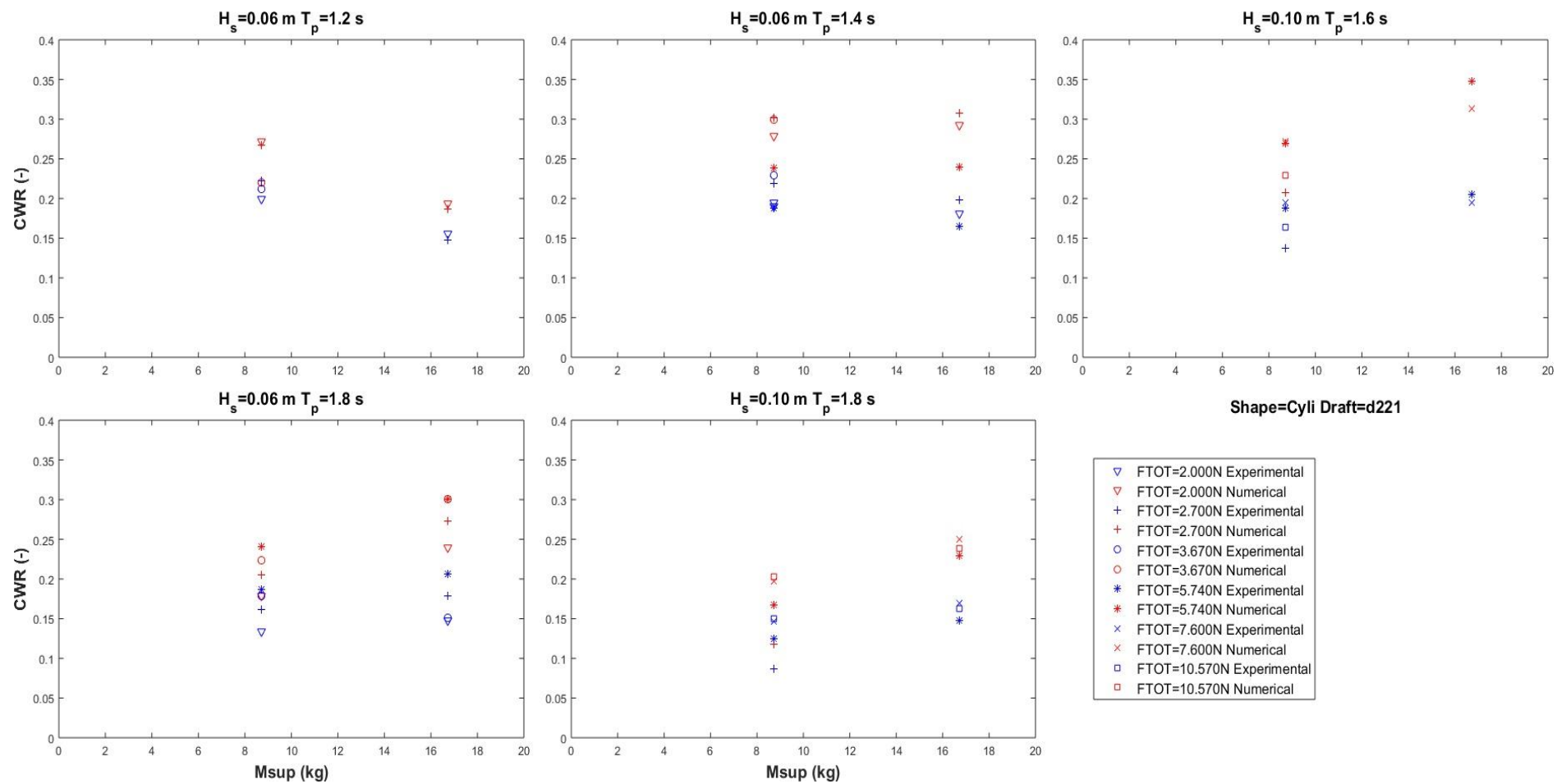
Figure C:26: Capture width ratio vs supplementary mass for constant sea state with varying damping force with. Cylinder shape, draft=185mm
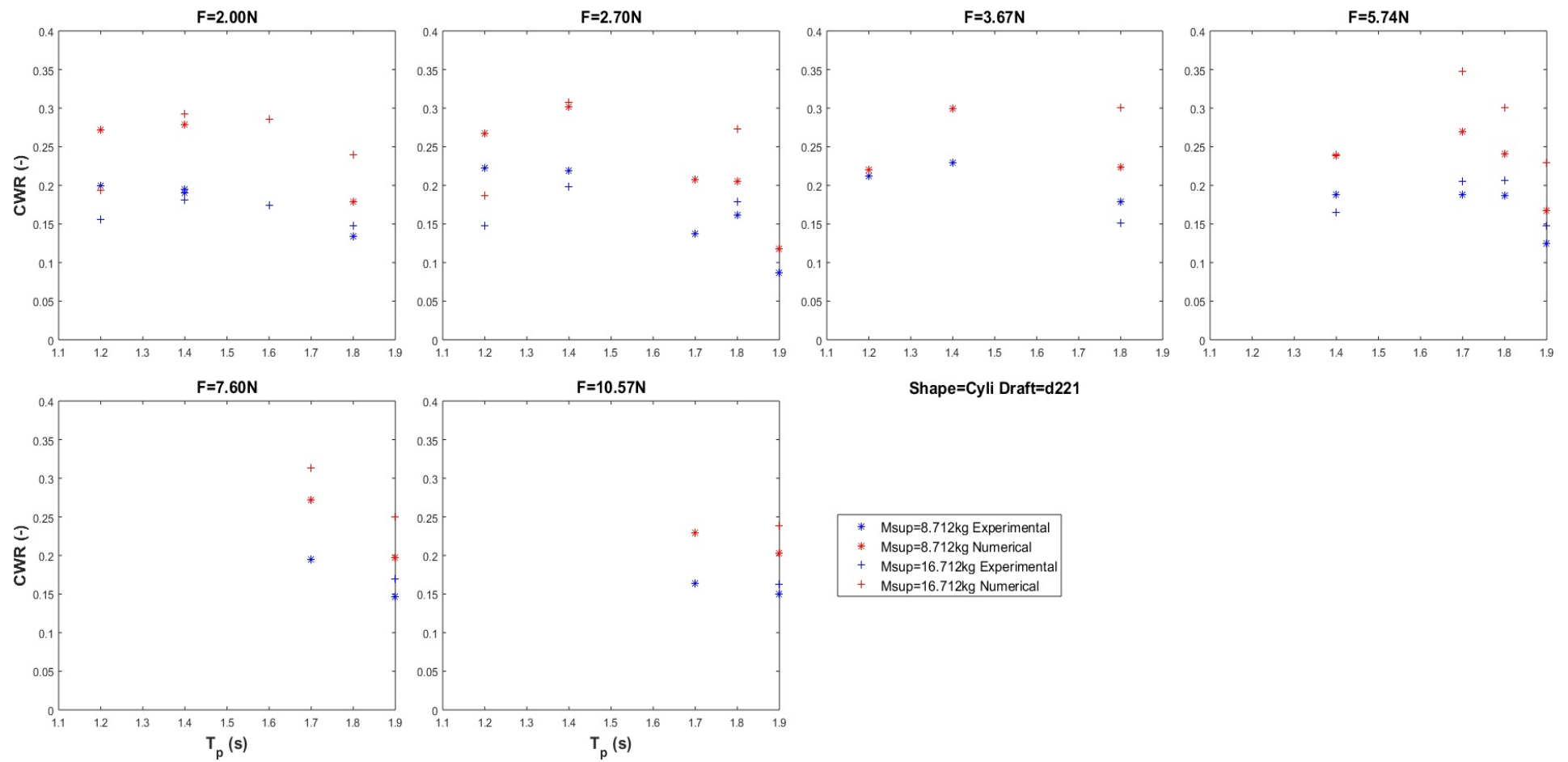
Figure C:27: Capture width ratio vs wave peak period for constant damping force with varying supplementary mass. Cylinder shape, draft=185mm
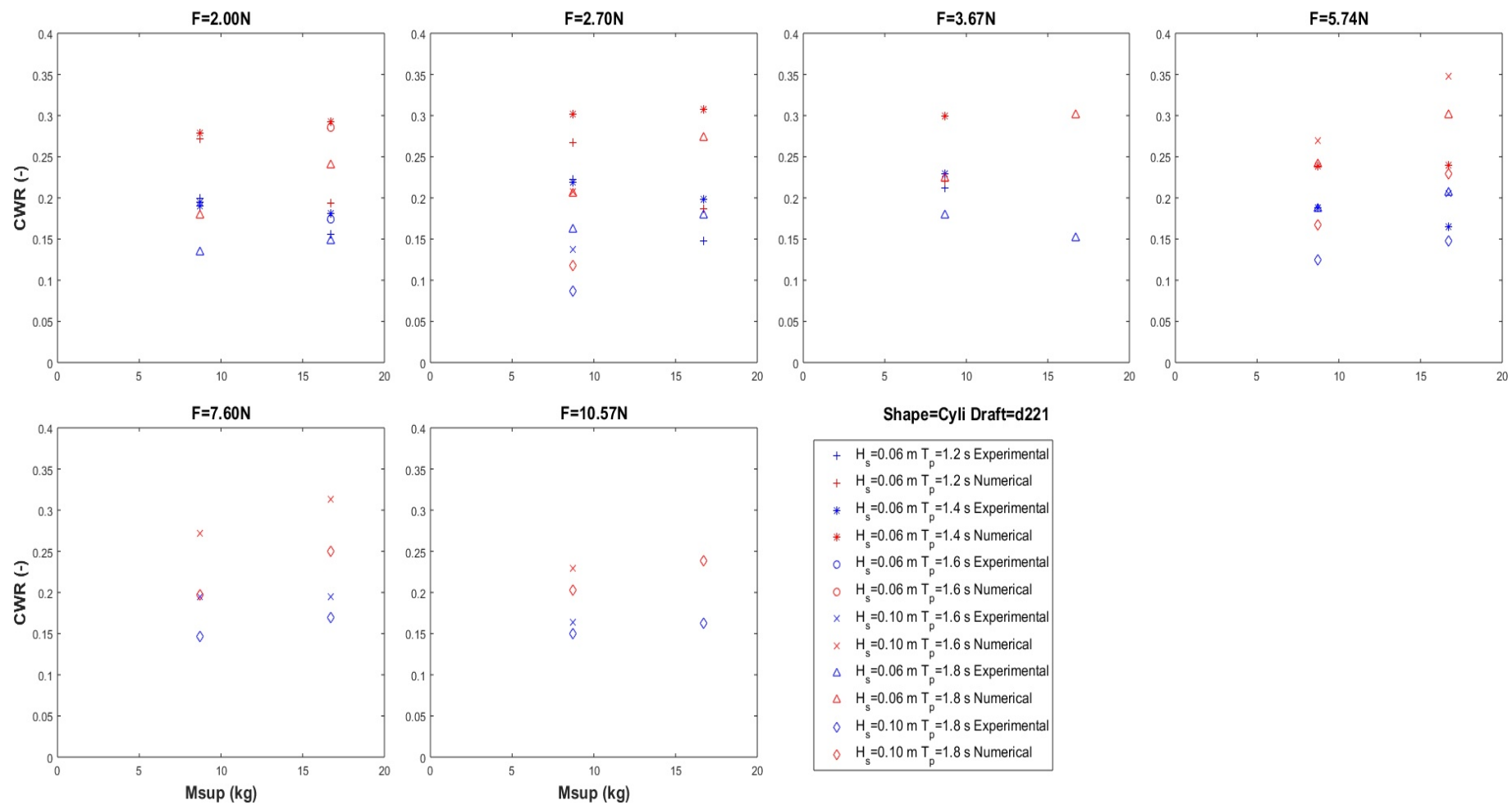
Figure C:28: Capture width ratio vs supplementary mass for constant damping force with varying sea state. Cylinder shape, draft=185mm
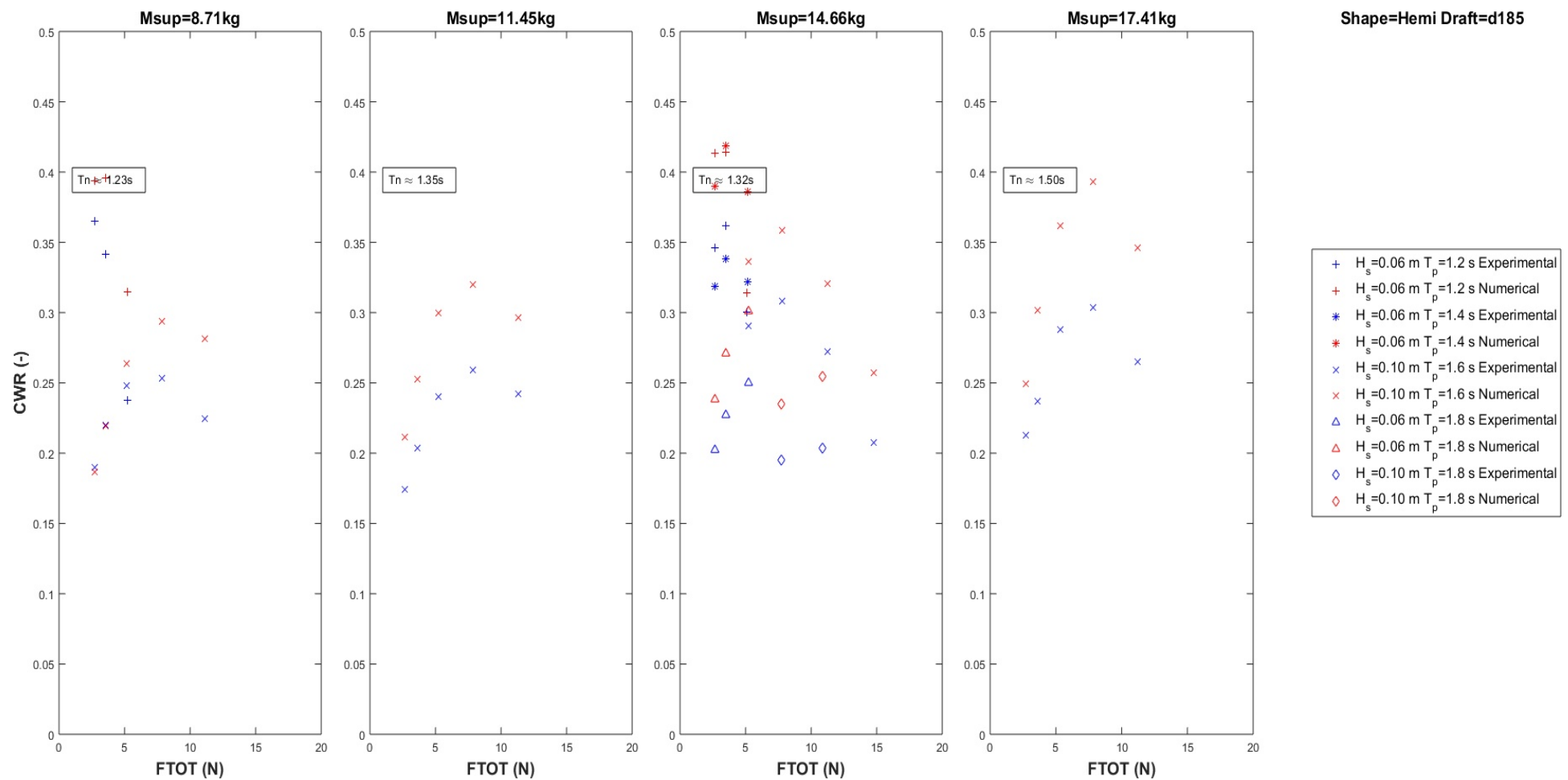
Figure C:29: Capture width ratio vs damping force for constant supplementary mass with varying sea state. Cylinder shape, draft=221mm
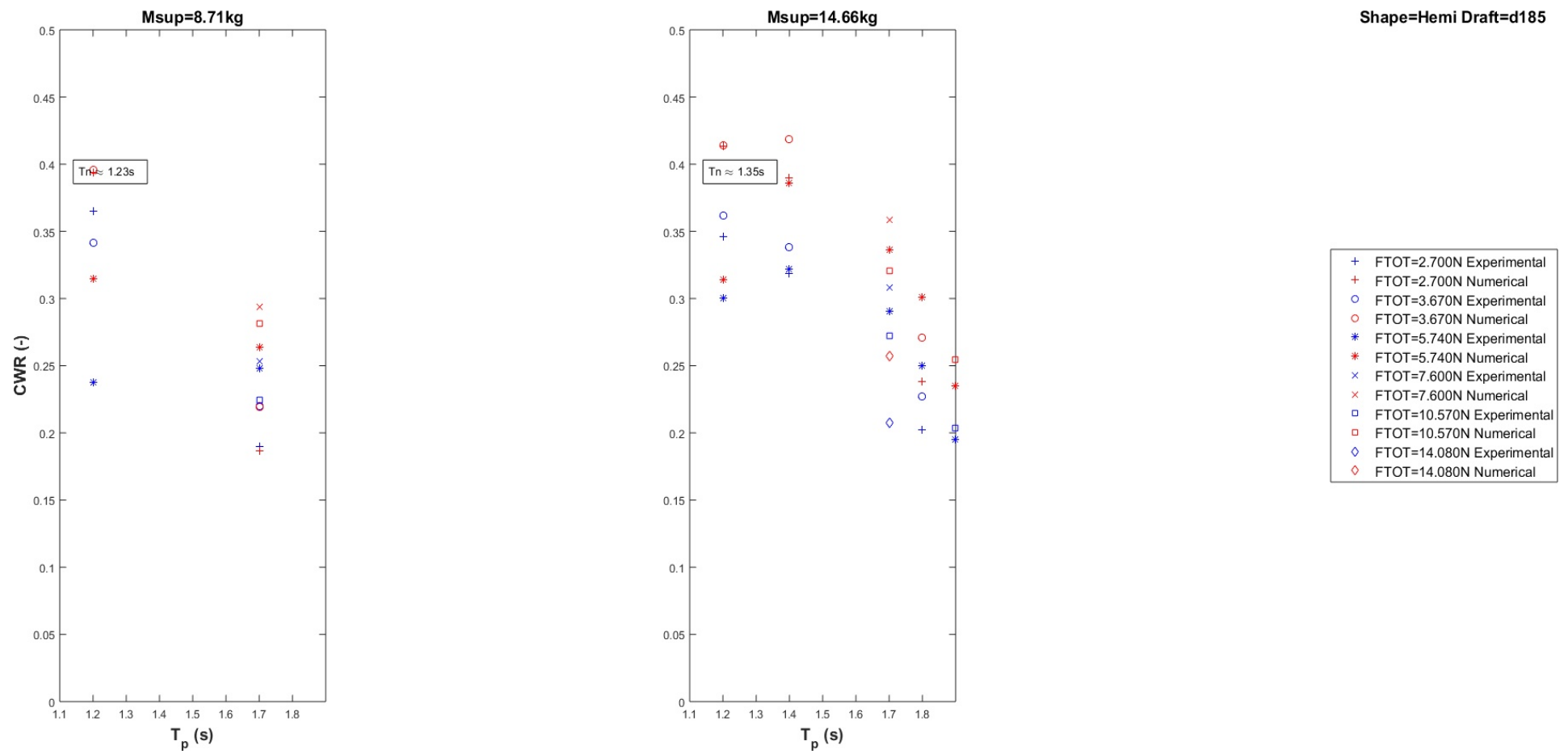
Figure C:30: Capture width ratio vs wave peak period for constant supplementary mass with varying damping force. Cylinder shape, draft=221mm

Figure C:31: Capture width ratio vs damping force for constant sea state with varying supplementary mass. Cylinder shape, draft=221mm

Figure C:32: Capture width ratio vs supplementary mass for constant sea state with varying damping force with. Cylinder shape, draft=221mm

Figure C:33: Capture width ratio vs wave peak period for constant damping force with varying supplementary mass. Cylinder shape, draft=221mm

378

Figure C:34: Capture width ratio vs supplementary mass for constant damping force with varying sea state. Cylinder shape, draft=221mm

Figure C:35: Capture width ratio vs damping force for constant supplementary mass with varying sea state. Hemisphere-cylinder shape, draft=185mm

Figure C:36: Capture width ratio vs wave peak period for constant supplementary mass with varying damping force. Hemisphere-cylinder shape, draft=185mm
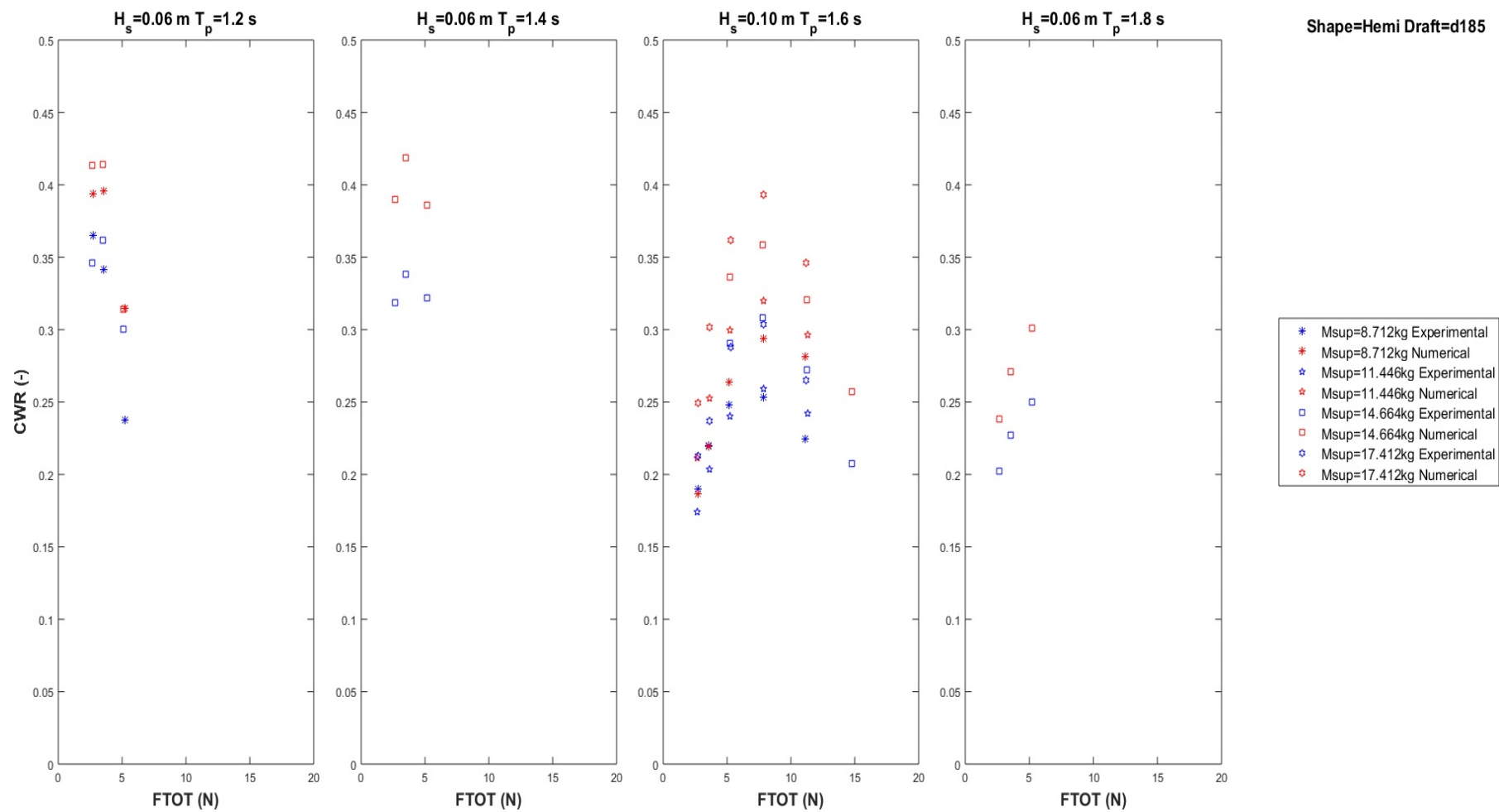
Figure C:37: Capture width ratio vs damping force for constant sea state with varying supplementary mass. Hemisphere-cylinder shape, draft=185mm
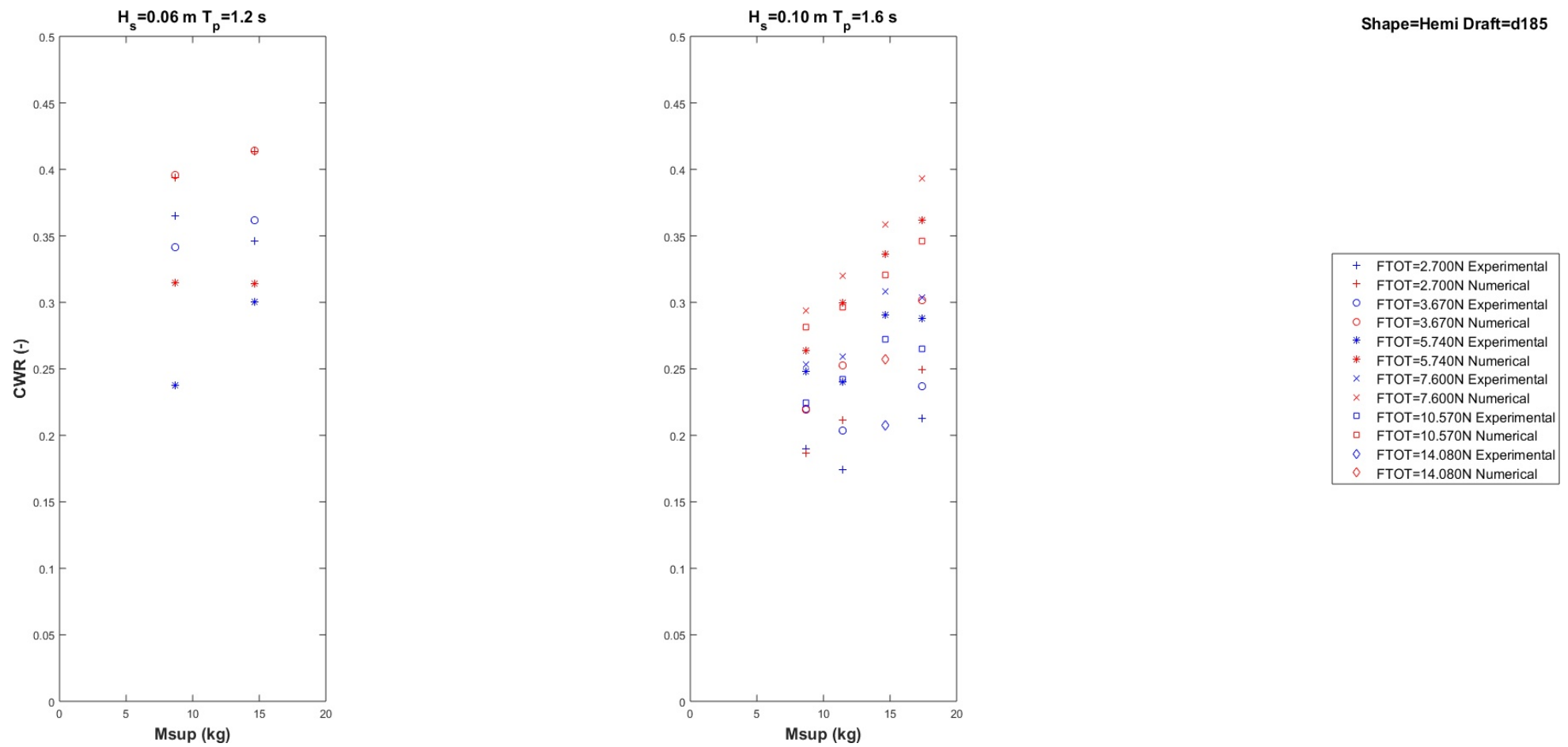
Figure C:37: Capture width ratio vs supplementary mass for constant sea state with varying damping force with. Hemisphere-cylinder shape, draft=185mm
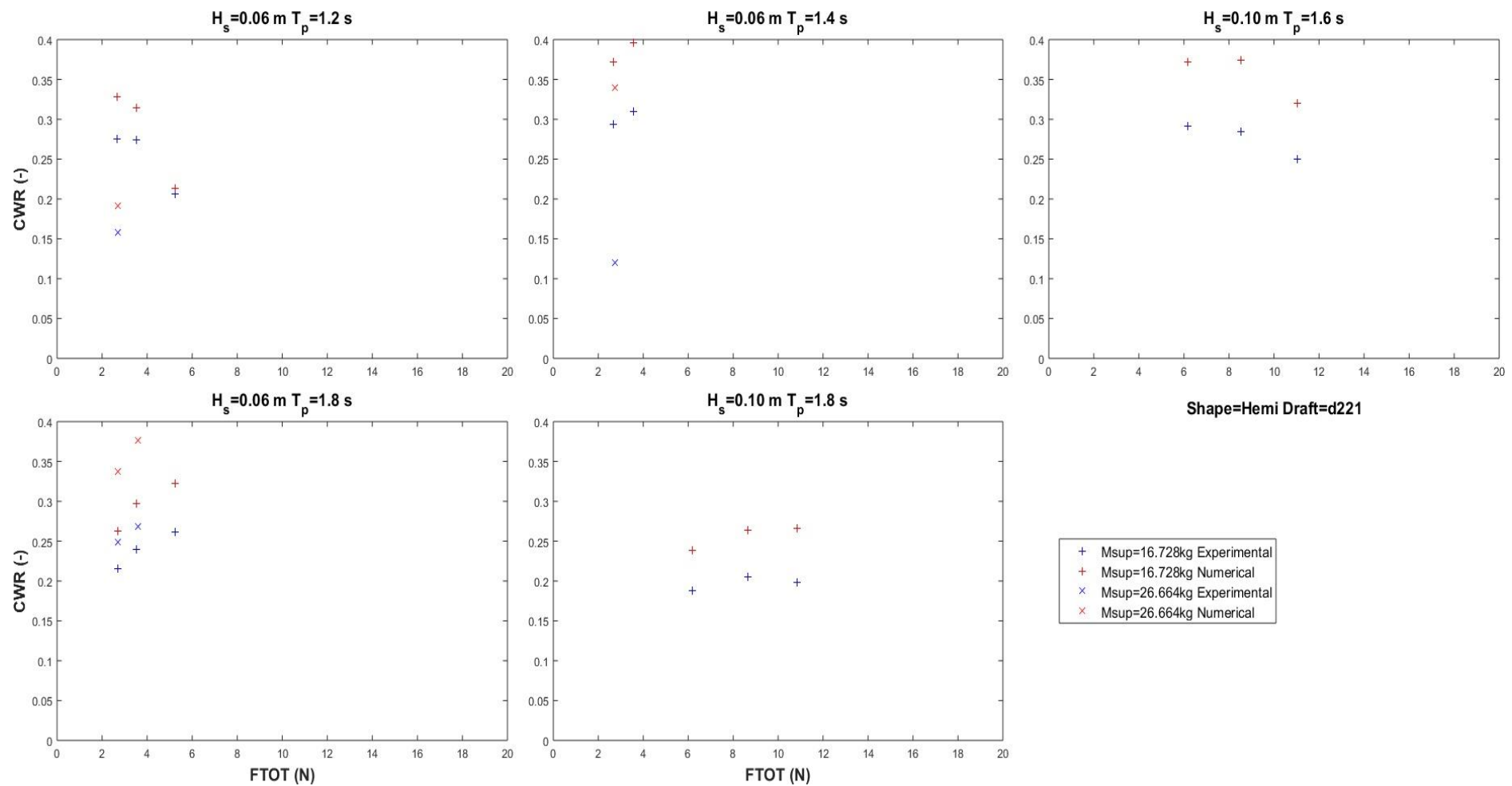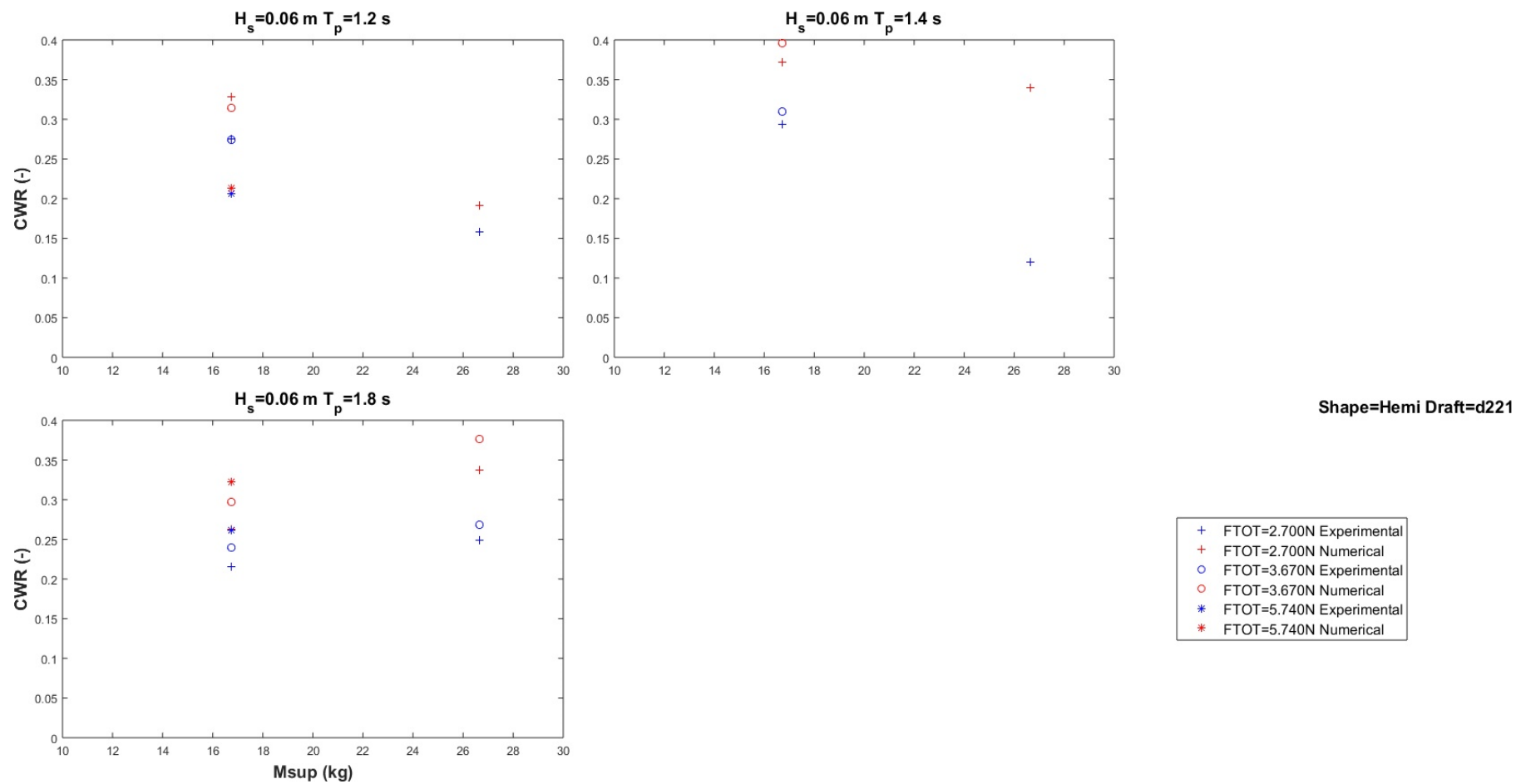
Figure C:38: Capture width ratio vs damping force for constant sea state with varying supplementary mass. Hemisphere-cylinder shape, draft=221mm

Figure C:39: Capture width ratio vs supplementary mass for constant sea state with varying damping force with. Hemisphere-cylinder shape, draft=221mm
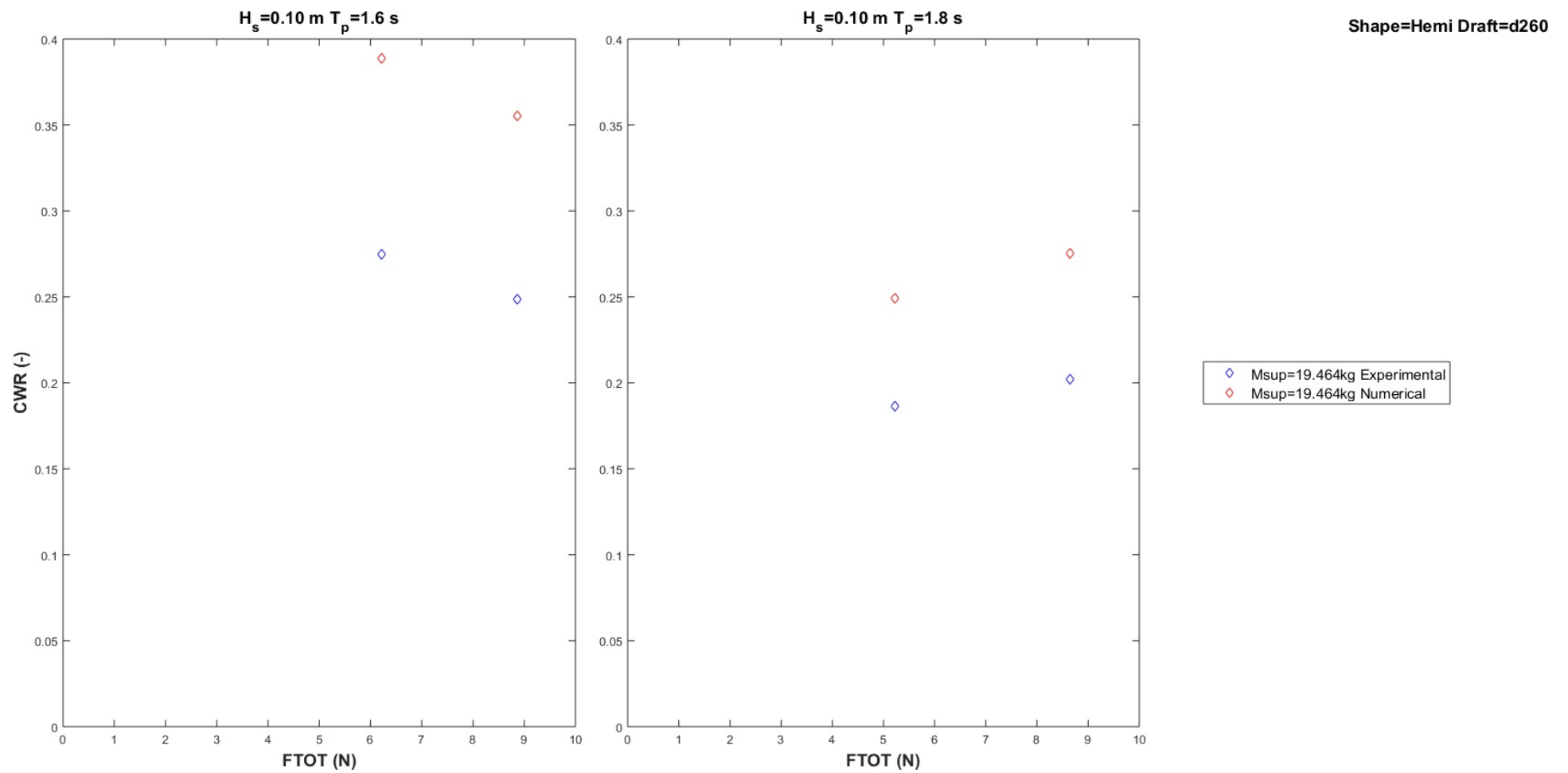
Figure C:40: Capture width ratio vs damping force for c constant sea state with varying supplementary mass. Hemisphere-cylinder, draft=260mm